The
University
Of
Sheffield.

# Access to Electronic Thesis

Author: Xiaoqing Jiang

Thesis title: Microstructure and Crystallographic Texture Evolution in Stationary Shoulder Friction Stir Welded Ti-6Al-4V

Qualification: PhD

# Microstructure and Crystallographic Texture Evolution in Stationary Shoulder Friction Stir Welded Ti-6Al-4V

# Xiaoqing Jiang

Department of Materials Science and Engineering
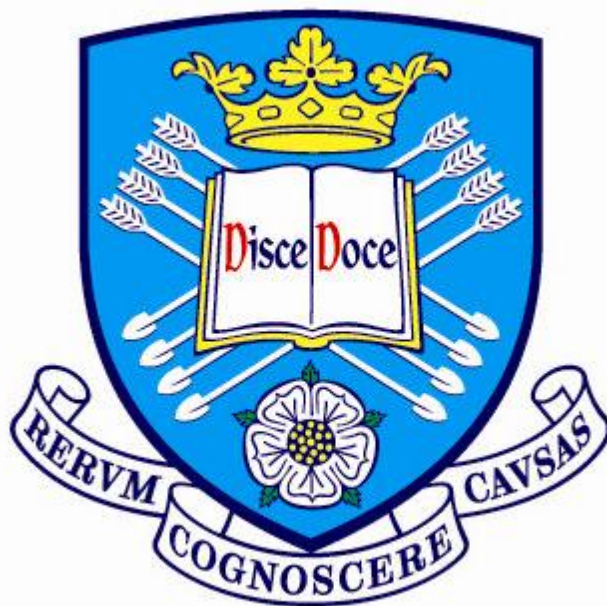
The University of Sheffield

Thesis submitted for the degree of Doctor of Philosophy

May 2012

# SUMMARY

Stationary shoulder friction stir welding with Ti-6Al-4V of 7mm thickness was undertaken by TWI Ltd and six welds with varying traverse speeds and rotation speeds were studied in terms of microhardness measurement, optical microscopy, scanning electron microscopy (SEM), and electron backscatter diffraction (EBSD). Data were processed by Sigma Plot 10.0, HKL channel 5 and quantitative metallographic analysis including linear intercept method and point counting method.

The weld zones were divided into four zones in this work, and they are the base material (BM) with equiaxed morphology, the heat affected zone (HAZ) with bimodal structure, thermo-mechanically affected zone (TMAZ) and the stir zone (SZ). Both the TMAZ and the SZ exhibit lamellar structure. Microhardness tests have been carried out on the cross sections, the normal section and the side sections for all the three welds with a constant rotation speed and on the cross sections for all the three welds with a constant traverse speed. Results showed that weld zones have slightly higher hardness than the BM; hardness at the advancing side (where tool rotation is as the same direction as the forward motion) is slightly harder than that at the retreating side (where tool rotation opposes the forward motion); an increased hardness was observed at the top surface regions of all the six welds and at the weld bottom of the two welds with 100 and 150mm/min traverse speed and microhardness distribution is most uniform in the four welds with a traverse speed of 150mm/min. Optical microscopy and scanning electron microscopy were used to investigate the cross sections on both horizontal and vertical lines revealing the microstructural evolution of the weld zones and the effect of traverse speed and rotation speed on the grain morphology of the bimodal structure and the lamellar structure, respectively.

EBSD runs were collected from the cross sections of all the six welds for texture analysis with step sizes of $2\mu m$ and $3\mu m$, and the texture analysis consists of the BM texture characterisation, the definition of TMAZ and HAZ, the representation of shear texture in the SZs, misorientation analysis of the welding edges of all the cross sections and two normal sections on the horizontal line. The BM was characterized by a classic rolling texture with equiaxed $\alpha_p$ grains showing macrozones; the HAZ and the TMAZ both have developed a texture type containing three components: TD component, 45° component and WD component, using Ari-Gur and Semiatin's notation (1998); the SZ exhibited shear texture dominated by D1 $(11\bar{2})[111]$ simple shear texture component.

## ACKNOWLEDGEMENTS

# LIST OF FIGURES

xxvii

# LIST OF TABLES

xxxi

# NOMENCLATURE

AS Advancing side

$\alpha_p$ Primary $\alpha$

BC Band contrast

BM Base material

CCD Charge-coupled device

DRV Dynamic recovery

DRX Dynamic recrystallization

EBSD Electron backscattering diffraction

EBSP Electron backscattered pattern

FEG Field emission gun

FSP Friction stir processing

FSW Friction stir welding

FSWed Friction stir welded

FSWs Friction stir welds

HAGBs High angle grain boundaries

HAZ Heat affected zone

IPF Inverse pole figure

LFW Linear friction welding

LAGBs Low angle grain boundaries

MUD Multiples of uniform density

NG Nugget zone

ODF Orientation distribution function

OIM Orientation image map

Pct Percent

PFs Pole Figures

RD, TD, ND Orthogonal axes during rolling process: RD, rolling direction, TD, transverse direction and ND, normal direction.

rpm Revolution per minute

RS Retreating side

SB Sharp boundary (between SZ and HAZ)

SD Shear direction

SEM Scanning Electron Microscopy

SFE Stacking fault energy

SPN Shear plane normal

SSFSW Stationary shoulder friction stir welding

SSFSWed Stationary shoulder friction stir welded

SSFSWs Stationary shoulder friction stir welds

Sx Thickness of the material sheared

SZ Stir zone

T Temperature

$T_\beta$ beta transus temperature

TMAZ Thermo-mechanically affected zone

WD, TD, ND Macroscopic orthogonal axes for FSW zones; WD, welding direction; TD, transverse direction; ND, normal direction

Z Atomic number

$\overset{g}{\varepsilon}$ Shear strain rate

Φ Euler angle of rotation about the X axis

φ1 First Euler angle of rotation about the Z axis

φ2 Second Euler angle of rotation about the Z axis

**Chapter 1 Introduction**

**1.1 Introduction to friction stir welding of titanium alloys**

The technology frontiers of friction stir welding (FSW) are rapidly evolving and there is great interest in extending the technology beyond aluminium to welding high performance and high melting temperature metals, for example titanium. However, a number of problems have been encountered in conventional friction stir welding of titanium alloys. In welds produced by conventional friction stir tools, most of the heat is generated at the surface/shoulder interface and a significant temperature gradient is produced through the thickness due to the low thermal conductivity of titanium, which often leads to poor weld quality and mechanical properties (Russell, 2003). To overcome this problem, TWI have developed a novel friction stir welding method called stationary shoulder friction stir welding (SSFSW) to eliminate the surface overheating problem and generate a more uniform heat distribution through the weld thickness (Russell et al., 2006, 2007). SSFSW uses a rotating probe located in a non-rotating shoulder, which slides over the surface of the material during welding. Thus, the shoulder generates little heat input during welding resulting in focussed heat generation around the probe, which improves process stability and eliminates the problem of surface overheating. Furthermore, deformation of the workpiece is dominated by the probe. In turn, TWI has been very successful in producing welds of high integrity with good mechanical properties. However, little work has been done on understanding how microstructure or crystallographic texture varies as a function of process variables such as traverse speed and rotation speed. If the process is to be successfully implemented then a detailed understanding of the microstructure and crystallographic texture is critical as most applications for this technology will be in structure critical components where most designers using titanium know that properties such as fatigue and creep resistance are very sensitive to the microstructure in the final product.

**1.2 Project aims**

This study aims to investigate how microstructure and crystallographic texture evolve as a function of traverse speed and rotation speed in Ti-6Al-4V welds produced by SSFSW. This is with the overall aim of determining the critical processing variables for producing optimum microstructure and thus best performance in-service.

## 1.3 Project objectives

In order to achieve the aforementioned aims the project has the following objectives:

1. Produce static shoulder friction stir welds for analysis at process conditions TWI believe are close to optimum for high weld integrity (rotation speed 900 rpm, traverse speed 150 mm/min) and also produce welds at potentially much lower heat inputs to investigate the possibility of sub beta transus welding.

2. Develop an understanding of how process parameters such as traverse force, downforce, torque, and rotation speed etc. influence weld integrity parameters such as process stability, porosity percentage and surface finish, and also investigate the effect of rotation speed and traverse speed on traverse force, down force and torque.

3. Detailed characterisation of the starting material in terms of microstructure and texture to ensure that any microstructure and texture observations in the weld can be directly related to the welding process or have to be interpreted as complex interactions between the starting material and the welding process.

4. Define the macroscopic location, size, shape of the weld zones as a function of process parameters.

5. Characterise the weld zones in terms of their microstructure and texture, with particular emphasis on how process parameters influence grain morphology, transformed microstructure and crystallographic texture.

6. Investigate if, like other studies on aluminium, simple shear is the major deformation mechanism by investigating crystallographic texture as a function of probe position.

7. Identify the possibility of variant selection during transformation and how this may be influenced by process parameters.


## 1.4 Thesis outline

Chapter 2 is a literature review. It introduces a general background to titanium alloys and the SSFSW technique, and describes previous work relevant to the present study including: the metallurgy of Ti-6Al-4V, the friction stir welding process, microstructure evolution during FSW of Ti-6Al-4V, and $\beta \rightarrow \alpha$ phase transformation in titanium including variant selection via texture analysis using by EBSD technique.

Chapter 3 describes the experimental procedures used in this work. It introduces the techniques to characterise the starting material and the weld zones. The experimental procedures include: sample preparation, SEM, EBSD, and descriptions of manual quantification of prior β grain size, volume fraction of primary α (αp) grain size and the thickness of the α laths measurement.

Chapter 4 describes the process of stationary shoulder friction stir welding of Ti-6Al-4V and how welding parameters affect heat input, surface quality and swept volume.

Chapter 5 concerns the work that was carried out to fully characterise the starting material used in this study and the weld zones developed during SSFSW. This chapter focused on the microstructural evolution of the SSFSW weld zones

Chapter 6 describes the crystallographic texture evolution of the SSFSW weld zones, concentrating on different texture types produced in different weld regions.

Chapter 7 summarises the effect of various welding parameters on the surface roughness, microhardness, microstructure and texture of the weld joints and suggests the optimum welding parameters.

Chapter 8 draws conclusions from this work.

Chapter 9 suggests future work to be undertaken.

**Chapter 2 Literature review**

**2.1 Titanium alloys and Ti-6Al-4V**

2.1.1 Introduction to titanium and its alloys

Since its commercial development in the 1940s, titanium and its alloys have been found to possess numerous applications in aerospace, chemical, automotive, architechture, sports and leisure medical, sports, and marine industries (Leyens and Peters, 2003). Currently titanium alloys are mainly used in the aerospace market for airframes and gas turbine engines applications such as discs and blades, rotor heads of helicopters due to weight saving, a high specific strength, an excellent corrosion resistance and a good combination of toughness, fatigue behaviour and creep resistance (Leyens and Peters, 2003; Lütjering and Williams, 2003).

2.1.2 Classification of titanium alloys

Pure titanium is an allotropic metal with melting point $1670\pm10\degree$C and two crystal structures: a high temperature body-centred cubic (bcc) crystal structure designated the beta ($\beta$) phase and a low temperature hexagonal close-packed (hcp) crystal structure designated the alpha ($\alpha$) phase. The transformation temperature called the $\beta$ transus temperature ($T_\beta$) for pure titanium is $882\pm2$ °C (Leyens and Peters, 2003 and Lütjering and Williams, 2003). Alloying elements which affect the phase fields are divided into three groups: $\alpha$ stabiliser which increases the $T_\beta$, $\beta$ stabiliser leading to the decrease of $T_\beta$ and phase neutral which have little or no influence on the $T_\beta$ (Figure 2.1(a)) (Lütjering and Williams, 2003). Strong $\alpha$ stabilising elements are the substitutional element aluminium and interstitial elements carbon, oxygen and nitrogen. $\beta$ stabilising elements are divided into two types: 1. $\beta$-isomorphous such as vanadium, molybdenum, niobium, and tantalum which exhibit complete mutual solubility with beta titanium and 2. $\beta$-eutectoid such as iron, manganese, and chromium which have restricted solubility in beta titanium and form intermetallic compounds by eutectoid decomposition of the beta phase. Phase neutral elements include zinc and tin. Furthermore, titanium alloys are classified into five groups and Figure 2.1(b) shows a schematic three dimensional phase diagram of the five groups of titanium alloys, corresponding to the $\alpha$ alloys, near $\alpha$ alloys, $\alpha+\beta$ alloys, metastable $\beta$ alloys and $\beta$ alloys (Lütjering and Williams, 2003; Leyens and Peters, 2003).
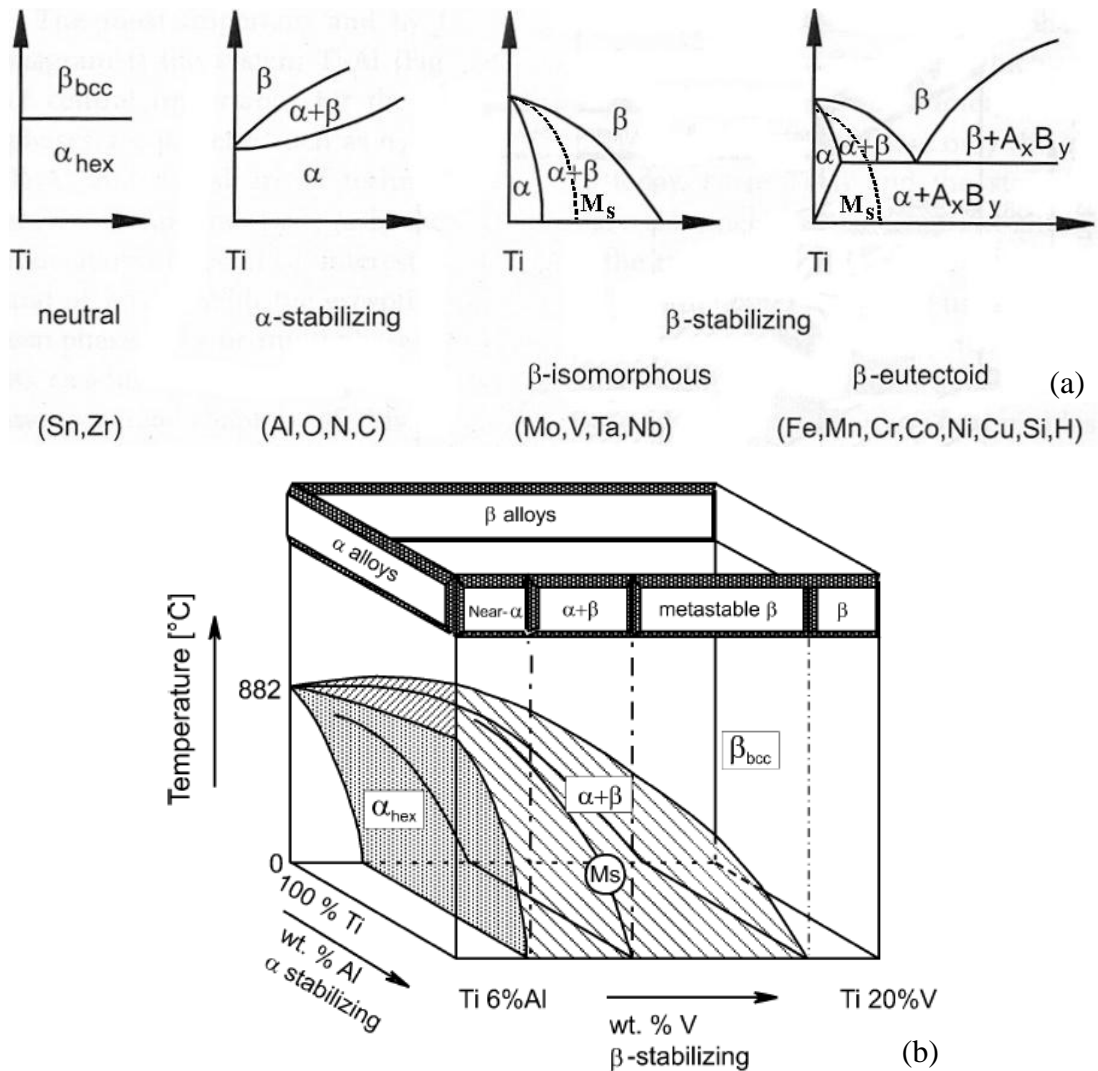
Figure 2.1 Phase diagrams classify titanium alloys: (a) Phase diagrams associated with alloying elements; (b) Three dimensional phase diagrams (Leyens and Peters, 2003)

### 2.1.2.1 α alloys and near α alloys

α alloys can be divided into two groups: α alloys and near α alloys. α alloys have 100 weight percentage (wt)% α phase with aluminium as the major alloying element and near α alloys consist of α phase and small amounts of β phase produced by the addition of 1-2wt% β stabilisers, such as molybdenum, silicon, which improves strength and workability (Joshi, 2006).

α alloys and near α alloys have excellent corrosion resistance and creep resistance in addition to medium mechanical strength, which is retained at temperature up to 600°C (Leyens and Peters, 2003). They are easily weldable, but with poor workability in the hot state (Kopeliovich, 2009). They are mainly used in process-engineering industries such as the chemical and petrochemical industries for excellent corrosion resistance and

deformability (Joshi, 2006), and they can also be used for pressures vessels, fan blades and the bleaching up sections for pulp and paper production (Lütjering and Williams, 2003). Examples of some of the major α alloys and near α alloys are shown in Table 2.1 in terms of alloy composition and $T_\beta$. Near α alloys can have exceptional temperature stability, and the best example is IMI834 (Ti-5.5Al-4Zr-4Sn-1Nb-0.6C-0.5Mo-0.35Si) which can be used up to 550°C with good fatigue and creep resistance (Joshi, 2006).

Table 2.1 Alloy composition and the $T_\beta$ for α and near-α titanium alloys (Donachie, 1988; Lütjering et al., 2010)

| Alloy type | | Alloy composition | $T_\beta$ (°C) |
|---|---|---|---|
| α -CP Ti | grade 1 | Ti–0.5Fe–0.4O–0.05N–0.08C–0.015H | 890 |
| | grade 2 | Ti–0.25Fe–0.08C–0.2O–0.03N–0.15H | 915 |
| | grade 3 | Ti–0.03Fe–0.2O–0.05N–0.08C–0.015H | 920 |
| | grade 4 | Ti–0.2Fe–0.15O–0.08C–0.015H | 950 |
| α | | Ti–5Al–2.5Sn (Ti–5–2.5) | 1040 |
| Near α | | Ti–8Al–Mo–1V (Ti–8–1–1) | 1040 |
| Near α | | Ti–6Al–5Zr–0.5Mo–0.25Si (IMI 685) | 1020 |
| Near α | | Ti–5.8Al–4Sn–4Zr–1Nb–0.5Mo–0.35Si (IMI 834) | 1040 |
| Near α | | Ti–6Al–2.75Sn–4Zr–0.4Mo–0.45Si (Ti–1100) | 1015 |
| Grade 7 | | Ti-0.2Pd | 915 |
| Grade 12 | | Ti-0.3Mo-0.8Ni | 880 |

*2.1.2.2 α+β alloys*

α+β alloys contain 4 to 6wt% β stabilisers which allow substantial amounts of β to be retained on cooling from the β phase field (Lütjering and Williams, 2003; Joshi, 2006). These alloys are mainly used for aircraft structural parts because of the excellent combination of properties such as high yield strength, high fatigue strength, high corrosion resistance, high elastic modulus and high temperature capability (Lütjering and Williams, 2003). Ti-6Al-4V is considered the most important α+β alloy used in the annealed condition or in the solution-treated and aged (STA) condition, and detailed

information on this alloy will be given in the following text. Other α+β alloys (Ti-6246, Ti-6222, Ti-17, etc.) are used in gas-turbine engines for temperature up to 400°C (Joshi, 2006). Table 2.2 shows the alloy composition and the $T_\beta$ for α+β alloys (Lütjering et al., 2010).

Table 2.2 Alloy composition and $T_\beta$ for α+β titanium alloys (Lütjering et al., 2010)

| α+β alloys | Alloy composition | $T_\beta$ (°C) |
|---|---|---|
| Ti-8-1-1 | Ti-8Al-1V-1Mo | 1040 |
| Ti-11 | Ti-6Al-2Sn-1.5Zr-1Mo-0.35Bi-0.1Si | 1015 |
| TIMETAL 1100 | Ti-5.9Al-2.6Sn-3.8Zr-0.4Mo-0.45Si | 1010 |
| IMI 679 | Ti-2.5Al-11Sn-5Zr-1Mo-0.2Si | 945 |
| IMI 685 | Ti-6Al-5Zr-0.5Mo-0.25Si | 1020 |
| IMI 829 | Ti-5.5Al-3.5Sn-3Zr-1Nb-0.25Mo-0.3Si | 1015 |
| IMI 834 | Ti-5.5Al-3.5Sn-3Zr-1Nb-0.25Mo-0.3Si-0.06C | 1045 |
| Ti-56-21-S | Ti-5Al-6Sn-2Zr-0.8Mo-0.25Si | 1005 |
| Ti-6-2-4-2 | Ti-6Al-2Sn-4Zr-2Mo-0.1Si | 995 |
| Ti-55-2-S | Ti-5Al-6Sn-2Zr-2Mo-0.25Si | 945 |
| Ti-3-2.5 | Ti-3Al-2.5V | 935 |
| Ti-6-4 | Ti-6Al-4V | 995 |
| Ti-6-6-2 | Ti-6Al-6V-2Sn | 945 |
| IMI 550 | Ti-4Al-2Sn-4Mo-0.5Si | 975 |
| Ti-55-24-S | Ti-5Al-5Sn-2Zr-4Mo-0.5Si | 975 |
| Ti-6-Q2 | Ti-6Al-2Sn-2Zr-2Mo-2Cr-0.5Si | 970 |
| Ti-6-2-4-6 | Ti-6Al-2Sn-4Zr-6Mo | 940 |
| TIMETAL 62S | Ti-6Al-2Fe-0.1Si | 1015 |
| Corona 5 | Ti-4.5Al-5Mo-1.5Cr | 935 |
| Ti-17 | Ti-5Al-2Sn-4Mo-4Cr | 890 |

*2.1.2.3 Metastable β alloys*

Metastable β alloys contain 10 to 15wt% of β stabilisers for β phase to be retained at room temperature in a metastable condition and small amounts of α-stabilising elements as strengthening element. These alloys have high strength, toughness, excellent hardenability, and forgeability over a wide range of temperatures, and they are used in aircraft structural applications (Joshi, 2006). Examples of metastable β alloys are shown in Table 2.3 in terms of alloy composition and the $T_β$ (Lütjering et al., 2010). Metastable β alloys are mainly used for the small parts in the aircraft, e.g. cargo handling fittings and landing gear of the Boeing 777 used Ti-10-2-3 (Leyens and Peters, 2003; Lütjering and Williams, 2003).

Table 2.3 Alloy composition and the $T_β$ for metastable β titanium alloys (Lütjering et al., 2010)

| Metastable β alloys | Alloy composition | $T_β$ (°C) |
|---|---|---|
| B 120 VCA | Ti-13V-11Cr-3Al | 720 |
| Beta III | Ti-11.5Mo-6Zr-4.5Sn | 760 |
| Beta C | Ti-3Al-8V-2Sn-6Cr-4Mo-4Zr | 795 |
| TIMETAL 10-2-3 | Ti-10V-2Fe-3Al | 800 |
| TIMETAL 15-3 | Ti-15V-3Cr-3Al-3Sn | 760 |
| TIMETAL 21S | Ti-15Mo-2.7Nb-3Al-0.2Si | 815 |
| TIMETAL LCB | Ti-4.5Fe-6.8Mo-1.5Al | 810 |
| Beta-CEZ | Ti-5Al-2Sn-2Cr-4Mo-4Zr-1Fe | 890 |
| SP 700 | Ti-4.5Al-3V-2Mo-2Fe | 900 |

*2.1.2.4 β alloys*

β alloys contain approximately 30% of β stabilisers like V, Mo, Nb, Ta, etc, for the β phase to be retained at room temperature (Joshi, 2006). β alloys have highest strength to weight ratios and excellent combination of strength, toughness, and fatigue resistance at large cross sections. However, these alloys have disadvantages of relatively high density,

small processing window, higher cost and difficult weldability compared to α+β alloys (Leyens and Peters, 2003).

The 'moly equivalent' (Mo Eq) is defined by equation 2.1.

$$Mo\ Eq = 1.0Mo + 0.67V + 0.44W + 0.28Nb + 0.22Ta + 1.6Cr + ...\ -1.0Al, \quad (2.1)$$

Equation 2.1 is used to indicate the β stability of an alloy (Bania, 1994) and Table 2.5 shows the major β alloys in terms of alloy composition, transus temperature, category, application and year of introduction in a descending order of their Moly Equivalency (Eylon, 1994).

Table 2.4 Composition, category, transus temperature, category, application and year of introduction of the major β titanium alloys (Eylon, 1994)

| Alloy composition | Commercial name | Category (Mo equivalent) | $T_\beta$, °C | Actual and potential applications | Year introduced |
|---|---|---|---|---|---|
| Ti35V15Cr | | Beta (47) | | Burn resistant alloy | 1990 |
| Ti40Mo | Alloy C | Beta (40) | | Corrosion resistance | 1952 |
| Ti30Mo | | Beta (30) | | Corrosion resistance | 1952 |
| Ti6V6Mo-5.7Fe-2.7Al | TIMETAL 125 | Metastable (24) | 704 | High strength aircraft fasteners | 1990 |
| Ti13V11Cr3Al | B120 VCA | Metastable (23) | 650 | Airframes. Landing gear, springs | 1952 |
| Ti1Al8V5Fe | 1-8-5 | Metastable (19) | 825 | Fasteners | 1957 |
| Ti12Mo6Zr2Fe | TMZF | Metastable (18) | 743 | Orthopedic implants | 1992 |
| Ti4.5Fe6.8Mo 1.5Al | TIMETAL LCB | Metastable (18) | 800 | Low cost, high strength alloy | 1990 |

| Ti15V3Cr1Mo5Nb3Al3Sn5Zr | VT35 | Metastable (16) | | High strength airframe castings | n.a. |
|---|---|---|---|---|---|
| Ti3Al8V6Cr4Mo4Zr | Beta-C | Metastable (16) | 795 | Oil-fields, springs, fasteners | 1969 |
| Ti15Mo | IMI205 | Metastable (16) | 727 | Corrosion resistance | 1928 |
| Ti8V8Mo2Fe3Al | 8-8-2-3 | Metastable (15) | 807 | High strength forgings | 1969 |
| Ti15Mo2.6Nb3Al0.2Si | Beta 21S | Metastable (13) | 807 | Oxidation/corrosion resist | 1989 |
| Ti15V3Cr3Sn3Al | 15-3 | Metastable (12) | 760 | Sheet, plate airframe castings | 1978 |
| Ti511.5Mo6Zr4.5Sn | Beta III | Metastable (12) | 745 | High strength | 1969 |
| Ti10V2Fe3Al | 10-2-3 | Metastable (12) | 800 | High strength forgings | 1971 |
| Ti5V5Mo1Cr1Fe5Al | VT22 | Metastable (12) | 850 | High strength forgings | n.a. |
| Ti5Al2Sn2Zr4Mo4Cr | Ti-17 | Beta-rich (5.4) | 885 | High strength, medium temperature | 1968 |
| Ti4.5Al3V2Mo2Fe | SP700 | Beta-rich (5.3) | 900 | High strength, SPF | 1989 |
| Ti5Al2Sn2Cr4Mo4Zr1Fe | Beta CEZ | Beta-rich (5.1) | 890 | High strength, medium temperature | 1990 |
| Ti3Nb13Zr | | Beta-rich (3.6) | | Orthopaedic implants | 1992 |

2.1.3 Ti-6Al-4V

Ti-6Al-4V is an α+β alloy containing 6% of aluminium and 4% of vanadium. Aluminium is added as α-phase stabiliser as a strengthen element due to the solution

strengthening effect. Vanadium stabilises ductile β phase and provides hot workability (Kopeliovich et al., 2009). Ti-6Al-4V is the most popular and most intensively developed titanium alloy for more than 50% usage in the alloys market (Leyens and Peters, 2003) and it was introduced by Timet in 1954 as the "workhorse" alloy of the industry (Timet, 2010). This alloy has moderately high tensile strength, good fatigue strength, high structural efficiency, excellent fatigue properties, highly corrosion resistance and intermediate fracture toughness. Moreover, this alloy has a good combination of strength and toughness but with generally lower strength than either Ti-662 or Ti-6246 (Chesnutt et al., 1976). It is mainly used for wing attach fitting, fan blades, non-rotating parts in aero-engines, tubular riser systems and steam turbine blades (Lütjering and Williams, 2003), air-frames, jet engine and rocket components, pressure vessels, fasteners, prosthetic implants, geothermal-well casings, automotive components and sports equipment (Timet UK Ltd). Major mechanical properties of Ti-6Al-4V are given in Table 2.5 (Thomas et al., 2007).

Table 2.5 Mechanical properties of Ti-6Al-4V (Thomas et al., 2007)

| Thermal Conductivity (W/m-K) | Thermal Expansion Coefficient (µm/m-°C) | Ultimate Tensile Strength (MPa) | Youngs Modulus (GPa) | Density (g/cm$^3$) |
|---|---|---|---|---|
| 6.7 | 9.2 | 950 | 113.8 | 4.43 |

*2.1.3.1 Microstructure of α+β titanium alloys*

The microstructure of α+β titanium alloys depends on thermal and mechanical processing sequence, morphology, volume fraction of αp phase and the prior β phase (Chesnutt et al., 1976). Donachie (2000) summarized the fully lamellar structure and bimodal structure of Ti-6Al-4V formed by air cooling and water quench from high temperature field of 1065°C and 955°C, respectively, as shown in Figure 2.2. And fully lamellar microstructure of titanium alloys is primarily determined by the cooling rates when cooled from the high temperature β phase field (Ahmed and Rack, 1998).
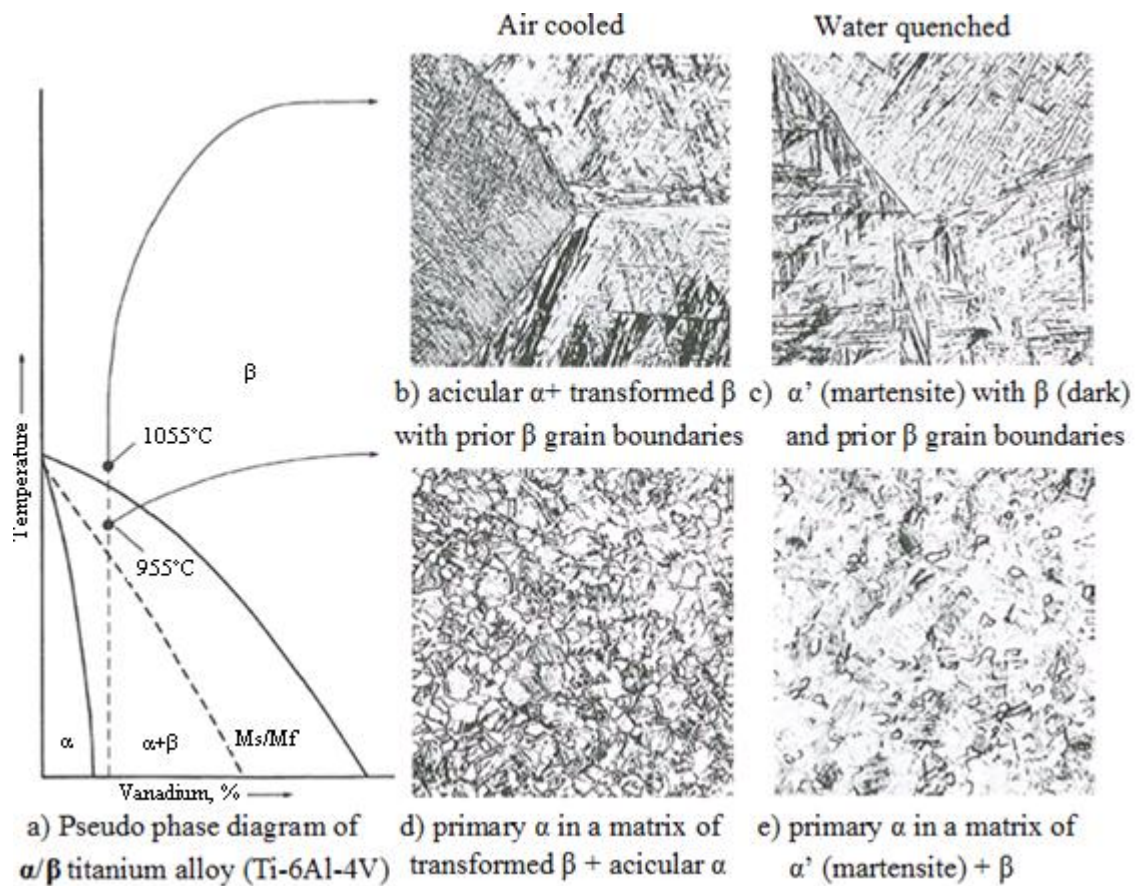
Figure 2.2 The microstructure of Ti-6Al-4V from different cooling processes adapted from Donachie (2000)

The fully lamellar structure can be classified as Basketweave structure, Widmansttättern structure and martensitic structure depending on the cooling rate from the β phase field. Lamellar structure becomes finer with increasing cooling rate (Stanford and Bate, 2004). And a detailed morphology characterisation of the fully lamellar structure under different cooling rates was investigated by Flower (1990), Wanjara and Jahazi (2005) and Joshi (2006). The α lath thickness of the Basketweave and Widmanstätten microstructure was as a function of the processing conditions. A very slow cooling rate will produce a lamellar microstructure with α lamellae in the form of packets or colonies and α laths on the prior β boundaries with retained β phase separating the intragranular α laths (Wanjara and Jahazi, 2005). At faster cooling rates, the microstructure consists of interleaved appearance Basketweave α of different orientations with grain boundary α and larger number of α colonies within each β grain; At more faster cooling rates, more α variants are nucleated and become finer, and are arranged as Widmanstätten array consisting of similarly aligned α laths within the prior β grains (Flower, 1990) due to larger driving force for transformation (Wanjara and

Jahazi, 2005). Moreover, Basketweave α microstructures are more likely to be formed in β-rich (α+β) titanium alloys at a slower cooling rate (Divinski et al., 1998). And Basketweave morphology can be changed to Widmanstätten morphology with increasing cooling rate or with decreasing alloying content (Joshi, 2006). There are two types of Widmanstätten α in Ti-Cr alloy, one is Basketweave type cooled upon the β phase field at cooling rate of 1.5°C/s and the other one is the Zig-Zag type produced at cooling rate of 15°C/s (Ahmed and Rack, 1998). An ultra-fine lamellar structure named martensitic microstructure consisting of fine long streaks of lamellae is generally resulted from quenching process (Flower, 1990; Baufeld et al., 2010) at very high cooling rates. Figure 2.3 is an example showing the structure changes from coarse lath lamellar structure (Widmanstätten structure) to martensite lamellar structure for Ti-6242 with increasing cooling rate from 1ºC/min to 8000ºC/min (Lütjering et al., 2000).
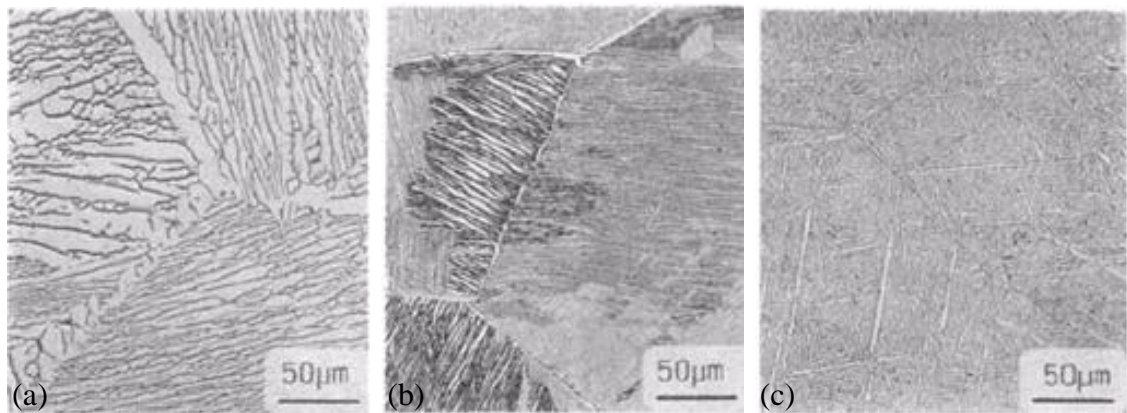


Figure 2.3 Effect of cooling rate from the β phase field on lamellar microstructures of Ti-6242: (a) coarse α laths; (b) fine α laths; (c) fully martensite structure at cooling rates of 1ºC/min, 100ºC/min and 8000ºC/min, respectively (Lütjering et al., 2000)

Microstructure after hot deformation of Ti-6Al-4V is influenced by the starting microstructure, deformation parameters (temperature, strain and strain rate). α grains become more elongated and refined with increasing strain from 0.2 to 1 (Warchomicka et al., 2010). A microstructural mechanism map for Ti-6Al4V with lamellar starting microstructure and equiaxed starting microstructure developed by Tamirisakandala et al. (2003) shown in Figure 2.6(a) and (b) was based on the experimental results indicating the influence of strain rate and temperature on the microstructure with different morphologies such as adiabatic shear banding, lamellae kinking and globularization.

13
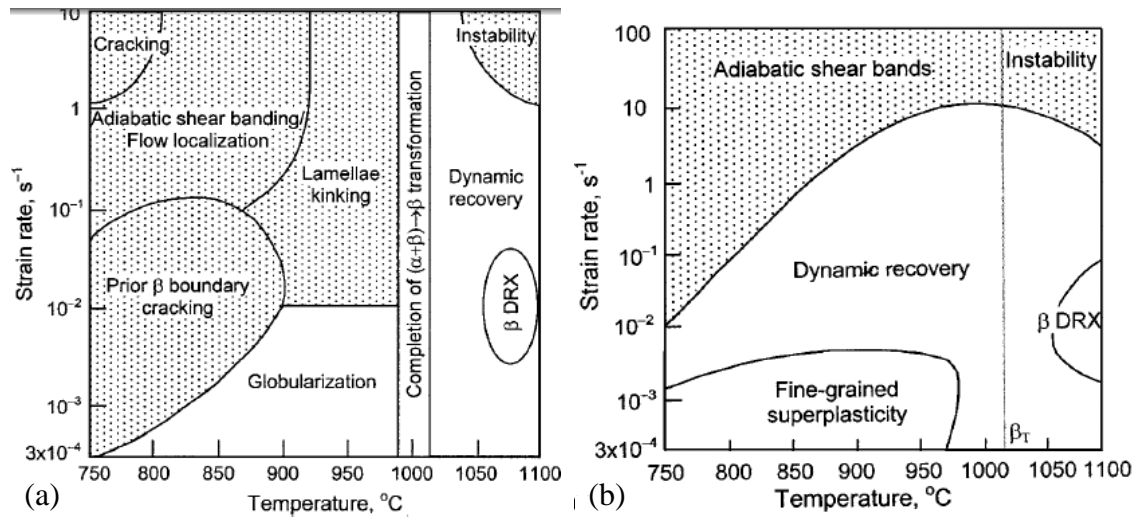
Figure 2.4 Processing map for hot working of standard grade Ti-6Al-4V with (a) a lamellar α+β starting microstructure; (b) an equiaxed starting microstructure ($\beta_T$: β transus) (Tamirisakandala et al., 2003)

Examples of the variety of microstructure morphologies depending on the strain rate range ranging $3 \times 10^{-4}$ to $10s^{-1}$ with a lamellar starting microstructure are shown in Figure 2.5 (Tamirisakandala et al., 2003).



14
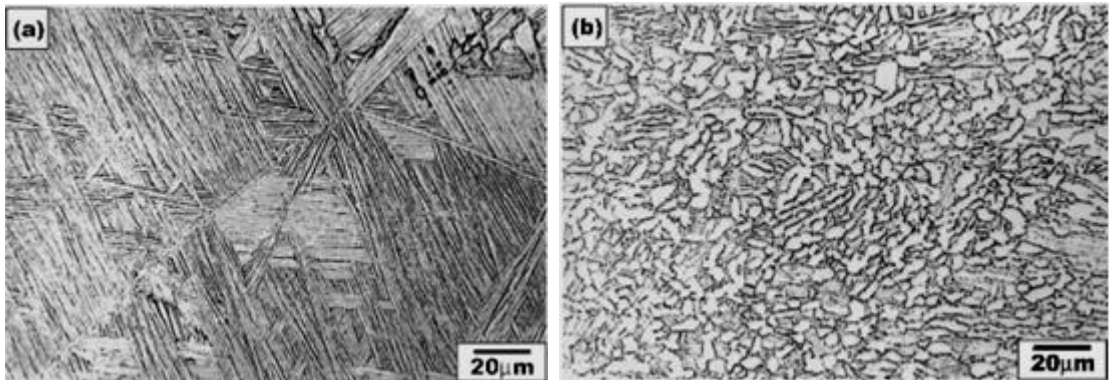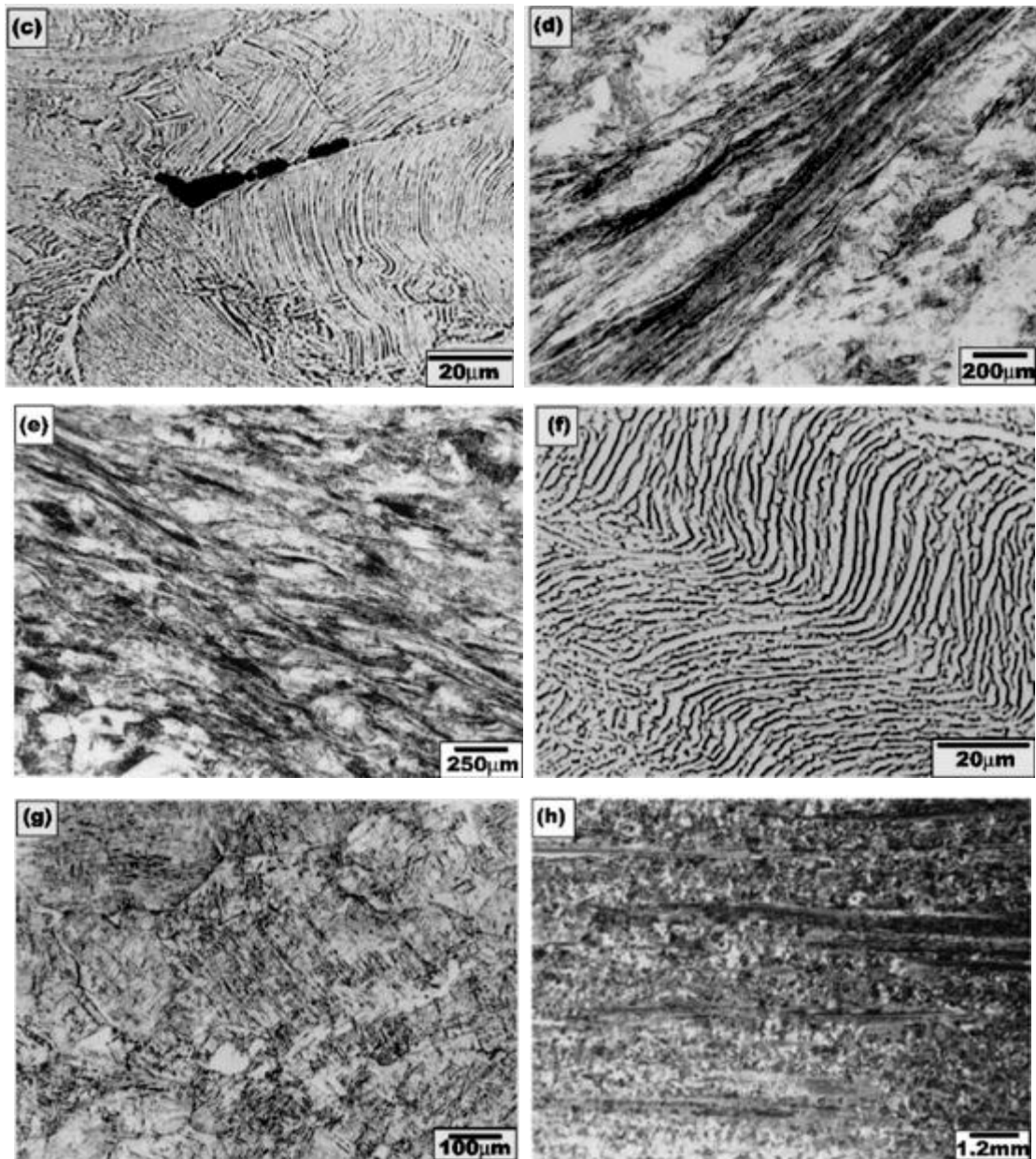
Figure 2.5 Representative micrographs of Ti-6Al-4V with strain rate range $3\times10^{-4}$ to $10s^{-1}$: (a) lamellar starting microstructure, (b) globularization, (c) prior β boundary cracking, (d) adiabatic shear banding and cracking, (e) flow localization, (f) lamellae-kinking, (g) β dynamic recrystallization, and (h) β instability (Tamirisakandala et al., 2003)

Cheng et al. (2010) have investigated the effect of strain on microstructure of laser welded Ti-6Al-4V and they found that the morphology transformed into lamella α at a strain of 43%; the prior β grains are elongated and broken at strain of 143%; at a strain of 229%, α lamellas are significantly globularized due to DRX, and lamellas are equiaxed at a strain of 397%.

15

Sub β transus forging from the higher α+β field and air cooled Ti-6Al-4V leads to bimodal structure consisting of primary α, fine secondary lamellar α and retained β within the prior β grains, as shown in Figure 2.6(a). Figure 2.6(b) shows fully equiaxed microstructure consisting of αp phase (white contrast) and retained β phase (black contrast) resulted from slowly cooling from the lower α+β field (Lütjering and Williams, 2003).
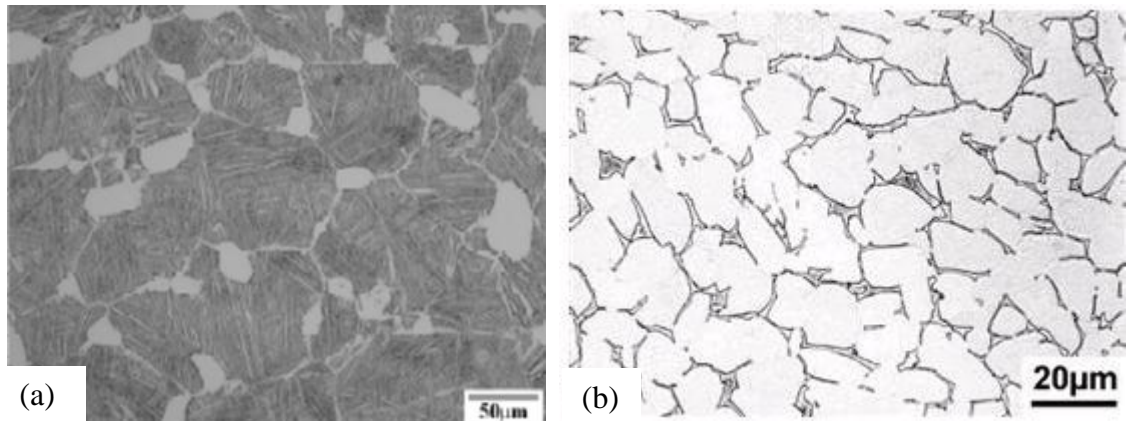


Figure 2.6 (a) Bimodal structure of Ti-6Al-4V; (b) fully equiaxed microstructure of Ti-6242 (Lütjering and Williams, 2003)

### 2.1.3.2 Microstructure and mechanical properties of Ti-6Al-4V

Many physical, chemical and mechanical properties of hexagonal metals depend on orientation, elastic modulus, Poisson's ratio, strength, ductility, toughness, magnetic permeability, the energy of magnetisation and other properties such as thermal expansivity and electrical conductivity (Hatherby and Hutchinson, 1979). The microstructure can largely affect the properties of titanium alloys and the microstructure can achieve the best properties by controlling thermomechanical treatments (Leyens and Peters, 2003). Lütjering and Williams (2003) and Gil et al. (2001) both observed that with decreasing cooling rates, tensile strength and yield stress decreases from the β phase field but ductility increases. Moreover, ductility will increase with decreasing microstructural unit size (grain size), such as the thickness of the α laths, prior β grain size, and the thickness of grain boundary α (GBα) at the β/β boundaries (Flower, 1990), however, tensile ductility is largely influenced by the prior β grain size by limiting the maximum slip length in the α laths at the β/β boundaries (Gil et al., 2001).

Microstructure unit size such as prior β grain size or colony size of the α and β lamellae and the width of the α lamellae in fully lamellar microstructures, can affect

16

fatigue properties of titanium alloys, e.g., the finer lamellae can enhance fatigue properties (Donachie, 2000). The fatigue crack propagation rates in Ti-6Al-4V depend on microstructure, as shown in Figure 2.7, a tortuous path for cracks was observed in the lenticular morphologies in both the equiaxed structure (Figure 2.9(a)) and bimodal structure (Figure 2.9(b)) (Goddard et al., 1989), however, elongated colony α or Widmanstätten α enhance fracture toughness (Flower, 1990).
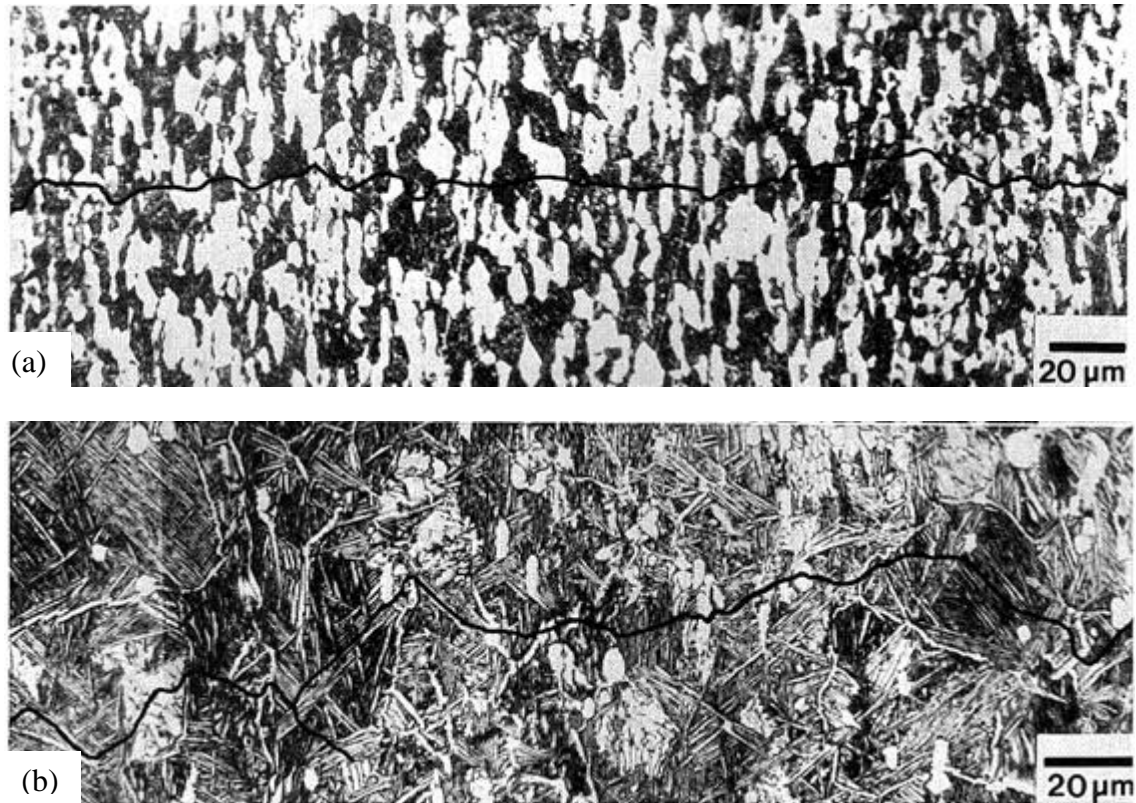


Figure 2.7 Optical micrographs of fatigue specimens of IMI 550, showing eventual path taken by propagating fatigue crack for two microstructures: (a) equiaxed α+β produced by annealing at 900°C; (b) microstructure containing small volume fraction of αp and Widmanstätten transformed β structure (Goddard et al., 1989)

The microcracks propagate faster within the intense slip bands in the coarse lamellar microstructure (Lütjering and Williams, 2003), e.g., cracks in annealed material tended to propagate at the α/β interface along Widmanstätten colony boundaries (Irving and Beevers, 1974). However, fine-scale microstructures retard crack nucleation and increase the strength and ductility, e.g. the martensitic structure have good microcrack propagation resistance (Lütjering and Williams, 2003).

The bimodal microstructure exhibits much higher ductility values compared to the fully lamellar structures (Lütjering and Williams, 2003). Equiaxed microstructures often

have high ductility and fatigue strength and can be superplastically deformed (Leyens and Peters, 2003). The mechanical properties of equiaxed microstructures of α+β titanium alloys are primarily influenced by the αp grain size and microcrack propagation rate increases with increasing αp grain size (Lütjering and Williams, 2003). Macrozones represent a cluster of αp grains with the same crystallographic orientation pointing their c axes into one unique direction, an example of macrozone is shown in Figure 2.8 for Timetal-834 (Thomas, 2007). Macrozones can act as a large effective grain leading to poor fatigue crack initiation performance (Lütjering and Williams, 2003).
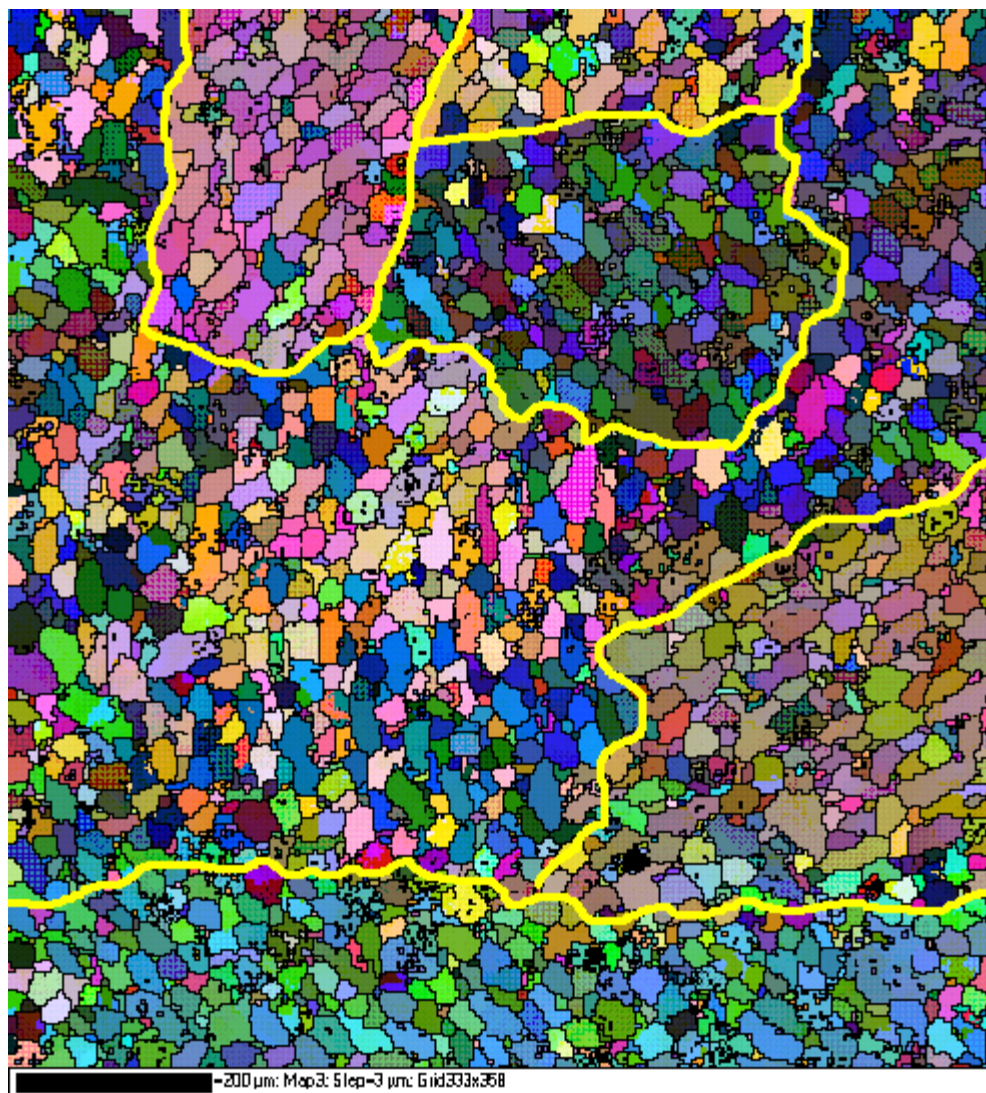


Figure 2.8 Example of macrozones indicated as enclosed yellow curves in an Euler colouring map of Timetal 834 with bimodal structure at room temperature (Thomas, 2005)

Wagoner et al. (2003) had made comparison between equiaxed microstructure and Widmanstätten microstructure using the same starting material and they found that the mechanical response of these two microstructures are similar at small strains; Most α grains in the undeformed equiaxed microstructure had a low dislocation density. However, the α phase in Widmanstätten structure has higher dislocation density.

## 2.2 Phase transformation in titanium alloys

### 2.2.1 Crystallographic structure

The atomic unit cells of the hexagonal close packed (hcp) α phase titanium in the low temperature field and the body-centred cubic (bcc) β phase titanium in the high temperature field are schematically shown in Figure 2.9 (Leyens and Peters, 2003).
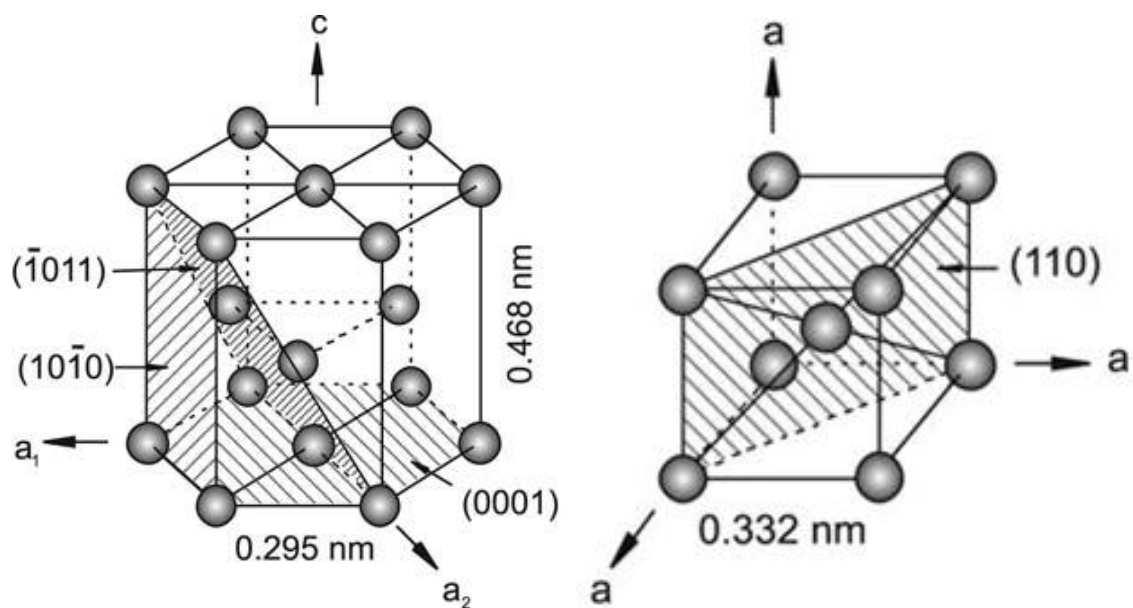


Figure 2.9 Atomic unit cells of room temperature hcp α and bcc β phase in high temperature field (Leyens and Peters, 2003)

Figure 2.10 is a schematic diagram showing phase transformations and texture in terms of volume faction of α and β phase of an α+β alloy at room temperature (20ºC), heated to high temperature α+β phase field at 928ºC and then cooled down to 20ºC, respectively (Bowen et al., 1991).
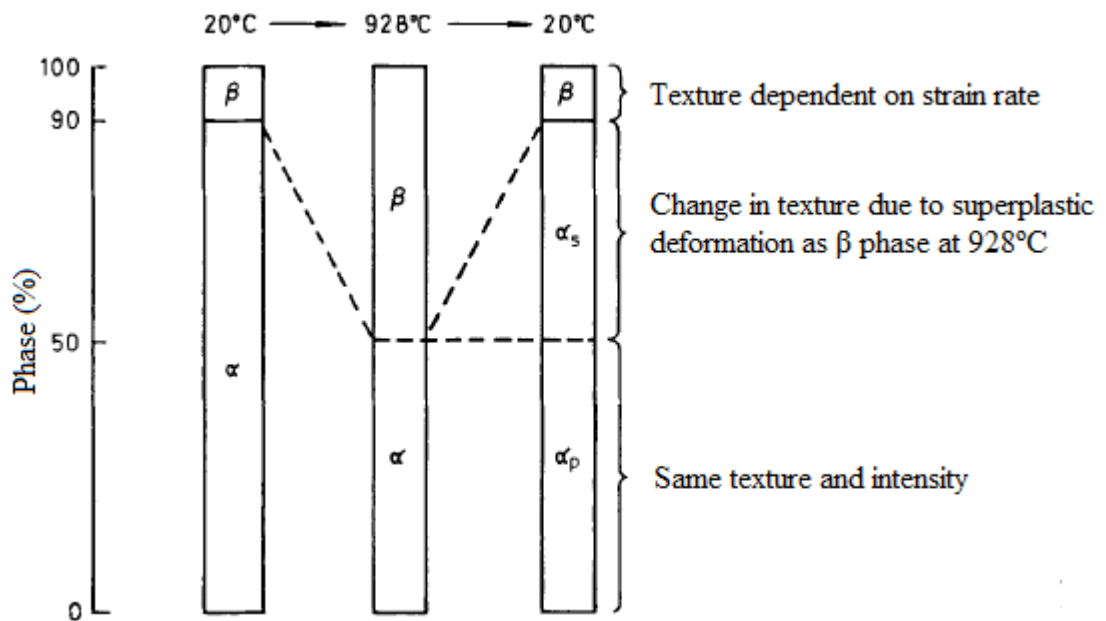
Figure 2.10 Schematic diagram showing phase transformations and texture of an α+β alloy (Bowen et al., 1991)

The β to α transformation is to follow the Burgers orientation relationship, see relationship 2.2 (Leyens and Peters, 2003), one example of the burgers orientation relationship is shown in Figure 2.11.

$$\{1\bar{1}0\}_\beta \| \{0001\}_\alpha$$
$$<111>_\beta \| <11\bar{2}0>_\alpha \tag{2.2}$$
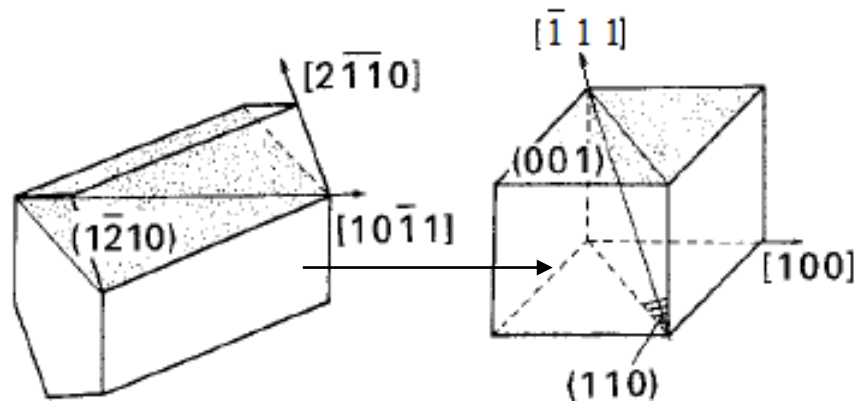


Figure 2.11 Illustration of the Burgers relationship (Zhu et al., 2003)

Burgers relationship is a useful tool to study texture in titanium and its alloys and it can be applied to phase separation of secondary α and αp in α+β alloys, variant selection

and reconstructed high temperature β phase from the orientation data of low temperature inherited α phase, etc.

## 2.2.2 Crystallographic indices

### 2.2.2.1 Miller indices

Lattice directions of planes are defined as the reciprocals of intercepts on the crystallographic axes of planes and are usually represented by miller indices in cubic systems. The miller indices of a plane are (hkl) and the intercepts with the axes are $1/h$, $1/k$, $1/l$. The miller indices (hkl) denote the smallest integer reduced by multiplying the reciprocal axis intercepts. The miller indices of a direction are (uvw) (Cullity, 1978). A list of the most commonly used texture notation is given below:

(hkl) describes the direction of a plane

{hkl} refers to family of planes

(uvw) is a direction

<uvw> describes family of directions

Miller notation (three axis notation) can be used both for bcc and hcp systems. If the direction <uvw> lies in the plane {hkl}, then: $hu+kv+lw=0$ (Weiss zone law-true in all crystal systems). In cubic system, <uvw> direction in Miller notation is perpendicular to {uvw} plane of the same indices, whereas, in hexagonal system, <uvw> direction is not perpendicular to {uvw} plane. For example, the $\{01\bar{1}0\}$ plane is perpendicular to direction $<\bar{1}100>$ in hcp systems (not <010> as in cubic system) which use Miller-Bravais system (Cullity, 1978; Kelly et al., 2000).

### 2.2.2.2 Miller-Bravais indices

A slightly different system of plane indexing is used in the hexagonal system. The unit cell of a hexagonal lattice is defined as two equal and coplanar vectors a1 and a2, at 120º to one another, and a third axis c at 90º (Cullity, 1978). In the hexagonal frame, lattice directions of planes can still be described by their reciprocal intercepts with respect to all four axes leading to the 'Miller-Bravais' indices (hkil) where

$$h + k + i = 0 \tag{2.3}$$

Thus the family of {100} planes which in the Miller system are (100), (010) and (1$\bar{1}$0) become (10$\bar{1}$0), (01$\bar{1}$0), and (1$\bar{1}$00) in the Miller-Bravais system. Thus one can see the advantage of the Miller-Bravais system that the same combination of integers describes the family of planes.

The four-axis indices [uvtw] of hexagonal system can be deduced from the three axes indices [UVW] in cubic system. The axis indices in the two systems are related in equation 2.4 (Cullity, 1978):

$$
\begin{aligned}
& u = (2U - V)/3 \\
U = u - t \quad & v = (2V - U)/3 \\
V = v - t \quad & t = -(u + v) = -(U + V)/3 \\
W = w \quad & w = W
\end{aligned}
\tag{2.4}
$$

Thus, [210] becomes [10$\bar{1}$0] and [100] becomes [2$\bar{1}$$\bar{1}$0], etc.

2.2.2 Displacive transformation and diffusional transformation

Phase transformation modes have been classified as diffusional and displacive transformations based on transformation mechanisms. Displacive transformations are athermal, while diffusional or reconstructive transformations are thermally activated. In diffusional (or reconstructive) transformations, the bonds between the near neighbour atoms are broken first and they are then reconstructed to form the product phase structure by random diffusional jumps. In contrast, atom movements in a displacive transformation is a cooperative movements of large numbers of atoms in a diffusionless process, which can be resulted from homogeneous distortion, shuffling of lattice planes, stationary displacement waves or a combination of these. Compared to thermally activated diffusional transformations, the displacive transformations do not require thermal activation, e.g. athermal martensitic transformation can occur by quenching (Banerjee and Mukhoparhyay, 2007).

Diffusional transformation result from slower cooling rate, i.e <20°C/s, which leads to the formation of massive α and diffusion controlled α in terms of various morphological forms (Majdic and Ziegler, 1973). Ahmed and Rack (1998) have examined the lamellar structure cooled from the β phase field at different cooling rates, as shown in Figure

2.12, where martensitic α', massive α (α$_m$) and diffusion controlled α were formed at cooling rate of 410°C/s-525°C/s, 410°C/s-20°C/s, 20-1.5°C/s, respectively.
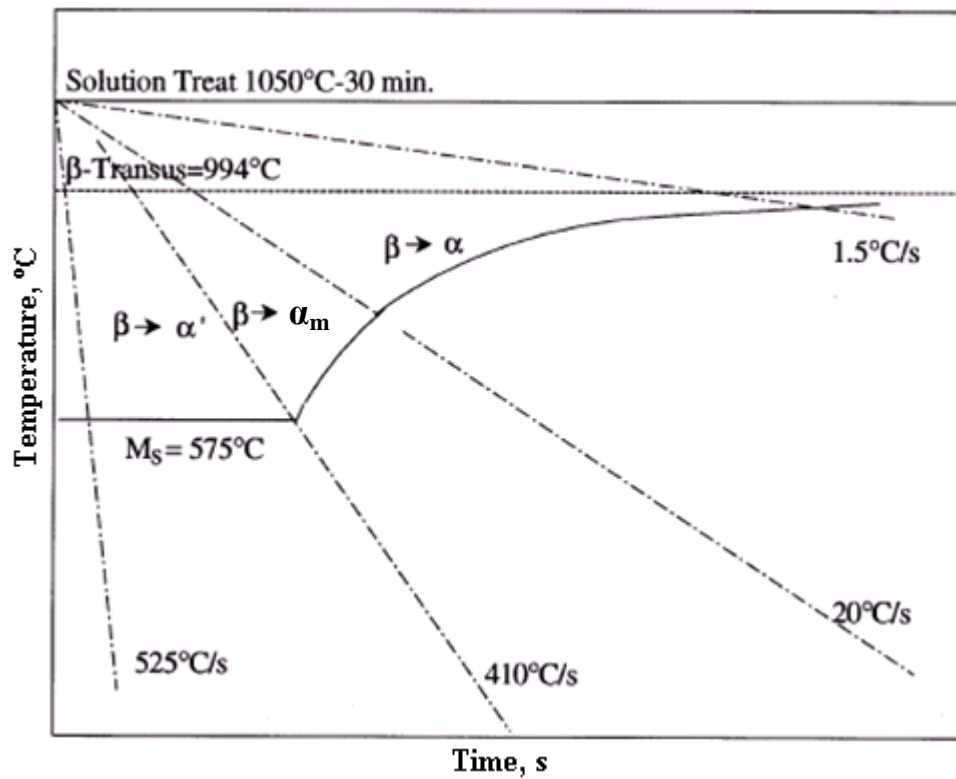


Figure 2.12 Schematic continuous cooling transformation diagram for Ti-6Al-4V under β solution treatment at 1050°C for 30 min (*M*s temperature: Majdic and Ziegler, 1973). (Ahmed and Rack, 1998)

Thus, cooling rates in excess of 410°C/s are required for Ti-6Al-4V to attain a completely martensitic microstructure (Majdic and Ziegler, 1973; Ahmed and Rack, 1998). For example, the martensitic microstructure transformed at quench rate ~500°C/s at the temperatures of 700-1000°C in Ti-6Al-4V (Stanford and Bate, 2005). It should be noted in Figure 2.12 that at the M$_s$ temperature, the driving force for martensitic transformation depends on the shear modulus of the alloy at the transformation temperature (Banerjee and Mukhoparhyay, 2007). Martensitic transformation is a typical kind of displacive transformations because martensite has fine plates with no retained β phase (Stanford and Bate, 2005; Banerjee and Mukhoparhyay, 2007). The pure titanium undergoes a martensitic transformation at temperature around 870°C (Jourdan et al., 1991).

Athermal martensite phase can be divided into hexagonal martensite α' and orthorhombic martensite α" depending on the alloy composition (Banerjee and

Mukhoparhyay, 2007). The most prevalent type is hexagonal martensite α' in massive or acicular morphology e.g. in high purity Ti and very dilute alloys and in alloys with a high martensitic transformation temperature (Lütjering et al., 1998; Lutjering and Williams, 2003). The massive martensite α' is composed of large packets of small parallel α laths of about 0.5-1μm thickness belonging to the same variant of the Burgers relation in irregular regions (size about 50-100μm). The acicular martensite α' contain individual α plates corresponding to variants of the Burgers relation (Lutjering and Williams, 2003). Ahmed and Rack (1998) found that a single hexagonal α' plate contains a combination of orthogonal orientated α' plates, dislocations, stacking faults and twin substructure. While the orthorhombic martensite α" crystal structure is a distorted hexagonal structure in titanium alloys with higher β stabilising element such as Mo, Nb, Ta, W, Re and in titanium alloys with Al and V (Lütjering et al., 1998) e.g. in a Ti-8.5Mo-0.5Si alloy with Mo and Si (Lütjering et al., 2000; Williams, 1973).

Morphological forms of diffusion controlled α are often characterized by Widmansttättern α, Basketweave α and grain boundary α (GBα). Van Bohemen et al. (2008) pointed out that the degree of α lath nucleation at the β/β boundaries can be classified into the following four types in diffusional deformation of titanium alloys: i. None of α plates at the β/β boundaries. ii. Considerable amount of α plates at one side of the β/β boundaries, none at the other side. iii. Few α plates at both sides of the β/β boundaries. iv. Many α plates at both sides of the β/β boundaries.

### 2.2.3 Variant selection in phase transformation

*2.2.3.1 Definition*

Twelve inherited α variants can be present within a single prior β grain after β to α transformation from high temperature β phase field of titanium alloys according to Burgers relationship. If all the 12 variants are equally selected, a smooth texture will be generated at room temperature, however, all variants do not often occur with the same probability due to the material transformation conditions. This phenomenon is called variant selection (Gey and Humbert, 2003). Thus, if no variant selection occurs, crystal planes and directions of the equivalent inherited 12 variants marked as V1-V12 are shown in Table 2.6 (Zhu et al., 1995).

Table 2.6 The 12 inherited variants during β-α phase transformation in titanium (Zhu et al., 1995)

| Variant number | Correspondence planes | Correspondence directions |
|:---:|:---:|:---:|
| V1 | $(011)_\beta \| (0001)_\alpha$ | $[\bar{1}\bar{1}1]_\beta \| [2\bar{1}\bar{1}0]_\alpha$ |
| V2 | | $[1\bar{1}1]_\beta \| [2\bar{1}\bar{1}0]_\alpha$ |
| V3 | $(\bar{1}01)_\beta \| (0001)_\alpha$ | $[1\bar{1}1]_\beta \| [2\bar{1}\bar{1}0]_\alpha$ |
| V4 | | $[111]_\beta \| [2\bar{1}\bar{1}0]_\alpha$ |
| V5 | $(0\bar{1}1)_\beta \| (0001)_\alpha$ | $[111]_\beta \| [2\bar{1}\bar{1}0]_\alpha$ |
| V6 | | $[\bar{1}11]_\beta \| [2\bar{1}\bar{1}0]_\alpha$ |
| V7 | $(101)_\beta \| (0001)_\alpha$ | $[\bar{1}11]_\beta \| [2\bar{1}\bar{1}0]_\alpha$ |
| V8 | | $[\bar{1}\bar{1}1]_\beta \| [2\bar{1}\bar{1}0]_\alpha$ |
| V9 | $(\bar{1}10)_\beta \| (0001)_\alpha$ | $[\bar{1}\bar{1}1]_\beta \| [2\bar{1}\bar{1}0]_\alpha$ |
| V10 | | $[111]_\beta \| [2\bar{1}\bar{1}0]_\alpha$ |
| V11 | $(110)_\beta \| (0001)_\alpha$ | $[1\bar{1}1]_\beta \| [2\bar{1}\bar{1}0]_\alpha$ |
| V12 | | $[\bar{1}11]_\beta \| [2\bar{1}\bar{1}0]_\alpha$ |

Any two of the 12 variants in Table 2.5 would give 144 possible combinations of misorientation between α and α variants (Wang et al., 2003). Gey and Humbert (2003) reported that the α variants inherited from the same β grain are characterized by specific misorientation angles of 10°, 60°-63°, 90° according to the Burgers orientation relation, as indicated in Table 2.6 with the corresponding axes. In the case of no variant selection, expected ratio for occurrence of the five misorientations of 10°529, 60°, 60°832, 63°262 and 90° is 1:2:3:2:2 (Wang et al., 2003). Two adjacent pixels of the α will form the same α colony if their relative misorientation angle is lower than a small value (e.g. 3°), and they belong to adjacent α colonies inherited from the same grain if their relative misorientation matches one of those angles shown in Table 2.7 (Gey and Humbert, 2003). Glavicic et al (2003a and b; 2004) developed a Monte-Carlo technique to determine the parent β orientations and find the inherited variants. Glavicic (Glavicic et al., 2003a and b) also developed a method to judge the likelihood of the adjacent variants belonging to the same parent β grain.

Table 2.7 Specific misorientations between variants inherited from the same parent β grain (Gey and Humbert, 2002; Wang et al., 2003)

| $\omega$ (angle) | $\overset{1}{n}$ (axis) |
| --- | --- |
| 0 | Identity |
| 10°529 | $(0001)$ |
| 60° | $(11\bar{2}0)$ |
| 60°832 | $(\overline{1.377}, \bar{1}, 2.377, 0.359)$ |
| 63°262 | $(\overline{10}, 5, 5, \bar{3})$ |
| 90° | $(1, \overline{2.38}, 1.38, 0)$ |

Textures can be formed during phase transformations either with or without variant selection, depending on heat treatment (Divinski et al., 1998). The study and the understanding of the texture changes and the variant selection mechanisms are keys to improve and optimise the properties of the products.

### 2.2.3.2 Mechanism of variant selection

Variant selections were observed when the β phase was strongly deformed in the β phase field (Zhu et al., 1995) and variant selection could not occur in cases with classical treatment in the β phase field (Gey and Humbert, 2002). For example, no variant selection occurred when the starting α phase was cold deformed (Moustahfid et al., 1997).

From a microscopic standpoint, variant selection may also be associated with the transformed α laths growing from the prior β grain in titanium alloys when α colonies precipitate from GBα at cooling rate less than 37ºC/s (Davies, 2009) and at low vanadium contents (<5%) in titanium alloys during slow diffusional transformations (Banerjee et al., 2004; Karthikeyan et al., 2008). It has been reported that in diffusional transformations with slower cooling rate, variant selection is a result of preferential nucleation of common variants growing into the β grains on either side of the β grain boundaries sharing common {0001} poles in the common {110} direction and the

common α variants grow and dominate the texture of the transformed β microstructure (Bhattacharyya et al., 2003 on Ti–6Al–2Sn–4Zr–6Mo; Stanford and Bate, 2004 on Ti-6Al-4V; Bhattacharyya et al., 2007; van Bohemen et al., 2008; Davies et al., 2011 on Ti-6Al-4V). Karthikeyan et al. (2008) pointed out the α-variants selected by GBα become the dominant variants for Ti-5Ta-1.8Nb. Daymond et al. (2010) have investigated the phase transformation of Zirconium alloy Zr–2.5Nb, and variant selection is also associated with α variants formed at β grain boundaries sharing common {0001} poles in the common {110} direction. Furthermore, the two adjacent β grains have common {110} poles at about 70% of the β grain boundaries. However, Seward et al. (2004) found that variant selection is due to preferential nucleation and/or growth of the GBα for pure titanium. Bhattacharyya et al. (2007) reported that the α colonies having common {0001} planes at the β grain boundaries will result in softer regions leading to crack nucleation and crack growth and reduce this possibility will increase resistance to high cycle fatigue crack growth propagation.

In a macroscopic scale, variant selection can be influenced by the applied stress, temperature, temperature gradient, thermal stress, texture, microstructure, cooling rate, β-phase chemical composition and stress distribution, etc. (Moustahfid et al., 1997; Divinski et al., 1998; Gey and Humbert, 2002; Zeng and Bieler, 2005; Humbert et al., 2005; Humbert et al., 2006, Daymond et al., 2010, Davies et al., 2011; Pilchak et al., 2011). Variant selection was due to deformation imposed on the material and severe deformation of the material in the β phase field (Gey and Humbert, 2002) and significant variant selection occurs upon martensitic transformation of Ti-6Al-4V by the elastic interaction (Stanford and Bate, 2004). Moustahfid et al. (1997) reported that favoured variants are linked to the slip systems {110}<111> and {112}<111> which caused the plastic deformation at the β phase field. Gey and Humbert (2002) observed few variants are close to the $\{10\bar{1}3\}/\{10\bar{1}3\} < 11\bar{2}0 >$ texture components in the Ti-40 sample cold rolled with 60% reduction. Zeng and Bieler (2005) have observed a strong variant selection in water quenched Ti-6Al-4V wires due to internal stresses between different α orientations. Humbert et al. (2006) suggested that variant selection is based on the minimum elastic strain energy. Daymond et al. (2010) found that variant selection was driven by the interaction between thermal stresses produced in the α-phase, the phase transformation strain and high levels of internal stress produced by cold work of Zr–2.5Nb alloy. Davies et al. (2011) pointed out that variant selection in titanium FSWs may be due to thermal stresses in the weld which leads to preferential

growth of certain variants or may be caused by the workpiece axes. Pilchak et al. (2011) found that variant selection is caused by the anisotropy in strains generated during the bcc to hcp phase transformation or due to dislocation activity on {110} planes in the β phase.

Variant selection in pure titanium and Ti-6Al-4V has been reported to be related with cooling rate using different welding methods by Leary et al. (2010) who proposed that variant selection was due to the growth of heterogeneously nucleated α variants within each prior β grain at lower cooling rates in conventional gas tungsten arc welding (GTAW); Variant selection may be related to the favorability of 60º boundaries at intermediate cooling rates such as InterPulse welding; at high cooling rates in laser or electron beam welding, the variant selection may be caused by homogeneous nucleation of certain variants and self-accommodation of stresses (Wang et al., 2003).

## 2.3 Restoration and deformation modes in titanium alloys

2.3.1 Restoration of titanium alloys

### 2.3.1.1 Grains and grain boundaries

Grains are defined as individual crystals to comprise the materials in polycrystalline metals. Grain boundaries are the interfaces between individual grains. The properties of grain boundaries depend on the misorientation between the adjacent grains (Humphreys, 2004).

Grain boundaries can be divided into three groups depending on the misorientation between the two adjacent grains, as shown in Figure 2.13. Low angle grain boundaries (LAGBs) consist of arrays of individual dislocations with misorientation less than 10º-15º, e.g., a symmetrical tilt boundary (Figure 2.13(a)); High angle grain boundaries (HAGBs) have larger misorientations more than 15º which are not from dislocations. There are certain HAGBs having high symmetry where many of the atom sites are common to both grains, called 'coincidence site boundaries' (CSL boundaries), example of which is the twin boundary (Σ3) (Humphreys, 2004; Humphreys, 2008).
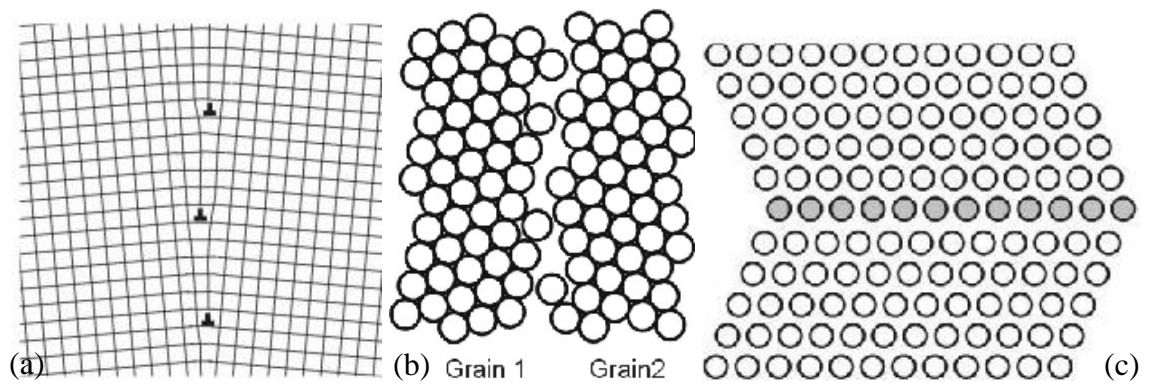
Figure 2.13 Three kinds of grain boundaries (GBs): (a) LAGBs; (b) HAGBs; (c) CSL (Σ3) boundaries (Humphreys, 2004; Humphreys, 2008)

HAGBs developed in materials deformed from medium to high strains can determine the flow stress, texture, recrystallization behaviour and the formability. And the mechanisms of the formation of HAGBs can be classified into microstructural mechanism and textural mechanism depending on the grain orientation, strain and deformation mode. Microstructural mechanism involves grain subdivision of the long boundaries such as dense dislocation walls and microbands and it can produce HAGBs with misorientations of 15°-30°, where misorientations increase steadily with increasing strain. The texture mechanism is associated with the different preferred textures of subdivided grains during deformation. In this case, texture components and misorientation relationship may lead to HAGBs ranging 20°-60° (Hughes and Hansen, 1997). In some circumstances, LAGBs can be moved to HAGBs and the movement of grain boundaries are driven by material flow or due to the local dislocation density differences (Gourdet and Montheillet, 2002).

### 2.3.1.2 Recovery and recrystallization

Recovery and recrystallization are competing processes and both are driven by the stored energy of the deformed state and the stored energy came from dislocation movements. Recovery is primarily due to changes in the dislocation structure and often measured by changes in the yield stress or hardness of the material (Humphreys, 2004). The dislocation density and the driving force of recovery increase with increasing strain (Sellars, 1978). At low strains, recovery is the dominant process, but at high strains, the dislocation density becomes high and provides a driving force for recrystallization (Sellars and Tegart, 1972). Recrystallization always leads to texture change during deformation process (Moustahfid et al., 1997), however, recrystallization may not affect

texture when a large volume fraction of second-phase particles are present (Wang and Huang, 2003).

Suitably high temperature following hot deformation is the dominant criterion for stationary recovery and stationary recrystallisation (Gourdet and Montheillet, 2002), such as subsequently annealing of a hot deformed material (Humphreys 2004), while a critical strain and high temperature are required for dynamic recrystallisation (DRX) which is characterised by concurrent generation and annihilation of dislocations (Arthur et al., 2007).

Dynamic recovery is rapid and extensive at high temperatures and is usually the only form of dynamic restoration mechanism for metals with high stacking fault energy (SFE) caused by a stacking fault, such as aluminium and its alloys, a-iron and ferritic steels and titanium alloys due to easily occurred dislocation climb and cross slip (Jonas et al., 1969; Humphreys, 2004). Dynamic recovery occurs at moderately high strain rates for Ti-6Al-4V (Tamirisakandala et al., 2003). For example, dynamic recovery has been reported to take place in compression, torsion and traction of Ti-6Al-4V (Takahashi et al., 1993) and beta CEZ alloys (Combres and Champin, 1992; Chaze and Montheillet, 1994). For $\alpha+\beta$ titanium alloys, DRX is the dominant deformation mode and occurs in the $\beta$ phase field region at lower strain rates and DRX increases with increasing deformation temperature (Banerjee and Mukhoparhyay, 2007; Tamirisakandala et al., 2003). DRX was observed in the fully lamellar structure in Ti-6Al-4V for strains above 0.3 (Warchomicka et al., 2010).

For most metallic materials, driving force for phase transformation is much higher than that for DRX, thus phase transformation is harder to occur compared to DRX during hot working process, but in practice only a small level of DRX was involved, even at 1050°C (Ding et al., 2002). DRX behaviour has been reported to change with grain size, strain rate, strain and alloying elements. DRX increased with decreasing initial grain size and increasing strain rate in fully lamellar structure of Ti-6Al-4V (Warchomicka et al., 2010) and also the degree of DRX increased with temperature (Ding et al., 2002). The DRX process was dominant in equiaxed morphology (Weiss and Semiatin, 1999). Banerjee and Mukhoparhyay (2007) have investigated the recrystallization behaviour of different alloyed titanium alloys and they found that the strain rate and temperature of the DRX domain both increased with increasing the alloying of oxygen content.

DRX is generally divided into discontinuous dynamic recrystallization (DDRX) and continuous dynamic recrystallization (CDRX). DDRX has clear nucleation and growth stages of new grains during deformation, such as subsequent annealing for the larger initial grain size and lower strains, but CDRX occurs at larger strains and smaller grain sizes and HAGBs may evolve. CDRX occurs in metals where recovery processes are slow, such as those with a low or medium SFE (copper, nickel and austenitic iron) (Humphreys, 2004). Moreover, in CDRX, the misorientation changes in terms of strain and nucleation sites for recrystallization were difficult to observe (Warchomicka et al., 2010). And DDRX can be transformed to CDRX by altering strains and grain sizes and increasing rolling reduction (Humphreys, 2004). High SFE metals undergo CDRX rather than DDRX. CDRX occurs in high SFE metals due to the movement of LAGBs into HAGBs by dynamic recovery at the strain exceeds 0.9 (Gourdet and Montheillet 2000; Gourdet and Montheillet, 2003; Ma et al., 2008). Moreover, CDRX leads to considerable grain refinement during hot deformation of high SFE alloys (Gourdet and Montheillet, 2003).

Dynamic recovery or DRX can occur in thermomechanical processing of Ti-6Al-4V near or above the β transus with varying strain and strain rate (Tamirisakandala et al., 2003). A strain rate of $1s^{-1}$ and a deformation strain of 0.7 gives 30 percent (pct) DRX at 1050°C (Ding et al. 2002; Ding and Guo, 2004), DRX occurs in the strain rate range $10^{-3}$-$10^{-1}s^{-1}$ at about 1100°C in Ti–6Al–4V (Seshacharyulu et al., 2002). DRX occurred with the strain and strain rate exceeding 0.7 and $0.5s^{-1}$ at 1050°C during linear friction welding (LFW) of Ti-6Al-4V, respectively (Wanjara and Jahazi, 2005).

Recrystallisation behaviour has been investigated for the welding of titanium alloy recently (Ma et al., 2008; Warchomicka et al., 2010; Cheng et al., 2010; Lang et al., 2010). Ma et al. (2008) have investigated friction stir processing (FSP) of Ti-6Al-4V and they reported that the TMAZ contains equiaxed α grains due to DRX. However, subgrains of the kinked lamellae of the SZ were formed by networks of LAGBs (<10°). CDRX occurred in the bimodal structure of Ti-6Al-4V due to newly formed subgrains within the elongated αp grains as strain increased (Warchomicka et al., 2010). And significantly globularization of α lamellar resulted in DRX during superplastic deformation of laser welded Ti–6Al–4V at a strain of 229% (Cheng et al., 2010). Except for recrystallization of the α phase, the β phase has undergone DRX in LFW of TC11 titanium alloys at high strain and strain rate (Lang et al., 2010).

### 2.3.2 Deformation modes

Slip and twinning are the two fundamental deformation modes in plastically deformed metals and alloys (Mahajan and Williams, 1973). The value of the SFE is the key parameter to determine which mode occurs in materials (Humphreys, 2004). SFE is lower in twinning than in slip and critical resolved shear stress (CRSS) for twinning is higher than that for slip (Blicharski et al., 1979). The presence of slip systems is controlled by the SFE, temperature (Hughes et al., 2000) and strain. At low strains (≤0.4), α-titanium deforms by both slip and twinning and the size of deformation twins decreases with increasing strain, whilst, slip is the only deformation mode in α-titanium at strains above 0.4 (Blicharski et al., 1979).

Slip is caused by glide of the crystal planes via dislocation movements on different glide planes (Mahajan and Williams, 1973). In single crystals, plastic deformation occurs when the CRSS reaches a critical value and Schmid factor is able to describe how easy it is for slip to occur for a particular slip system (Channel 5, 2005) and it is shown in equation 2.5.

$$\tau R = \tau A \cos\theta \cos\phi \qquad (2.5)$$

In this equation, $\cos\theta \cos\phi$ is the Schmid factor, $\theta$ is the angle between the load axis and the slip direction (normal to the slip plane), $\phi$ is the angle between the load axis and the slip direction. $\tau A$ and $\tau R$ are the applied and resolved stress, respectively (Swygenhoven et al., 1999).

Slip is the dominant mechanism in hcp materials at high homologous temperatures, <a> slip systems are the most common slip systems consisting of basal <a> $\{0001\} < 11\bar{2}0 >$, prismatic <a> $\{10\bar{1}0\} < 11\bar{2}0 >$ and pyramidal <a> $\{10\bar{1}1\} < 11\bar{2}0 >$. <c+a> slip: the $<11\bar{2}3>$ directions on first order $\{10\bar{1}1\}$ and second order $\{11\bar{2}2\}$ planes, as shown in Figure 2.14 (Dunst and Mecking, 1996; Balasubramanian and Anand, 2002; Schillinger et al., 2006). Predominant slip system is prismatic <a> slip $\{10\bar{1}0\} < 11\bar{2}0 >$ while the slip system pyramidal <a> $\{10\bar{1}1\} < 11\bar{2}0 >$ seldom occurs (Humphreys and Hatherly, 1995). <a> dislocation systems were easy to determine, however, the <c+a> dislocations were difficult to find. And the CRSS of <c+a> pyramidal glide is two times larger than that of prismatic slip and <c+a> glide was

strongly reduced with high oxygen content in titanium alloys. Moreover, the activation of <c+a> slip requires much higher CRSS compared to the activation of <a> slip (Wang and Huang, 2003 and Zaefferer, 2003). Other slip systems are <c+a> slip in $\{10\bar{1}1\} < 1\bar{1}23 >, \{11\bar{2}2\} < 11\bar{2}3 >$ (Schillinger et al., 2006).
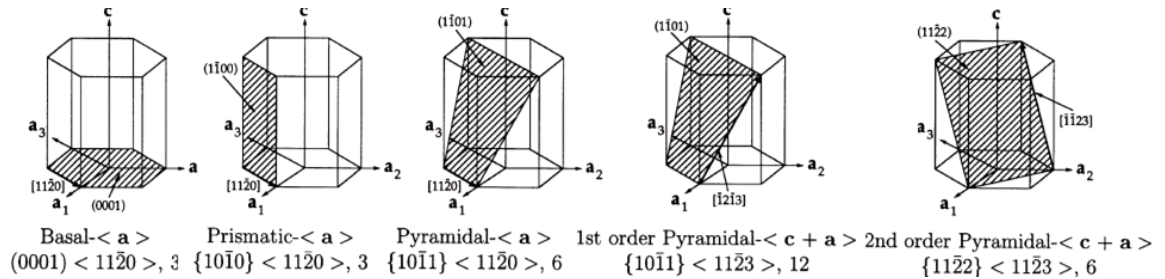


Figure 2.14 Basal <a>, prismatic <a>, pyramidal<a> slip systems, and first- and second-order pyramidal <c+a> slip systems in hcp materials (Balasubramanian and Anand, 2002)

Textures and microstructures can be affected by slip processes depending on the SFE and temperature. Low value of SFE will result in new texture components and similar deformation microstructures will be developed in different materials if they have similar slip pattern and textures, regardless of the SFE (Hughes et al., 2000).

Deformation twinning is another deformation mechanism involving grain subdivision of the dislocation boundaries depending on the SFE, strain and temperature (Hughes et al., 2000). And it is increased with decreasing the deformation temperature and increasing strain rate. Deformation twinning may occur in metals with a low value of SFE because the shape of material is difficult to change during plastic deformation by slip alone. For example, twinning is a major deformation mode in bcc metals at low temperature or high strain rates and in fcc metals with low SFE<25mjm$^{-2}$ (Humphreys, 2004), such as Cu, Zn alloys (Danaf et al., 1999) and austenite stainless steels (Kestenbach and Meyers, 1976), However, deformation twinning is difficult to occur in hcp metals due to high value of SFE compared to bcc metals with low values of SFE, e.g. twinning is hardly observed in high SFE materials such as Al alloys (Gray III, 1988). However, deformation twinning is the dominant mechanism for strain in the c-axis at low homologous temperatures for hcp metals (Balasubramanian and Anand, 2002). Deformation twinning systems for hcp crystals and titanium alloys are shown in Figure 2.15 and Figure 2.16, respectively and twinning systems in pure titanium is $\{10\bar{1}2\} < 10\bar{1}1 >$ (Humphreys and Hatherly, 1995). Deformation occurs mainly by

twinning at rolling reductions below 40%, whereas, slip is the main deformation mode when rolling reductions is more than 40% (Singh and Schwarzer, 2001). And in all cases, the degree of twinning depends on the orientations (Humphreys, 2004).
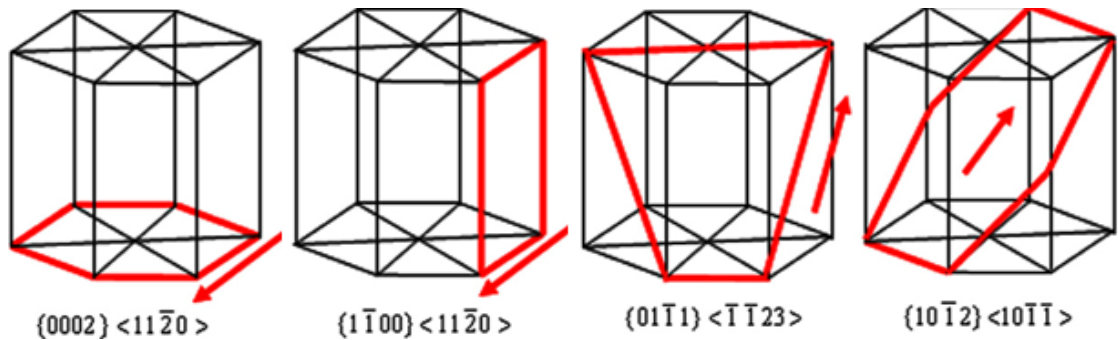


Figure 2.15 Planes and directions for dislocation guide and habit plane for deformation twinning for hcp crystals (Choi et al., 2007)
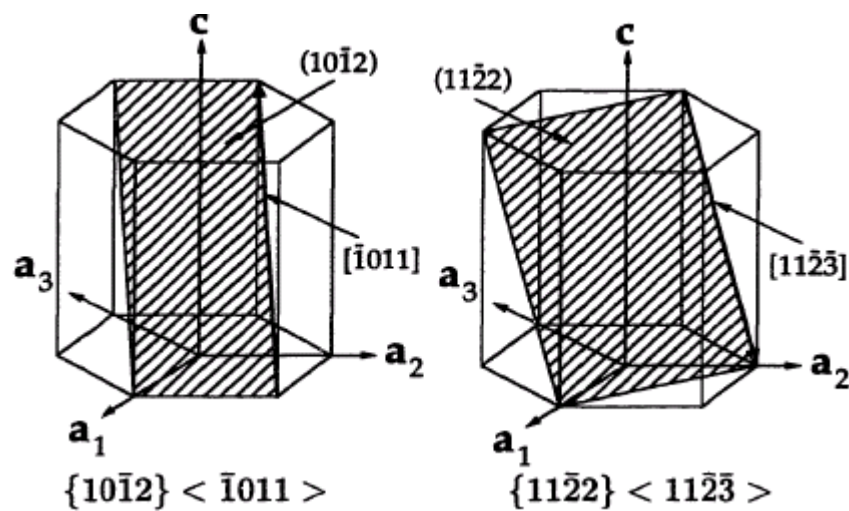


Figure 2.16 Twin systems in room-temperature deformation of hcp titanium alloys (Balasubramanian, 1998)

Zaefferer (2003) have investigated the effect of twinning on ductility in different titanium alloys and he noted that the low ductility of T60 is due to the absence of twinning and <c+a> glide because of high oxygen content; the higher ductility of T40 is explained by the lower CRSS for <c+a> glide, <a> pyramidal glide and deformation twinning; the good ductility of Ti-6Al-4V is due to the small grain size and the relative reduction of the SFE on basal planes by interstitial oxygen with the combination of twinning and <c+a> glide. (Zaefferer, 2003).

**2.4 EBSD technique and texture analysis**

2.4.1 Principles of the EBSD system

Recently electron backscatter diffraction (EBSD) technique has been used as an important tool for quantitative characterization of grains and subgrains, the local orientations of materials, or the relationship between microstructure and crystallographic texture can be measured directly by EBSD (Humphreys, 2001). Figure 2.17 shows a schematic representation of an EBSD setup (Crystallographic institute, 2008). The lattice planes can be reflected on the screen as a diffraction pattern called Electron backscatter Kikuchi patterns (EBSPs) which are then measured by sensitive CCD cameras, feed into computer software and indexed and another computer is used to operate stage and beam control. An optional electron detector is mounted below the phosphor screen to receive the electrons scattered in the forward direction from the sample (Schwatz et al., 2000; Davies, 2009).
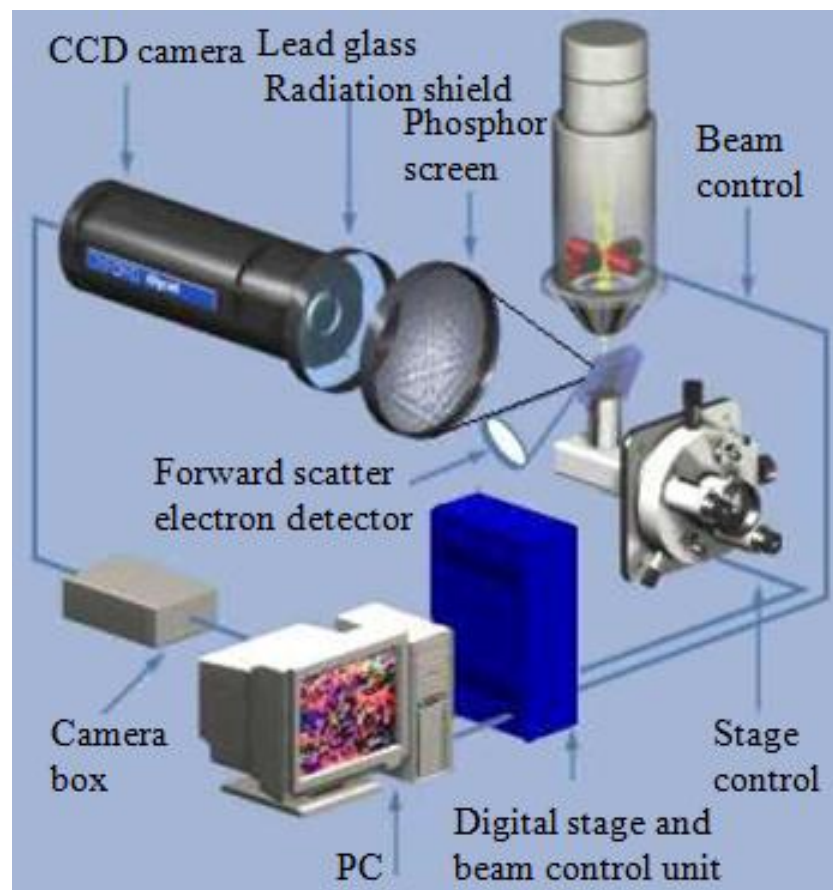


Figure 2.17 Schematic diagram of EBSD detection equipment arrangement showing the experimental set-up for recording EBSD (Crystallographic institute, 2008)

### 2.4.2 Texture

*2.4.2.1 Definition of texture*

Texture is the preferred orientation in the crystals of polycrystalline metals (Hatherby and Hutchinson, 1979). Texture is subdivided into macro-texture and micro-texture. Macro-texture shows a profile of diffracted intensities based on a large sample volume and is characterised by X-ray diffraction and neutron diffraction. While micro-texture analysed by EBSD and Transmission electron microscopy (TEM) is composed of individual orientations relative to their location in a specimen (Randle and Engler, 2000). Texture can greatly determine physical, chemical and mechanical properties of polycrystalline metals, e.g. elastic modulus, Poisson's ratio, strength, ductility and toughness (Hatherby and Hutchinson, 1979).

*2.4.2.2 Description of texture*

Texture can be represented as orientation and misorientation (Randle and Engler, 2000). Orientation is usually represented by pole figures, Euler angles and Euler space or orientation distribution function (ODF) and a full representation of texture developed by Randle and Engler (2000) is shown in Figure 2.18, where the representation of orientation is circled by the left dashed frame and representation of misorientation is contained in the right dashed frame. For example, texture can be defined in one of the three ways (Channel 5, 2005).

1. Euler angles, e.g. Goss (0º, 45º, 90º)

2. Crystallographic indices (100) [$\bar{1}$10]

3. Fibre texture <110> fibre parallel to the rolling direction
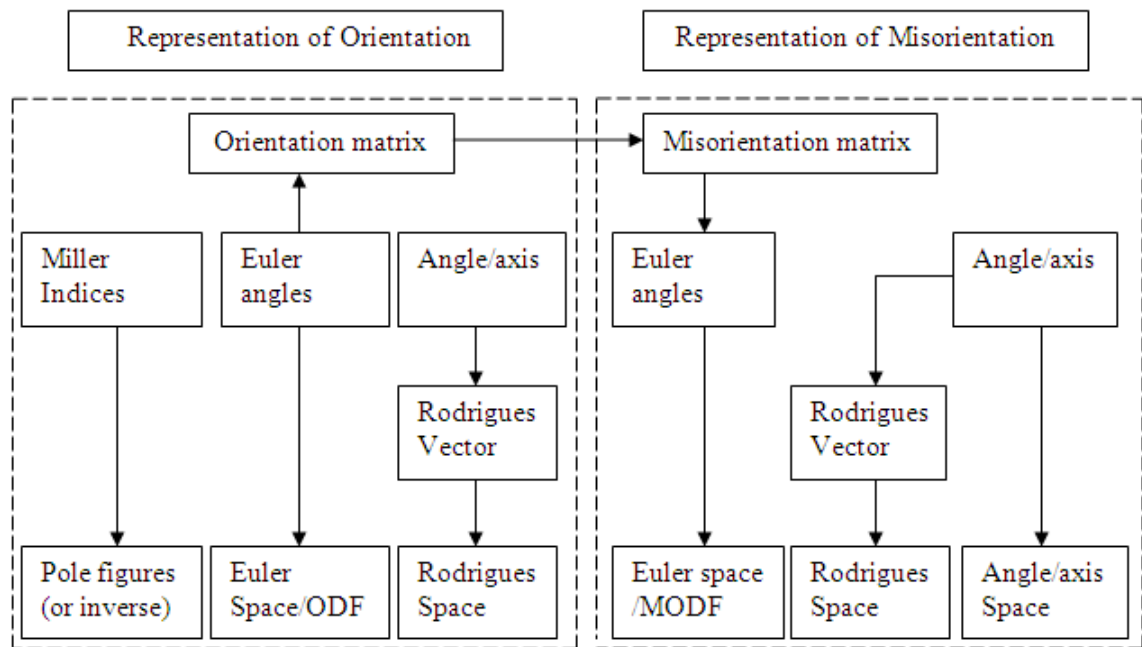
Figure 2.18 Representation of orientation and misorientation (Randle and Engler, 2000)

Crystallographic textures generally depend on the deformation degree, the deformation mode, and the temperature of deformation. Usually the intensity of the texture increases with increasing deformation degree (Leyens and Peters, 2003), e.g., sharpness of the texture increases with increasing deformation, such as rolling reduction (Blicharski et al., 1979); hot deformation (Moustahfid et al., 1997; Gourdet and Montheillet, 2000; Davies, 2009); rolling (Gey and Humbert, 2002); increased strain/ strain rate (Johnson et al., 2003); torsion (Baczynski and Jonas; 1996); extrusion (Gazder et al., 2006) and friction stir welding process (Reynolds et al., 2005; Knipling and Fonda, 2009; Fonda and Knipling, 2010; Jiang et al., 2010; Davies et al., 2011).

*2.6.2.3 Orientation and misorientation*

Orientations describes a relation between two coordinate systems (Kocks et al., 1998), corresponding to the crystal coordinate system and the specimen coordinate system. The crystal coordinate system is defined as the crystal direction such as [001], [010] and [110] in cubic systems and [0001], [11$\bar{2}$0] and [10$\bar{1}$0] in hexagonal systems. The specimen coordinate system depends on the processing route, for example, the specimen coordinate system consists of rolling direction (RD), transverse direction (TD) and normal direction (ND) in rolling (Randle and Engler, 2000).

The orientation is expressed and stored in the form of Euler angles: $\varphi 1$, $\Phi$ and $\varphi 2$, as noted by Bunge (Bunge, 1982). Euler angles are formed according to four steps as shown in Figure 2.19: A. the crystal coordinate system $K_B$ (X'Y'Z') lies parallel to the sample coordinate system $K_A$ (XYZ); B. $K_B$ is rotated around the Z'-axis through the angle $\varphi 1$; C. $K_B$ is rotated with respect to the orientation B) around the X'-axis through the angle $\Phi$; D. $K_B$ is rotated with respect to the orientation C) around the new Z'-axis through the angle $\varphi 2$ (Bunge, 1982; Randle and Engler, 2000).
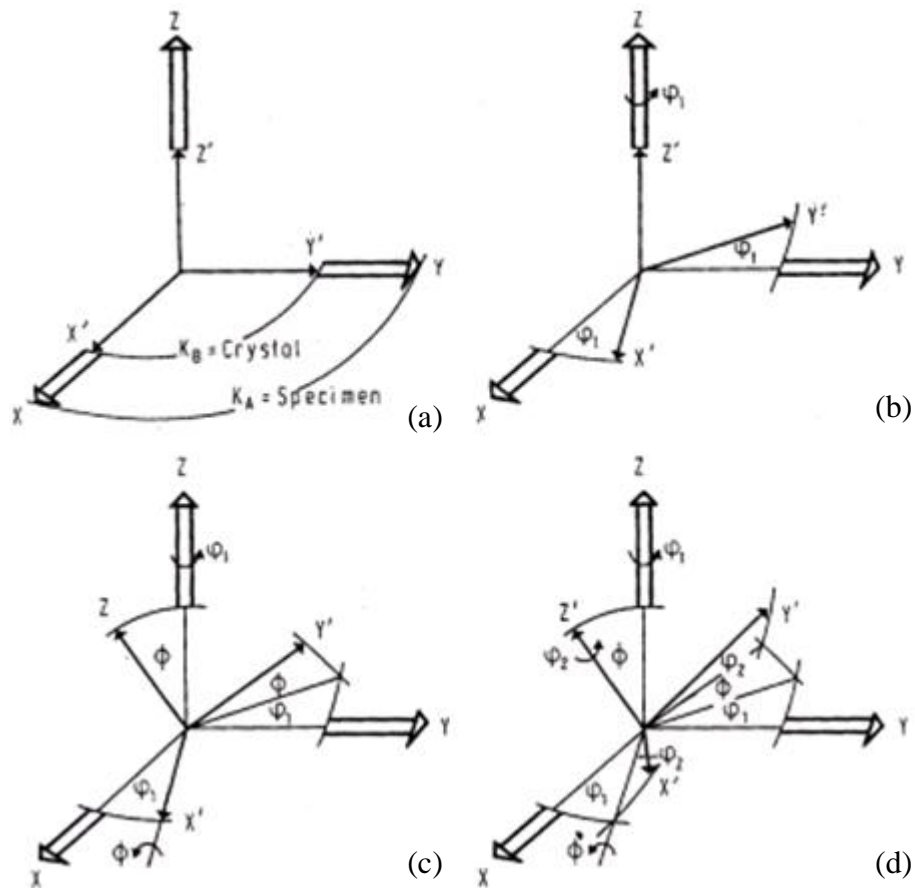


Figure 2.19 Bunge's definition for the three Euler angles $\varphi 1$, $\Phi$, $\varphi 2$ (Bunge, 1982)

As mentioned before, orientation can also be represented in a three-dimensional orientation space called Euler space with coordinates given by the three Euler angles $\varphi 1$, $\Phi$, $\varphi 2$, where each orientation g corresponds to a point in the Euler space. Orientation matrix g is given by equation 2.6 as function of the three Euler angles $\varphi 1$, $\Phi$, $\varphi 2$ (Bunge, 1982; Randle and Engler, 2000).

$$g = \begin{bmatrix} \cos\varphi_1\cos\varphi_2 - \sin\varphi_1\sin\varphi_2\cos\phi, \sin\varphi_1\cos\varphi_2 + \cos\varphi_1\sin\varphi_2\cos\phi, \sin\varphi_2\sin\phi \\ -\cos\varphi_1\sin\varphi_2 - \sin\varphi_1\cos\varphi_2\cos\phi, -\sin\varphi_1\sin\varphi_2 + \cos\varphi_1\cos\varphi_2\cos\phi, \cos\varphi_2\sin\phi \\ -\sin\varphi_1\sin\phi, -\cos\varphi_2\sin\phi, \cos\phi \end{bmatrix}$$

(2.6)

Misorientation is the relative rotation of one orientation to another orientation, for example, the difference in orientation between neighbouring grains in a specimen (Kocks et al., 1998; Davies, 2009). The misorientation matrix $\Delta g$ is calculated from the orientations of grain A and grain B: $g_A$ and $g_B$, and the crystal lattice of grain A was brought into coincidence with the crystal lattice of grain B though a rotation $\Delta g$ which is given by equation 2.7 and 2.8, indicating the rotation from $g_A$ to $g_B$, with $g_A$ chosen as the reference orientation (Kocks et al., 1998; Randle and Engler, 2000).

$$\Delta g = g_B * g_A^{-1}$$

(2.7)

$$\Delta g = \begin{bmatrix} \Delta g11 & \Delta g12 & \Delta g13 \\ \Delta g21 & \Delta g22 & \Delta g23 \\ \Delta g31 & \Delta g32 & \Delta g33 \end{bmatrix}$$

(2.8)

Misorientation is often described by a rotation axis n, and an angle ω (axis/angle representation). The axis of rotation n is a common crystallographic direction of the two crystal lattices and the angle of rotation ω represents the rotation around the axis n required to bring the two crystal lattices into coincidence (Kocks et al., 1998). Misorientation axes n in sample coordination system describe how the misorientation axes are arranged relative to the specimen for a chosen range of misorientation angles. While in crystal coordination system, misorientation axes n shows how crystallographic direction align with the misorientation axes for a chosen range of misorientation angles (Channel 5, 2005).

The angle of rotation ω is given by equation 2.9.

$$\omega = \cos^{-1}\{(\Delta g_{11} + \Delta g_{22} + \Delta g_{33} - 1)/2\}$$

(2.9)

The axis of rotation n can be described by matrix as given in equation 2.10 (Kocks et al., 1998).

$$(n_1, n_2, n_3) = \frac{(\Delta g_{23} - \Delta g_{32}, \Delta g_{31} - \Delta g_{13}, \Delta g_{12} - \Delta g_{21})}{\sqrt{((\Delta g_{23} - \Delta g_{32})^2 + (\Delta g_{31} - \Delta g_{13})^2 + (\Delta g_{12} - \Delta g_{21})^2}} \qquad (2.10)$$

A misorientation between two lattices only can be described in 24 different ways because some of rotation angles and axes represent the same misorientation due to the symmetry in cubic systems (Randle and Engler, 2000). The lowest angular rotation for a given misorientation is called disorientation (Davies, 2009).

**2.5 Friction stir welding process**

2.5.1 Introduction to friction stir welding

Friction stir welding (FSW) was first developed and patented by the Welding Institute (TWI), Cambridge, UK in 1991 (Thomas et al., 1991) as a solid state process which eliminates some of the welding defects caused by fusion welding such as hot cracking, porosity and it has no hazards of welding fume, spatter, ultraviolet or electromagnetic radiation (Threadgill and Martin, 2008). FSW has been widely applied in a variety of materials, especially for aluminium and its alloys and FSW with titanium and its alloys was developed by TWI in 1997 via TWI group sponsored project (GSP 5689) (http://www.twi.co.uk/j32k/unprotected/band_1/research_gsp5689_intro.html).

The FSW process generates very high strains and strain rates, both of which are substantially higher than that found in the conventional (e.g. solid state) metalworking processes e.g. extrusion, rolling, forging, etc (Ma et al., 2008; Threadgill et al., 2009). The principal features of FSW are shown Figure 2.20. In the FSW process, the rotating tool probe is plunged into the workpiece and welding (frictional) heat is generated by rubbing the tool probe and tool shoulder against the workpiece (Threadgill and Martin, 2008). And the welding material will be softened by frictional heat between the welding tool and the workpiece with peak temperature below the melting point, which allows the translation of the welding tool along the weld line to form a solid state bond (Hansen, 2003). Jata et al. (2004) found that peak temperatures in FSW of titanium alloys are lower than that in fusion welds which has the problems such as grain growth in the

40

HAZ and embrittlement due to contamination by interstitial elements (O, N, C). A characteristic asymmetry was observed between the two sides of the weld due to combination of the tool translation and rotation and is characterised by the advancing side (AS) and the retreating side (RS). At the AS, the tool rotation has the same direction as the forward motion, whilst, the tool rotation opposes the forward motion at the RS (Threadgill et al., 2009). A FSW study of Ti-6Al-4V by Pilchak et al. (2007a) proposed that both the strain and temperature profiles in the SZ and the TMAZ can vary significantly at both the AS and the RS because of asymmetry of the process. Computer simulation results of the FSW process by Vilaca et al. (2005) and Heurtier et al. (2006) reported that the temperature and strain at the AS are higher than that at the RS because the tool rotation and the tool velocity are in the same direction at the AS.
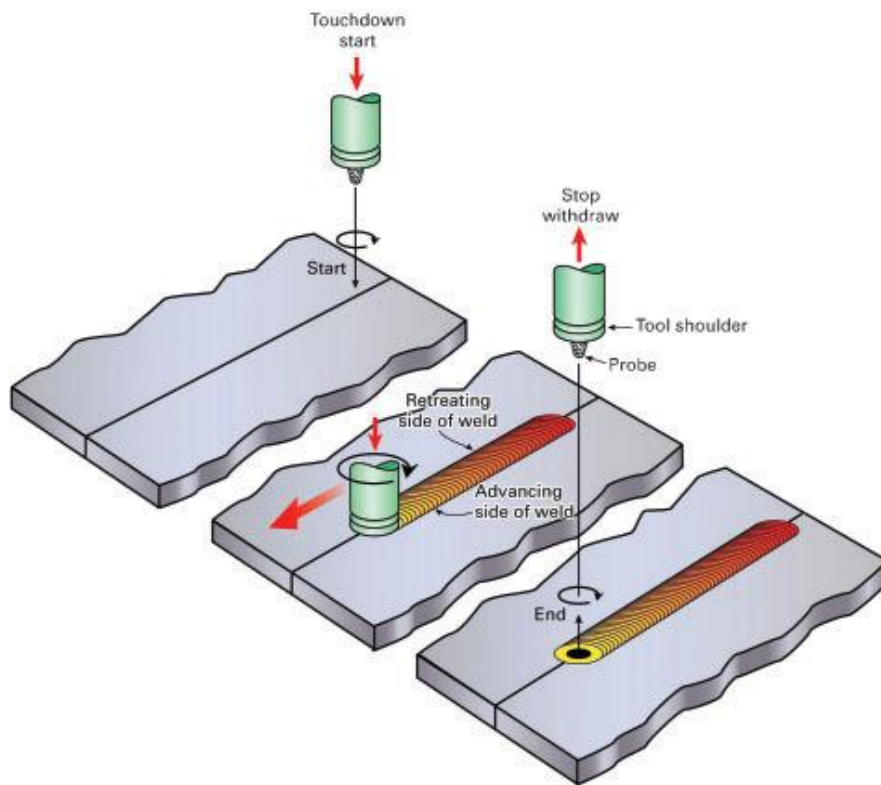


Figure 2.20 Schematic diagram of FSW process (Threadgill, 2007)

### 2.5.1.1 Heat generation

Frictional heat is mainly generated by the high normal pressure and shearing action of the shoulder (Threadgill et al., 2009). And there are two main heat sources in FSW: the friction heat generated at the interface between the tool probe and the workpiece and the plastic deformation heat that generated near the tool probe consisting of three parts: (a)

heat generated by shearing of the material; (b) heat generated by friction on the threaded surface of the probe; and (c) heat generated by friction on the vertical surface of the probe (Song and Kovacevic, 2003).

Threadgill et al. (2009) pointed out that the heat input is a complex function of the process parameters such as traverse speeds, rotation speeds and down force, the alloy being welded and the tool design. However, Peel et al. (2006) found no correlation between the temperature and the input power or heat in FSW of aluminium alloys and he also reported that the heat input and temperature of the backing plate are more strongly dependent on the rotation speed rather than on traverse speed under the tool.


*2.5.1.2 Stationary shoulder friction stir welding*

Stationary Shoulder Friction stir welding (SSFSW) was first developed by TWI in 2006 primarily to improve the FSW of titanium based alloys by generating a more uniform heat input through the weld cross section. SSFSW used a rotating probe located in a non-rotating shoulder which slides over the surface of the specimen during welding, and this produces a focussed heat input around the tool probe eliminating the problem of surface overheating. However, when rotating shoulder are used, the poor thermal conductivity of titanium leads to a significant temperature gradient through the thickness of the welds during the welding process, this results in poor weld quality and mechanical properties (Jiang et al., 2010).

The cross sectional view of SSFSW is shown in Figure 2.21 and the SSFSW equipment is mainly composed of 15 components. A rotating tool pin (component 11) held within a sliding shoe (component 10) is located in a non-rotating shoulder (component 7). The stationary shoulder drags the rotating pin along the welding direction without touching the upper surface of workpiece. Inert gas provided by a gas chamber (component 14) fixed on the welding head is to prevent contamination of elements such as oxygen, hydrogen and nitrogen. The SSFSW weld head is shown in Figure 2.22 with an external view and an underneath view (Russell et al., 2007).
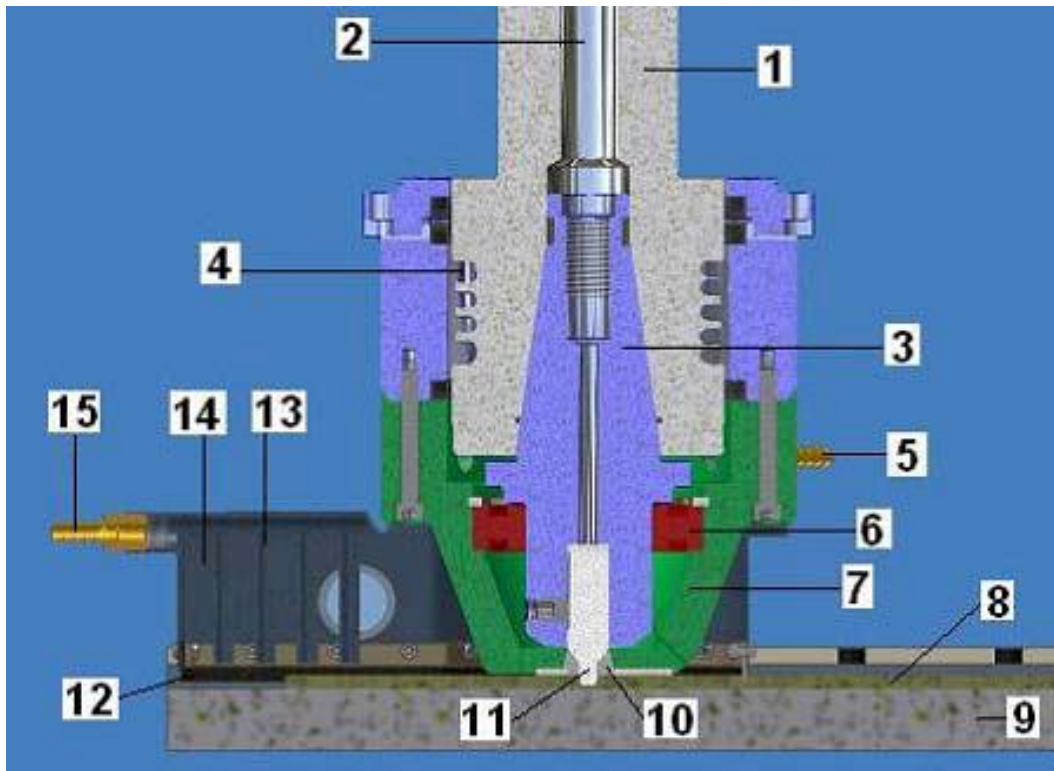
| | | |
|---|---|---|
| (1) Rotating Spindle | (6) Support Bearing | (11) Rotating Tool Pin |
| (2) Draw Bar | (7) Stationary Tool Head | (12) Sliding Seal |
| (3) ISO 50 Tool Holder | (8) Work-piece | (13) Argon Supply |
| (4) Water Cooling Jackets | (9) Backing Plate | (14) Gas Chamber |
| (5) Argon Input | (10) Sliding Shoe | (15) Inert Gas Input |

Figure 2.21 The cross section view of SSFSW (Russell et al., 2007)
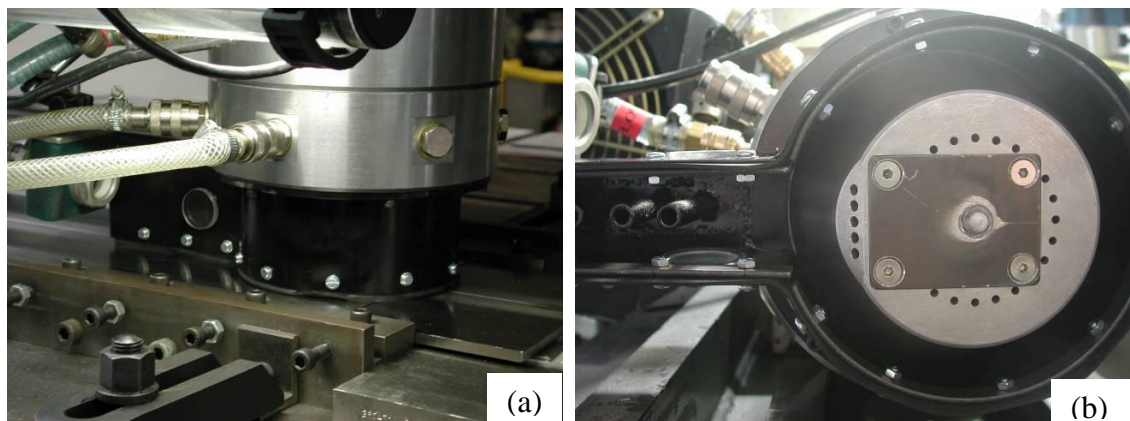


Figure 2.22 The SSFSW welding head: (a) External view; (b) underneath view
(Russell et al., 2007)

43

## 2.5.2 Advantages and disadvantages of FSW

Main advantages of FSW process can be classified into process benefits, component design benefits and environmental benefits (Kallee and Mistry, 1999; Harris and Norman, 2003; Threadgill and Martin, 2008).

Process benefits in manufacturing by FSW include solid phase, single pass and fully mechanised process; The absence of melting resulting in less weld contamination; excellent weld quality with no porosity which can arise in fusion welding; FSW provides welds with low distortion and reduced residual thermal stresses due to the low heat input; Able to join wrought to cast products; Position can be easily chosen at 1-Dimensional, 2- Dimensional and 3- Dimensional; Joints are made with low distortion and shrinkage; No shielding gas or filler wire required for most materials; Excellent forming and tensile properties, good dimensional stability and repeatability and excellent metallurgical properties in the joint area; Fine-grained microstructure in the weld region, leading to improved mechanical properties.

Component design benefits of FSW include improved manufacturing quality control, Less complex processing; Improved component accuracy and tolerances; Improved structural stiffness for torsional rigidity; Reduction in manpower and Improved operation time; Repeatable resulting in less structural conservatism and possible over-design.

Environmental benefits are: No hazards in welding fume, spatter, UV and electromagnetic radiation; No special surface treatment is required and it is applicable to poor pre-weld edge profiling or cleaning.

SSFSW can produce high quality solid-phase welds with excellent mechanical properties; welded components have relatively low distortion/shrinkage. SSFSW has high efficiency with low energy consumption and it is able to join non-fusion-weldable grades (Assessment of SSFSW, 2007).

Disadvantage of FSW includes slow traverse speeds compared to other fusion welding methods for thin section material; Workpiece must be rigidly clamped; Backing bar required for single sided welding; Keyhole at the end of each weld; Cannot make fillet welds or any geometry which requires a fillet; Equipment can be expensive (Threadgill and Martin, 2008).

There are four common imperfections in FSW including lack of penetration, voids, joint line remnants and keyhole (exit hole) (Fuller, 2007; Smith and Hinrichs, 2011).

1. Lack of penetration/kissing bond

Inadequate tool pin length or insufficient plunge depth will lead to the lack of penetration or kissing bond which will appear differently with changing joint configuration (Smith and Hinrichs, 2011), e.g., incomplete root penetrations is due to variations in the plate thickness, poor alignment of tool and joint interface and improper tool design (e.g. FSW pin is too distant from the support anvil) (Fuller, 2007).

2. Voids

Voids usually occur at the AS, and they may or may not break through the surface of the FSWs. Void formation involves insufficient forging pressure, too high of traverse speed and insufficient work piece clamping (Leonard and Lockyer, 2003).

3. Remnant oxides or lazy-s defect.

Remant oxide traces (lazy-s defects) have s-shaped structures because of insufficient cleaning of workpieces prior to welding or insufficient deformation at the faying surface interface (Fuller, 2007; Smith and Hinrichs, 2011). They may reduce stationary and fatigue properties of the welds (Smith and Hinrichs, 2011) and are always seen in FSW of aluminium alloys (Ahmed, 2009).

4. Keyhole (exit hole) at the end.

Keyhole is generated at the end of the weld after the tool material has been plugged out from the work piece (Smith and Hinrichs, 2011). Arbegast (2007) has developed a so-called refill welding process to fill the key hole for friction stir spot welding.

2.5.3 FSW parameters

*2.5.3.1 Tool types (probe and shoulder)*

In traditional FSW, tool shoulders are designed to produce heat on surface of the work piece through friction and material deformation and downward force is also produced by the tool shoulder (Fuller, 2007). The first shoulder design was the concave shoulder (Thomas et al., 1991), which is the most commonly used shoulder types developed for FSW (Nelson et al., 1999; Reynolds and Lockwood, 1999; Brinckmann et al., 2000; Nelson et al., 2000; Sorensen and Nelson, 2003; Lienert et al., 2003a and b; Chen and Maginness 2004; Fujii et al., 2004; Record et al., 2004; Savolainen et al., 2004 and Sorensen et al., 2004). Easily machined concave shoulders produce FSWs with good quality. Features are added to increase the amount of material deformation produced by

the shoulder (Thomas et al., 1996; Dawes and Thomas, 1999). These features have been classified into five types, corresponding to scrolls (Brinckmann et al., 2000; Zettler et al., 2004), knurling, scoops (Dawes and Thomas, 1999), grooves and concentric grooves (Brinckmann et al., 2000, Dawes and Thomas, 1999) (Figure 2.23) and they can be machined onto any tool shoulder profiles of concave, flat and convex.
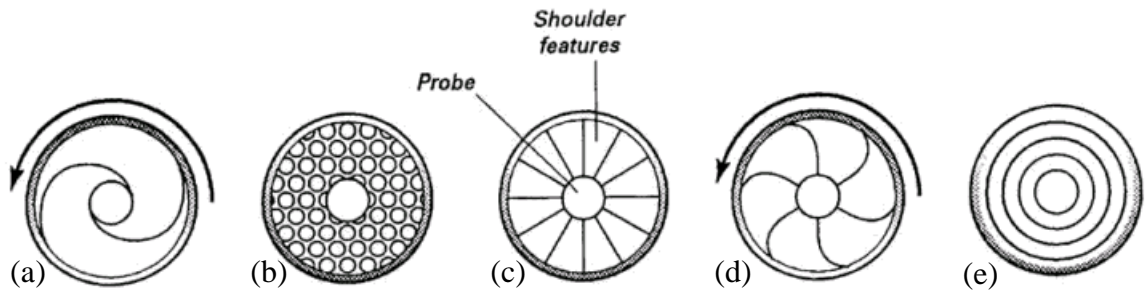


Figure 2.23 Different shoulder features used to improve material flow and shoulder efficiency: (a) scrolls; (b) knurling; (c) scoops; (d) grooves; (e) concentric grooves (Thomas et al., 1996)

Another commonly used shoulder type is the scroll shoulder which has 'a flat surface with a spiral channel cut from the edge of the shoulder toward the center', as shown in Figure 2.24. Scrolled shoulder can easily been subjected to displacement compared to the concave shoulder. And it is unable to weld work piece with complex curvatures and with large thickness variation along the weld length (Fuller, 2007).



Figure 2.24 Photograph of a scrolled shoulder tool and a truncated cone pin containing three flats (Fuller, 2007)

There is a rarely used shoulder type named convex shoulder which has a convex profile (Thomas et al., 1996) and the only reported success using this tool shoulder was

46

on a friction stir welded 0.4mm sheet with a convex shoulder of 5mm diameter (Nishihara and Nagasaka, 2004).

Scialpi et al. (2003) developed three shoulder geometries for FSW with an aluminium alloy using an non-threaded cylindrical pin and the shoulders are characterized by three different features: 1. Scroll ($T_S$), a smaller shoulder size was used in the modified scroll shoulder; 2. Cavity ($T_C$), the cavity in the concave shoulder can form a compressed annular ring of workpiece material around the pin and prevent the removal of plasticized material; 3. Fillet ($T_F$), the fillet was developed to reduce stress concentration and increase the effective contact surface. Figure 2.25 shows the $T_{FS}$ (scroll+ cavity), $T_{FC}$ (fillet+ cavity), and $T_F$ tools. The shoulder type $T_{FC}$ with fillet and cavity is the best tool among the three tools due to the fact that it increases the size of the joint in terms of longitudinal and transverse length and provides the best crown surface (Scialpi et al., 2003).
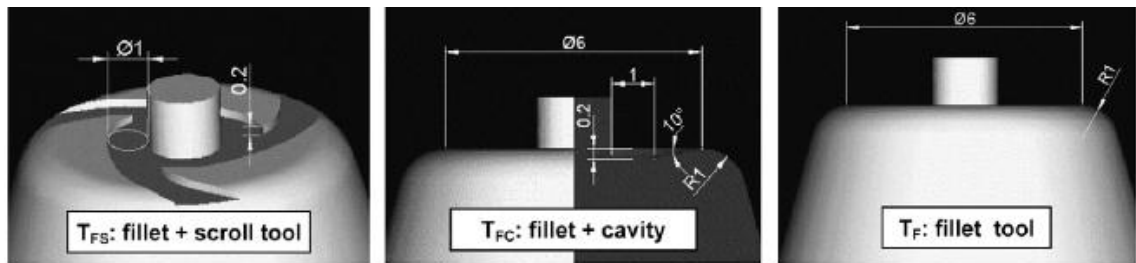


Figure 2.25 Tool types with the main dimensions in mm (Scialpi et al., 2003)

The general requirements of the tool materials for FSW are to have high temperature strength, low reactivity, manufacturability and toughness (Sorensen, 2004); ambient and elevated-temperature strength to prevent tool fracture or distortion for the duration of FSW; elevated-temperature stability to maintain strength and dimensional stability during the time of use; wear resistance in order not to change the tool shape by removing tool features which is associated with weld quality and defects; tool reactivity; fracture toughness (Lienert et al., 2003a) to prevent lateral movement during spindle rotation and to avoid premature tool fracture, machinability, uniformity in microstructure and density and availability of materials (Fuller, 2007). FSW of "hard" materials such as nickel alloys, stainless steels and titanium alloys, unlike aluminium alloys ("soft" alloys) require robust wear resistant, high temperature alloy and high strength tool materials to withstand high temperatures and high heat output (Jata et al., 2004). Table 2.8 shows a list of selection for the tool materials (Fuller, 2007).

47

Table 2.8 Summary of current FSW tool materials (Fuller, 2007)

| Alloy | Thickness, mm | Tool material |
|---|---|---|
| Aluminium alloy | <12 | Tool steel, WC-Co |
| | <26 | MP159 |
| Magnesium alloys | <6 | Tool steel, WC |
| Copper and copper alloys | <50 | Nickel Alloys, PCBN*, tungsten alloys |
| | <11 | Tool steel |
| Titanium alloys | <6 | Tungsten alloys |
| Stainless steels | <6 | PCBN*, tungsten alloys |
| Low-alloy steel | <10 | WC, PCBN* |
| Nickel alloys | <6 | PCBN* |

PCBN: Polycrystalline Cubic Boron Nitride

Tool steel is a low cost material that is widely used for welding or processing of aluminium and lower melting point materials, such as magnesium, lead, zinc and so on (Smith and Hinrichs, 2011) and it have been widely used in FSW of aluminium alloys for its easy availability and machinability, low cost and established material characteristics (Nelson et al., 1999 and 2000).

The refractory metals such as tungsten, molybdenum, tungsten-rhenium, super abrasives polycrystalline cubic boron nitride (PCBN), nickel and cobalt-based alloys, niobium and tantalum have high strength and good ductility, as well as good creep and corrosion resistance and they are used for high temperature capabilities and high densities (Lienert et al., 2003a, Sorensen 2004, Subramanian et al., 2003; Sutton et al., 2006; Liu et al., 2010a; Smith and Hinrichs, 2011). Tungsten-base alloys have been used in FSW of copper alloys, nickel-aluminium bronze, titanium alloys and steels (Lienert et al., 2003a and b, Subramanian et al., 2003, Sutton et al., 2006, Liu et al., 2010a, Smith and Hinrichs, 2011). However, tungsten tools exhibit poor room temperature toughness and rapid tool wear (Sorensen, 2004).

Tungsten carbide is a low to moderate cost material used in lower to moderately higher melting point materials. It has good wear properties, but too brittle (Smith and Hinrichs, 2011). And it has been reported to have smooth and uniform thread surfaces
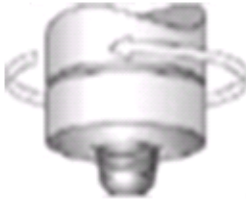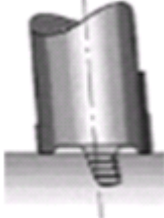
for the FSW of Al 6061 (Colligan, 2000). Carbides are commonly used due to superior wear resistance and good fracture toughness (Fuller, 2007).

Tungsten Rhenium (W-Re) is a high cost material used to weld steel and titanium alloys for high temperature and high strength (Fuller, 2007; Smith and Hinrichs, 2011), but tool wear caused by W-Re is significant (Sorensen, 2004). High cost PCBN tool material is primarily used for welding steel and it was manufactured at extreme pressures and temperatures (Smith and Hinrichs, 2011).

Nickel and cobalt base alloys were developed to have high strength, good ductility, creep resistance and corrosion resistance. These alloys derive their strength from precipitates (Fuller, 2007; Smith and Hinrichs, 2011). They exhibit yield strengths higher than 500MPa at 1000ºC and have been applied for high softening temperature materials such as mild steel, ultra-high carbon, cp-Ti and Ti-6Al-4V (Sato et al., 2011).

Apart from the tool types, tool geometry has the most important influence on material flow, process loads, traverse speed, and the uniformity of microstructure and properties in FSW (Mishra and Ma, 2005). There are six tool probe types designed by TWI as summarized in Table 2.9 which also lists the used examples, and they are the Cylindral, Whorl[TM], MX triflute[TM], Flared triflute[TM], A-skew[TM] and Re-stir[TM], where the Whorl[TM] type has basic variants of five types as shown in Figure 2.26 and shoulder profiles used on the Whorl[TM] type are displayed in Figure 2.27 (Dawes and Thomas, 1999).

Table 2.9 Selection of tools designed at TWI (Thomas et al., 2003; Nandan et al., 2008; Fuller, 2007)

| Tool | Cylindral | Whorl[TM] | MX Triflute[TM] | Flared Triflute[TM] | A-skew[TM] | Re-stir[TM] |
|---|---|---|---|---|---|---|
| Schematics |  |  |  |  |  |  |
| Tool pin shape | Cylindrical with threads | Tapered with threads | Threaded, tapered with three flutes | Triflute with flute ends flared out | Inclined cylindrical with thread | Tapered with threads |
| Ratio of pin volume to cylindrical pin volume | 1 | 0.4 | 0.3 | 0.3 | 1 | 0.4 |
| Swept volume to pin volume ratio | 1.1 | 1.8 | 2.6 | 2 | Depends on pin angle | 1.8 |
| Used examples | Thomas et al., 1991; Nelson et al., 2000; Brinckmann et al., 2000; aluminium alloys | Thomas et al., 2001; Thomas et al., 2002; aluminium alloys | Thomas et al., 2001; Strangwood et al., 2004; aluminium alloys | Colegrove and Shercliff, 2004, for an aluminium alloy | Thomas et al., 2002 for an aluminium alloy | Thomas, 2003 for 5083-O aluminium alloy |
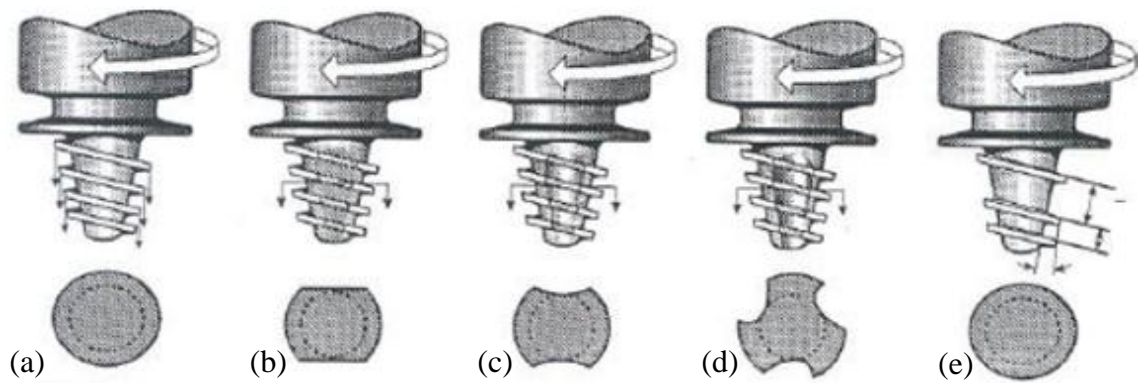
Figure 2.26 Basic variants of the Whorl[TM] type of FSW tool: (a) Oval shape, (b) Paddle shape, (c) Two re-entrant, (d) Three sided probe, (e) Changing spiral form (Dawes and Thomas, 1999)
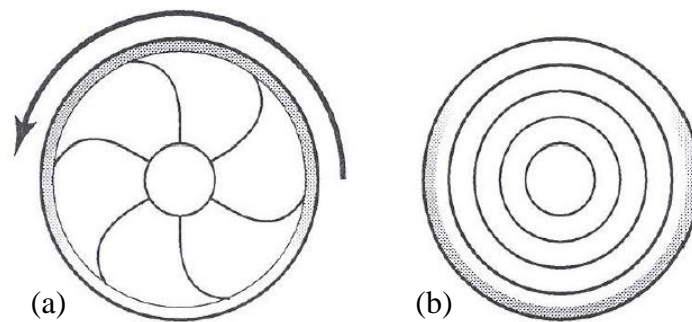


Figure 2.27 Shoulder profiles used on the Whorl[TM] tool (view from underneath shoulder): (a) Scoop; (b) Concentric grooves (Dawes and Thomas, 1999)

The design features of the two tool types: the Whorl[TM] and the MX Triflute[TM], which are able to reduce welding force, enable easier flow of plasticized material, facilitate the downward augering effect, and increase the interface between the pin and the plasticized material, thereby increasing heat generation. The MX Triflute[TM] probe with square grooves reduces the displaced volume by about 70% compared to 60% reduction by the Whorl[TM] probe with threaded shapes because square grooves in the MX Triflute[TM] probe can enable the additional tool surface area forcing or downforce (Thomas et al., 2001; Smith and Hinrichs, 2011). In addition, the Whorl[TM] probe can easily traverse the work piece and a cylindrical tool than the MX Triflute[TM] probe. However, the MX Triflute[TM] has more complex appearance compared to the Whorl[TM] probe, which ensures full penetration of the weld line material, and eases material flow (Harris and Norman, 2003).

*2.5.3.2 Welding parameters*

Tool rotation speed and tool traverse speed are the two most important parameters for FSW. It has been reported that the peak weld temperature, hardness, texture strength, grain size in the weld zones increases with increasing rotation speed and with decreasing traverse speed. Moreover, the rotation speed has larger effect on the peak weld temperature and microstructure unit size such as the thickness of the $\alpha$ laths in the stir zone (SZ) compared to the traverse speed and the rotation speed was the dominating factor affecting heat generation and the peak weld temperature in FSW of aluminium alloys, magnesium alloy, pure copper, and titanium alloys (Querin et al., 2009; Zhou et al., 2010a; Attallah and Salem, 1999 for an aluminium alloy, Commin et al. 2009, Xue et al. 2010; Edwards and Ramulu, 2010; Grujicic et al., 2011). Both higher rotation speed and lower traverse speed generates larger grained microstructures due to higher temperature, longer exposure times and more intense stirring and mixing of material due to higher friction heating, whereas the traverse speed is the dominating parameter in determining material stirring at the weld root and the formation of flaws (Mishra and Ma, 2005; Grujicic et al., 2011). A FSW study of Ti-6Al-4V by Edwards and Ramulu (2010) reported that the peak temperature at the weld surface increased by 146°C with increasing rotation speed from 200 to 400rpm, but peak temperatures were not affected by varying traverse speed from 50 to 150mm/min with a constant rotation speed of 300rpm. For a given traverse speed, an optimum rotation speed can produce welds with highest strength and ductility for FSW with high strength AA7010 alloy. As the travel speed increases, the rotation speed should be increased to maintain this condition (Hassan et al., 2003).

Fujii et al. (2010) have recently performed FSW of pure Ti joints and they found that the dislocation densities inside the equiaxed grains in the SZ with bimodal structure decreases with increasing traverse speed. An investigation of FSW of AA6082 by Cavalierea et al. (2008) found that tensile stress increases with increasing strain; the yield and tensile strengths of the FSWed aluminium joints increases significantly with increasing traverse speed (Cavaliere et al., 2008; Ren et al., 2007), whilst, the tensile properties are not noticeably affected by the rotation speed except for the tensile properties of one sample with a reduced ductility (Ren et al., 2007).

**2.6 Friction stir welding with titanium and its alloys**

2.6.1 Introduction

Titanium is intrinsically difficult to weld by FSW, due to its low thermal conductivity and limited hot working temperature range, which results in focused heat input at the weld surfaces. It is almost impossible to generate satisfactory welding conditions using conventional approaches. While SSFSW developed by TWI can generate more or less uniformly distributed heat input through the weld thickness, reducing some of the welding problems encountered in conventional FSW and giving excellent welds (Threadgill and Martin, 2008)

FSW of titanium alloys has to be performed either in vacuum or an inert gas atmosphere to prevent contamination on titanium alloys by oxygen and hydrogen from the ambient environment as a drawback causing brittle (Threadgill and Martin, 2008). Both alloy composition and microstructure determine the weldability of titanium alloys Generally, titanium alloys become easier to weld with increasing volume fraction of the α phase, e.g. unalloyed pure titanium and α alloys are easily weldable and α and α+β alloys are easier to weld than β alloys (Lütjering and Williams, 2003). Some reports of FSW of titanium alloys are available in conference proceedings or have been presented at conferences (Lienert et al., 2000; Helder and Subramanian 2003; Lienert et al., 2000; Goetz and Jata, 2001; Helder and Subramanian, 2003; Ramirez and Juhas, 2003; Jiang et al., 2010) and journal papers were found on FSW of titanium alloys in terms of microstructural evolution, textural evolution and mechanical test (Lienert et al., 2001; Lienert et al., 2003b; Juhas et al., 2000; Chen and Maginness, 2004; Jata et al., 2004; Lee et al., 2005, Mishra and Ma, 2005, Reynolds et al., 2005a, Pilchak et al., 2007 a and b, Pilchak et al. 2008 b; Querin et al., 2009; Pilchak and Williams, 2011; Zhang et al., 2008 a and b; Mironov et al. 2008 a and b; Mironov et al., 2009; Knipling and Fonda, 2009; Zhou et al., 2009; Cheng et al., 2010, Fonda and Knipling, 2010, Edwards and Ramulu, 2010; Edwards et al., 2010; Fujii et al., 2010; Liu et al., 2010 b; Mironov et al., 2010; Zhang et al., 2010; Zhou et al., 2010a and b; Fratini et al., 2010; Liu and Zhou, 2010; Davies et al., 2011; Pilchak et al., 2011; Knipling and Fonda, 2011).

2.6.2 FSW zones of titanium alloys

Macroscopic weld zones for FSW have been determined to consist of the following four zones as commonly found in the literature: Base material (BM), heat affected zone

(HAZ), thermo-mechanical affected zone (TMAZ) and nugget zone (NG) according to Threadgill (2007). A thermal cycle may be experienced in the BM but without deformation; the region next to the BM is the HAZ which has experienced a peak weld temperature to generate microstructure change but without deformation; the TMAZ undergoes deformation to change the microstructure in terms of grain shape. The recrystallised region is often called the 'nugget (NG)' or 'dynamically recrystallised region' and used extensively for FSW of aluminium alloys. The NG has sufficiently high deformation and temperature to generate new grain boundaries through recrystallization mechanisms in aluminium alloys (Threadgill et al., 2009).

However, titanium alloys has a high melting point and low thermal ductility, which means that it is not possible to assign the same microstructure terms to FSW of titanium alloys as that to the FSW of aluminium alloys, in the literature, weld zones in FSW of titanium alloys are generally divided into the BM, the HAZ, the TMAZ and the stir zone (SZ) (Pilchak et al., 2007a and b; Pilchak et al., 2008; Pilchak and Williams, 2011; Zhang et al., 2008a and b; Mironov et al., 2008a and b; Mironov et al., 2009; Zhou et al., 2009; Zhang et al., 2010; Fratini et al., 2010; Liu and Zhou, 2010; Knipling and Fonda, 2011) which will be discussed in detail in the following text.

*2.6.2.1 Base material (BM)*

Base material (BM) is remote from the weld, the BM is not affected by heat in terms of microstructure changes or properties, and it may have experienced a thermal cycle from the weld but without deformation. The BM has not experienced thermal cycle or deformation to change microstructure of this region (Pilchak et al. 2007a; Threadgill et al., 2009).

*2.6.2.2 Heat affected zone (HAZ)*

Heat affected zone (HAZ) is the region close to the BM and microstructure and/or properties of the HAZ have been modified by the weld thermal cycle, but no apparent plastic deformation is detected by light microscopy (Threadgill et al., 2009). The HAZ can have either lamellar structure, bimodal structure or equiaxed structure for FSW of Ti-6Al-4V depending on the microstructure of the BM. HAZ can exhibit lamellar structure if the BM has fully lamellar structure, e.g, a study of FSP with Ti-6Al-4V by Pilchak et al. (2007a) with a lamellar starting microstructure reported no detectable

plastic strain in the colony α microstructures of the HAZ, which are beneficial to high-cycle fatigue strength. Whilst, Zhang et al. (2008a) found that the HAZ having the lowest hardness contained a bimodal microstructure consisting of equiaxed αp and α+β lamellar structure within the prior β grains while the base material (BM) had a deformed α+β lamellar microstructure in FSW of Ti-6Al-4V. Another study on FSW of pure titanium by Zhang et al. (2008b) reported that the HAZ exhibits an equiaxed bimodal microstructure consisting of much finer αp grains compared to that in the BM with an equiaxed microstructure.

Macrozones are often observed in the bimodal microstructure. As aforementioned earlier, a macrozone is composed of necklaces of equiaxed αp grains sharing the same orientation or close c-axes, e.g. in a bimodal structure of Ti-6Al-4V (Germain et al., 2008). The c axes are mainly aligned with the tensile directions (Biavant et al., 2002), which is probably linked to variant selection during the β to α transformation of the macrozones (Germain et al., 2005). Fatigue cracks are initiated on the basal plane or the prismatic plane, but no crack can be found in the macrozone if they are both difficult (Biavant et al., 2002).

### 2.6.2.3 Thermo-mechanically affected zone (TMAZ)

The region next to the HAZ is the thermo-mechanically affected zone (TMAZ) which has been plastically deformed by the FSW tool and the heat, but without recrystallization (Threadgill et al., 2009). Mishra and Ma (2005) reported that the TMAZ experiences both temperature and deformation during FSW/FSP. The TMAZ underwent plastic deformation but without recrystallization due to insufficient deformation strain, and it was not found in the weld zones of FSW of titanium alloys in some studies (Juhas et al., 2000 on Ti-6Al-4V; Zhang et al. 2008a and b on Ti-6Al-4V and pure Ti; Lee et al. 2005 on pure Ti) as evidenced by a sharp boundary (SB) found between the SZ and HAZ. Furthermore, Fonda and Knipling (2010) found that the weld nugget of FSW of a near α alloy Ti-5111 has a very refined grain size surrounded by a very narrow (<100μm wide) TMAZ and no HAZ is apparent.

### 2.6.2.4 Stir zone (SZ)

Close to the TMAZ is the SZ which have experienced the highest temperatures and the highest strains and the process parameters such as rotation speed and travel speed, depth

of plunge/down force and tilt angle would define the microstructure in the SZ by affecting the strain field imposed during processing and microstructure (Pilchak et al., 2007a). The SZ can either have bimodal structure or lamellar structure depending on the BM structure and the peak weld temperature. In most conditions for FSW of α+β titanium alloy, a full lamellar microstructure is formed in the SZ with peak weld temperature exceeding the β transus temperature (Ramirez and Juhas, 2003; Mironov et al. 2008 a and b; Zhang et al., 2008a; Zhang et al., 2010; Zhou et al., 2010a). In some cases, bimodal structure was formed in the SZ (Juhas et al., 2000, Pilchak et al., 2007a and b, 2008; Zhou et al., 2009; Zhou et al., 2010b; Liu et al., 2010b; Fujii et al., 2010). SZ with bimodal structure was observed for the weld for 400rpm and 25, 50 and 75mm/min and characterized by dislocation-free equiaxed αp indicating fully dynamic recrystallization (DRX) (Zhou et al., 2009; Zhou et al., 2010b; Humphreys and Hatherly, 2004). This observation agrees with the results reported by Juhas et al. (2001). However, randomly oriented twins and a high dislocation density were observed in the SZ of the FSW of Ti-6Al-4V (Pilchak et al., 2008; Lienert et al., 2001). A FSW study of pure Ti by Fujii et al. (2010) reported that the bimodal microstructure formed in the SZ is due to the fact that DRX resulted in a significant decrease in the grain size and increase in hardness.

Fine lamellae are formed in transformed β in the SZ of the weld for 400rpm and 100mm/min, basket-weave α+β lamellae observed in the SZ contains dislocation-free colony α as well as α colonies with low dislocation density in the weld for 600rpm and 75mm/min (Zhou et al., 2010a). Zhang et al. (2008b) found that the SZ showing fully lamellar structure with refined prior β grains exhibited higher hardness than the BM. Fine equiaxed α grains in the SZ have superior fatigue crack initiation resistance, while the coarse lamellar microstructure is more resistant to fatigue crack growth (Pilchak et al., 2007a) and local coarsening of the α laths resulted from the fine scale of the microstructure FSW of Ti-6Al-4V lead to a slight softened SZ with dislocation-free equiaxed α grains and dislocation-free colony α+β laths (Juhas et al., 2000).

Examples for published references of the SZs having both bimodal structure and lamellar structure in FSWed titanium alloys are shown in Table 2.10.

Table 2.10 Examples of the SZ**s** in FSWed titanium alloys from published references

| Authors | Starting material | Traverse speed, mm/min | Rotation speed, rev/min | Plunge depth, mm | SZ features |
|---|---|---|---|---|---|
| Pilchak et al., 2007a, Ti-6Al-4V | Lamellar structure | 102 | 100 | Not mentioned | fine equiaxed $\alpha_p$; randomly oriented twins; a high dislocation density |
| Fujii et al., 2010, pure Ti | Equiaxed structure | 50, 100, 200, 300 | 400 | 2 | equiaxed grain structure and low density of dislocations at lower traverse speed |
| Zhou et al., 2009, Ti-6Al-4V | Bimodal structure | 50 | 400 | 1.8 | Bimodal structure; dislocation-free equiaxed $\alpha_p$; DRX leads to grain refinement; |
| Zhou et al., 2010a, Ti-6Al-4V | Bimodal structure | 75 | 500, 600 | 1.8 | Above $\beta$ transus; $\alpha$ colonies with low dislocation density; lowest hardness; high HAGBs |
| Zhou et al., 2010b, Ti 64 | Bimodal structure | 25, 50, 75, 100 | 400 | 1.8 | Bimodal structure, DRX; dislocation-free equiaxed $\alpha p$; lowest hardness; refined structure; |
| Liu et al., 2010b, Ti-6Al-4V | Bimodal structure | 25, 50 | 400 | 2 | Bimodal structure, DRX, much finer equiaxed $\alpha p$ |
| | | 100 | 400 | 2 | Dislocation-free equiaxed $\alpha p$ grains, ultra-fine $\alpha p$ sub-grains; DRX not complete |

| | | | | | |
|---|---|---|---|---|---|
| Fratini et al., 2010, Ti-6Al-4V | Not mentioned | 50 | 300, 500 | 3 | Bimodal structure with smaller αp grain size compared to the BM due to DRX |
| | | | 700, 1000 | 3 | Hardness decreases with decreasing average grain size as the increase of the rotation speed |
| Liu and Zhou, 2010, TC4 titanium alloy | Bimodal structure | 50 | 400 | 2 | Bimodal structure; equiaxed αp grains have low dislocation density; lowest hardness due to DRX |
| Mironov et al., 2010, Ti-15V-3Cr-3Al-3Sn, Metastable β | Bimodal structure | 60 | 400 | 3 | Lamellar structure, simple shear texture with 111 and 110 partial fibre textures (D1, D2, E, E2, J, J2, F), DDRX |
| Zhang et al., 2010, pure Ti | Lamellar structure | Not mentioned | 200-400 | Not mentioned | Torsion texture; finer grain structure compared to the BM; Both CDRX and DDRX |
| Zhang et al., 2008a, Ti-6Al-4V | Deformed lamellar structure | 60 | 300, 400, 500, 600 | 2 | Lamellar structure higher strength and elongation than the BM due to finer a laths |
| Zhang et al., 2008b, pure Ti | Equiaxed structure | 50 | 200 | 2 | Smaller prior β grain size compared to the BM; DRX |
| Knipling and Fonda, 2011, Ti-5111 | Lamellar structure | 51 | 140 | 12.5 | Equiaxed prior β grains due to DRX; shear texture with D2 $\{\bar{1}\bar{1}2\}<111>$ and P1 $\{\bar{1}100\}<11\bar{2}0>$ |

2.6.3 Tool/workpiece interaction

Tool wear mechanisms in conventional FSW of Ti alloys can be classified into abrasive wear and chemical wear. Abrasive wear is the wear of the tool probe in the root areas of the weld and chemical wear is due to dissolution of the tool probe material into the work piece in the surface areas of the weld (Russell and Blignault, 2006). Tool wear in FSW is primarily due to chemical wear and tool wear (W contamination) observed in the weld centre was due to temperatures and frictional forces (Klingensmith et al., 2005) or caused by the grain refinement effect, the Ti borides and PCBN tool debris (Zhang et al., 2008b).

Significant tool wear caused by submicron tungsten rich particle was observed at both the weld surface and the weld centre of the SZ with bimodal structure after FSP of investment cast Ti-6Al-4V using W-Re tool and partial dissolution of the tungsten-rich particles into the SZ locally stabilised the β phase in the SZ (Pilchak et al., 2007b). Lienert et al. (2001) have investigated FSW of Ti-6Al-4V and they found that the greatest amount of tool wear was resulted from the plunging process. It has been reported that the AS has experienced more significant tool wear than the RS of the weld because the tool rotation direction opposes the tool travel direction (Klingensmith et al., 2005), however, Pilchak et al. (2007b) observed more tool wear at the RS because the particles were transported to the RS during deformation.

A study of FSW of mild steel using tool materials included both molybdenum and tungsten based alloys by Lienert et al. (2003a) reported that tool wear has altered the tool dimensions and reduced tool life and tensile properties. However, FSW of SUS304 stainless steel using an Ir10%Re welding tool was without significant tool wear (Miyazawa et al., 2011).

2.6.4 Hardness

A FSW of pure titanium using PCBN tool by Zhang et al. (2008) found that high level of hardening of material in the weld zones can be attributed to the microstructural features of the surface layer and the SZ has the highest hardness at the top surface due to grain refinement and PCBN tool debris and Ti borides. Hardness increases from 340VHN in the BM to 370VHN in the SZ of FSW of Ti-6Al-4V (Lienert et al., 2000). However, the weld centre and the weld bottom of the SZ of FSW of Ti-6Al-4V showing a slight softening

trend may be due to the fine scale of the microstructure and grain size effects have the strongest influence on hardness in titanium alloys (Juhas et al., 2000).

Microstructural investigation of FSW of pure titanium by Lee et al. (2005) showed that the higher hardness spot in the weld nugget is a denser twinned region with high dislocation density, while the lower hardness spot in the weld nugget is a region containing lower twin density and grain boundary serration. The material can be hardened by deformation twin by a reduction in the slip length (Hall-Petch effect) in addition to the increased hardness of the twin region (Kalidindi et al., 2003)

### 2.6.5 Shear texture in FSW of titanium alloys

Shear texture was reported in the final texture of torstion extrusion (Baczynski and Jonas 1996) and equal channel angular extrusion (ECAE) (Gazder et al., 2006) for bcc materials and ideal orientations were generated from the shear texture. Baczynski and Jonas (1996) investigated the textures of two interstitial free (IF) steels and a high purity α-iron after deformation in torsion in the temperature range 20-500°C. The seven important ideal orientations are identified on the {110} pole figure in Figure 2.28. At room temperature, these ideal orientations are F{110}<001>, J1 $\{0\bar{1}1\} < \bar{2}11 >$, J2 $\{1\bar{1}0\} < \bar{1}\bar{1}2 >$, D1$\{11\bar{2}\}$<111>, D2$\{\bar{1}\bar{1}2\}$<111>, E1$\{01\bar{1}\}$<111>, and E2 $\{0\bar{1}1\}$ <111>, as shown in Table 2.11 with the shear direction and the three Euler angles indicating the corresponding orientations (Gazder et al., 2006).

Figure 2.28 The {110} pole figure displaying ideal orientations observed during torsion tests (Gazder et al., 2006)

Table 2.11 Some important torsion ideal orientations (Shear direction (SD) is that of positive shear ($\theta$) axis) (Gazder et al., 2006)

| Orientation | SPN | SD[+] | $\varphi 1$ | $\Phi$ | $\varphi 2$ |
|---|---|---|---|---|---|
| D1 | $\{11\bar{2}\}$ | <111> | 125.3 | 45.0 | 0.0 |
| D2 | $\{\bar{1}\bar{1}2\}$ | <111> | 54.7 | 45.0 | 0.0 |
| E1 | $\{01\bar{1}\}$ | <111> | 39.2 | 65.9 | 26.6 |
| E2 | $\{0\bar{1}1\}$ | <111> | 90.0 | 35.3 | 45.0 |
| F | $\{110\}$ | <001> | 180.0 | 45.0 | 0.0 |
| J1 | $\{0\bar{1}1\}$ | $<\bar{2}11>$ | 30.0 | 54.7 | 45.0 |
| J2 | $\{1\bar{1}0\}$ | $<\bar{1}\bar{1}2>$ | 90.0 | 54.7 | 45.0 |

Baczynski and Jonas (1996) have observed an increase of D1$\{11\bar{2}\}$ <111> and a decrease of D2$\{\bar{1}\bar{1}2\}$<111> in textures measured in twisting under fixed end testing conditions with an increase of strain from 0.5 to 1.9 and consequently, D2 component will disappear at strain about 1.9. Texture evolution study of IF-steel (bcc) subjected to ECAE by Gazder et al. (2006) reported that texture developed by ECAE follows the simple shear deformation and increasing accumulated strain of IF-steel resulted in the strengthening of E1$\{01\bar{1}\}$<111> and D1$\{11\bar{2}\}$ <111> type components and the weakening of J2$\{1\bar{1}0\}$ < $\bar{1}\bar{1}2$ > orientations. A study on the microstructural evolution during FSP of pure iron by Mironov et al. (2008) revealed that the SZ resulted from a simple shear deformation exhibited D1$\{11\bar{2}\}$ <111> shear texture component and the stir zone is dominated by $\{11\bar{2}\}$ <111> slip. Texture analysis of friction stir welding of titanium alloys have been carried out recently and high temperature β texture of the stir zone has been reported to follow the simple shear texture of bcc materials (Reynolds et al., 2005a, Mironov et al., 2008, Knipling and Fonda, 2009; Pilchak, 2009; Fonda and Knipling, 2010; Pilchak and Williams 2011; Jiang et al., 2010; Davies et al., 2011). Reynolds et al. (2005a) examined the texture evolution of friction stir welding of β titanium alloy Timetal 21S sheets and they reported that the SZ texture has developed D2 shear texture component which agrees with the bcc torsion texture. Mironov et al. (2008a) has recently performed FSW of Ti-6Al-4V with a 500rpm rotating rate and a 60mm/min traverse speed and they found that retained β phase in the SZ has experienced simple shear deformation due to $\{110\}$<111> slip and shear texture component J2$\{1\bar{1}0\}$ < $\bar{1}\bar{1}2$ > was observed in retained β phase, however, results were based on a small scaled map. Knipling and Fonda (2009) investigated the texture of the weld exit hole of FSWed near α titanium alloys Ti-5111 and they reported that the high temperature reconstructed β phase and the inherited α phase both exhibit D2 shear texture component $\{\bar{1}\bar{1}2\}$<111>. Later on, Fonda and Knipling (2010) have reported that the deposited friction stir welds of near-α Ti-5111 alloy are dominated by hcp P1 $\{\bar{1}100\}$<11$\bar{2}$0 > shear texture at slow weld speeds due to the shear stress caused by the tool rotating and bcc D2 $\{\bar{1}\bar{1}2\}$<111> textures at the fast weld speed due to poor coupling at the deposited weld. Pilchak and Williams (2010) have observed that simple shear texture was developed in the fully lamellar structure of both the transition zone and stir zone, shear texture component consist of E1/E2 orientations with an intensity of 9.8 times random and the D2 component with an intensity of 4 times random.

Ahmed (2009) has developed a method to rotate the current dataset in the reference coordinate system (TD, WD, ND) into a new dataset in shear reference frame (FSW shear [θ, Z, r] reference frames) via a program written by Visual Basic. Net by two rotations, as shown in the following text: (1) a rotation α about the ND and (2) a tilt angle β about a direction perpendicular to the ND, which are shown schematically in Figure 2.29. In the weld centre, θ lies perpendicular to the WD and Z was tilted at an angle β; at the welding edges of the NG, θ is parallel to the WD for the AS and in the opposite direction for the RS.



(a)                                                                 (b)
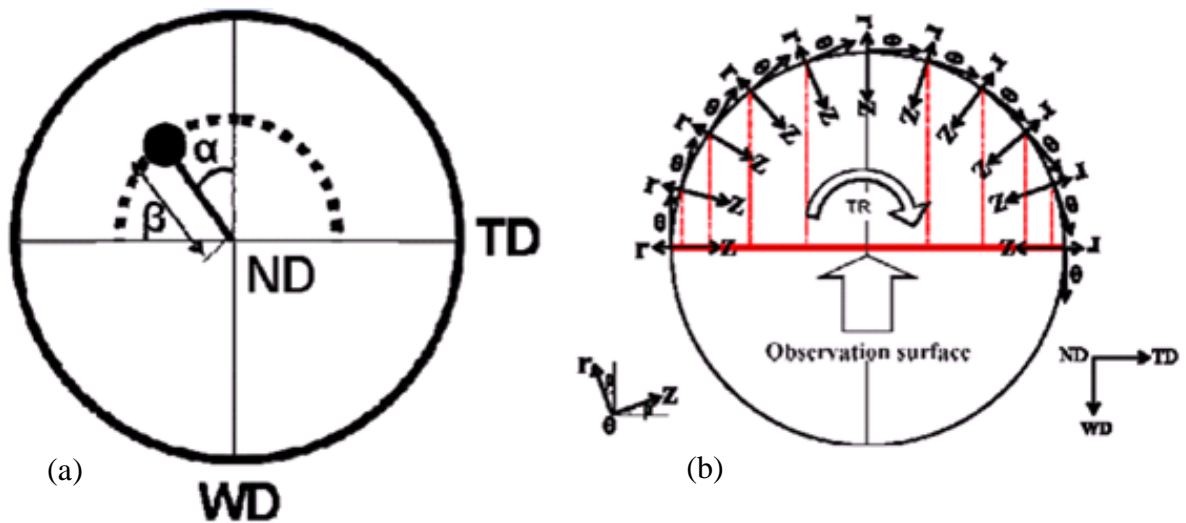
Figure 2.29 (a) Schematic diagram of the location of the intense (110) pole of the shear texture at angles α and β. Note that in the current analysis, α was considered positive for an anti-clockwise rotation about the ND and negative for a clockwise rotation; (b) Schematic diagram showing the FSW shear (θ, Z, r) reference frames (Ahmed, 2009)

To transform the reference coordinate system TD, WD, ND to the local θ, Z, r, a new orientation matrix Gr is defined as multiplying the two rotations from the original orientation matrix G: 1. Rα, which rotates G about ND by an angle α, as a rotation about ND of the shear reference frame; 2. Rβ, which rotates the new orientation matrix about TD through an angle β as tilted in shear reference frame for a tapered probe, whereas, for a parallel tool probe, β=0. Gr represents the orientation of the point of interest with respect to the local shear reference frame, and it is given by equation 2.11 (Ahmed, 2009).

$$Gr = GR_\alpha R_\beta \qquad\qquad (2.11)$$

Where $G$, $R\alpha$ and $R_\beta$ are shown in equation 2.12, in the present study using a parallel tool probe, $R_\beta$=1. The angle $\alpha$ is given by equation 2.13 (Ahmed, 2009).

$$G = \begin{bmatrix} g11 & g12 & g13 \\ g21 & g22 & g23 \\ g31 & g32 & g33 \end{bmatrix} \quad R\alpha = \begin{bmatrix} Cos\alpha & Sin\alpha & 0 \\ -Sin\alpha & Cos\alpha & 0 \\ 0 & 0 & 1 \end{bmatrix} \quad R_\beta = \begin{bmatrix} 1 & 0 & 0 \\ 0 & Cos\beta & Sin\beta \\ 0 & -Sin\beta & Cos\beta \end{bmatrix} \qquad (2.12)$$

$$\alpha = \sin^{-1}\left(\frac{X}{NGr}\right) \tag{2.13}$$

Where $X$ is the distance from the centre of the weld and $NGr$ is the radius of the NG at the point of interest. A visual basic program will be used to transfer the above transformations to the EBSD dataset.

## 2.7 Summary

This literature survey has shown that there have been a number of studies on the process, properties, microstructure and crystallographic texture in friction stir welded titanium alloys over the last 15 years. However, there have been very few studies conducted on SSFSW and general systematic studies of the effect of process parameters such as rotation speed and traverse speed. Moreover, there is still a significant understanding required to optimize this process in terms of microstructure in order to ensure good properties in service. Thus, the aim of this thesis is to understand microstructure and texture evolution in static shoulder weld joints and provide the optimum process parameters for best performance in-service.

## Chapter 3 Experimental procedure

### 3.1 Materials

The as-received material was Ti-6Al-4V (Timetal 6-4 ASTM Grade 5 Mil T-9047) in the form of 7mm thick plate provided by Timet UK limited with a test certificate and its composition is given in Table 3.1. The β transus ($T_β$) for this alloy is 996±14 ℃ (Timet, 2010).

Table 3.1 Chemical Analysis of As-Received Material (wt%) – Balance Ti

|  | Fe | V | Al | C | O | N | B | Y | OE | OT | ON |
|---|---|---|---|---|---|---|---|---|---|---|---|
| **Top** | 0.14 | 3.98 | 6.44 | 0.01 | 0.19 | 0.006 | <0.001 | <0.001 | <0.05 | <0.20 | 0.388 |
| **Bot.** | 0.16 | 4.05 | 6.49 | 0.01 | 0.17 | 0.005 | <0.001 | <0.001 | <0.05 | <0.20 | 0.36 |

OE = Others (impurities) Each

OT = Other (impurities) Total

ON = Oxygen + Nitrogen

The as-received microstructure (Figure 3.1) contained approximately 82 vol.% equiaxed $α_p$(average diameter of 17.3μm) and 18 vol.% retained β phase with no evidence of secondary α.
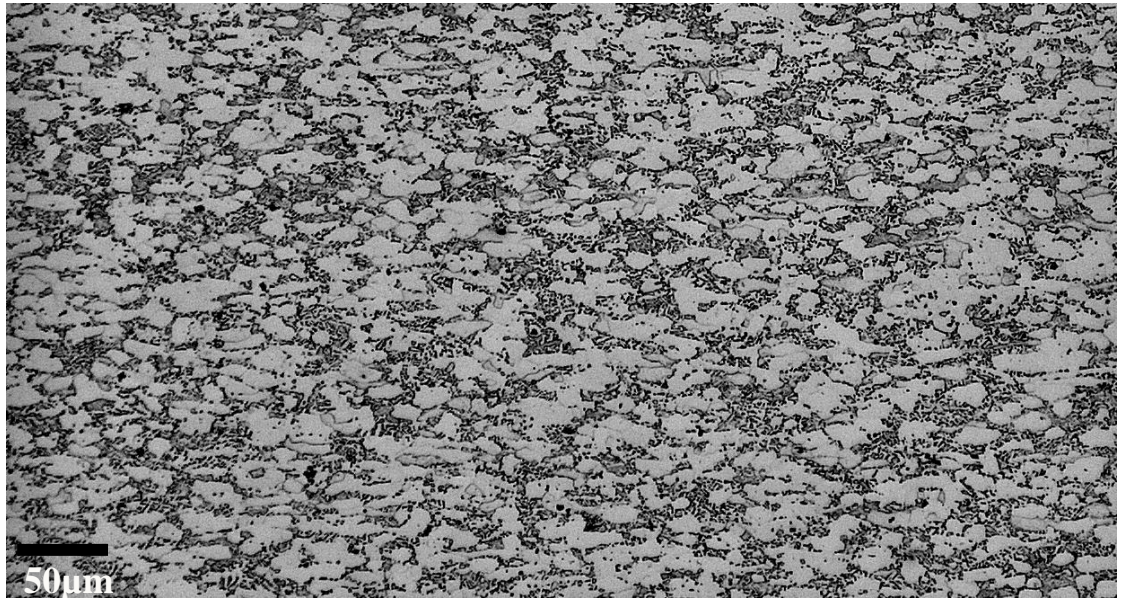


Figure 3.1 As-received as rolled base material microstructure

**3.2 Friction stir welding of Ti-6Al-4V**

3.2.1 Stationary shoulder friction stir welding

Stationary shoulder Friction stir welding (SSFSW) was carried out by TWI Ltd, Yorkshire, UK using a precision spindle RM2 FSW machine manufactured by Transformation Technologies Inc. (Figure 3.2). Detailed specifications of the machine are shown in Table 3.2. The machine possesses a moving table and a fixed rigid spindle head and highly concentric spindle designed specifically for welding with ceramic tool materials. A ceramic backing bar with less than 0.05mm flatness tolerance across the 0.5m traversing length was mounted on the machine table. All of the welds were performed in force control mode allowing the tool to maintain a consistent contact depth with the workpiece surface.

Table 3.2 The specification of the precision FSW machine

| Maximum downforce, kN | Maximum traverse force, kN | Maximum lateral force, kN | Spindle drive power, kW | Maximum rotation speed, rev/min | Maximum torque, N·m | Mode capability |
|---|---|---|---|---|---|---|
| 100 | 45 | 45 | 37 | 2250 | 225 | Force control |

The tool shoulder used for the welds was made of Si3N4 with 17.75mm diameter while the probe pin was made of Tungsten Rhenium (W-25%Re) of 6.1mm length and 9.8mm diameter with a 2mm radius. The shoulder and probe geometries are shown in Figure 3.2 and Figure 3.3, respectively. Three welds named as W4, W5, and W6 were made at a rotation speed of 900rpm and traverse speeds of 50mm/min, 100mm/min and 150mm/min and three welds named W19, W20 and W21 were made at a traverse speed of 150mm/min and rotation speeds of 800rpm, 600rpm, and 400rpm, respectively. Previous work at TWI (private communication Jonathan Perrett, TWI, 2009) has shown that a rotation speed of 900rpm and a traverse speed of 150mm/min produce a weld of high integrity. Thus welds W4, W5 and W6 were produced at conditions close to what was considered optimum. It was expected that heat input produced in these three welds would produce a peak weld

temperature above the $T_\beta$. Thus to investigate the possibility of sub β transus welding, welds W19, W20 and W21 were produced where there was an expectation that there would be a lower heat input, particularly for welds W20 and W21.

Rotation speed, traverse speed and forward movement revolution are shown in Table 3.3 for the six welds. Forward movement per revolution F (mm/rev) is defined as the ratio of traverse speed to rotation speed and it is a key parameter in optimising welding parameters (C. Dawes, TWI. Ltd) and F is given by equation 3.1.

$$F= \upsilon / \omega \qquad (3.1)$$

Where $\upsilon$ = traverse speed (mm/min), $\omega$ = rotation speed (rev/min)

All welds were done with the welding direction parallel to the rolling direction of the as-received material. Specimen welding axes for this research was defined using a similar convention for rolling i.e. welding direction (WD), transverse direction (TD) and normal direction (ND) as shown in Figure 3.4.
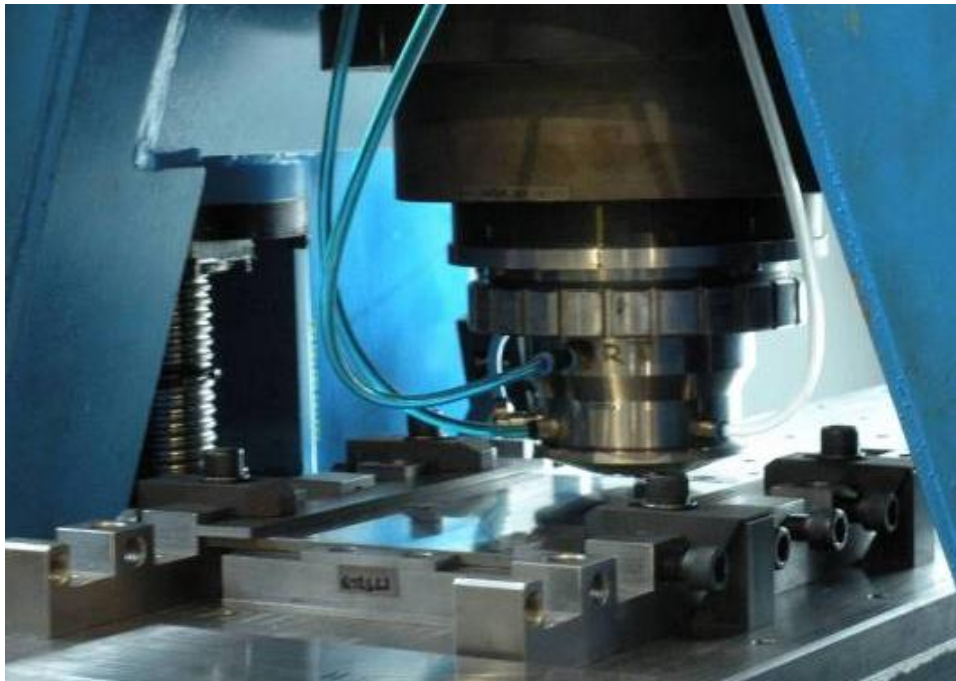


Figure 3.2 Photograph of the precision FSW machine
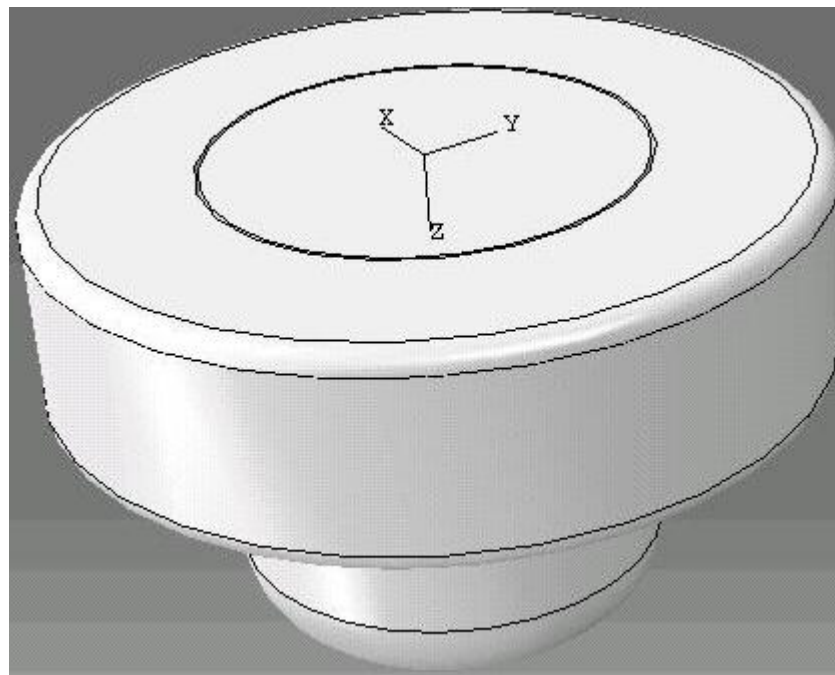
Figure 3.3 Shoulder and probe schematically show

Table 3.3 Welding parameters for the six welds in Ti-6Al-4V

| Weld No | Rotation speed ($\omega$), rev/min | Traverse speed ($\upsilon$), mm/min | Forward movement revolution ($\upsilon/\omega$), mm/rev |
|---|---|---|---|
| W4 | 900 | 50 | 0.056 |
| W5 | 900 | 100 | 0.111 |
| W6 | 900 | 150 | 0.167 |
| W19 | 800 | 150 | 0.189 |
| W20 | 600 | 150 | 0.25 |
| W21 | 400 | 150 | 0.375 |
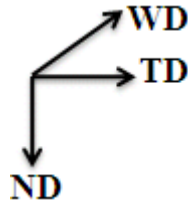
Figure 3.4 Specimen welding axes: welding direction (WD), transverse direction (TD) and normal direction (ND)

## 3.3 Analytical techniques

3.3.1 Sample preparation

*3.3.1.1 Sectioning and mounting*

Specimens were sectioned such that microstructure could be investigated perpendicular to the WD (cross sections), ND (normal sections) and TD (side sections). Normal sections, cross sections and side sections were analysed for the three welds with 900rpm rotation speed but only cross sections were analysed for the three welds with 150mm/min traverse speed.

A cutting plan of the three welds W4, W5, W6 is referred to Figure 3.5. In Figure 3.5, three cross sectional samples (A4, B4 and C4) sized 29mm×6mm×7mm were sectioned through the transverse direction of the entire weld zone from the adjacent regions along the weld length. Three cross sections (D4, E4 and F4) sized 29mm×10mm×7mm were sectioned in to 15 side sections, each cross section corresponds to five side sections, four of which were sized 10mm×6mm×7mm with another one sized 10mm×5mm×7mm; another three cross sections named G4, H4 and I4 were sized 29mm×10mm×7mm and cut into 9 normal sections and each of them was sized 29mm×10mm×2.333mm. Red lines drawn on the sections represent the regions to be investigated. Similar explanations can be found for all the sections of W5 and W6, as shown in Figure 3.5(b) and Figure 3.5(c). Surfaces to be investigated are indicated in Figure 3.6(a, b and c).

69

(a)

Cross sections

Normal sections

Side sections



(b)

Cross sections

Normal sections

Side sections

(c)

Cross sections

RS

AS

Side sections

Normal sections

RS

AS

Figure 3.5 Cutting plan for the three welds: (a) W4; (b) W5 and (c) W6



(a)

AS

A4 A5 A6

ND

RS

TD

WD

Observation surface

71
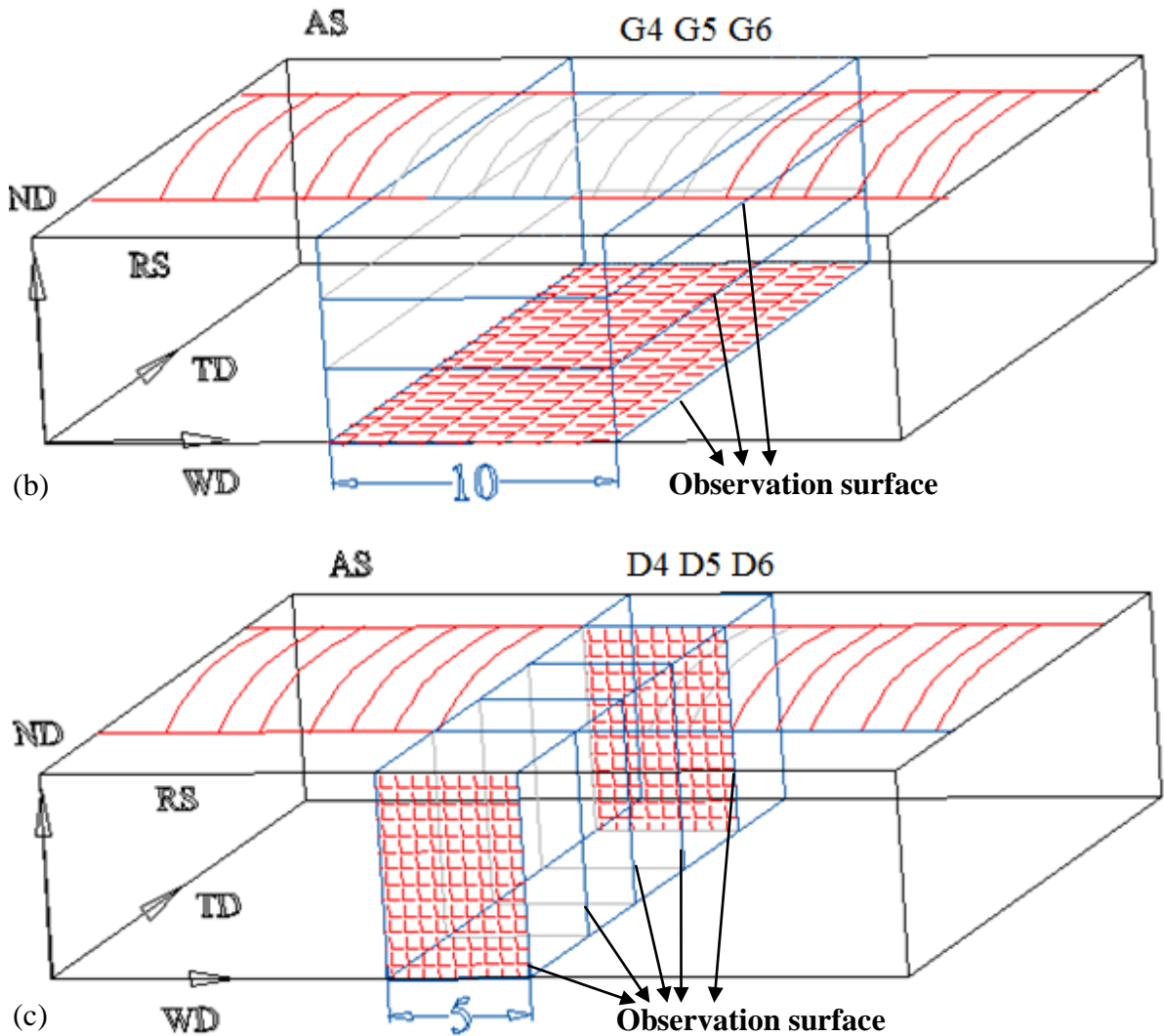
Figure 3.6 Surfaces to be investigated: (d) cross sections; (e) normal sections; (c) side sections

Sectioned samples were then mounted into a cylinder of 32mm diameter non-conducting Bakelite using standard procedures.

### 3.3.1.2 Grinding and polishing

The grinding and polishing procedures were carried out on an automatic Phoenix 4000 and Abramin sample preparation system. Progressively finer grades of silicon carbide grinding paper (240, 600, 800, 1200 grit) were used for grinding. After grinding, initial polishing was carried out with 9μm diamond suspension followed by final polishing using a polishing

72

cloth with a combined solution of 90% colloidal silco suspension and 10% hydrogen peroxide ($H_2O_2$, 30% w/v).

### 3.3.1.4 Etching

Etching was undertaken using the standard titanium etch of Kroll's Reagent consisting of 1-3ml hydrofluoric acid, 2-6ml nitric acid and 100ml water. Specimens were then immersed in the solution for about 15 seconds.

### 3.3.2 Surface roughness measurement

Surface profile measurements of the as-welded surface were undertaken using Surtronic 3+ device produced by Taylor Hobson pneum Ltd as shown in Figure 3.7. This enabled the production of surface profile maps of the as-welded surface by taking a number of linear profiles at 1mm intervals.



Figure 3.7 Taylor Hobson Surtronic 3+ 9V 112/1590 Surface Tester

### 3.3.3 Microhardness test

Microhardness hardness maps were produced for a number of samples using a MITUTOYO Microhardness Tester. In all cases maps were obtained from indentations at 0.5mm interval in the horizontal direction and 1mm interval in the vertical direction. A load of 0.3 kg was applied for 15 seconds.

### 3.3.4 Optical microscopy

Optical micrographs used for the study of the microstructure were taken using a Riechert Junge Polyvar B-Met.

### 3.3.5 Scanning electron microscopy (SEM)

To study the microstructures at higher magnifications, scanning electron microscopy was carried out using a field emission gun Inspect F and Sirion Scanning Electron Microscope (FEGSEM) at accelerating voltage of 15kV and spot size of 5 and micrographs were taken at secondary mode (SE) and backscattered mode (BSE).

### 3.3.6 X-ray energy dispersive spectroscopy (X-EDS)

FEI Inspect F and FEI Sirion Field Emission Gun scanning electron microscope were used to perform X-EDS provided by EDAX Inc. USA and X-EDS used the same image from the microscope.

### 3.3.7 Electron back scatter diffraction (EBSD)

EBSD systems produced by Oxford instruments HKL Denmark are fitted to FEI Sirion field emission gun Sirion microscope (FEGSEM) and FEI Inspect F FEGSEM. EBSD investigations are performed using FEI Sirion FEGSEM and FEI Inspect F FEGSEM. The FEGSEM is equipped with a HKL Nordlys CCD (Charge Coupled Device) video camera with solid state sensors, the data acquisition and processing are carried out using the HKL Channel 5 software. Channel 5 MapStitcher are used to create a large graph by stitching the individual maps together. Required dimension for the EBSD specimen is that width should be no more than 10mm and height no more than 5mm, length can be 10mm, 20mm, 30mm and 50mm depending on the sample holders. And the sample surface for EBSD should be free of surface layers or contaminations which are detrimental to the electron beam by sticking to the beam and deteriorating the EBSD Kikuchi patterns.

Parameters used in EBSD data acquisition for the present study are shown in Table 3.4.

Table 3.4 Parameters used in EBSD data acquisition for this work

| Parameters | Magnification | Beam Voltage | Timing per Frames | Step Size | Camera binning | Camera gain | No of bands |
|---|---|---|---|---|---|---|---|
| Value | 100-400 times | 20KeV | 8-12 | 0.2-2 µm | 4×4 pixels | High | 4-6 |

### 3.3.7 Manual measurements

#### *3.3.7.1 Linear intercept method for grain size measurement*

Grain size measurements by linear intercept method were developed for measuring the αp grain size and prior β grain size:

  1. αp grain size from the optical micrographs.

  2. Prior β grain size from the reconstructed Euler maps of high temperature β phase. The prior β grain boundaries are indicated by the grain boundary maps of the reconstructed EBSD maps

#### *3.3.7.1 Point counting method for volume fraction measurement*

  Point counting method was used to measure the volume fraction of the αp grains in the BM and the HAZ and the volume fraction of retained β phase in the SZ with 95% confidence limits, as shown in the following:

  1. Volume fraction of the αp grains in the base material with equiaxed structure and retained β phase in the HAZ with bimodal structure by Secondary electron micrographs.

  2. Volume fraction of the low temperature retained β phase in the SZ with lamellar structure by EBSD maps. Volume fraction measurement of retained β phase was done by point counting of pixels in Euler maps.

#### *3.3.7.3 α laths thickness measurement*

The thickness of the α laths is calculated as the equilibrium size using the classic Arrheius energy formulation at temperature T, as given in equation 3.2 (Charles and Järvstråt, 2008).

$$t^{eq}_{\alpha-lath} = ke^{-R/T}$$

(3.2)

The constant k is given by equation 3.3.

$$k=K_0 \exp (-Q_g/RT)$$

(3.3)

Where $K_0$ is a constant in which the specific interfacial energy of the grain boundary is included, Qg is the activation energy of the process, T is the temperature in Kevin degrees and R is the gas constant (Gil et al., 2001). The parameters $k$ =18433 and $R$=10044 (Charles and Järvstråt, 2008).

## 3.4 Summary

This chapter explains the friction stir welding experiments undertaken in addition to the experimental procedures to characterise the starting material and the weld zones in terms of sample preparation, SEM, EBSD, and descriptions of manual measurements of grain size, volume fraction and the thickness of the α laths.

**Chapter 4 Stationary shoulder friction stir welding of Ti-6Al-4V**

**4.1 Introduction**

In this chapter, the results of SSFSW with six welds of 7mm thickness using the same FSW tool but with varying traverse speeds and rotation speeds are presented and discussed. The cross sections, normal sections and side sections were examined using surface profile measurement and hardness test. Heat input was calculated according to the weld record and swept volume was calculated based on dimensions of the cross sections. The effect of the welding parameters on surface roughness, heat input, swept volume and microhardness were discussed.

4.1.1 Three welds with 900rpm rotation speed

Figure 4.1 shows the transverse view of the three butt welds made at a constant rotation speed of 900rpm and various traverse speed at 50mm/min (W4), 100mm/min (W5) and 150mm/min (W6), respectively, along the longitudinal direction.
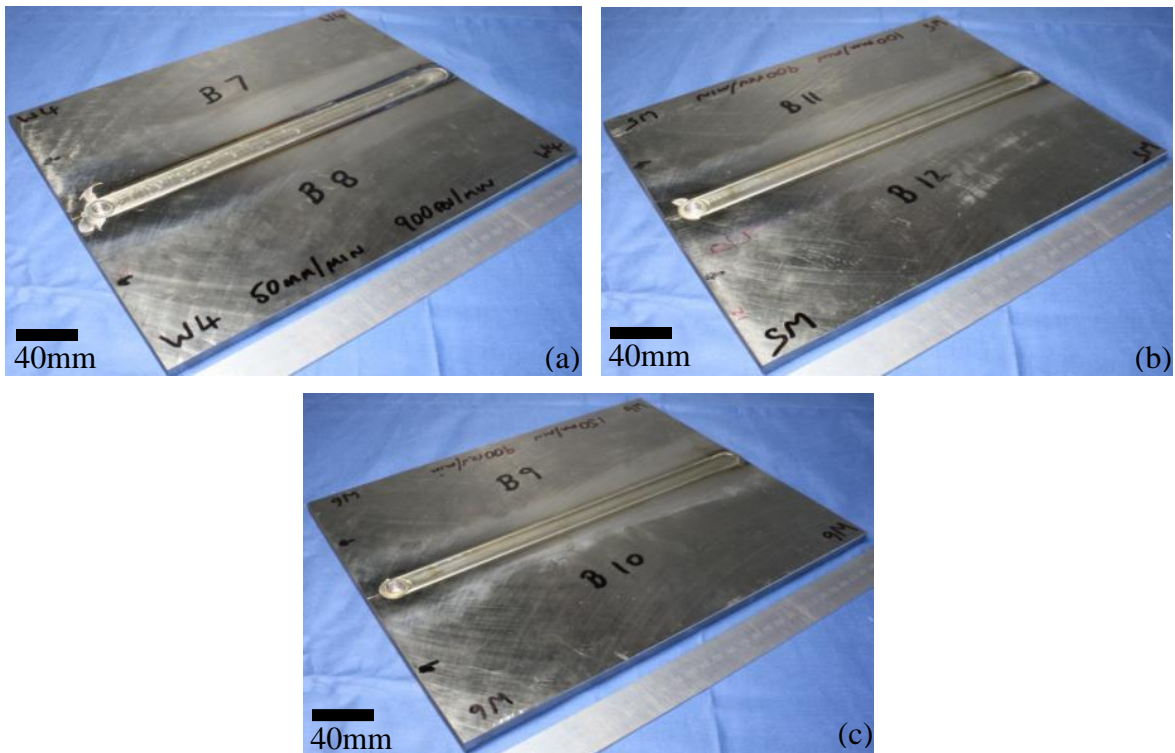


Figure 4.1 Photographs of the surfaces of the three welds (a) W4, (b) W5 and (c) W6

The FSW process parameters such as traverse force (X-force), down force (Z-force), pin depth, torque, traverse speed and rotation speed were recorded automatically by the friction stir welding machine and then output into Microsoft excel worksheets. Figure 4.2 shows the process parameters of the three welds W4, W5 and W6 given as a function of time.



(a)



(b)
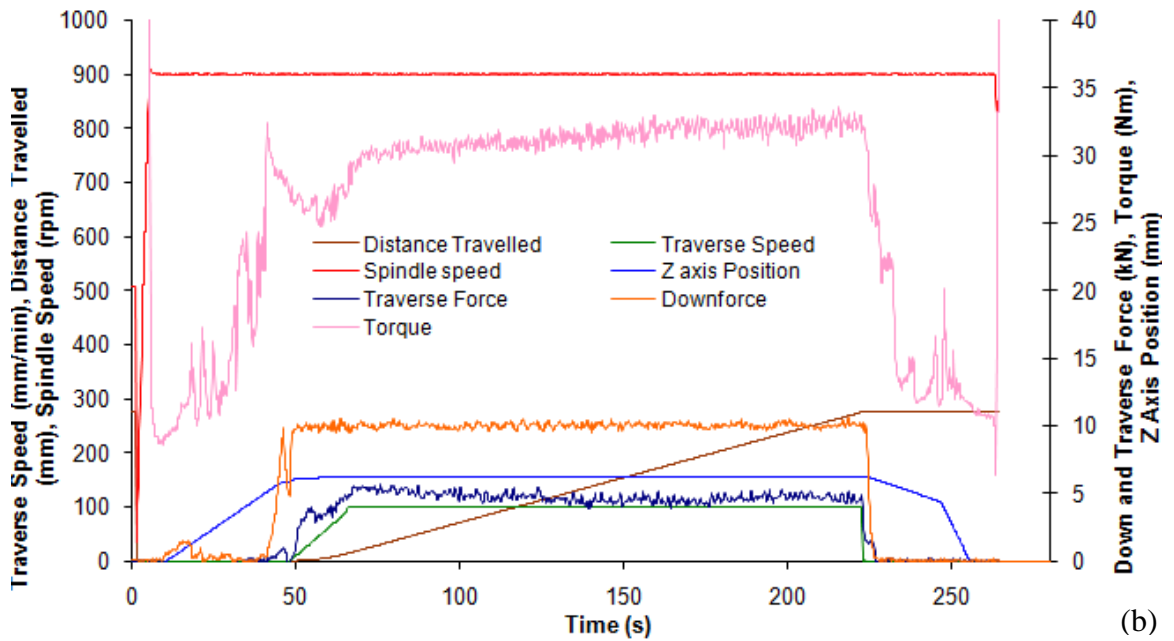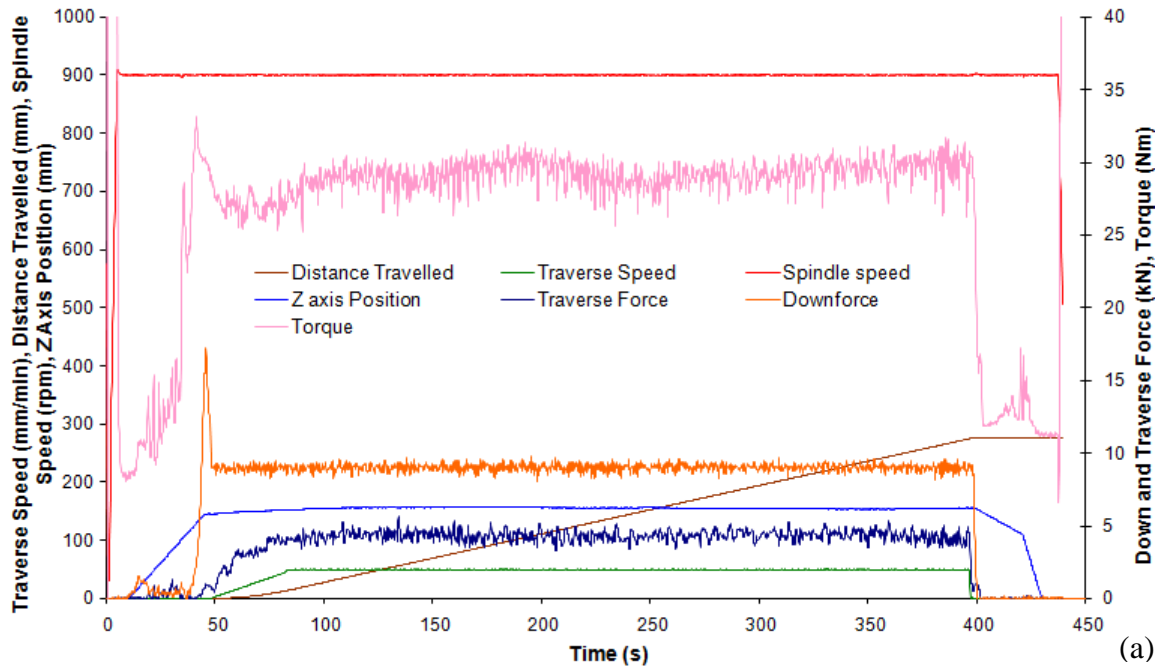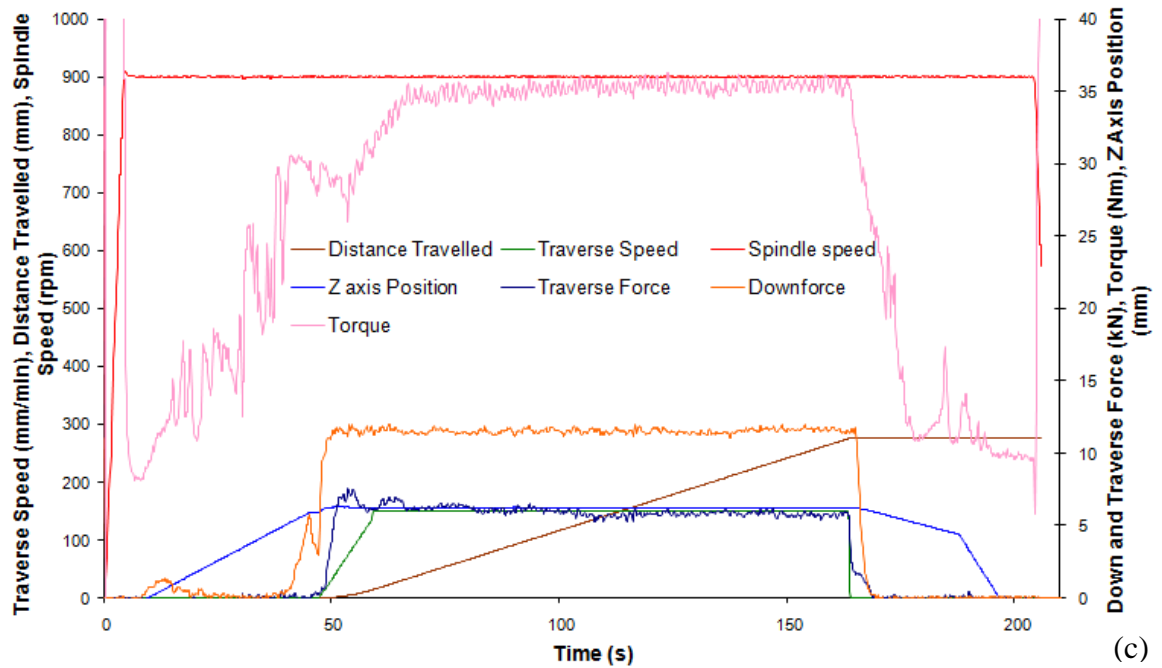
Figure 4.2 Weld records loaded at the three traverse speeds: (a) W4 (50mm/min); (b) W5 (100mm/min) and (c) W6 (150mm/min); Distance travelled (mm), Rotation speed (rpm), Z Axis position (mm), Down and Traverse Force (kN), Torque (N·m)

In order to find out how process parameters such as traverse force, downforce and torque influence weld integrity parameters such as process stability, porosity percentage and surface finish, the welding process parameters were referred to the average value, as shown in Table 4.1. Traverse force, down force and torque given as a function of position along the whole weld length (in mm) of the welds W4, W5 and W6 are shown in Figure 4.3.

Table 4.1 Average process parameters for the three welds W4, W5 and W6

| Weld No | Spindle Torque, N·m | Down Force, kN | Traverse Force, kN | Rotation speed, rev/min | Traverse speed, mm/min |
|---------|---------------------|----------------|--------------------|-----------------------|----------------------|
| W4 | 30 | 8.86 | 4.84 | 900 | 50 |
| W5 | 31.5 | 10.4 | 5.2 | 900 | 100 |
| W6 | 35.6 | 11.8 | 6.2 | 900 | 150 |
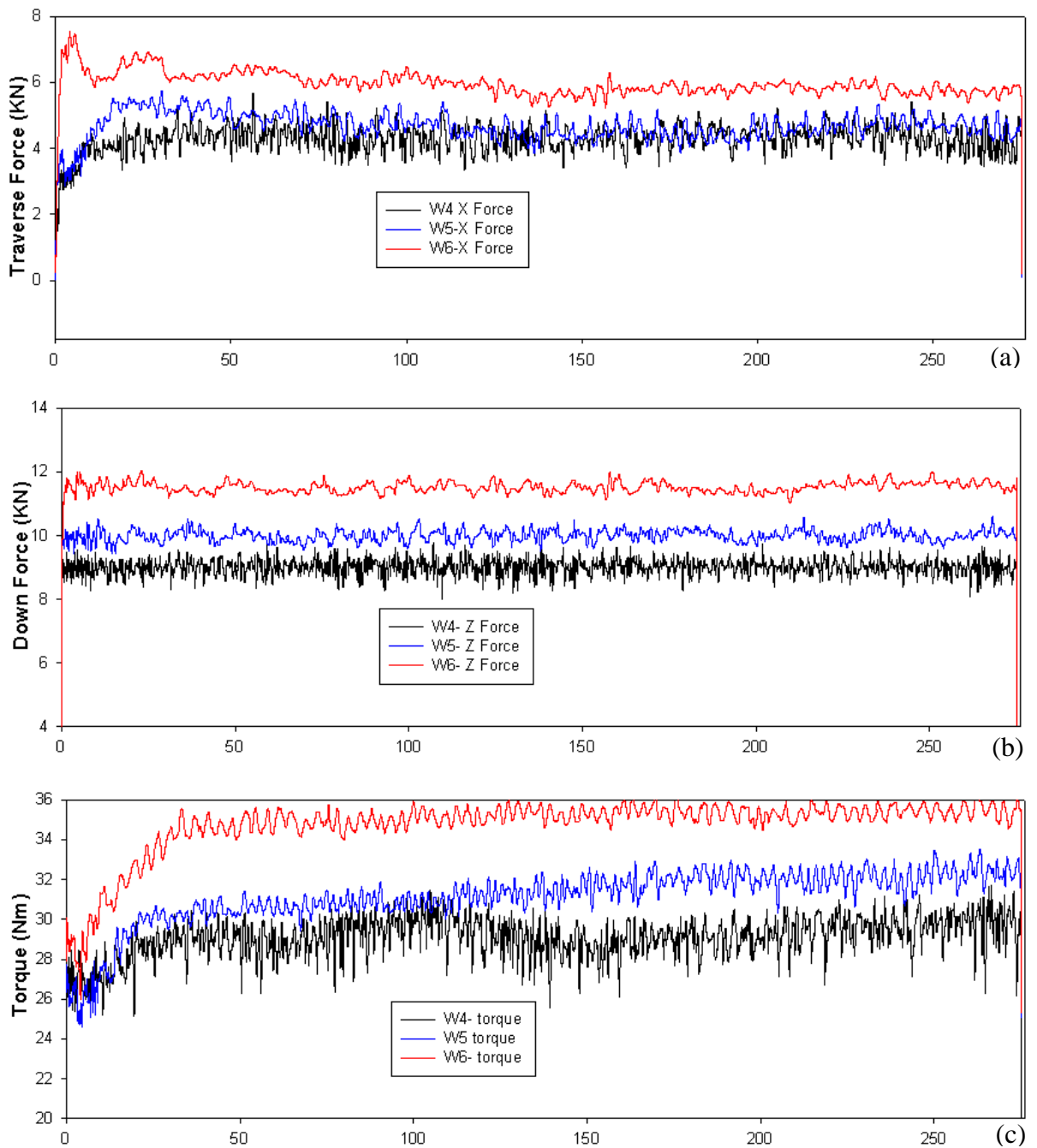
Figure 4.3 Traverse force, down force and torque given as a function of position along the whole weld length (in mm) of the three welds: (a) W4, (b) W5 and (c) W6

4.1.2 Three welds with 150mm/min traverse speed

Figure 4.4 shows photographs of the surfaces of the three butt welds W19, W20 and W21 made at a constant traverse speed of 150mm/min and various rotation speeds at 800rpm, 600rpm and 400rpm, respectively. The weld records of W19, W20 and W21 along the

whole weld length are displayed in Figure 4.5 showing the process parameters of the three welds W19, W20 and W21 given as a function of time, respectively. Welding process parameters shown in Figure 4.5 were referred to the average value of the parameters shown in Table 4.2. Traverse force, down force and torque given as a function of position along the whole weld length (in mm) of the welds W19, W20 and W21 are shown in Figure 4.6.
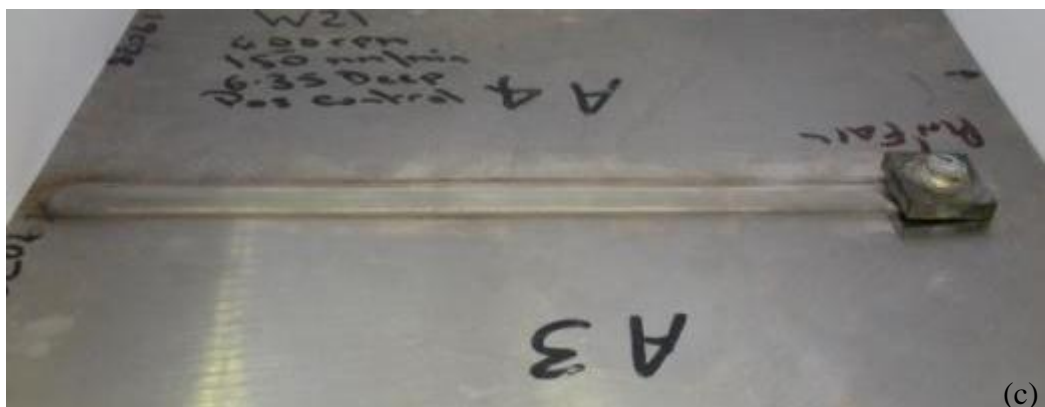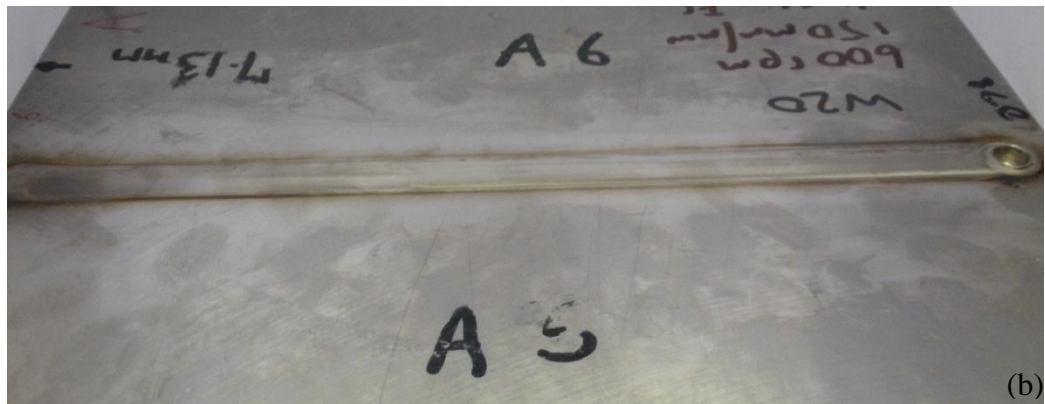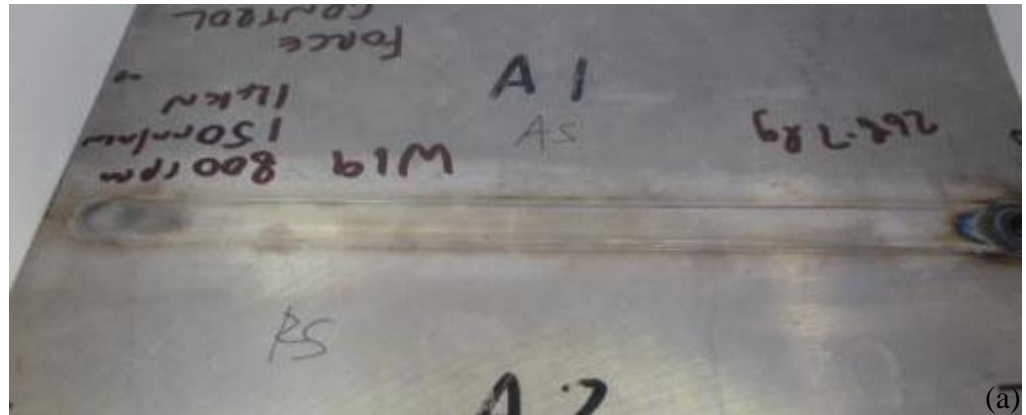
Figure 4.4 Photographs of the surfaces of the three welds: (a) W19 (800rpm); (b) W20 (600rpm); (c) W21 (400rpm)

(a)


(b)
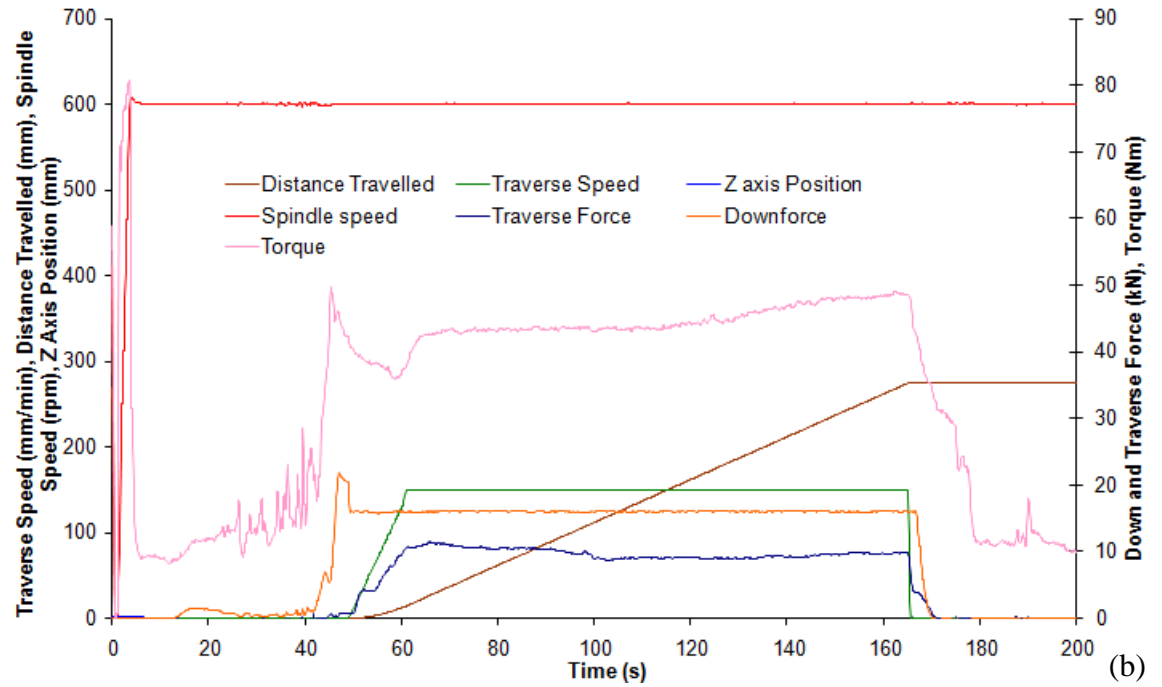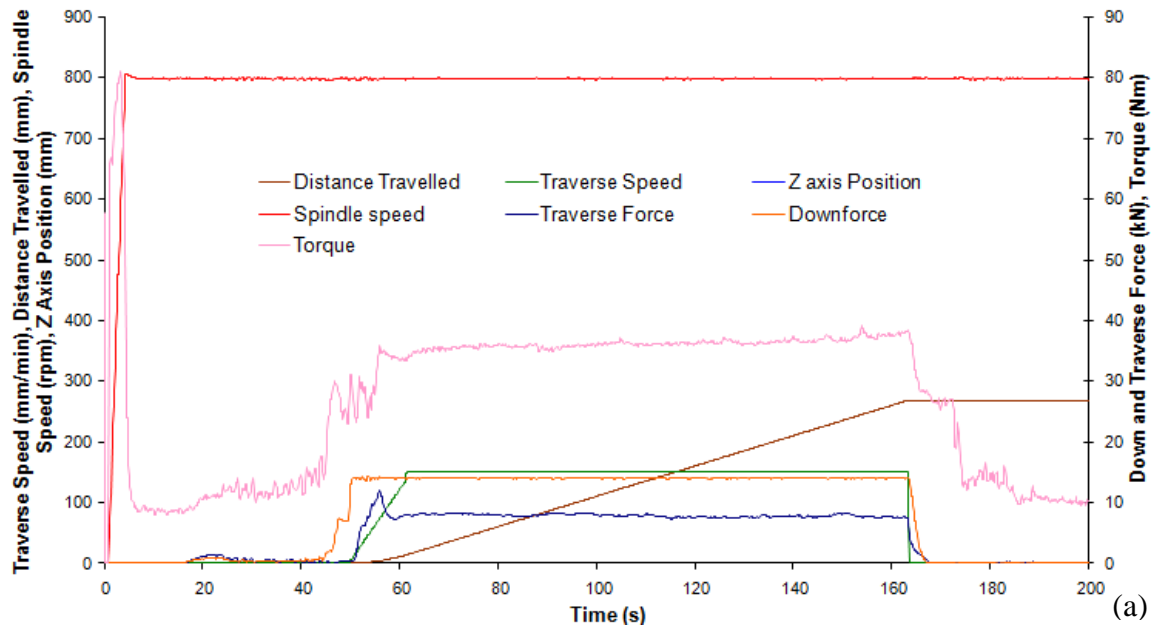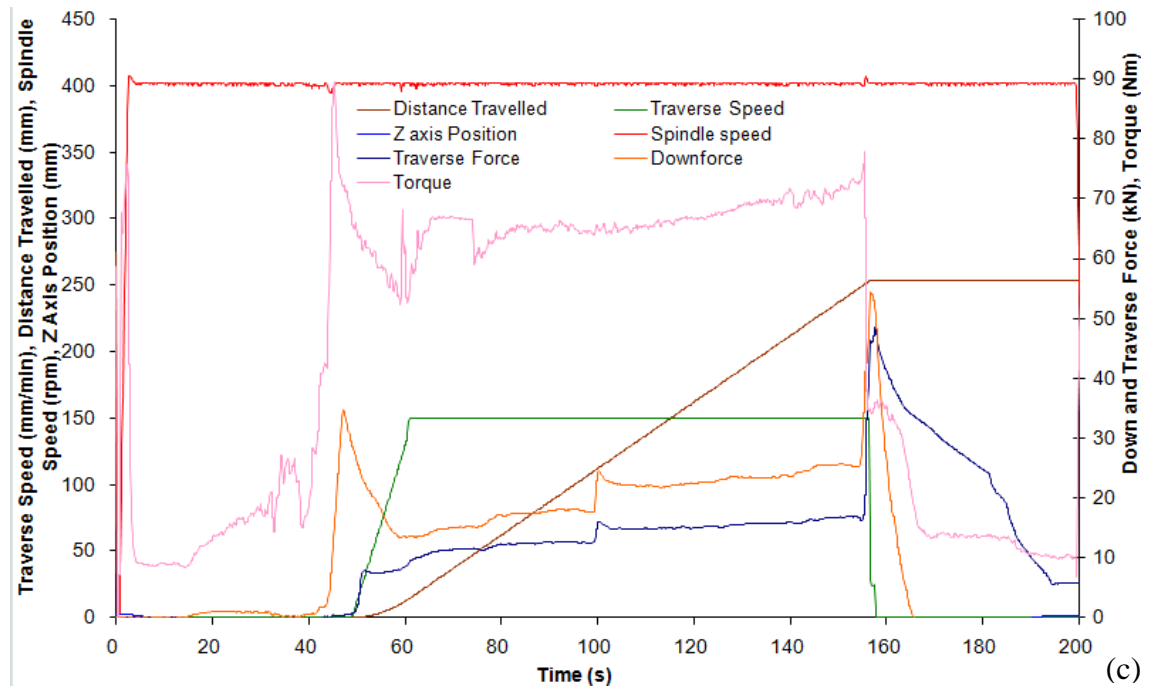
Figure 4.5 Weld records loaded at the three rotation speeds: (a) W19 (800rpm), (b) W20 (600rpm) and (c) W21 (400rpm); Distance travelled (mm), Rotation speed (rpm), Z Axis position (mm), Down and Traverse Force (kN), Torque (N·m)

Table 4.2 Average process parameters for the three welds W19, 20 and 21

| Weld No | Spindle Torque, N·m | Down Force, kN | Traverse Force, kN | Rotation speed, rev/min | Traverse speed, mm/min |
|---------|---------------------|----------------|--------------------|-----------------------|-----------------------|
| W19 | 36 | 14 | 8 | 800 | 150 |
| W20 | 40 | 16.5 | 10 | 600 | 150 |
| W21 | 65 | 18 | 15 | 400 | 150 |
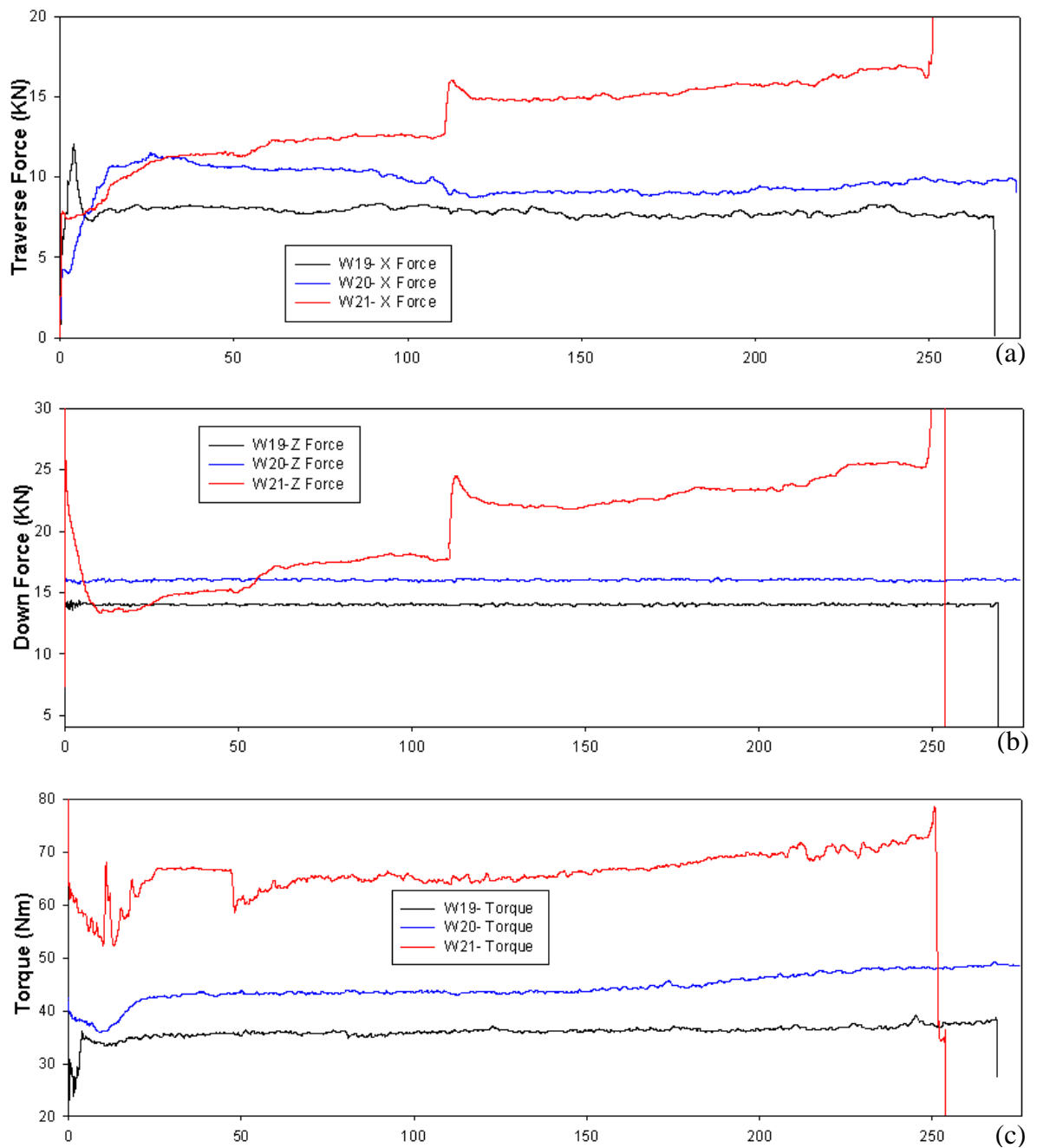
Figure 4.6 Traverse force, down force and torque given as a function of position along the whole weld length (in mm) of the welds: (a) W19 (800rpm), (b) W20 (600rpm) and (c) W21 (400rpm)

## 4.2 Calculation of heat input and swept volume

4.2.1 Heat input calculation

Heat input is important in determining the width of HAZ, the minimum strength in the weld region and it also influences other performance criteria, e.g. corrosion resistance, grain size,

84

formability (Threadgill and Martin, 2008), microhardness, surface quality and weld defects. Calculation of heat input is given by equation 4.1 and heat input was calculated from the original data of the weld records and the calculation method is given in equation 4.2 (Ahmed, 2009). This is the calculation for energy input. Heat input equation usually has an efficiency factor K, we assume K=1 because all the welds were done in the same condition. Thus, heat input equals to energy input.

Heat input (HI)= K*power/ travel speed= K*torque (T)×angular velocity ($\omega$) / travel speed ($\upsilon$)                                                                                                  (4.1)

Heat input (HI) = $\dfrac{\omega T}{\upsilon}$ =2π·r·T/(1000*V) (kJ/mm)                                                (4.2)

Where $\omega = \dfrac{2\pi r}{60}$, HI is the heat input, kJ/mm; K is the efficiency factor=1; T is the torque, N·m; r stands for rotating speed, rev/min (rpm) and $\upsilon$ is the traverse speed, mm/min.

Heat input line profiles of the six welds W4, W5, W6, W19, W20 and W21 along the whole welding distance are shown in Figure 4.7 and Table 4.3 shows the average heat input for each weld. The key point from these results is that the three welds W19, W20 and W21 have similar heat input as that of the optimum weld W6 suggesting that sub β transus welding may not have been achieved.
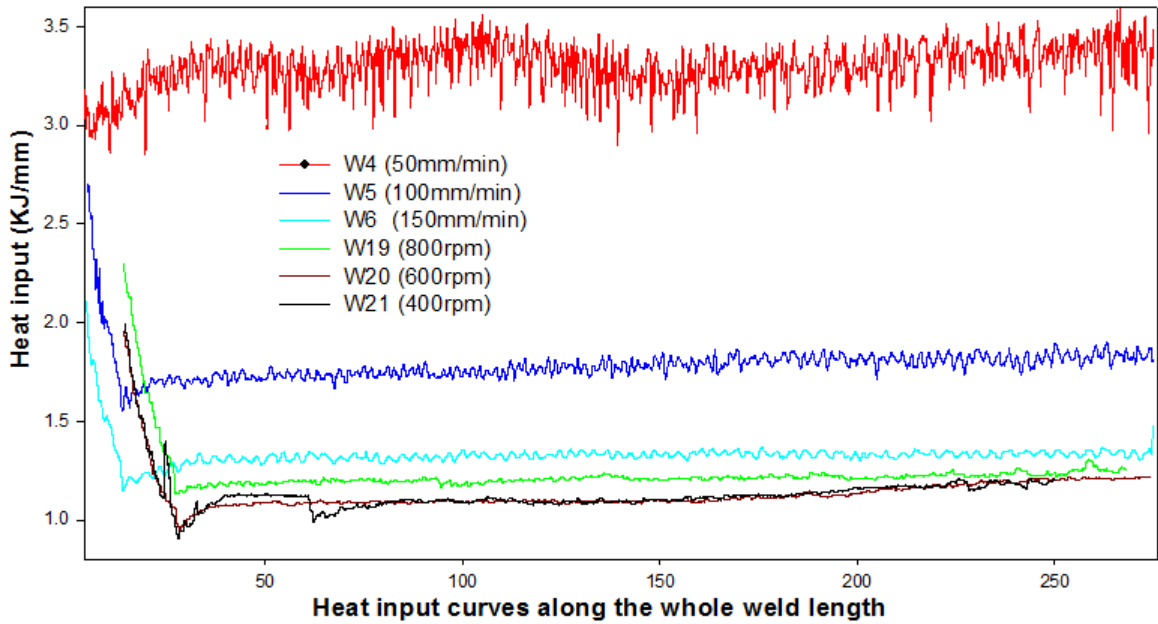
Figure 4.7 Heat input line profiles of all the six welds W4, W5, W6, W19, W20 and W21 along the whole weld length

Table 4.3 Average heat input of all the six welds

| Weld No | W4 | W5 | W6 | W19 | W20 | W21 |
|---|---|---|---|---|---|---|
| Average Heat input, kJ/mm | 3.29 | 1.79 | 1.33 | 1.23 | 1.13 | 1.12 |

4.2.2 Swept volume calculation

Swept volume is the volume of the material swept by the tool in each revolution and it is given by equation 4.3 (Adapted from TWI).

Swept volume $(mm^3/rev)$ = Swept area $(mm^2)$ x Forward movement revolution (mm/rev)     (4.3)

Figure 4.8 and Figure 4.9 show the schematic cross sectional view of the weld zones of all the six welds W4, W5, W6, W19, W20 and W21, respectively, and characterization of the weld zones will be given in Chapter 5 in terms of microstructure. As seen in Figure 4.8

and Figure 4.9, all the weld zones have a basin-like shape and a narrow region showing joint lines consisting of inner joint line and outer joint line in the welding edge at both AS and RS. In this way, the swept area becomes the region encircled by the two inner joint lines at the AS and the RS, the weld surface and the weld bottom. In order to calculate the swept volume, the weld zones were put in a coordinate system, and then the inner joint lines and the coordinates constitute the mathematic allotropic curves. After few trials of curve simulation, the allotropic curve approaches to the curve $y=ax^4+c$.

Thus the swept area A is given in equation 4.4:

$$A= 7W-2\times\int_{S}^{E}(ax^4+c)dx=7W-2\{a(E^5-S^5)/5+c(E-S)\} \tag{4.4}$$

And swept volume V is given in equation 4.5:

$$V=\text{Swept area}\times \text{Forward movement revolution} = A*v/\omega \tag{4.5}$$

Swept volume calculation results of all the six welds are shown in Table 4.4.

Table 4.4 Swept volumes of all the six welds W4, W5, W6, W19, W20 and W21

| Weld No | W, mm | S, mm | E, mm | $y=ax^4+c$ | Swept area A, mm$^2$ | Swept volume V, mm$^3$/rev |
|---------|-------|-------|-------|------------|--------------------|--------------------------|
| W4 | 17.75 | 6.5 | 8.875 | $0.0016x^4$-2.828 | 109.86 | 6.15 |
| W5 | 17.75 | 5.5 | 8.875 | $0.0013x^4$-1.211 | 106.42 | 11.82 |
| W6 | 17.75 | 5.25 | 8.875 | $0.00128x^4$-0.98 | 105.74 | 17.66 |
| W19 | 17 | 5 | 8.5 | $0.00152x^4$-0.95 | 100.57 | 19 |
| W20 | 16 | 4.5 | 8 | $0.0019x^4$-0.779 | 95.512 | 23.88 |
| W21 | 15 | 4 | 7.5 | $0.00241x^4$-0.616 | 95.14 | 35.74 |
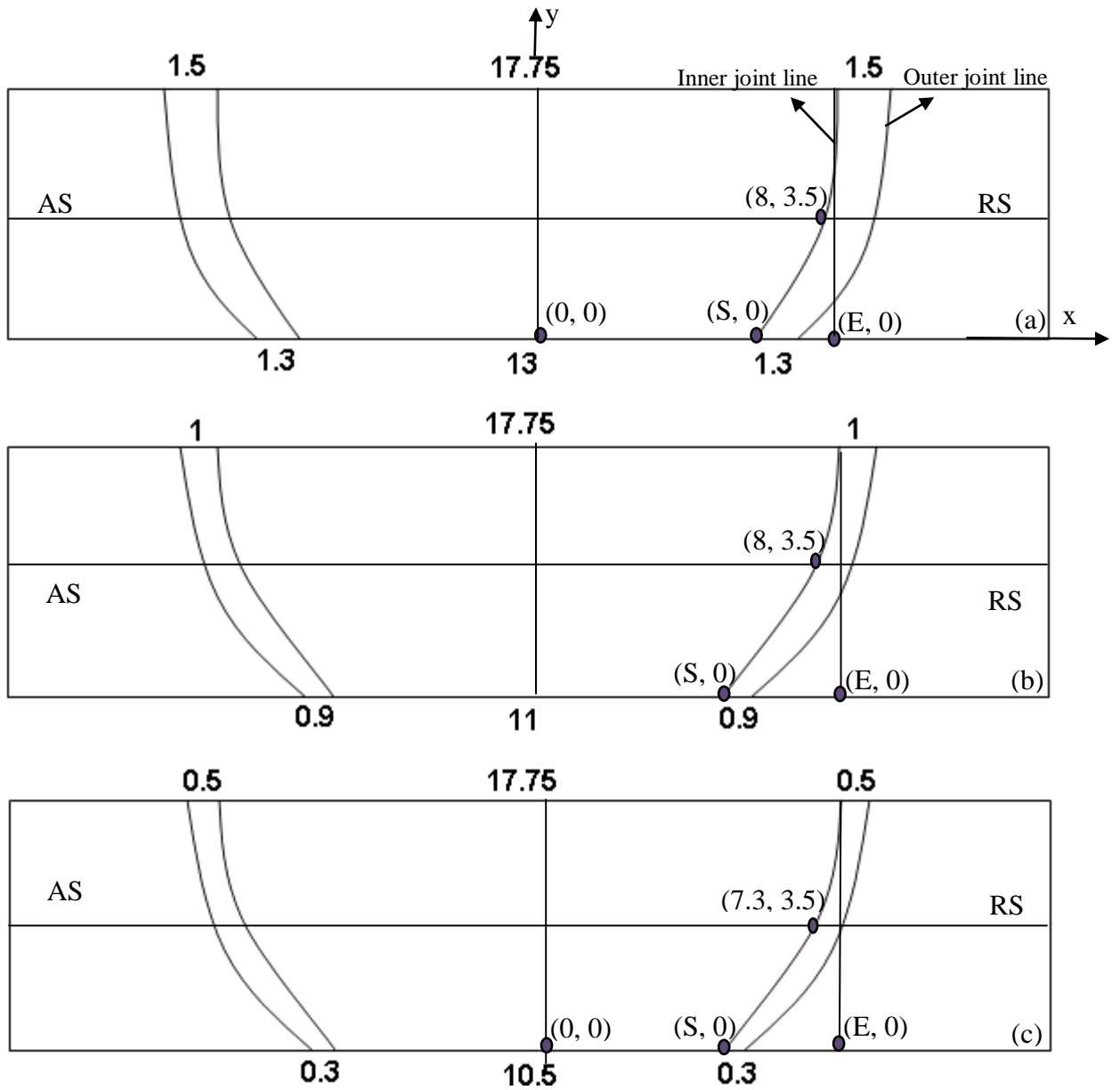
Figure 4.8 Schematic cross sectional view of the weld zones of (a) W4, (b) W5 and (c) W6
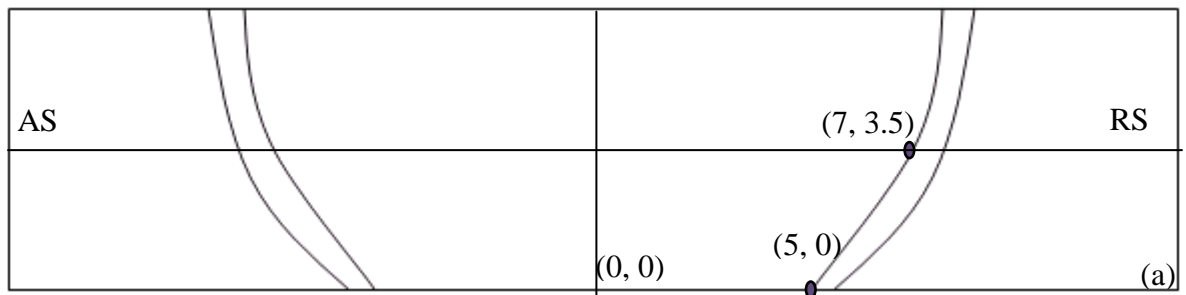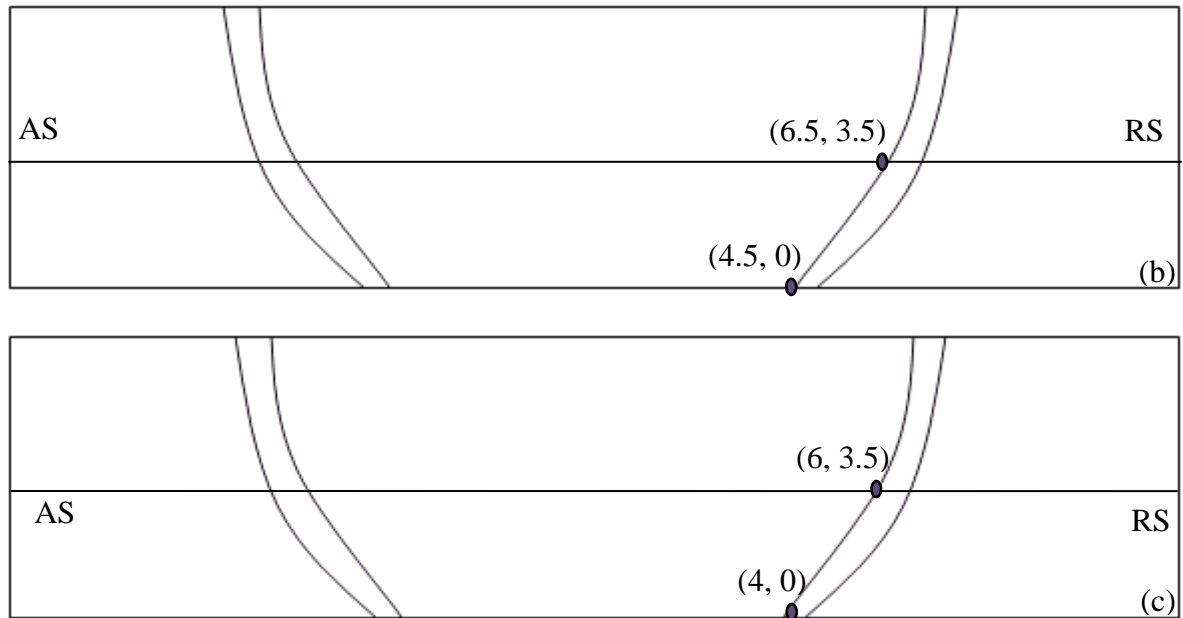
Figure 4.9 Schematic cross sectional view of the weld zones of (a) W19, (B) W20 and (c) W21

## 4.3 Surface profiles of the welds

4.3.1 Surface profiles of W4, W5 and W6

All three welds with a constant rotation speed of 900rpm were free of macroscopic defects. Figure 4.10 shows the photographs of the weld surface of the three welds W4, W5 and W6 with a constant traverse speed. Microscopically, all the three welds had relatively flat surfaces, but there are rings observed at the weld surfaces of all the three welds, which are associated with the rotation of the tool. It is seen that the ring spacing was most irregular at the slowest traverse speed whilst at the highest traverse speed the ring spacing became more uniform. Line profiles of transverse sections exported as three dimensional graphs by Sigma plot 10.0 were used to reveal surface roughness of the weld surfaces along the whole weld length, as shown in Figure 4.11. Figure 4.11 again suggests that ring spacing was most irregular at the slowest traverse speed and it became much more uniform with increasing traverse speed from 50 to 100 and 150mm/min. However, Figure 4.11(c) shows that W6 has a bump at the AS of the weld surface due to insufficient down force.

| W4(50mm/min) | W5(100mm/min) | W6(150mm/min) |
|---|---|---|
| | | |
| | 10mm | WD ← |
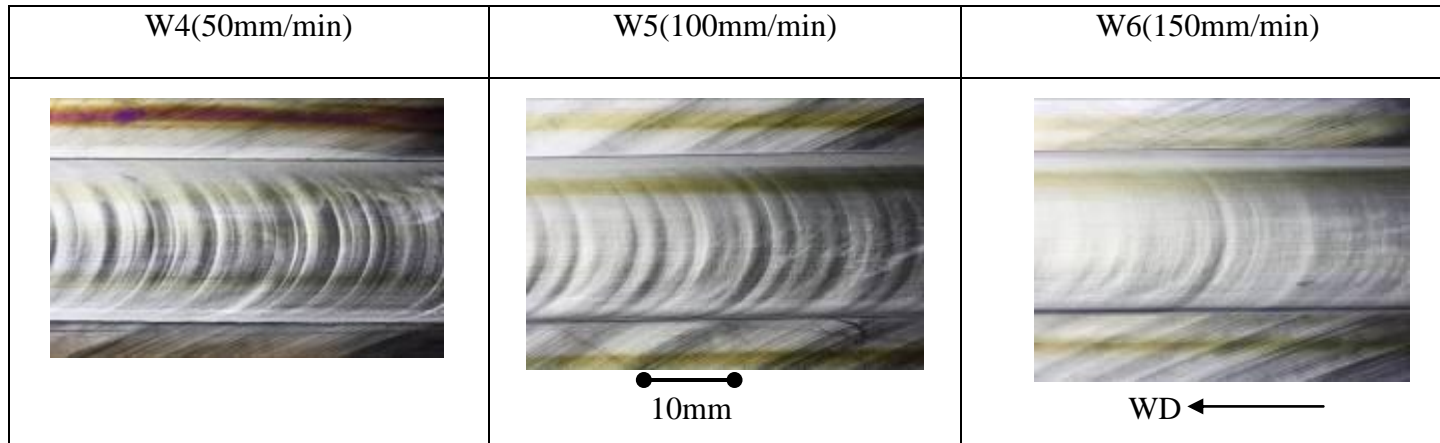
Figure 4.10 Photographs of the weld surface of the three welds W4, W5 and W6, up RS down AS, black arrow indicates the welding direction (WD)



(a)
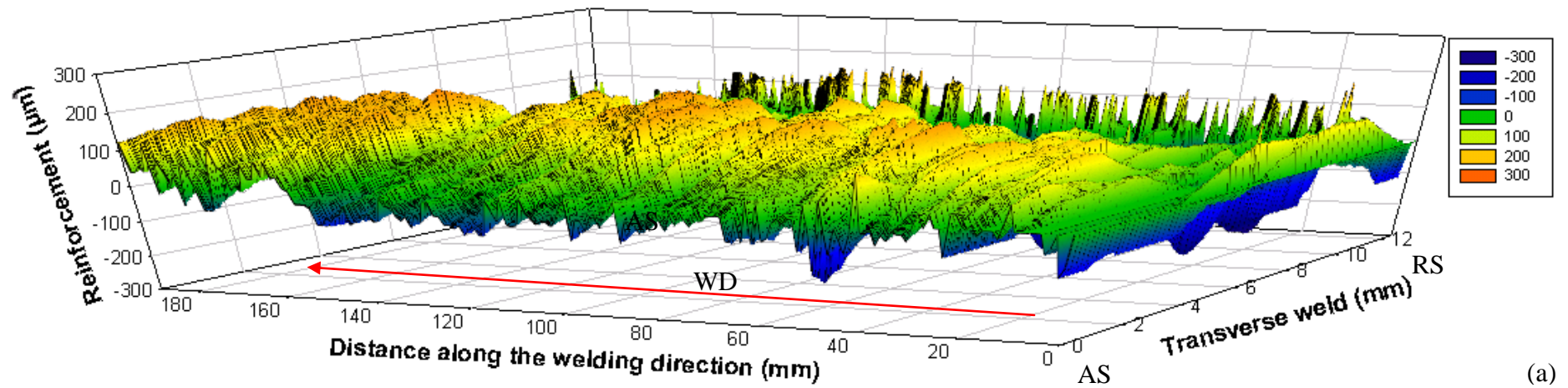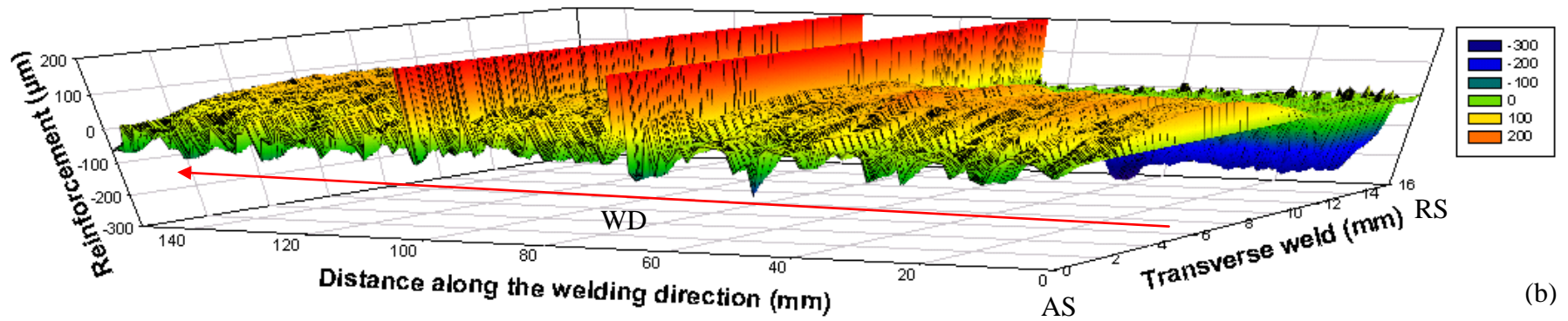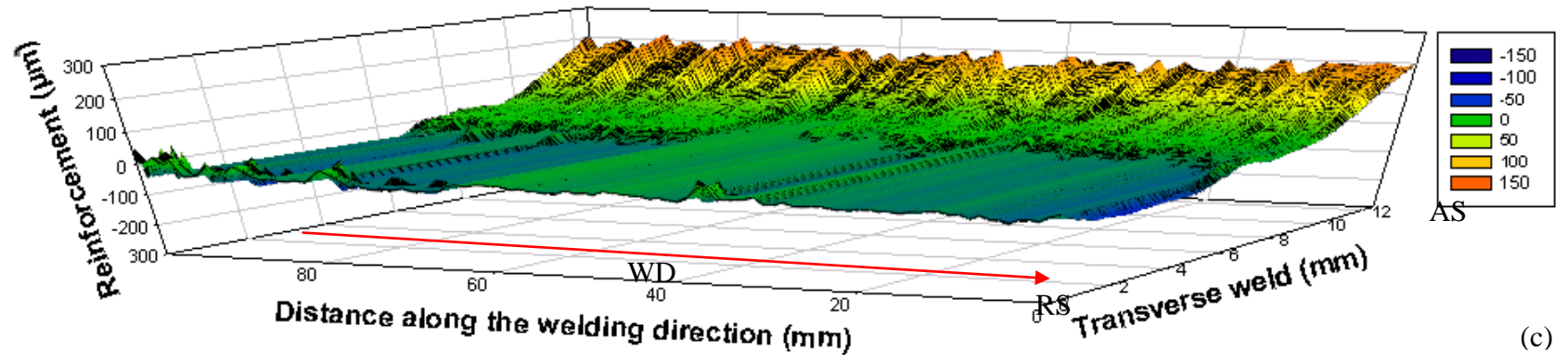
Figure 4.11 Surface profile maps along the whole weld length of (a) W4, (b) W5, and (c) W6, 150mm/min; red arrow indicates the WD

4.3.2 Surface profiles of W19, W20 and W21

Figure 4.12 shows the photographs of the weld surface of the three speeds W19, W20 and W21 with a constant traverse speed of 150mm/min. It can be seen that surfaces were smooth in W19. However, in W20 and W21, material has not been fully penetrated at the RS showing a concave gap of 0.5mm depth at the RS of the cross sections of W20 and W21. It was shown in Section 4.3.1 that the weld W6 has a bump at the AS of the weld surface due to insufficient down force of 11.8kN. This problem was eliminated in the W19 using a higher down force of 13.9kN and a slower rotation speed of 800rpm.

| W19 (800rpm) | W20 (600rpm) | W21 (400rpm) |
|---|---|---|
|  |  10mm |  WD |
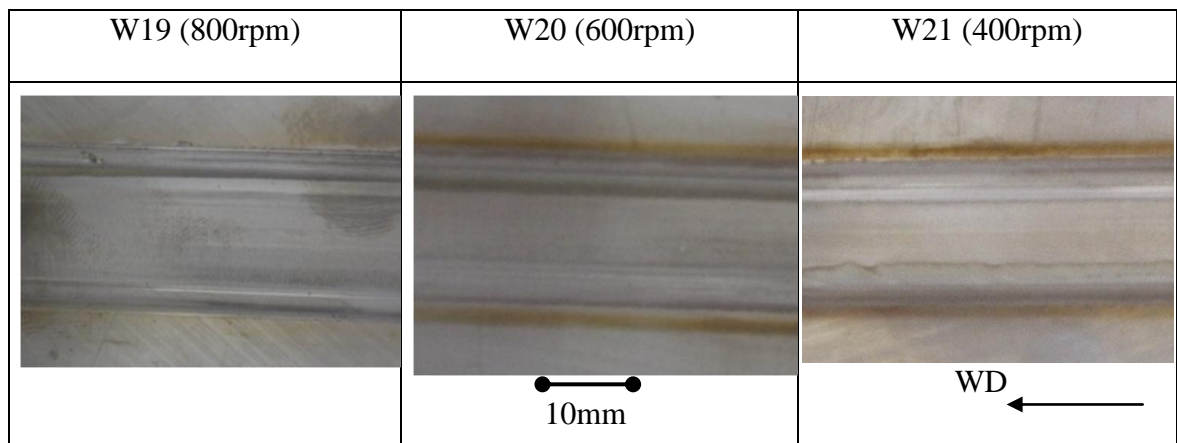
Figure 4.12 Photographs of the weld surface for the three speeds with a constant traverse speed, black arrow indicates the welding direction (up RS down AS)

## 4.4 Microhardness profiles

Microhardness tests were carried out on the cross sections, side sections and normal sections at 0.5mm interval in horizontal direction and 1mm interval in vertical direction for the three welds W4, W5 and W6 with 900rpm rotation speed. The cross sections cut from the three traverse welds were named as W4A4, W5A5 and W6A6, respectively. The normal sections were taken from the weld surface, the weld centre and the weld bottom, respectively, and the side sections were sectioned 6mm to the weld edge at both the AS and the RS. All the sections are indicated in the cutting plan as shown in Figure 4.13 and a detailed cutting plan is referred to the experimental procedure in Chapter 3. There are one cross section, three normal sections and five side sections for each weld, and each section

was used for three times for microhardness test, microscopy and EBSD, respectively, resulting in 81 samples for all the sections of three welds W4, W5 and W6, e.g., for microhardness test of the weld W4, cross section was named W4A4; 4.6.a, 4.7.a and 4.8.a were named for the normal sections; the side sections of W4 were named as 4.1.a, 4.2.a, 4.3.a and 4.4.a, where 4.1.a and 4.4.a were cut from the AS of the welding edge and the RS of the welding edge, respectively, 4.2.a and 4.3.a were from the stir zone. Similarly, the side sections of W5 named as 5.1.a, 5.2.a, 5.3.a and 5.4.a: 5.1.a and 5.4.a were cut from the AS of the welding edge and the RS of the welding edge, respectively, 5.2.a and 5.3.a were from the stir zone, 5.6.a, 5.7.a and 5.8.a were for the normal sections. And the side sections of W6 were named as 6.1.a, 6.2.a, 6.3.a and 6.4.a: 6.1.a and 6.4.a were cut from the AS and the RS of the weld edge, respectively, and 6.2.a and 6.3.a were from the stir zone.
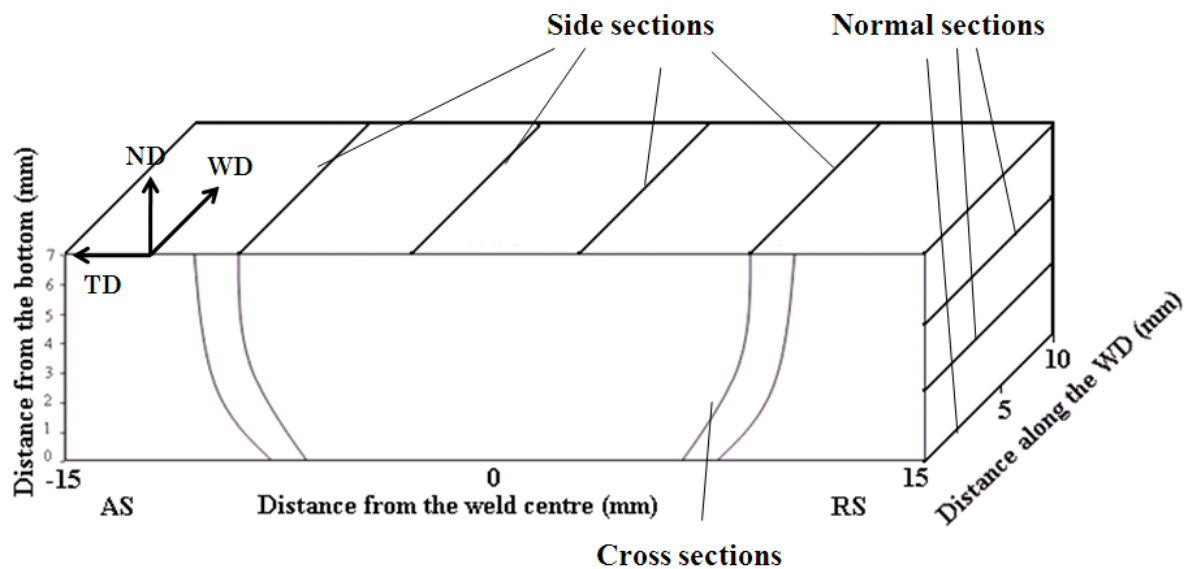


Figure 4.13 Illustration of the sectioning of side sections and normal sections of the welds W4, W5, W6

4.4.1 Microhardness profiles of W4, W5 and W6

Microhardness tests on the cross sections, the side sections and the normal sections were carried out with 0.5mm interval in horizontal direction and 1mm interval in vertical direction for all the three welds W4, W5 and W6 with a constant rotation speed of 900rpm.

Microhardness profiles of the cross section, side sections and normal sections of W4 are shown in Figure 4.14. Figure 4.14(a) shows the microhardness profile of the weld W4 taken from the cross section of the weld W4 (W4A4). Figure 4.14(b), Figure 4.14(c), Figure 4.14(d) and Figure 4.14(e) are the microhardness profiles of the side sections 4.1.a, 4.2.a, 4.3.a and 4.4.a, respectively. Figure 4.14(f) shows the microhardness profile of the bottom normal section 4.8.a. It should be noted that the higher hardness surface layer of 1.4mm deep observed at the weld surface exhibits interweaved region of higher hardness and lower hardness as shown in 4.2.a (Figure 4.14(c)) where the distance between the high hardness regions corresponds to the width between spaced rings at the weld surface. Thus, interweaved regions of higher and lower hardness observed on the surface of 4.2.a (Figure 4.14(c)) corresponded to the spaced rings observed in the weld surface of W4 (Figure 4.1(a)).



(a)



(b)



(c)
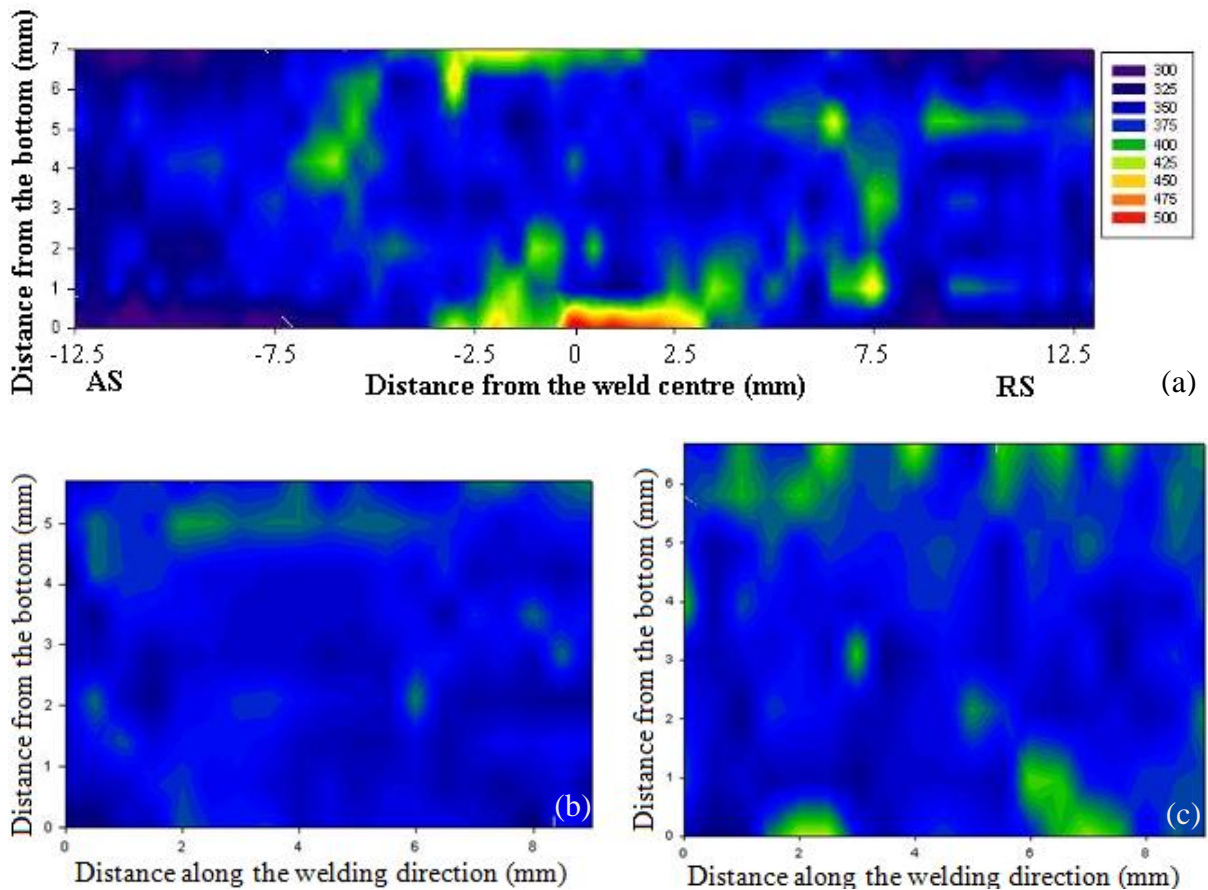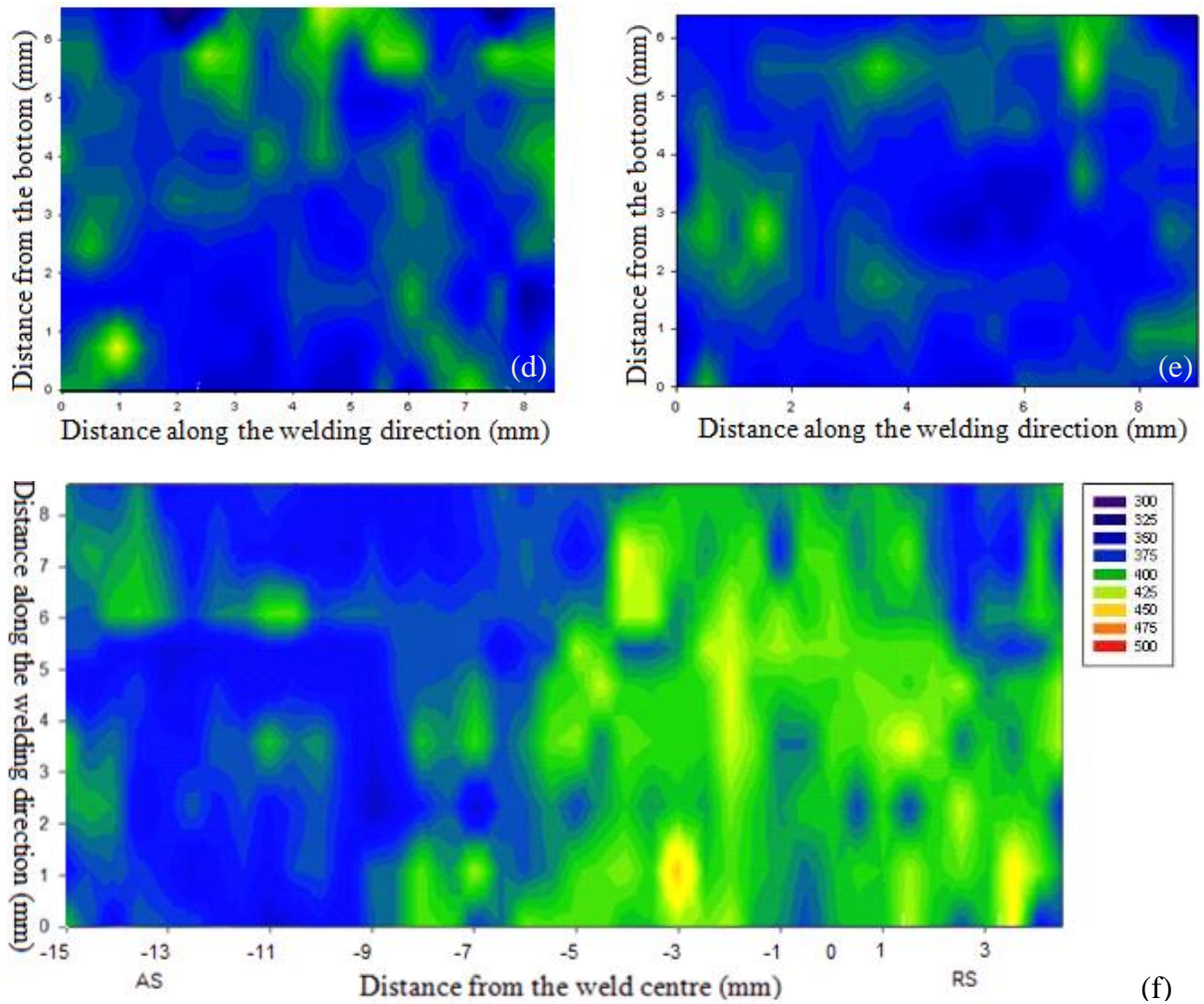
Figure 4.14 Microhardness profile of the cross section: (a) W4A4; the side sections: (b) 4.1.a, (c) 4.2.a, (d) 4.3.a, (e) 4.4.a and the normal section: (f) 4.8.a

Figure 4.15 show the microhardness profiles of the cross section, side sections and normal sections of the weld W5. Figure 4.15(a) is the microhardness profile of the cross section W5A5. Figure 4.15(b-e) show the microhardness profiles of the side sections 5.1.a, 5.2.a, 5.3.a and 5.4.a, respectively. Microhardness profiles of the normal sections 5.6.a, 5.7.a and 5.8.a are displayed in Figure 4.15(f), (g) and (h), respectively.

(a)

(b)

(c)

(d)

(e)

(f)

(g)



(h)
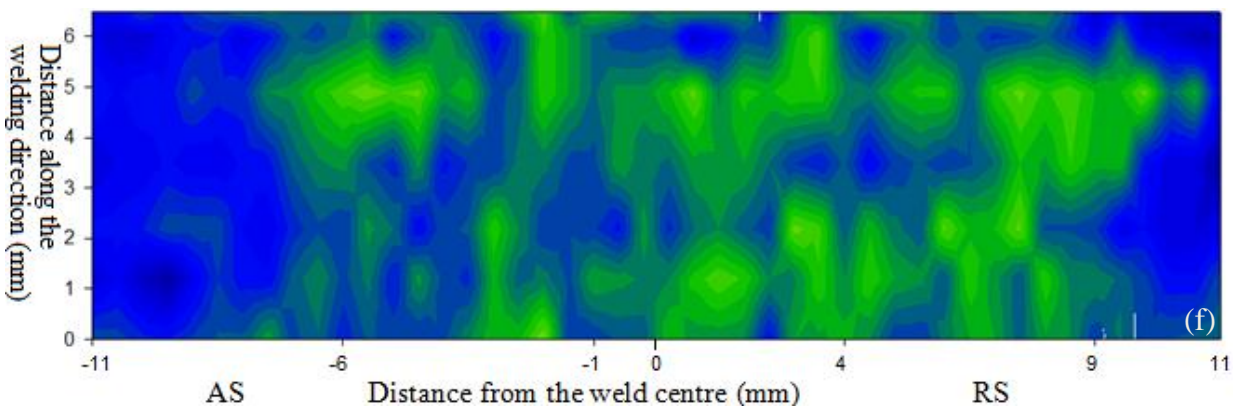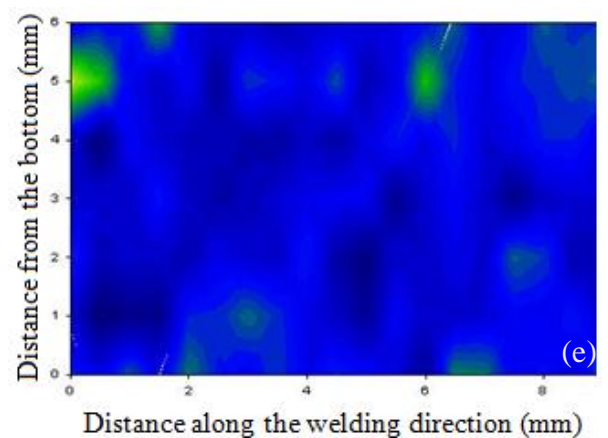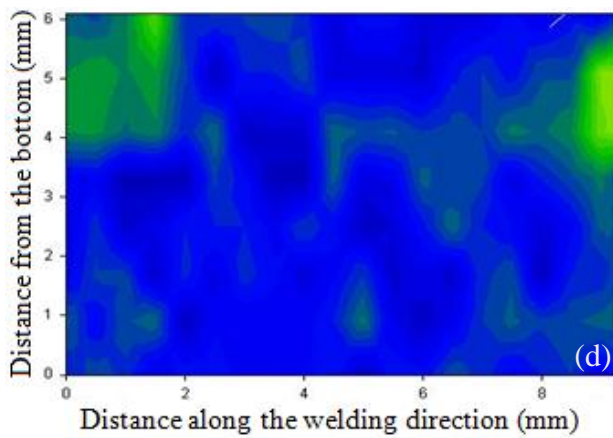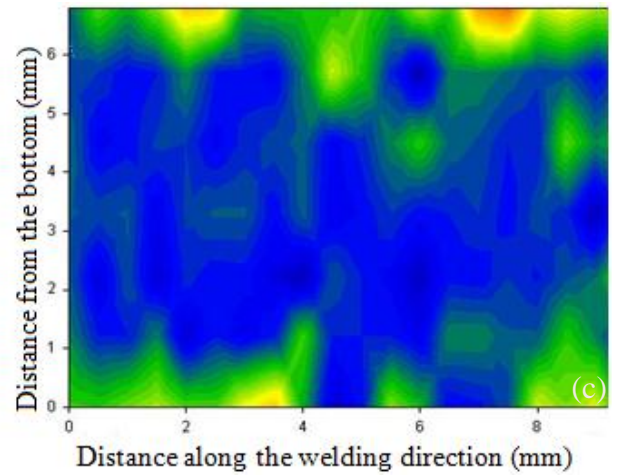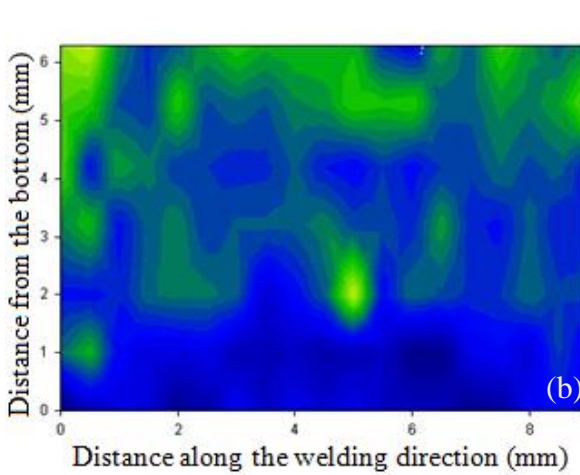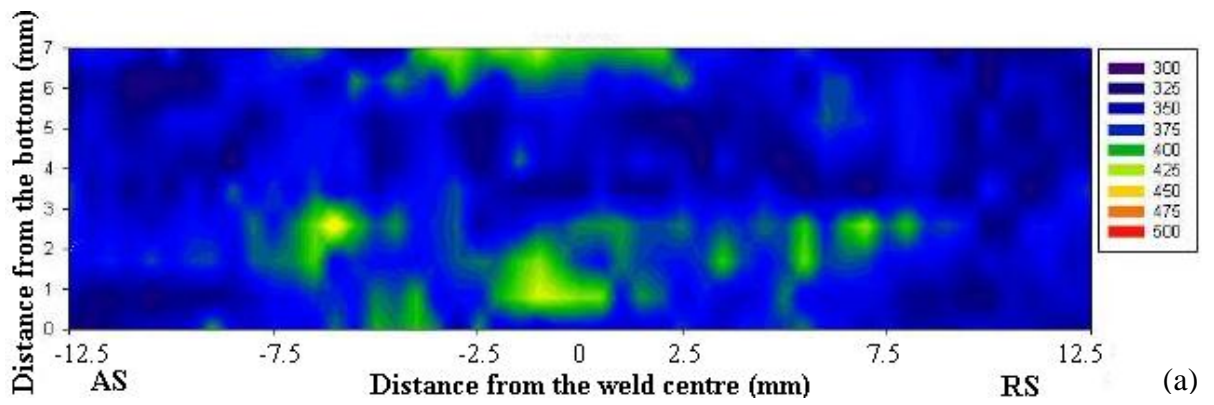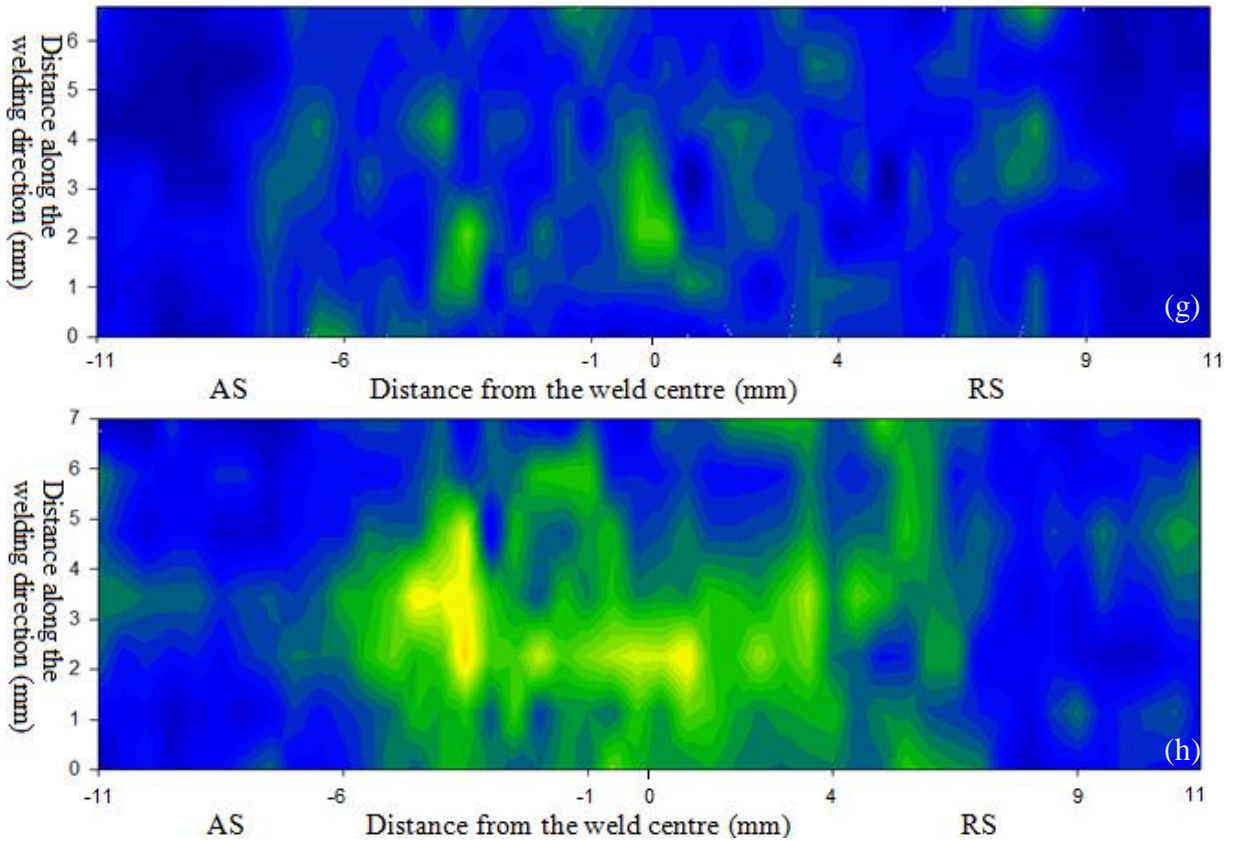
Figure 4.15 Microhardness profiles of the cross section (a) W5A5; the side sections: (b) 5.1a, (c) 5.2.a, (d) 5.3.a, (e) 5.4.a; and the normal sections: (f) 5.6.a, (g) 5.7.a, (h) 5.8.a

Figure 4.16 show the microhardness profiles of the cross section, side sections and normal section of the weld W6. Figure 4.16(a) is the microhardness profile of the cross section W6A6. Figure 4.16(b-e) show the microhardness profiles of the side sections 6.1.a, 6.2.a, 6.3.a and 6.4.a, respectively. Figure 4.16(f) shows the microhardness profile of the bottom normal section 6.8.a.



(a)
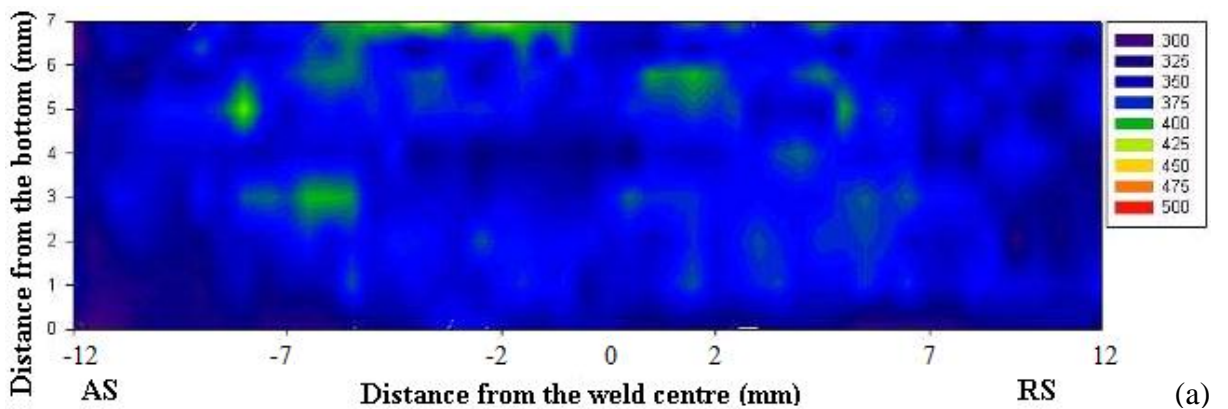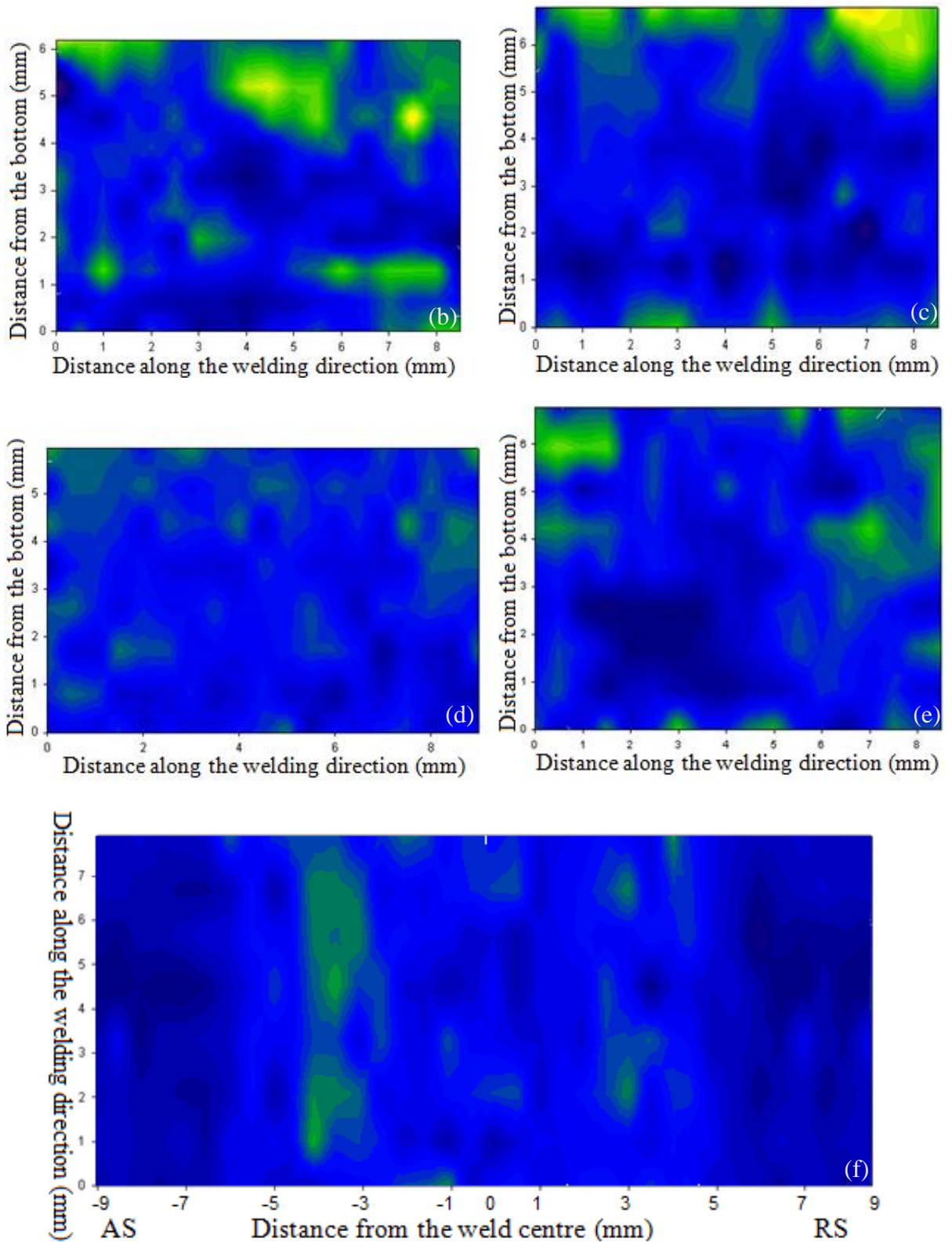
Figure 4.16 Microhardness profiles of the cross section: (a) W6A6; the side sections: (b) 6.1a, (c) 6.2.a, (d) 6.3.a, (e) 6.4.a; and the normal section: (f) 6.8.a

### 4.4.2 Microhardness profiles of W19, W20 and W21

Microhardness tests on the cross sections of the three welds W19, W20 and W21 with a constant traverse speed of 150mm/min were carried out with 0.5mm interval in horizontal direction and 1mm interval in vertical direction. And the microhardness profiles of the cross sections of the three welds W19, W20 and W21 are shown in Figure 4.17(a), (b) and (c), respectively.
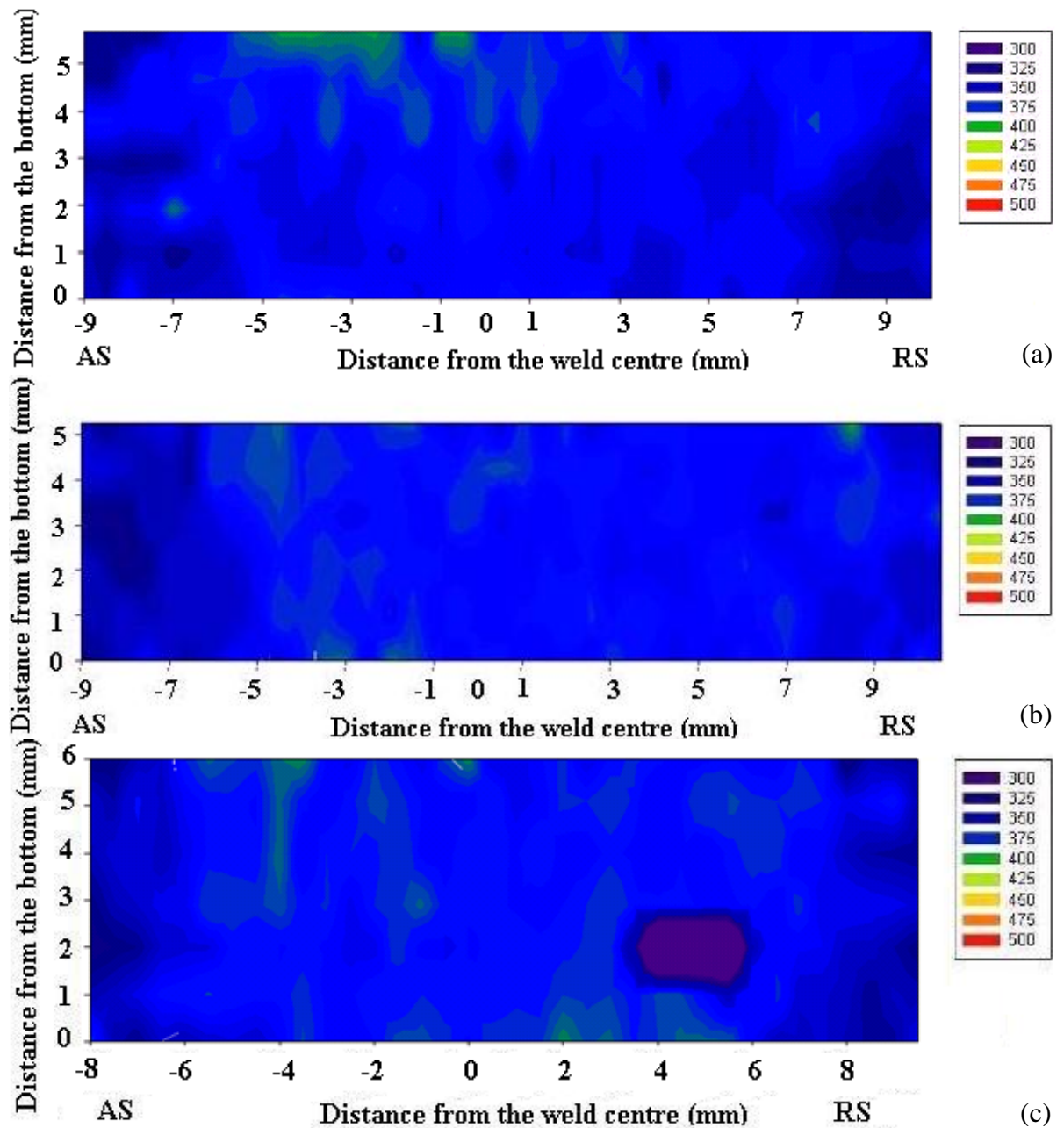


Figure 4.17 Microhardness profiles of the cross sections: (a) W19, (b) W20 and (c) W21

## 4.5 Effect of traverse speed and rotation speed

4.5.1 Relationship between the process parameters

It is seen in Figure 4.2 that traverse force and torque were not stable during the welding process of W4, while all the other process parameters were smoothly distributed during SSFSW of W5 and W6. This would suggest that FSW of W4 with 50mm/min traverse speed was the least stable process compared to the welds W5 and W6 using higher traverse speeds, which could be attributed to the highest heat generated during SSFSW of W4 due to the fact that the lowest traverse speed results in more exposure time for heating. It is seen from Table 4.1 and Figure 4.2 that both traverse force, down force and torque increase with increasing traverse speed. A comparison of traverse force for all the three welds W4, W5 and W6 in Figure 4.3(a) shows that traverse force was the largest in the weld W6 with 150mm /min traverse speed and it increased by 19% when traverse speed increased from 100 to 150mm/min. However, the weld W5 had a slightly larger traverse force compared to the weld W6 at the beginning of the welding process (<50mm), however, as the welding process went on, the traverse force received the same value for the two welds W5 and W6 during welding. It is clearly observed in Figure 4.3(b) that down force has increased by 17% and 13% with increasing traverse speed from 50 to 100 and 100 to 150mm/min, respectively, and down force was most uniformly distributed along the whole weld length for all the three welds W4, W5 and W6 compared to traverse force and torque. It was shown in Figure 4.3(c) that torque increased greatly at welding distance of 0 to 50mm before it reached a steady value at a welding distance of larger than 50mm for all the three welds W4, W5 and W6. In comparison of torque for all the three welds W4, W5 and W6, it is seen from Figure 4.3(c) that torque has increased by 5% and 13% with increasing traverse speed from 50 to 100 and 100 to 150mm/min, respectively.

Figure 4.5 indicated that all the process parameters were smoothly distributed during SSFSW of W19 (800rpm) and W20 (600rpm) except for torque, which shows a slight oscillation at the welding distance of 60 to 160mm. However, most of the process parameters during SSFSW of the weld W21 were not stable; this could indicate that SSFSW of W21 was not stable due to insufficient rotation speed, which result in poor weld quality such as porosity observed at the weld surface of W21. It is seen from Table 4.2 and Figure 4.6 that both traverse force, down force and torque increase with decreasing rotation

speed. A comparison between all the three welds W19, W20 and W21 in Figure 4.6(a) shows that traverse force was the largest in the weld W21 with 400rpm rotation speed and it increased by 50% as the rotation speed decreased from 600 to 400rpm, however, there was a 25% increase in traverse force as the rotation speed decreased from 800 to 600rpm. It is also seen that the lowest traverse force was steadily distributed along the whole weld length of W19 and traverse force became less irregular with decreasing rotation speed from 800 to 600 and 400rpm. It is clearly observed in Figure 4.6(b) that down force was stable along the whole weld length for the two welds W19 and W20, while W21 had a non-stable traverse force during the welding process indicating poor welding condition. In comparison of the welds W19 and W20, down force has increased by 10% with decreasing rotation speed from 800 to 600rpm. It is shown in Figure 4.6(c) that torque was most stable along the whole weld length for the two welds W19 and W20 and torque was much more uniformly distributed along the welding distance of W21 compared to traverse force and down force. A comparison can be made on torque between the three welds W19, W20 and W21 and it was observed that torque has largely increased by 62.5% with decreasing rotation speed from 600 to 400rpm compared to the 11% increase of torque with decreasing rotation speed from 800 to 600rpm, this meant that a greater value of torque applied in SSFSW of W21 was able to stabilise the welding process.

To summarize, both traverse force, down force and torque increase with increasing traverse speed and both traverse force, down force and torque increase with decreasing rotation speed. This is in agreement with Edwards and Ramulu (2010) who reported that the forge loads, travel loads and torques decreased with increasing rotation speeds and the forge loads, travel loads and torques increased with increasing travel speed. It should be noted that the increase in the traverse force is largely due to the decrease of temperature and is partially caused by the decreased material flow between the die cavity and the back side of the tool probe (Longhurst, 2009). And the microstructure will vary with the sharp changes of down force at the edge of the shoulder (Chen and Kovacevic, 2003).

4.5.2 Effect of welding parameters on heat input and surface quality

The heat input results in Figure 4.7 and Table 4.3 show that the weld W4 with the lowest traverse speed has the greatest heat input, and heat input has decreased greatly by 45.5%

with increasing traverse speed from 50 to 100mm/min, while the heat input has reduced by 28% with increasing traverse speed from 100 to 150mm/min, this meant that the material has higher heat input at lower traverse speed and the reduction of heat input in not linear; heat input decreased slightly with decreasing rotation speed from 900 to 800 and 600rpm and the reduction of heat input is nearly linear. It should be noted that the two welds W20 and W21 have similar heat input, which can be attributed to much higher process parameters used in W21 compared to W20, e.g. torque, traverse force and down force. It is seen that heat input was most uniformly distributed in the two welds W6 and W19 along the whole weld length. The results demonstrated that the traverse speeds had largely influenced on heat input compared to the rotation speeds.

Figure 4.10 provides the photographs of the surface of the three welds W4, W5 and W6 with a constant rotation speed of 900rpm indicating that the weld surfaces became significant smoother with increasing traverse speed from 50 to 100 and 150mm/min at a constant rotation speed of 900rpm. Three dimensional graphs of the surfaces of the three welds W4, W5 and W6 shown in Figure 4.11 again suggests that the surfaces became significantly smoother with increasing traverse speed indicating process stability increases with increasing traverse speed. The data, however, also confirms a greater variation in the bump at the AS of the weld surface for Weld W6 compared to the weld W19 and highest bump at the AS was observed on the weld surface of W6 due to insufficient down force. This possibly suggests that with increasing traverse speed, a greater down force is required to get ideal surface flatness. Due to much lower heat input, surfaces were smooth in the three welds W19, W20 and W21 with a constant traverse speed of 150mm/min (Figure 4.12). It is seen that W19 has a relatively flat surface, especially at the AS, where a much lower bump of 1mm was observed compared to the bump of 2.5mm at the AS of W6. However, in the two welds W20 and W21, material has not been fully penetrated at the RS showing a concave gap of 0.5mm depth at the RS of the cross sections.

4.5.3 Effect of welding parameters on swept volume

It is clearly seen in Table 4.4 that as traverse speed increased from 50 to 100mm/min, swept volume increased by 92% and swept volume increased by 49% from W4 (50mm/min) to W5 (100mm/min) and W5 to W6 (150mm/min); swept volume increased by 7.6%, 25.7%

and 49% with decreasing rotation speed from 900 to 800, 600 and 400rpm. Swept volume results showed that as traverse speed increased, swept volume increased and swept volume increased with decreasing rotation speed.

4.5.4 Effect of welding parameters on microhardness

Microhardness profiles were presented for all the three welds W4, W5 and W6 with a constant rotation speed in terms of cross sections, side sections and normal sections and cross sections for the three welds W19, W20, W21 with a constant traverse speed. It can be seen from the microhardness profiles of the cross sections of all the six welds W4, W5, W6, W19, W20, W21 (Figure 4.14(a), Figure 4.15(a), Figure 4.16(a), Figure 4.17(a), Figure 4.17(b), Figure 4.17(c)) and all the normal sections of W5  (Figure 4.15(f), (g) and (h)) that hardness of the weld zones is slightly higher than that of the BM with a slight increase of hardness at the weld surface and the weld bottom. Microhardness profiles of the side sections of W6 (Figure 4.16(b-e)) also suggest that microhardness of the weld zones is slightly higher than that of the BM with a little increase at the weld surface. It is seen that the HAZ with bimodal structure at the welding edge, which lies in-between the inner joint line and outer joint line, has the lowest hardness, which could be attributed to the fact that the combined frictional force and down force have softened the material in the HAZ during SSFSW process. It was shown that the equiaxed structure in the BM has lower hardness compared to the lamellar structure in the SZ which has the highest hardness, this meant that materials in the SZ have experienced the highest peak temperature and the greatest deformation.

   Thin high hardness layers at the weld surface were observed at the AS of the SZs for all the six welds W4, W5, W6, W19, W20 and W21 as seen in the six cross sections W4A4, W5B5, W6A6, W19, W20 and W21, side sections 4.2.a, 5.2.a and 6.2.a (Figure 4.14(a), Figure 4.15(a), Figure 4.16(a), Figure 4.17, Figure 4.14(c), Figure 4.15(c) and Figure 4.16(c)) and normal section 5.6.a (Figure 4.15(f)), moreover, the highest microhardness was also found at the weld bottom, as shown in the microhardness profiles of the side sections 4.2.a and 4.3.a and normal section 4.8.a and 5.8.a (Figure 4.14(b), Figure 4.14(c), Figure 4.14(f) and Figure 4.15(h)). It is seen that microhardness of the weld bottom 5.8.a (Figure 4.15(h)) is higher than that of the weld surface 5.6.a (Figure 4.15(f)) and weld

centre 5.7.a (Figure 4.15(g)), indicating that the weld bottom is harder than the weld surface and the weld centre of W5. It was shown that higher hardness observed at both the weld surface and the weld bottom could be attributed to greater heat input or extra cold work, and/or tool material infiltration, as the tool material is W-Re.

It should be noted that hardness at the AS is generally higher than that at the RS, as shown in the micrographs of the cross sections W4A4, W5A5, W6A6, W19, W20 and W21, side sections 5.1.a, 5.2.a, 5.3.a, 5.4.a, 6.2.a 6.3.a and the normal section 6.8.a (Figure 4.15(a), Figure 4.15(a), Figure 4.16(a), Figure 4.17, Figure 4.15(b), Figure 4.15(c), Figure 4.15(d), Figure 4.15(e), Figure 4.16(b), Figure 4.16(c) and Figure 4.16(f)), In a direct comparison of the microhardness profiles between all the four side sections of W5, microhardness of 5.2.a is slightly higher than that of 5.3.a as shown in Figure 4.15(c) and Figure 4.15(d). Similarly, microhardness of 6.2.a is slightly higher than that of 6.3.a as shown in Figure 4.16(c) and Figure 4.16(d). The results demonstrate that the microhardness at the AS is slightly higher than that at the RS for W6. Microhardness profile of 6.8.a shows that the AS is harder than the RS and the weld zones have higher hardness than the BM (Figure 4.16(f)). This observation is consistent with the hardness results obtained from the cross section W6A6. The higher hardness at the AS could be due to the fact that the AS has experienced slightly higher peak weld temperature than the RS. Moreover, a FSP study of Ti-5111 by Rubal et al. (2010) also reported that the peak weld temperature is generally 20°C higher at the AS than that at the RS, however, the reason why the AS has higher peak weld temperature has not been explained. It is very likely that the material at the RS has been pushed away to the AS by the tool rotation, which results in greater material flow at the AS than that at the RS and this would contribute to higher peak weld temperature and much more deformation experienced at the AS compared to that at the RS.

It can be seen that in the microhardness profiles of the cross sections of the three welds W4, W5 and W6 with a constant rotation speed, hardness in the weld zones increased with decreasing traverse speed from 150 to 100 and 50 mm/min ((Figure 4.14(a), Figure 4.15(a) and Figure 4.16(a)), this is due to the fact that low traverse speed results in more heating time and higher heat input. As heat input decreased, peak weld temperature experienced in the weld zones decreased with increasing traverse speed. The hardness distributions in W4A4 and W5B5 were not uniform due to the uneven temperature distribution in the weld zones where higher heat input was generated. However, the cross section W6A6 with the

highest traverse speed has the most uniformly distributed microhardness indicating more uniformly distributed heat input. There is not much variation of hardness in the three welds with rotation speeds of 800, 600 and 400rpm, as shown in Figure 4.17, due to much lower heat input compared to the previous welds W4, W5 and W6, the three welds W19, W20 and W21 with a constant traverse speed of 150mm/min had uniformly distributed hardness which is similar to the hardness of the BM. However, a slightly higher hardness was observed at the AS of the weld surface of W19, W20 and W21, and a hole was observed through the thickness of the cross section of W21 because of incomplete penetration resulted from the insufficient rotation speed. In the case of a low rotation speed and a high traverse speed, this lack of penetration defect at the RS is seen as void defects due to insufficient heating and deformation (Edwards and Ramulu, 2009).

Interweaved regions of higher hardness and lower hardness observed on the surface of 4.2.a shown in Figure 4.14(c) suggest that the tool material W and Re might have infiltrated into the weld surface resulting in a higher hardness layer of 1.4mm deep and 0.3mm wide. In comparison of the hardness of the work piece and tool probe, the hardness of the probe is much higher than that of the work piece. This means that the tool material has possibly infiltrated into the work piece to 1.4mm deep on the weld surface. The spaced rings and interweaved regions could be associated with the tool rotation. In SSFSW, material in the weld zones was rotated from the trailing edge of the shoulder to the leading edge and the rings were then generated on the weld surface at the trailing edge, thus, visible spacing was formed between these rings when the tool was travelling along the welding direction.

To summarize, the weld zones are slightly harder than the BM, the HAZ has the lowest heat input due to the softened material in the HAZ; hardness at the AS is slightly higher than that at the RS due to the higher peak weld temperature experienced at the AS; thin higher hardness layers observed in the weld surface of all the three welds W4, W5 and W6 and the weld bottom of the weld W4 and W5 were possibly resulted from the tool material infiltration; Microhardness is much more uniformly distributed in the four welds W6, W19, W20 and W21 with 150mm/min traverse speed.

## 4.6 Summary

This chapter presented the results of all the six welds using the same workpiece material and the same tool material under different welding parameters. Weld records indicated the influence of process parameters on weld integrity and the effect of rotation speed and traverse speed on traverse force, down force and torque were also investigated. The results showed that surfaces of the welds and heat input in the weld zones have altered with varying welding parameters. Also the hardness results showed the weld zones in terms of cross sections, normal section and side sections. Results of swept volume were also presented. The main findings from this chapter were summarised in the following two charts in Figure 4.18.
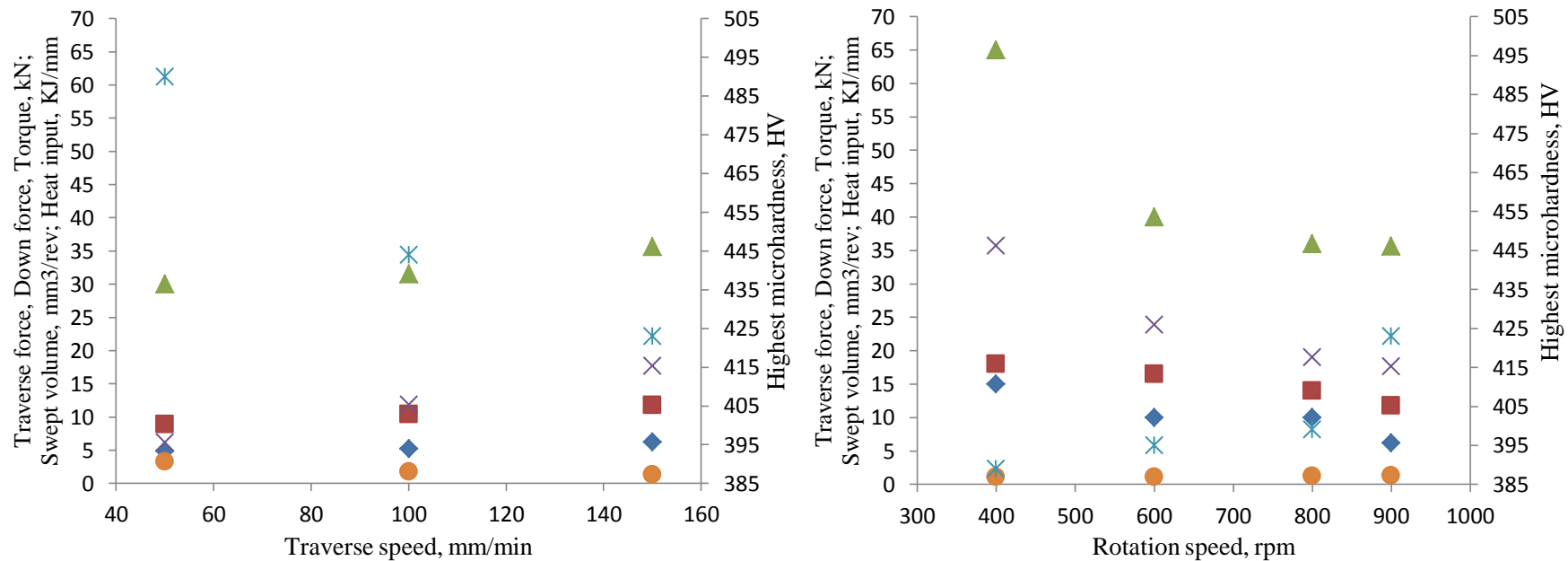


Figure 4.18 A summary of the main findings from Chapter 4,

◆Traverse force, kN ■Down force, kN ▲Torque, N·m ✕Swept volume, mm3/rev ✳Highest microhardness, HV ●Heat input, KJ/mm

**Chapter 5 Microstructural evolution of the SSFSW weld zones**

**5.1 Introduction**

This chapter presents work that was carried out to investigate microstructural evolution in SSFSWed Ti-6Al-4V plates in terms of cross sections, normal sections and side sections with varying weld parameters using optical microscopy and SEM. Tool/workpiece interaction was studied by X-EDS and the relationship between tool wear, microstructure and microhardness were also studied.

**5.2 Optical and SEM microstructures**

5.2.1 Transverse cross section view of a SSFSW weld

A typical transverse cross section of a friction stir weld is shown in Figure 5.1, and the AS and the RS are the short terms for the retreating side and the advancing side, respectively.
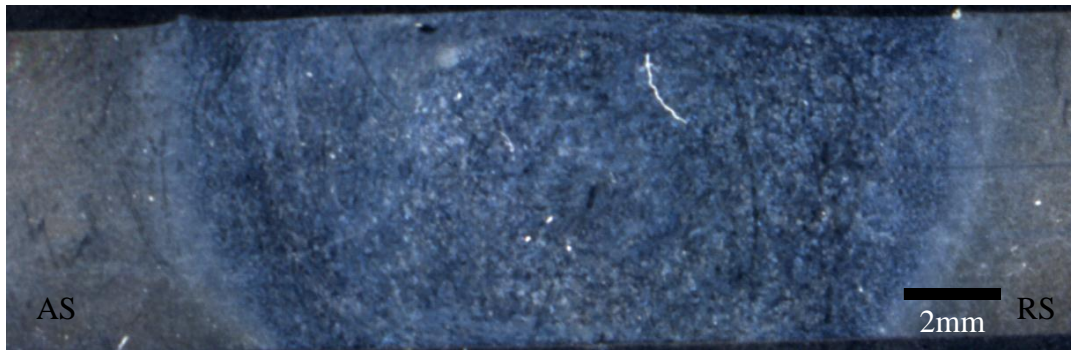


Figure 5.1 A typical transverse cross section of a friction stir weld in Ti-6Al-4V

As mentioned in the literature review of Chapter 2, it is difficult to differentiate the TMAZ from the NG (nugget zone) in titanium alloys because titanium transforms from β to α and it is difficult to distinguish the recrystallized region and the non-recrystallized region of the transformed lamellar structure between the adjacent regions of the welds in the case of the weld zones having peak weld temperature above the $T_\beta$. Thus, in the present study, the weld zones are divided into the base material (BM), heat affected zone (HAZ), thermo-mechanical affected zone (TMAZ) and the stir zone (SZ), where the HAZ and the TMAZ are the transition zones (TZ) between the BM and the SZ. Microstructure of these weld zones were characterised by SEM and the weld zones have been divided into fully equiaxed

structure in the BM, bimodal structure, coarse lamellar structure and fine lamellar structure from the welding edge to the weld centre.

5.2.2 Base material microstructure

The BM has undergone a thermal cycle with no microstructure change or deformation. In order to provide more detailed information about the BM microstructure, optical microscopy and SEM were carried out on the BM in terms of side section at lower and higher magnifications, respectively. The BM exhibits the equiaxed structure consisting of αp phase in the formed of equiaxed α grains and retained β phase located between the αp grains as shown in Figure 5.2 as an optical micrograph from a side section 6.1.b with welding axes WD, TD and ND shown on the right. Figure 5.3(a) and Figure 5.3(b) are the secondary electron micrographs taken at higher magnifications. It is seen from Figure 5.2 that the αp grains were elongated along the welding direction (WD), namely, the rolling direction (RD), which was due to the rolled condition of the as-received material. Secondary electron micrographs in Figure 5.3 show that the equiaxed αp grains contain subgrains due to DRX (Humphreys, 2004).
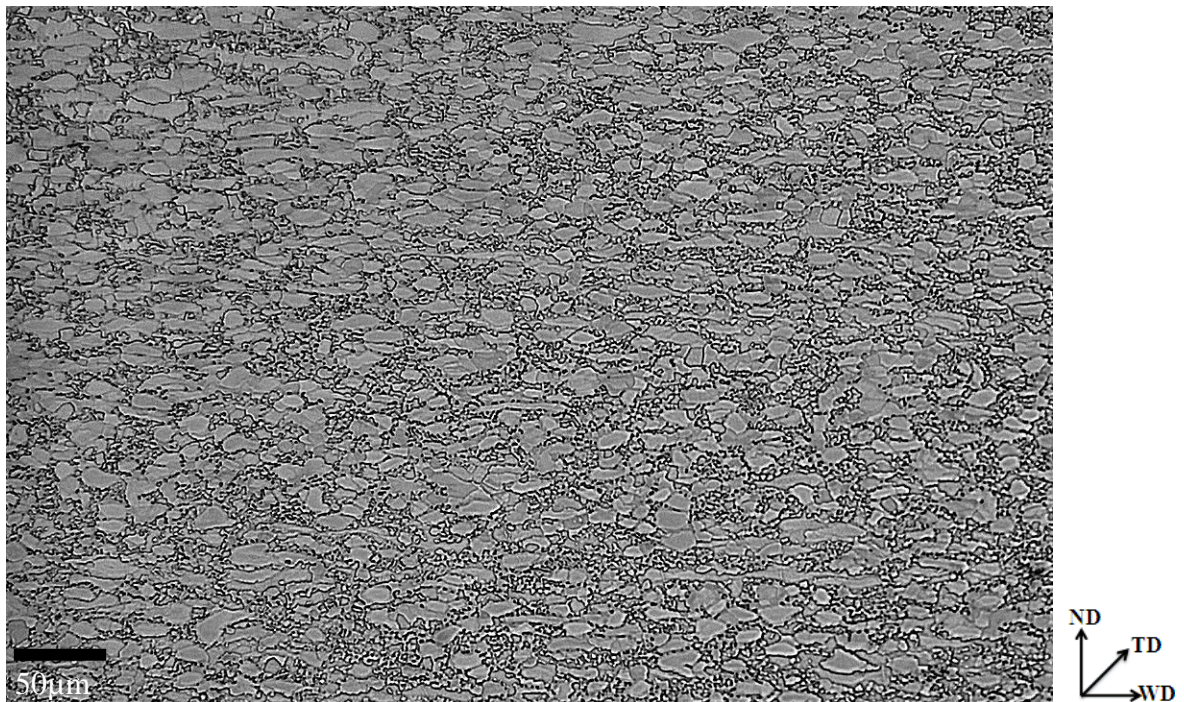


Figure 5.2 Optical micrograph of the BM taken from the centre of the side section 6.1.b
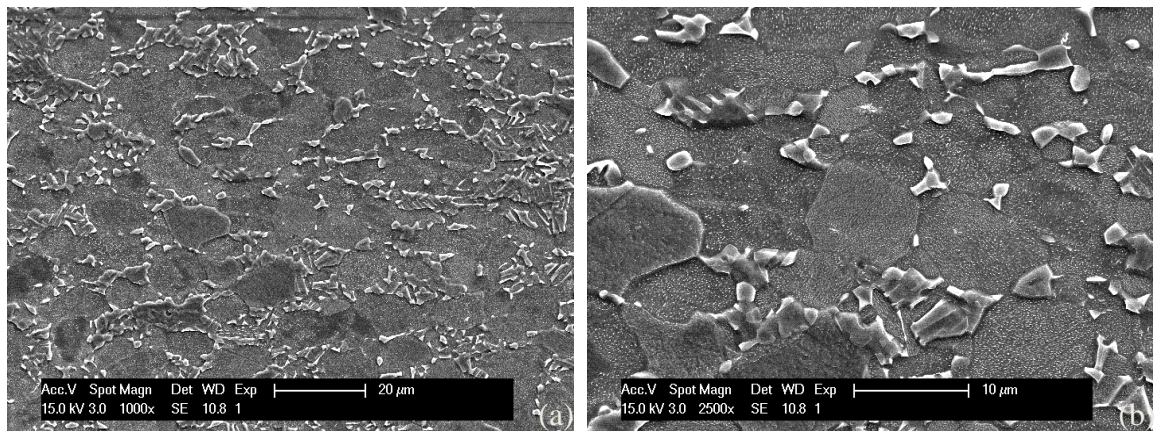
Figure 5.3 Secondary electron micrographs of the BM taken from the centre of the side section 6.1.b at magnifications of (a) ×1000 and (b) ×2500

### 5.2.3 Transition zone structure (HAZ and TMAZ)

Transition zones consisting of part of the BM, the whole HAZ and partially TMAZ were examined by the SEM taken from the BM, the whole HAZ and part of the TMAZ at both the AS and the RS of the weld zones. Secondary electron micrographs of the surface, centre and bottom of the transition zones at both the AS and the RS of W4 are shown in Figure 5.4, Figure 5.5 and Figure 5.6, respectively. Secondary electron micrographs of the surface, centre and bottom of the transition zones at both the AS and the RS of W5 are shown in Figure 5.7, Figure 5.8 and Figure 5.9, respectively. Similarly, the secondary electron micrographs of the weld surface, the weld centre and the weld bottom of the transition zones at both the AS and the RS of the other four welds W6, W19, W20 and W21 are shown from Figure 5.10 to Figure 5.21.
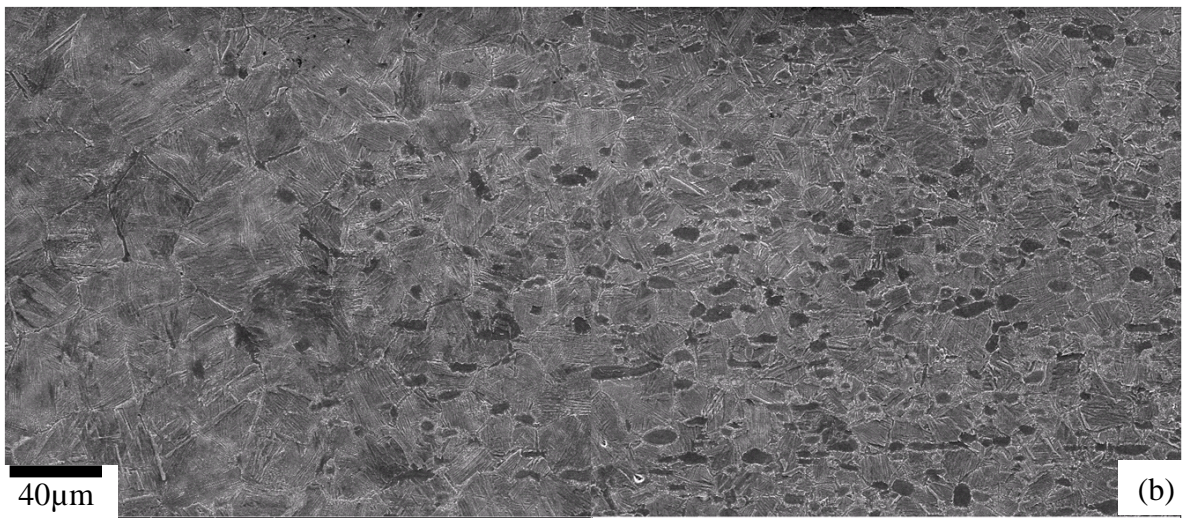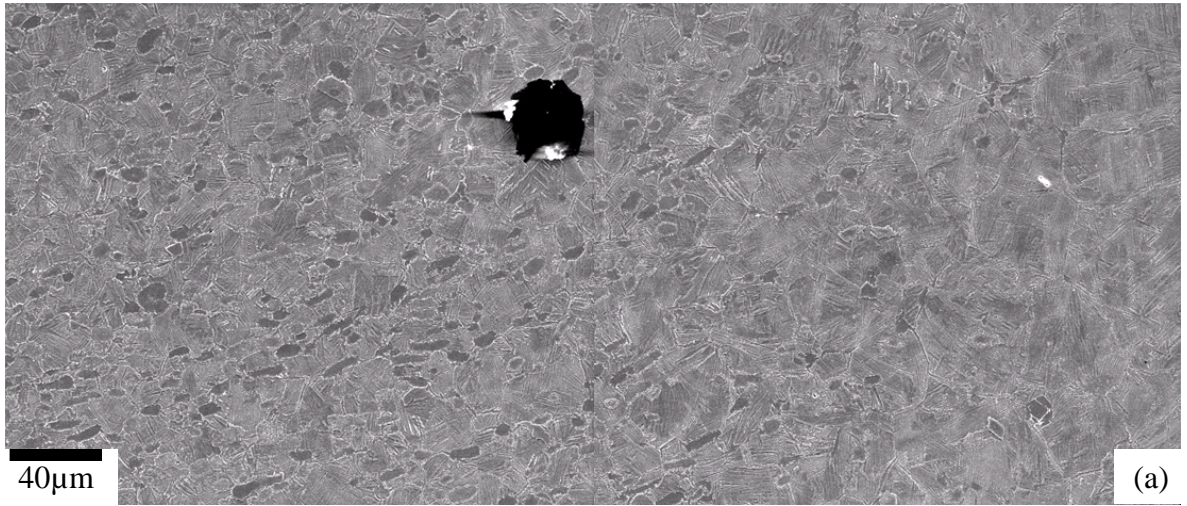
Figure 5.4 Secondary electron micrographs of the surface transition zone of the weld W4 at (a) the AS and (b) the RS

(b)

40μm
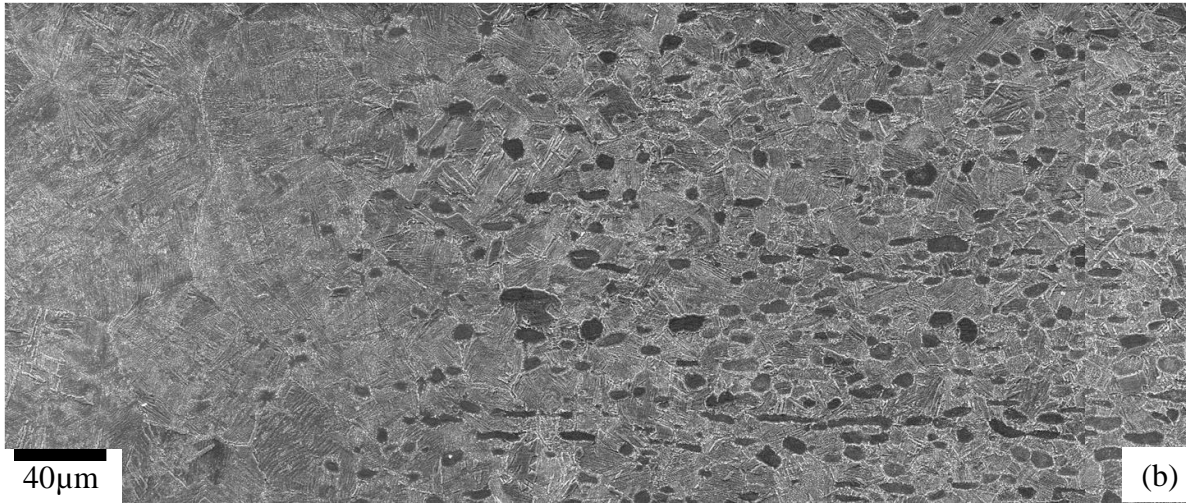
Figure 5.5 Secondary electron micrographs of the centre transition zone of the weld W4 at
(a) the AS and (b) the RS



(a)

40μm



(b)

40μm
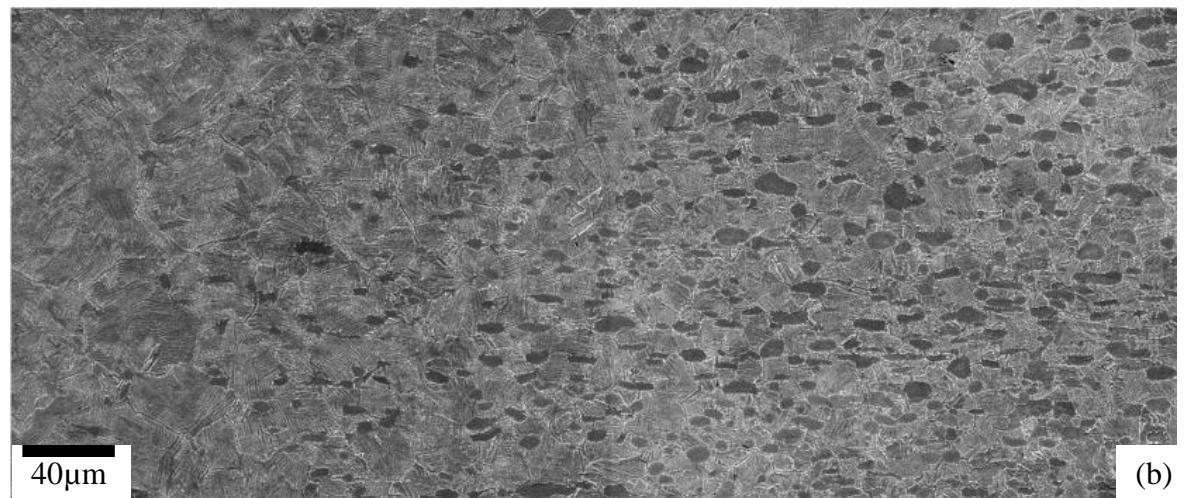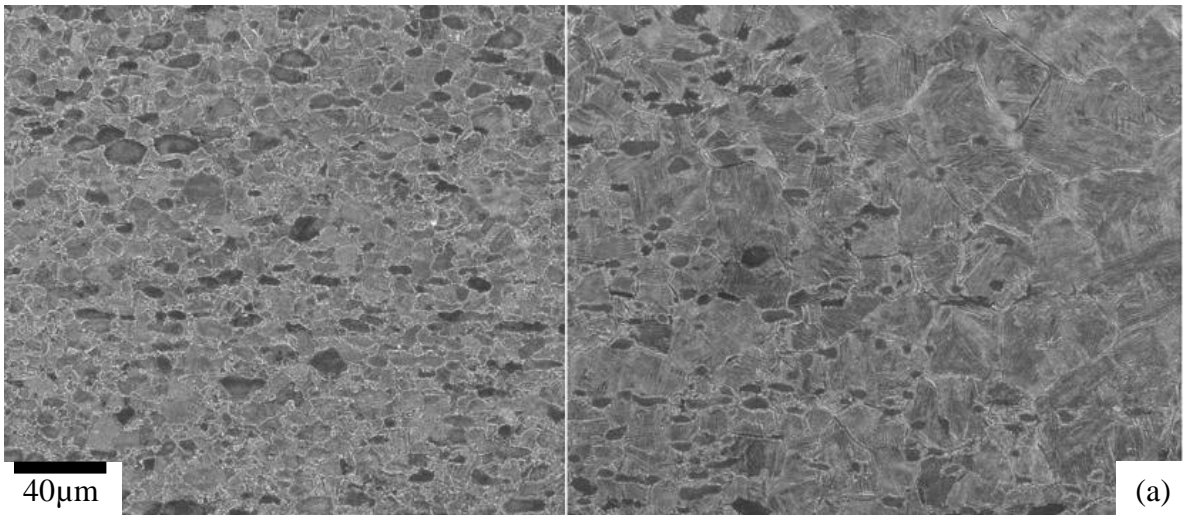
Figure 5.6 Secondary electron micrographs of the bottom transition zone of the weld W4 at
(a) the AS and (b) the RS

40μm

(a)



40μm

(b)
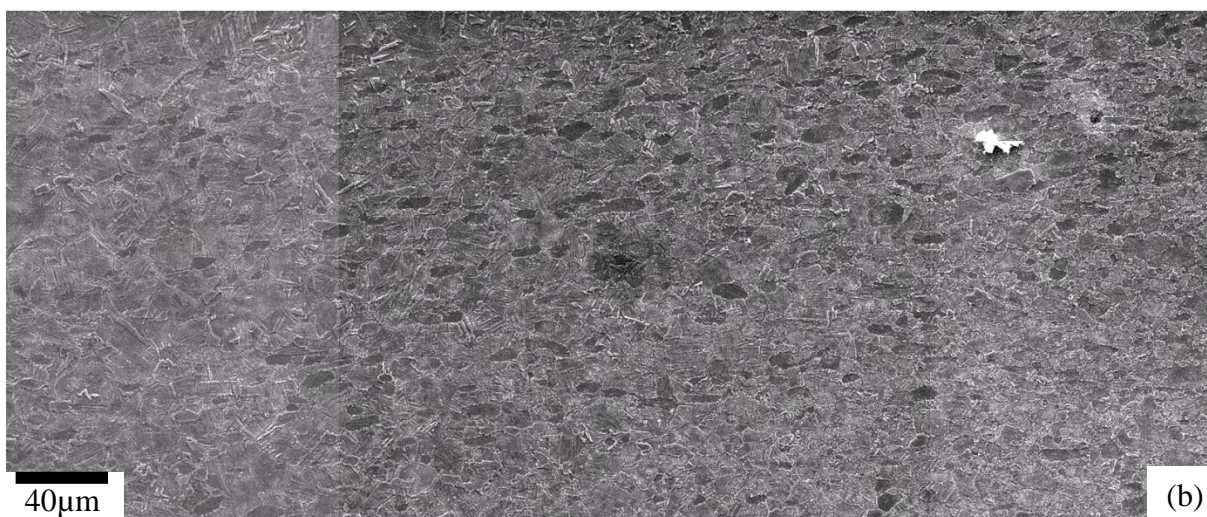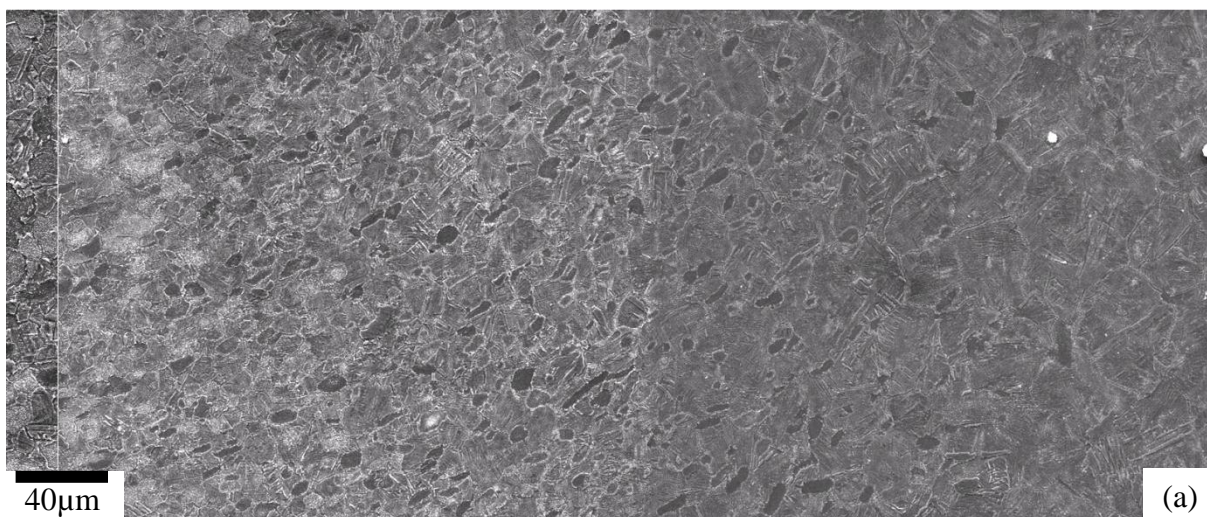
Figure 5.7 Secondary electron micrographs of the surface transition zone of the weld W5 at (a) the AS and (b) the RS



40μm

(a)

(b)
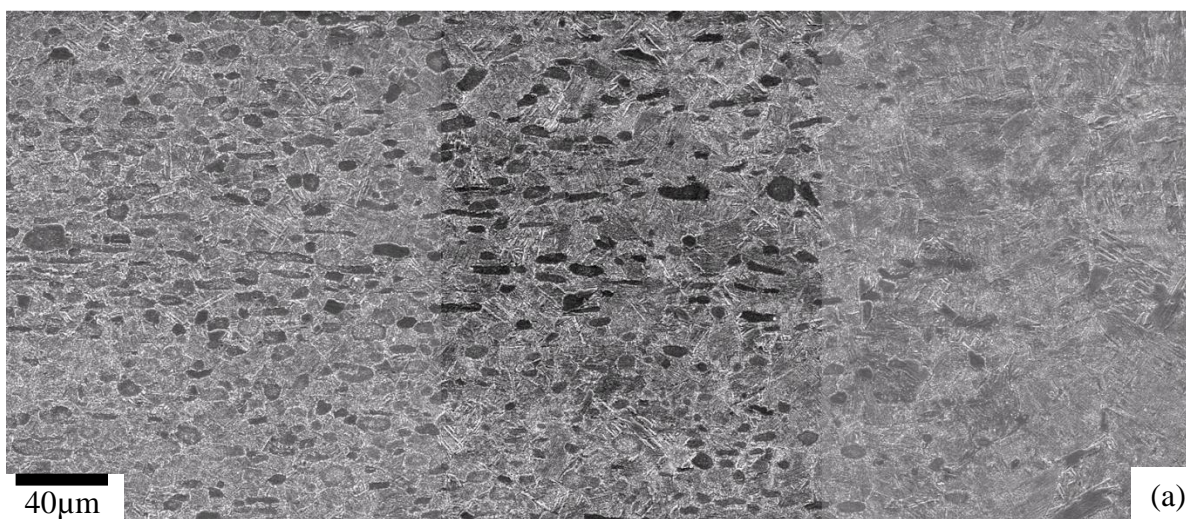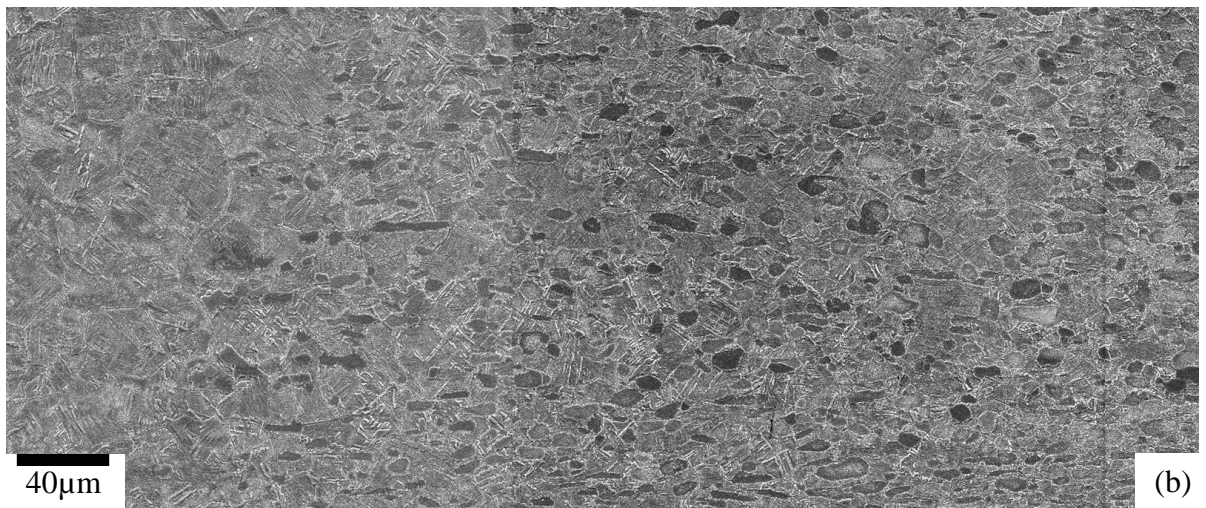
Figure 5.8 Secondary electron micrographs of the centre transition zone of the weld W5 at (a) the AS and (b) the RS



(a)



(b)
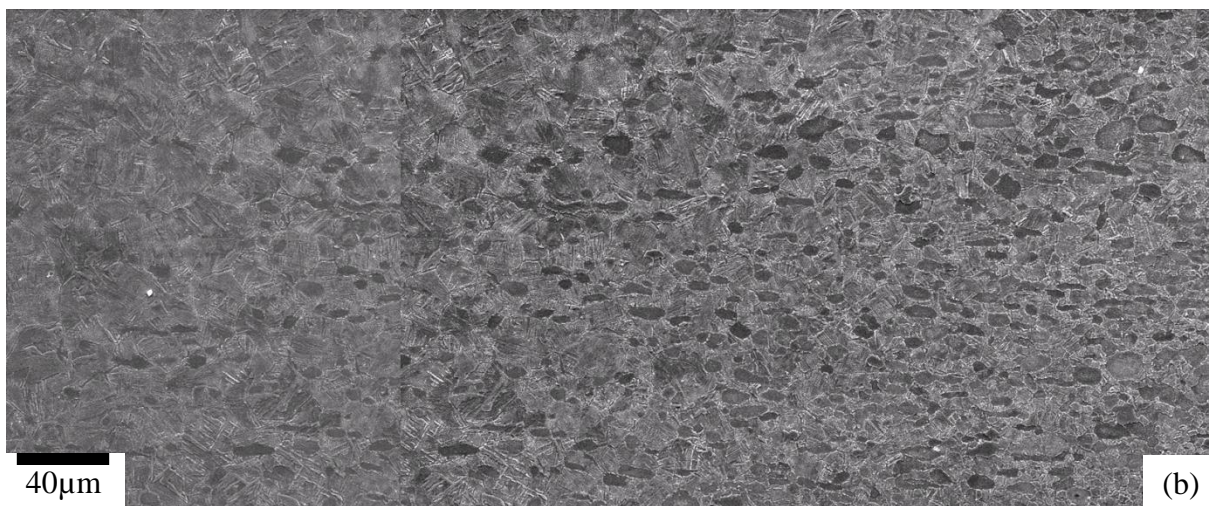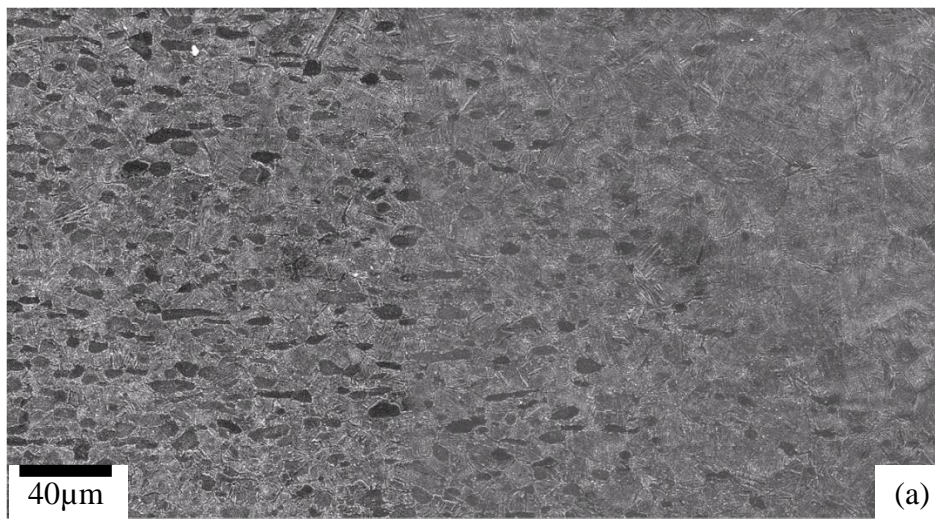
Figure 5.9 Secondary electron micrographs of the bottom transition zone of the weld W5 at (a) the AS and (b) the RS

(a)

40µm



(b)

40µm
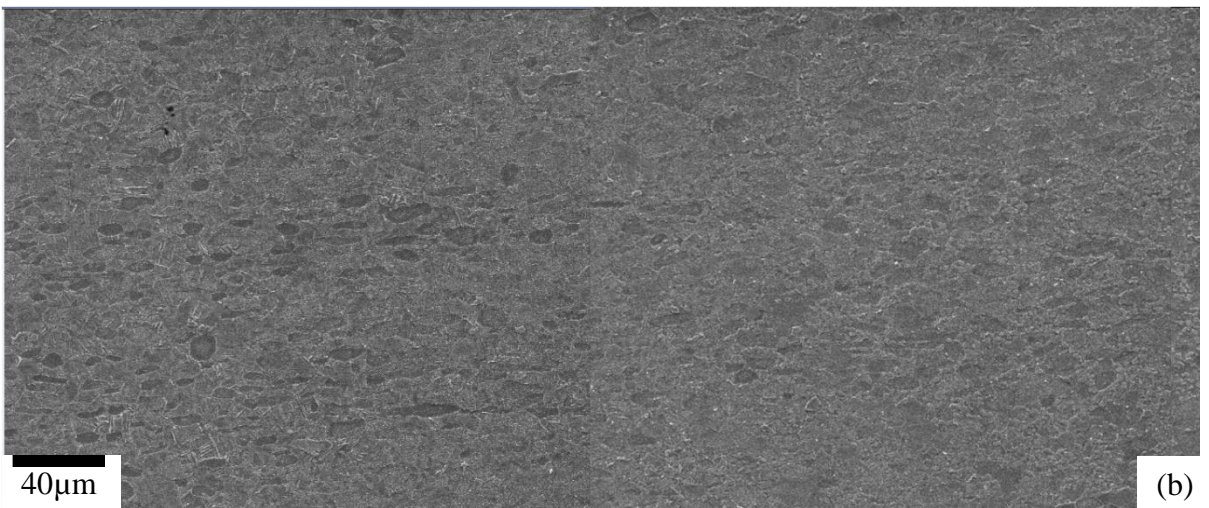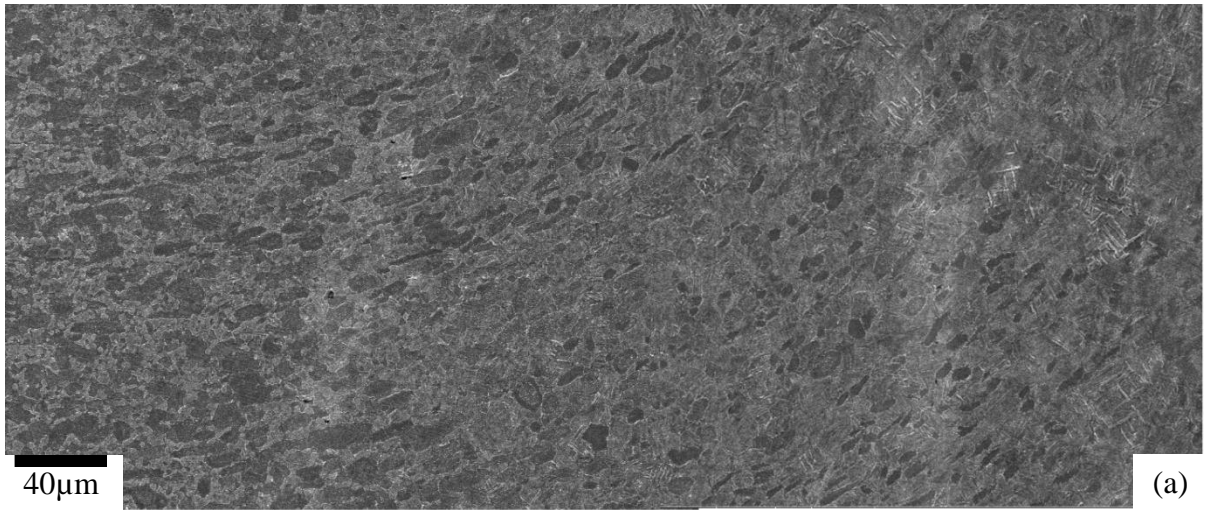
Figure 5.10 Secondary electron micrographs of the surface transition zone of the weld W6 at (a) the AS and (b) the RS



(a)

40µm

114
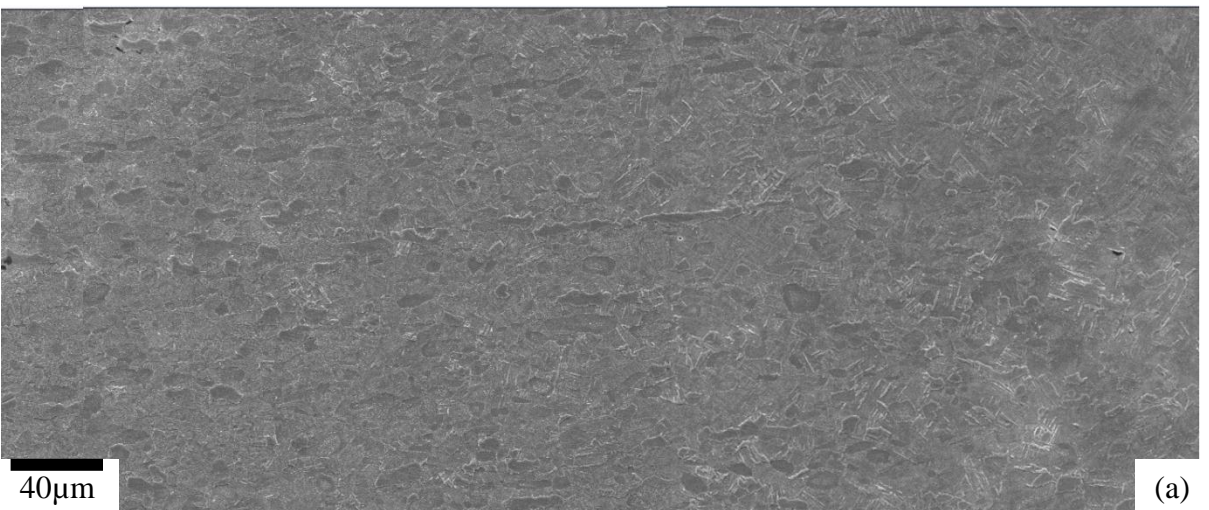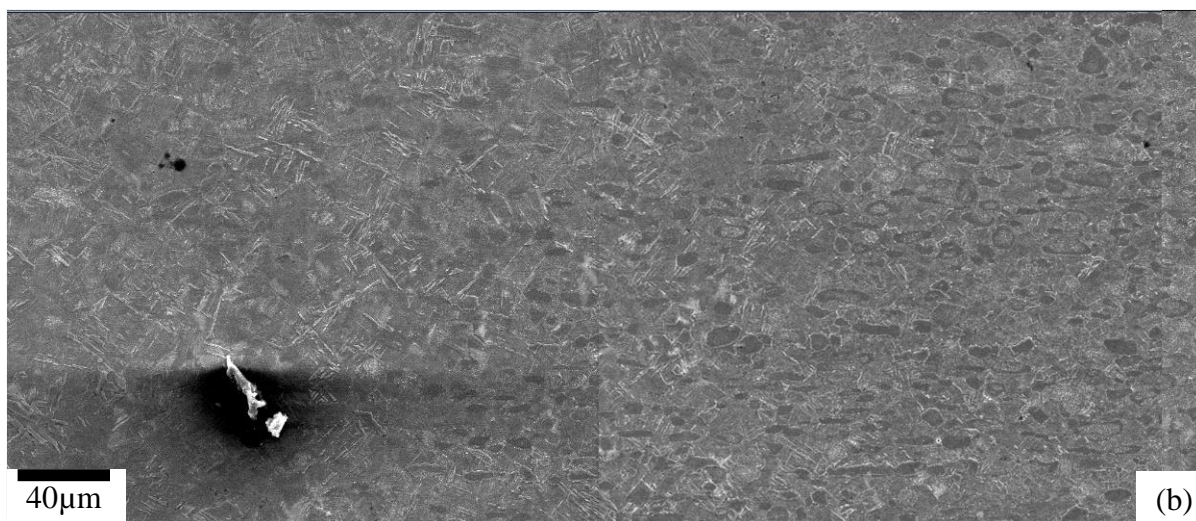
Figure 5.11 Secondary electron micrographs of the centre transition zone of the weld W6 at (a) the AS and (b) the RS
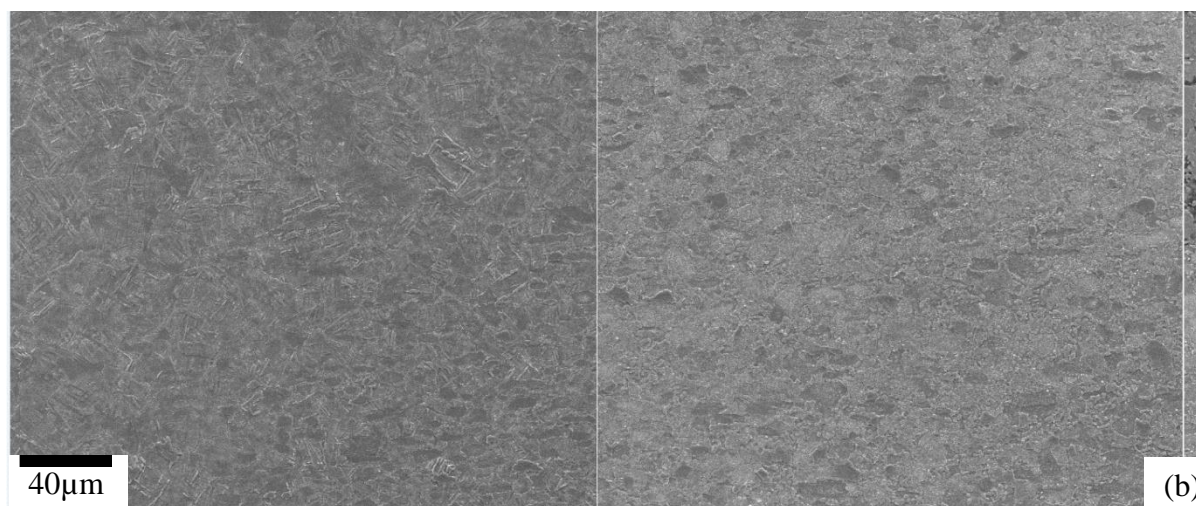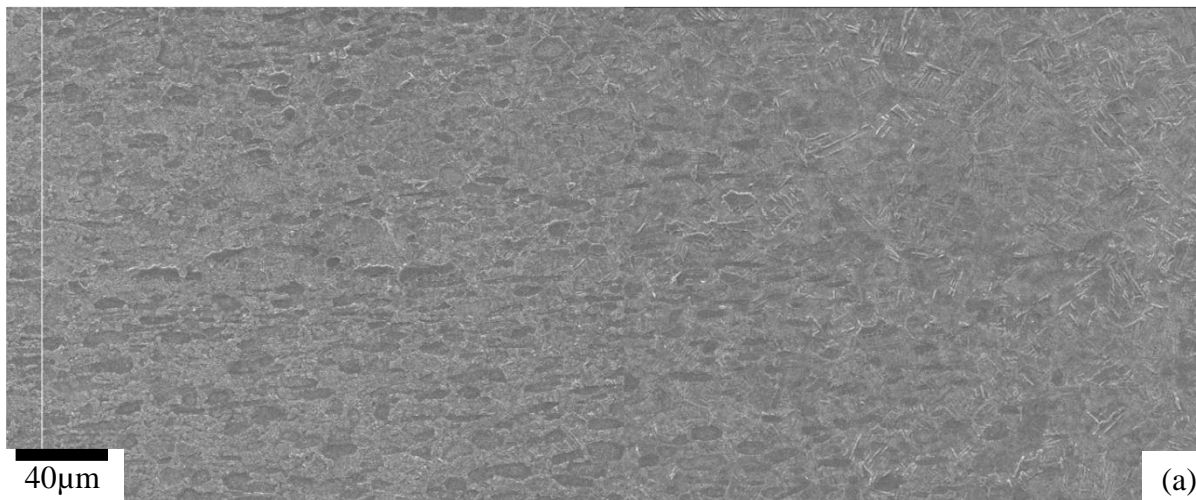




Figure 5.12 Secondary electron micrographs of the bottom transition zone of the weld W6 at (a) the AS and (b) the RS
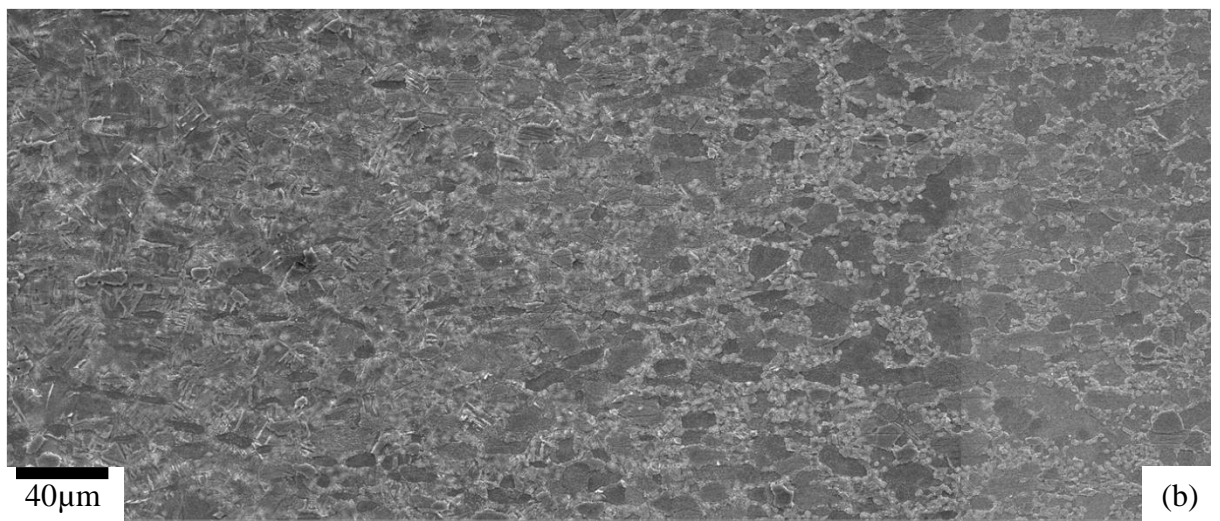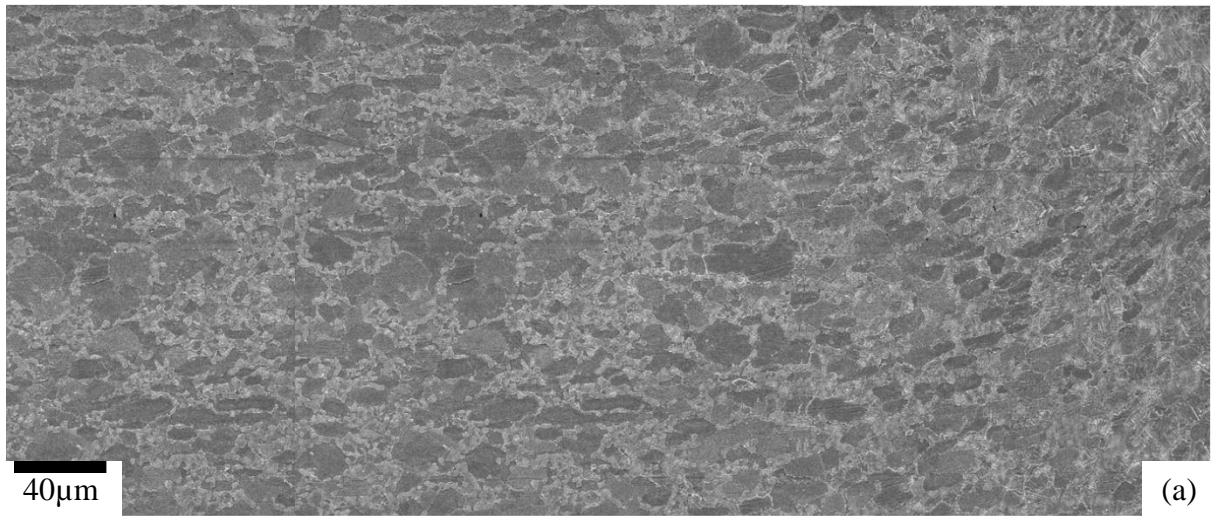
Figure 5.13 Secondary electron micrographs of the surface transition zone of the weld W19 at (a) the AS and (b) the RS

(b)
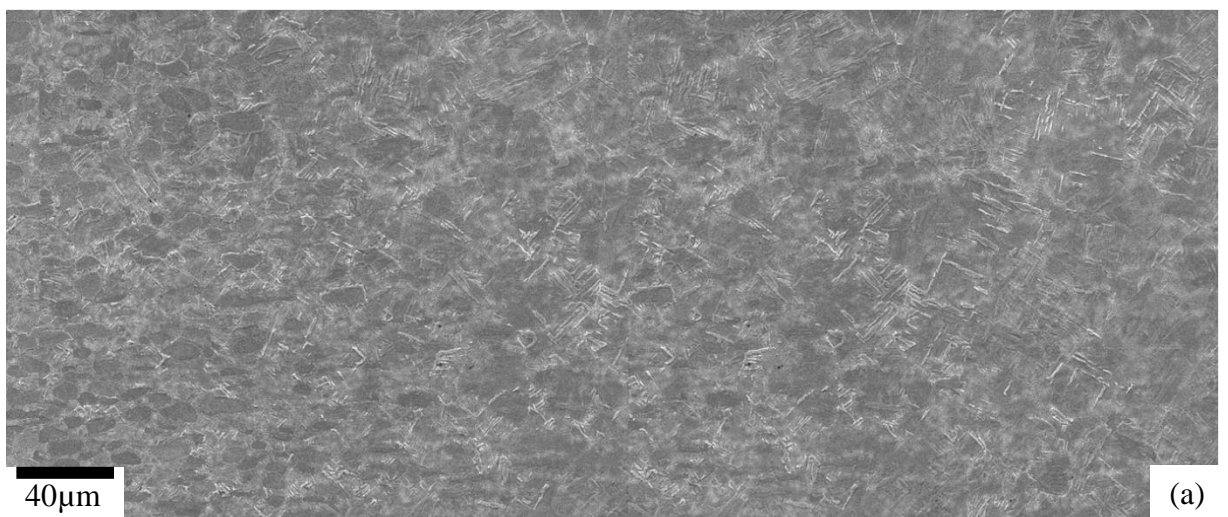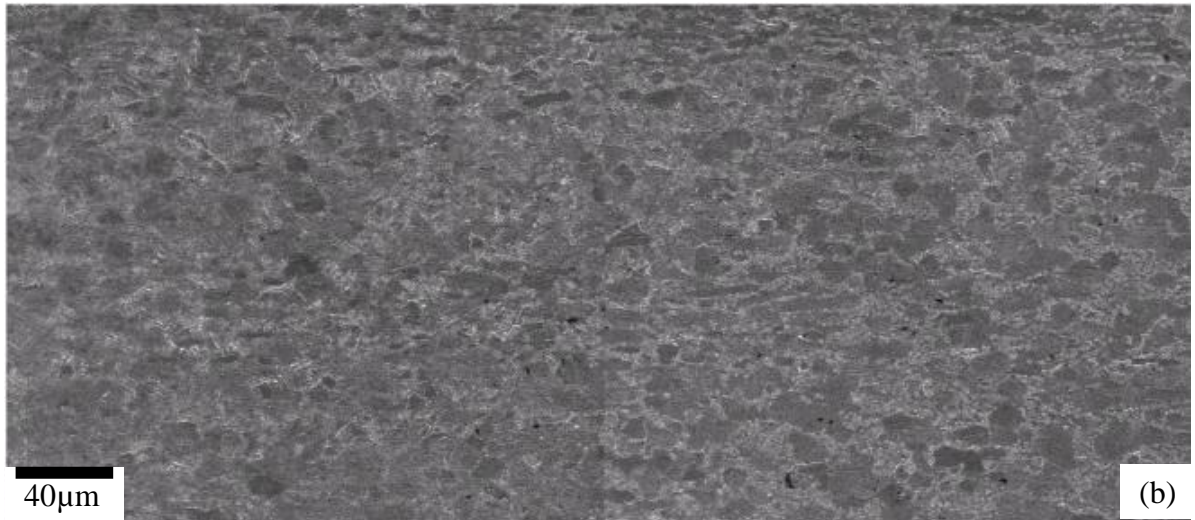
Figure 5.14 Secondary electron micrographs of the centre transition zone of the weld W19 at (a) the AS and (b) the RS



(a)



(b)
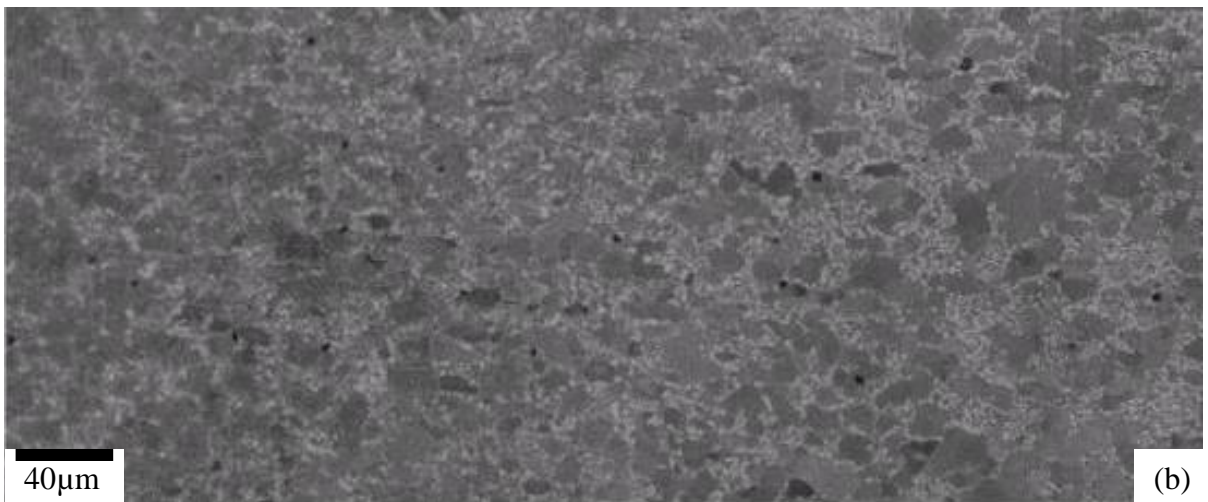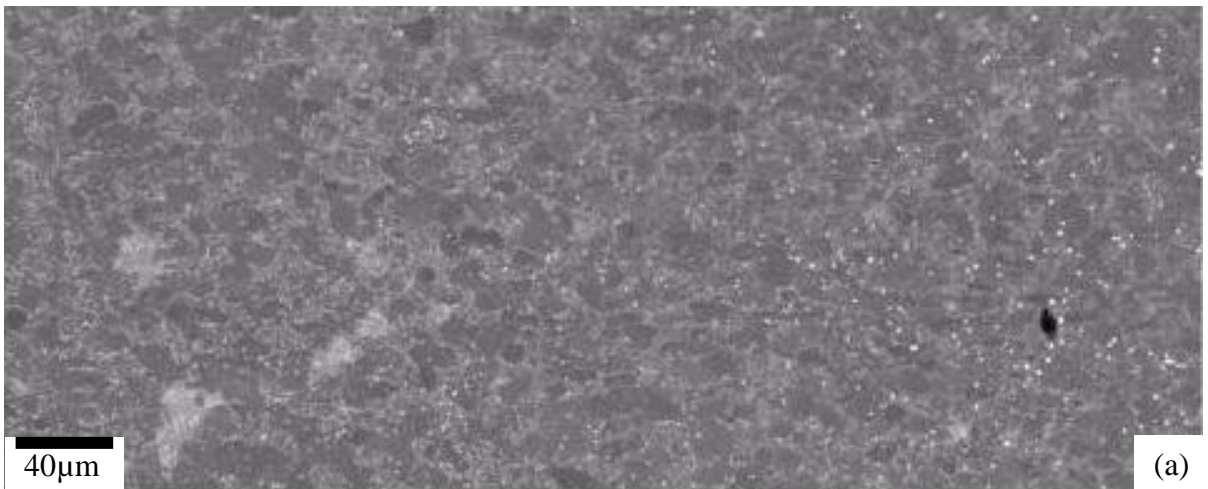
Figure 5.15 Secondary electron micrographs of the bottom transition zone of the weld W19 at (a) the AS and (b) the RS
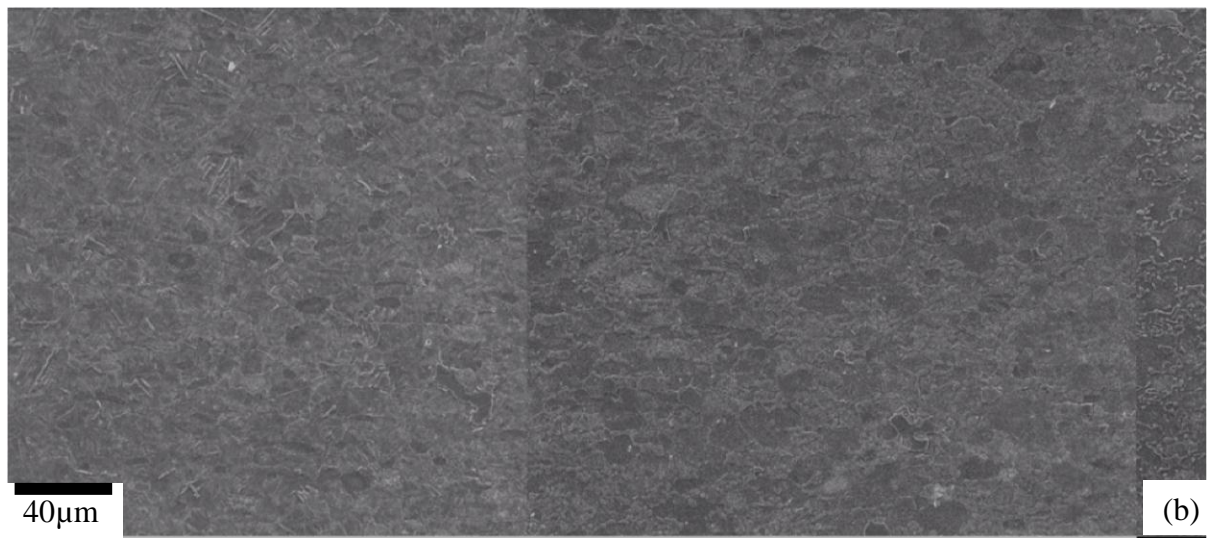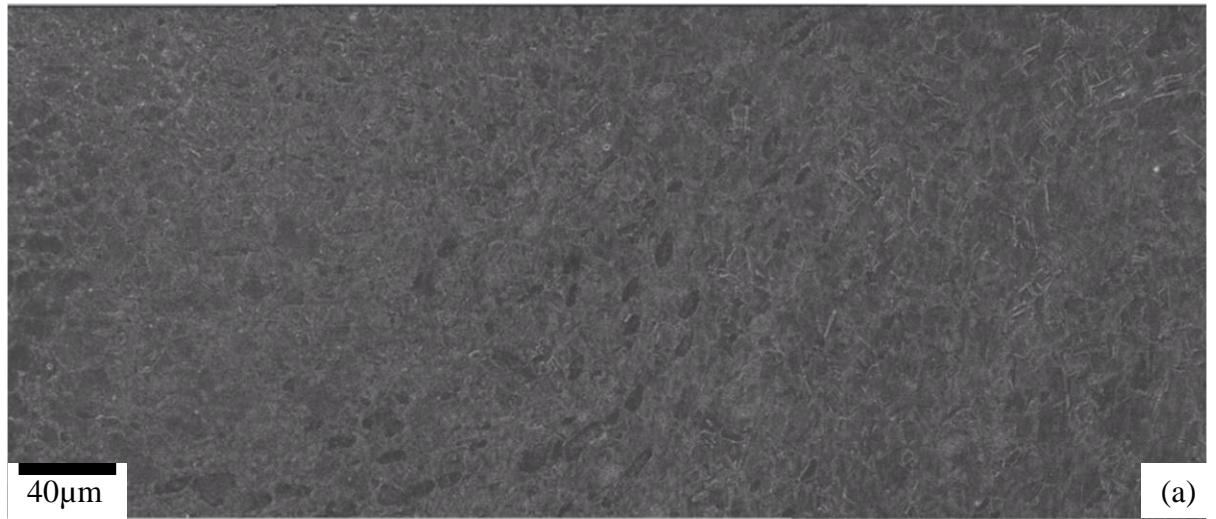
Figure 5.16 Secondary electron micrographs of the surface transition zone of the weld W20 at (a) the AS (b) the RS

40µm

(b)
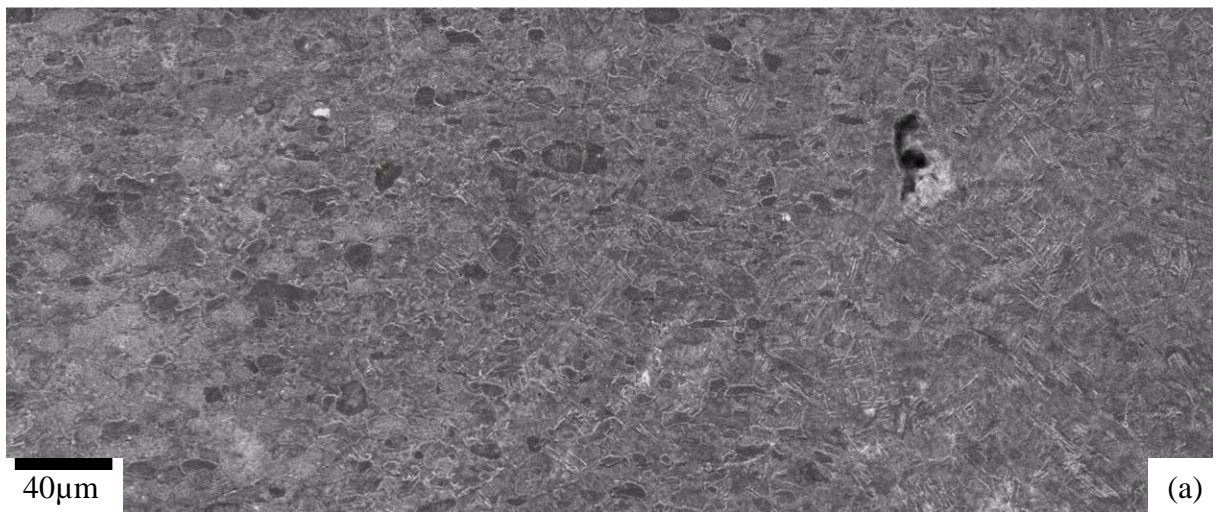
Figure 5.17 Secondary electron micrographs of the centre transition zone of the weld W20 at (a) the AS and (b) the RS



40µm

(a)



40µm

(b)
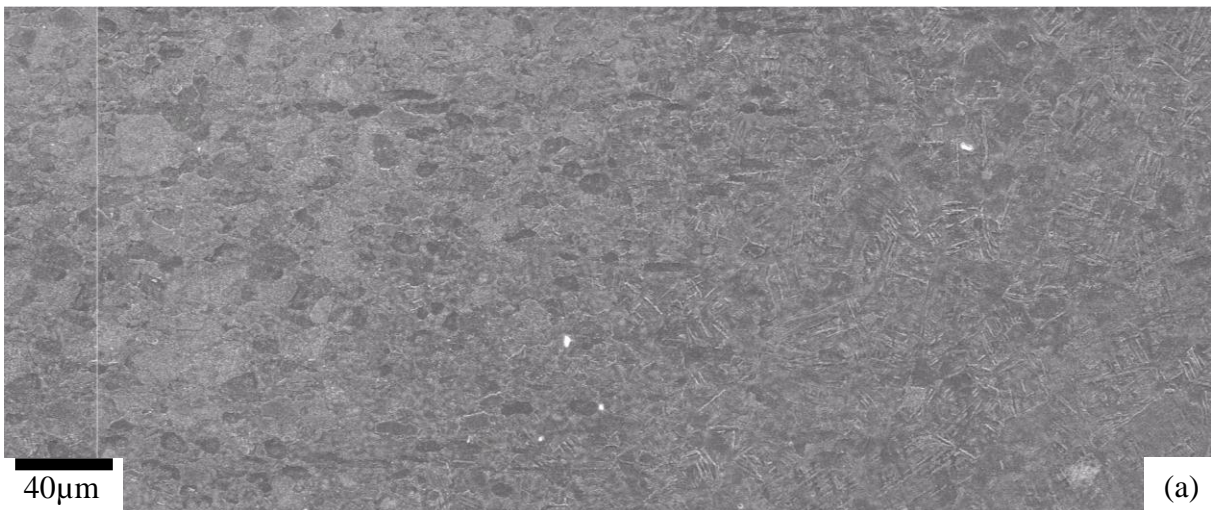
Figure 5.18 Secondary electron micrographs of the bottom transition zone of the weld W20 at (a) the AS and (b) the RS

40μm

40μm

(a)

(b)
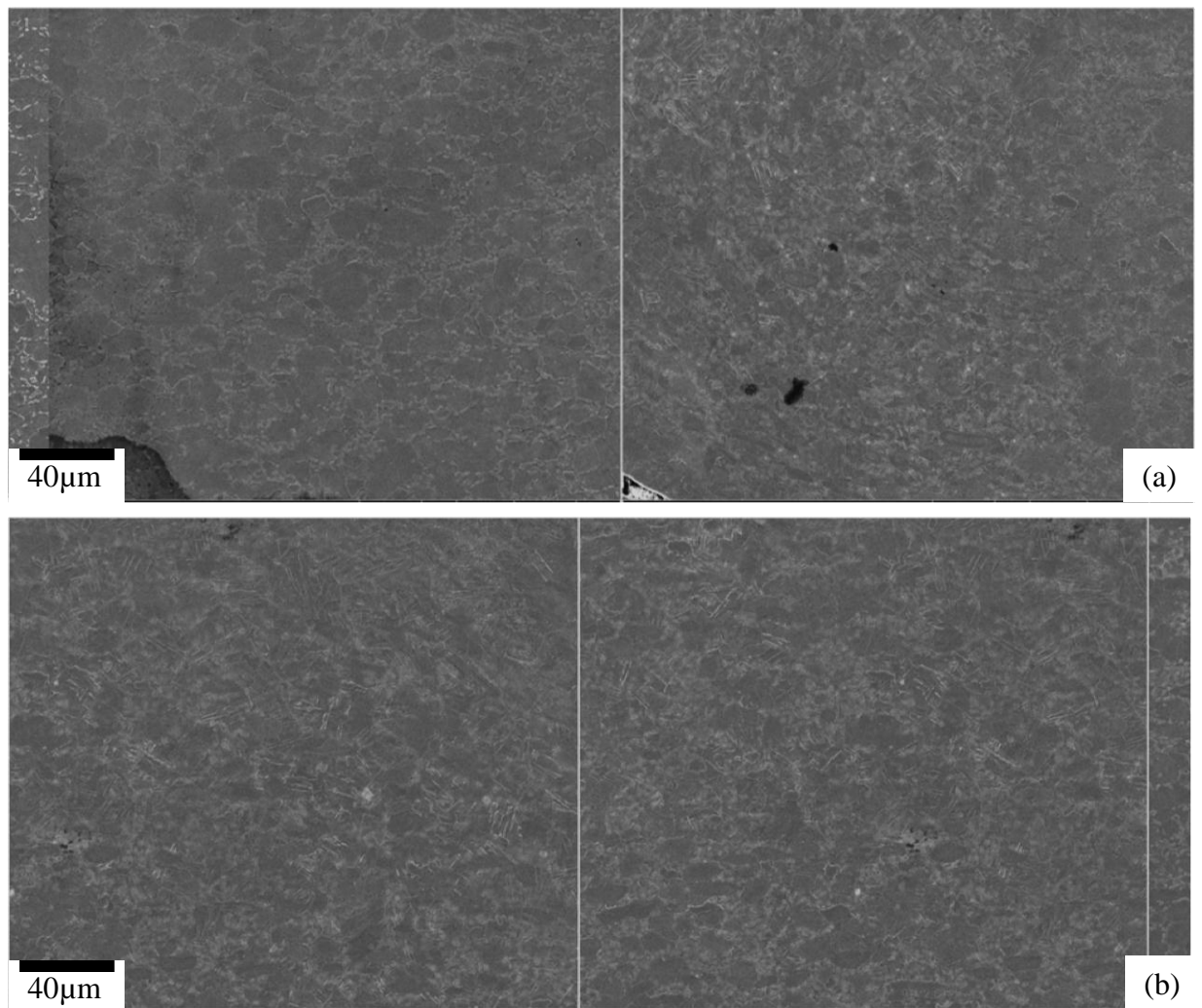
Figure 5.19 Secondary electron micrographs of the surface transition zone of the weld W21
at (a) the AS and (b) the RS



40μm

(a)
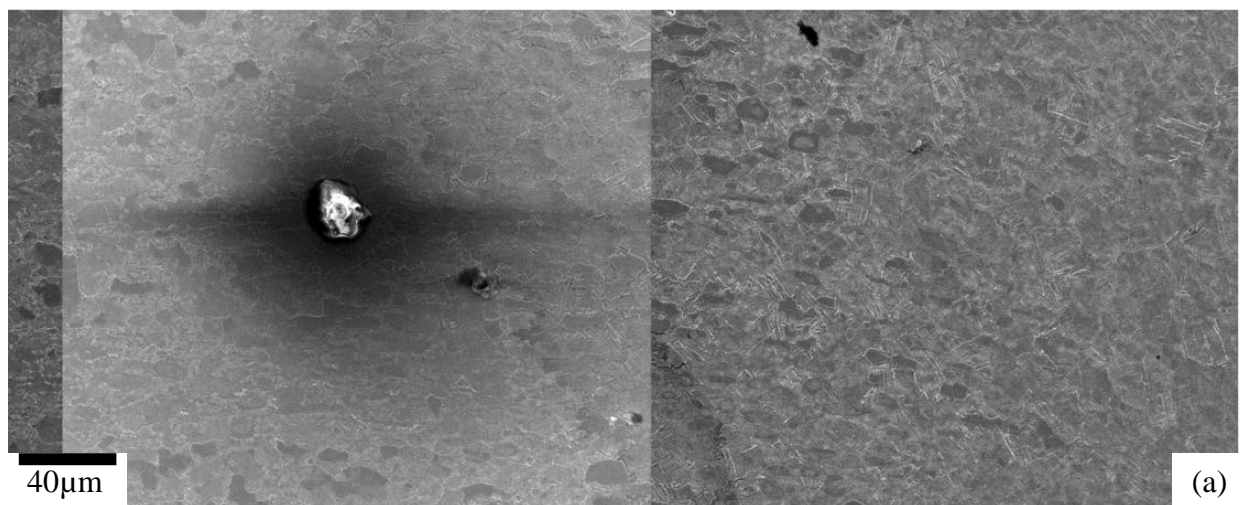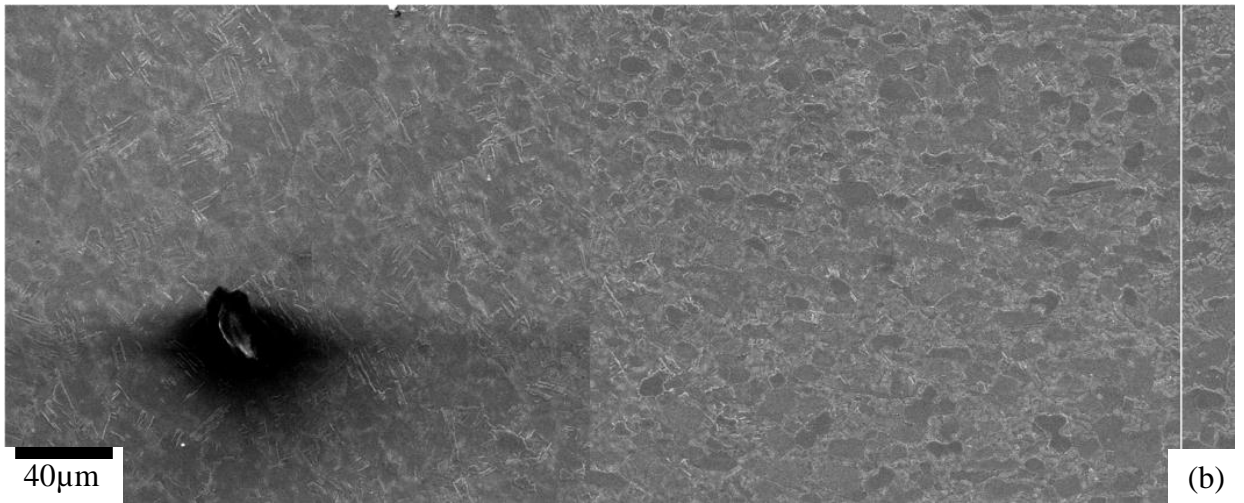
Figure 5.20 Secondary electron micrographs of the centre transition zone of the weld W21
at (a) the AS and (b) the RS
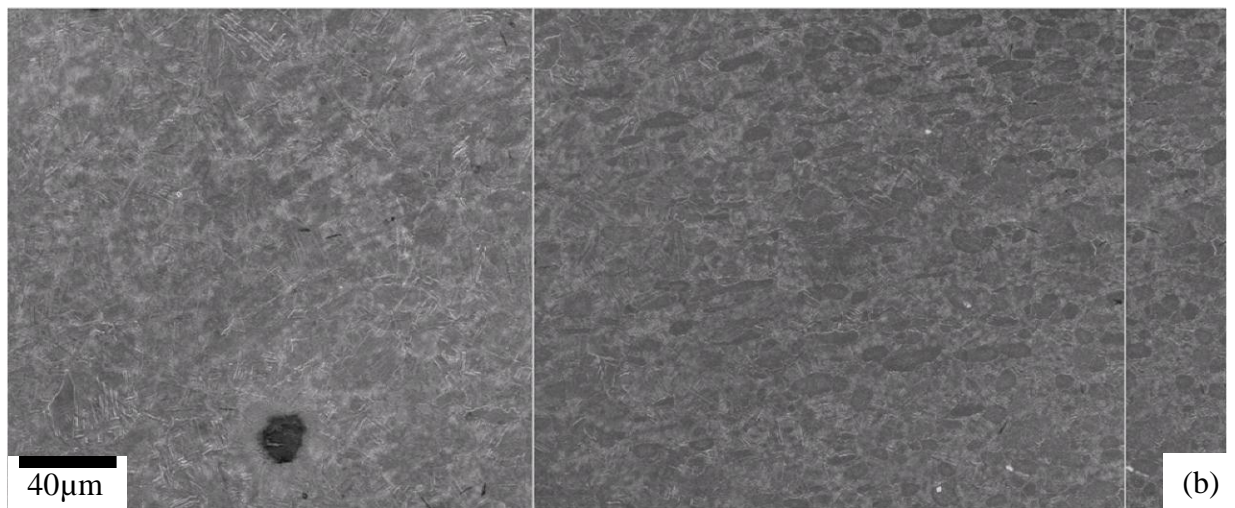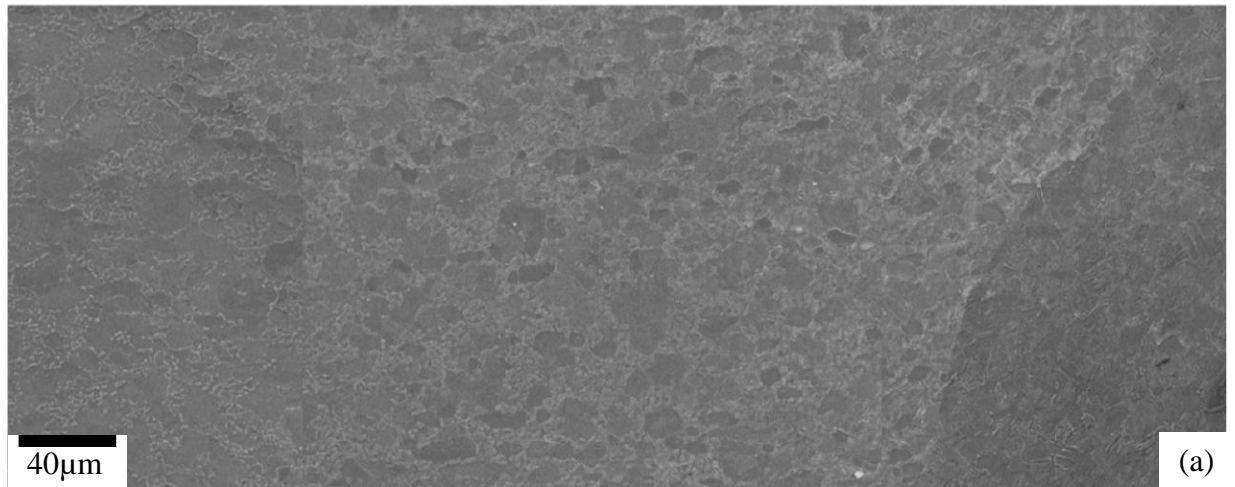


Figure 5.21 Secondary electron micrographs of the bottom transition zone of the weld W21
at (a) the AS and (b) the RS

5.2.4 Bimodal structure

In the case of the BM having equiaxed structure, the heat affected zone of FSW of Ti-6Al-4V has been reported to have a bimodal microstructure consisting of equiaxed $\alpha_p$ grains and fine transformed lamellar $\alpha+\beta$ laths (Zhang et al., 2008a; Juhas et al., 2000). This region is partially defined as the heat affected zone (HAZ) as they were affected by temperature which generated a microstructure change from the equiaxed structure to the bimodal structure but with no visible deformation. Figure 5.22 shows the secondary electron micrographs of the central bimodal structure of the weld zones adjacent to the equiaxed structure in the BM from the three welds W4, W5 and W6 with 900rpm rotation speed at both the AS and the RS, respectively. Figure 5.22(a) is a high magnification micrograph obtained from the bimodal structure at the RS of W4B4, Figure 5.22(c) shows the bimodal structure at the AS of W5B5. Figure 5.22(b) shows a high resolution micrograph of the central bimodal structure at the RS of W6B6. Figure 5.22(e) displays the central bimodal structure at the AS of the surface normal section 5.6.b while the $\alpha_p$ grains are elongated along the transverse direction (TD) (Figure 5.22(c)). Table 5.1 shows the width of the bimodal structure and volume fraction of $\alpha_p$ phase in the weld centre at both the AS and the RS of the three cross sections W4B4, W5B5 and W6B6

Table 5.1 Width of the bimodal structure and volume fraction of $\alpha_p$ phase in the weld centre of the three cross sections W4B4, W5B5 and W6B6

| Weld No | | W4 | W5 | W6 |
|---|---|---|---|---|
| Traverse speed, mm/min | | 50 | 100 | 150 |
| Width of the bimodal structure, μm | AS | 580 | 450 | 420 |
| | RS | 660 | 550 | 420 |
| Volume fraction of $\alpha_p$ at the AS, % | | 50 | 55 | 60 |
| Volume fraction of $\alpha_p$ at the RS, % | | 53 | 58 | 62 |
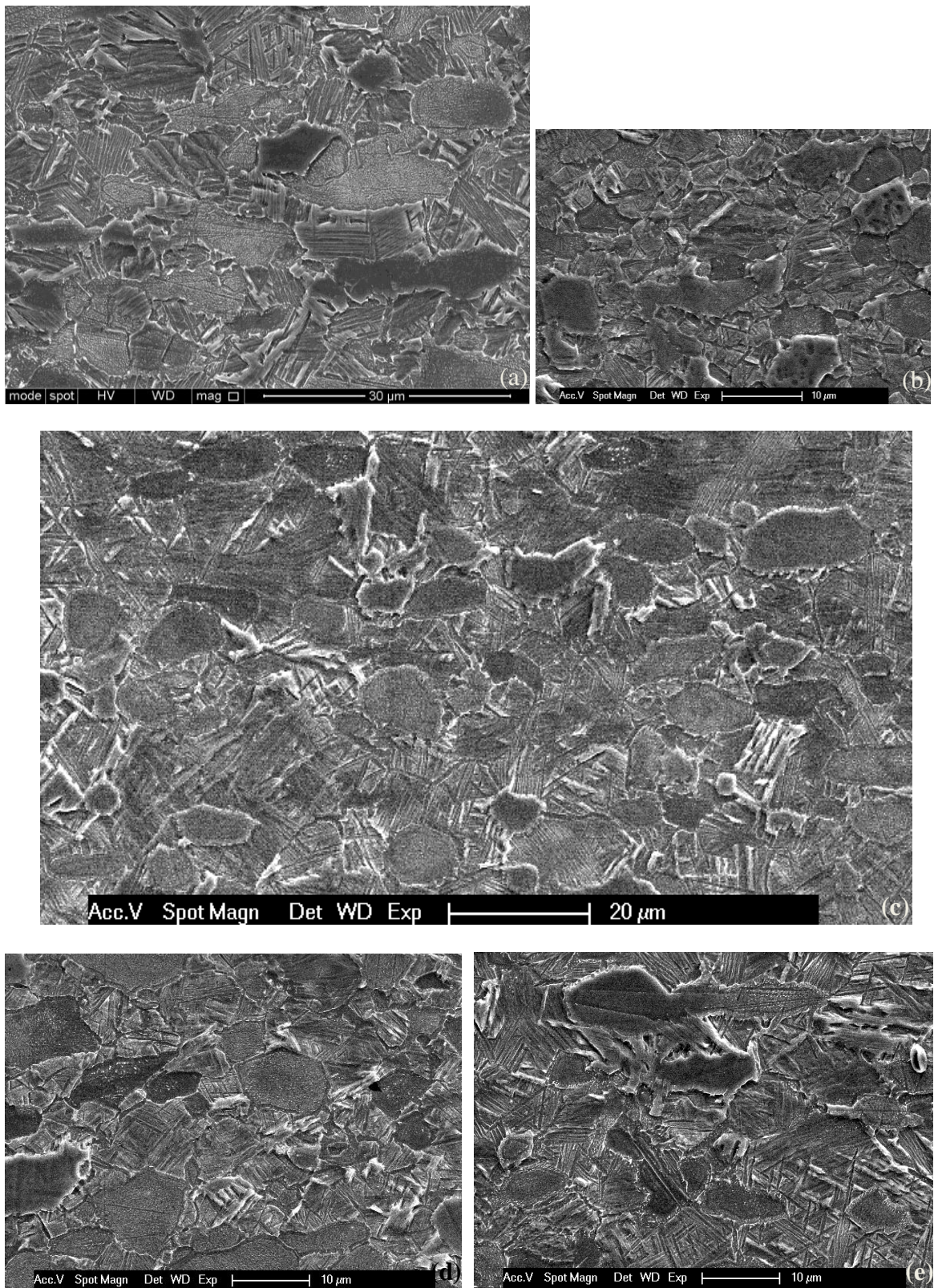
Figure 5.22 Secondary electron micrographs of the central bimodal structure at the RS of the three welds with 900rpm rotation speed: (a) W4B4, (b) W6B6, (c) W5B5, and at the AS (d) W6B6; (e) 5.6.b

123

High resolution secondary electron micrographs of the central bimodal structure at the AS of the three welds W19, W20 and W21 with a constant traverse speed of 150mm/min are shown in Figure 5.23(a), (b) and (c), respectively, and Figure 5.23(d) is a micrograph taken from the central bimodal structure at the RS of W21. Table 5.2 shows the width of the bimodal structure and volume fraction of αp phase in the weld centre at both the AS and the RS of W19, W20 and W21.
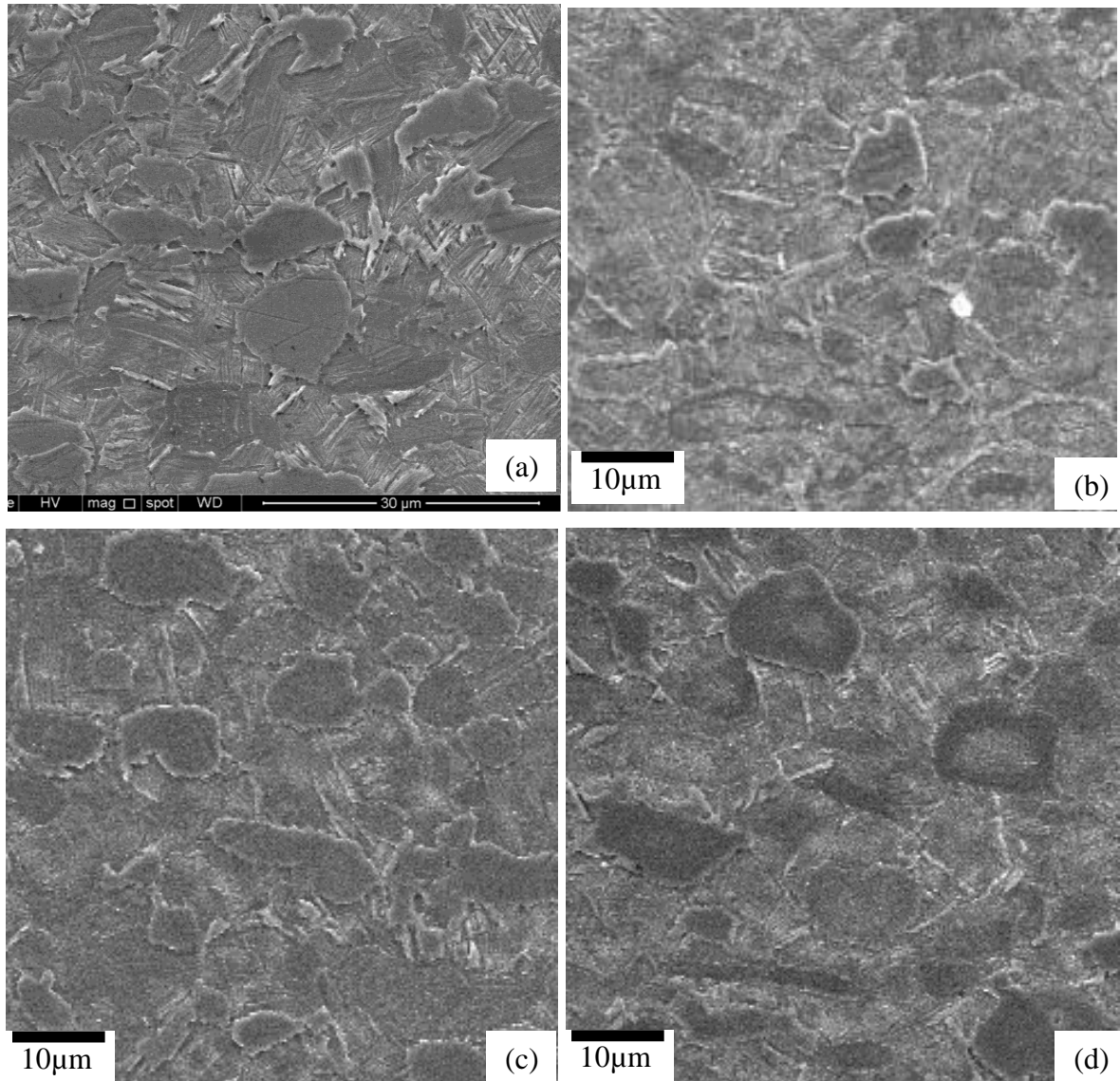


Figure 5.23 Secondary electron micrographs of the central bimodal structure at the AS of the three welds (a) W19, (b) W20, (c) W21 and at the RS of (d) W21

Table 5.2 Width of the bimodal structure and volume fraction of αp phase in the weld centre of the three welds W19, W20 and W21

| Weld No | | W19 | W20 | W21 |
|---|---|---|---|---|
| Rotation speed, rpm | | 800 | 600 | 400 |
| Width of the bimodal structure, μm | AS | 250 | 200 | 180 |
| | RS | 300 | 220 | 195 |
| Volume fraction of $\alpha_p$ at the AS, % | | 70 | 73 | 76 |
| Volume fraction of $\alpha_p$ at the RS, % | | 72 | 75 | 77 |

5.2.5 Coarse lamellar structure adjacent to the bimodal structure

As we move away from the welding edge to the weld centre, volume fraction of αp phase in the bimodal structure was gradually diminishing to 0pct and the microstructure has been changed to a coarse lamellar structure of 800-1000μm length containing coarse α laths, which is typical of material cooled above the β transus. A typical coarse lamellar structure is shown as an optical micrograph in Figure 5.24 and the coarse lamellar structure taken from the weld centre at both the AS and the RS of the cross sections of all the six welds W4, W5, W6, W19, W20 and W21 are shown from Figure 5.25 to Figure 5.30 as Secondary electron micrographs.

20µm
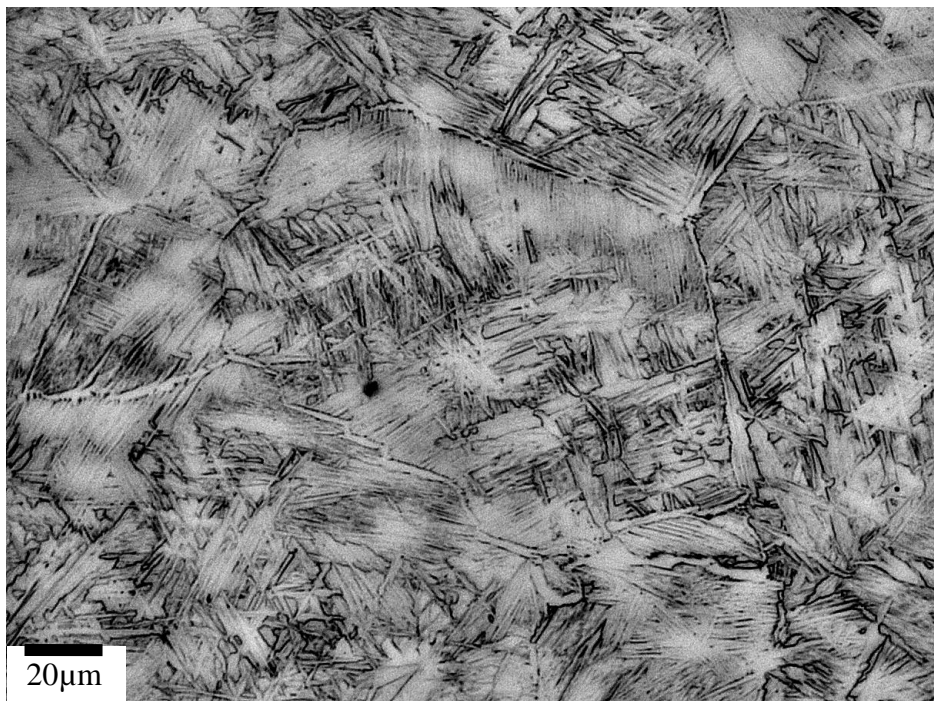
Figure 5.24 Optical micrograph of the coarse lamellar structure adjacent to the bimodal structure of 4.4.b
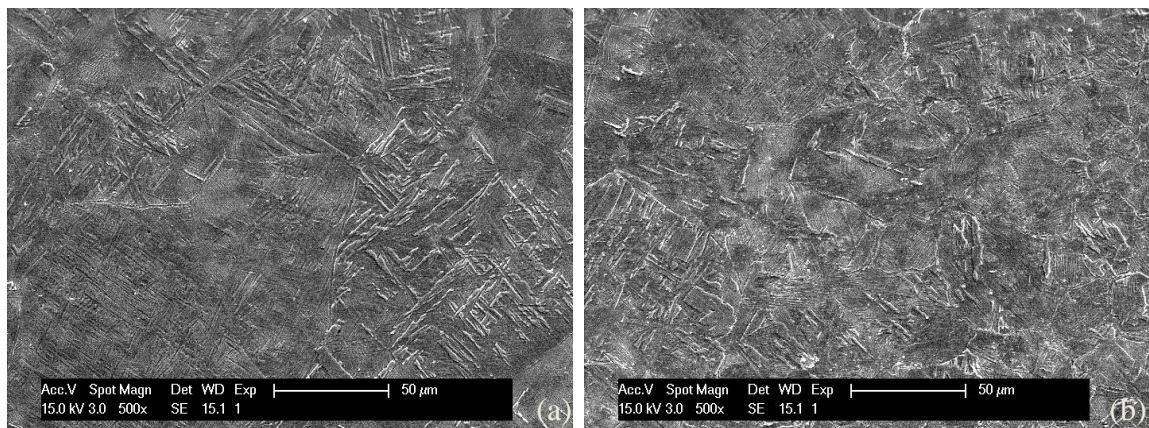


Figure 5.25 Secondary electron micrographs of the coarse lamellar structure of W4 at (a) the AS and (b) the RS
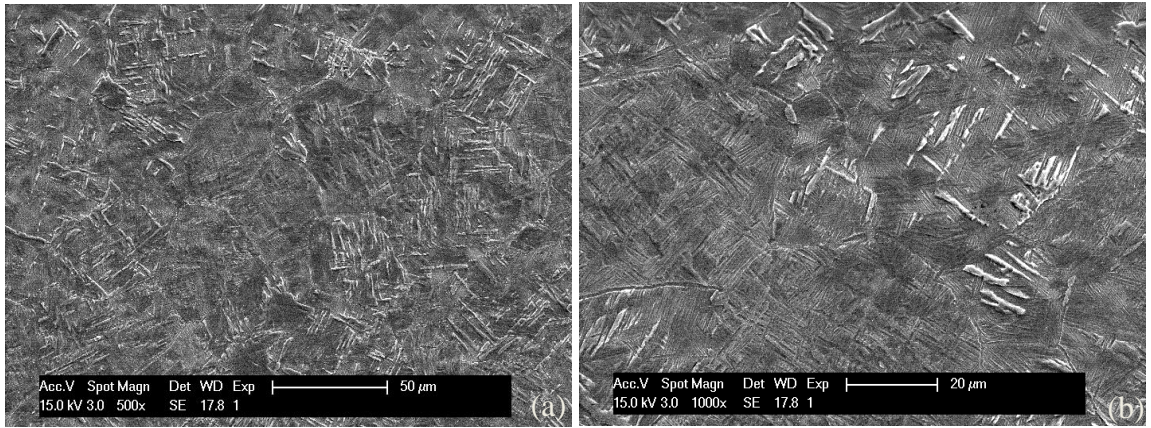
Figure 5.26 Secondary electron micrographs of the coarse lamellar structure of W5 at (a) the AS and (b) the RS
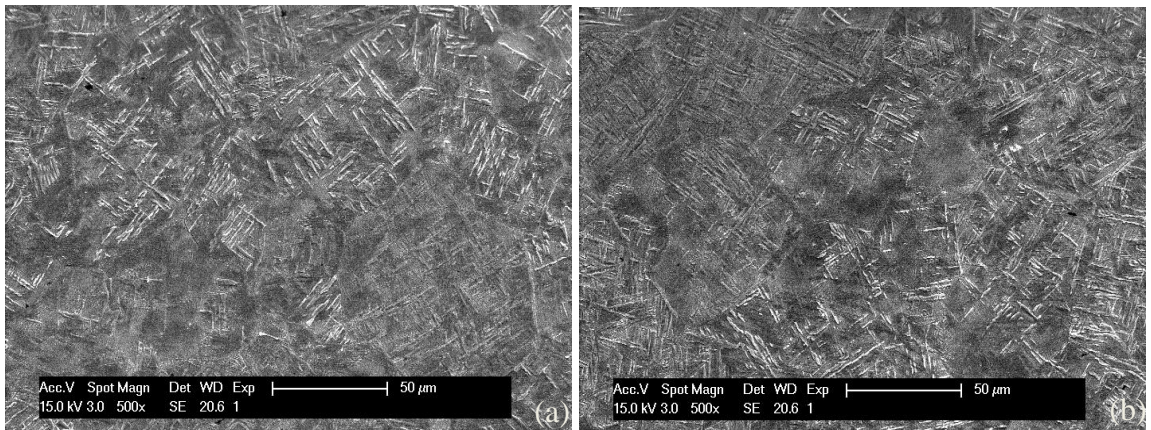


Figure 5.27 Secondary electron micrographs of the coarse lamellar structure of W6 at (a) the AS and (b) the RS
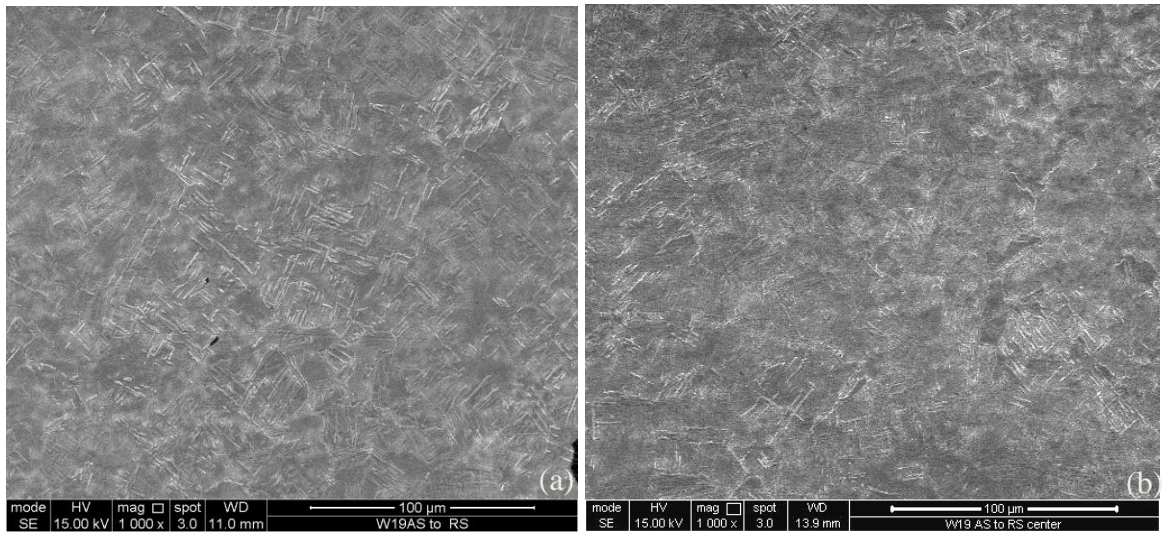


Figure 5.28 Secondary electron micrographs of the coarse lamellar structure of W19 at (a) the AS and (b) the RS

127
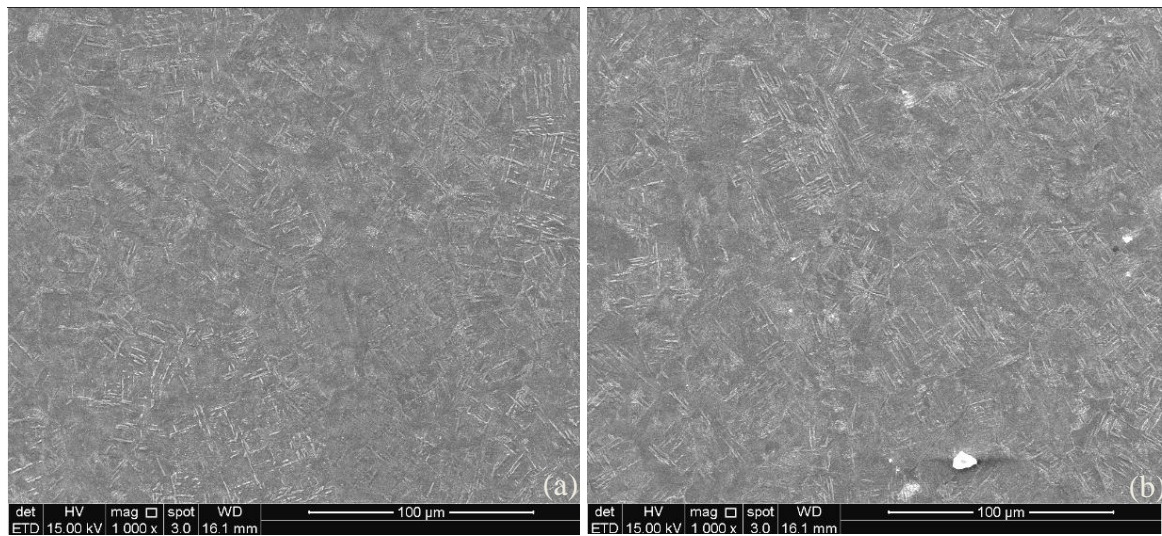
Figure 5.29 Secondary electron micrographs of the coarse lamellar structure of W20 at (a) the AS and (b) the RS
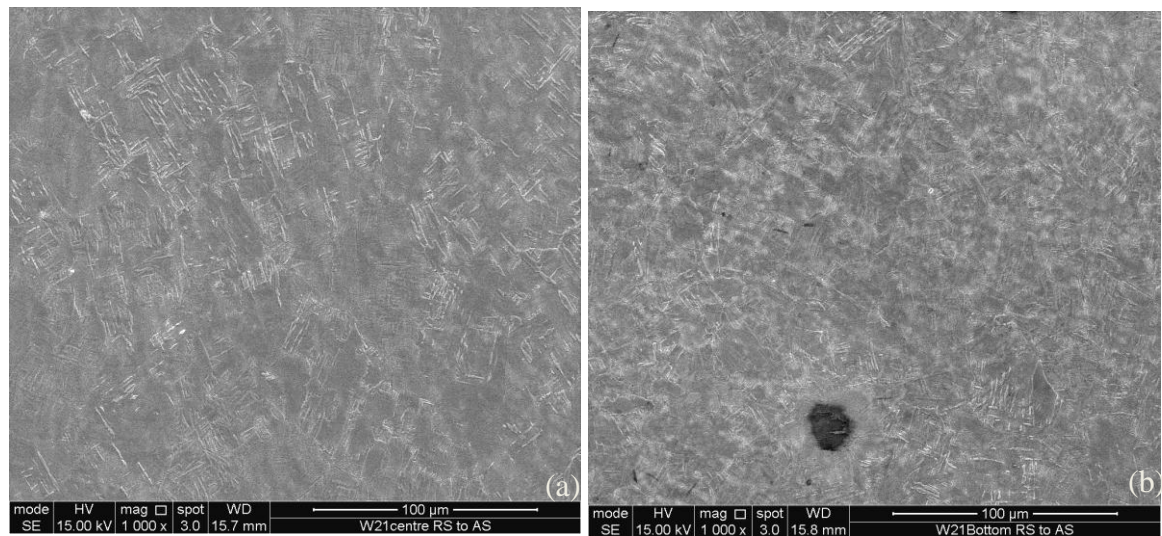


Figure 5.30 Secondary electron micrographs of the coarse lamellar structure of W21 at (a) the AS and (b) the RS

## 5.2.6 Fine lamellar structure of the stir zone

Further into the weld centre, fine lamellar structure just adjacent to the coarse lamellar structure was observed in the weld zones of all the six welds dominating the microstructure in the weld centre, and the width of the fine lamellar structure ranges from 14.5 to 17mm depending on the welding parameters. The fine lamellar structure contains much finer $\alpha$ laths and larger prior $\beta$ grains compared to the coarse lamellar structure, which could be

128

resulted from higher temperature and more deformation experienced in the fine lamellar structure. Thus, the weld region with the fine lamellar structure is defined as stir zone (SZ) in this work. SEM analysis was carried out on the SZ of the cross section W4B4 on both the central horizontal and central vertical lines and the regions selected for vertical and horizontal measurement are indicated as vertical and horizontal arrowed red lines in Figure 5.31, respectively. Figure 5.32(a) to Figure 5.32(j) show the secondary electron micrographs from the weld bottom to the weld surface of the SZ in W4B4 on the central vertical line. Secondary electron micrographs of the adjacent lamellar regions selected from the AS to the RS on the central horizontal line of W4B4 are shown from Figure 5.33(a) to Figure 5.33(f).
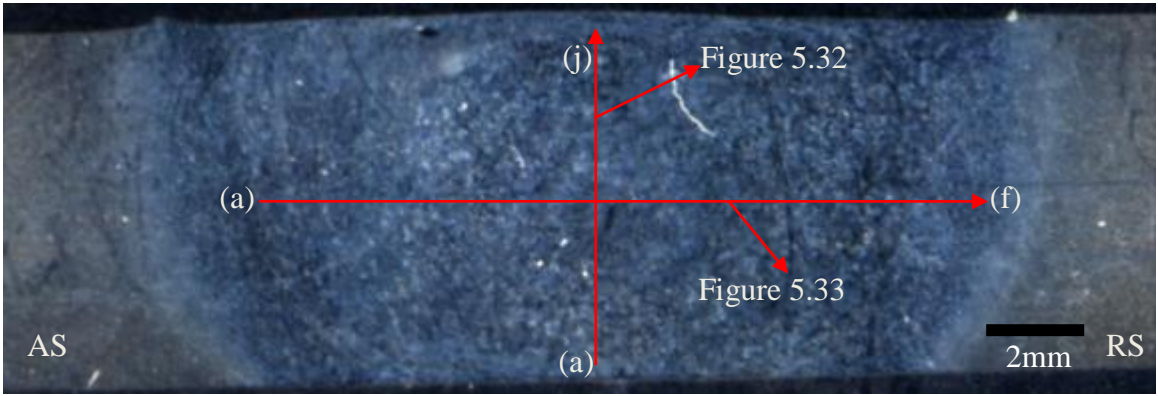


Figure 5.31 Indication of the two measurements taken from the SZ of W4B4
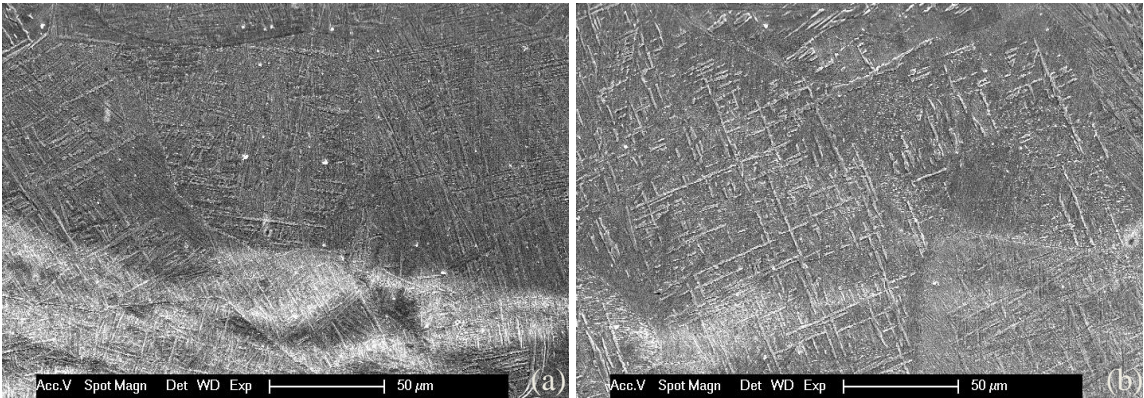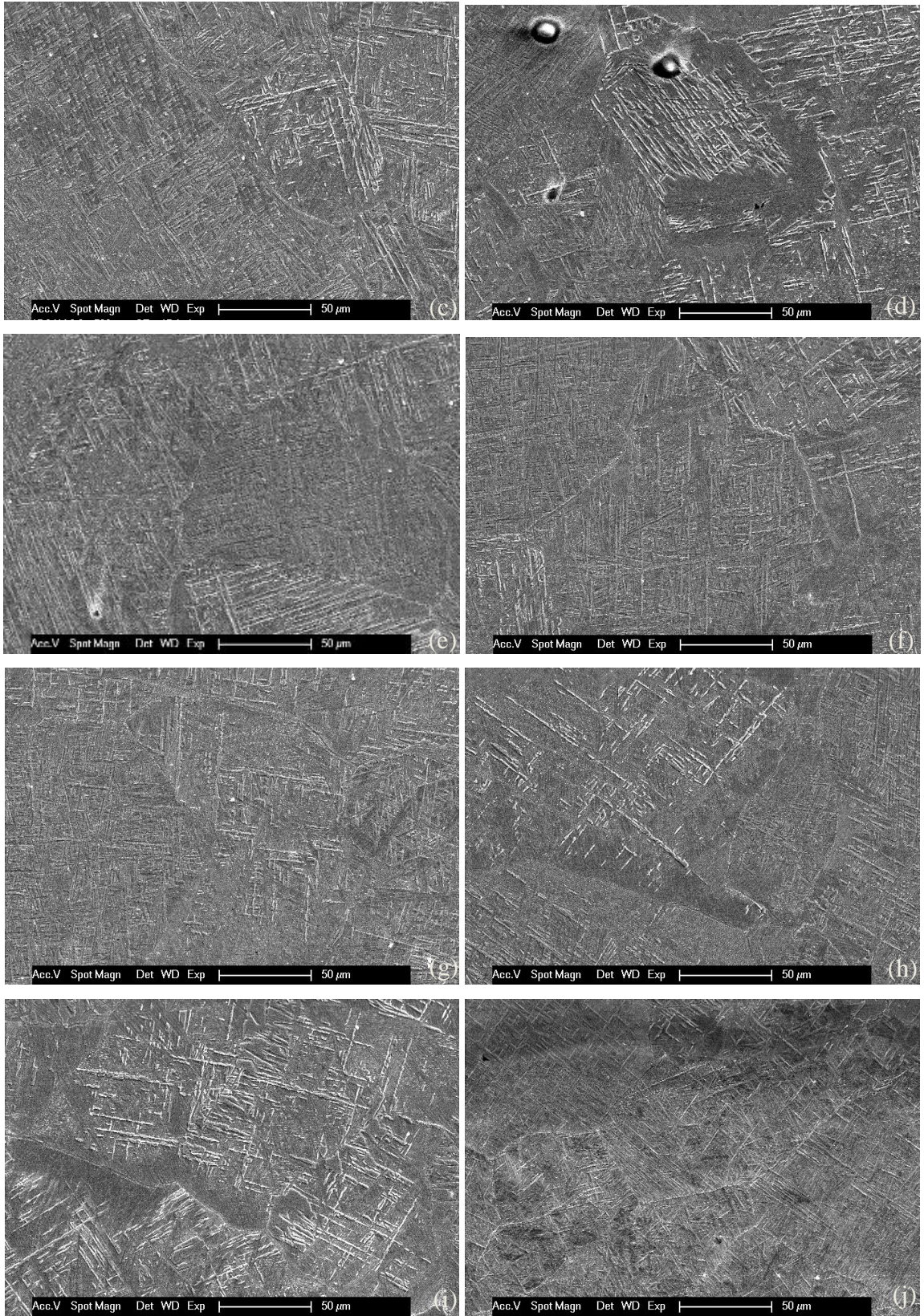
Figure 5.32 (a-j) Secondary electron micrographs from the weld bottom to the weld surface of the SZ in W4B4 on the central vertical line: Y coordinate of a, b, c, d, e, f, g, h, i, j: -2.5, -2, -1.5, -1, 0, 1, 2, 3, 4, 4.5

130
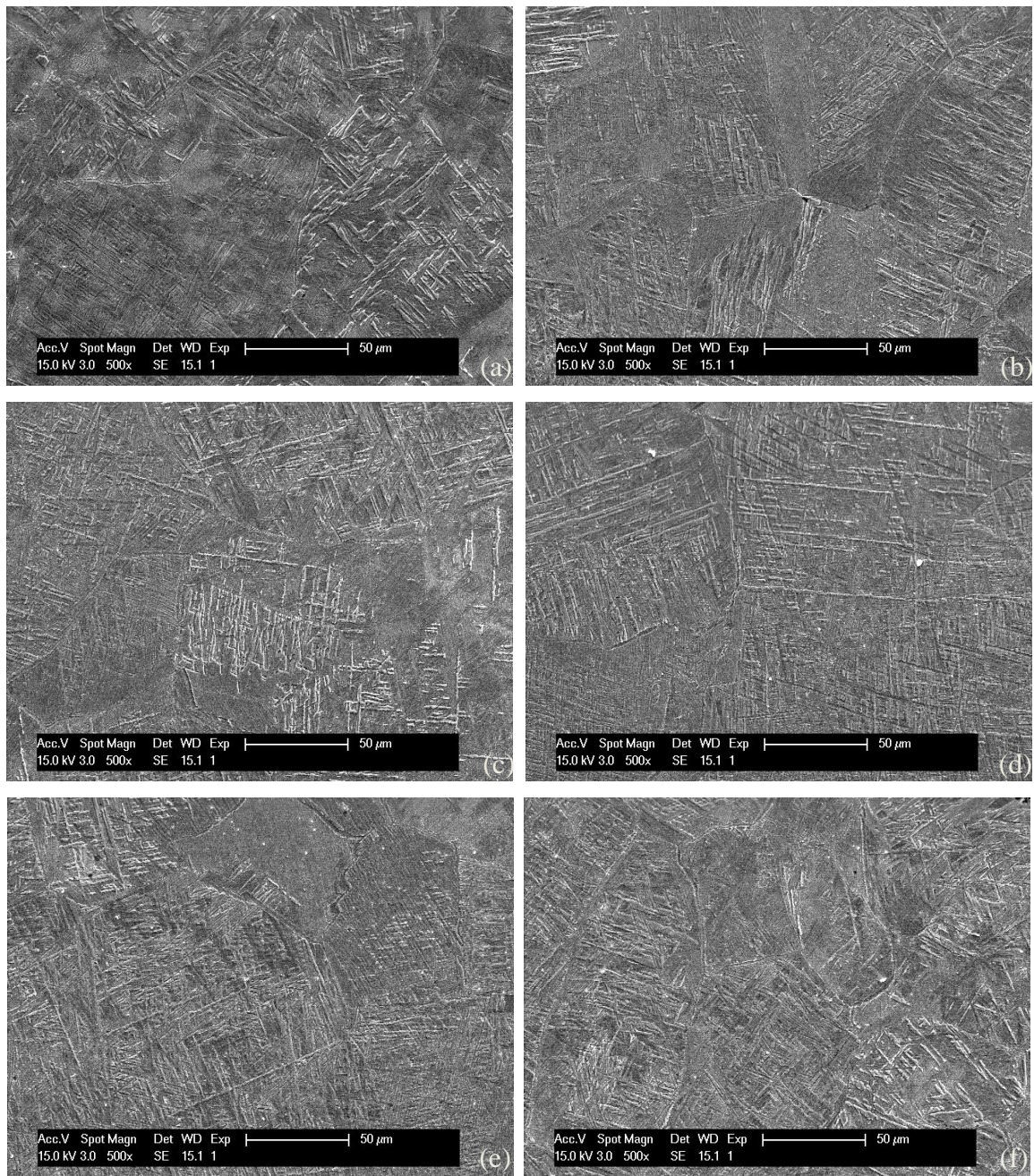
Figure 5.33 (a-f) Secondary electron micrographs from the AS to the RS of the SZ in W4B4 on the central horizontal line, X coordinate of a, b, c, d, e, f: -7.5, -3.5, -1.5, 1.5, 3.5, 7.5

The same measurements using SEM were carried out on the other two cross sections W5B5 and W6B6. SEM analysis was carried out on the SZ of the cross section W5B5 and the regions selected for vertical and horizontal measurement are indicated as vertical and horizontal arrowed red lines in Figure 5.34, respectively. One measurement was obtained

from the weld bottom to the weld surface of the SZ in W5B5 on the central vertical line, results of which is shown in Figure 5.35; Figure 5.36(a-h) show the secondary electron micrographs from the AS to the RS of the lamellar structure in the SZ of W5B5 on the central horizontal line.
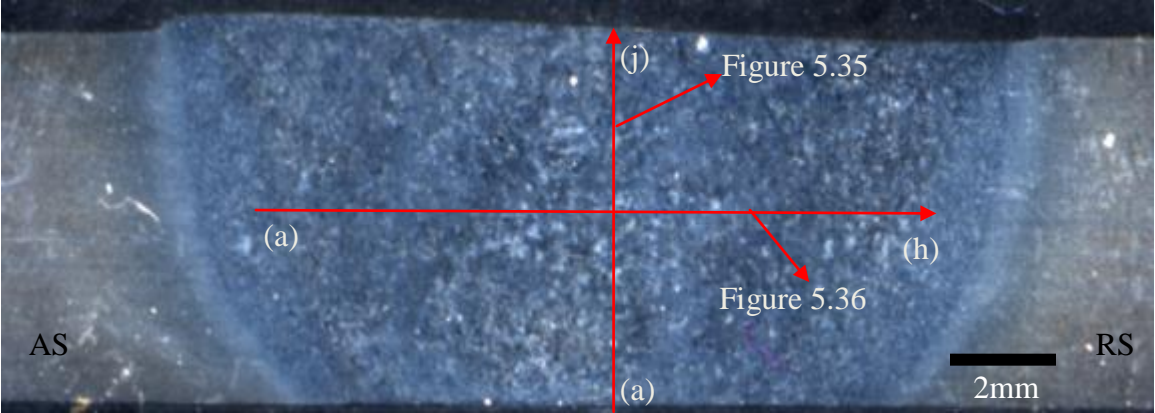


Figure 5.34 Indication of the two measurements taken from the SZ of W5B5
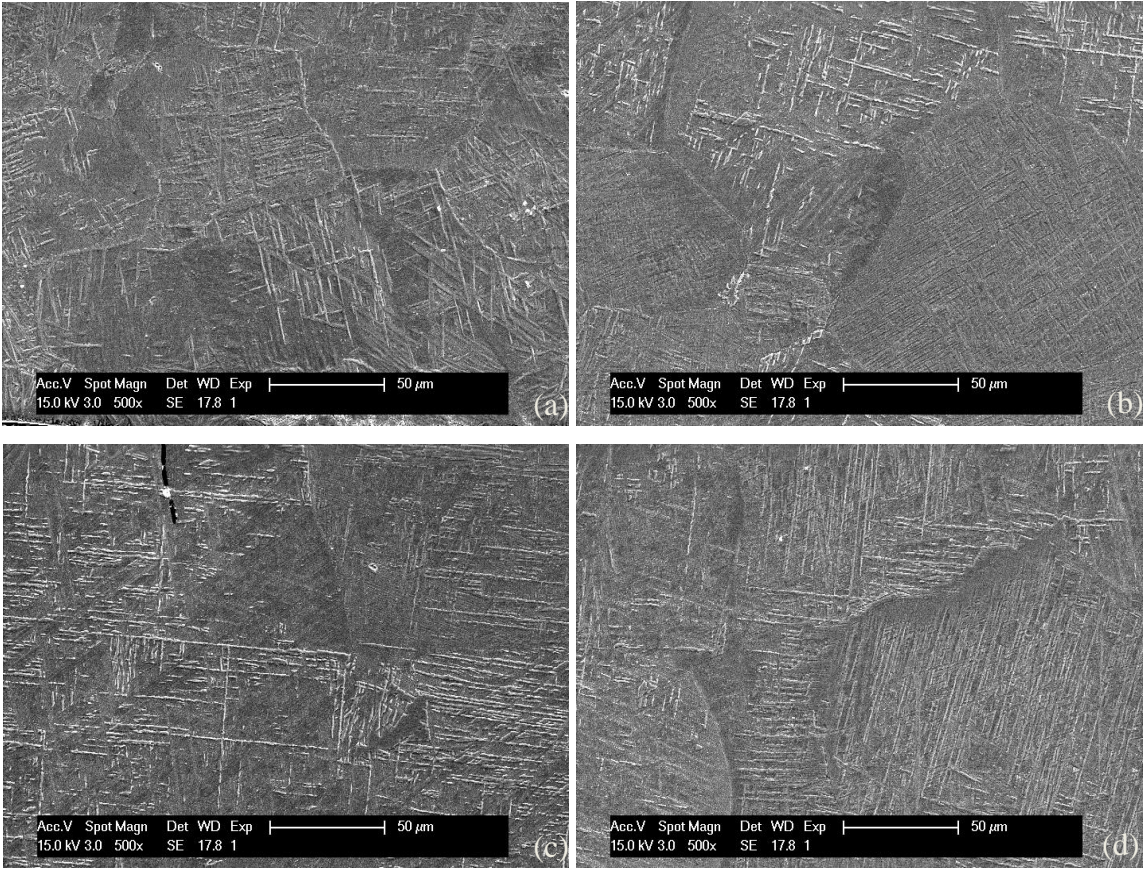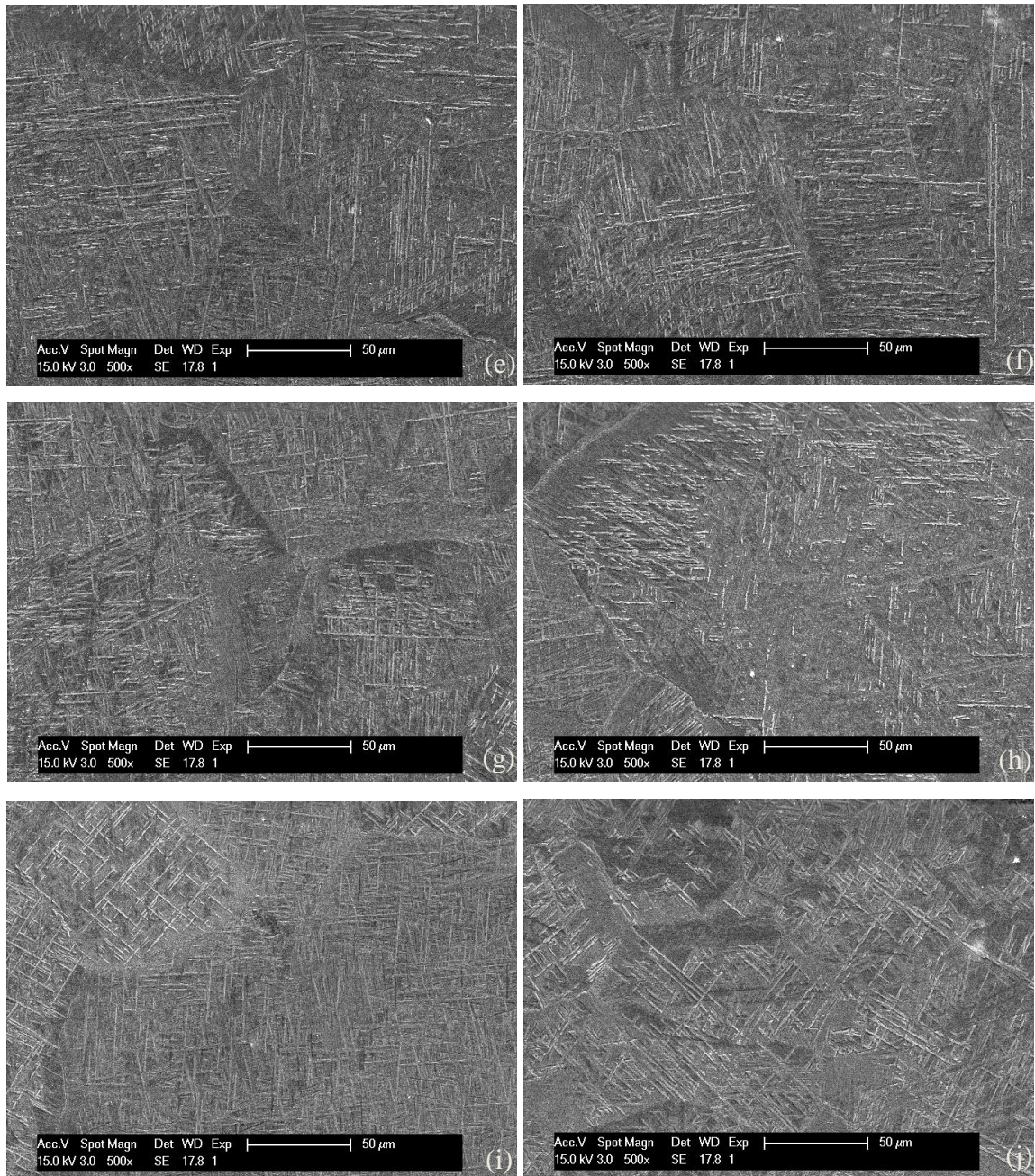
Figure 5.35 (a-j) Secondary electron micrographs from the weld bottom to the weld surface of the SZ in W5B5 on the central vertical line, Y coordinate of a, b, c, d, e, f, g, h, i, j: -2.8, -2, -1, 0, 0.85, 1, 1.5, 2.5, 4, 4.4

133
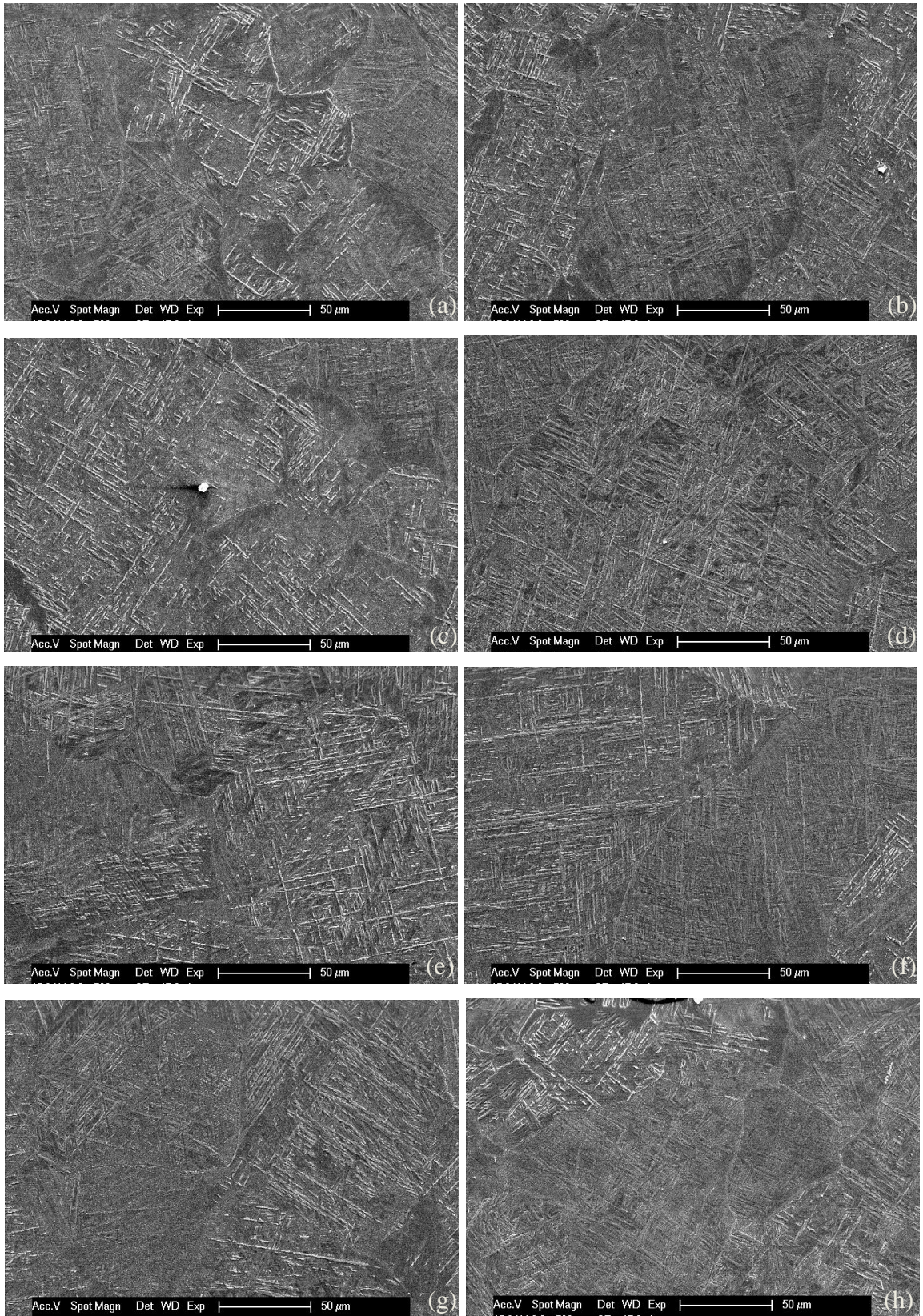
Figure 5.36 (a-h) Secondary electron micrographs from the AS to the RS of the SZ in W5B5 on the central horizontal line, X coordinate of a, b, c, d, e, f, g, h: -7, -6.5, -6, -4, -2, 2, 4, 6

SEM analysis was carried out on the SZ of the cross section W6B6 on both the central horizontal and vertical lines; the regions selected for vertical and horizontal measurement are indicated as vertical and horizontal arrowed red lines in Figure 5.37, respectively. One measurement was obtained from the weld bottom to the weld surface of the SZ in W6B6 on the central vertical line, results of which is shown in Figure 5.38 as Secondary electron micrographs; Figure 5.39 show the secondary electron micrographs from the AS to the RS of the lamellar structure in the SZ on the central vertical line. Secondary electron micrographs from the weld bottom to the weld surface in the SZ centre of W6B6 on the central vertical line are displayed in Figure 5.38(a-h). Figure 5.39(a-h) shows the secondary electron micrographs obtained from the AS to the RS of the lamellar structure in the SZ of W6B6 on the central horizontal line.
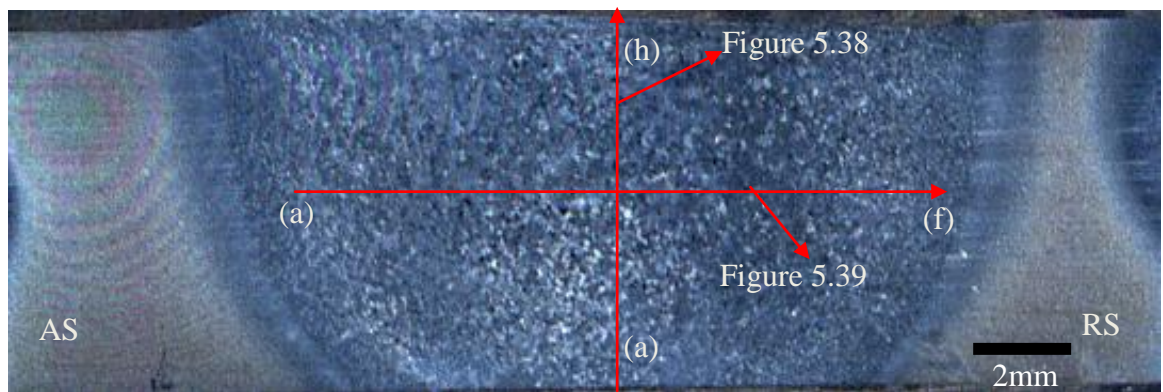


Figure 5.37 Indication of the two measurements taken from the SZ of W6B6
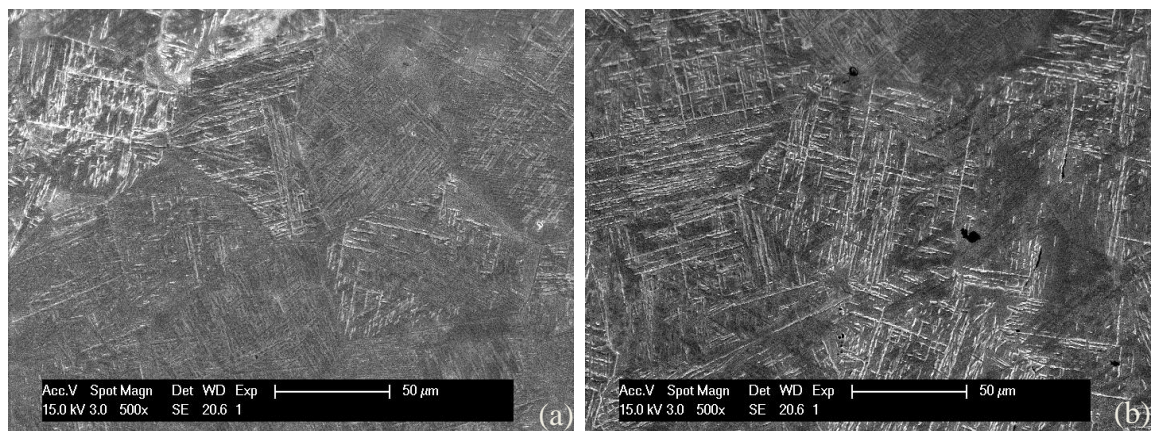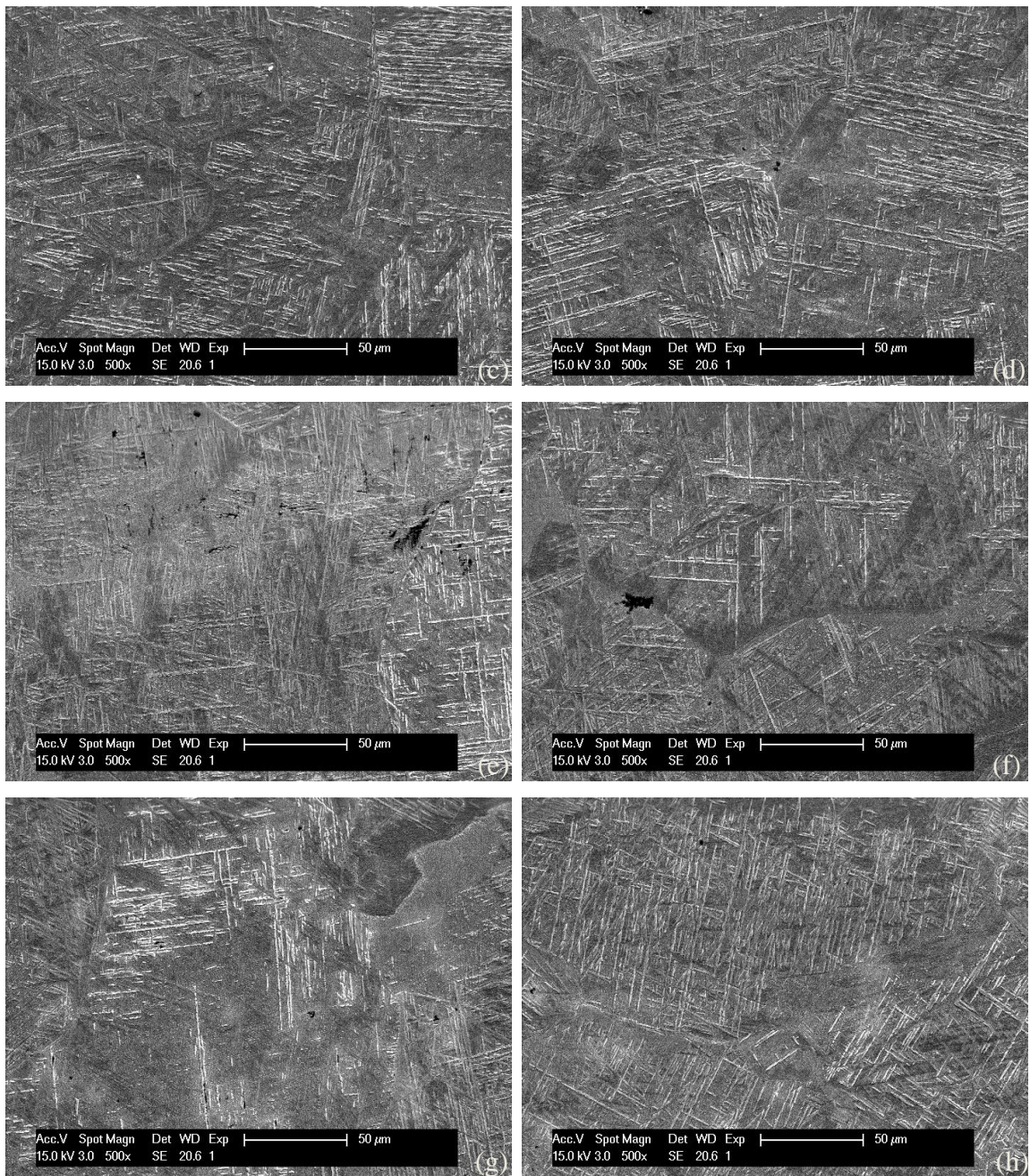
Figure 5.38 (a-h) Secondary electron micrographs from the weld bottom to the weld surface of the SZ in W6B6 on the central vertical line, Y coordinate of a, b, c, d, e, f, g, h,: -2, -1, 0, 1, 2, 3, 4, 4.7
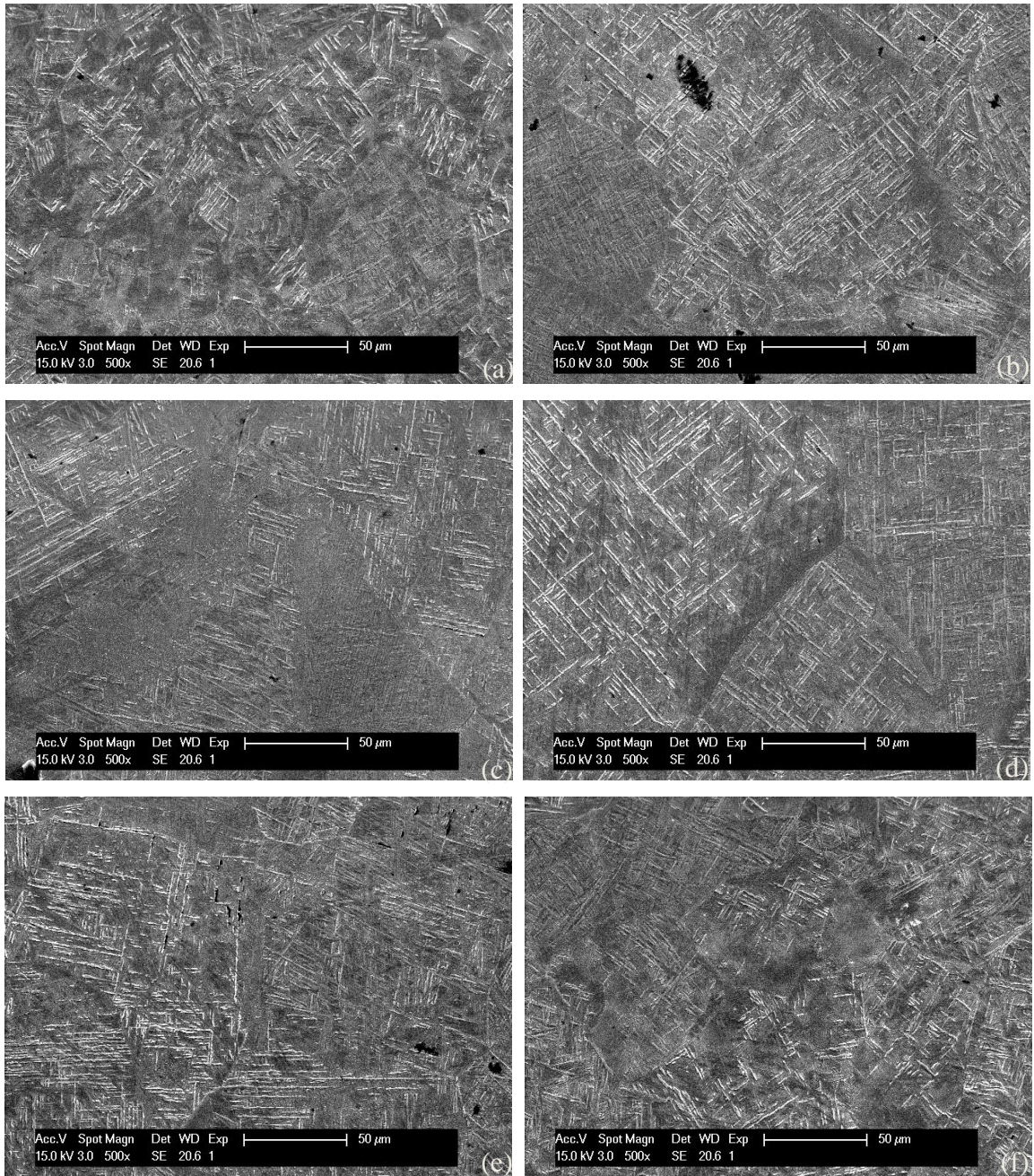
Figure 5.39 (a-f) Secondary electron micrographs taken from the AS to the RS of W6B6 on the central horizontal line, X coordinate of a, b, c, d, e, f: -7, -6.1, 0, 2, 4, 6

SEM analysis was carried out on the SZ of the cross section W19 on both horizontal and central vertical lines; the regions selected for vertical and horizontal measurement are indicated as vertical and horizontal arrowed red lines in Figure 5.40, respectively. Figure 5.41(a-j) shows the secondary electron micrographs obtained from the weld bottom to the weld surface in the centre of the SZ in W19 on the central vertical line and Secondary

electron micrographs obtained from the AS to the RS of the lamellar structure at the weld surface of the SZ in W19 on a horizontal line are shown in Figure 5.42(a-h).
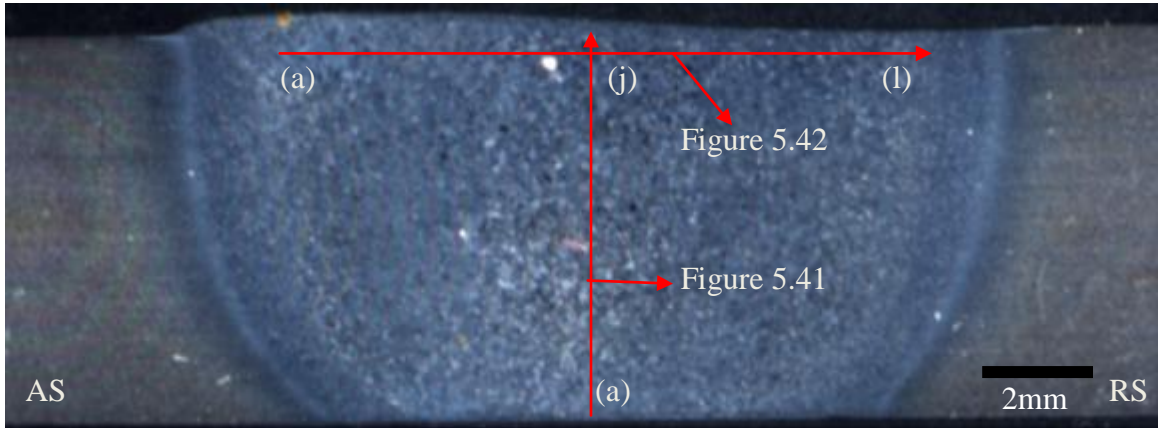


Figure 5.40 Indication of the two measurements taken from the SZ of W19
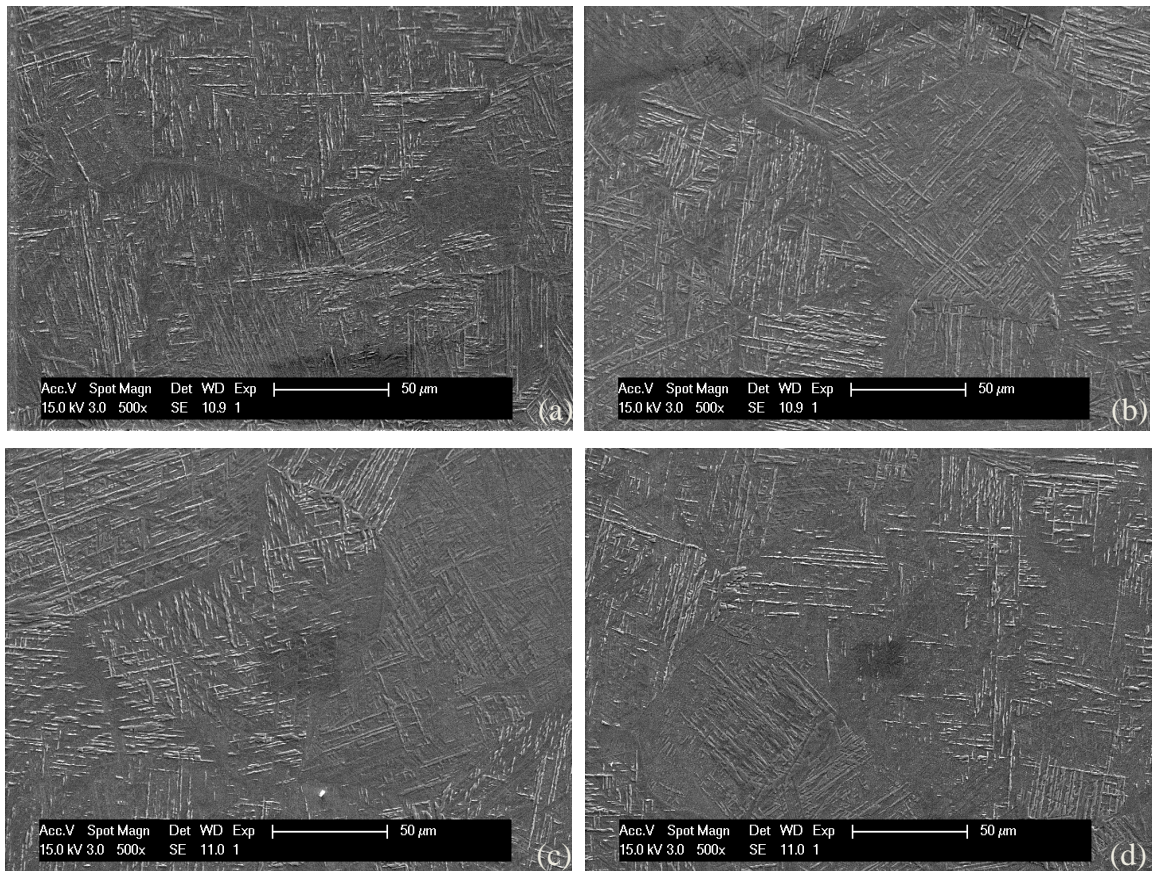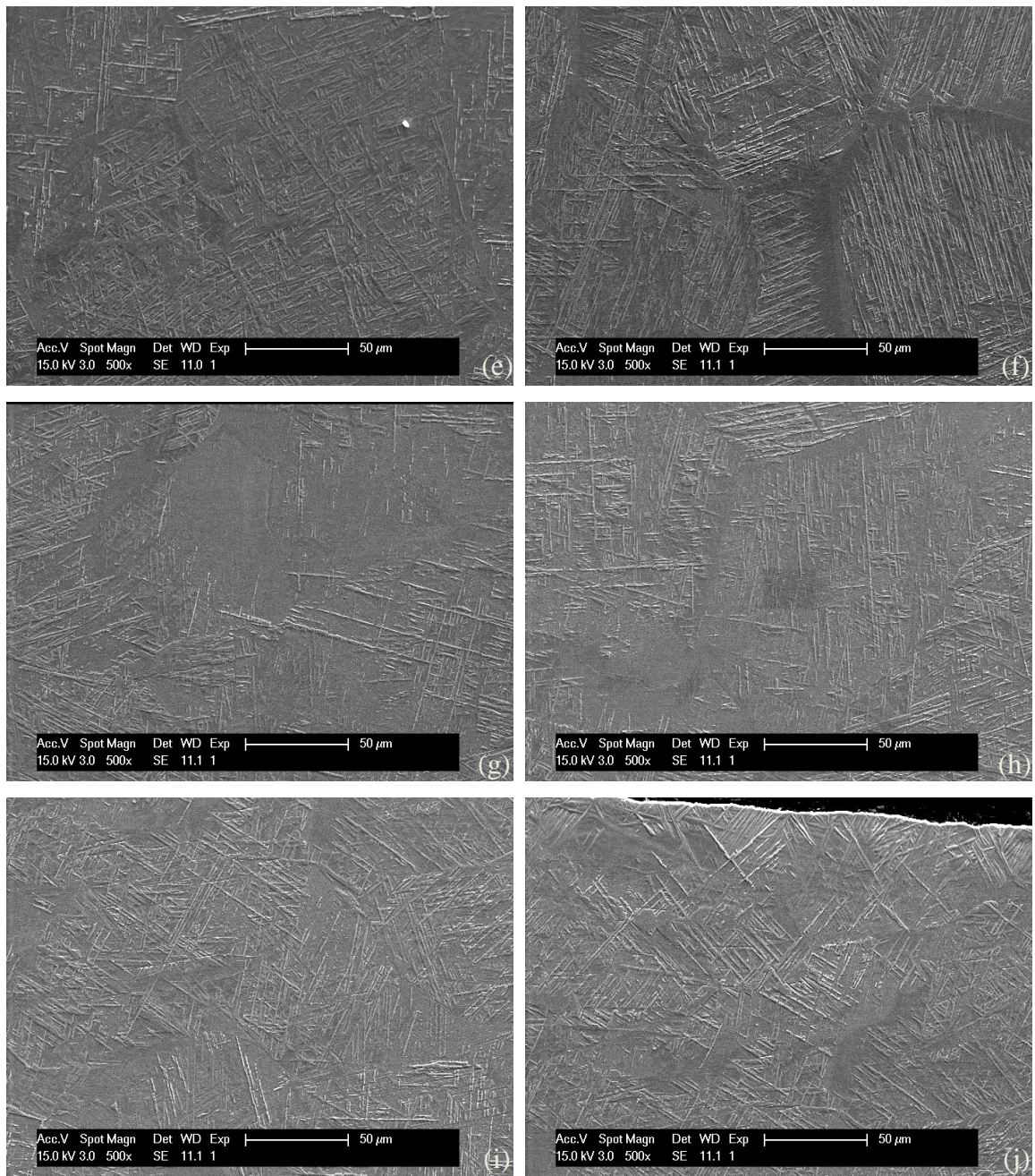
Figure 5.41 (a-h) Secondary electron micrographs from the AS to the RS of the SZ in W19 on the central vertical line, Y coordinate of a, b, c, d, e, f, g, h, i, j: Y= -3.5, -2.4, -1.3, -0.4, 0, 0.3, 1.2, 2.1, 3, 3.5
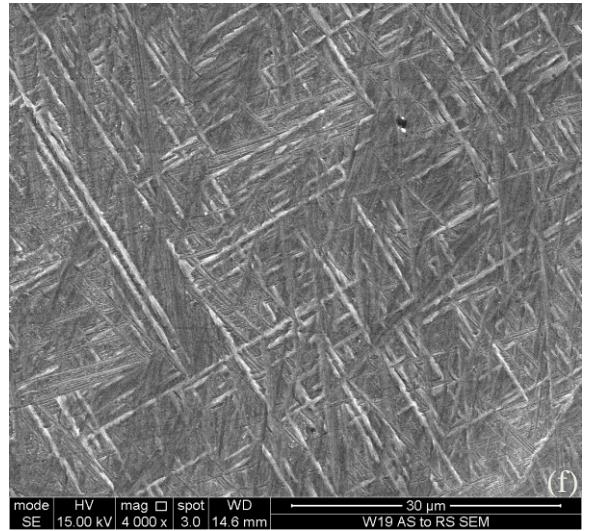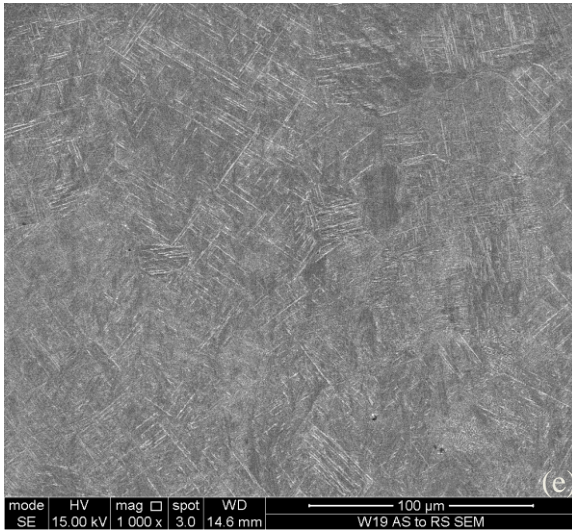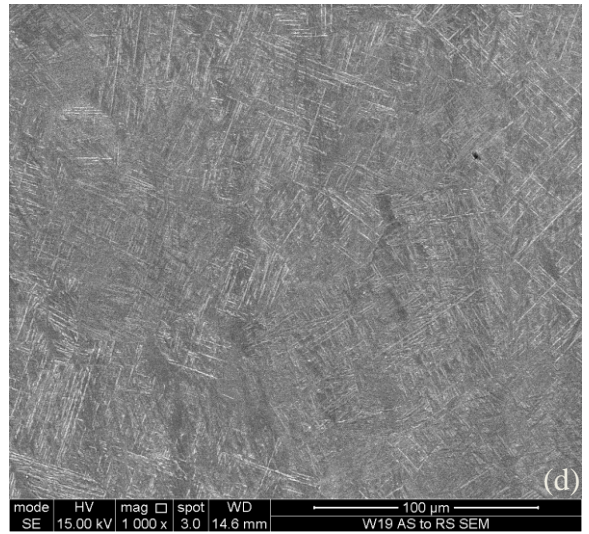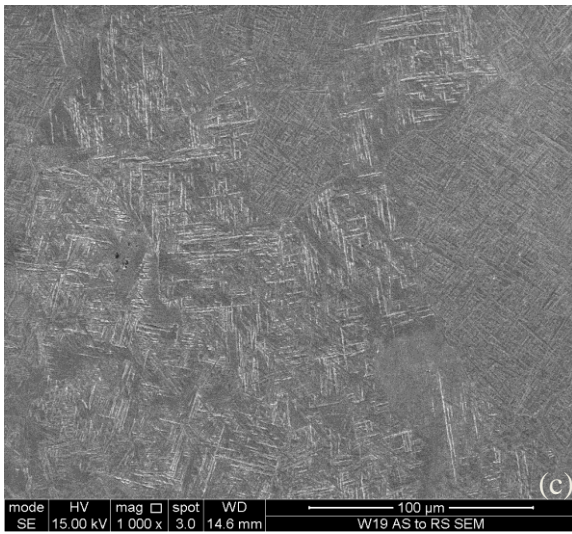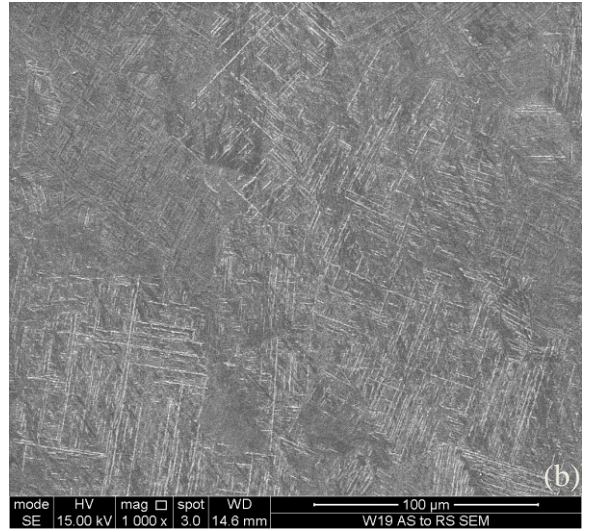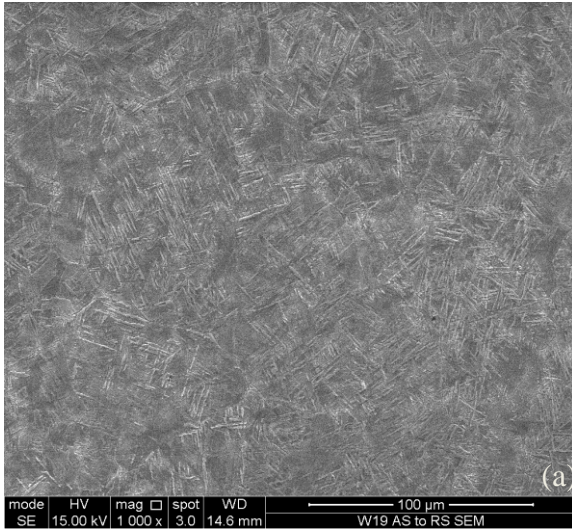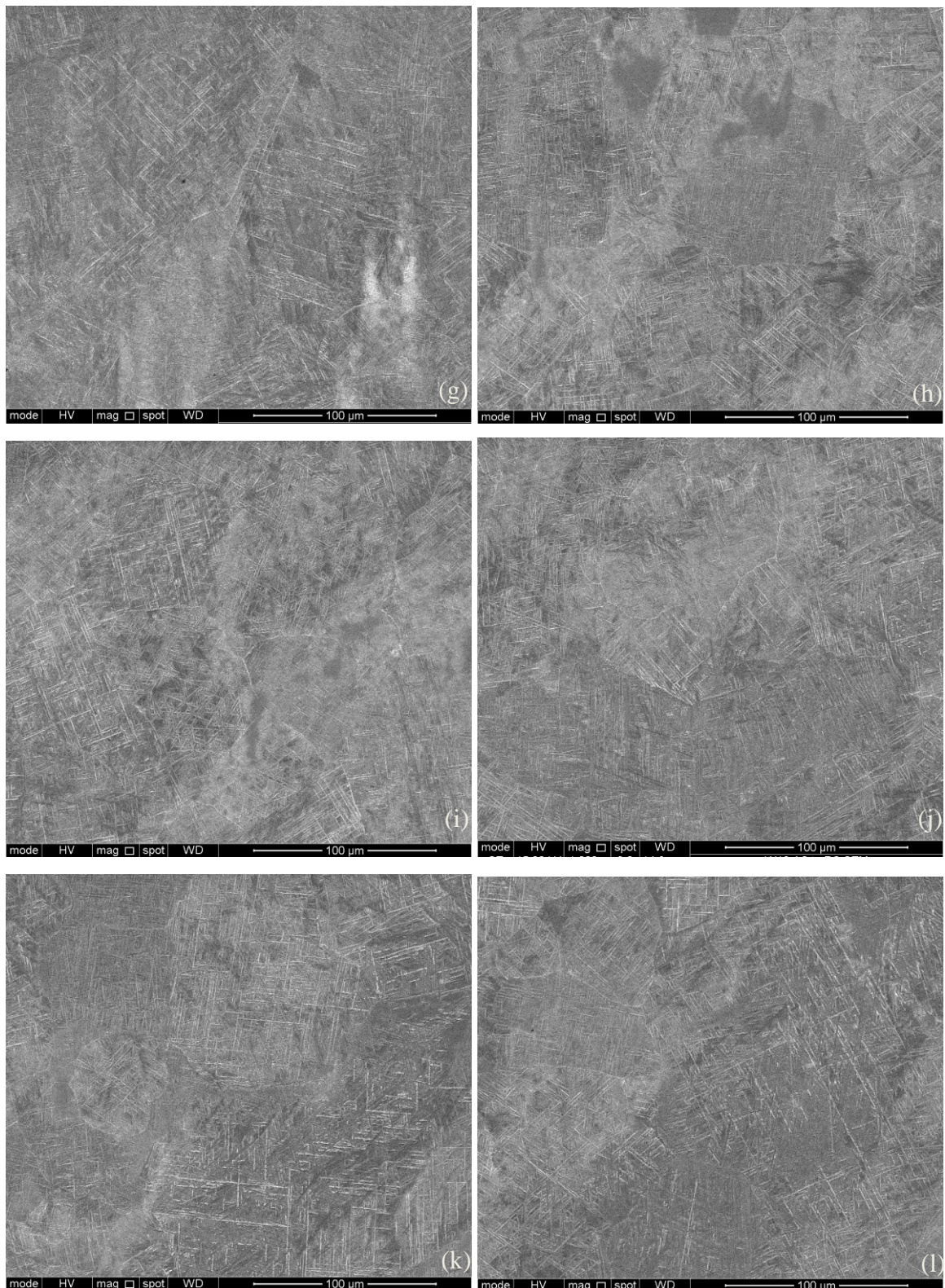
Figure 5.42 (a-l) Secondary electron micrographs from the AS to the RS of the SZ in W19 on the central horizontal line, X coordinate of a, b, c, d, e, f, g, h, i, j, k, l : -7, -6.3, -5.6, -4.2, -2.8, -1.4, 0, 1.4, 2.8, 4.2, 5.6, 6.3

SEM analysis was carried out on the SZ of the cross section W20 on both the central horizontal and vertical lines, and the regions selected for vertical and horizontal measurement are indicated as vertical and horizontal arrowed red lines in Figure 5.43, respectively. Secondary electron micrographs obtained from the weld bottom to the weld surface of the lamellar structure in the SZ of W20 on the central vertical line are shown in Figure 5.44(a-h). Figure 5.45(a-h) shows the secondary electron micrographs from the AS to the RS of the lamellar structure in the SZ of W20 on the central horizontal line.
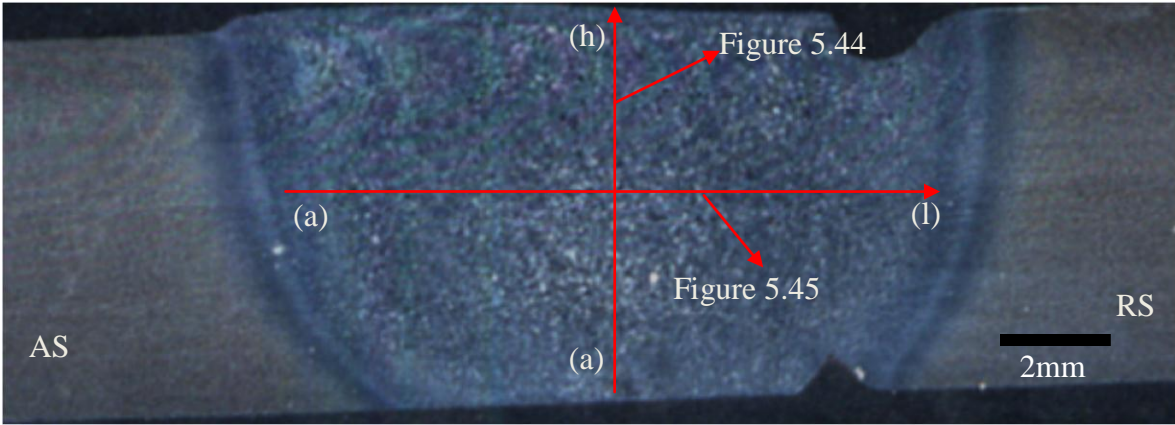


Figure 5.43 Indication of the two measurements taken from the SZ of W20
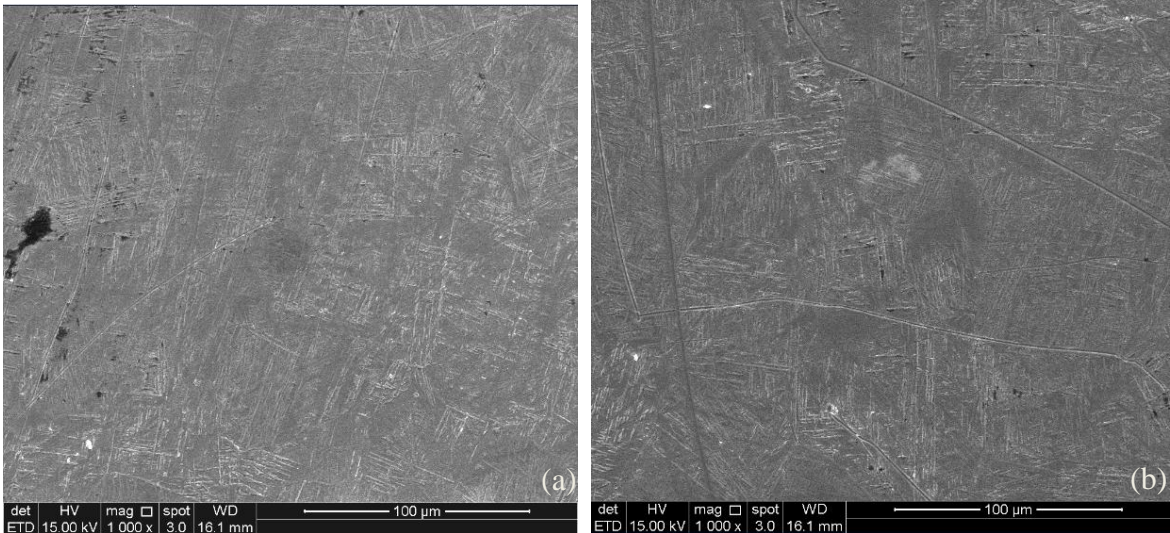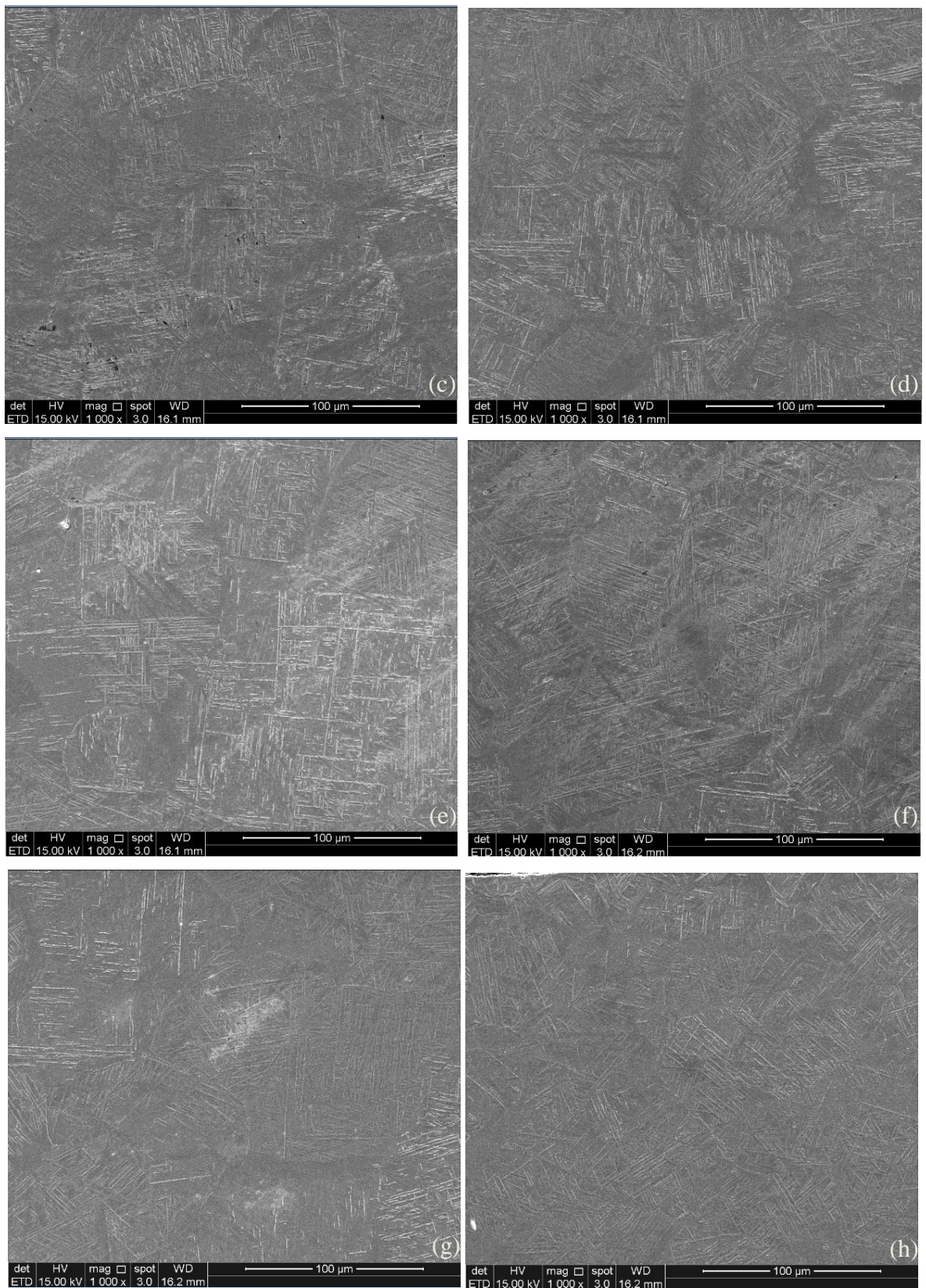
Figure 5.44 (a-h) Secondary electron micrographs from the weld bottom to the weld surface of the SZ in W20 on the central vertical line, Y coordinate of a, b, c, d, e, f, g, h: 0, 1.1, 1.9, 2.9, 4, 5.1, 6.2, 6.7

143
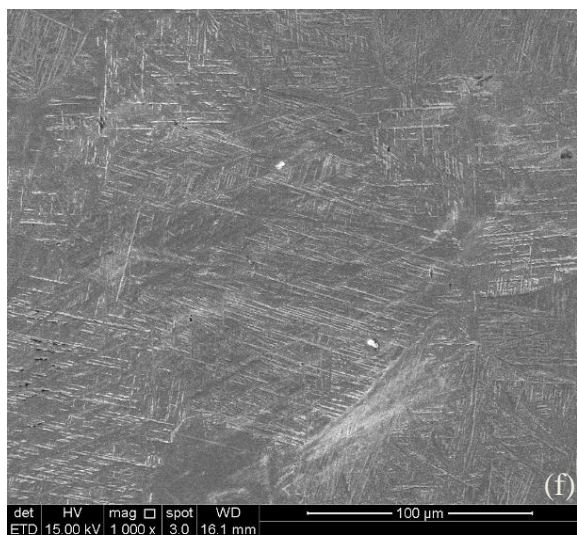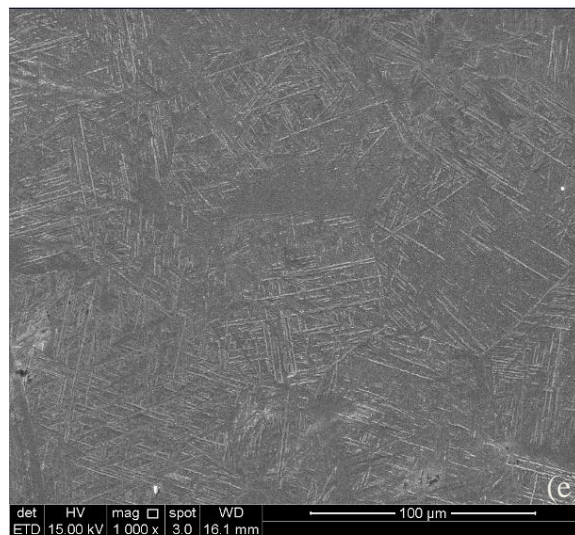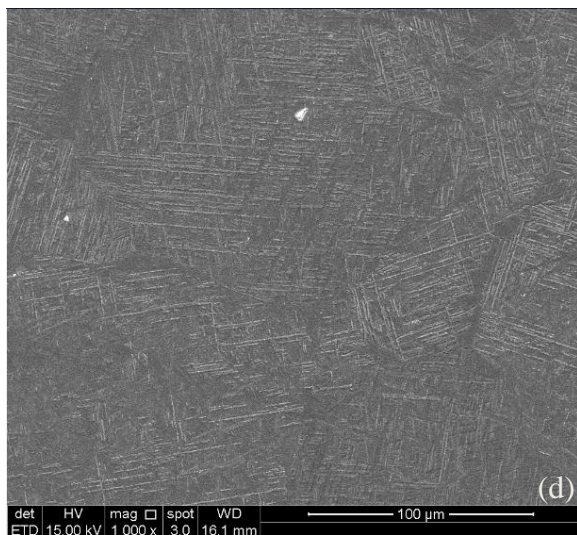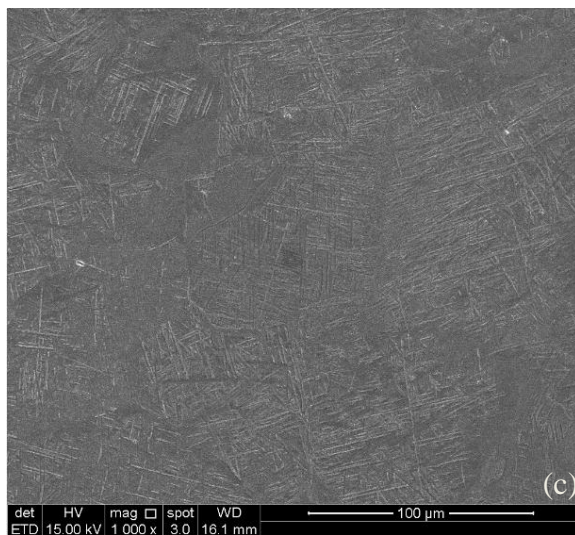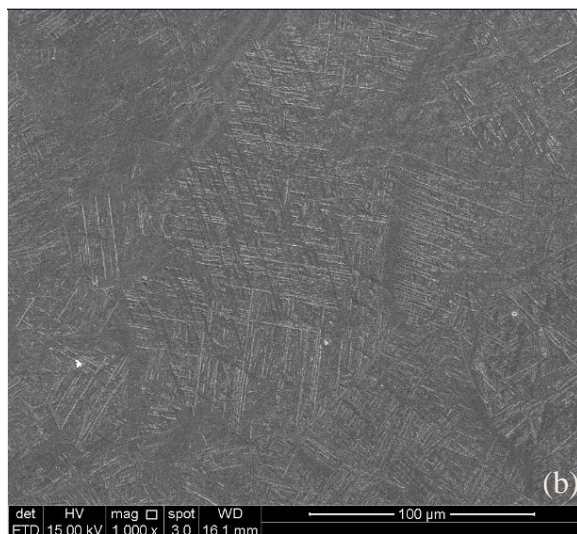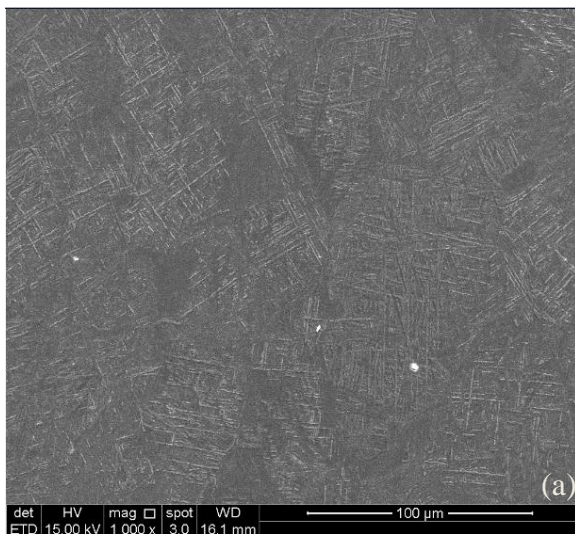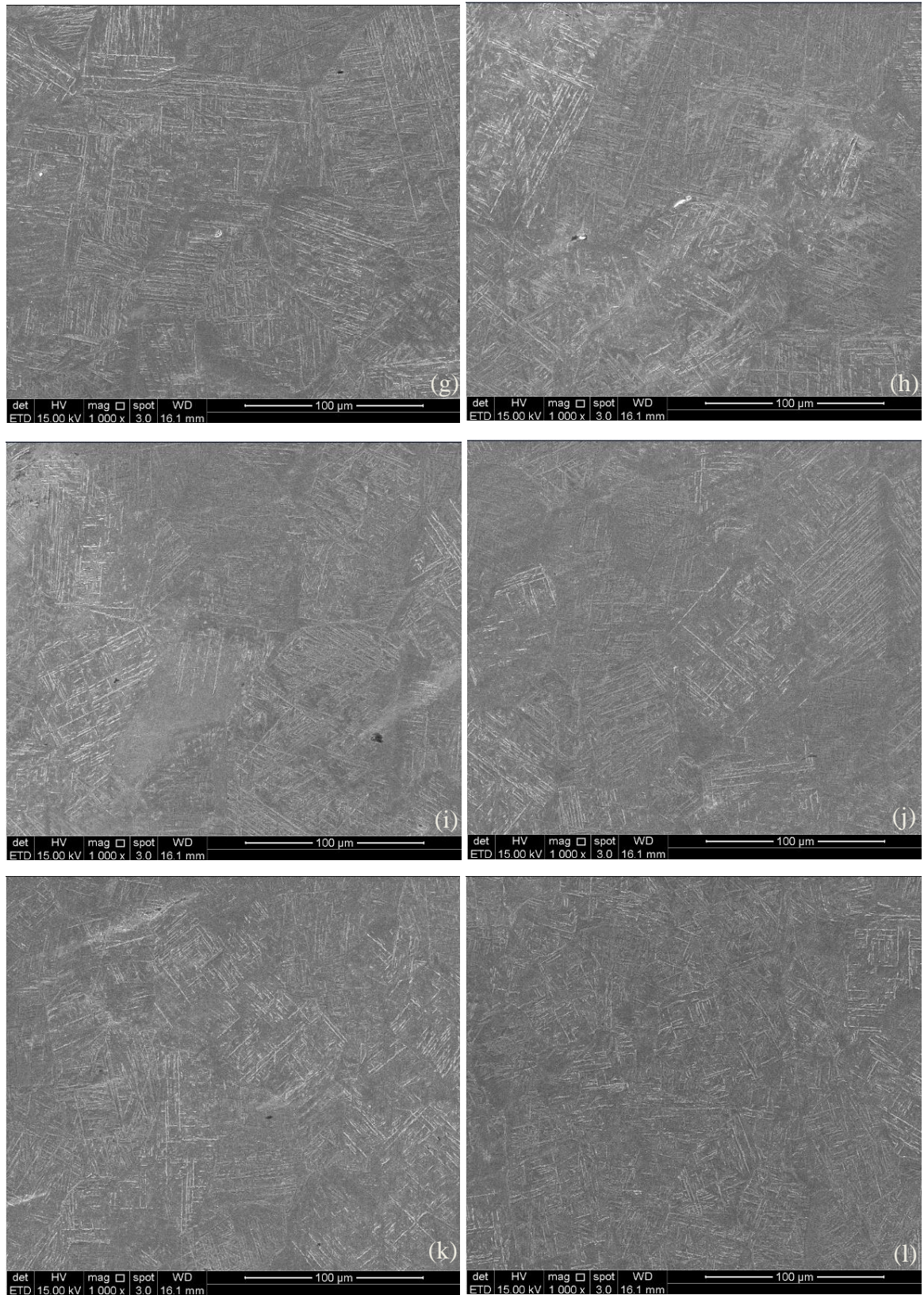
Figure 5.45 (a-j) Secondary electron micrographs from the AS to the RS of the SZ in W20 on the central horizontal line, X coordinate of a, b, c, d, e, f, g, h, i, j, k, l: -4.95, -4.05,-3.15, -2.25, -1.35, -0.45, 0.45, 1.35, 2.25, 3.15, 4.05, 4.95

SEM analysis was carried out on the SZ of the cross section W21 on both the central horizontal and central vertical lines, the regions selected for vertical and horizontal measurements are indicated as vertical and horizontal arrowed red lines in Figure 5.46, respectively. One measurement was obtained from the weld bottom to the weld surface of the SZ in W21 on the central vertical line, results of which is shown in Figure 5.47 as secondary electron micrographs. Figure 5.48 show the secondary electron micrographs taken from the AS to the RS of the lamellar structure in the weld centre of SZ in W21 on the central horizontal line.
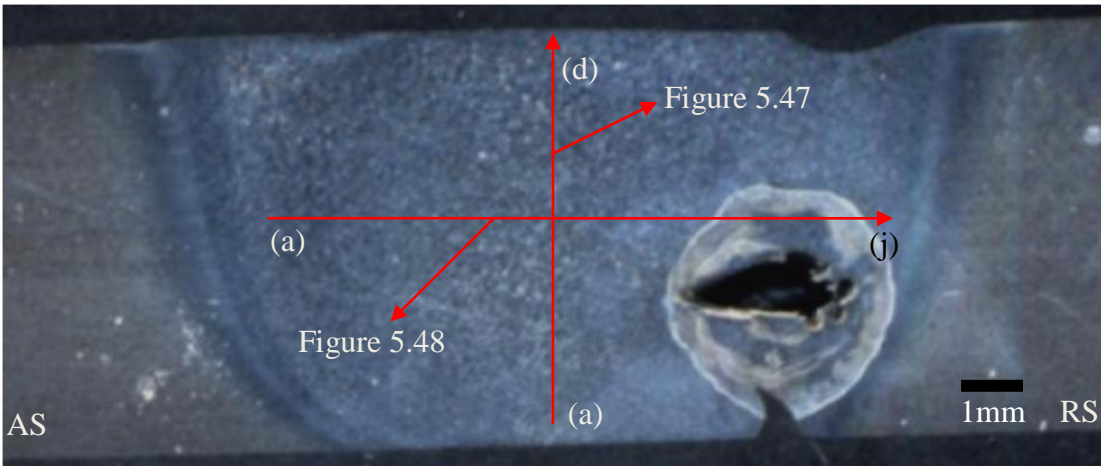


Figure 5.46 Indication of the two measurements taken from the SZ of W21



146
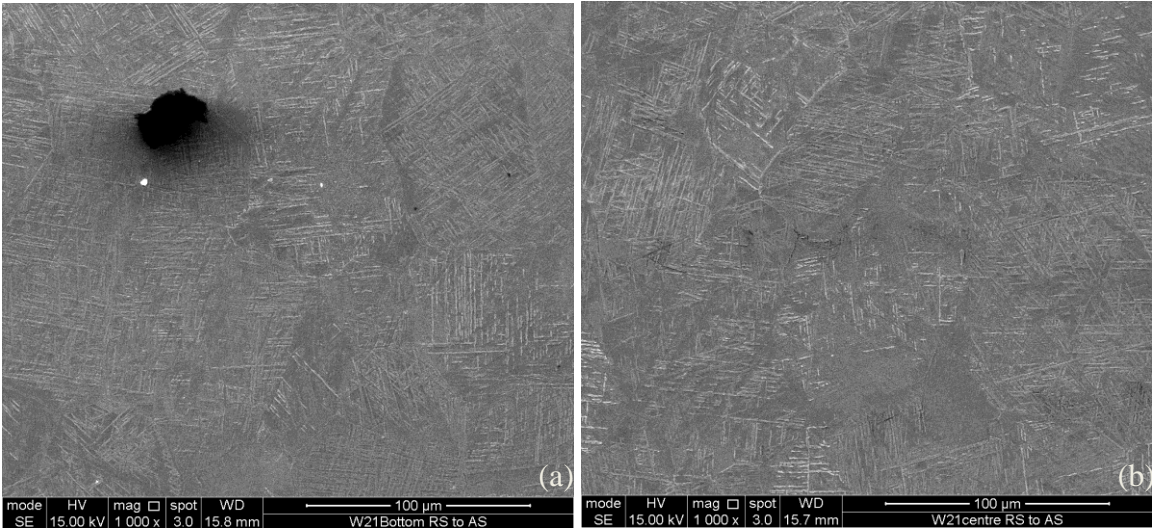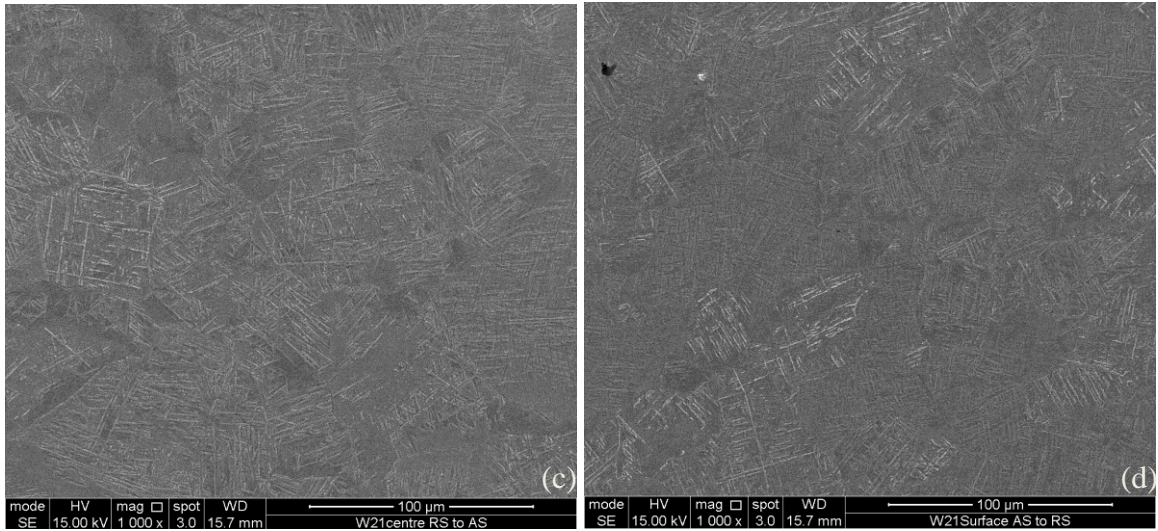
Figure 5.47 (a-d) Secondary electron micrographs from the weld bottom to the weld surface of the SZ in W21 on the central vertical line, Y coordinate of a, b, c, d: 0, 3.6, 4.6 and 6.9
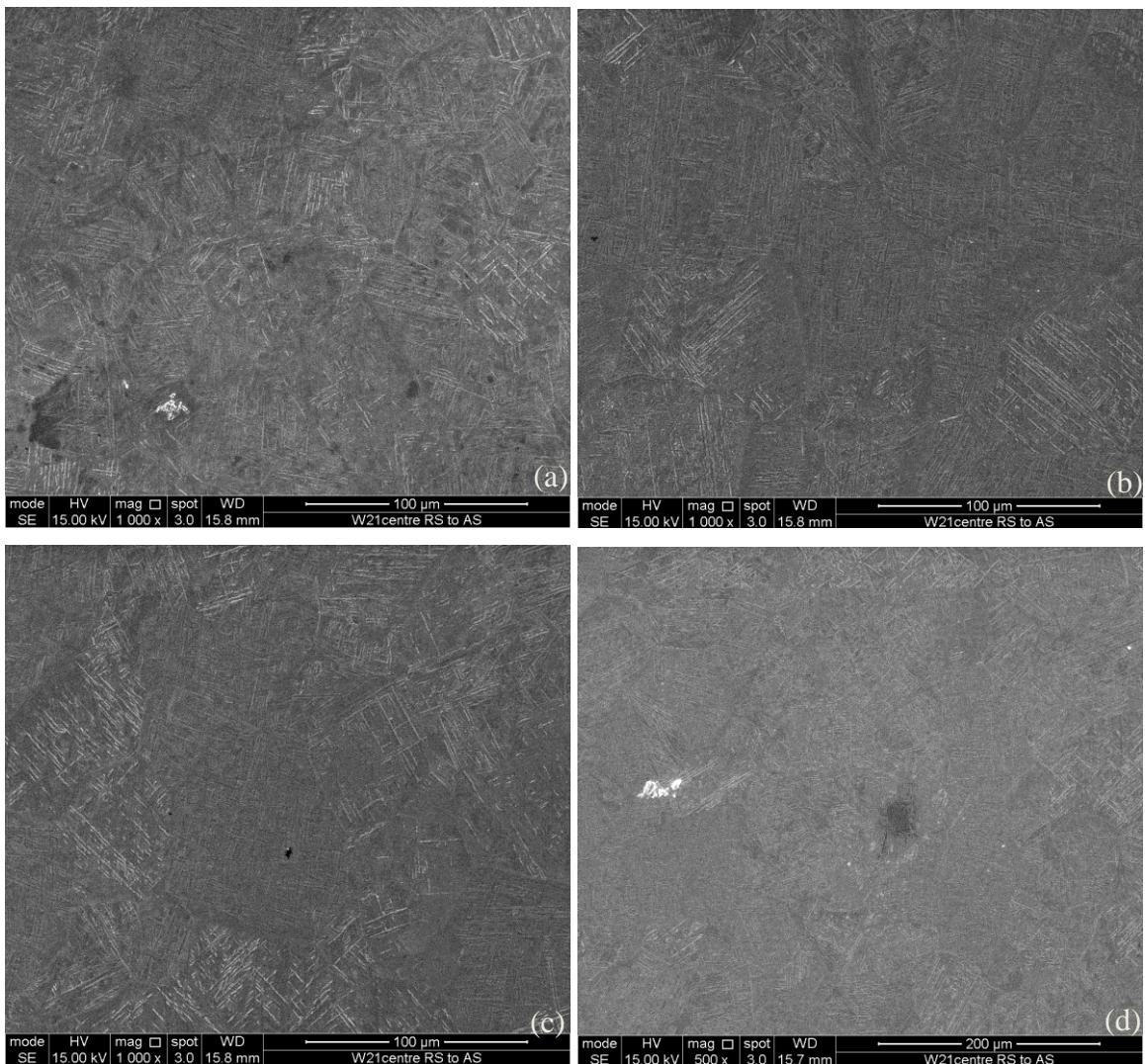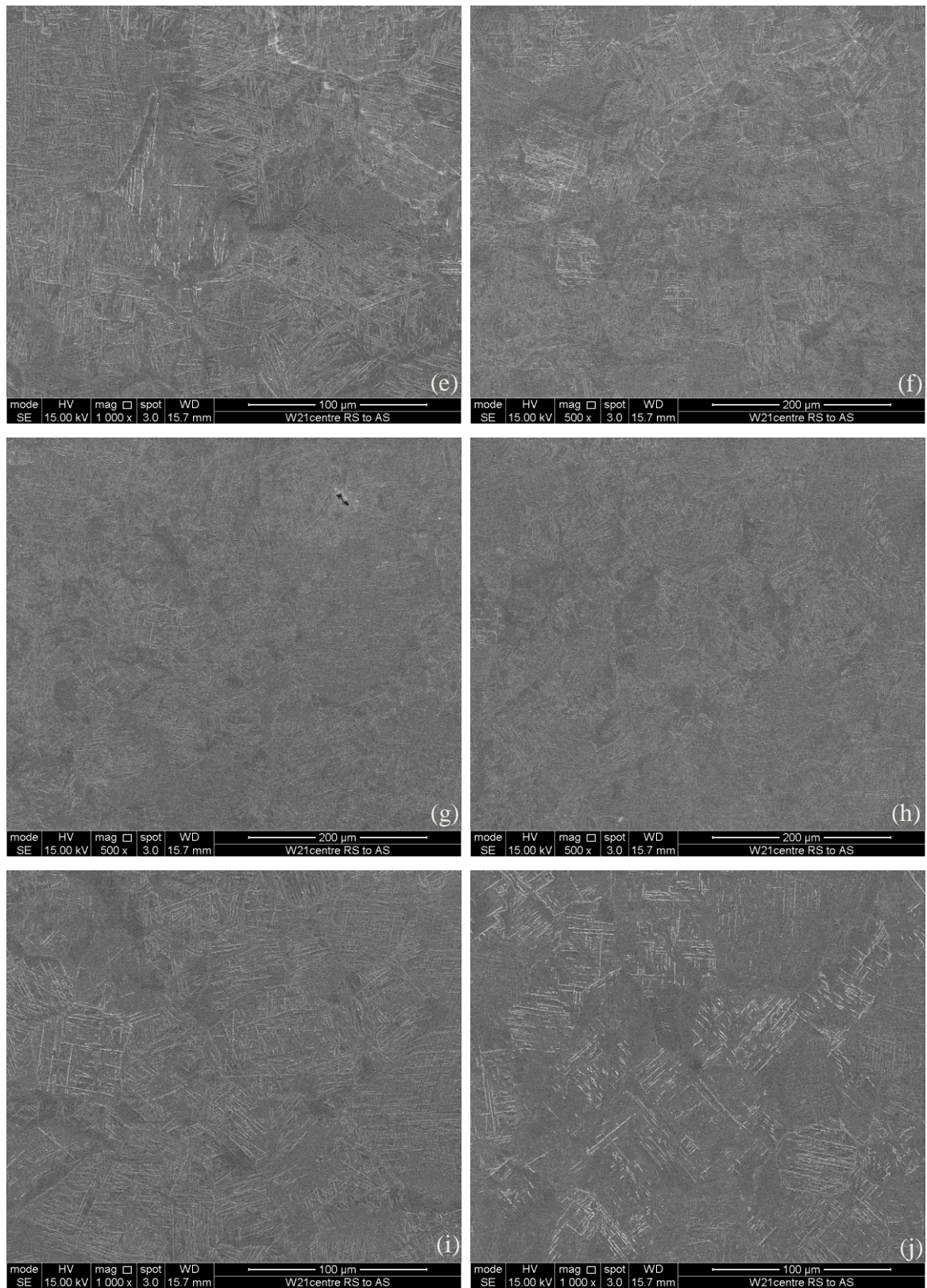
Figure 5.48 (a-j) Secondary electron micrographs from the AS to the RS of the SZ in W21 on the central horizontal line, X coordinate: a, b, c, d, e, f, g, h, i, j: -4.75, -3.75, -2.75, -1.25, -0.25, 0.75, 2.25, 2.75, 3.75, 4.75

Secondary electron micrographs of the fine lamellar structure taken from the normal sections 4.6.b, 5.6.b and 6.8.b are shown in Figure 5.49, Figure 5.50 and Figure 5.51, respectively, indicating different α morphologies, such as basketweave and colony morphologies, and α+β laths growing from the prior β grain boundaries (Figure 5.49, Figure 5.50(b)). Figure 5.52(a-f) displays the backscatter electron micrographs of the fine lamellar structure from the side section 4.3.b.
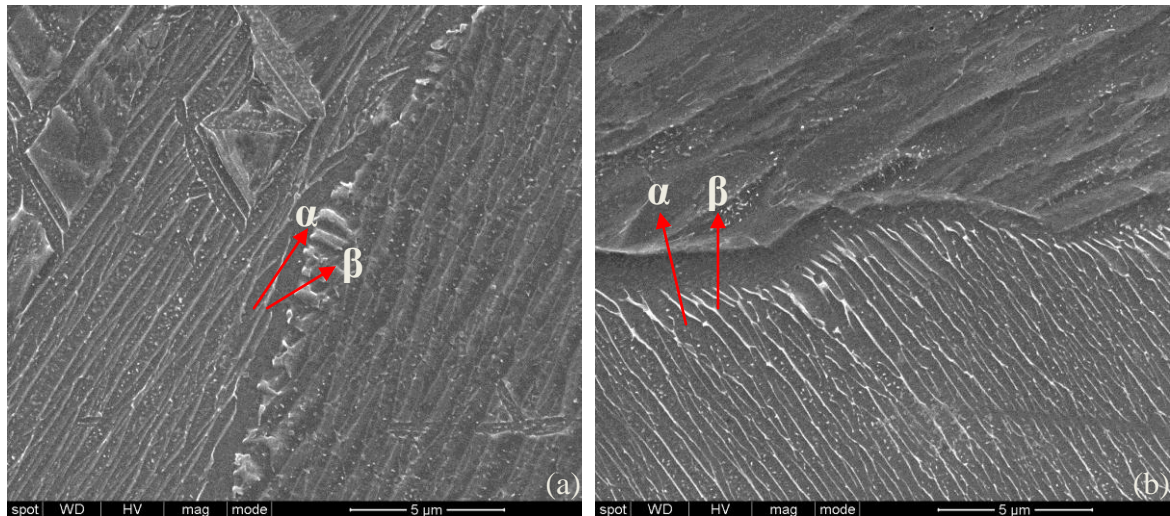


Figure 5.49 (a) and (b) Secondary electron micrographs from the fine lamellar structure of 4.6.b, black contrast is the α phase and light contrast represents retained β phase in the form of thin interlath between α laths
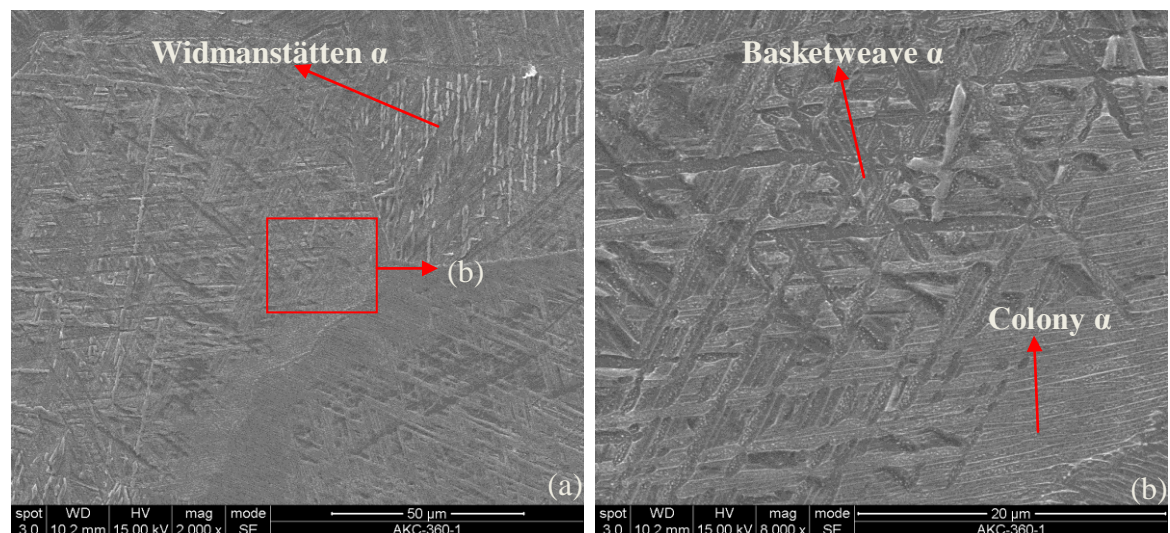


Figure 5.50 Secondary electron micrographs show the fine lamellar structure 1mm to the weld centre at the RS of 5.6.b at (a) low and (b) high magnification showing the α laths of basketweave and colony morphologies, respectively

149
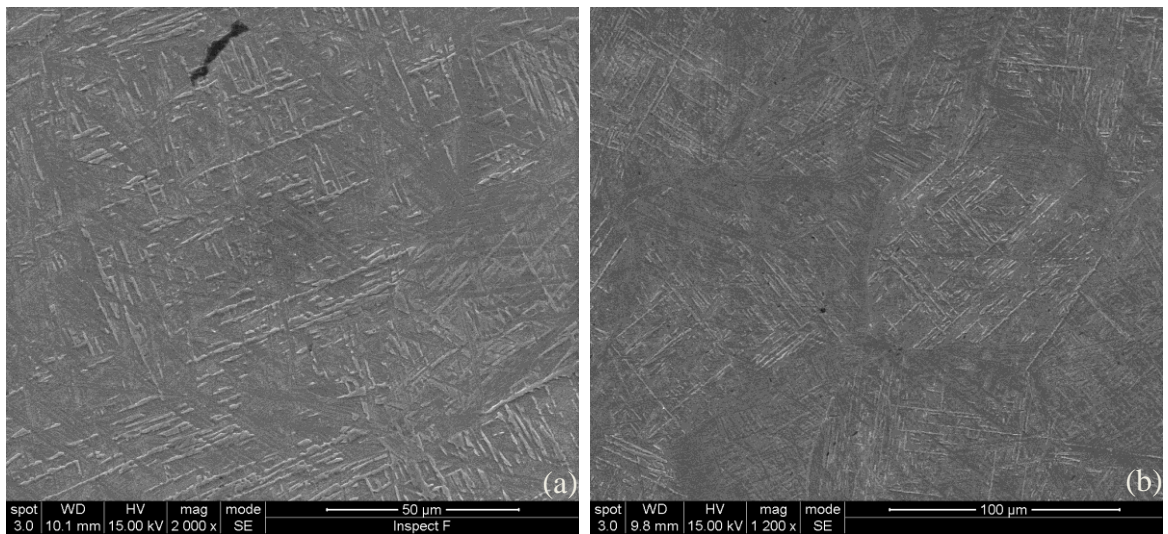
Figure 5.51 Secondary electron micrographs from the SZ centre of 6.8.b at (a) the weld surface; (b) the weld centre



150
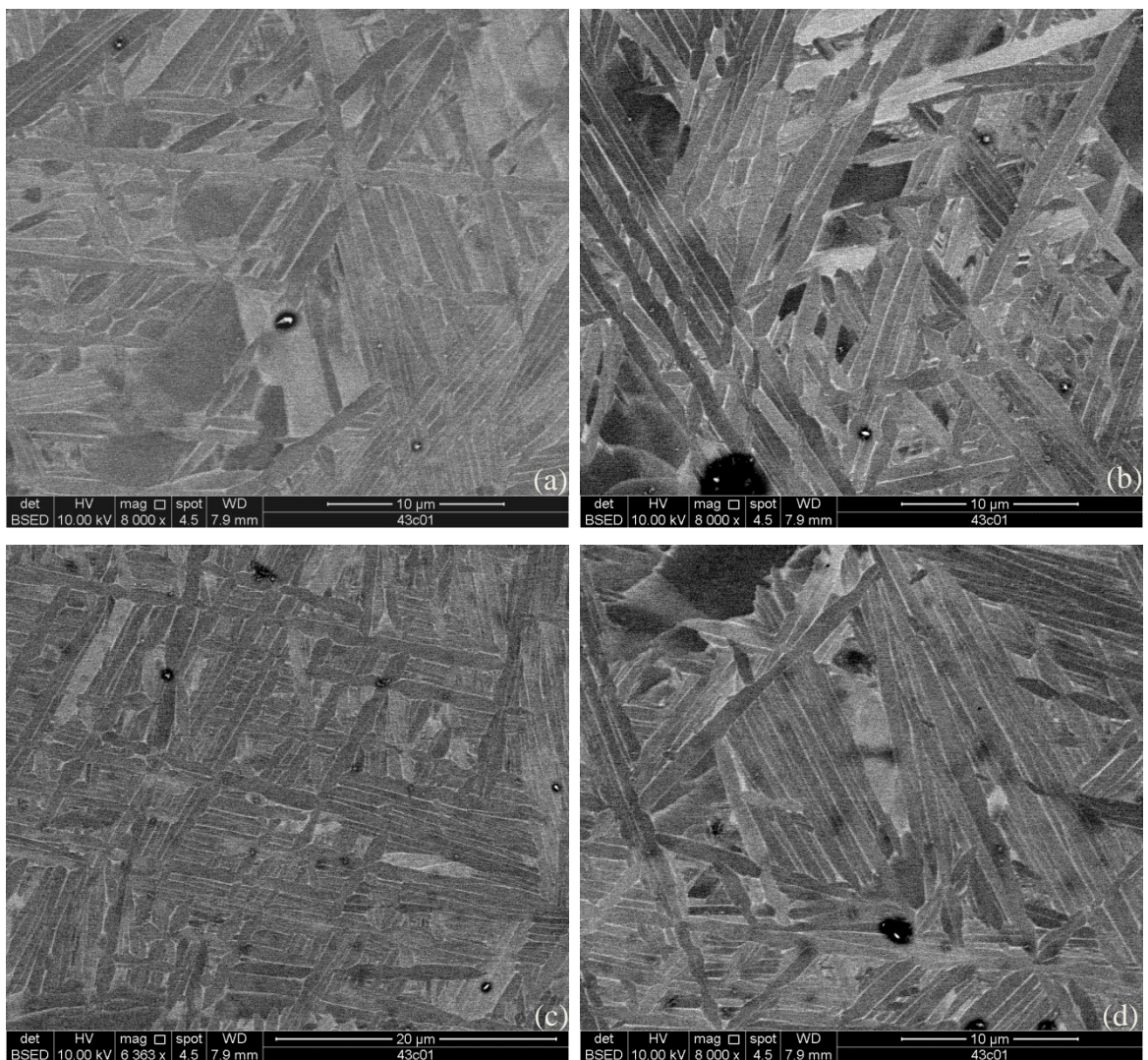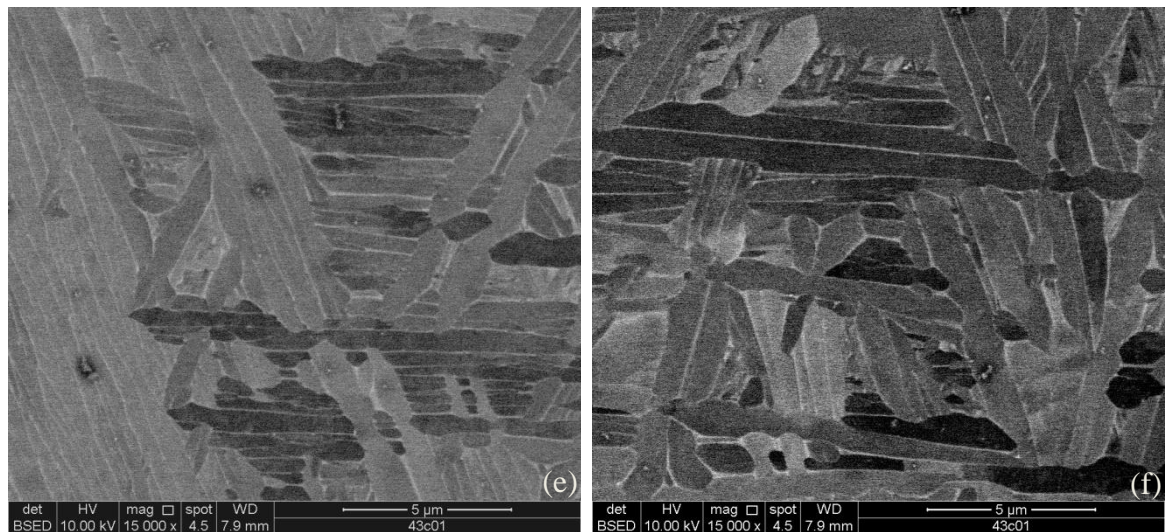
Figure 5.52 (a-f) Backscatter electron micrographs from the fine lamellar structure of 4.3.b

### 5.2.7 Interesting microstructure observation

#### 5.2.7.1 Bump at the AS of the weld W6

It was previously discussed in Chapter 4 that a bump was observed at the AS of the weld surface of W6 (900rpm) due to insufficient down force. To understand how this bump formed in the SSFSW process, SEM was carried out on the bump at the AS of the weld surface of W6, and Figure 5.53 shows the secondary electron micrographs from the bump of W6. Figure 5.53(a) is a stitched secondary electron micrograph, and detailed micrographs were selected from the two red rectangular regions, results of which are shown in Figure 5.53(b) and Figure 5.53(c), respectively. Figure 5.53(b) shows that the refined microstructure above the equiaxed structure is composed of fine $\alpha$p grains of 2μm and retained $\beta$ phase. Moreover, in Figure 5.53(c), adjacent to the fine equiaxed structure, the refined microstructure above the bimodal structure is a fine bimodal structure consisting of a small amount of $\alpha$p grains of less than 2μm. It should be noted that, further into the weld centre, the refined microstructure is similar to the classic lamellar structure. The results demonstrate that the refined microstructure in the bump is within the two red rectangular boxes as indicated in Figure 5.53(a) and length of this region with refined microstructure is approximately 435μm.
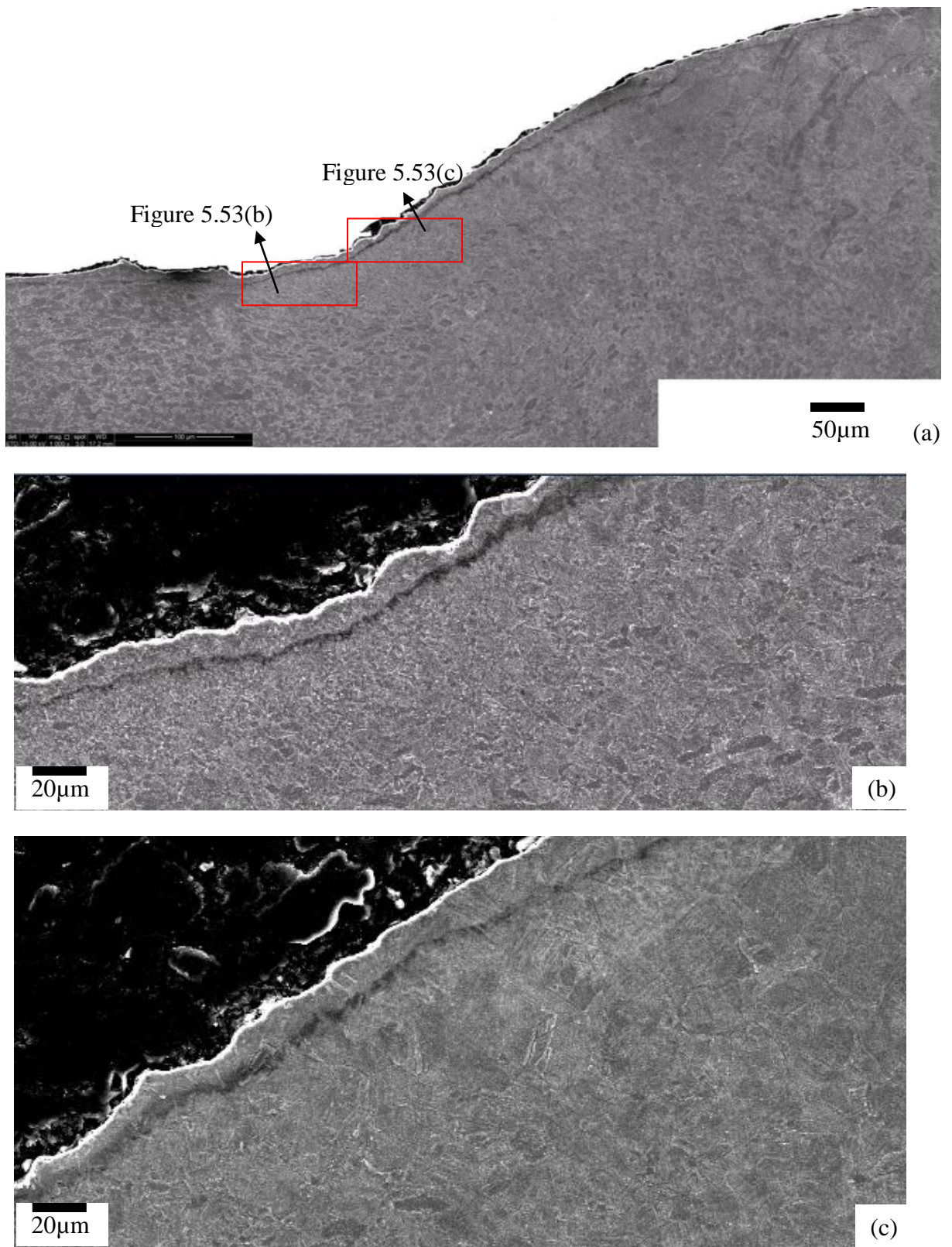
Figure 5.53 Secondary electron micrographs of the bump at the AS of the weld surface of W6: (a) stitched micrographs; and (b) and (c): two secondary electron micrographs taken from the stitched micrographs enclosed by the two red rectangular regions in (a)

*5.2.7.2 Microstructure observed at the notches on W20 and W21*

SEM was carried out on the notch region at the RS of the weld surface of W20, and Figure 5.55 shows the secondary electron micrographs taken from the notch region of W20. Figure 5.55(a) and Figure 5.55(b) show the detailed micrographs of the two red rectangular regions indicated in Figure 5.54, respectively. It can be seen in the micrographs of the notch regions in Figure 5.55(a) and (b) that the microstructure retained the classic lamellar structure in the notch region.
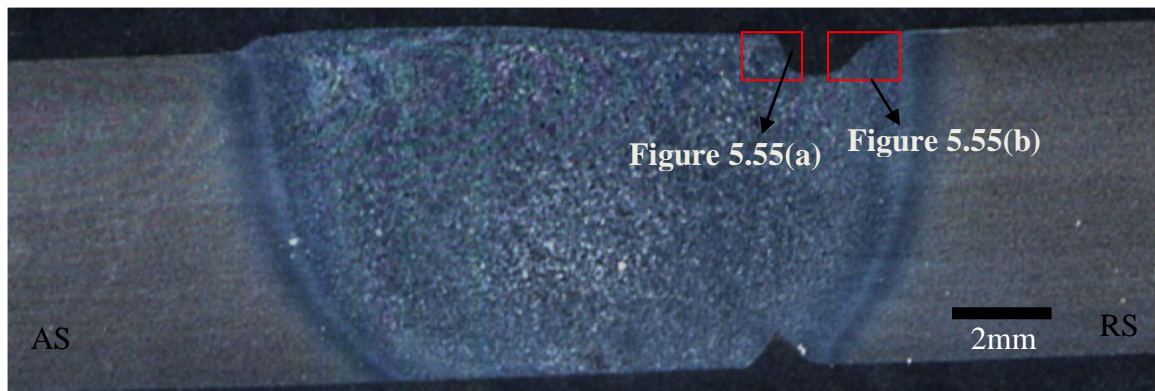


Figure 5.54 Macro section of W20 indicates surface notch regions at the RS
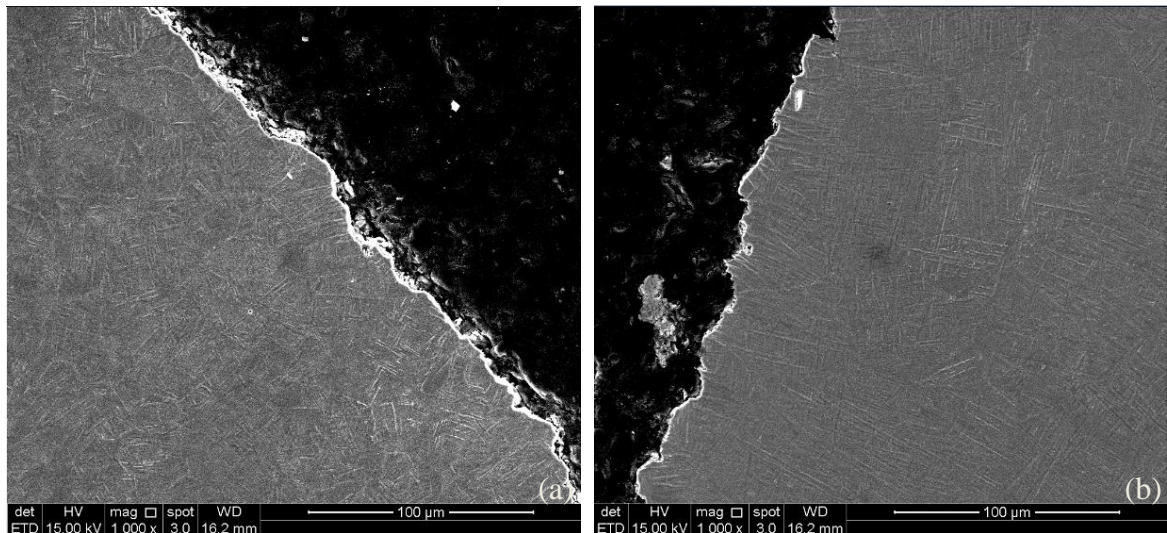


Figure 5.55 Secondary electron micrographs of the surface notch region at the RS of the welding edge of W20 enclosed by the two red rectangular regions in Figure 5.54: (a) left; (b) right

Figure 5.56 shows the secondary electron micrographs taken from the notch region of W21. Figure 5.57(a) and Figure 5.57(b) show the detailed micrographs of the three red rectangular regions enclosed in Figure 5.56, respectively. Figure 5.58 shows the SEM microgaphs of the bimodal strucutre and the equiaxed structure obtained from the weld surface next to the notch region and the bimodal structure at the top surface of W21 at low and high magnification are shown in Figure 5.58(a) and (b), respectively. Secondary electron micrographs at low and high magnification shown in Figure 5.58(c) and (d) exhibit the bimodal structure just below the top surface and the equiaxed structure at the top surface of the BM are shown at low and high magnification in Figure 5.58(e) and (f), respectively. It was shown in Figure 5.57 that the notch region at the RS of the weld surface exhibit the classic lamellar structure, whereas, grain refinement has occurred in both the bimodal structure and the equiaxed structure adjacent to the notch region at the top surface, as indicated in Figure 5.58. Figure 5.58(b) shows that the refined microstructure above the bimodal structure, which is just adjacent to the notch region, consists of fine $\alpha_p$ grains of approximately 1.9µm and secondary $\alpha+\beta$ laths. Figure 5.58(f) displays that the refined microstructure above the equiaxed structure is composed of much finer $\alpha_p$ grains of 1.1µm and retained $\beta$ phase.
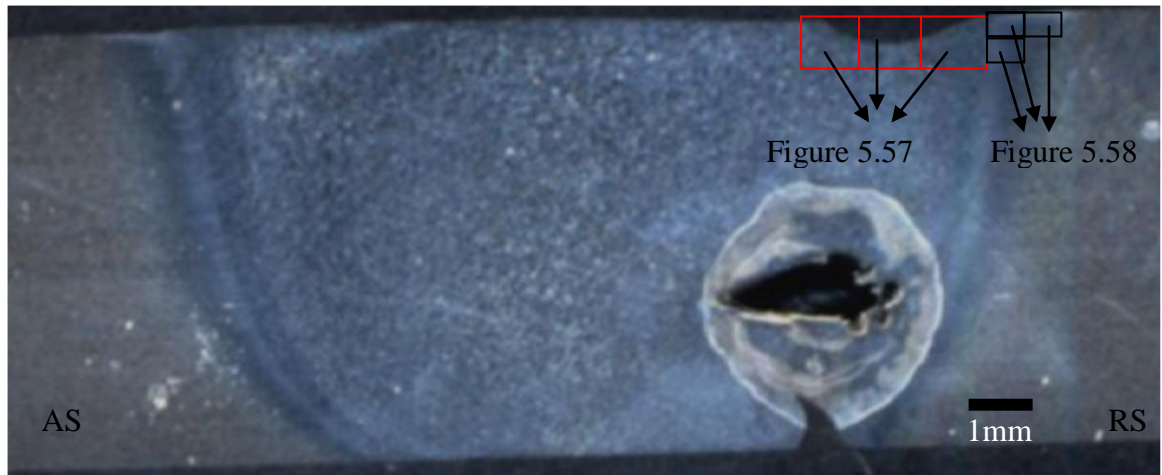


Figure 5.56 Macro section of W21 indicates surface notch regions at the RS
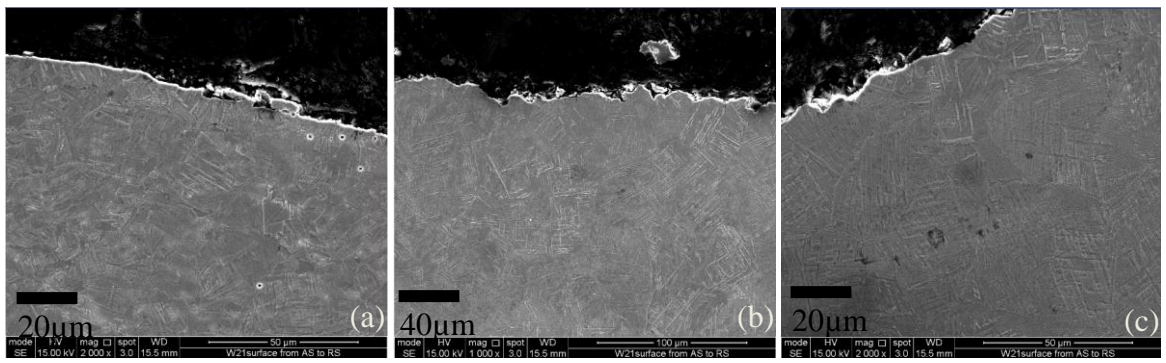
Figure 5.57 Secondary electron micrographs of the surface notch region at the RS of the welding edge of W21 enclosed by the three adjacent red rectangular regions in Figure 5.56 at magnifications of (a) 2000, (b) 1000 and (c) 2000
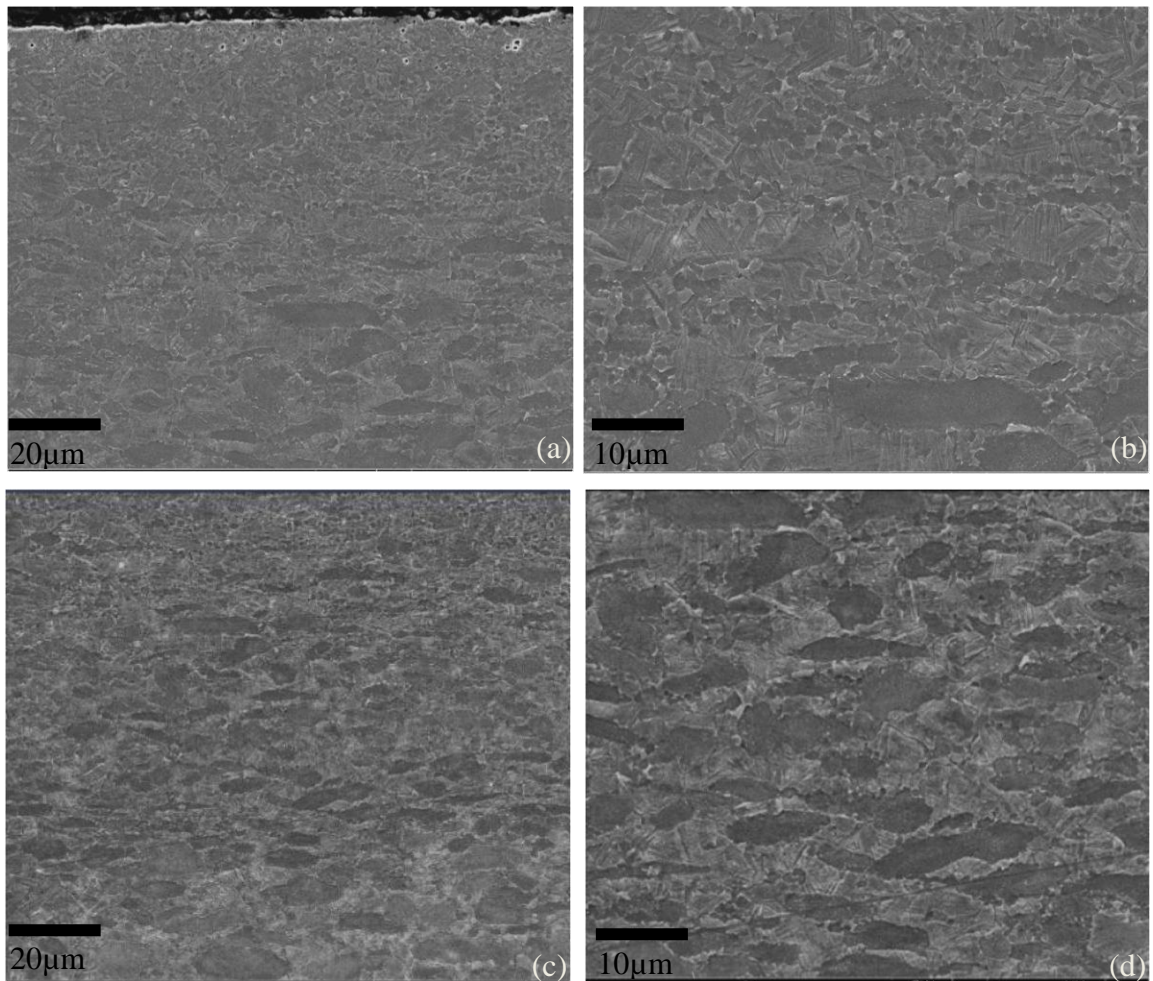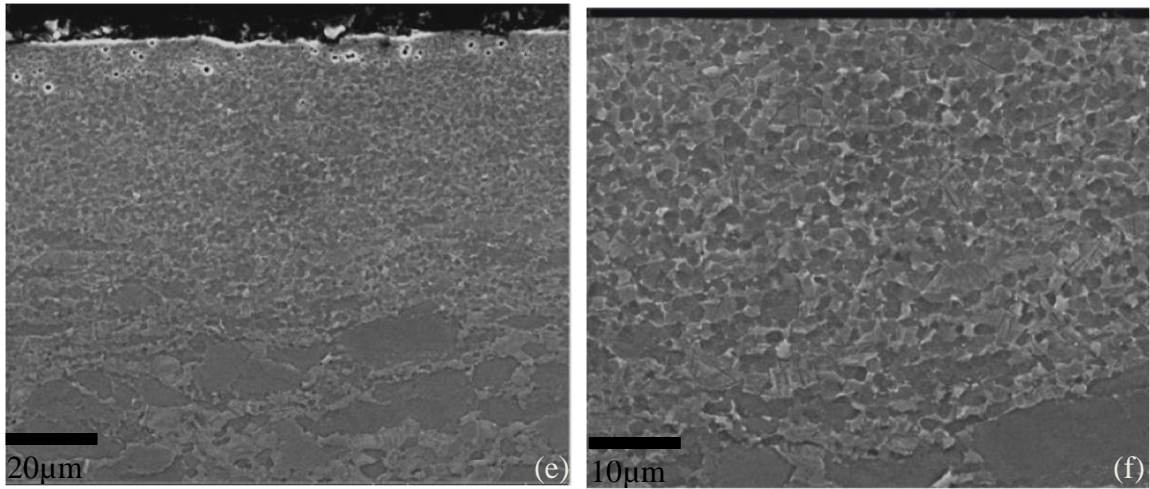
Figure 5.58 Secondary electron micrographs obtained from the weld surface next to the notch region of W21 from AS to RS enclosed by the three adjacent red rectangular regions in Figure 5.57 show the bimodal structure at the top surface at (a) low and (b) high magnification; the bimodal structure just below the top surface at (c) low and (d) high magnification; the equiaxed structure at the weld surface in the BM at (e) low and (f) high magnification

## 5.2.8 α laths thickness measurement

Manual measurements have been carried out on the thickness of GBα and α laths to analyze the influence of traverse speed and rotation speed on the thickness of the α laths in the fully lamellar structure of all the six welds W4, W5, W6, W19, W20 and W21. Secondary electron micrographs were taken from the SZs of the three welds W4, W5 and W6 with a constant rotation speed of 900rpm. However, due to text limit, measurement results of the thickness of the α laths for the three welds W19, W20 and W21 are not shown here. Figure 5.60, 5.62 and 5.64 show morphology of the α laths in the transformed lamellar structure in the three cross sections W4B4, W5B5 and W6B6, and Figure 5.59, 5.61, 5.63 are the stitched optical micrographs showing indication of the regions for the secondary electron micrographs. Measurement of the thickness of the α laths in the lamellar structure were carried out on each Secondary electron micrograph and the results for the three welds W4, W5 and W6 were shown in Table 5.3, Table 5.4 and Table 5.5, respectively.

The measurements including the thickness of GBα suggest that the corresponding secondary electron micrographs were taken from more than two prior β grains, while the measurements without the thickness of GBα indicate the secondary electron micrographs

were inside the single prior β grains. It can be seen that Figure 5.60(d) belonging to the TMAZ of the weld W4 contains much shorter and thicker α+β laths compared to the laths in the SZ. In the SZ, except for colony α and GBα, the other α laths are in the form of Widmanstätten structure and basketweave structure as indicated in Figure 5.60(a), (b) and (c), since colony α has been observed in the microstructure, thus the cooling rate experienced must be less than 50°C/s and retained β phase appears as thin layers separating the parallel α laths (Davies, 2009). α+β laths and α colonies are commonly observed in the SZ. It is clearly seen that α+β laths are always located at the regions adjacent to GBα or GBα are surrounded by the α+β laths, as shown in Figure 5.60(c) of W4B4, Figure 5.62(b, c) of W5B5 and Figure 5.64 (a,d) of W6B6.
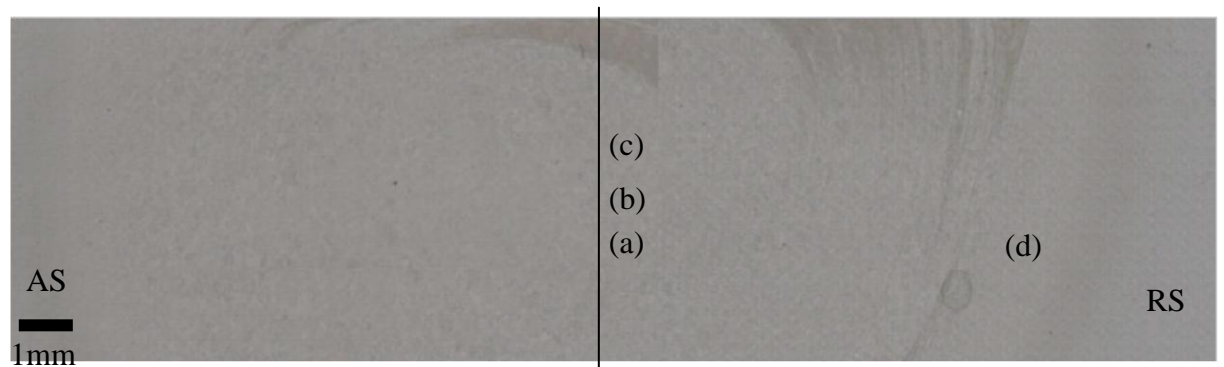


Figure 5.59 Stitched optical micrographs showing the indication of secondary electron micrographs of the weld W4



157
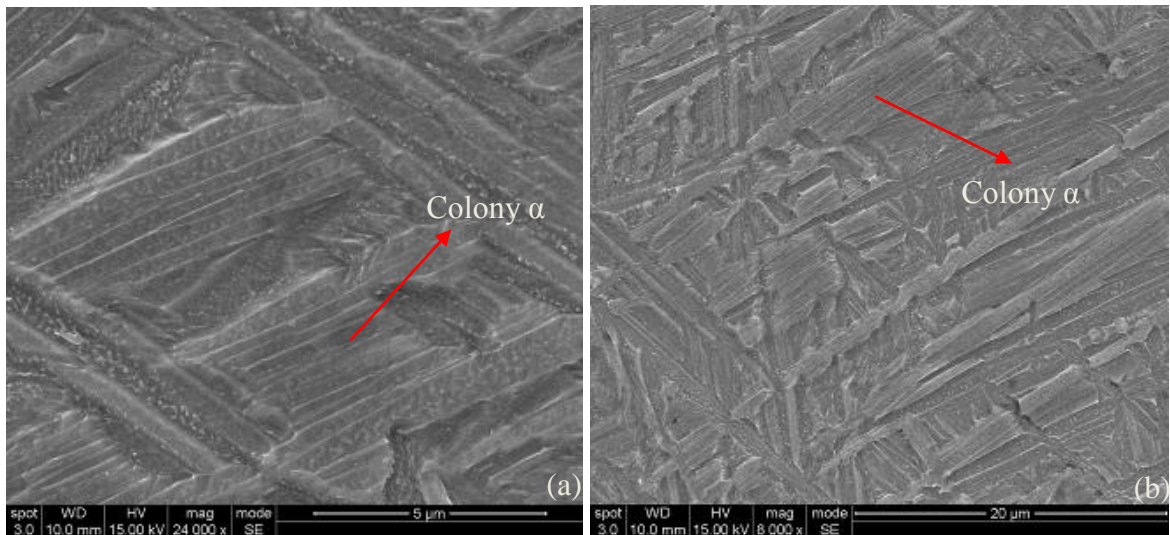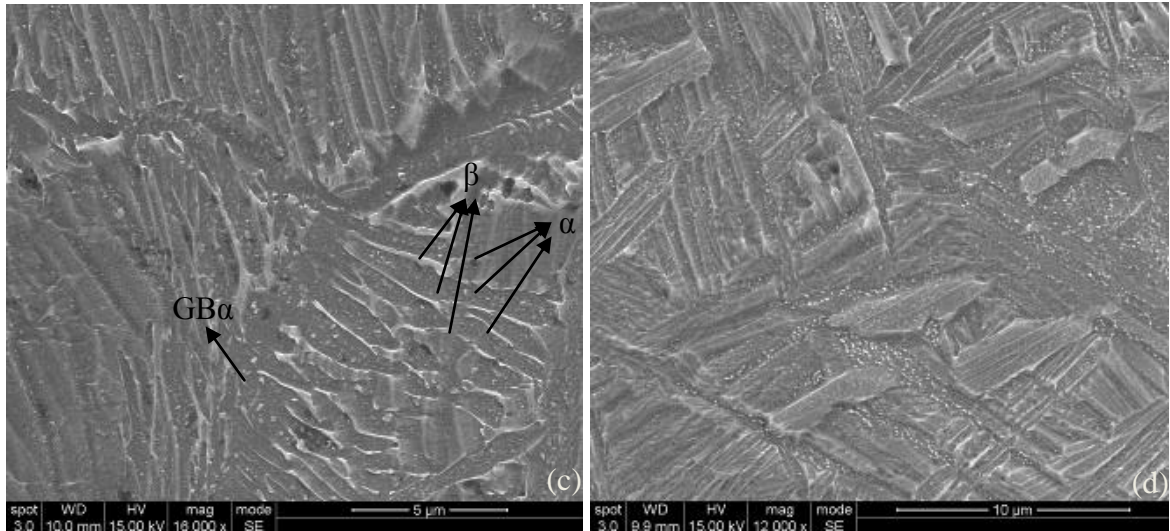
Figure 5.60 (a-d) Secondary electron micrographs corresponding to the indicated area in Figure 5.59 of W4

Table 5.3 The thickness of the α laths in the weld zone of W4 on a vertical line

|  | Coordinates | Minimum, μm | Mostly appeared, μm | Maximum, μm | GBα thickness, μm |
|---|---|---|---|---|---|
| a | 0,0.5 | 0.24 | 0.57 | 1.43 | N/A |
| b | 0, 2 | 0.21 | 0.36 | 1.32 | 1.14 |
| c | 0, 3.5 | 0.24 | 0.44 | 2.5 | 1.08 |
| d | 7.6, -0.3 | 0.24 | 0.59 | 2.1 | N/A |
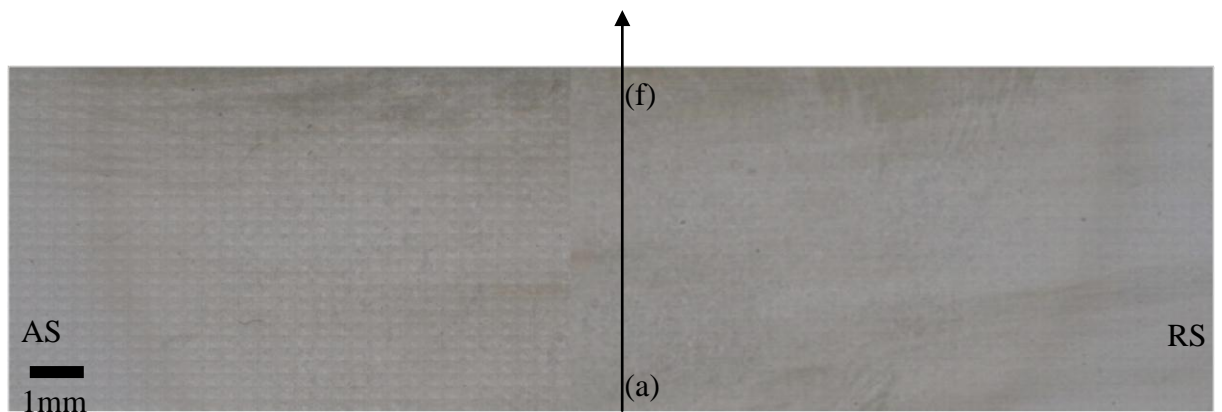


Figure 5.61 Stitched optical micrographs showing the indication of secondary electron micrographs of the weld W5

158
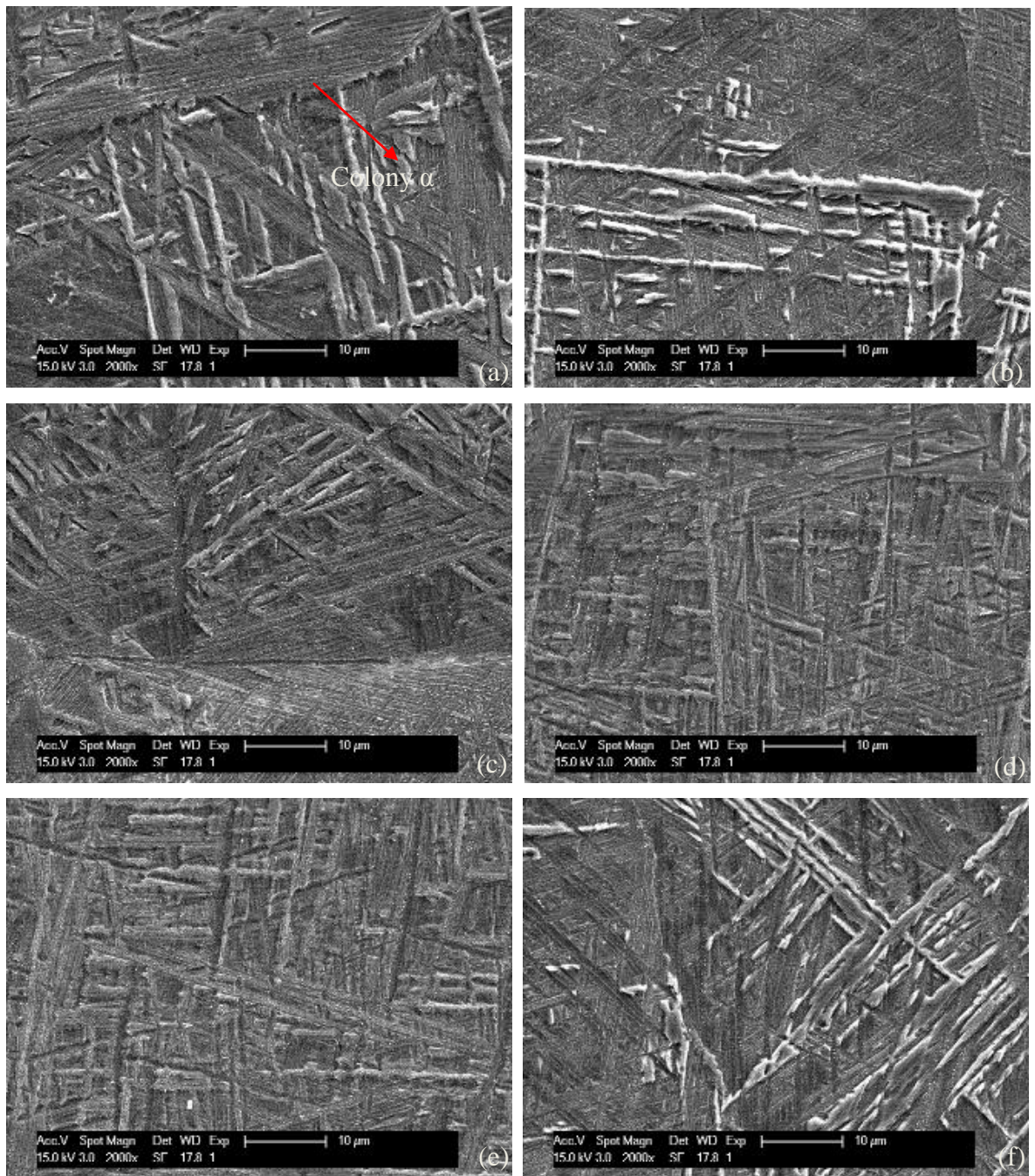
Figure 5.62 (a-f) Secondary electron micrographs corresponding to the indicated area in Figure 5.61 of W5

Table 5.4 The thickness of the α laths in the weld zone of W5 on a vertical line

| | Coordinates | Minimum, μm | Mostly appeared, μm | Maximum, μm | GBα length, μm |
|---|---|---|---|---|---|
| a | 0, -2.8 | 0.24 | 0.95 | 2.38 | N/A |
| b | 0, -1.5 | 0.24 | 0.57 | 1.4 | 3.2 |
| c | 0, -0.5 | 0.24 | 0.52 | 1.9 | 0.48 |
| d | 0, 0.5 | 0.24 | 0.48 | 1.9 | N/A |
| e | 0,2 | 0.24 | 0.95 | 2.38 | N/A |
| f | 0,4 | 0.24 | 0.48 | 0.95 | 0.71 |
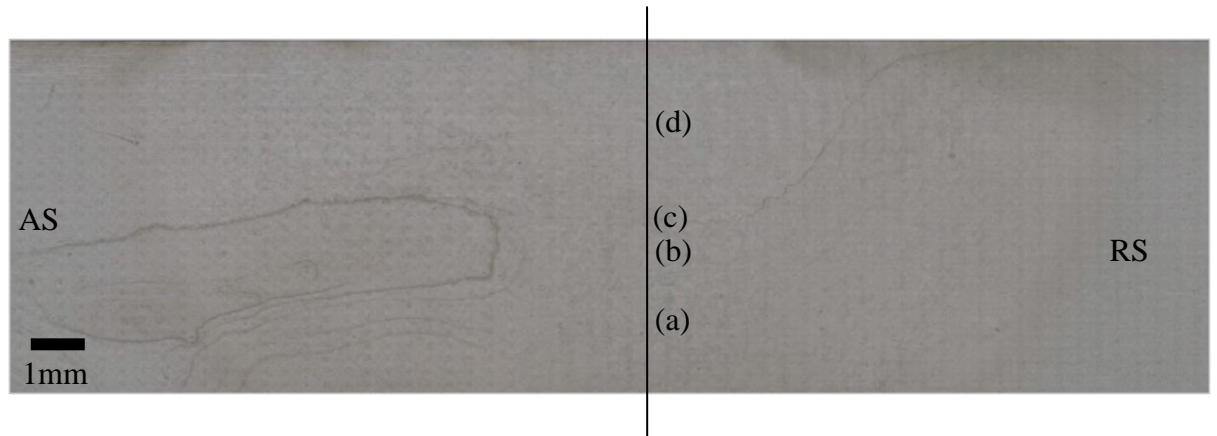


Figure 5.63 Stitched optical micrographs showing the indication of secondary electron micrographs of the weld W6
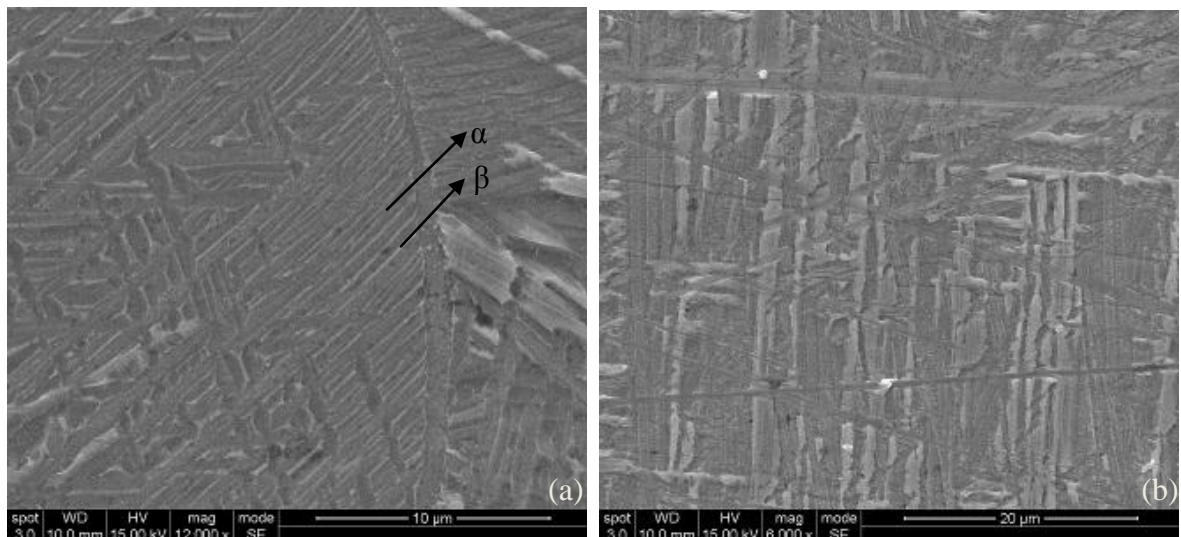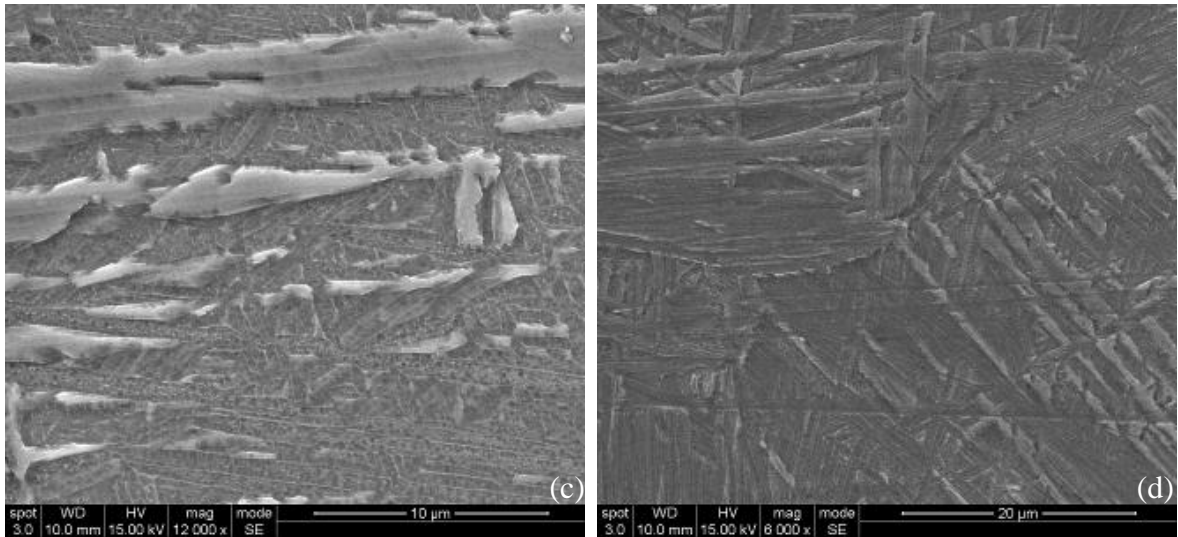
Figure 5.64 (a-d) Secondary electron micrographs corresponding to the indicated area in Figure 5.63 of W6

Table 5.5 The thickness of the α laths in the weld zone of W6 on a vertical line

|  | Coordinates | Minimum, µm | Mostly appeared, µm | Maximum, µm | GBα length, µm |
|---|---|---|---|---|---|
| a | 0.1,-2.47 | 0.29 | 0.58 | 2 | 1 |
| b | 0, -0.25 | 0.58 | 0.77 | 1.92 | N/A |
| c | 0, 0.18 | 0.2 | 0.9 | 2.92 | N/A |
| d | -0.3, 4.05 | 0.2 | 1.0 | 2 | 1.2 |

**5.3 X-EDS characterization of the weld zones**

5.3.1 Introduction

5.3.2 X-EDS analysis on the α phase and β phase in the BM

An obvious difference between chemical compositions of αp phase and that of retained β phase of the equiaxed structure in the BM is shown in Figure 5.65 in terms of weight percentage of aluminium and vanadium. Secondary electron micrograph of part of the equiaxed structure of the BM is shown in Figure 5.65(a) and Figure 5.65(b) shows the X-EDS spectrums on αp phase and retained β phase, respectively. It is seen that retained β

phase contains less aluminium and more vanadium compared to αp phase because vanadium stabilised β phase and aluminium stabilised α phase.
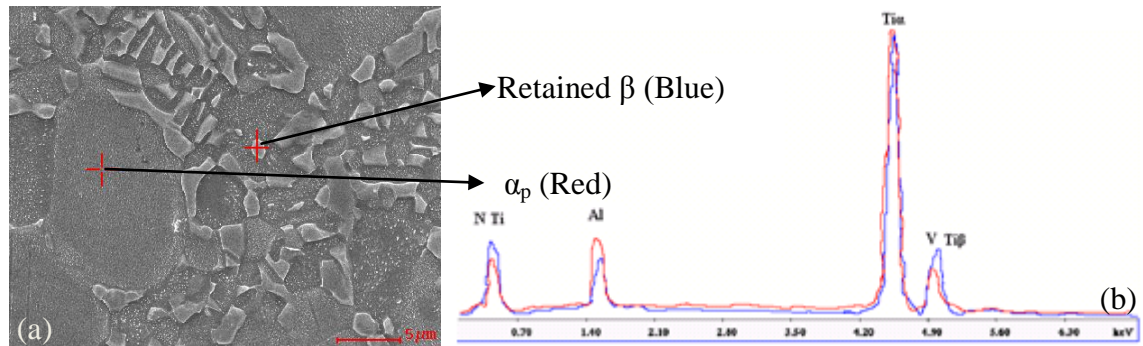


Figure 5.65 (a) Secondary electron micrograph and (b) X-EDS spectrums of αp phase and retained β phase in the BM

5.3.3 Examples of small debris in the microstructure

Small debris including TiC, C or O has been investigated in microstructures of the weld zones and the BM through X-EDS analysis in terms of spectrums and elemental maps. Only defects seen as black dots and white dots in the welds of all the sections through X-EDS analysis were observed at 500 magnification or higher magnification, where 20% of the black dots are mainly carbon, 80% of the black dots are titanium carbides (C>Ti or Ti>=C). Zhu et al. (1998) found that TiC particulate reinforced Ti–6Al–4V composite have enhanced strength and creep properties compared to Ti–6Al–4V due to altering of the matrix microstructure by TiC particulates. Moreover, the white dots were also observed in the BM as well as the black dots. It should be noted that the fine white dots of no more than 1μm are usually silco particles coming from the polishing material in sample preparation step. Examples of those white and black dots are shown from Figure 5.66 to Figure 5.69. Figure 5.66 are X-EDS elemental maps of the black particles in the centre of W6B6, showing that the black particle contains carbon. An X-EDS spectrum analysis on another black dot from W6B6 is shown in Figure 5.67 and this black dot also contains carbon, which is seen as a defect. Figure 5.68 are X-EDS elemental maps of the white dots observed in the centre of W4B4 indicating that white dots are carbon particles. Figure 5.69 shows the same X-EDS spectrums for a black region in the weld W4 and a white dot in the weld W6, both of them consist of Ti, Al, V, N, C and they have the same amount of carbon

element. It was observed that black dots and white dots were part of the BM and they retained in the weld zones, this reassures that the SSFSW with Ti-6Al-4V was defect free.
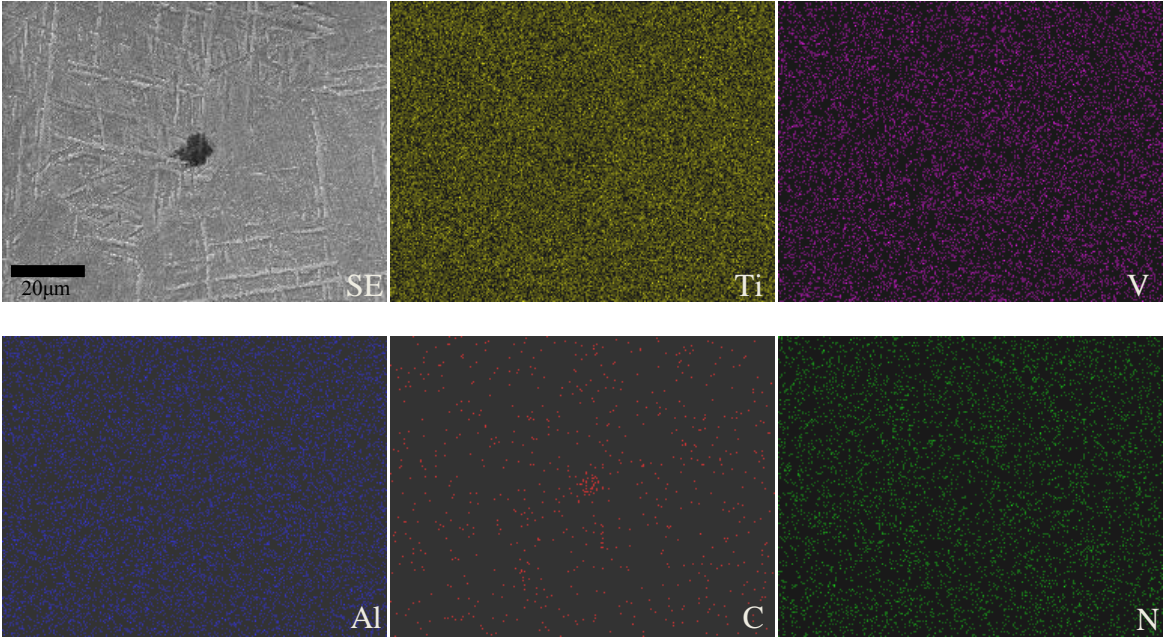


Figure 5.66 X-EDS elemental maps of the carbon particle observed in the centre of W6B6
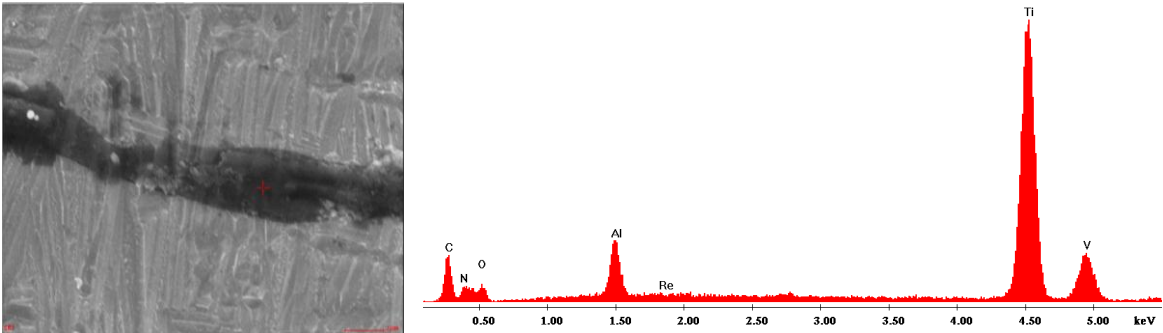


Figure 5.67 X-EDS spectrum of the black region from W6B6
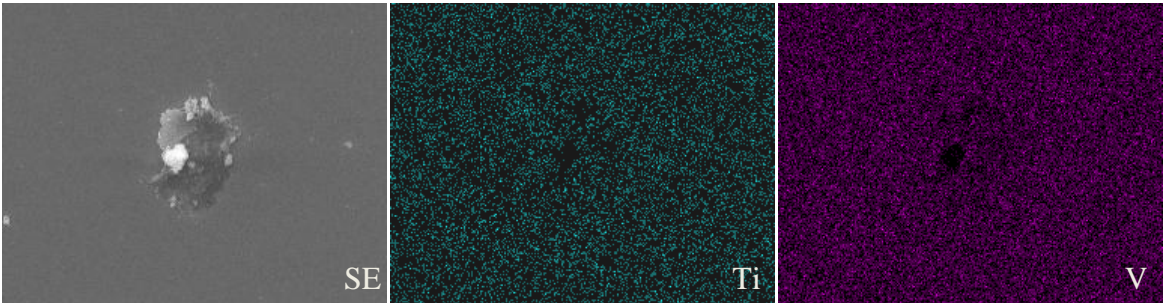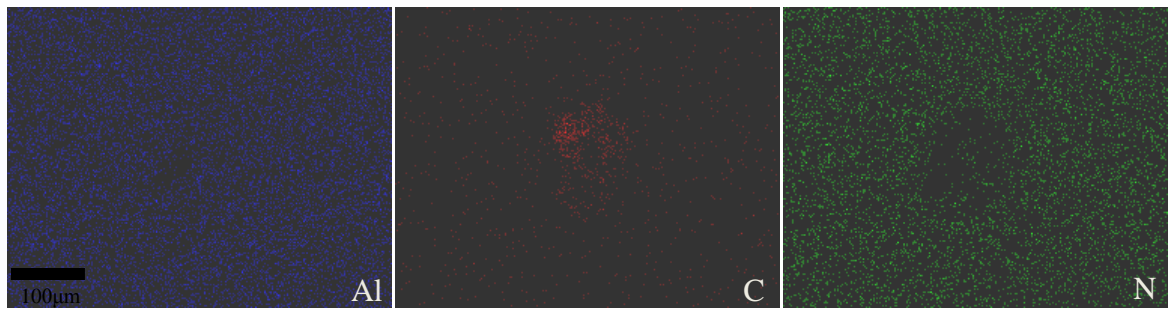
Figure 5.68 X-EDS elemental maps of the carbon particle observed in the centre of W4B4
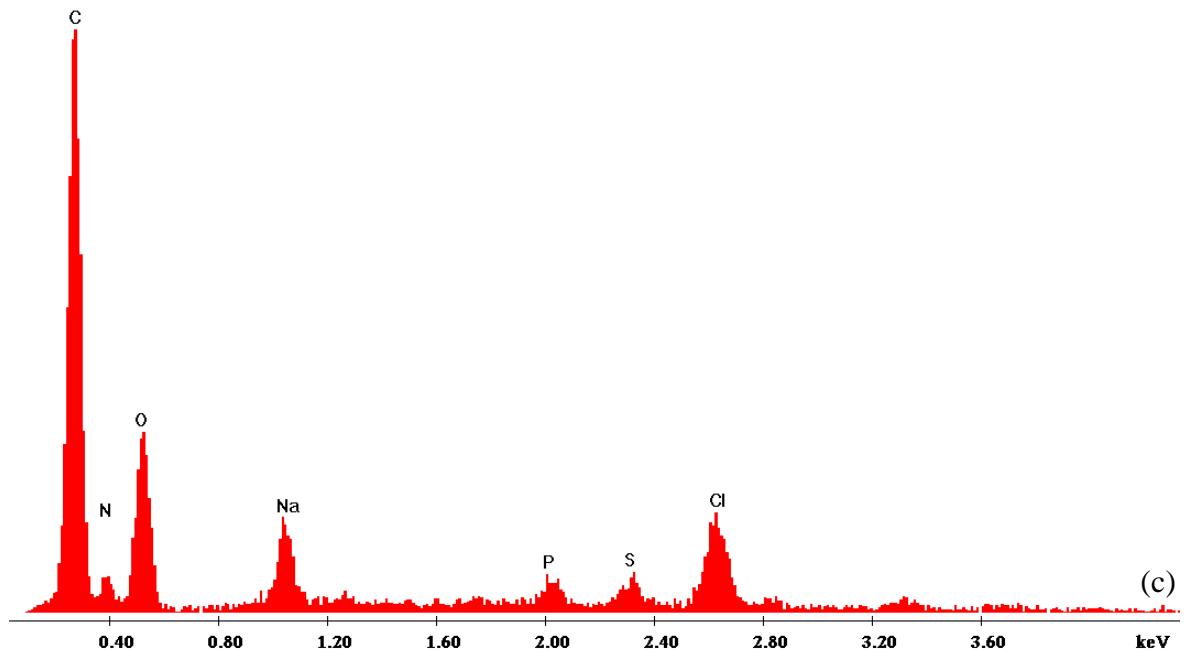


Figure 5.69 The same X-EDS spectrums (c) for: (a) a black region in the weld W4 and (b) a white dot in the weld W6

5.3.3 Tool/ work piece interaction

Tool/ work piece interaction has been investigated in the fully lamellar structure of the cross sections, the normal sections and the side sections in terms of Secondary electron micrographs, X-EDS analysis and EBSD data.

*5.3.3.1 Cross section observation*

Figure 5.70(a) shows an secondary electron micrograph taken from the weld bottom at the AS of the cross section W4B4 showing "ring" structure which consists of two kinds of microstructures: Area 1 with dark contrast and Area 2 with light contrast. X-EDS spectrum analysis of Area 1 and Area 2 is shown in Figure 5.70(b). The results show that Area 2 with light contrast contains a small amount of tungsten (W) and rhenium (Re), and this region is called "W-Re containing region" in the present work. A detailed SEM analysis was carried out on the fully lamellar structure of W4B4; in order to characterize the non W-Re containing region and W-Re containing region, Figure 5.71(a) shows the secondary electron micrographs of a non W-Re containing region consisting of classic lamellar structure with mixed basketweave and Widmanstätten morphologies. Whilst, Figure 5.71(b) displays that W-Re containing region has an unknown fine lamellar structure consisting of much finer α laths compared to much coarser α laths in the classic lamellar structure. Figure 5.71(c) and (d) are the secondary electron micrographs of another W-Re containing region at the weld surface at low and high magnification, respectively. The "ring structure" from the weld surface in Figure 5.71(a) showing interweaved hardness, as discussed in the previous section 4.1, could be caused by the rotation of the tool pin. It is clearly seen from the spectrum peaks of W and Re in Figure 5.71(b) that probe material W and Re have infiltrated into the weld bottom of the weld W4 in the form of W-Re compound.

W-Re containing region sized 3.15mm by 2.72mm was also evident at the AS of the top surface of W5B5, as shown in Figure 5.72(a), which contain a large part of "ring structure" consisting of interweaved regions of dark and light contrast, and the region with light contrast is the W-Re containing region, which was indicated as a red elliptical circle at the weld surface. And the corresponding high resolution secondary electron micrograph of W-Re containing region is shown in Figure 5.72(b). Figure 5.72(c) shows the secondary electron micrograph of a non W-Re containing region just adjacent to the W-Re containing

region. W-Re containing region was not found at the AS of the weld surface of W6B6, but it was found at the top surface of W6 on the central vertical line, as shown in Figure 5.73(a) and Figure 5.73(b) displays the non W-Re containing region of W6.
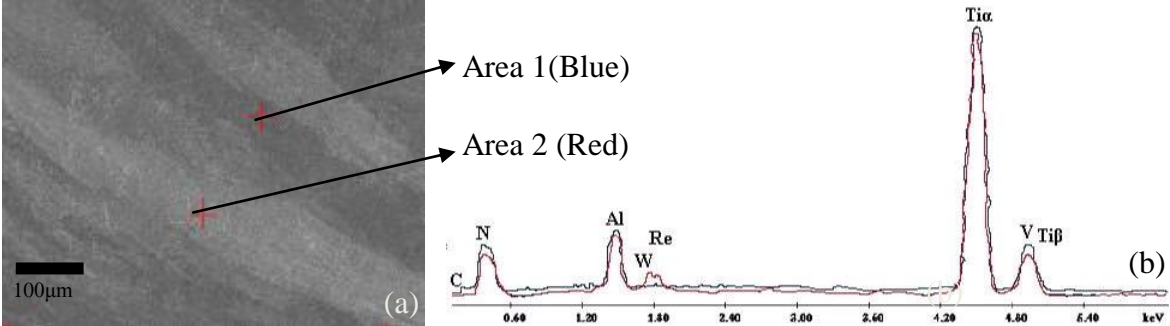


Figure 5.70 X-EDS spectrum analysis from the weld bottom of W4B4 indicating infiltration of the tool material
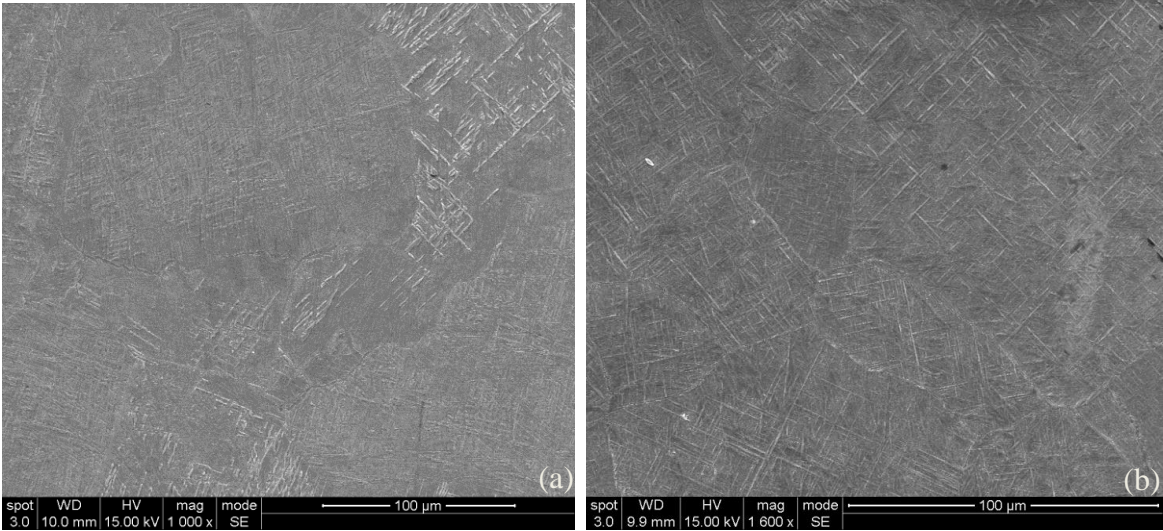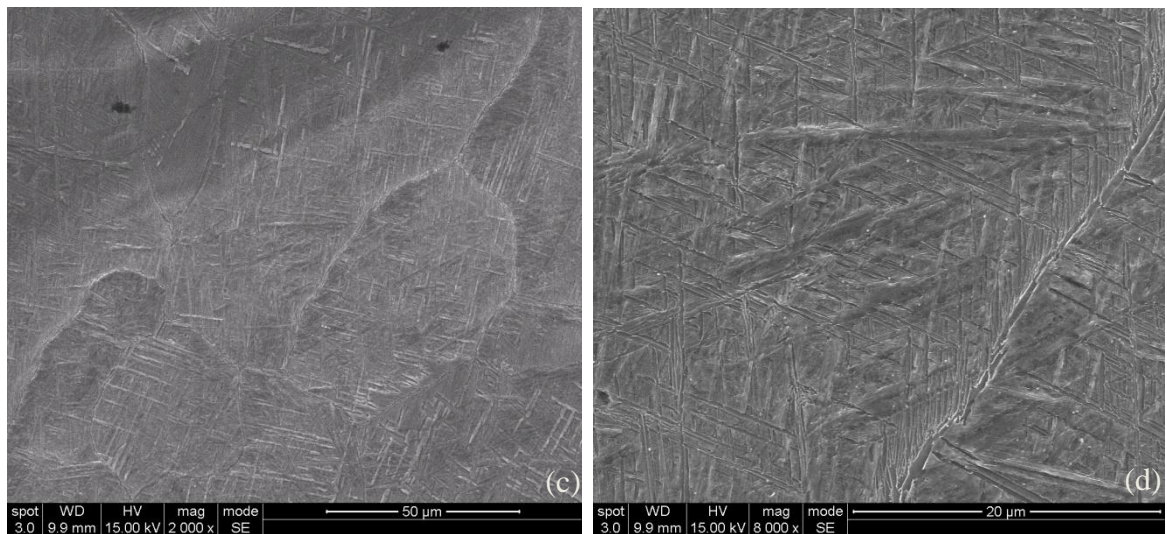
Figure 5.71 Secondary electron micrographs of (a) a non W-Re containing region; (b) a W-Re containing region from the weld bottom of W4B4; Secondary electron micrographs of the W-Re containing region of the weld surface at (c) low and (d) high magnification
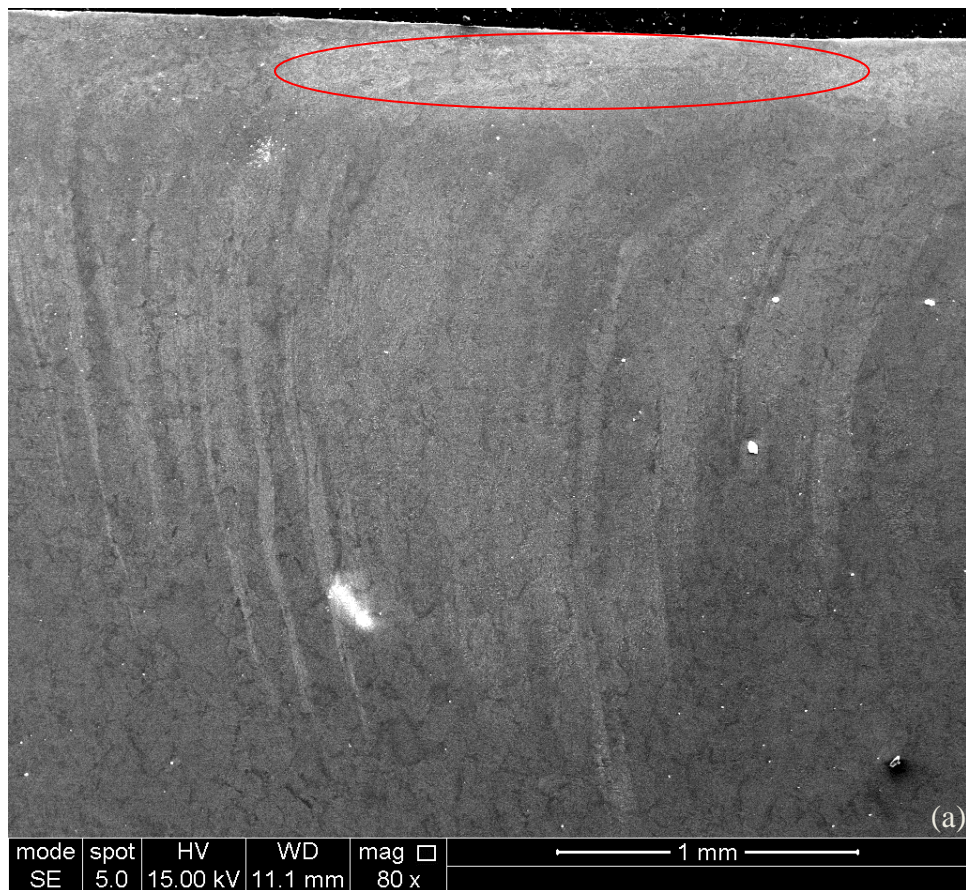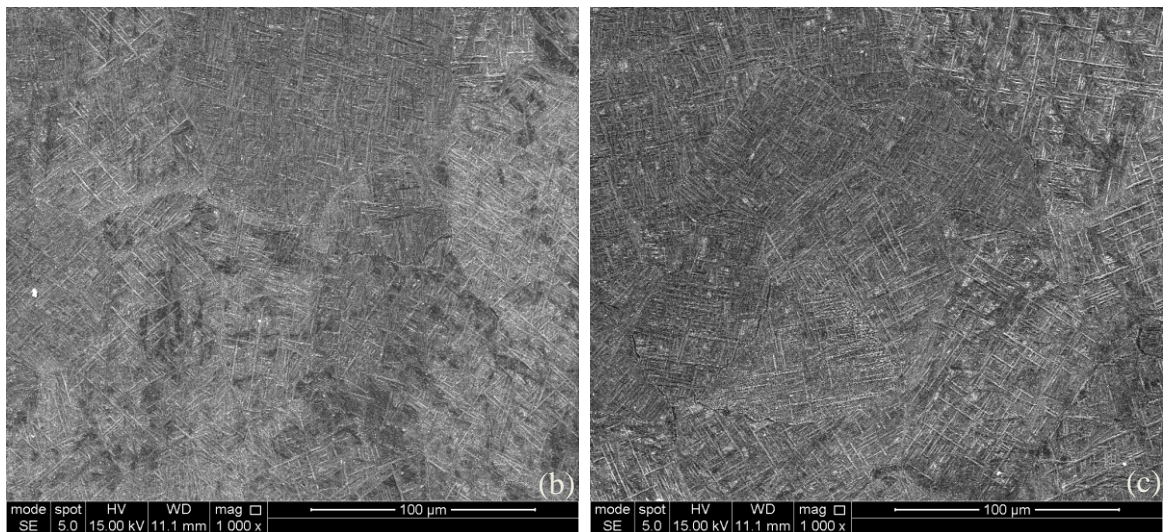
Figure 5.72 Secondary electron micrographs taken from the AS of the top surface of W5B5 at (a) low magnification; high magnified secondary electron micrographs of (b) a W-Re containing region and (c) a non W-Re containing region
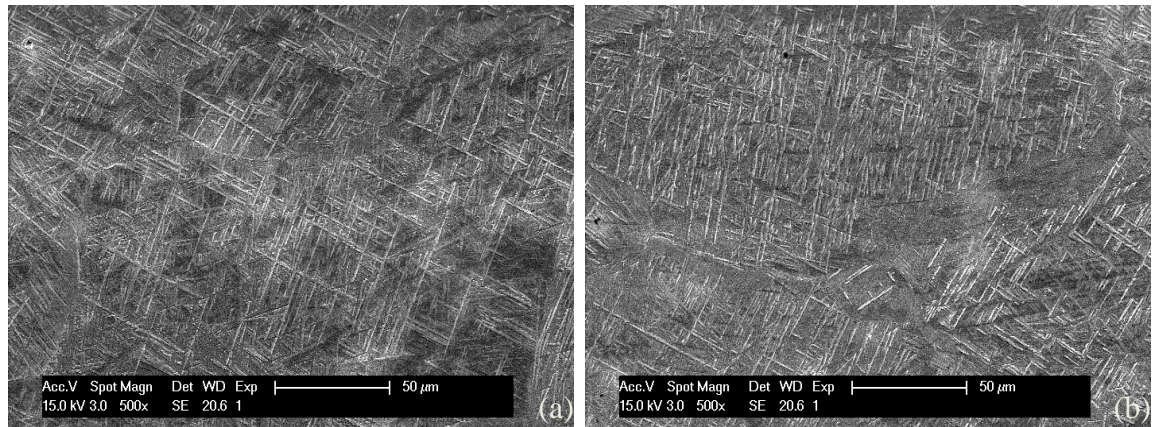


Figure 5.73 Secondary electron micrographs of (a) a W-Re containing region; (b) a non W-Re containing region from the weld surface of W6B6

Figure 5.74 shows the secondary electron micrographs taken from the AS of the weld surface of the weld W19. Figure 5.74(a) is a micrograph from the region sized 3.55mm by 2.47mm and the whole W-Re containing region was sized 145μm by 146μm. Figure 5.74(b) shows the detailed "ring structure" or W-Re containing region enclosed by the red rectangular box in Figure 5.74(a) and Figure 5.74(c) is a high resolution secondary electron micrograph of this region. X-EDS elemental maps of Figure 5.74(b) and Figure 5.74(c) are shown in Figure 5.75 and Figure 5.76, respectively.

168
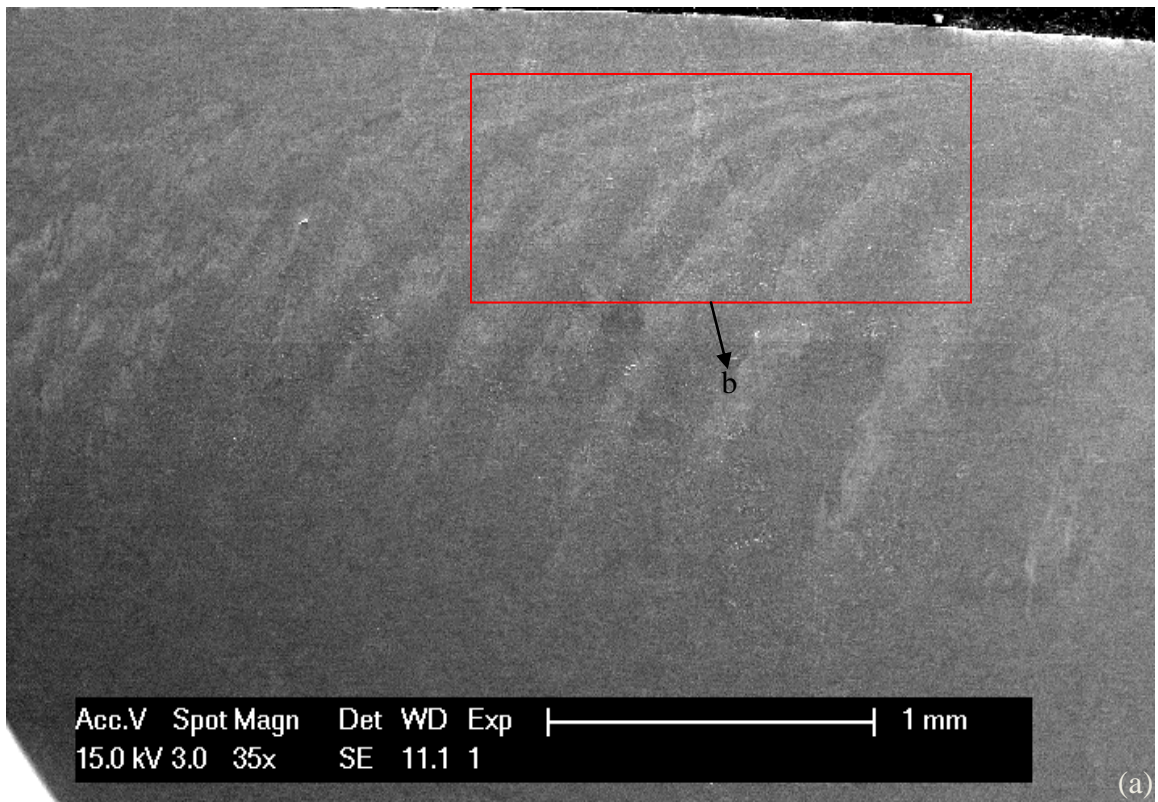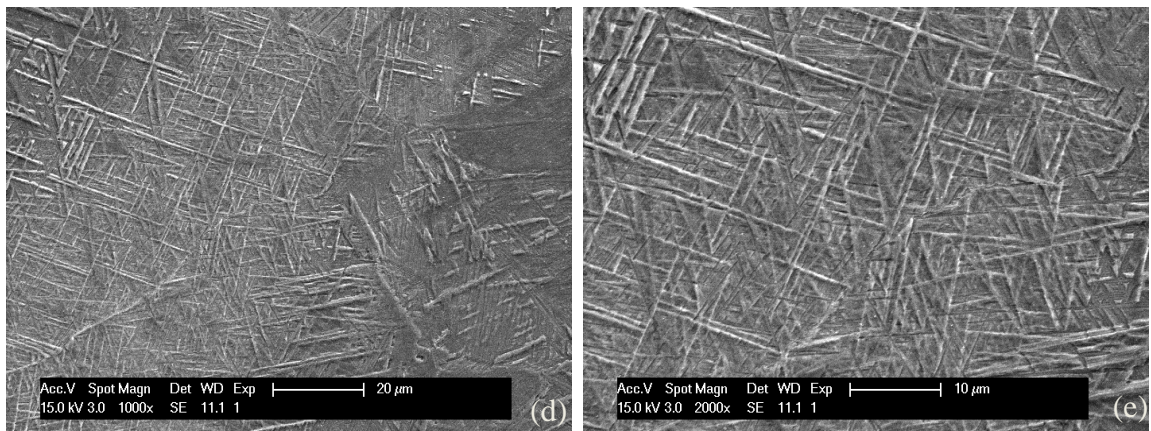
Figure 5.74 Secondary electron micrographs from the AS of the weld surface of W19: (a) the first "ring structure" at (b) low and (c) high magnification; another "ring structure" at (d) low and (e) high magnification
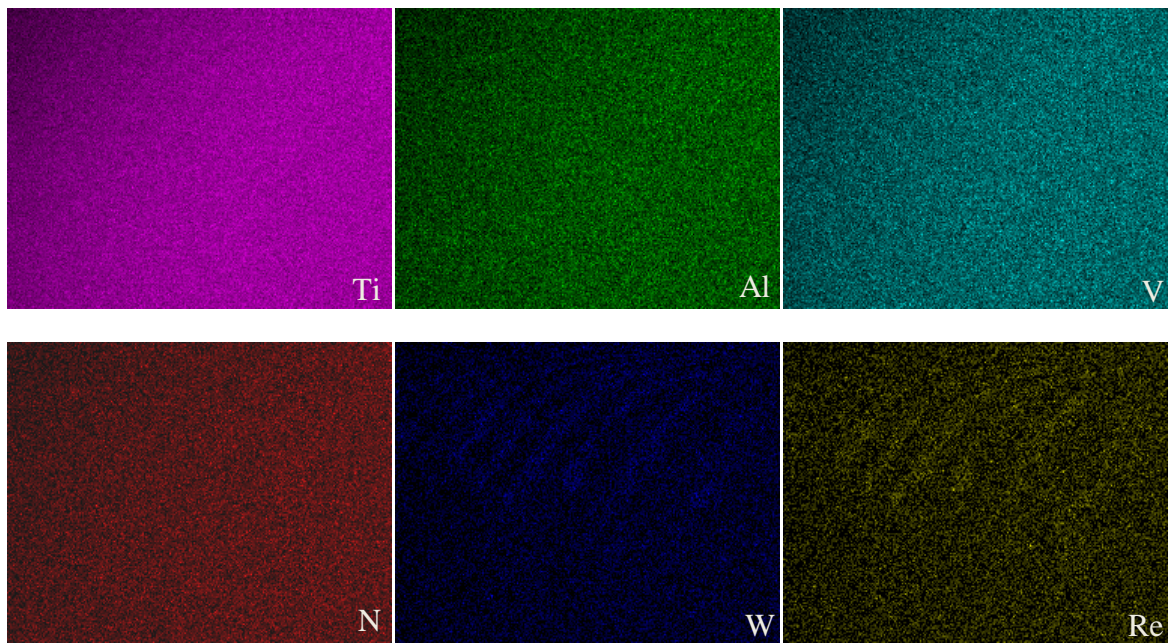


Figure 5.75 X-EDS elemental maps of Figure 5.74(b)
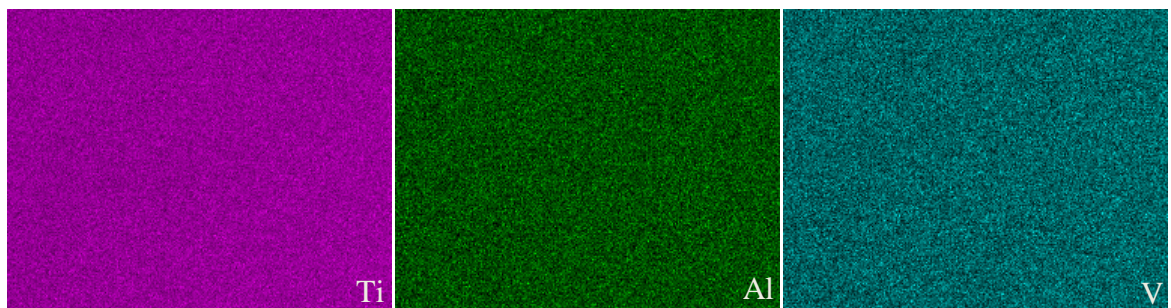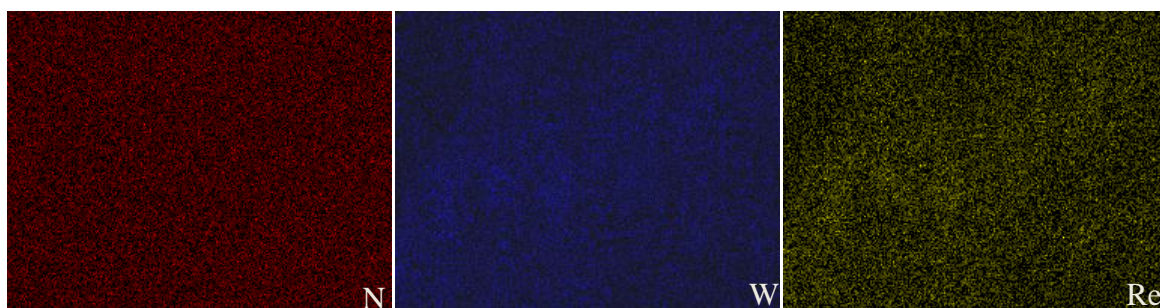
Figure 5.76 X-EDS elemental maps of Figure 5.74 (c)

*5.3.3.2 Normal section and side section observation*

A normal section sample named as 4.8.c was cut from the weld bottom of W4, as shown in Figure 5.77(a) and the analysis area was taken from the back of the weld, results are shown in Figure 5.77(b-g). Figure 5.77(b) is a detailed optical micrograph taken from the part of Figure 5.77(a), where the "ring" structure consists of two kinds of microstructures: Type 1 (dark contrast) and Type 2 (light contrast). Type 2 belongs to the classic lamellar structure in the SZ while type 1 is an unknown fine lamellar structure belonging to the W-Re containing region. Misorientation angle distribution of the W-Re containing region is shown in Figure 5.77(c). Figure 5.77(d) is the reconstructed β texture of the whole map. Euler colouring map of Type 1 structure using 0.2μm step size is shown in Figure 5.77(e) and the corresponding misorientation angle distribution histogram is shown in Figure 5.77(f) where a 30º angle is a large deviation from the burgers angles which was assumed to be the misorientation angle between the adjacent prior β grains. Figure 5.77(g) is a reconstructed map of the W-Re containing region at 0.5μm step size indicating that the unknown fine lamellar structure in the W-Re containing region consists of fine α laths resembling martensitic structure, Later on, an X-EDS elemental analysis of the "ring" structure region was carried out on the "ring structure" in Figure 5.77 and results were shown in Figure 5.78. The high resolution secondary electron micrographs of a W-Re and a non W-Re containing region of 4.8.b are shown in Figure 5.79(a) and Figure 5.79(b), respectively. Evidence of tool wear were also found in the normal section 4.6.b and side section 4.2.b. Figure 5.80 shows the "ring structure" in an optical micrograph of the lamellar structure at the AS of the welding edge of 4.6.b, where the W-Re containing regions appear as black contrast. The same "ring structure" was also observed at the top surface of 4.2.b, as shown in Figure 5.81.
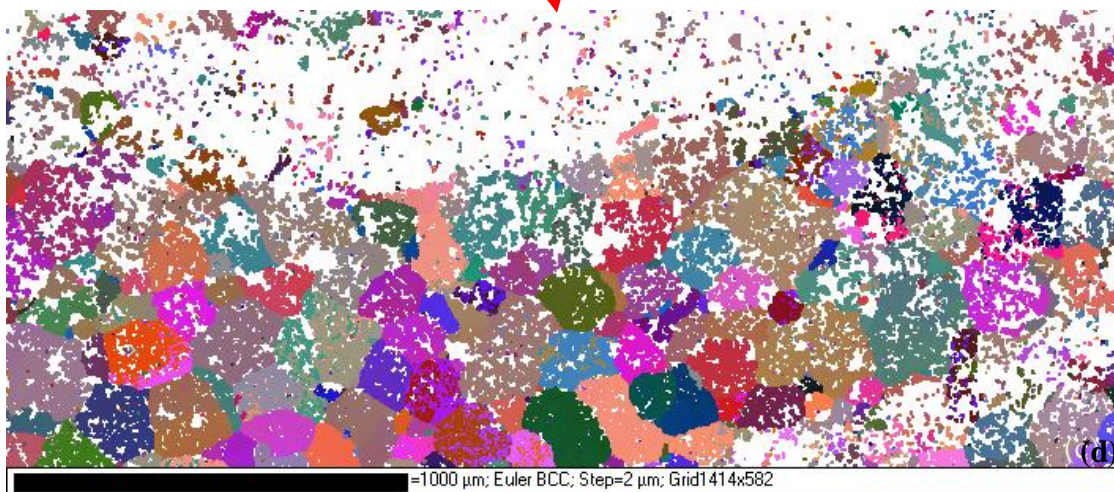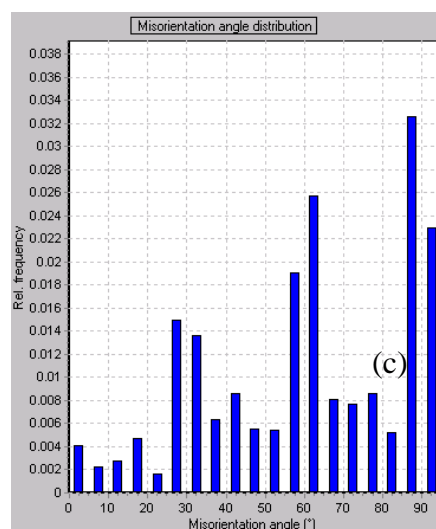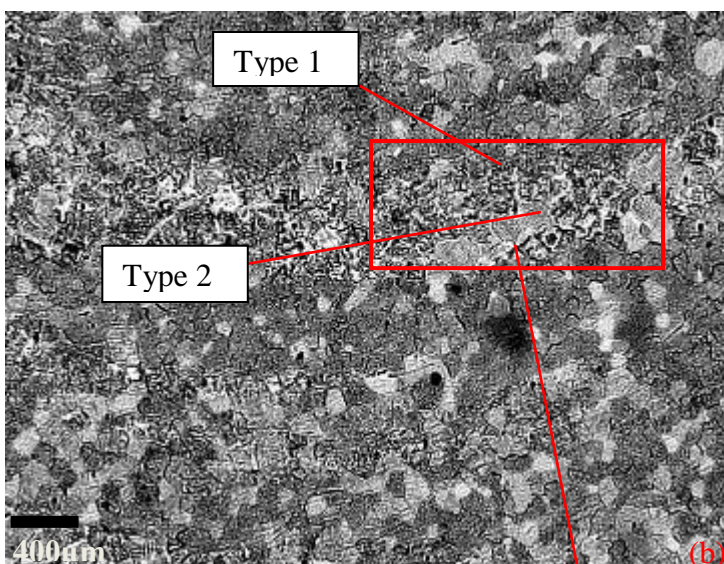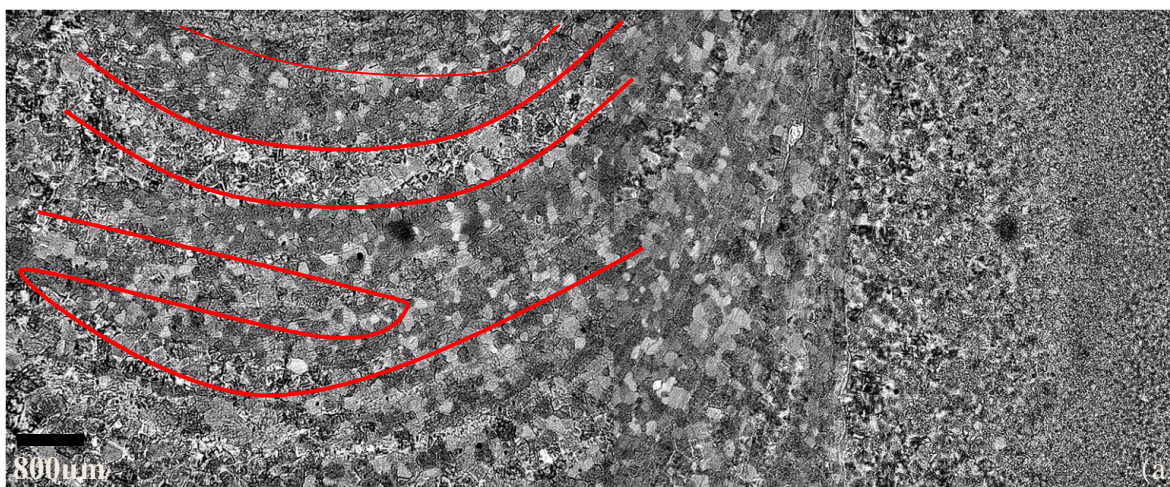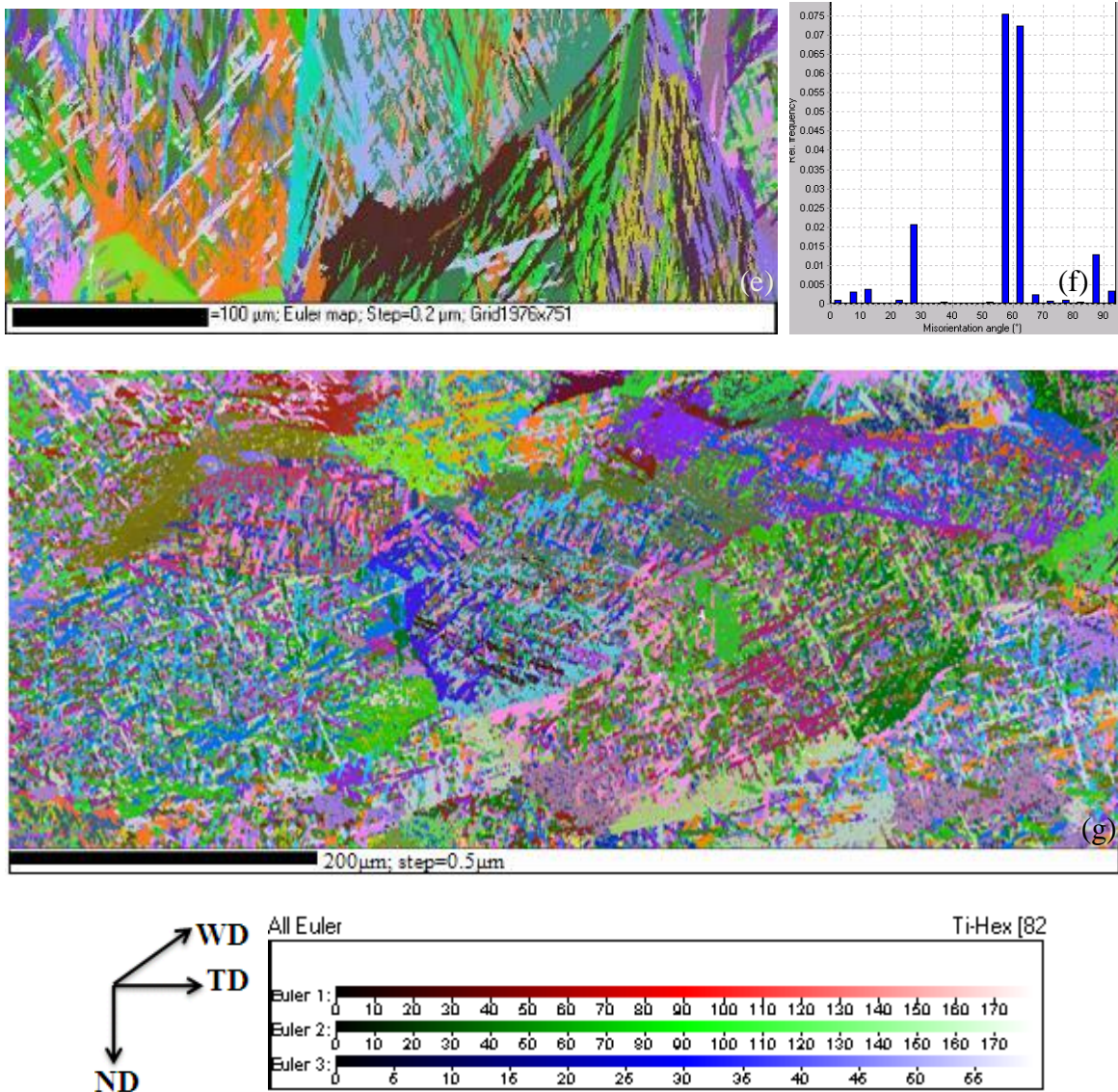
Figure 5.77 (a) Optical micrograph obtained from the weld centre and welding edge at the RS of 4.8.b showing "ring" structure, (b) a detailed region selected from the "ring structure" (c) misorientation angle distribution histogram of Type 1 structure of W-Re containing region; (d) reconstructed high temperature β texture of the red rectangular region of (b); (e) a detailed EBSD Euler map of Type 2 structure (classic lamellar structure in the SZ); (f) misorientation angle distribution histogram of Type 2 structure; (g) high resolution EBSD Euler map of Type 1 structure
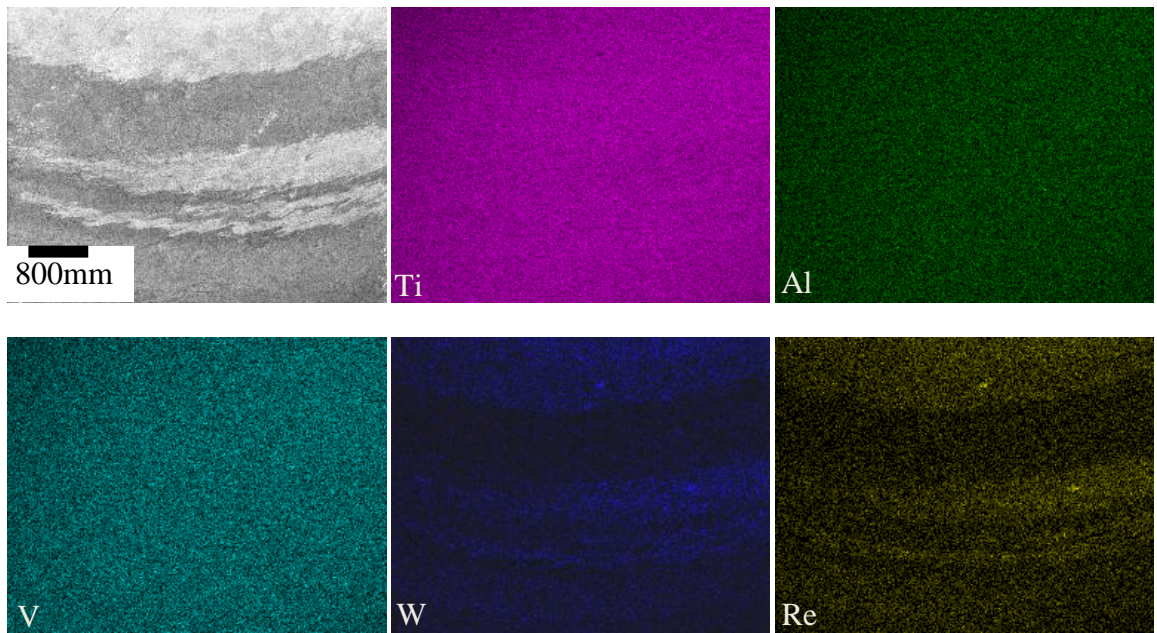
Figure 5.78 X-EDS elemental map of the "ring structure" shown in Figure 5.77(a) and (b)
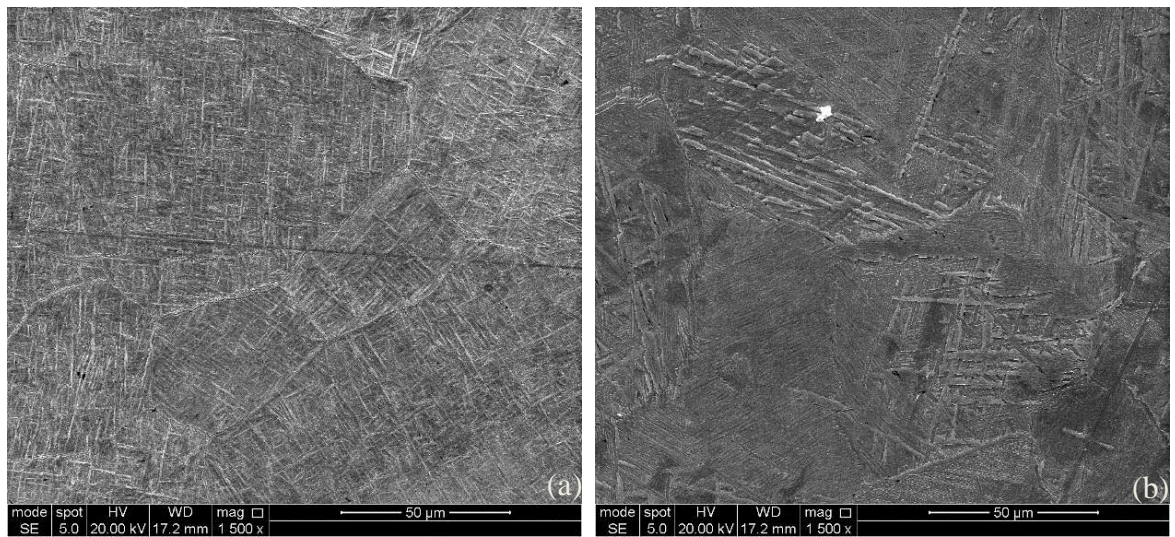


Figure 5.79 Secondary electron micrographs of (a) a W-Re containing region and (b) a non W-Re containing region from 4.8.b
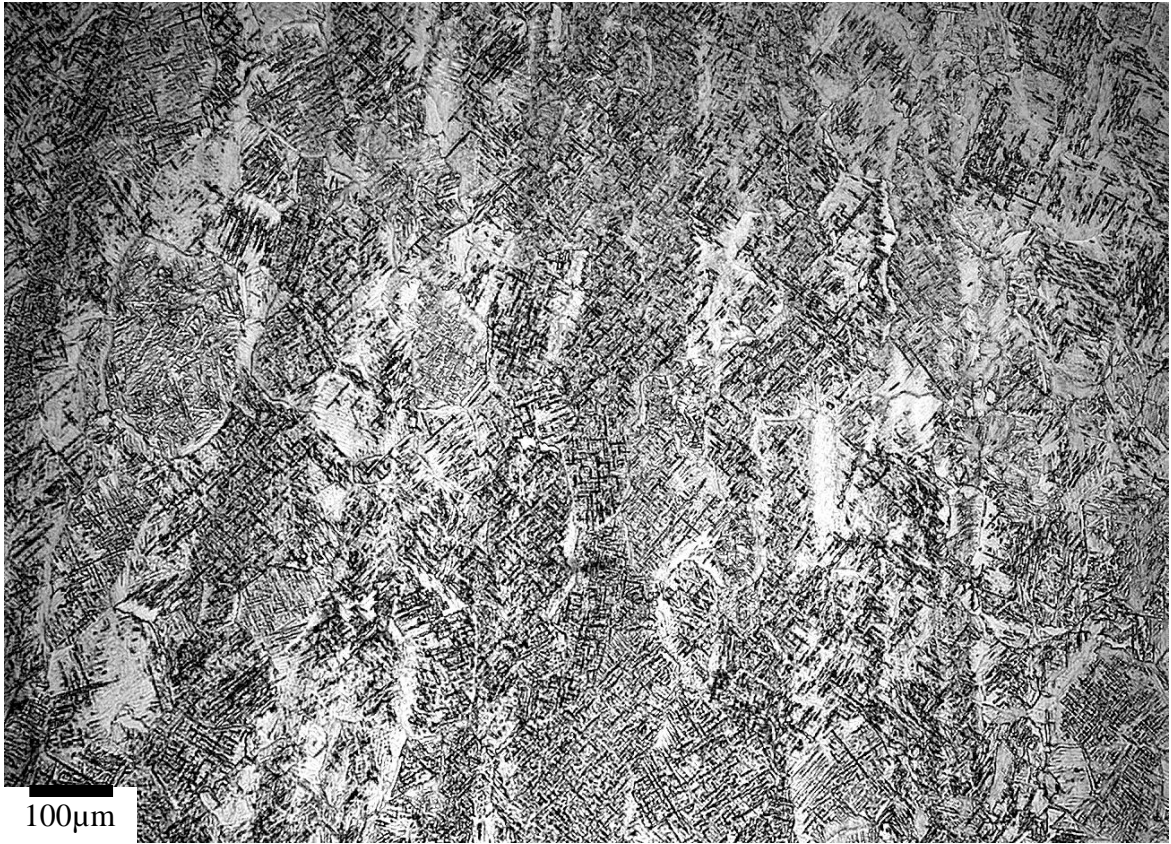
Figure 5.80 Optical micrograph of the lamellar structure adjacent to the AS of the welding edge of 4.6.a and the W-Re containing regions appear as black contrast
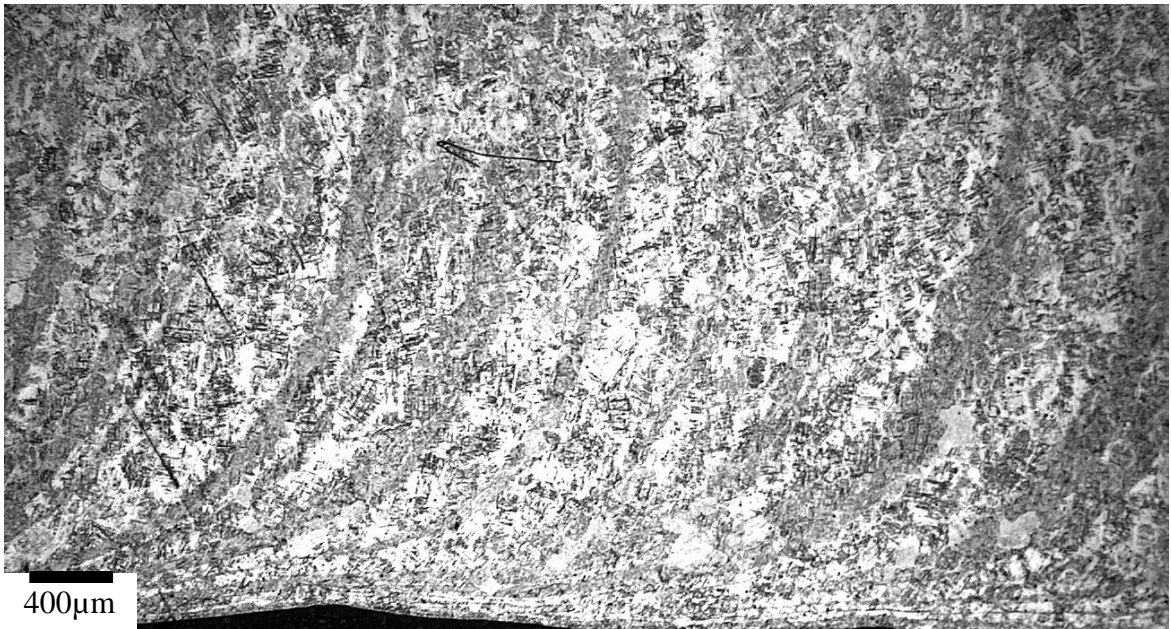


Figure 5.81 Optical micrograph from the top surface of 4.2.a, the W-Re containing regions appear as black contrast

175

**5.4 Effect of welding parameters on microstructure**

5.4.1 Influence of welding parameters on the bimodal structure

On a horizontal line of the SSFSWs, the weld zones are divided into the BM, the HAZ, the TMAZ and the SZ with corresponding equiaxed structure, bimodal structure and lamellar structure. Each weld joint has two HAZs, two TMAZs at both the AS and the RS of the welding edge and SZ in the weld centre. The differences in bimodal structure of the weld zones of the six welds W4, W5, W6, W19, W20 and W21 can be attributed to different welding parameters in those regions. The αp grains were both present in the equiaxed structure of the BM and the bimodal structure of all the six welds, which indicates that the peak weld temperature at those region did not exceed the β transus. Moreover, the bimodal structure contains αp phase of much lower volume fraction compared to αp phase in the equiaxed structure in the BM. This meant that the temperature was sufficiently high in the bimodal structure to cause the retained β grains present in the BM to grow and depletion of the αp grains and transforming to a lamellar α+β structure on cooling. Bimodal structure possibly belongs to the HAZ. Bimodal structure of all the six welds are analysed in terms of shearing effect at the AS of the weld surface, the width of the bimodal structure, αp grain size and volume fraction of αp phase.

It is seen from the AS of the weld surface of the weld W4 (Figure 5.4 (a)) that the αp grains in the bimodal structure are aligned along the direction which rotates about 45° anticlockwise around the transverse direction (TD), this is called the "shearing effect" in this work, which were also observed at the AS of the weld surface of all the other five welds (Figure 5.7(a), Figure 5.10(a), Figure 5.13(a), Figure 5.16(a) and Figure 5.19(a)), this is possibly due to the great material flow from the probe at the AS of the weld surface as the tool was translating during welding and pushing the material from the RS to the AS. However, in the bimodal structure at the RS of the weld surface, the αp grains were equiaxed and elongated along the transverse direction (TD), thus the shearing effect was not observed at the RS of the bimodal structure (Figure 5.4(b), Figure 5.7(b), Figure 5.10(b), Figure 5.13(b), Figure 5.16(b) and Figure 5.19(b)). Moreover, the shearing effect was not observed at both the AS and the RS of the weld centre or the weld bottom of the bimodal structure, as shown in Figure 5.5(a and b), Figure 5.6(a and b), Figure 5.8(a and b), Figure 5.9(a and b), Figure 5.11(a and b), Figure 5.12(a and b), Figure 5.14(a and b), Figure 5.15(a

176

and b), Figure 5.17(a and b), Figure 5.18(a and b), Figure 5.20 (a and b) and Figure 5.21 (a and b).

The total length of the central transition zone at the AS of the weld W4 is 0.65mm and it is much wider than that of the weld W6 (0.4mm). Length of the central transition zone at the AS of the weld W19 is 0.25mm, as shown in Figure 5.5(b), Figure 5.11(b) and Figure 5.14(b). The length of the surface transition zone at the AS of W4, W6 and W19 is 0.7mm, 0.4mm and 0.25mm, respectively (Figure 5.5(a), Figure 5.11(a) and Figure 5.14(a)). Length of the bottom transition zone at the AS of W4, W6 and W19 is 0.6mm, 0.35mm and 0.2mm (Figure 5.5(c), Figure 5.11(c) and Figure 5.14(c)). This meant that the gradient of the temperature profiles at the welding edges of the weld W4 was the most flat, and this gradient became deeper with increasing traverse speed; the gradient was deeper in the weld with lower rotation speed.

A detailed comparison can be made between the bimodal structure of all the six welds by comparing the width of the bimodal structure in the weld centre at both the AS and the RS. It was shown in Table 5.1 and Table 5.2 that, as traverse speed increased from 50 to 100 and 150mm/min, the width of the bimodal structure decreased from 580μm to 450μm and 420μm at the AS and the width of the bimodal structure decrease from 660μm to 550μm and 420μm at the RS; as rotation speed decreased from 900 to 800, 600 and 400rpm, the width of the bimodal structure decreased from 420μm to 250μm, 200μm and 180μm at the AS; the width of the bimodal structure decrease from 420μm to 300μm, 220μm and 195μm at the RS. This result demonstrates that the width of the bimodal structure decreased with increasing traverse speed and it decreased with decreasing rotation speed. It should be noted that the width of the bimodal structure is much larger at the RS compared to that at the AS for W4 and W5 with 50 and 100mm/min traverse speeds, indicating that the microstructure at the RS is more diffuse than that at the AS.

In comparison of the bimodal structure of the central transition zones and bottom transition zones of the three welds W4, W5 and W6 with a constant rotation speed of 900rpm at both the AS and RS in terms of volume percentage of αp grains and αp grain size, as shown in Figure 5.5(b and c), Figure 5.8(b and c), Figure 5.11(b and c), Figure 5.14(b and c), Figure 5.17(b and c) and Figure 5.20(b and c), material in the bimodal structure of the weld W4 has smaller volume percentage of αp grains compared to W5 and the weld W5

has smaller volume percentage of αp grains than the weld W6. As traverse speed increased from 50 to 100 and 150mm/min, the volume fraction of the αp grains increased from 50, 55 and 60pct at the RS of the central bimodal structure (Table 5.2). This would suggest that volume percentage of the αp grains increases with increasing traverse speeds due to lower peak weld temperature in the bimodal structure when traverse speed increases. This meant that peak temperature experienced in the bimodal structure was the highest in the weld W4 with the lowest traverse speed and it decreased with increasing traverse speed. It is seen from Table 5.2 that W6 has larger αp grains than W5 and W5 has larger αp grains than W4 (Figure 5.5 (b and c), Figure 5.8 (b and c), Figure 5.11(b and c), Figure 5.14(b and c), Figure 5.17(b and c) and Figure 5.20(b and c)). Thus, the αp grain size in the bimodal structure increases with increasing traverse speed. This also indicates that peak weld temperatures experienced in the bimodal structure of the weld W4 at both the AS and the RS are much higher compared to that in the bimodal structure of the weld W5 and as traverse speed decreases, the bimodal structure experiences slightly higher peak weld temperature enabling the gradually consumption of the αp grains, thus resulting in smaller αp grain size. This result shows agreement with a FSW study of Ti–6Al–4V by Liu et al. (2010b) who investigated the bimodal structure in the SZ at traverse speeds of 25, 50 and 100mm/min and a constant rotation speed of 400rpm and reported that the αp grain size in the bimodal structure increases with increasing traverse speed.

Compared to the weld W6 with 900rpm rotation speed, the αp grains in the bimodal structure at both the AS and the RS of the welding edge of W19 with a 800rpm rotation speed were greater and they accounted for increased volume percentage, this indicated that the region with bimodal structure at both the AS and the RS of the weld W6 have experienced higher peak weld temperature compared to that of the weld W19.

A direct comparison can be made between the central bimodal structure of all the three welds W19, W20 and W21 by comparing volume fraction of the αp grains (Table 5.2). It is seen from Table 5.2 that as rotation speed decreased from 800 to 600 and 400rpm, volume fraction of the αp grains increased from 70, 73 and 76pct at the AS of the central bimodal structure. And volume fraction of the αp grains increased with decreasing rotation speed at the RS of the central bimodal structure, results of which are not shown here. This meant that peak temperature experienced in the bimodal structure was the highest in the weld W19 with 800rpm rotation speed and it decreased with decreasing rotation speed from 800 to

600 and 400rpm. In comparison of the bimodal structure in the weld surface, in the weld centre and the weld bottom at both the AS and the RS of the welding edges of the three welds W19, W20 and W21, W21 has larger αp grains than W20 and W20 has larger αp grains than W19 (Figure 5.13, Figure 5.14 and Figure 5.15, Figure 5.16, Figure 5.17 and Figure 5.18, Figure 5.19, Figure 5.20 and Figure 5.21). This meant that the αp grain size in the bimodal structure increases with decreasing rotation speed and volume fraction of αp phase increases with decreasing rotation speed.

It can be seen that the bimodal structure at the AS is slightly different from that at the RS in terms of volume fraction of the αp grains (Table 5.1 and Table 5.2) and the αp grains are generally smaller at the AS than that at the RS in the bimodal structure and transition zone at the AS has a much smaller volume fraction of the αp grains than that at the RS, as shown in all the 18 figures (Figure 5.4 to Figure 5.21) due to the fact that more αp grains have been consumed by the adjacent lamellar structure as a result of phase transformation. Thus, there is more consumption of the αp grains by retained β phase in the HAZ at the AS than that at the RS; this would suggest that material at the AS of the HAZ has experienced a slightly higher peak weld temperature than that at the RS.

It can be concluded that the peak weld temperature in the region with bimodal structure decreased with increasing traverse speed and it increased with increasing rotation speed. The αp grain size in the bimodal structure increases with increasing traverse speed and decreasing rotation speed; volume fraction of the αp grains increases with increasing traverse speed and decreasing rotation speed; the αp grains in the bimodal structure are generally smaller at the AS compared to that at the RS indicating in the HAZ, the AS has experienced a slightly higher peak weld temperature than the RS.

5.4.2 Influence of welding parameters on the lamellar structure

The lamellar structure which has experienced peak weld temperature above the $T_\beta$ has been divided into coarse lamellar structure and fine lamellar structure, in order to define the TMAZ and the SZ. And influence of traverse speeds and rotation speeds on the lamellar structure of the six welds has been investigated in terms of α laths morphology, which can be obtained from comparison of the cross sections of all the six welds W4, W5, W6, W19, W20 and W21 on both the central horizontal and vertical lines.

It was shown in Figure 5.24 that the coarse lamellar structure in the weld W4 contain a substantial amount of α colonies and clear GBα at the prior β grain boundaries and the region with the coarse lamellar structure might be the TMAZ or the SZ. The TMAZ has been defined as the region next to the HAZ, which has undergone both temperature and deformation caused by the rotation of the tool and down force during FSW but without recrystallization due to smaller strain or not enough time at a certain temperature (Pilchak et al., 2007b). However, the TMAZ is difficult to be differentiated from the HAZ in bimodal structure due to the fact that in the bimodal structure 30-50μm to the coarse lamellar structure, materials might have or have not experienced deformation. If this region has undergone deformation, then it belongs to the TMAZ then the coarse lamellar structure could be inside the SZ; if the region has not experienced deformation, then the coarse lamellar structure would belong to the TMAZ. In order to clarify this fact, a method has been developed to define the HAZ and the TMAZ by EBSD technique, and will be discussed in Chapter 6. And the TMAZ is expected to have the coarse lamellar structure (Figure 5.24- Figure 5.30) and the SZ has the fine lamellar structure (Figure 5.32-Figure 5.48) for all the six welds W4, W5, W6, W19, W20 and W21.

The SZ exhibits a basin-like shape significantly widening towards the upper surface. This shape is frequently observed in the SSFSWs and may be attributed to the strong influence of the tool shoulder on material flow during conventional FSW (Threadgill, 2007). However, this basin-like shape is due to the 2mm radius at the edge of the probe in the present study using SSFSW method with a non-rotating shoulder. Secondary electron micrographs of the fine lamellar structure were taken from the weld bottom to the weld surface of the SZ for all the six welds on a vertical line, as shown in Figure 5.32, Figure 5.35, Figure 5.38, Figure 5.41, Figure 5.44 and Figure 5.47 and from the AS to the RS on a horizontal line, as shown in Figure 5.33, Figure 5.36, Figure 5.39, Figure 5.42, Figure 5.45 and Figure 5.48. All those secondary electron micrographs of the cross sections from all the six welds W4, W5, W6, W19, W20 and W21 show that the SZ is characterized by a fully transformed lamellar structure with the prior β grain boundaries delineated by allotriomorphic grain boundary α (GBα), and the interiors of the prior β grains contain colony α, basketweave α and Widmanstätten α. Moreover, the thickness of the α laths decreased and the number of α colonies decreased moving from the TMAZ at the AS to the weld centre and from the TMAZ at the RS to the weld centre due to the increase of peak

temperature and increased cooling rate. It was later shown in Figure 5.60 that the SZ centre consists mainly of basketweave α and Widmanstätten α and the TMAZ contain a substantial amount of colony α and GBα, this would indicate that the SZ centre has a large amount of Widmanstätten α and basketweave α structure and the number of colony α and GBα increase as moving from the weld centre to the TMAZ.

Figure 5.49, Figure 5.50 and Figure 5.51 show the secondary electron micrographs of the fine lamellar structure from the normal sections 4.6.b, 5.6.b and 6.8.b, respectively. It can be seen from Figure 5.49(a) and (b) that the parallel α laths actually consist of α laths and much thinner β laths and the α laths are coloured with black contrast and light contrast is for retained β phase in the form of thin laths. The α and β phases are both indicated as red arrows. These typical α+β morphologies were observed in the fine lamellar structure of the SZ of all the six welds. Figure 5.52(a-f) are the backscatter electron micrographs of the fine lamellar structure from the side section 4.3.b showing high resolution micrographs of the fine lamellar structure in the SZ of the weld W4 consisting of basketweave and Widmanstätten morphology. It is also seen from Figure 5.52 that retained β phase in the form of β laths lying between the α laths is shown with light contrast. The average thickness of the α laths is approximately 1 to 2μm and the thickness of the β laths is about 0.1μm.

In comparison of the lamellar structure in the TMAZ and the SZ, the α morphology in the TMAZ and the SZ look different due to different peak temperature experienced in those regions. The TMAZs at both the AS and the RS have a large amount of colony α, thicker GBα and thicker α laths, however, with increasing distance from the TMAZ to the weld centre, the SZ structure is characterised by less colony α, thinner GBα and thinner α laths, whilst the TMAZ contains much shorter and thicker α laths compared to the α laths in the SZ. This meant that the SZ has experienced higher cooling rate than the TMAZ due to the higher peak temperature experienced in SZ. In the SZ, except for colony α and GBα, the other α laths are in the form of Widmanstätten and basketweave morphology as indicated in all of the micrographs of the SZ, in which Widmanstätten structure has fine α lamella than that seen in the basketweave structure suggesting the regions with Widmanstätten structure have experienced faster cooling rate than the regions with basketweave structure. Basketweave structure contains interweaved appearance basketweave α of different orientations, and the lamellar α lath is shorter, and GBα is broken up while Widmanstätten

structure consists of Widmanstätten array of α plates of similarly aligned α laths within the prior β grains at faster cooling rate (Flower, 1990; Yue et al., 2009).

In comparison of the fine lamellar structure on the central horizontal line of the SZs, morphology of the fully transformed lamellar structure have changed significantly with changing distance from the weld centre due to different peak weld temperature and cooling rate. It was observed that, in the secondary electron micrographs from the AS to the RS of the lamellar structure in the SZ centre on a horizontal line of all the six welds W4, W5, W6, W19, W20 and W21 (Figure 5.33 (W4), Figure 5.36 (W5) Figure 5.39 (W6), Figure 5.42 (W19), Figure 5.45 (W20), and Figure 5.48 (W21)), the thickness of the α laths decreased and the number of α colonies decreased with decreasing distance from the weld centre, on the other hand, the thickness of the α laths slightly increased and α colonies increased in the lamellar structure from the weld centre to either the AS or the RS of the welding edge (Figure 5.33, Figure 5.36, Figure 5.39, Figure 5.42, Figure 5.45 and Figure 5.48). It was previously demonstrated in Section 2.1.3.1 that slower cooling rate leads to thicker α laths and larger α colonies. Thus, difference between the AS, weld centre and the RS in the lamellar structure could be attributed to the fastest cooling rate in the weld centre and slower cooling rate in the regions deviated from the weld centre. This would suggest that peak weld temperature and cooling rate experienced in the weld centre were the highest and they both decreased with increasing distance from the weld centre to the welding edge at both the AS and the RS.

Each secondary electron micrograph on the central vertical line of SZs of all the six welds indicate that although those micrographs both exhibit fully transformed lamellar α, lamellar α morphology has changed slightly when it is seen from the weld bottom to the weld surface of each weld (Figure 5.32, Figure 5.35, Figure 5.38, Figure 5.41, Figure 5.44 and Figure 5.47). At the weld bottom of the regions, the microstructure contains a large amount of colony α, GBα and basketweave α and Widmanstätten α, however, the amount of colony α decreased as the decrease of distance from the weld centre on the central vertical line, and at the same time, GBα became thinner and α laths became finer, this indicates cooling rate experienced in the regions along the central vertical line of SZs gradually increased from the weld bottom to the weld centre and from the weld surface to the weld centre due to the increase of peak weld temperature from the weld bottom to the weld centre and the increase of peak weld temperature from the weld surface to the weld centre on the central vertical

line of the SZs. It can be concluded that in each weld, the α laths became thicker, the amount of colony α decreased with decreasing distance from the weld centre on the central vertical line, and simultaneously, GBα became thinner and the α laths became finer (Figure 5.32, Figure 5.35, Figure 5.38, Figure 5.41, Figure 5.44 and Figure 5.47).

Table 5.6 lists heat input and the lamellar morphology in the weld centre of all the six welds and the corresponding micrographs is referred to the figure numbers, it is seen that the α morphology consists of basketweave α and Widmanstätten α, colony α and GBα in the weld centre and no massive or martensite α have been observed, thus cooling rate in this work did not exceed 20°C/s according to the continuous cooling transformation diagram of Ti-6Al-4V in Chapter 2 (Ahmed and Rack, 1998, Figure 2.15). Figure 5.82(a-f) shows the percentage of different morphologies of the α phase on the central horizontal lines from the AS to the RS of the weld zones consisting of the HAZ, the TMAZ and the SZ in terms of area fraction and the percentage of different morphologies of the α phase from the weld bottom to the weld centre along the central vertical lines in the SZ of all the six welds is shown in Figure 5.83 in terms of area fraction. It was shown in Figure 5.82(a-f) that in each weld, the area fraction of basketweave α and Widmanstätten α is the largest in the weld centre and it is slightly larger at the AS than that at the RS; on the other hand, the weld centre has the smallest area fraction of colony α and GBα which are greater with increasing distance from the weld centre to the TMAZ at both the AS and the RS.

The results also demonstrate that the area fraction of basketweave α and Widmanstätten α, colony α and GBα were similar for the three welds W4, W5 and W6 with a constant rotation speed and different traverse speeds. Furthermore, a comparison can be made between the secondary electron micrographs of SZs of the three welds W4, W5 and W6 on the central vertical line by comparing the thickness of the α laths. It can be seen in Figure 5.32, Figure 5.35 and Figure 5.38 that thickness of the α laths increased slightly and the amount of colony α increased slightly with increasing traverse speed indicating that the cooling rate in the SZs decreases slightly as the increase of traverse speed because the thickness of the α laths increases with decreasing cooling rate (Gil et al., 2001; Senkov et al., 2002; Stanford and Bate, 2004).

Effect of rotation speed on microstructure refinement was also studied, as shown in the secondary electron micrographs of SZs of the three welds W19, W20 and W21 on the

central vertical line (Figure 5.41, Figure 5.44 and Figure 5.47), the α laths became thicker with decreasing rotation speeds and Figure 5.82(d-f) and 5.83(d-f) show that the decrease of the area fraction of basketweave α and Widmanstätten α and the increase of the area fraction of colony α and GBα were both significant with decreasing rotation speed either from the AS to the RS of the weld zones on the central horizontal line or from the weld bottom to the weld centre along the central vertical lines in the SZ for all the threes welds W19, W20 and W21, indicating that the cooling rate in the SZs decreases significantly with decreasing rotation speed.

Table 5.6 Heat input and lamellar morphology in the weld centre of all the six welds

| Weld No. | Heat input, kJ/mm | Figure No. | Lamellar morphology |
|---|---|---|---|
| W4 | 3.29 | Figure 5.32(f) | basketweave α and Widmanstätten α, GBα |
| W5 | 1.79 | Figure 5.35(h) | basketweave α and Widmanstätten α, GBα |
| W6 | 1.33 | Figure 5.38(f) | basketweave α and Widmanstätten α, colony α, GBα |
| W19 | 1.23 | Figure 5.41(e) | basketweave α and Widmanstätten α, colony α, GBα |
| W20 | 1.13 | Figure 5.44(d) | basketweave α and Widmanstätten α, colony α, GBα |
| W21 | 1.12 | Figure 5.47(b) | basketweave α and Widmanstätten α, colony α, GBα |

(a) Distance from the weld centre, mm

(b) Distance from the weld centre, mm

(c) Distance from the weld centre, mm

(d) Distance from the weld centre, mm

185
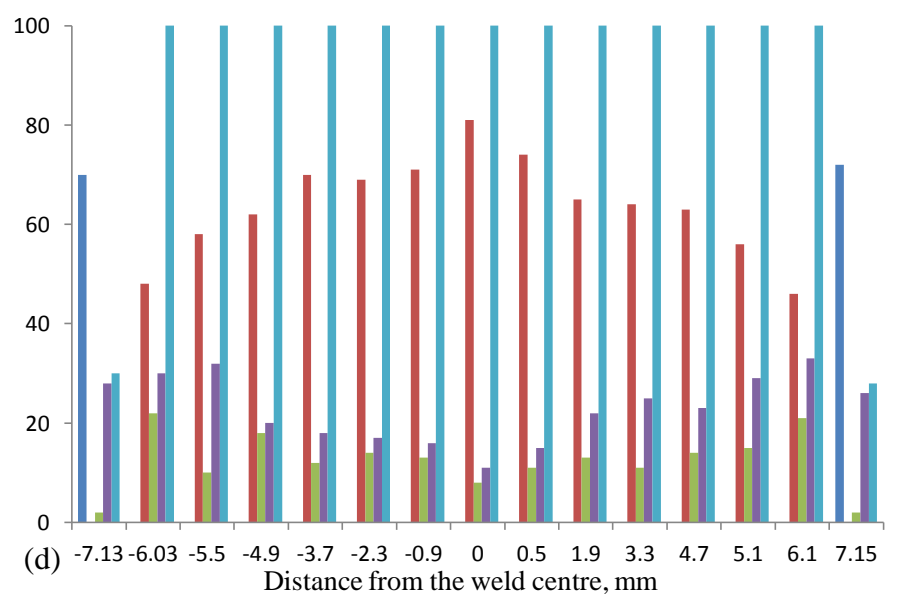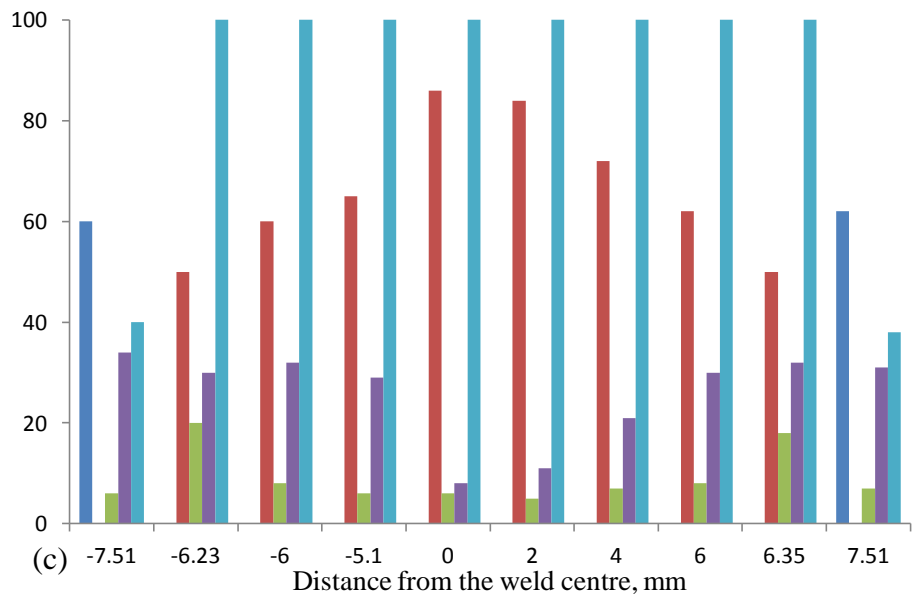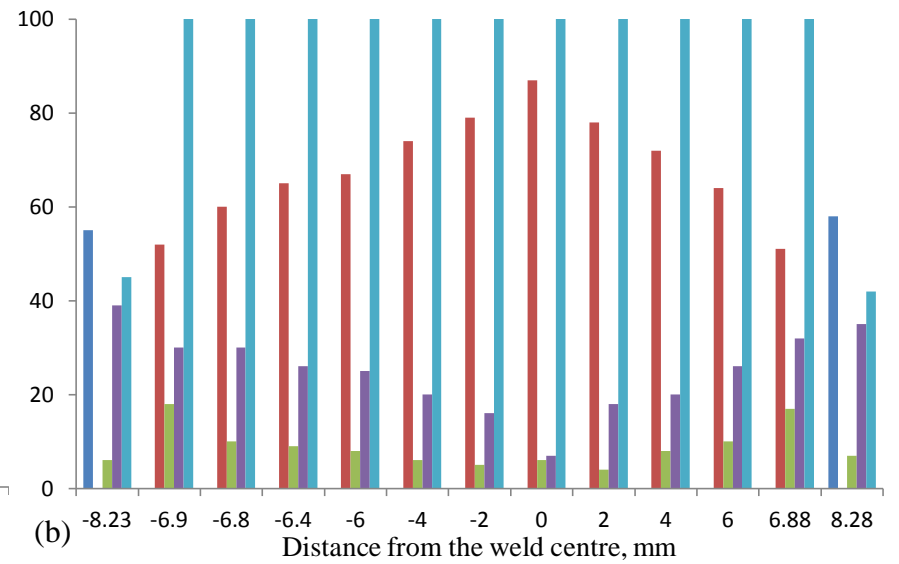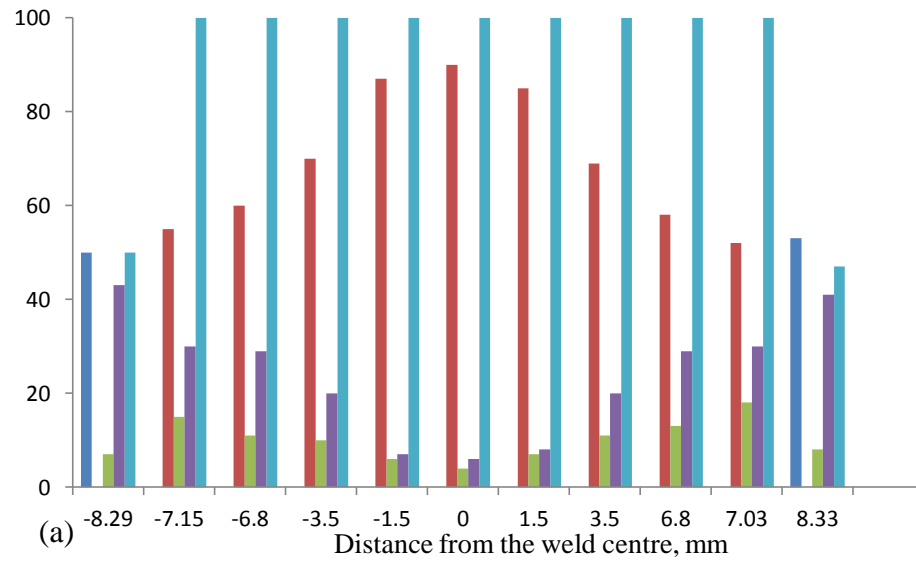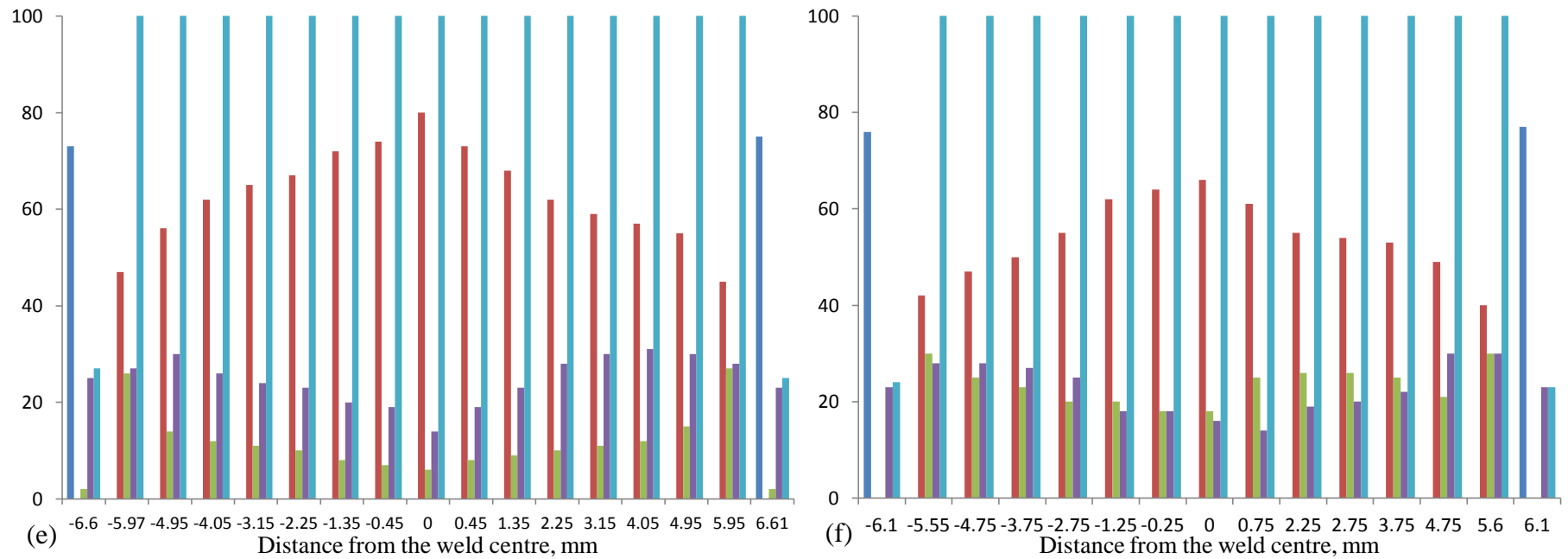
Figure 5.82 Percentage of different morphologies of the α phase along the central horizontal lines from the AS to the RS in the weld zones (HAZ, TMAZ and SZ) of (a) W4 (b) W5 (c) W6 (d) W19 (e) W20 and (f) W21,

■Primary α ■Basketweave α+Widmanstätten α ■GBα ■Colony α ■Transformed β phase
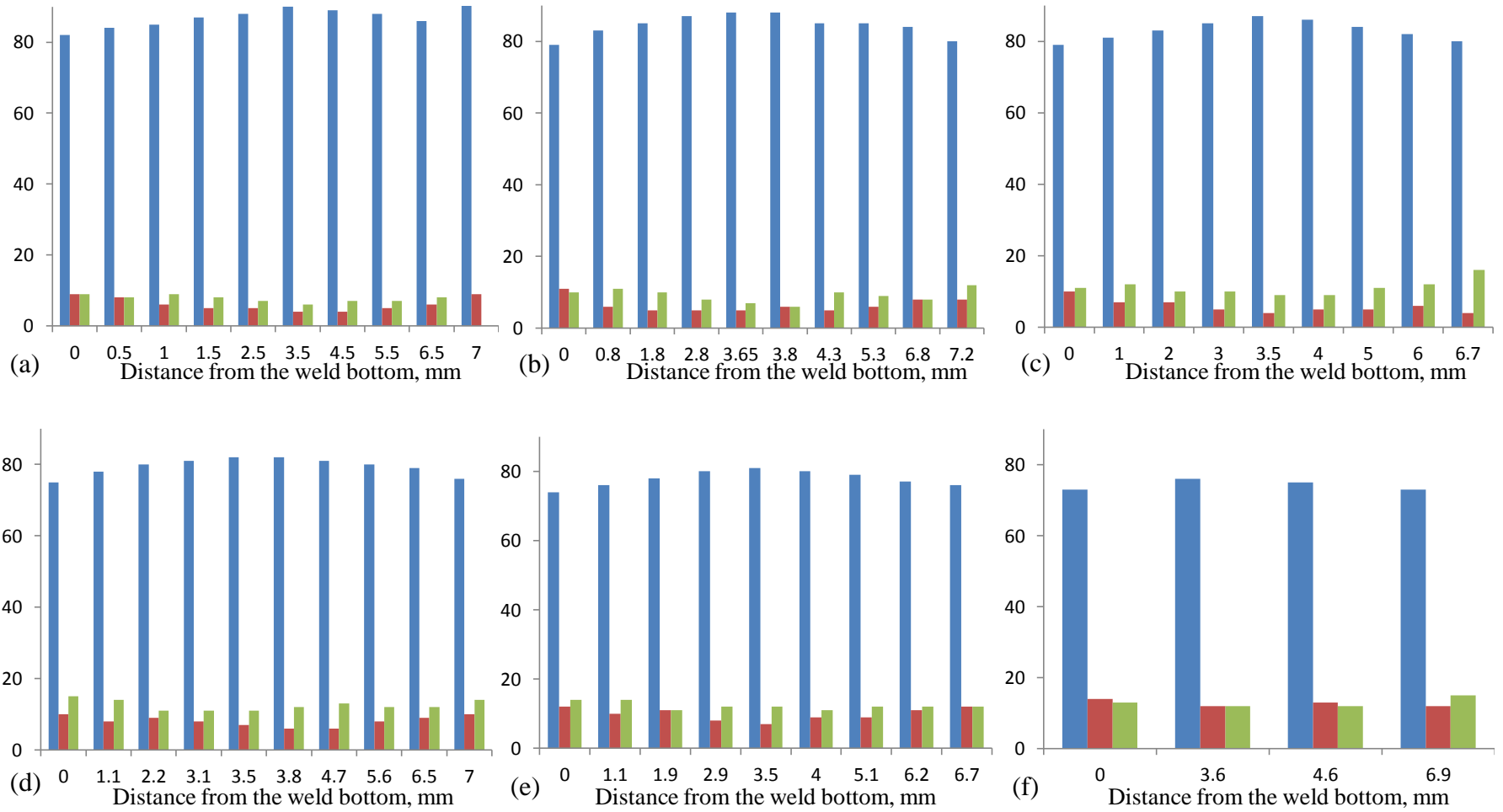
Figure 5.83 Percentage of different morphologies of the α phase along the central vertical lines in the SZ of (a) W4 (b) W5 (c) W6 (d) W19 (e) W20 and (f) W21,

The average thickness of the α laths in the weld centre as a function of heat input for all the six welds is shown in Figure 5.84 with vertical error bars and best fit curve. It is clearly seen that the average thickness of the α laths decreases significantly with increasing heat input from 1.1 to 1.5kJ/mm and there is a slight decrease in the average thickness of the α laths when heat input increases from 1.5 to 3.3kJ/mm indicating that cooling rate in the weld centre increases significantly with increasing rotation speed and increased slightly with decreasing traverse speed. Figure 5.85(a) and (b) shows the average thickness of the α laths in the weld centre as a function of traverse speed and rotation speed with vertical error bars and fit curves, respectively. The results demonstrates that firstly, the fit curve y=0.37/ln(x) (y= average thickness of the α laths, in μm and x= heat input, in kJ/mm) can be used to describe the relationship between the thickness of the α laths and the cooling rate in this work. Gil et al. (2001) investigated the thickness of the α laths as a function of cooling rate in Ti-6Al-4V, as shown in Figure 5.86 at temperature of 1050°C, 1100°C, 1150°C and 1200°C and heat treatment times of 5, 10, 15, 20, 30, 60 and 120min, respectively, indicating that the α laths become thinner with increasing cooling rate. Because the prior β grain size in the work of Gil et al. (2001) is much larger than the present study, thus we would expect to see a much wider lamellar size for them compared to us for the same cooling rate due to less nucleation sites in the prior β grains, e.g, for the α laths of 5μm, cooling rate is approximately 1°C/s in Figure 5.86, whilst, the required cooling rate for the α laths of 5μm in this work would be much smaller than 1°C/s, and this would suggest that the influence of cooling rate on the thickness of the α laths in this work has the same trend as that reported by Gil et al. (2001);  Figure 5.85(a) and (b) in conjunction with the results of the α laths thickness measurement in 5.2.8 both demonstrate that not much variation in the thickness of the α laths was observed along the central vertical line of the SZs for the three welds W4, W5 and W6 with varying traverse speeds (Table 5.3, Table 5.4 and Table 5.5), whilst, the thickness of the α laths increased significantly with decreasing rotation speed in the three welds W19, W20 and W21 with varying rotation speeds, thus, the rotation speed has much stronger effect on the thickness of the α laths compared to the traverse speed although heat input has increased greatly as traverse speed increases, which shows agreement with Attallah and Salem (1999) for an aluminium alloy who found that grain size in the SZ is largely affected by the tool rotation speed, whilst the traverse speed did not show a significant effect on the grain size.
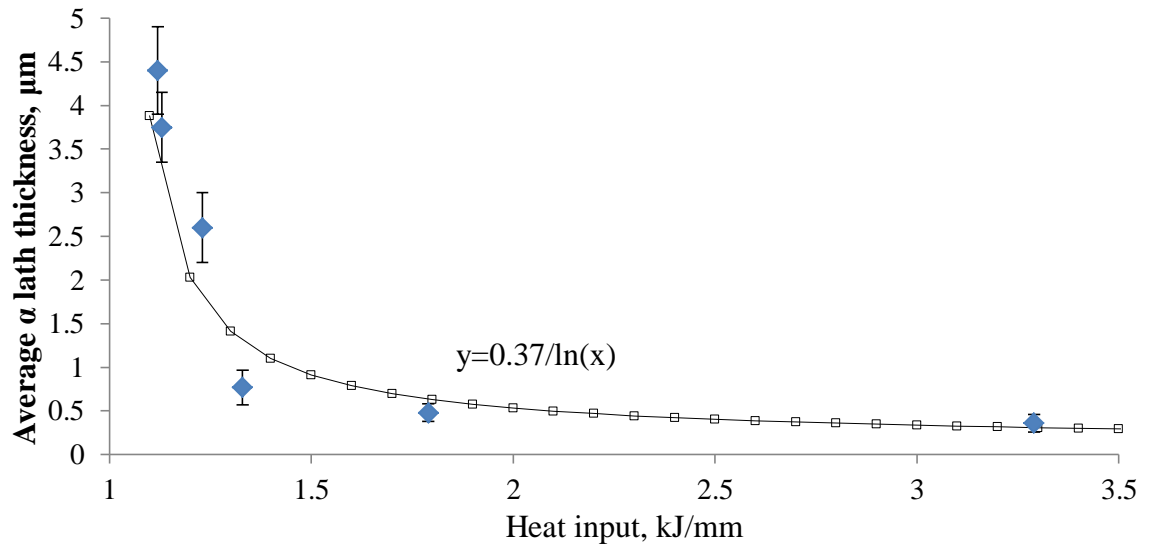
Figure 5.84 Average thickness of the α laths in the weld centre plotted against heat input for all the six welds W4, W5, W6, W19, W20 and W21
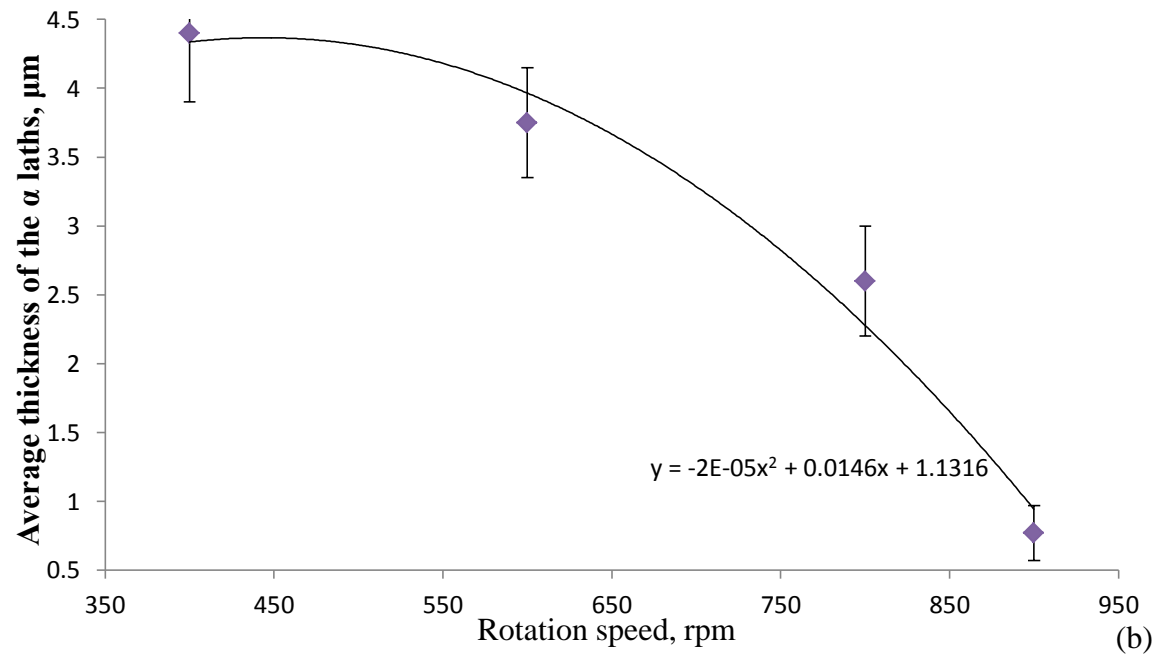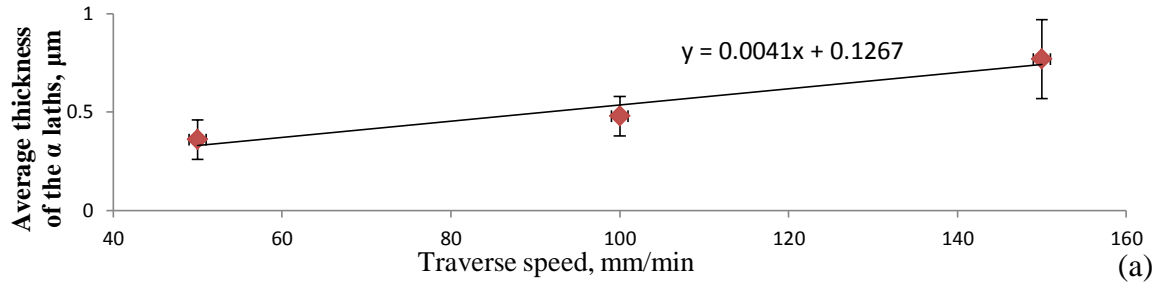


Figure 5.85 Average thickness of the α laths in the weld centre plotted against (a) traverse speed with a constant rotation speed and (b) rotation speed with a constant traverse speed
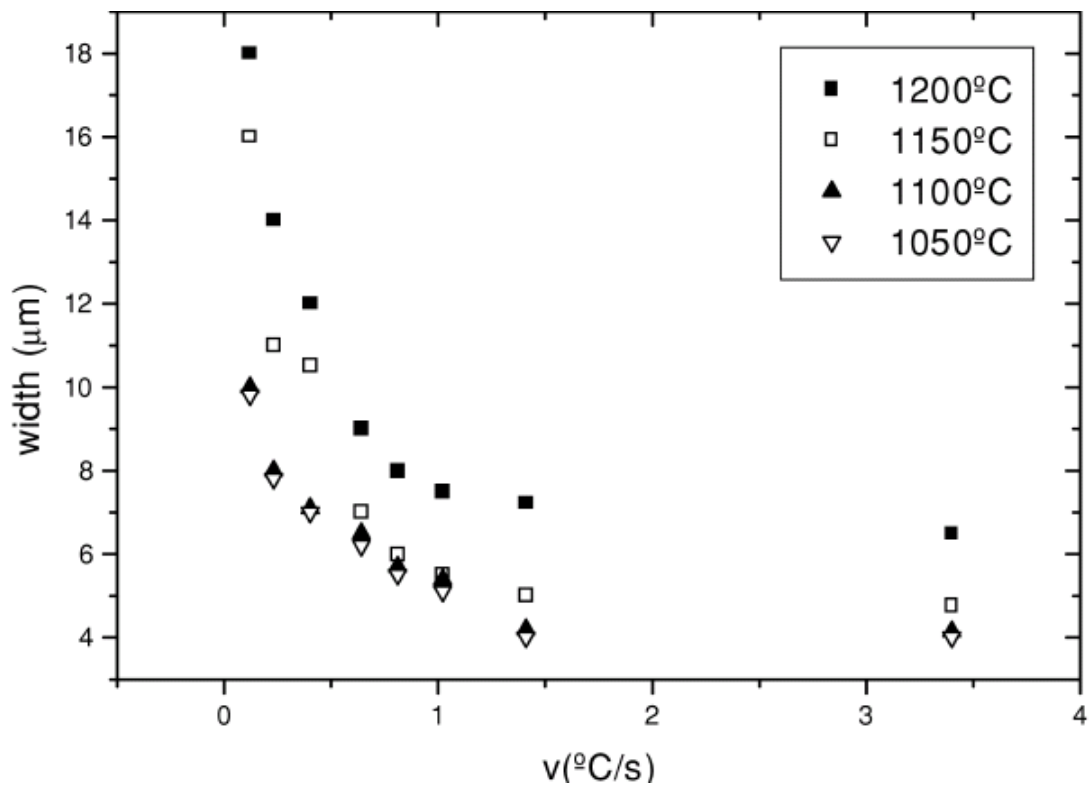
Figure 5.86 Width of α-Widmanstätten plates in relation to the cooling rate (Gil et al., 2001)

**5.5 Tool wear, microstructure and microhardness**

Tool wear were found at the weld surface and weld bottom (centre) in both the cross section, the normal sections and the side sections at the AS of the weld W4 (as shown from Figure 5.63 to Figure 5.71); W5 contains a small amount of tool wear at the AS of the weld surface (Figure 5.72), which was observed in the cross section W5B5 only, and the region contaminated by tool wear was sized 2.1mm by 0.6mm (Figure 5.71); The top surface of the weld W6 along the centre vertical line has shown evidence of tool wear (Figure 5.72). However, tool wear was not found at the AS of the weld surface of W6, while a region sized 1.6mm by 0.8mm was believed to be caused by tool wear at the AS of the weld surface of W19 (Figure 5.73), however, tool wear were not observed in the two welds W20 and W21.

Misorientation angle distribution of Type 1 structure (W-Re containing region) (Figure 5.77(d) in the normal section 4.8.c from the weld bottom of W4 demonstrates that W-Re containing region structure partially obeys the burgers relation indicating that it might be resulted from the severe deformation of the SZ which leads to the breaking of the burgers

190

relation, as seen in the misorientation angle distribution histogram of Type 1 structure (Figure 5.77(d)). In W-Re containing region, the α laths are too thin to be indexed or reconstructed at large step size of 2μm, that is why the W-Re containing region in Type 1 structure are seen as blank region in the reconstructed map when 2μm step size was used (Figure 5.77(e)), whilst, those regions can be fully reconstructed when 0.5μm step size was used (results are not shown here). A more detailed X-EDS elemental analysis of the W-Re containing region reassures that a small amount of W and Re have appeared in the region of Type 1 structure while Type 2 structure regions contain no W or Re (Figure 5.77). This would again suggest that the tool probe material W and Re have infiltrated into the weld bottom of W4 and changed the transformation kinetics of this area, which resulted in grain refinement.

It has been previously shown that the tool material W and Re have infiltrated into all the four welds W4, W5, W6 and W19. As tool material, W-Re has much higher hardness compared to the BM, thus tool wear may be related with the higher hardness observed in all the welds in terms of cross sections, side sections and normal sections in Section 4.4. Recall the microhardness profiles of W4A4, 4.2.a, 4.3.a and 4.8.a (Figure 4.14(a), Figure 4.14(c), Figure 4.14(d) and Figure 4.14(f)) in Section 4.4.1 in conjunction with the corresponding X-EDS analysis of the weld surface and weld bottom of the cross section W4B4 in Section 5.3.3 showed that the weld surface and weld bottom with higher hardness could be the W-Re containing area. The tool wear results in a higher hardness layer of 1.4mm deep and 0.3mm wide at the AS of the weld surface of W5, as shown in W5B5 and 5.6.b (Figure 4.14(a) and Figure 4.14(f)). A FSW study of Ti-6Al-4V by Zhang et al. (2008b) also reported that tool wear occurring as PCBN debris and Ti borides resulted in higher hardness in the fine lamellar structure on the top surface of the SZ.

Recall the interweaved regions of higher hardness and lower hardness observed on the surface of 4.2.a corresponding to the "ring structure" associated with the tool rotation in the photograph of the weld surface of W4 that the interweaved regions may be caused by W-Re infiltration, which was proved by X-EDS spectrum analysis of the "ring structure" in the cross section W4B4. X-EDS elemental maps of the "ring structure" in the centre of the normal section 4.8.b have shown that material in the "ring structure" contains interweaved regions of W-Re containing region and non W-Re containing region (Figure 4.14(c)). It was previously shown that the non W-Re containing region has a classic lamellar structure

consisting of GBα, colony α, basketweave α and Widmanstätten α, which is similar to the fine lamellar structure in the SZ of all the six welds. And the W-Re containing region contains a martensite like ultra-fine lamellar structure appearing as light contrast with substantially finer α laths compared to the classic fine lamellar structure. In W-Re containing region of the weld bottom of W4, as Figure 5.71(a) shows, the thickness of the α laths is between 0.17μm and 0.27μm and thickness of GBα is 0.57μm; while the thickness of the α laths is between 0.45μm, 1.13μm and 1.36μm in the non W-Re containing region (Figure 5.71(b)). This would suggest that W-Re has infiltrated into the four welds W4, W5, W5 and W19 in the form of solution resulting in changing of the transformation behaviour, whereupon martensite like structure is formed at normally the same cooling rate as the region next to it does not have dissolved W-Re region which formed lamellar structure.

## 5.6 Summary

In this chapter the effect of traverse speed and rotation speed on the microstructure of the weld zones have been investigated and the influence of tool wear on microstructure and hardness were also studied. The results showed a variation of lamellar structure with varying welding parameters, from the weld surface to the weld bottom of the SZ and from the AS to the RS of the SZ. The main findings from this chapter were summarised in the following two charts in Figure 5.87.
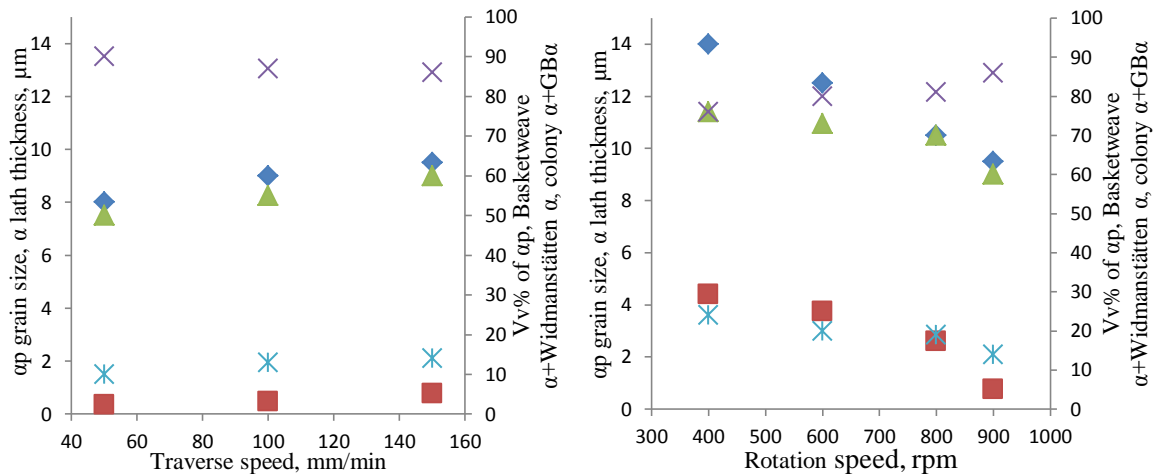


Figure 5.87 A summary of the main findings from Chapter 5:
◆ αp grain size, μm ■ α lath thickness, μm ▲ Vv% of αp phase ✕ % of basketweave α+Widmanstätten α ✳ % of colony α and GBα

**Chapter 6 Crystallographic texture evolution of the SSFSW weld zones**

**6.1 Introduction**

This chapter presents work that was carried out to investigate crystallographic texture evolution in the SSFSWs of Ti-6Al-4V specimens in terms of cross sections and normal sections with varying weld parameters using EBSD. A method was developed to define the TMAZ and the HAZ, and misorientation analysis shows the evolution and movement of the HAGBs and the LAGBs in the weld zones. Finally, variant selection which has occurred in the SZs were investigated and manual measurements were also carried out to determine the αp grain size in the BM, prior β grain size in the SZ and volume fraction of retained β phase and transformed β phase in the weld zones.

**6.2 Crystallographic texture**

6.2.1 Base material texture

As demonstrated in the previous section, the BM was an as received as rolled Ti-6Al-4V which has an equiaxed structure consisting of αp and a small amount of β phase located at the αp grain boundaries and it has clearly experienced a peak temperature well below the $T_\beta$. EBSD was performed on the BM and some of the HAZ adjacent to the BM of the cross sectional sample using a 2μm step size and 200 magnifications with α phase indexed only. Figure 6.1(a) is an inverse pole figure colouring (IPF) map taken from part of the BM showing that the equiaxed structure in the BM was composed of macrozones lying in the ND/TD plane. IPF colour key is shown in Figure 6.1(c), where the basal planes are represented by the red component and the blue component represents the prismatic planes. Figure 6.1(b) is a macrozone map of the corresponding cross section which shows accumulated regions of red pixels and blue pixels. Macrozones are the regions of aligned grains with similar crystallographic orientations and macrozone colouring maps were obtained by using an in-house software. Colour key for macrozone maps is seen in Figure 6.1(d) which is plotted as colour intensity against the percentage of neighbours which have disorientation less than 15° to the central pixel in one defined grid and the default number of neighbours is 100. In the present study, macrozones are determined as the region having disorientations less than 15° between the central pixel and their neighbouring orientations in the case of the number of the neighbouring orientations is more than 50. The pixels inside

193

the macrozones disorientated less than 15º from more than 60 neighbouring orientations were coloured from green to red depending on the percentage of neighbours. Figure 6.1(e) shows the {0001} pole figure of the room temperature α texture in the BM. Figure 6.2(a) shows a high resolution IPF map enclosed by the black rectangular box in (a) using smaller step size. Figure 6.2(b) is the corresponding grain boundary misorientation map, where misorientations between 2° and 15° are coloured silver and pixels with misorientations greater than 15° are coloured black. Thus, misorientation of 15º was used to separate the low angle grain boundaries (LAGBs) from the high angle grain boundaries (HAGBs). High resolution grain boundary misorientation maps from the blue component and the red component are shown in Figure 6.2(c) and (d), respectively.

According to the IPF colour key in Figure 6.1(c), macrozones are oriented along the basal planes (the red component) and prismatic planes (the blue component) in Figure 6.1(a). Figure 6.1(a) shows that the as-rolled BM is characterised by large elongated macrozones, and majority of the αp grains within the macrozones (Figure 6.1(c)) were oriented along the basal planes {0001} as red component and prismatic planes {$10\bar{1}0$} as blue component. Macrozones can deteriorate the mechanical properties of metals especially the fatigue performance, e.g., macrozones were reported to initiate fatigue cracks along the αp grains which are oriented along the basal planes and prismatic planes in Ti-6Al-4V and Ti-6246, respectively (Biavant et al., 2002; Szczepanski et al., 2008). Texture of the BM is shown in Figure 6.1(e), which is displayed in terms of basal planes {0001}, prismatic planes {$10\bar{1}0$} and the pyramidal planes {$11\bar{2}0$}. In unit of multiples of uniform density (MUD) represents the strength of the clustering of poles, thus, MUD is used to represent the texture strength. It is clearly seen that the BM texture exhibits a classic rolled structure which shows good agreement with the rolling texture reported in the literature (Leyens and Peters, 2003; Schwartz et al., 2000). It was observed in the {0001} pole figure (Figure 6.1(e)) that the αp texture of the BM developed from rolling had one part of the basal poles aligned with the WD (RD) and another part of the basal poles aligned with the TD. The pole intensity of the basal poles at the TD is twice higher than that at the WD (RD), which means the number of the basal poles at the TD is almost twice larger than the number of the basal poles at the WD. This is possibly because the αp grains are elongated along the TD. It was observed that the texture type is a transverse texture (T-texture) developed from the rolling temperature at 960ºC (Peters et al., 1984).

(a)
=2000 µm; IPF hcp; Step=2 µm; Grid2354x1598

Figure6.2 (a)



(b)
=2000 µm; IPF hcp; Step=2 µm; Grid2354x1598

WD
TD
ND

195
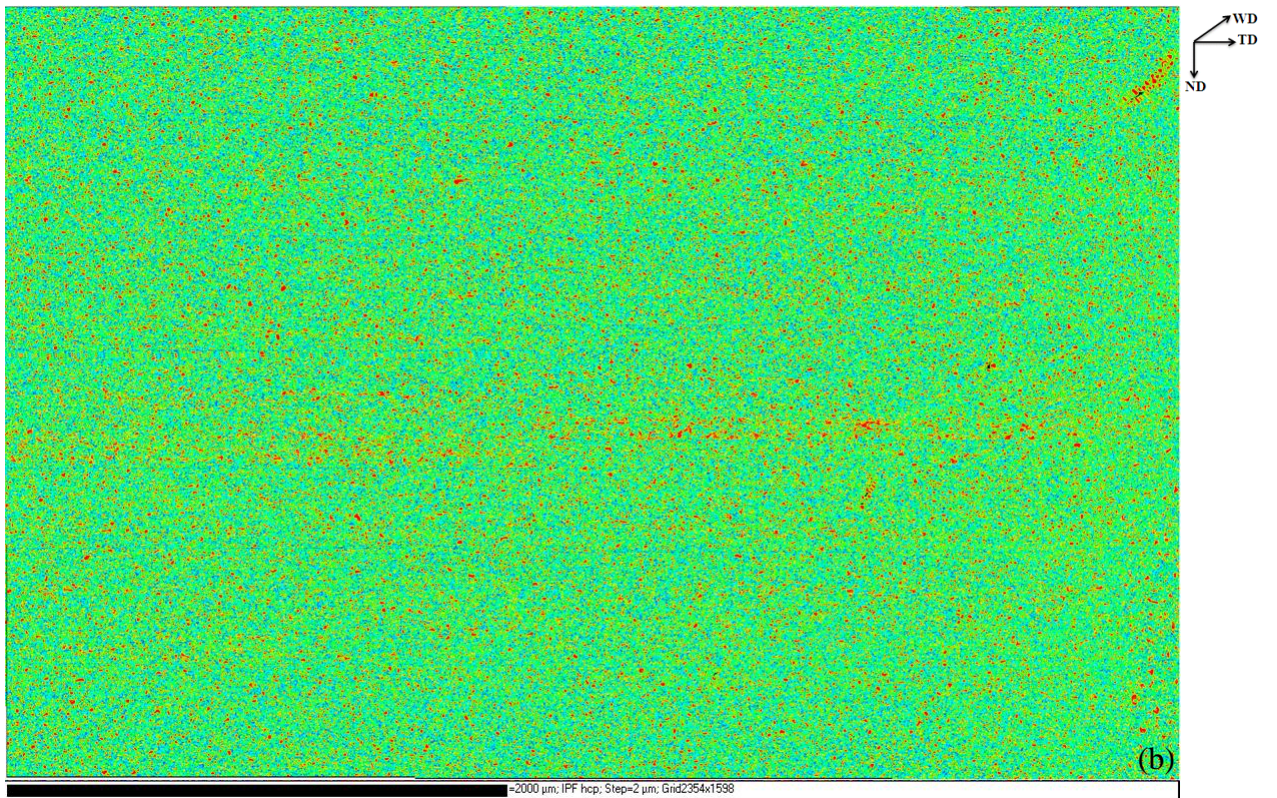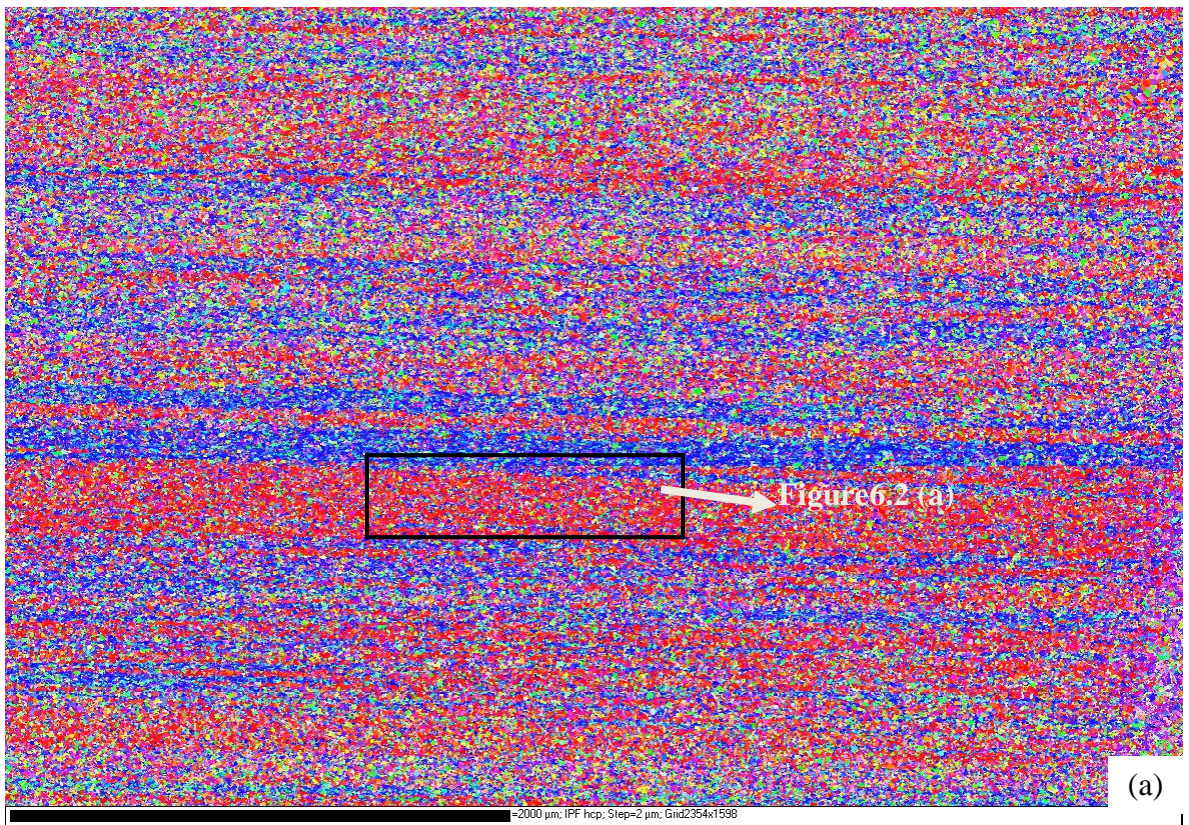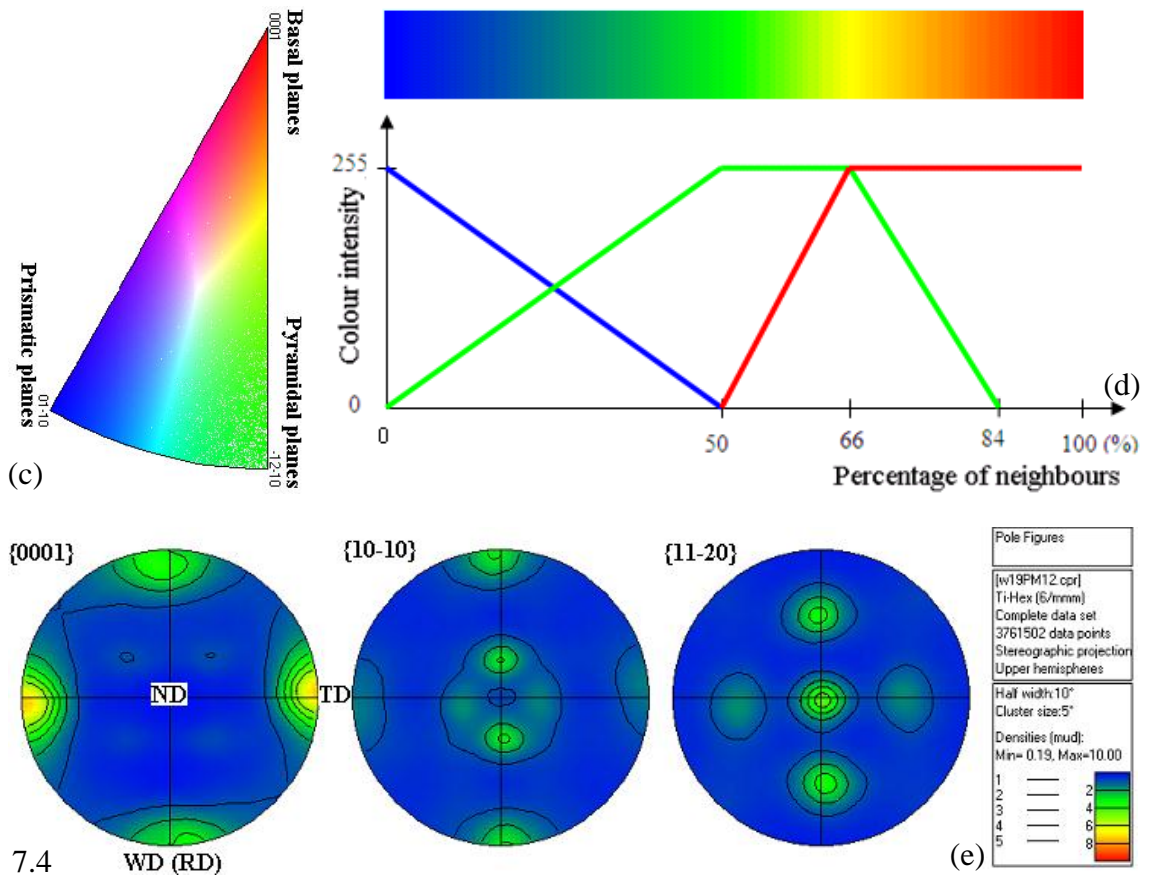
Figure 6.1 BM texture from a cross section with low resolution EBSD maps: (a) IPF map sized 5000×3176μm$^2$ and the welding axes ND, TD and WD is shown on the right, (b) macrozone map (c) IPF colour key, (d) colour key of the macrozone maps, (e) {0001}, {10$\bar{1}$0} and {11$\bar{2}$0} pole figures

196

=500 μm; GB015; Step=1 μm; Grid1248x388
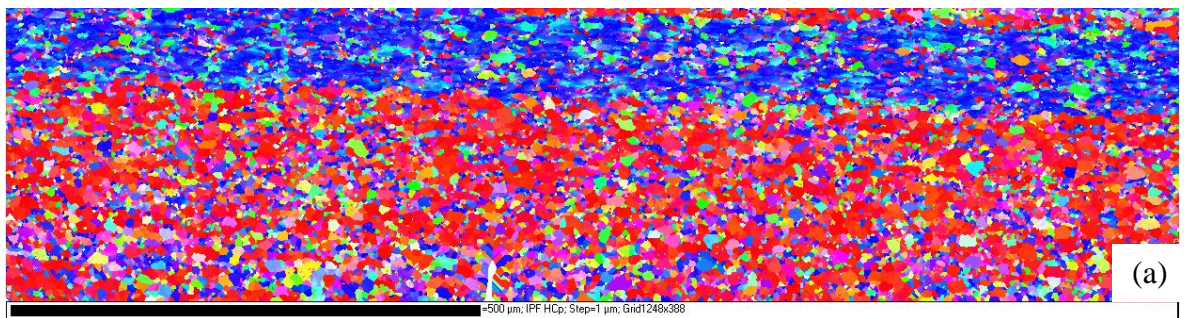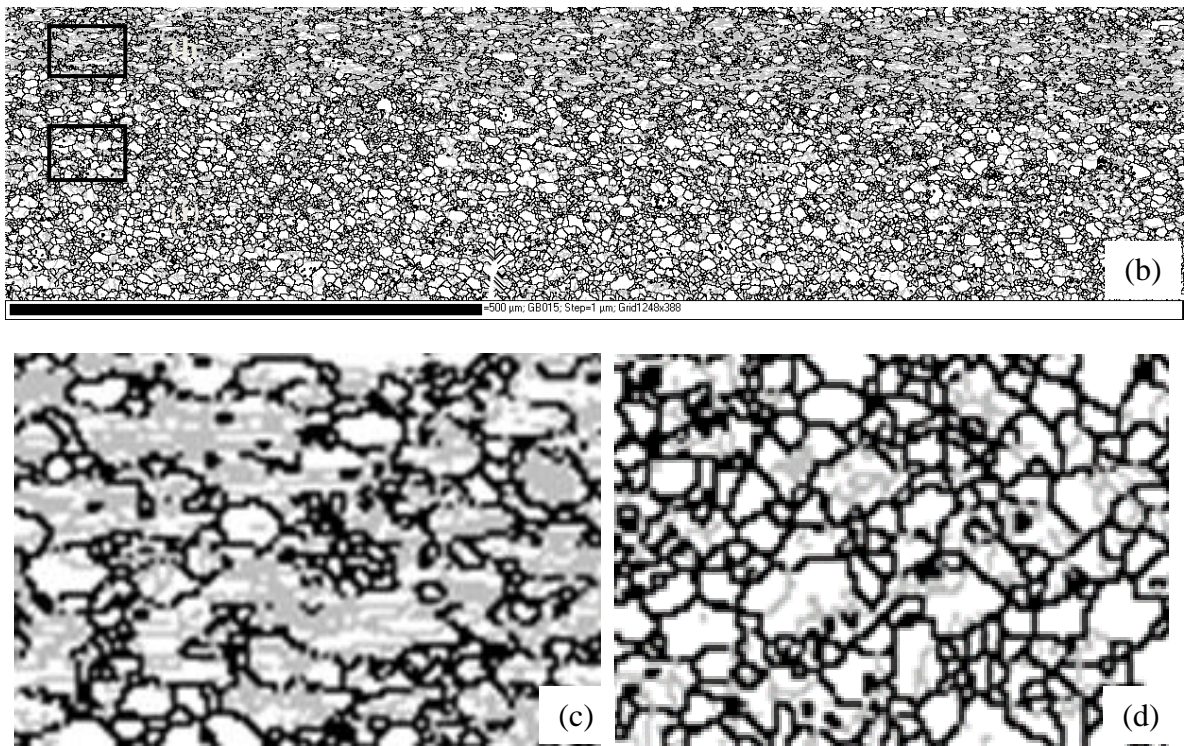
Figure 6.2 (a) IPF map enclosed by the black rectangular box in Figure 6.1(a), (b) grain boundary misorientation map, where LAGBs (2º-15º) and HAGBs (15º-94.5º) are depicted as silver and black lines, respectively; high resolution grain boundary misorientation map from (c) the blue component and (d) the red component

High resolution orientation imaging maps (OIM) of the texture in the BM obtained from a side section using a 0.5μm step size are displayed in Figure 6.3. And the welding axes, IPF colour key, PF colour key are shown at the bottom of the figures. Figure 6.3(a) is an IPF map and macrozone colouring map of this region is shown in Figure 6.3(b). Region A (red component) and region B (blue component) were indicated as black rectangular boxes in (a). $\{0001\}$, $\{10\bar{1}0\}$ and $\{11\bar{2}0\}$ pole figures for the IPF maps of the whole part, region A and region B are shown in Figure 6.3(c), (d) and (e), respectively. Moreover, high resolution OIM resembling the red region A in Figure 6.2 were obtained from a cross section using a 0.2μm step size, and the results are shown in Figure 6.4(a-c) as EBSD maps. And Figure 6.4(d) displays the $\{0001\}$, $\{10\bar{1}0\}$ and $\{11\bar{2}0\}$ pole figures of the α phase.

197

(a)



(b)



{0001}   {10-10}   {11-20}

(c)
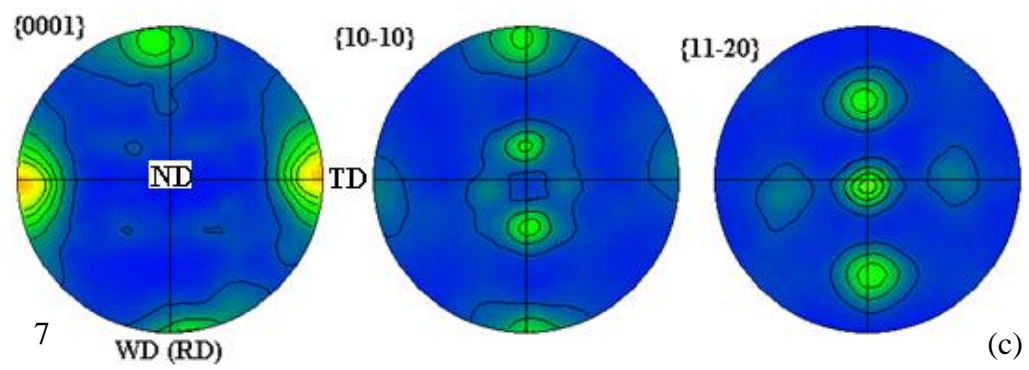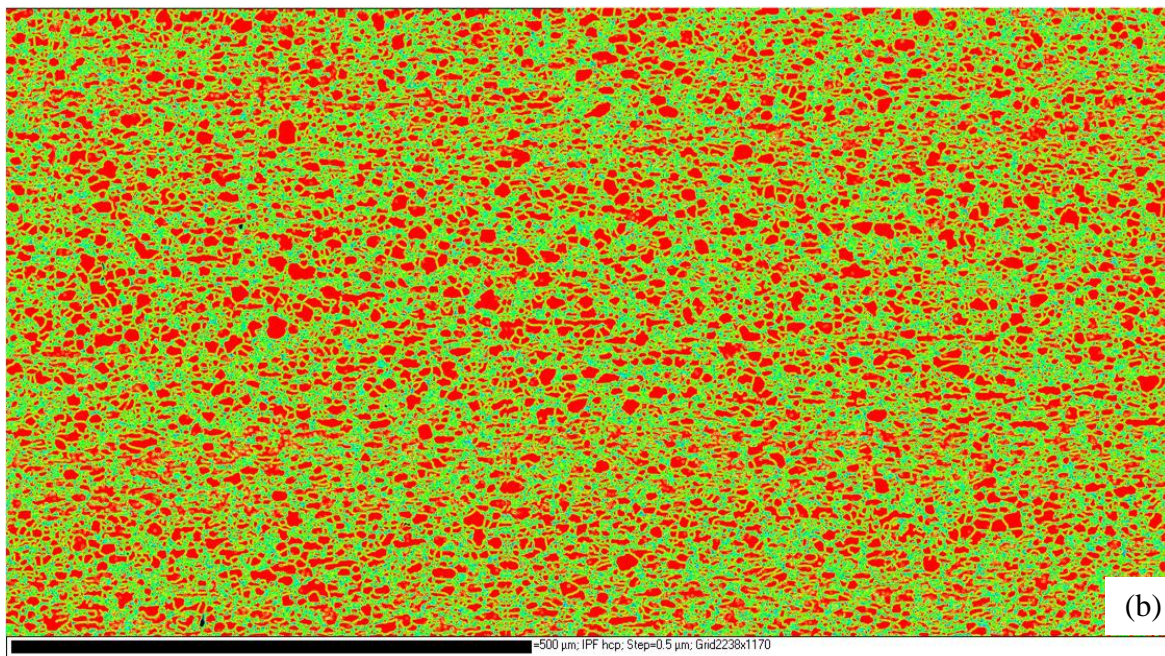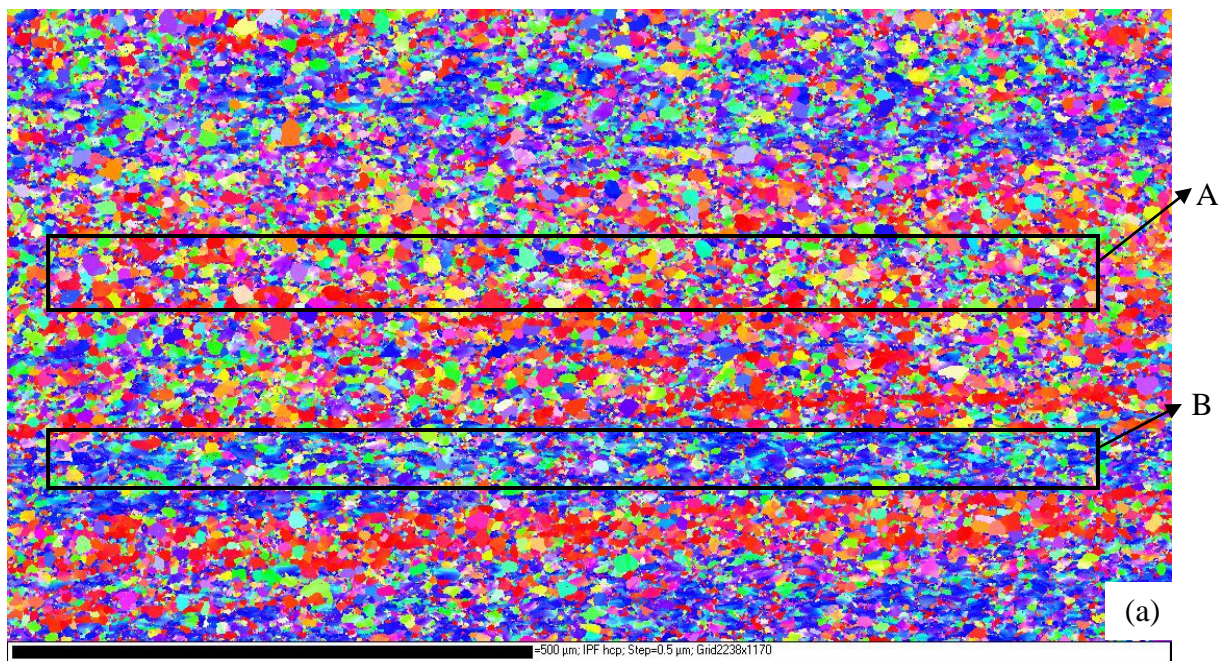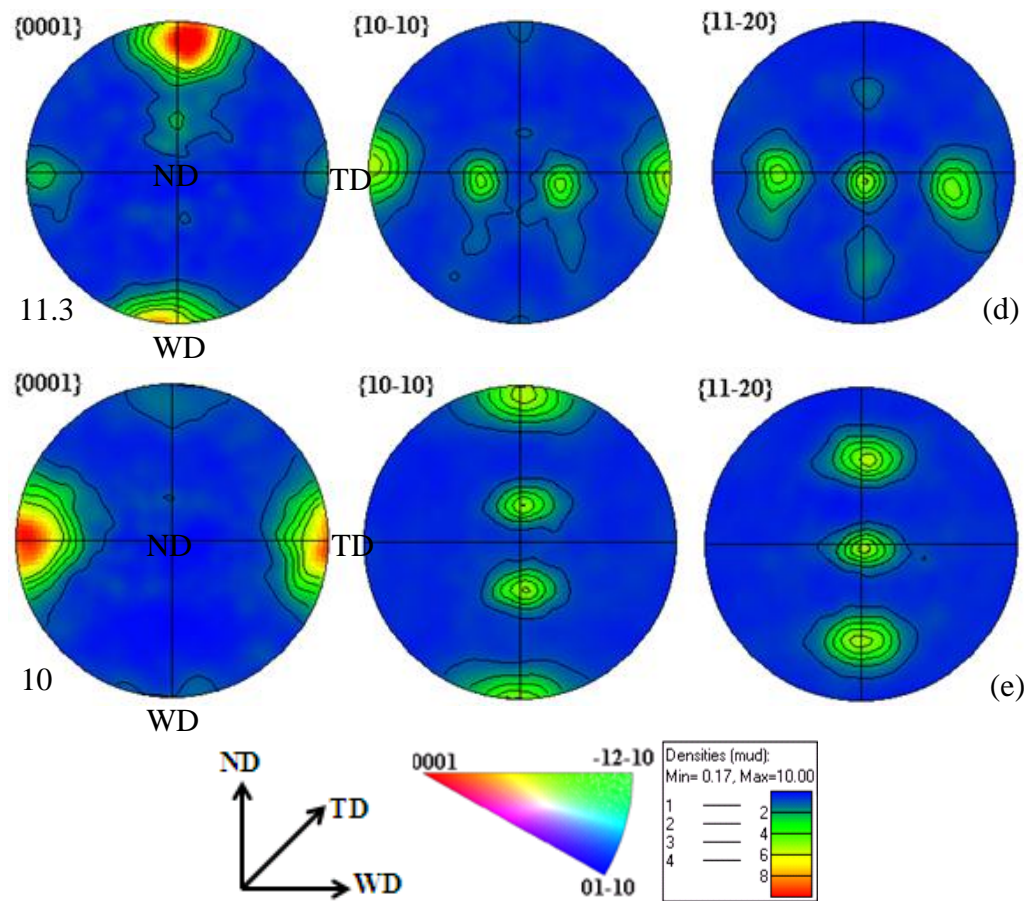
Figure 6.3 Representation of the BM texture from the side section at the AS using a 0.5µm step size: (a) IPF map; (b) macrozone map; {0001}, {10$\bar{1}$0} and {11$\bar{2}$0} pole figures of the α phase of (c) the whole part; (d) red rectangular region A; (e) blue rectangular region B
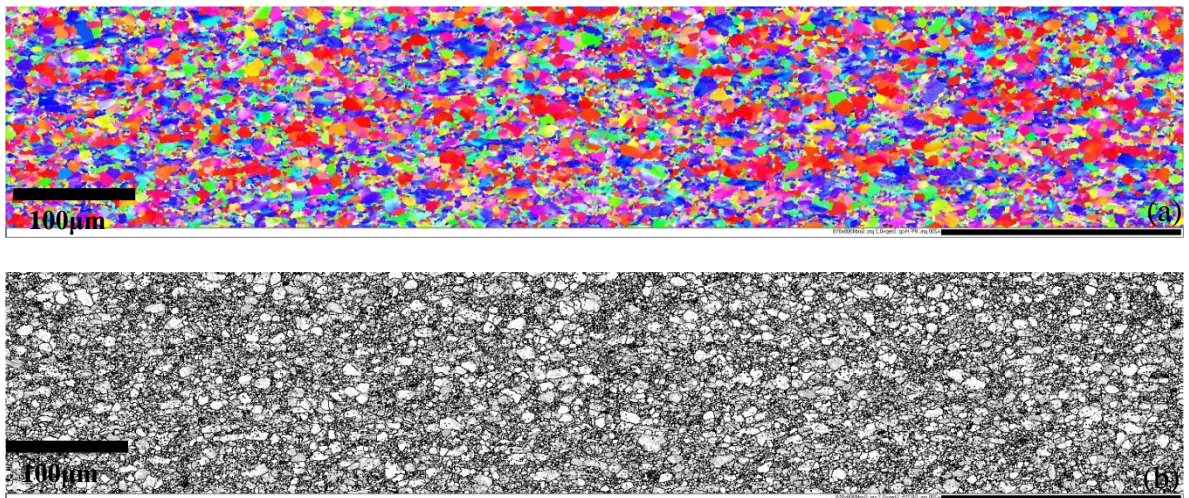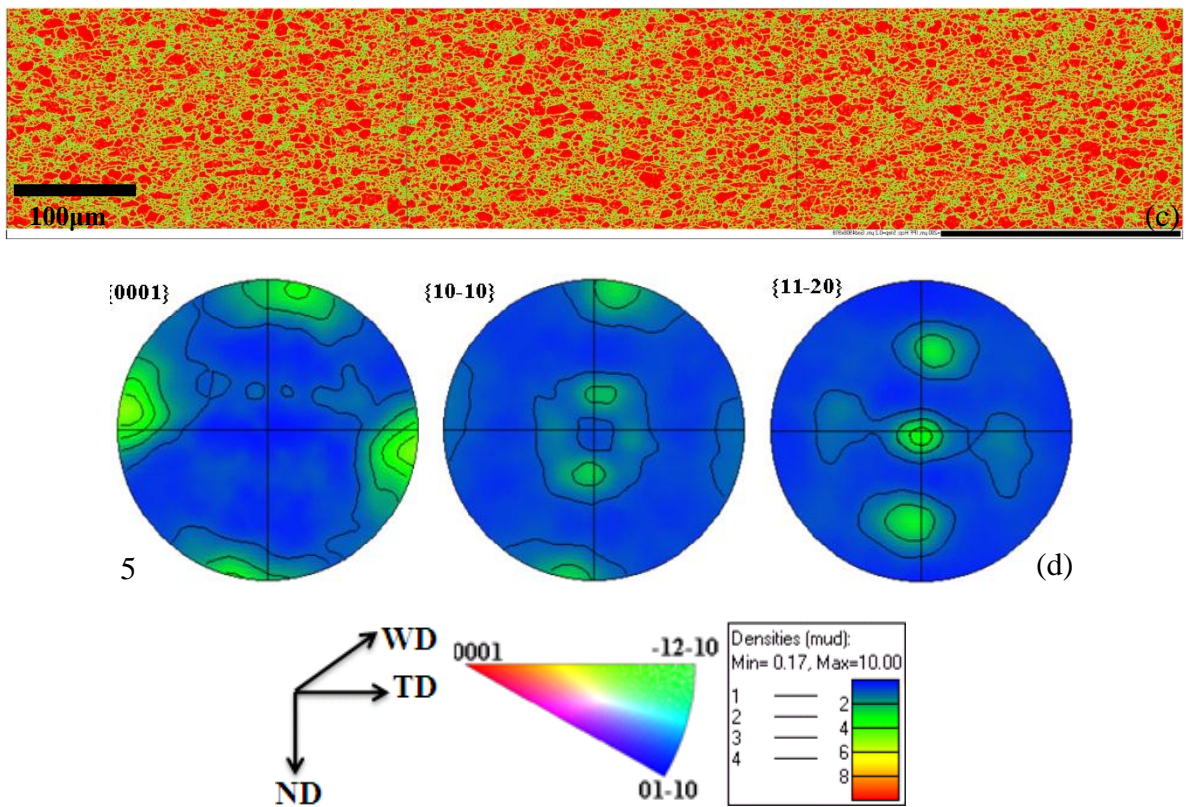
Figure 6.4 High resolution OIM resembling the red region A in Figure 6.2 from a cross section using a 0.2µm step size: (a) IPF map; (b) macrozone map; (c) macrozone colouring map; (d) map of deviation from the average; (e) {0001}, {10$\bar{1}$0} and {11$\bar{2}$0} pole figures of the α phase

In comparison of low resolution OIM in Figure 6.1 and high resolution OIM map in Figure 6.3 and Figure 6.4, a larger amount of grains less than 1µm were indexed using smaller step sizes of 0.5µm and 0.2µm, however, indexing is not possible using a 2µm step size. It can be seen that in high resolution orientation maps using 1µm step size, most of the pixels were indexed as red component of similar orientations (Figure 6.3(a)). It was observed that in both low and high resolution OIM (Figure 6.3 and Figure 6.4), there are a small amount of basal poles with low density appeared close to the ND and they may be produced during thermal process in the BM due to increased amount of plastic strain accommodated by αp phase (Salem 2000). It is clearly seen in Figure 6.4(a) that the IPF map is composed of several macrozones elongated along the WD (RD), and those macrozones consist of red components of approximately 60% and blue component of 40%, which were enclosed in the two rectangular regions, corresponding to A (red rectangular region) and B (blue rectangular region). Figure 6.3(d) and Figure 6.3(e) show that {0001}

poles in region A (red rectangular region) are mostly orientated at the WD (RD) with density of 11.3MUD while in Region B (blue rectangular region), {0001} poles are mostly orientated at the TD with density of 10MUD. Grain boundary misorientation maps of the blue component and the red component in Figure 6.2(c) and (d) show that the blue component (region B) has a large amount of LAGBs compared to the red component (region A), as clearly seen in low resolution grain boundary misorientation maps of the two components A and B in Figure 6.2(b), which meant that the blue component contains a much larger number of subgrains compared to the red component, resulting in higher texture strength at the TD in {0001} PF, as shown in Figure 6.1(e).

6.2.2 Texture representation of the weld zones

Crystallographic texture in FSWs of Ti-6Al-4V has been reported to follow the simple shear texture by many researchers (Mironov et al., 2008; Knipling and Fonda, 2009; Fonda and Knipling, 2010; Zhang et al., 2008a; Davies et al., 2011) and the simple texture observed in the titanium FSWs shows agreement with the shear texture developed from torsion tests or extrusion tests (Montheillet et al., 1984; Baczynski and Jonas, 1996 and Li et al., 2005), and it is to follow the simple shear deformation of bcc materials. Zhang et al. (2010) reported that the similar shear texture development during FSW of pure titanium is due to shear deformation by the tool shoulder. As aforementioned in Section 2.6.5, the six typical bcc shear texture components are D1 $(11\bar{2})[111]$, D2 $(\bar{1}\bar{1}2)[111]$, E $(01\bar{1})[111]$, $\bar{E}$ $(0\bar{1}1)[111]$, J $(0\bar{1}1)[211]$, $\bar{J}$ $(1\bar{1}0)[112]$ and F $(110)[001]$. D1 and D2 are the two most important shear texture components developed in the SZs of titanium friction stir welds.

   To best illustrate the texture developed in the weld zones, three orthogonal directions (ND, TD and WD) were arranged as the ND put in the centre of the pole figure with the TD at the right and the WD at the bottom (Biavant et al., 2002). The shear axes: the shear direction and the shear plane normal (SPN) generated by the shearing action of the probe were then closely related with the welding axes. In SSFSWs, the shear direction (SD) is tangent to the tool probe, that is to say, the SD is parallel to the transverse direction (TD) and thus the shear plane normal (SPN) perpendicular to the SD is parallel to the welding direction (WD). A drawing resembling pole figure can be obtained as shown in Figure 6.4 with superimposed D1 shear texture component, and the welding axes ND, TD and WD,

the SD and the SPN were also indicated. This pole figure is a colour key for the representation of texture. In order to rotate the current coordinate systems into the shear reference frame, most of the pole figures were rotated 270° anti-clockwise around the TD for aligning the WD with the SPN for the cross sectional samples, rotation of pole figures from EBSD data of the cross sections collected in different ways were done in a program, and the rotation of pole figures for the normal sections and the side sections can be referred to the appendix.
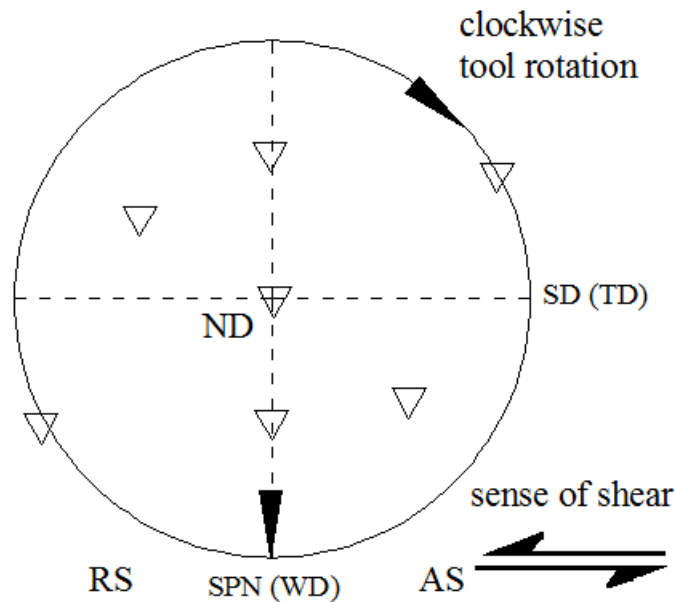


Figure 6.5 Pole figure key with superimposed ideal orientation, shear directions and the welding axes TD, ND and WD showing D1 shear texture component

*6.2.2.1 Texture of W4*

Texture analysis of the weld W4 was carried out on the cross section W4C4 and EBSD data was acquired from the whole weld zone using a 2μm step size. Due to the huge dataset, EBSD maps were acquired from the five parts, corresponding to Set 1, Set 2, Set 3, Set 4 and Set 5, as shown in Figure 6.6. In order to show how the texture in the α phase evolves across the weld zones from the RS to the AS, Figure 6.7(a and b) to Figure 6.11 (a and b) of Set 1, Set 2, Set 3, Set 4 and Set 5 show the IPF maps of the weld zones of cross section W4C4 on a horizontal line and the corresponding {0001} pole figures of the low temperature α phase at the 1-2mm intervals. In the IPF map (Figure 6.7(a)), the inverse

202

colours denote the orientations of the individual α laths, which are coloured with respect to the welding direction (WD) and similar orientations are displayed in similar colours. Similarly, for the ND at the centre of the weld, Figure 6.7(c and d) to Figure 6.11(c and d) of Set 1, Set 2, Set 3, Set 4 and Set 5 show the corresponding texture of the reconstructed high temperature β phase on a horizontal line. It should be noted that the welding axes of the map, IPF map colour key for both the α phase and β phase, and pole figure density bar are shown at the bottom of the figures. Figure 6.7 to Figure 6.11 show texture evolution from the weld bottom to the weld surface, and texture strength was reflected as pole intensity. The maximum and minimum density of the {0001} PFs and {110} PFs for all the five parts are shown in Table 6.1.

Low temperature α texture has generally higher texture strength than the reconstructed high temperature β texture when compare the pole intensity of each pole in {0001} and {110} pole figures for all the five parts. A direct comparison can be made between the basal plane texture ({0001} and {110} PFs) of both the α and β phases for all the five parts by comparing texture strength (pole intensity) from the weld bottom to the weld surface and it was observed in both the low temperature α texture and high temperature reconstructed β texture that texture strength is the highest in the weld centre (Figure 6.9) and the weld bottom (Figure 6.11) has higher texture strength than the weld surface (Table 6.1). Except for the weld surface, the AS has higher texture strength than the RS for all the other four parts.

The banded "ring structure" observed on the weld surface of W4 can be seen in the band contrast (BC) map and misorientation map in Figure 6.7a). It was shown that the prior β grains tend to align with the tangent surface of "ring structure" or distorted along the tangent surface of "ring structure". Black contrast in the band contrast (BC) map is the W-Re containing region and light contrast represents the non W-Re containing region. In the W-Re containing region with black contrast in BC map, the prior β grains tend to align with the surface of "ring structure". It is seen that W-Re containing region has higher HAGBs fraction and higher texture strength compared to the non W-Re containing region and α texture of the W-Re containing region has the highest texture strength as 11.3MUD. The blank region seen at the AS of the weld bottom (Figure 6.10(b)) without indexing was not able to be reconstructed using a 2μm step size, which was attributed to much finer grain size in this blank region compared to that in the classic lamellar structure and this blank

region was believed to be the W-Re containing region which has ultra-fine lamellar structure, as previously shown in Section 5.3.3.1, where the average thickness of the α laths in the W-Re containing region is less than 0.2μm. It can be seen that direction of the prior β grains is parallel to the direction of the banded structure from the weld centre to the welding edge at the AS of the weld surface of W4. This meant that tool probe was off-centred during SSFSW, and it wears more on one side than the other side, leading to the refined banded structure.
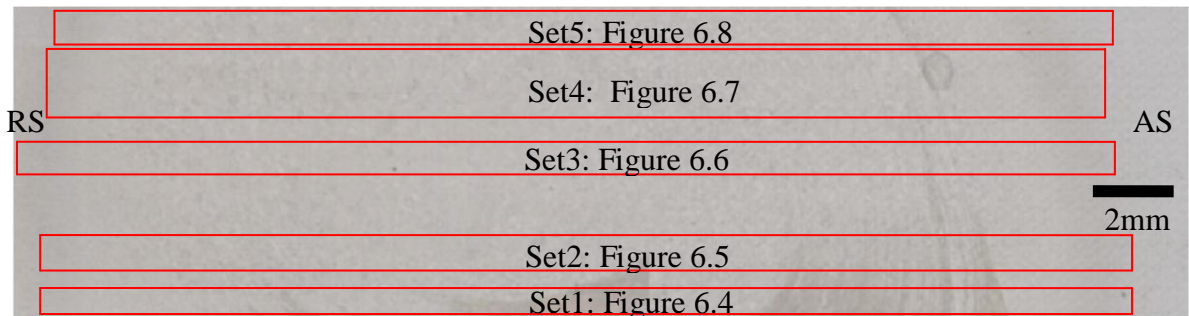


Figure 6.6 Illustration of the five sections obtained from the whole weld zone of W4C4

Table 6.1 Pole intensity of the {0001} PFs and {110} PFs for the low temperature α texture and reconstructed high temperature β texture of all the five parts of W4B4

|  |  | Set1 | Set2 | Set3 | Set4 | Set5 |
|---|---|---|---|---|---|---|
| {0001} PFs | Max. density | 11.3 | 7.8 | 11.6 | 8.2 | 9.3 |
|  | Min. density | 3.6 | 3 | 3.1 | 2.7 | 2.1 |
| {110} PFs | Max. density | 9.9 | 6.4 | 8.6 | 12.6 | 6.4 |
|  | Min. density | 3.1 | 3 | 2 | 2.8 | 2.3 |
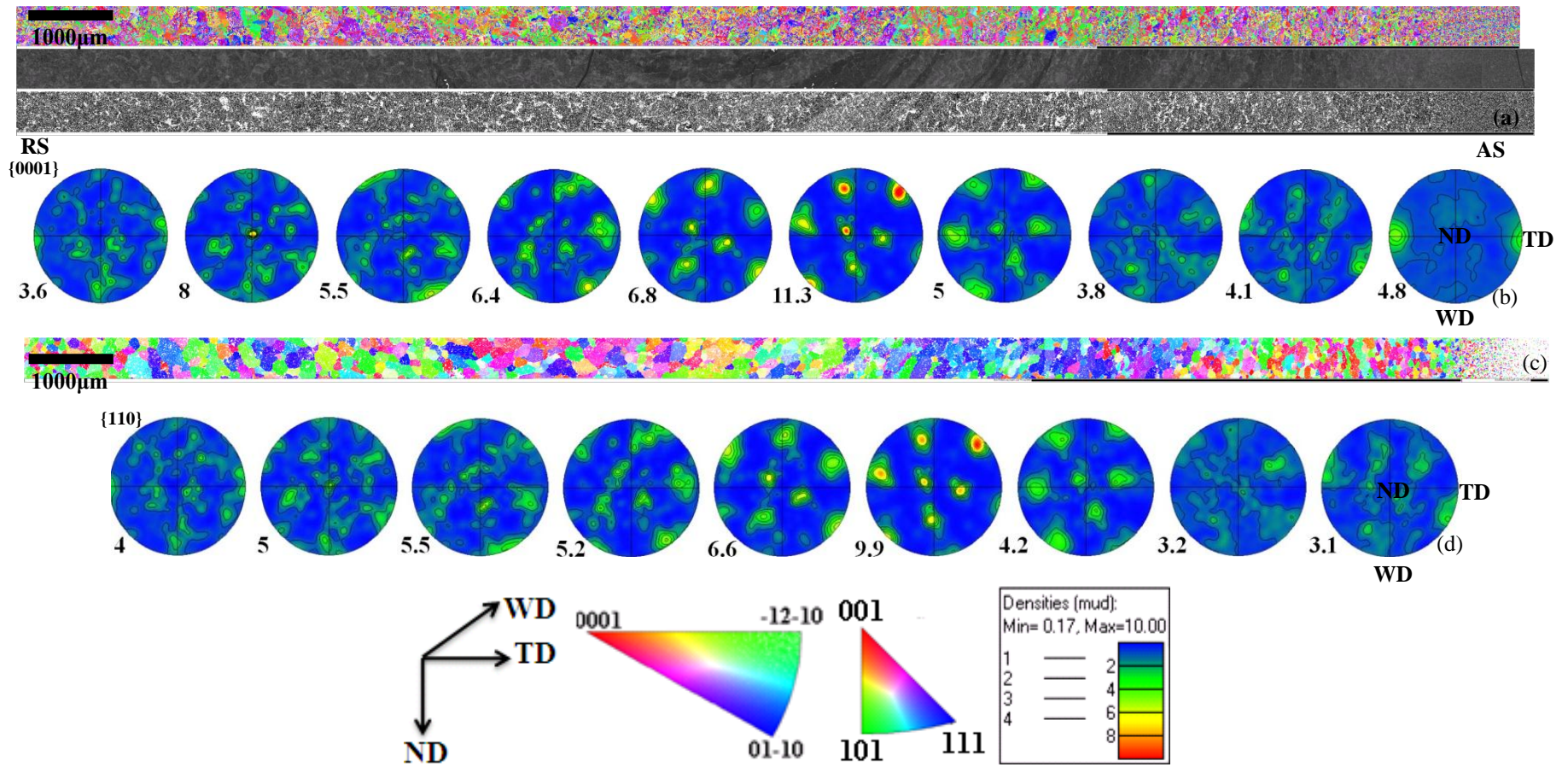
Figure 6.7 EBSD data of Set1 sized 17806μm×460μm obtained from the RS to the AS of W4: (a) IPF map, band contrast map and grain boundary misorientation map with boundaries of 2º-15º coloured silver and boundaries larger than 15º coloured black; (b) {0001} pole figures of the low temperature α phase; (c) IPF map after reconstruction; (d) {110} pole figures of the reconstructed high temperature β phase
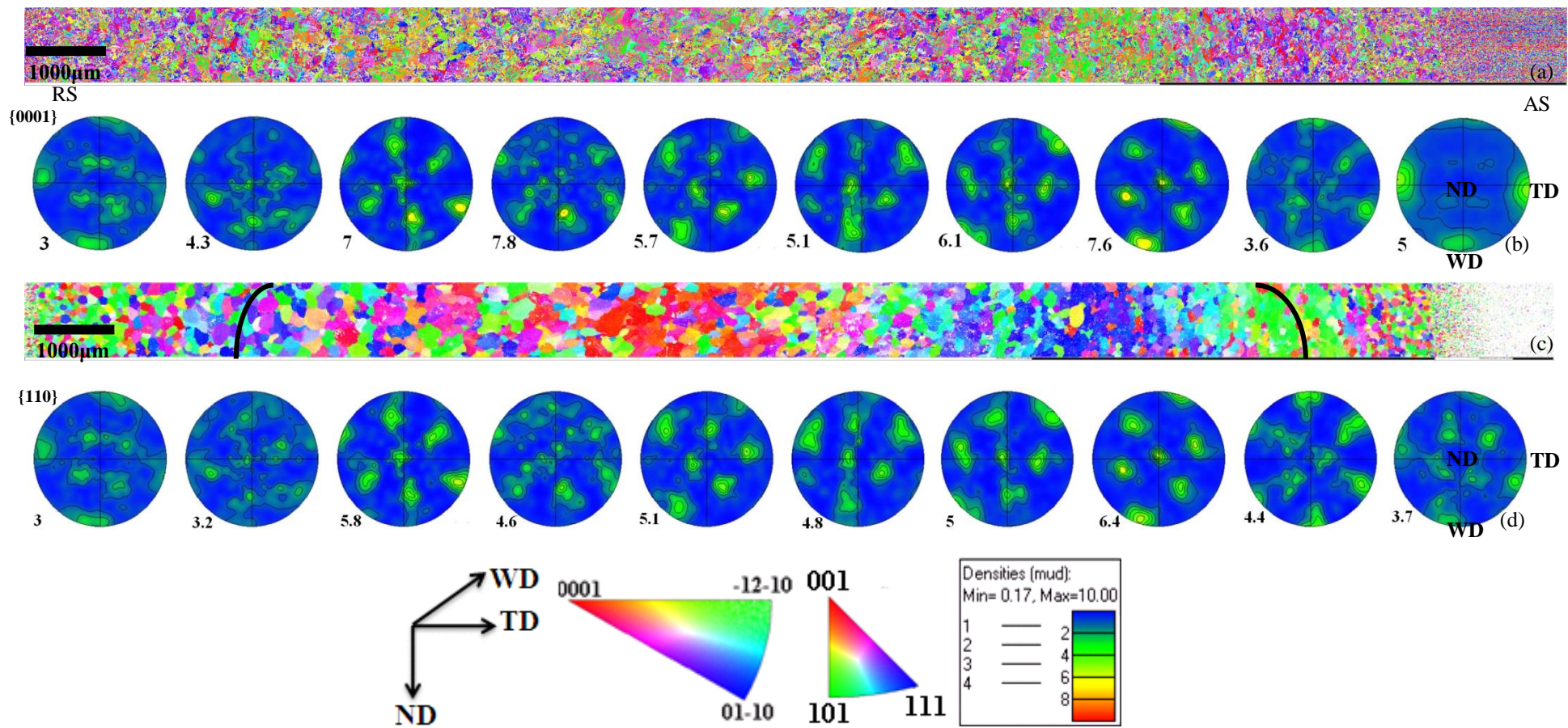
Figure 6.8 EBSD data of Set2 sized 18976μm×900μm obtained from the RS to the AS of W4: (a) IPF map and (b) {0001} pole figures of the low temperature α phase; (c) IPF map after reconstruction with superimposed black curves explained in the text; (d) {110} pole figures of the reconstructed high temperature β phase with maximum density
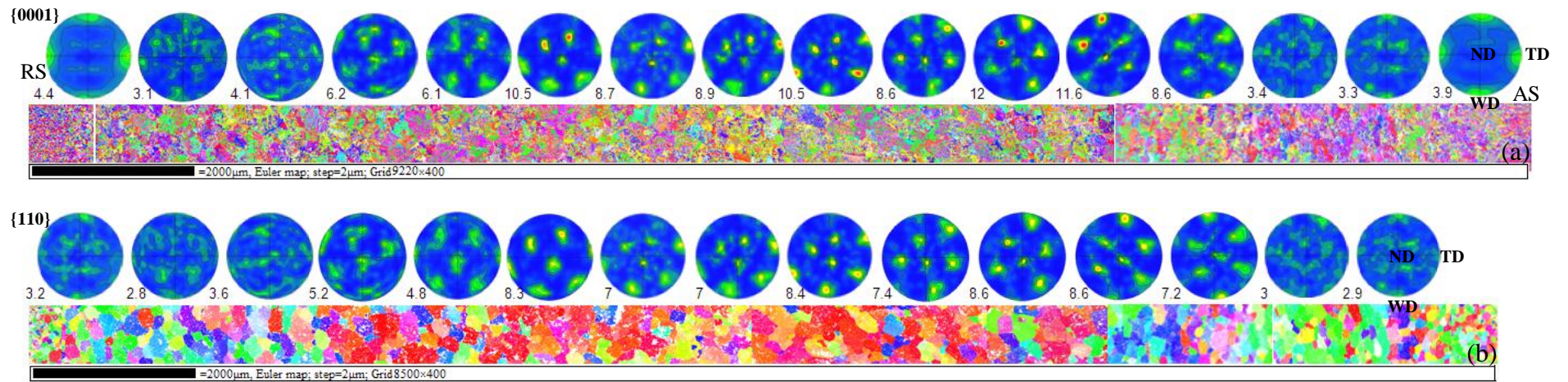
Figure 6.9 EBSD data of Set3 sized 18440μm×800μm from the RS to the AS of W4: (a) IPF maps and {0001} pole figures of the low temperature α phase with maximum density (c) IPF maps after reconstruction and {110} pole figures of the reconstructed high temperature β phase with maximum density

{0001}

4.1    4    3.1    7.9    7.1    8.2    7    4.1    5.2    2.7

ND    TD
WD

5.2    3.6    3.3    4    12.6    9.3    5.5    4.8    5.9    2.8

(b)

(a)

(c)
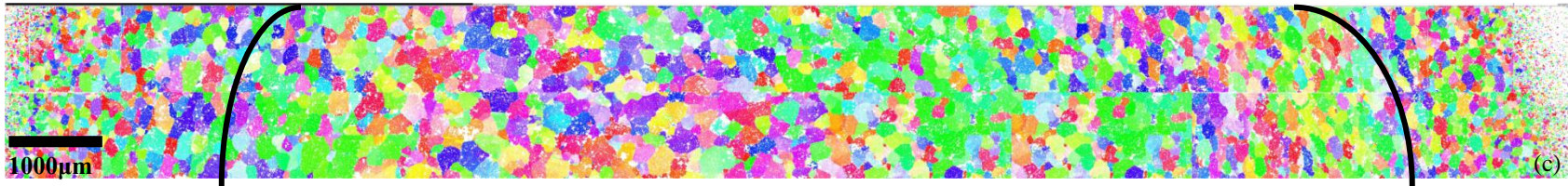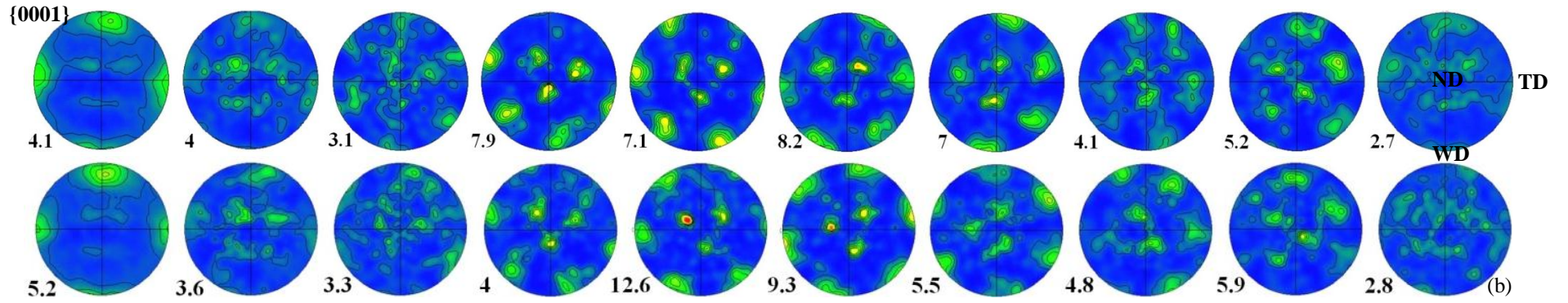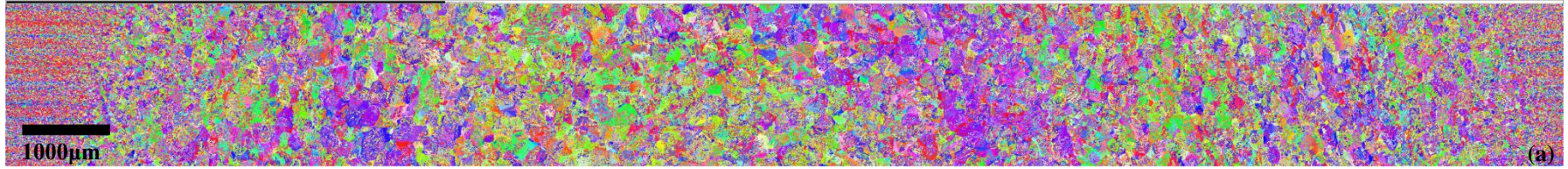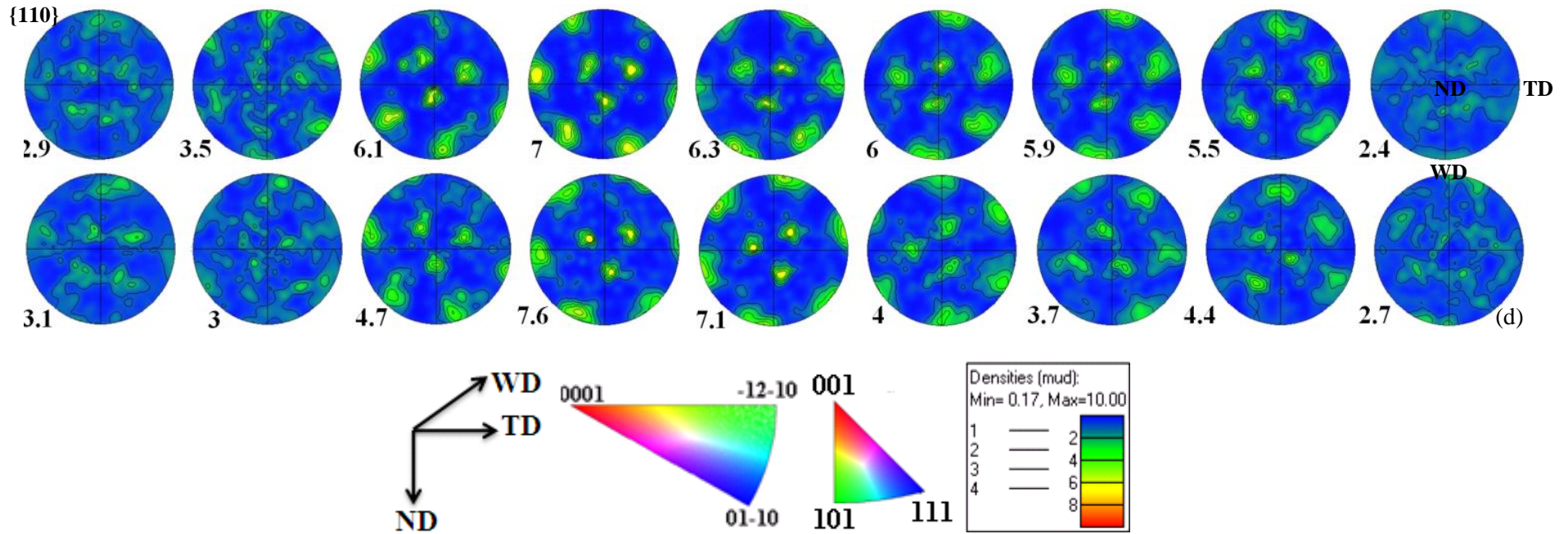
Figure 6.10 EBSD data of Set4 sized 17750μm×1840μm obtained from the RS to the AS of W4: (a) IPF map and (b) {0001} pole figures of the low temperature α phase; (c) IPF map after reconstruction with superimposed black curves explained in the text; (d) {110} pole figures of the reconstructed high temperature β phase with maximum density
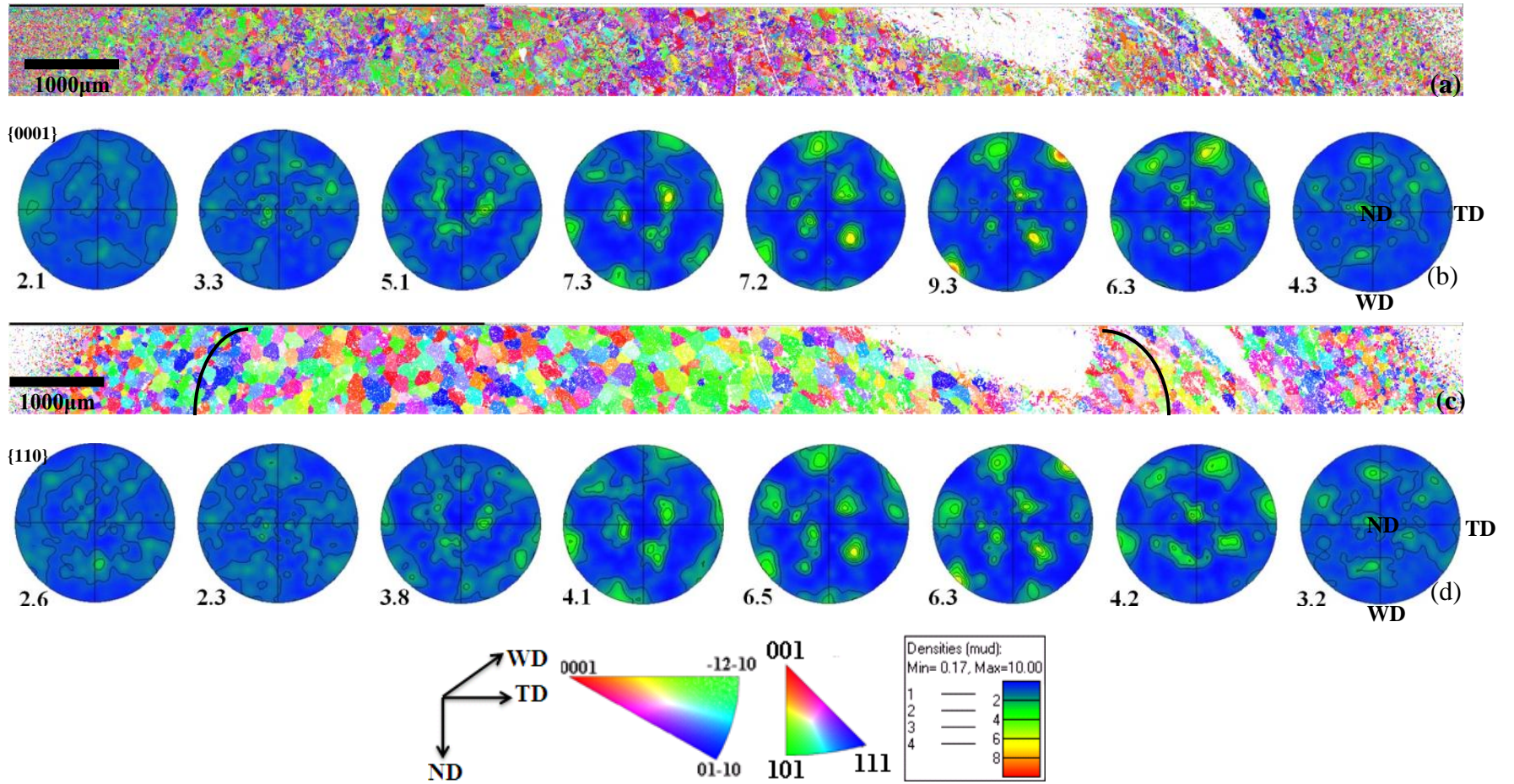
Figure 6.11 EBSD data of Set5 sized 15302μm×920μm obtained from the RS to the AS of W4: (a) IPF map and (b) {0001} pole figures of the low temperature α phase; (c) IPF map after reconstruction with superimposed black curves explained in the text; (d) {110} pole figures of the reconstructed high temperature β phase with maximum density

*6.2.2.2 Texture of W5*

Figure 6.12 indicates the EBSD data obtained from the five parts of the weld cross section W5C5, corresponding to Set1, Set 2, Set 3, Set 4 and Set 5 drawn as red rectangular. Figure 6.13(a and b) to Figure 6.17(a and b) show the IPF maps of the whole length of the weld zones at the 1-2mm intervals and the {0001} PFs of the low temperature α phase texture on a horizontal line. And Figure 6.13(c and d) and Figure 6.17(c and d) describe texture of the corresponding reconstructed high temperature β phase in terms of IPF map and {110} PFs. It should be noted that the welding axes of the map, IPF map colour key for both the α phase and β phase, and pole figure density bar are shown at the bottom of figures. The maximum and minimum density of the {0001} PFs and {110} PFs for all the five parts are shown in Table 6.2.

D1 shear texture component was observed in both the α and β texture of all the five parts (Figure 6.13(b and d), Figure 6.14(b and d), Figure 6.15(b and d), Figure 6.16(b and d), Figure 6.17(b and d)). It is also seen that the AS has higher texture strength than the RS for all the five parts. Low temperature α texture has generally higher texture strength than the reconstructed high temperature β texture when compare the pole intensity of each pole in {0001} and {110} pole figures for all the five parts and it was also observed in both low temperature α texture and high temperature reconstructed β texture that texture strength is the highest in the weld centre (Figure 6.15) and the weld bottom (Figure 6.17) has higher texture strength than the weld surface (Figure 6.12).
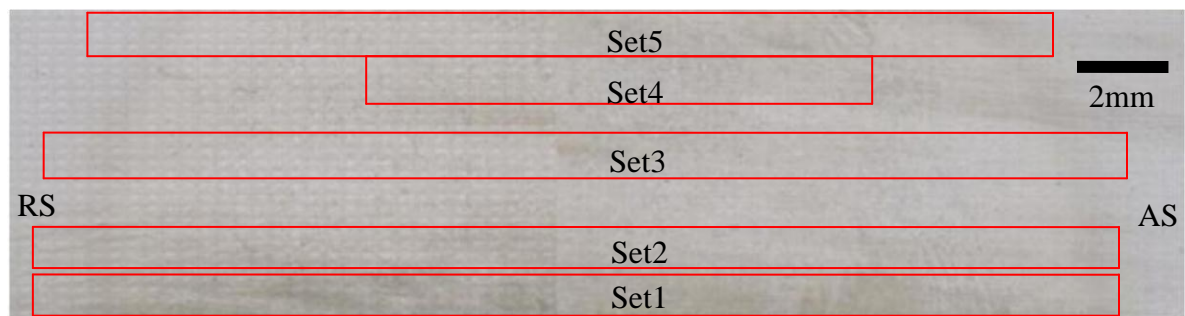


Figure 6.12 Illustration of the five sections obtained from the whole weld zone of W5
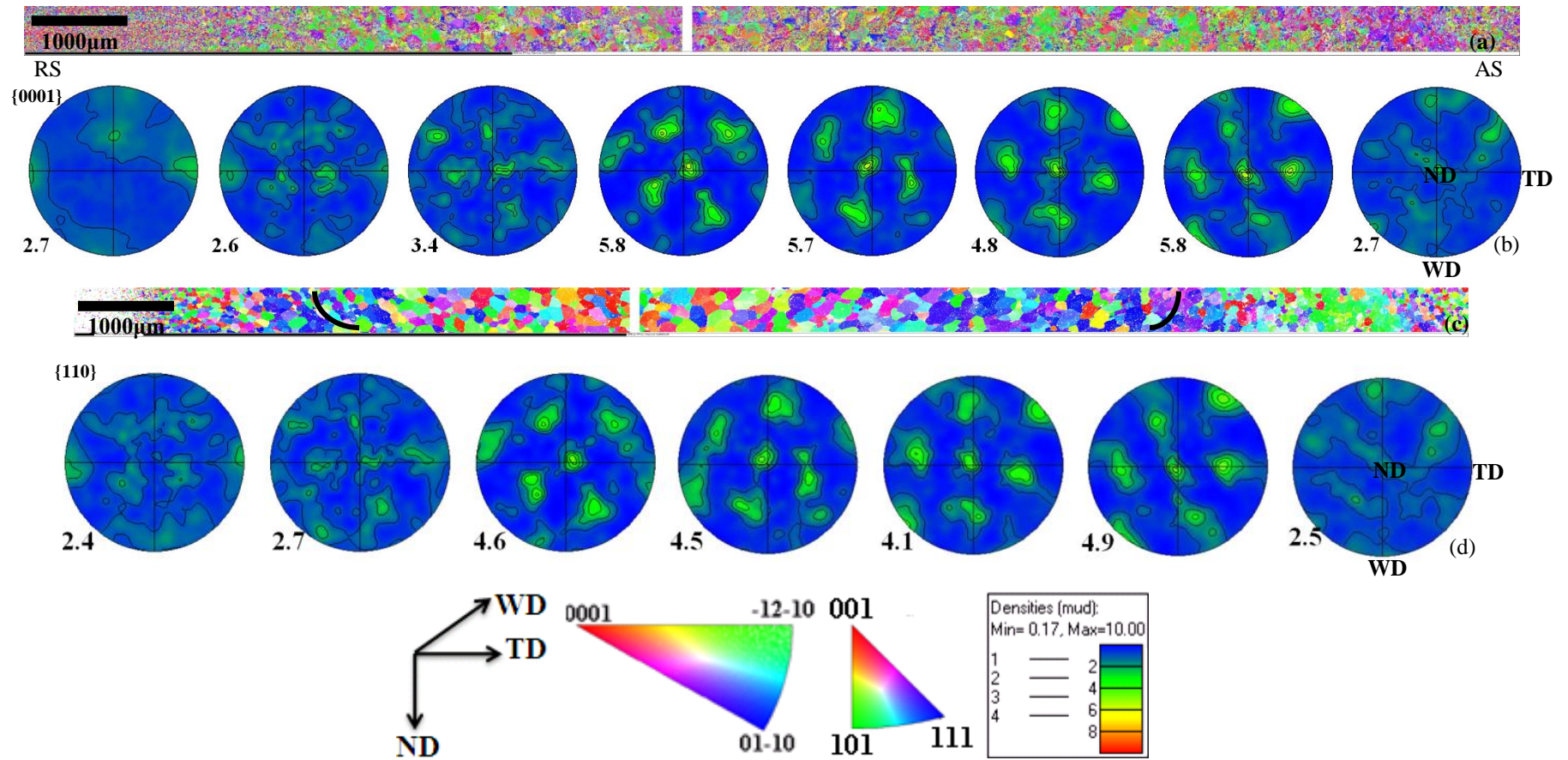
Figure 6.13 EBSD data of Set1 (very surface) sized 15348μm×460μm obtained from the RS to the AS of W5: (a) IPF map and (b) {0001} pole figures of the low temperature α phase; (c) IPF map after reconstruction with superimposed black curves explained in the text; (d) {110} pole figures of the reconstructed high temperature β phase with maximum density
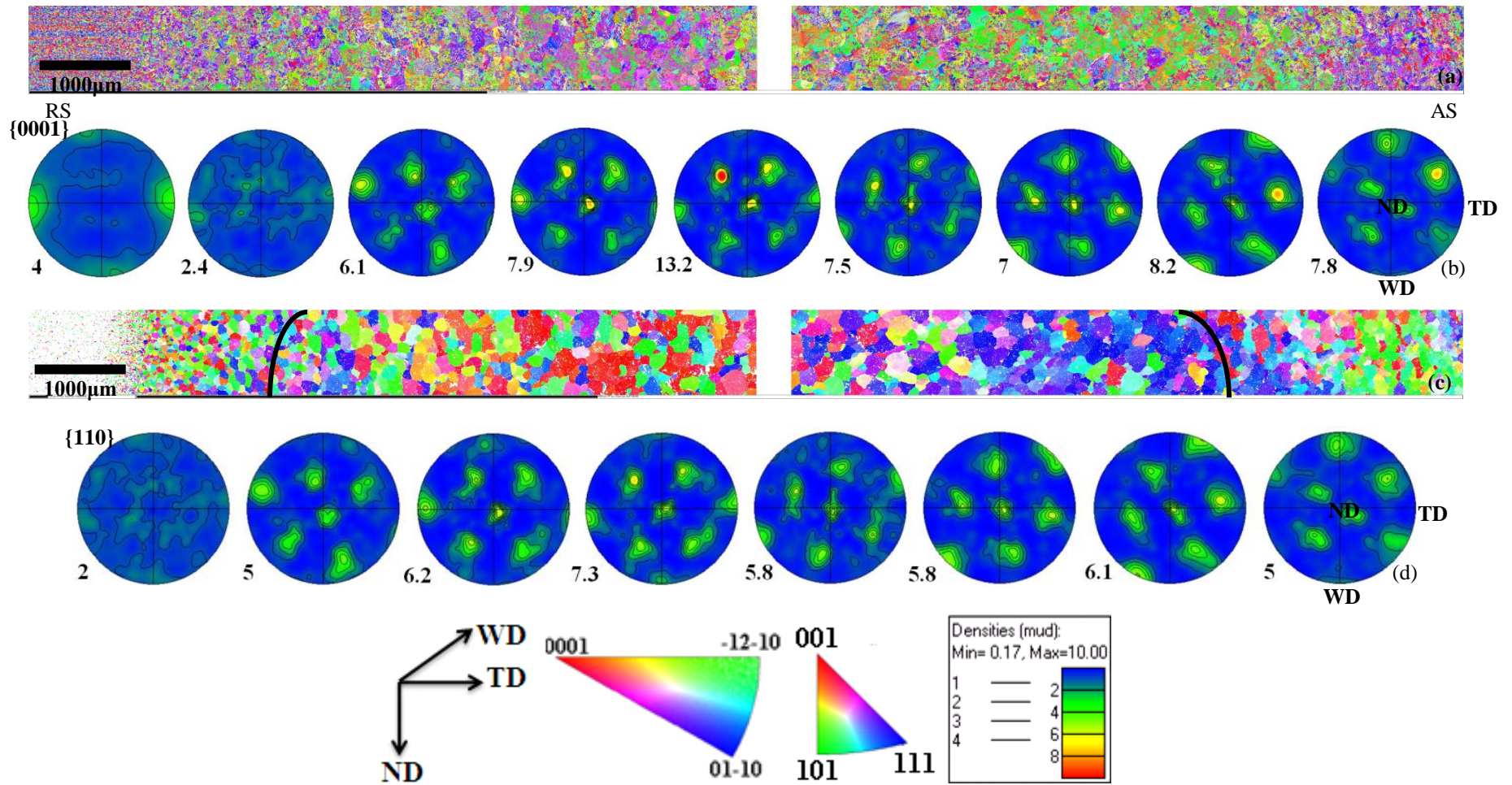
Figure 6.14 EBSD data of Set2 (2mm below the weld surface) sized 15680μm×920μm obtained from the RS to the AS of W5: (a) IPF map and (b) {0001} pole figures of the low temperature α phase; (c) IPF map after reconstruction with superimposed black curves explained in the text; (d) {110} pole figures of the reconstructed high temperature β phase with maximum density
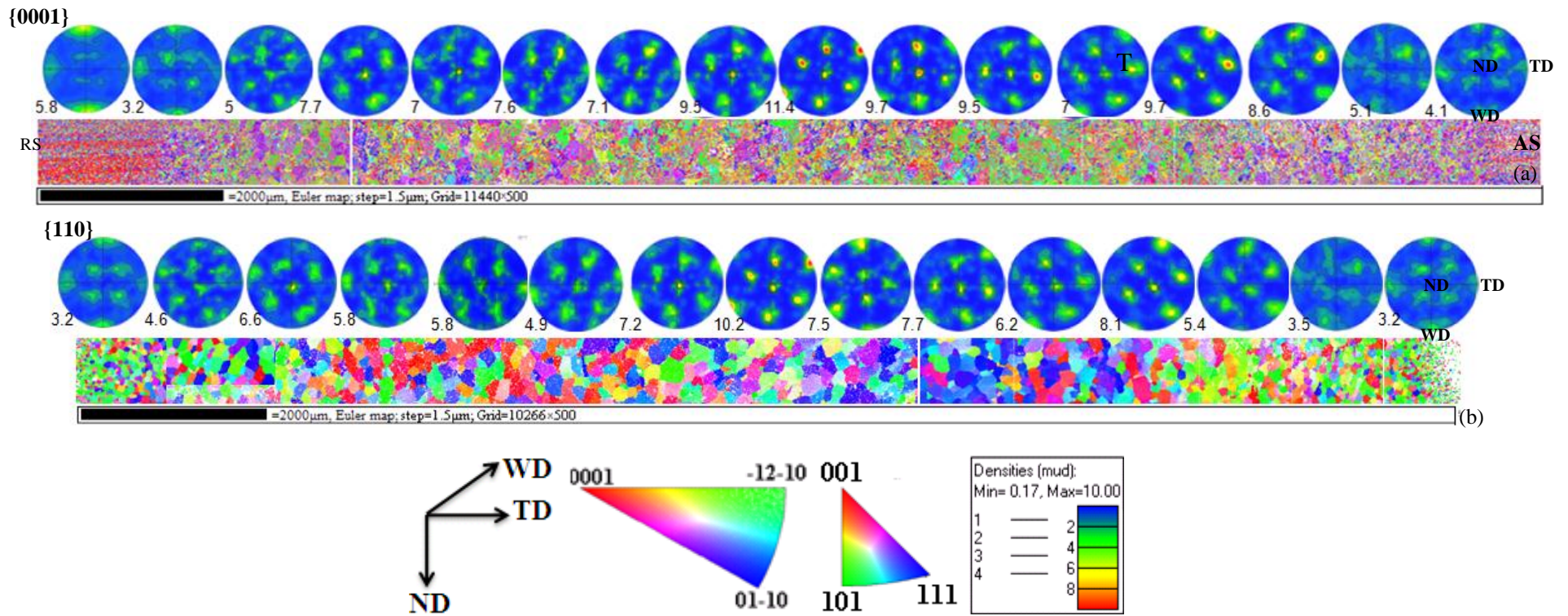
Figure 6.15 EBSD data of Set3 sized 22880μm×1000μm obtained from the RS to the AS of W5: (a) IPF map and (b) {0001} pole figures of the low temperature α phase with maximum density; (c) IPF maps after reconstruction with superimposed black curves explained in the text; and the corresponding: (d) {110} pole figures of the reconstructed high temperature β phase with maximum density
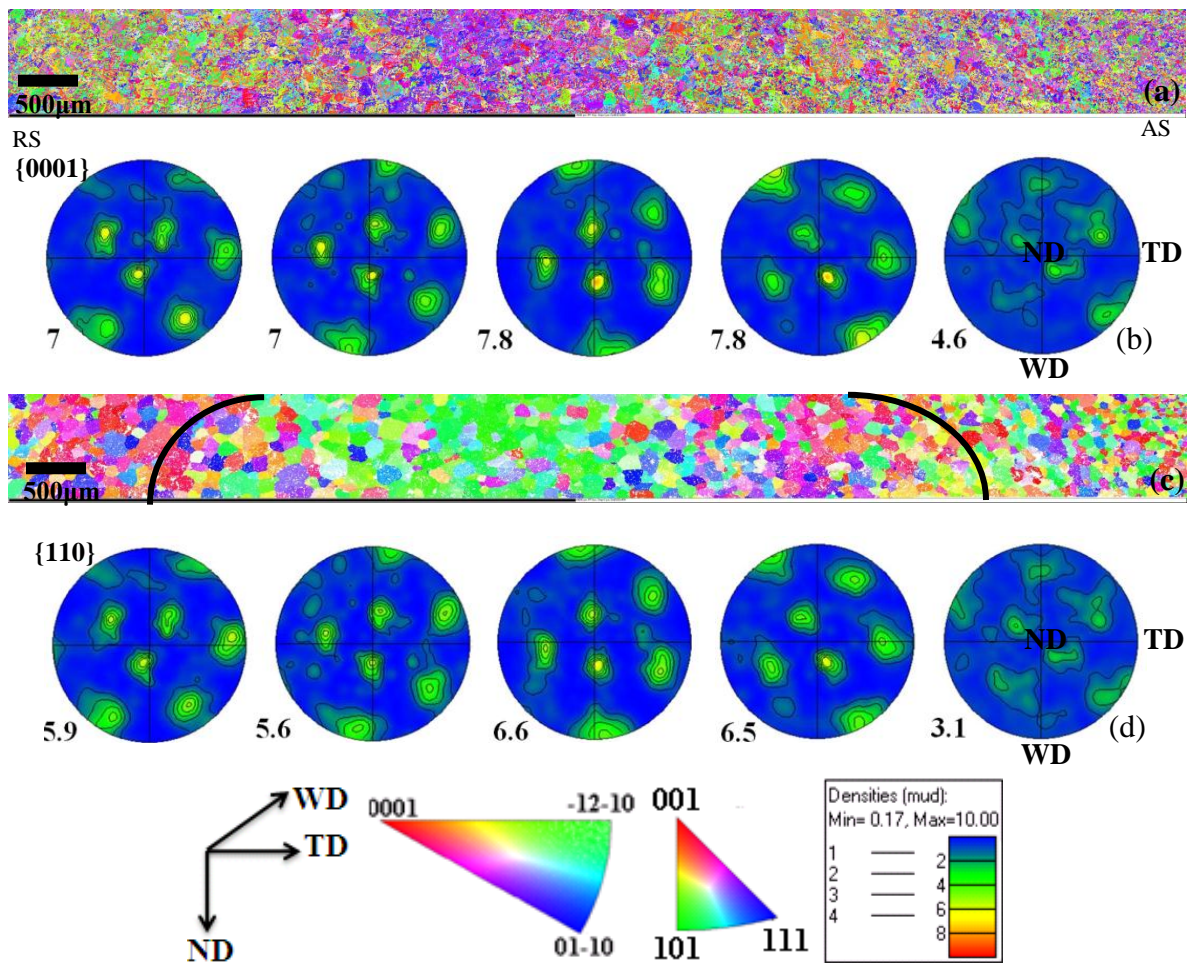
Figure 6.16 EBSD data of Set4 (1.5mm above the weld bottom) sized 10406μm×916μm obtained from the RS to the AS of W5: (a) IPF map and (b) {0001} pole figures of the low temperature α phase; (c) IPF map after reconstruction with superimposed black curves explained in the text; (d) {110} pole figures of the reconstructed high temperature β phase with maximum density
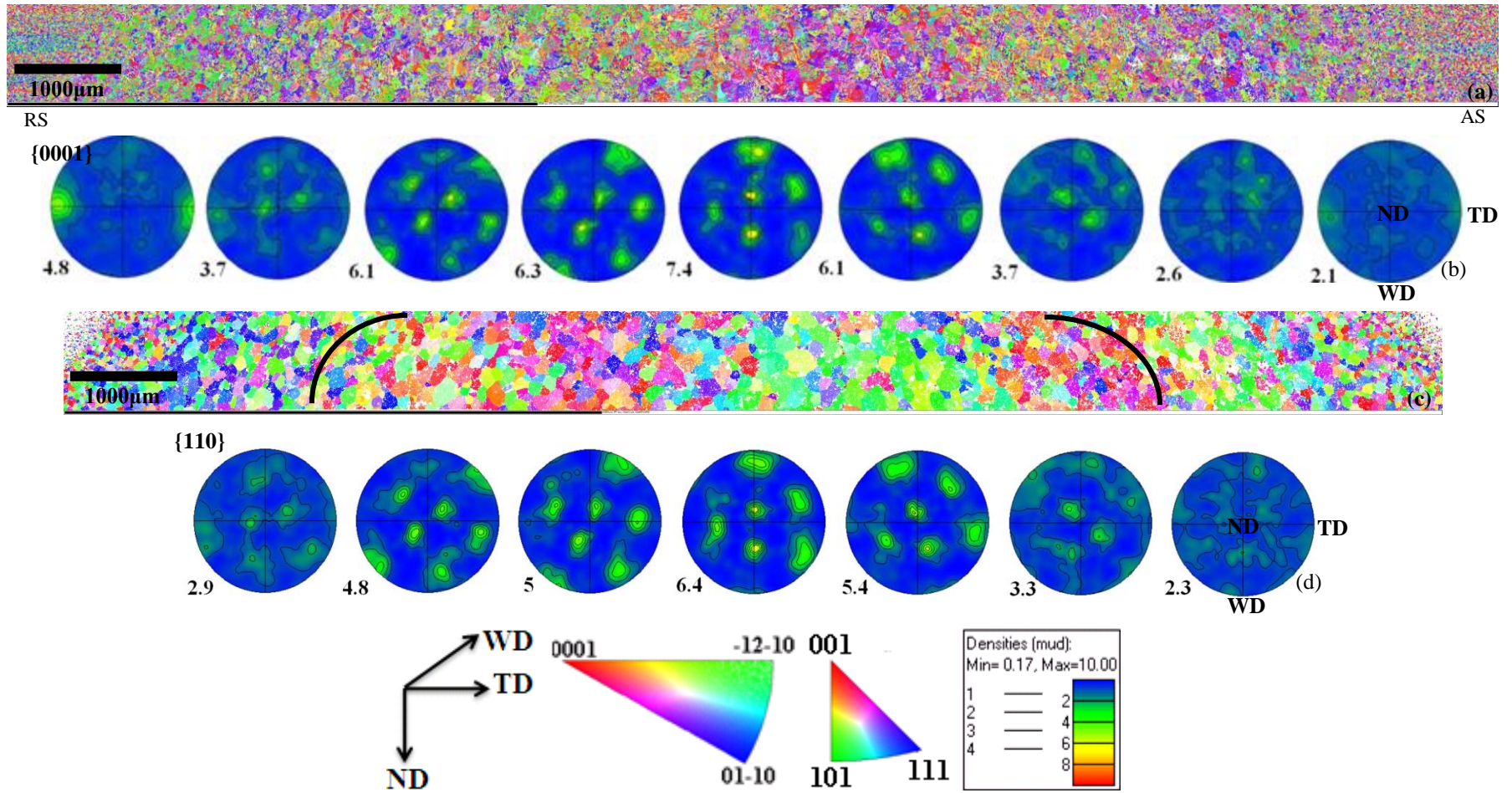
Figure 6.17 EBSD data of Set5 (at the very bottom) sized 14078μm×920μm obtained from the RS to the AS of W5: (a) IPF map and (b) {0001} pole figures of the low temperature α phase; (c) IPF map after reconstruction with superimposed black curves explained in the text; (d) {110} pole figures of the reconstructed high temperature β phase with maximum density

Table 6.2 Pole intensity of the {0001} PFs and {110} PFs for the low temperature α texture and reconstructed high temperature β texture in all the five parts of W5B5

|  |  | Set1 | Set2 | Set3 | Set4 | Set5 |
|---|---|---|---|---|---|---|
| {0001} PFs | Max. density | 5.8 | 13.2 | 11.4 | 7.8 | 7.4 |
|  | Min. density | 5.7 | 2.4 | 3.2 | 4.6 | 2.1 |
| {110} PFs | Max. density | 4.9 | 7.3 | 10.2 | 6.6 | 6.4 |
|  | Min. density | 2.4 | 2 | 3.2 | 3.1 | 2.3 |

*6.2.2.3 Texture of W6*

Texture analysis of the weld W6 has been carried out on the cross section W6C6, data were taken from the RS to the AS and five EBSD runs using a 2μm step size were obtained from the weld surface, the weld centre and the weld bottom corresponding to the five parts: Set1, Set 2 and Set 3, Set4 and Set5, as shown in Figure 6.18. In order to show how the texture in the α phase evolves across the weld zones in the TD, Figure 6.19(a and b) to Figure 6.23(a and b) show the IPF maps of the weld zones on horizontal lines and the corresponding {0001} pole figures of the low temperature α phase at the 1-2mm intervals. Similarly, for the ND at the centre of the weld, Figure 6.19(c and d) to Figure 6.23(c and d) are the corresponding IPF maps and {110} pole figures of the reconstructed high temperature β phase on horizontal lines. It should be noted that the welding axes of the map, IPF map colour key for both the α phase and β phase, and pole figure density bar are shown at the bottom of figures. The maximum and minimum density of the {0001} PFs and {110} PFs for all the five parts are shown in Table 6.3.

It can be seen from Figure 6.19 to Figure 6.23 that the low temperature α texture has generally higher texture strength than the reconstructed high temperature β texture for all the five parts. The AS has higher texture strength than the RS in the weld centre Set 2; the weld centre has higher texture strength than the weld surface and the weld bottom Set 5 and the weld surface; the weld surface has higher texture strength than the weld bottom (Set 4 and Set 5).
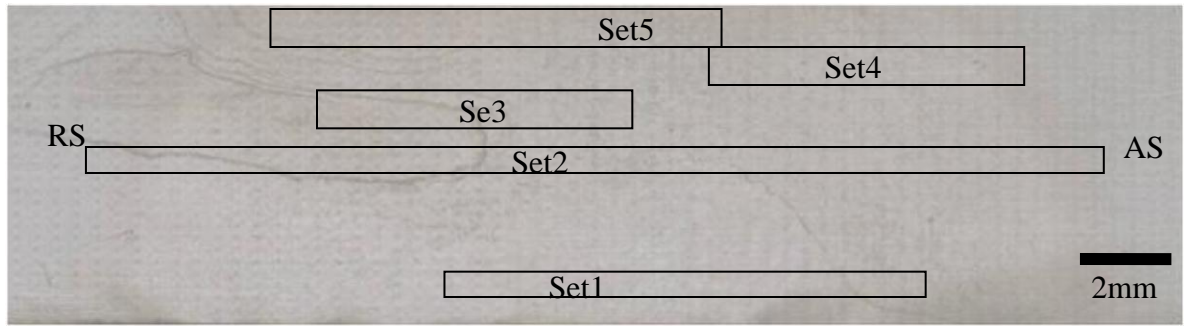
Figure 6.18 Illustration of the four sections obtained from the whole weld zone of W6
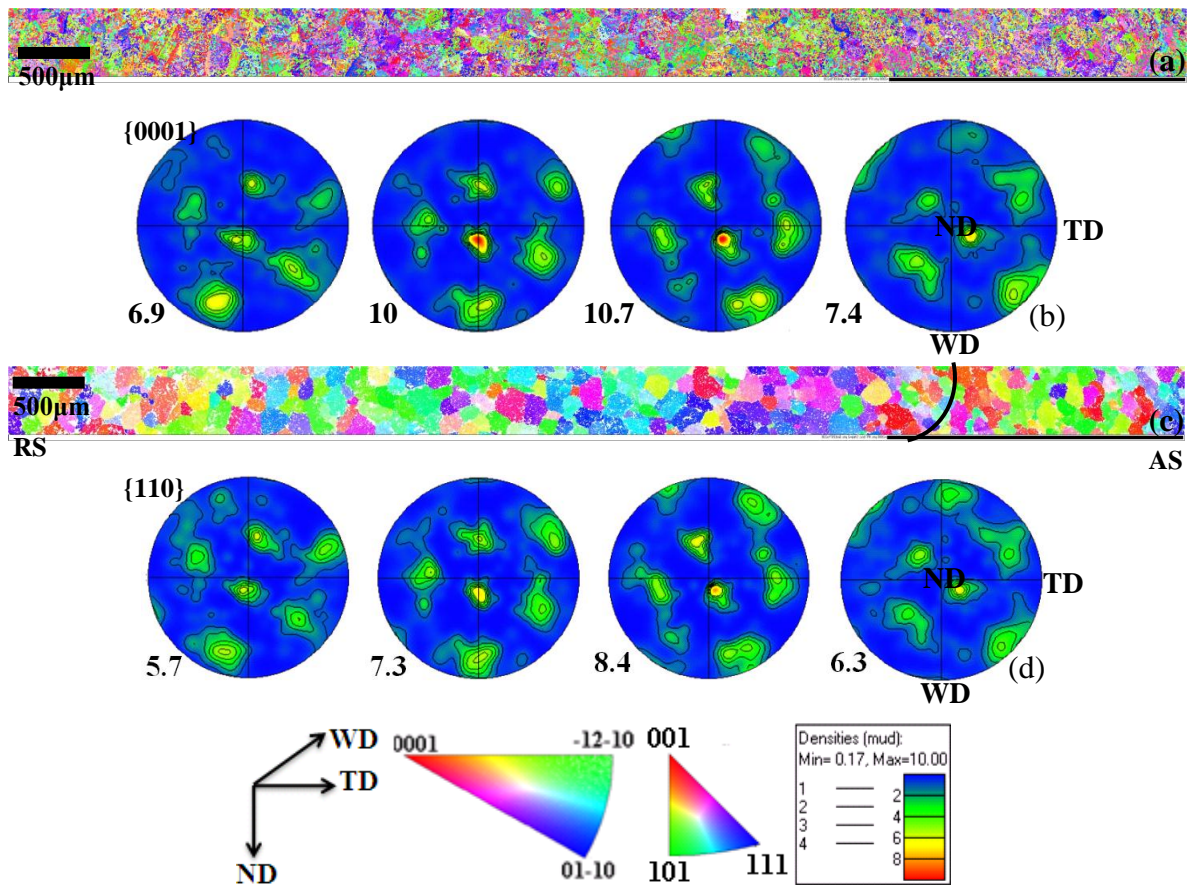


Figure 6.19 EBSD data of Set1 (Y=-2) sized 7958μm×460μm obtained at the AS of W6C6: (a) IPF map and (b) {0001} pole figures of the low temperature α phase; (c) IPF map after reconstruction with superimposed black curves explained in the text; (d) {110} pole figures of the reconstructed high temperature β phase with maximum density
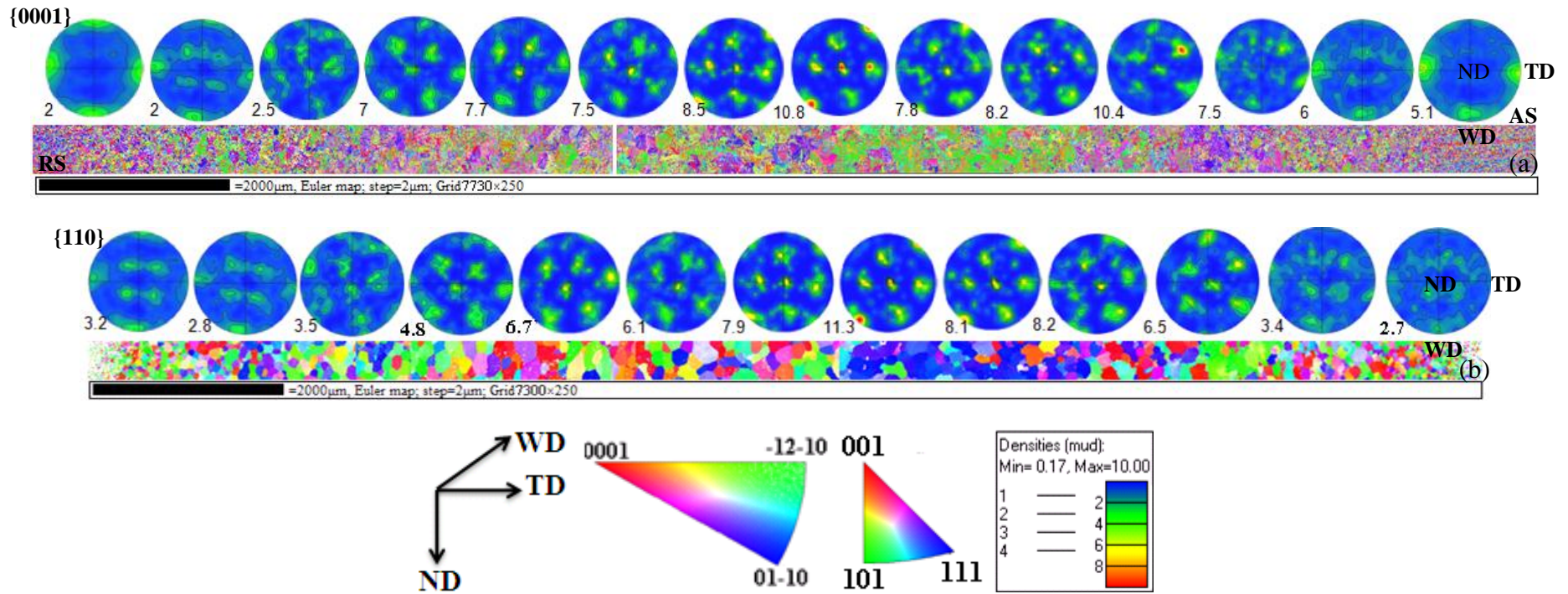
Figure 6.20 EBSD data of Set2 (centre) sized 15460μm×500μm obtained from the RS to the AS of W6C6: (a) IPF maps of the whole length of the weld zones and the corresponding: (b) {0001} pole figures of the low temperature α phase with maximum density; (c) IPF map after reconstruction and (d) the corresponding {110} pole figures of the reconstructed high temperature β phase with maximum density
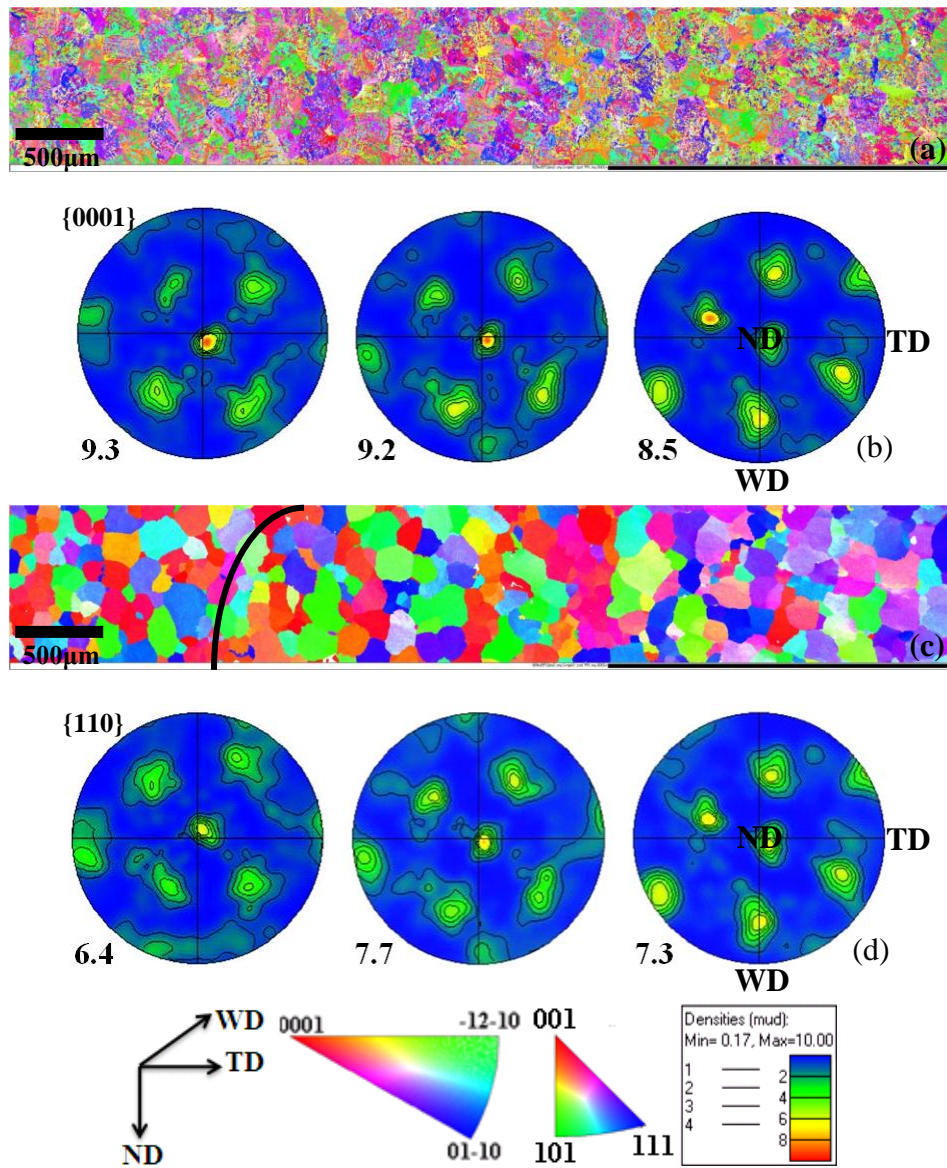
Figure 6.21 EBSD data of Set3 (Y=1.2) sized 5510μm×918μm obtained at the RS of W6C6: (a) IPF map and (b) {0001} pole figures of the low temperature α phase; (c) IPF map after reconstruction with superimposed black curves explained in the text; (d) {110} pole figures of the reconstructed high temperature β phase with maximum density
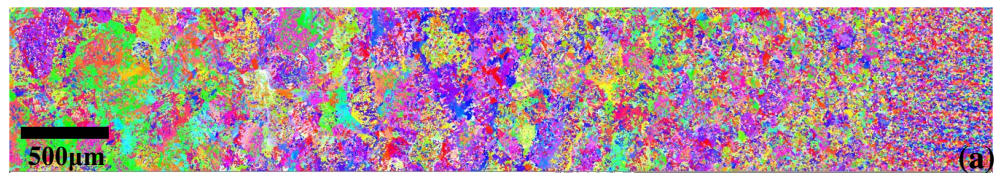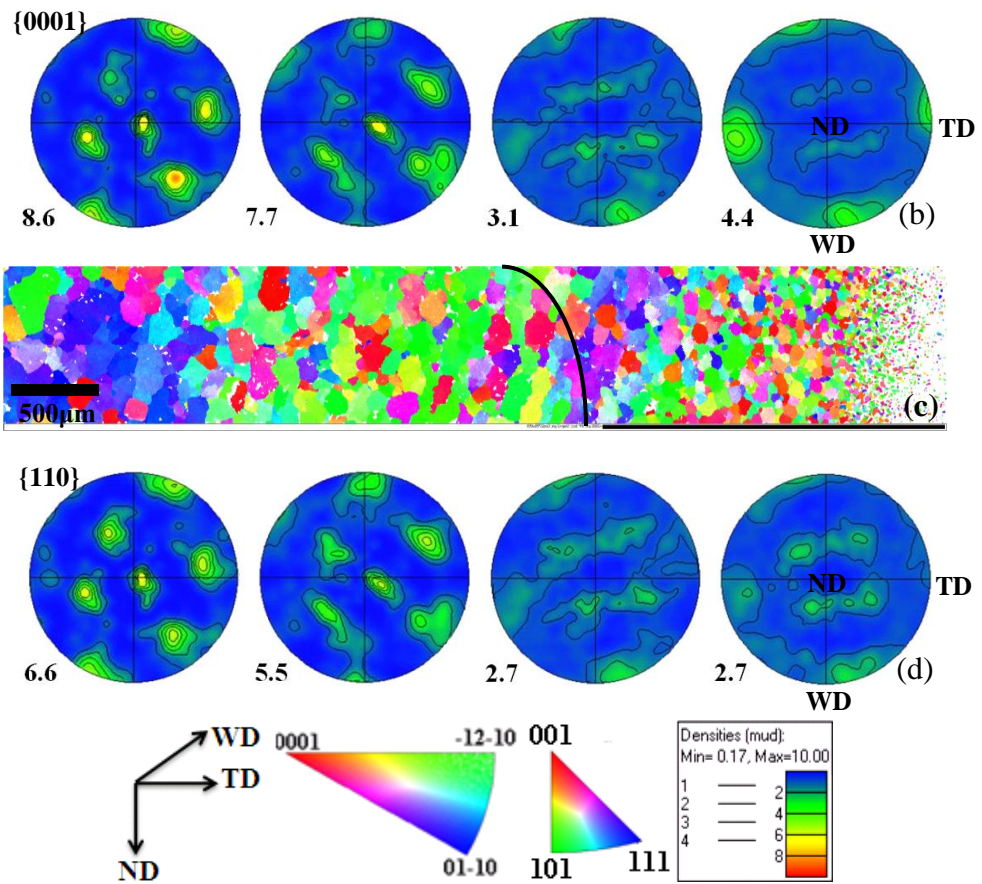
Figure 6.22 EBSD data of Set4 (Y=2.2) sized 5510μm×918μm obtained at the AS of W6C6: (a) IPF map and (b) {0001} pole figures of the low temperature α phase; (c) IPF map after reconstruction with superimposed black curves explained in the text; (d) {110} pole figures of the reconstructed high temperature β phase with maximum density
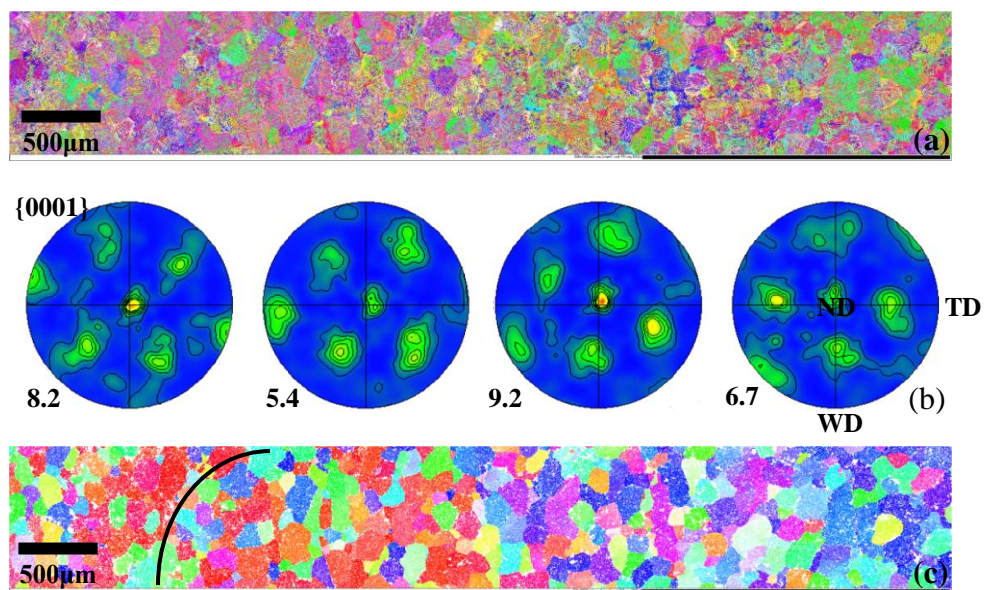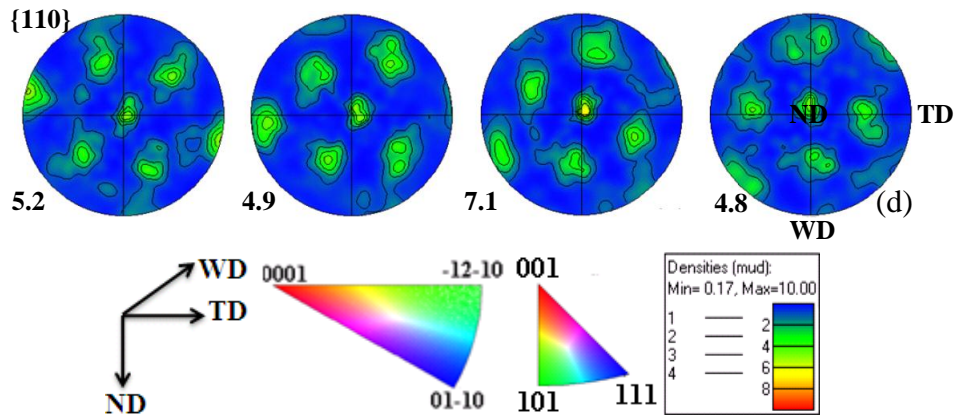
Figure 6.23 EBSD data of Set5 (Y=3) sized 7346μm×918μm obtained from the RS to the weld centre of W6C6: (a) IPF map and (b) {0001} pole figures of the low temperature α phase; (c) IPF map after reconstruction; (d) {110} pole figures of the reconstructed high temperature β phase with maximum density

Table 6.3 Pole intensity of the {0001} PFs and {110} PFs for the low temperature α texture and reconstructed high temperature β texture in all the five parts of W6C6

|  |  | Set1 | Set2 | Set3 | Se4 | Set5 |
|---|---|---|---|---|---|---|
| {0001} PFs | Max. density | 10.7 | 10.8 | 9.3 | 8.6 | 9.2 |
|  | Min. density | 6.9 | 2 | 8.5 | 3.1 | 5.4 |
| {110} PFs | Max. density | 8.4 | 11.3 | 7.3 | 6.6 | 7.1 |
|  | Min. density | 5.7 | 2.7 | 6.4 | 2.7 | 4.8 |

*6.2.2.4 Texture of W19*

Texture analysis of the weld W19 has been carried out on the cross section, data were taken from the RS to the AS and EBSD run using a 2μm step size was obtained from the weld surface to two thirds of the plate thickness, and the area was indicated as a red rectangular, and the blue rectangular represents another EBSD run with 1μm step size taken from the bump at the AS of the weld surface, as shown in Figure 6.24. In order to show how the texture of the low temperature α phase evolves across the weld zones in the TD, Figure 6.25(a) and (b) show the IPF maps of the weld zones at the 1-2mm intervals and the corresponding {0001} pole figures of the low temperature α phase on a horizontal line. For convenience, the map has been divided into five parts corresponding to part1, part2, part3,

part4 and part 5 at the 0.9mm interval. Similarly, for the ND at the centre of the weld, Figure 6.26(a) and (b) are the corresponding IPF map and {110} pole figures of the reconstructed high temperature β phase on a horizontal line. And texture of the blue rectangular region (bump region) at the AS of the top weld surface of W19 is shown in Figure 6.27(a-d). The maximum and minimum density of the {0001} PFs and {110} PFs for both the α and β texture of all the five parts are shown in Table 6.4.

Low temperature α texture has generally higher texture strength than the reconstructed high temperature β texture when compare the pole intensity of each pole in {0001} and {110} pole figures for all the five parts. It is seen that the SZ exhibits D1 shear texture component from the weld bottom to the weld surface. When compare the texture strength (pole intensity) from the weld bottom to the weld surface as shown in Figure 6.25, Figure 6.26, Figure 6.27 and Table 6.4, texture strength is the highest in the weld centre and it decreased with increasing distance from the weld centre. It should be noted that the AS has higher texture strength than the RS for all the five parts, as seen in {0001} and {110} PFs of both the α and β phases (Figure 6.26). It should be noted that the top surface contains a surface layer of fine prior β grain size of approximately 20μm and a region of 440μm by 500μm with much finer prior β grain size was seen in the bump region, as enclosed by a black rectangular region (Figure 6.27).



Figure 6.24 Macro section of W19 with red rectangular box indicating the area for EBSD analysis

{0001}

5.5    3.8    5    6.1    7.9    9.1    11.3    5.7    3.9

ND    TD
WD

9.5    4.5    4.1    7.8    8.4    8.6    12.3    5.4    6

8.1    4.6    8.1    7.9    7.3    8.4    6    7    5

RS    AS

1000μm

(a)
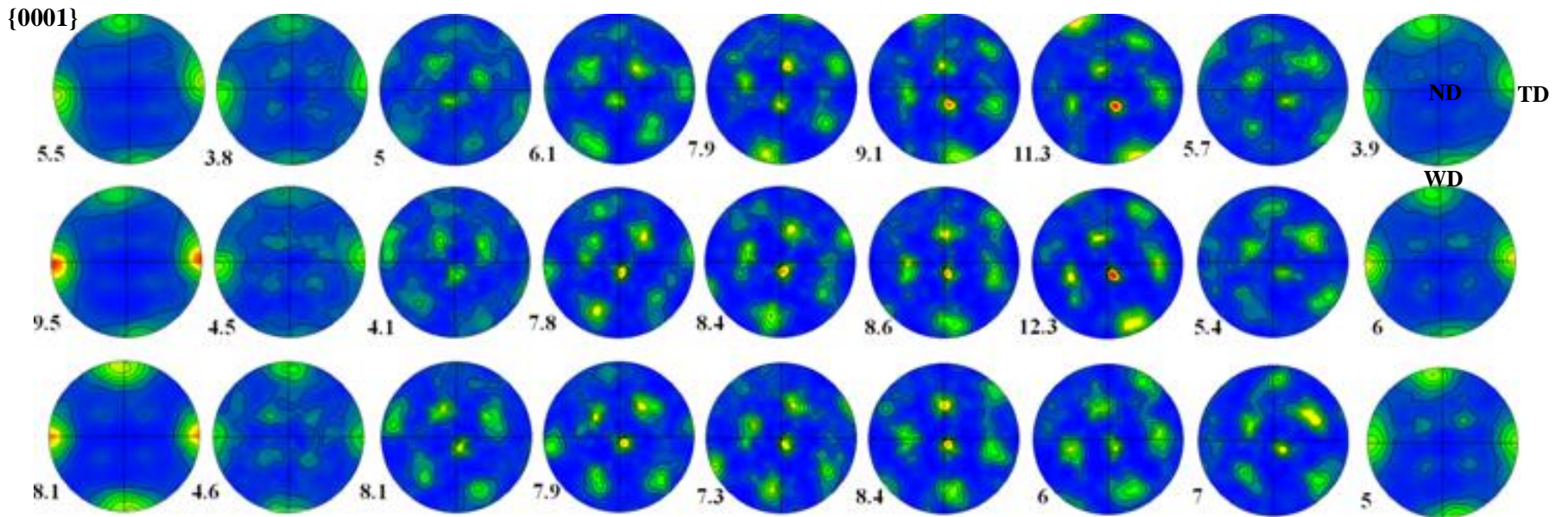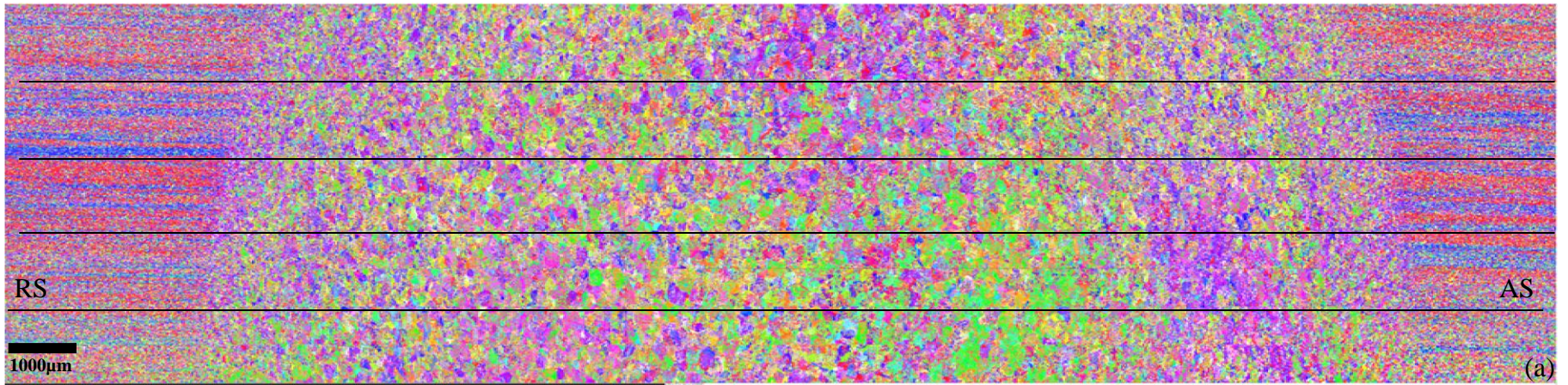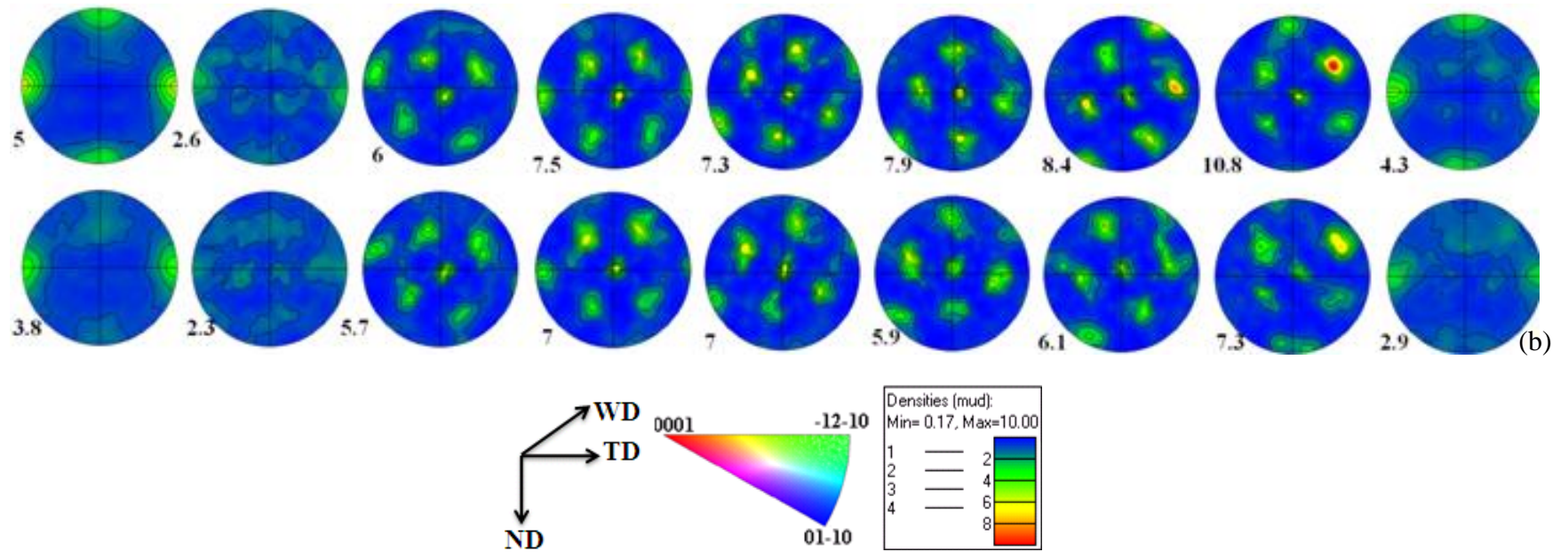
Figure 6.25 EBSD data sized 22880μm×1000μm obtained from the RS to the AS of W19: (a) IPF maps of the whole length of the weld zones and (b) the corresponding {0001} pole figures of the low temperature α phase with maximum density

{110}

2.4    5    5.6    6    8    7    5.4    2.83

2.3    4.3    6.9    7.6    8.8    9    4.7    3.6

ND    TD

WD

(a)

1000μm
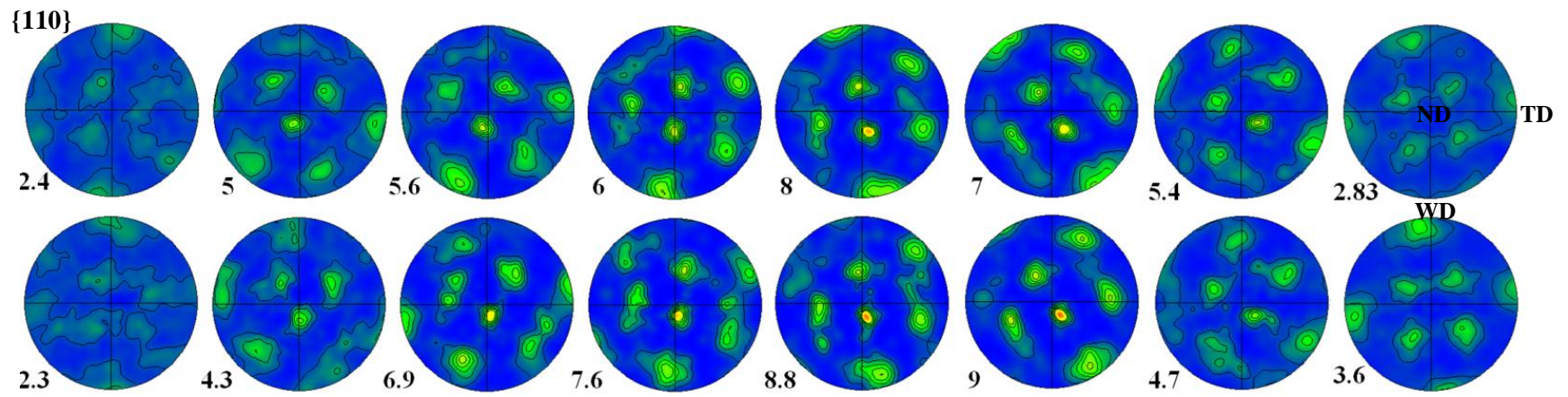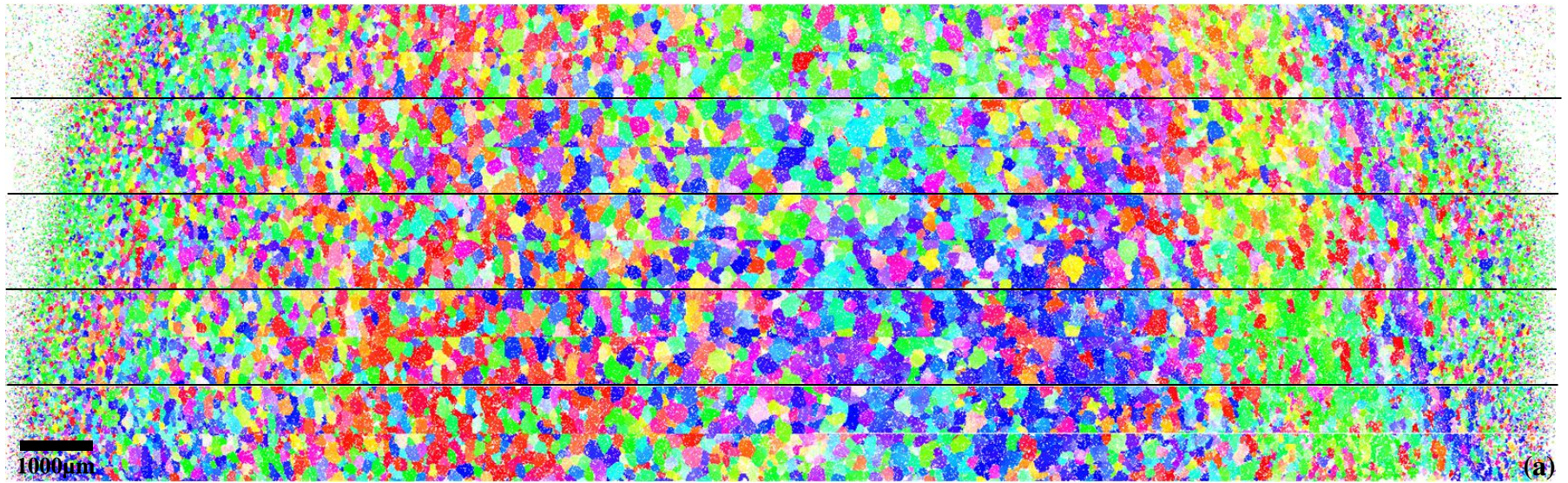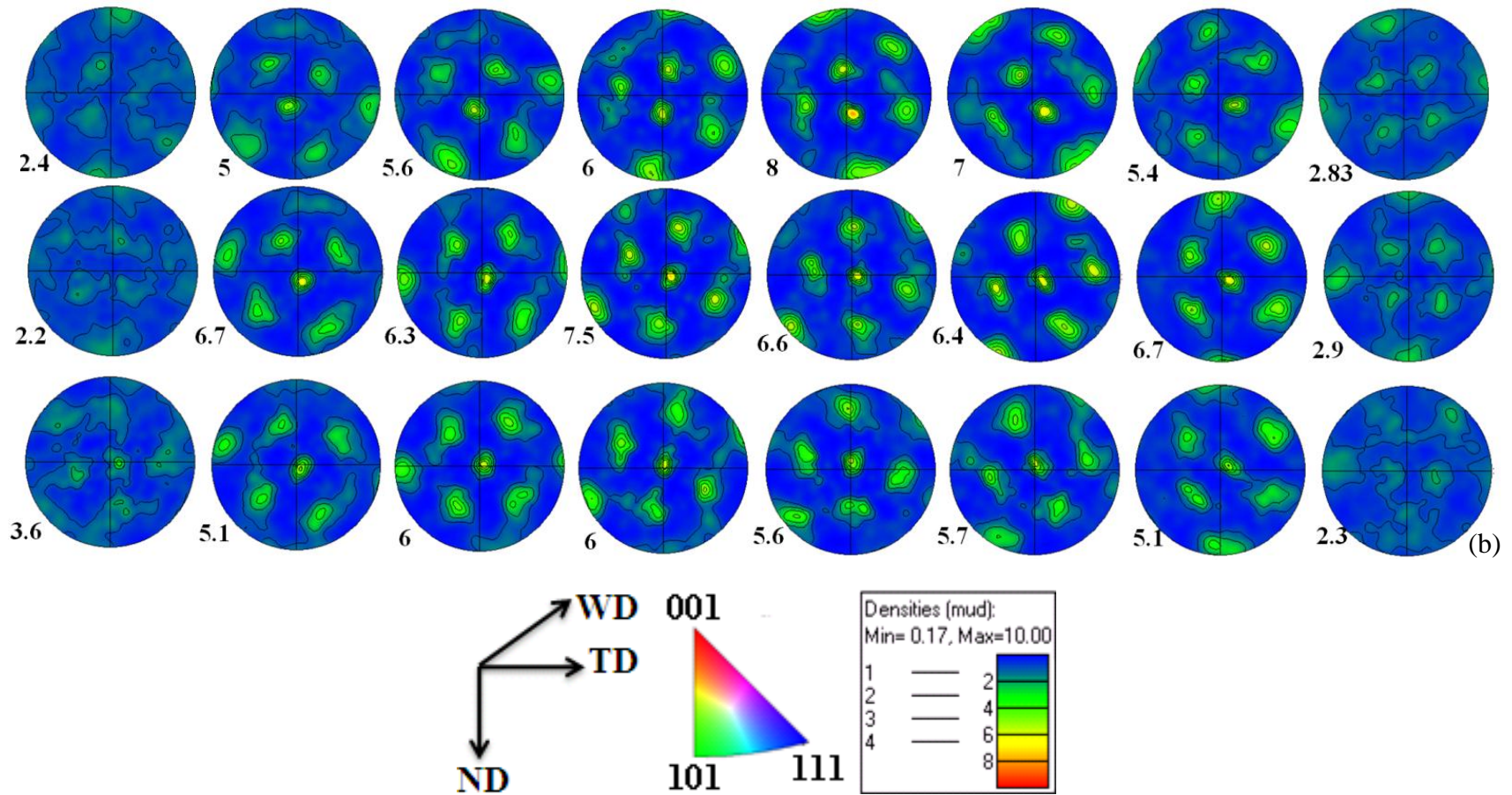
Figure 6.26 (a) IPF maps after reconstruction and (b) the corresponding {110} pole figures of the reconstructed high temperature β phase with maximum density
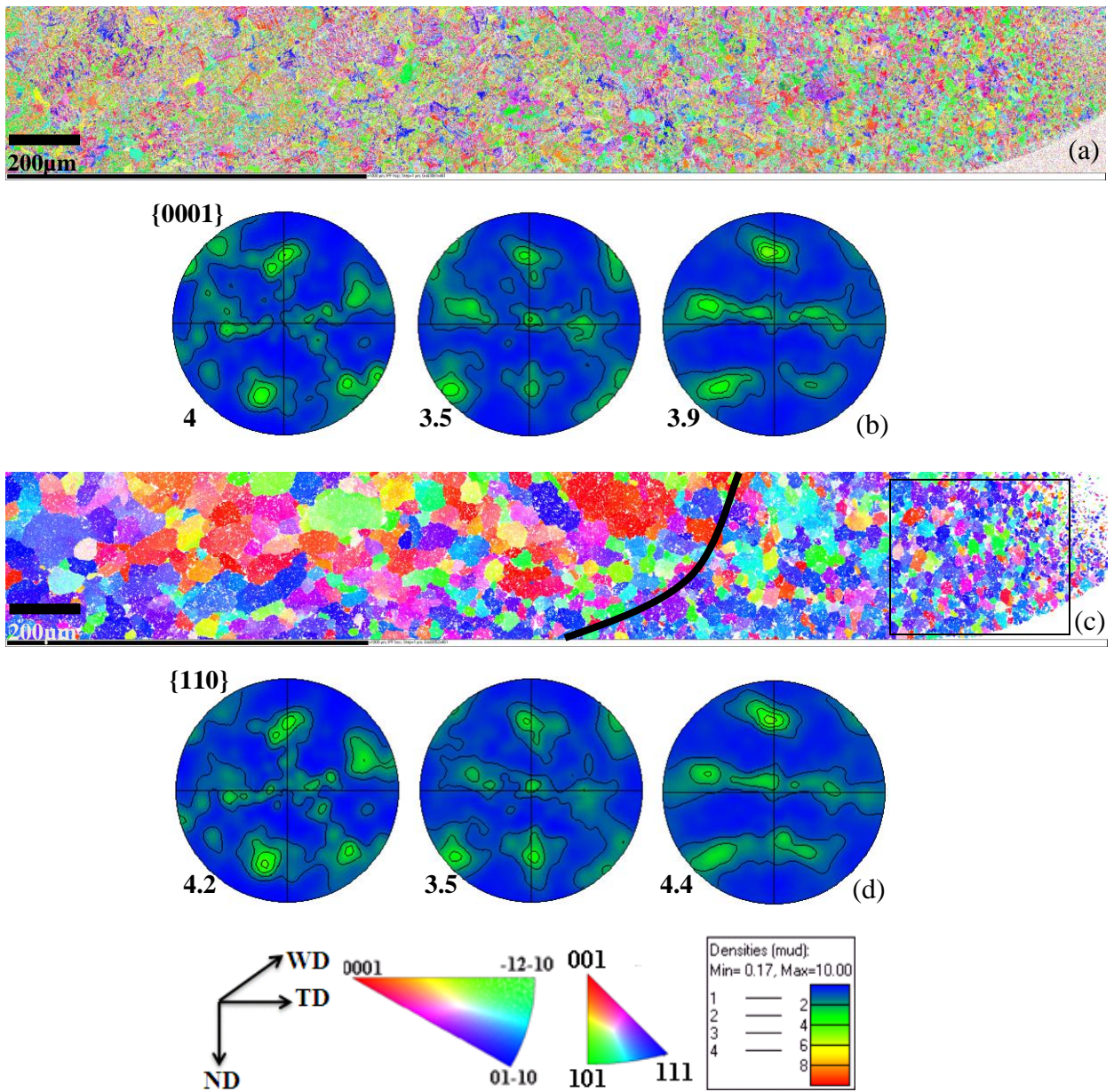
Figure 6.27 EBSD data sized 3061μm×461μm obtained at the AS on the top weld surface of W19: (a) IPF map and (b) {0001} pole figures of the low temperature α phase; (c) IPF map after reconstruction with superimposed black curves explained in the text; (d) {110} pole figures of the reconstructed high temperature β phase with maximum density

Table 6.4 Pole intensity of the {0001} PFs and {110} PFs for the low temperature α texture
and reconstructed high temperature β texture of W19

|  |  | Set1 | Set2 | Set3 | Set4 | Set5 |
|---|---|---|---|---|---|---|
| {0001} PFs | Max. density | 11.3 | 12.3 | 8.1 | 10.8 | 7.3 |
|  | Min. density | 3.8 | 4.1 | 4.6 | 4.3 | 2.3 |
| {110} PFs | Max. density | 8 | 9 | 8.1 | 7.5 | 5.7 |
|  | Min. density | 2.4 | 2.3 | 2.6 | 2.2 | 2.3 |

*6.2.2.4 Texture of W20*

In Figure 6.28, a red rectangular in the macrograph of W20 indicates the IPF map sized 20.2mm by 1.366mm from the RS to AS of the weld W20. Figure 6.29(a) and (b) are the IPF maps of the whole length of the weld zones in the weld centre of W20 and the corresponding {0001} pole figures of the low temperature α phase at the 1-2mm intervals on a horizontal line. Similarly, for the ND at the centre of the weld, Figure 6.29(c) and (d) shows texture of the reconstructed high temperature β phase on a horizontal line. It should be noted that the welding axes of the map, IPF map colour key for both the α phase and β phase, and pole figure density bar are shown at the bottom of figures. The maximum and minimum density of the {0001} PFs and {110} PFs for both the α and β texture are shown in Table 6.5. It can be seen that the weld centre exhibits D1 shear texture component and the AS has higher texture strength than the RS.
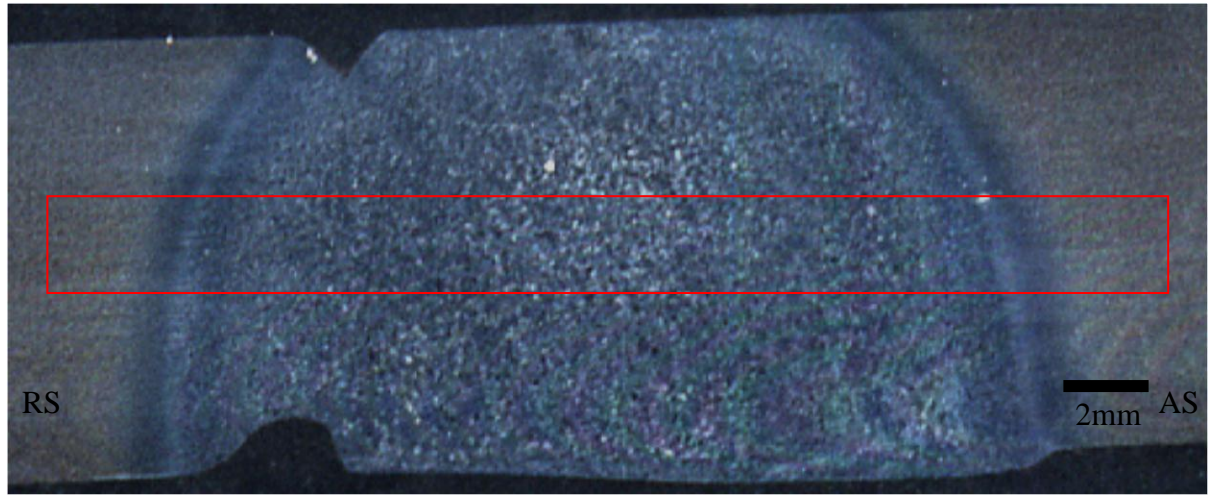
Figure 6.28 Macro section of the weld W20

Table 6.5 Pole intensity of the {0001} PFs and {110} PFs for the low temperature α texture and reconstructed high temperature β texture of W20

|  | {0001} PFs | | {110} PFs | |
|---|---|---|---|---|
|  | Max. density | Min. density | Max. density | Min. density |
| Set1 | 8.3 | 3.1 | 7.1 | 2.6 |
| Set2 | 8.8 | 2.7 | 7.1 | 3.2 |

{0001}

9.2  3.1  9  7.3  7.9  8.3  8  4.6  11.2  ND  TD  WD

2.7  8.3  8.2  5.7  8.8  7.1  5.8

(b)



{110}

2.6  6.4  5.4  6  6.5  7.1  3  ND  TD  WD

3.2  6.5  6.8  5.4  9.3  7.1  3.4

(d)
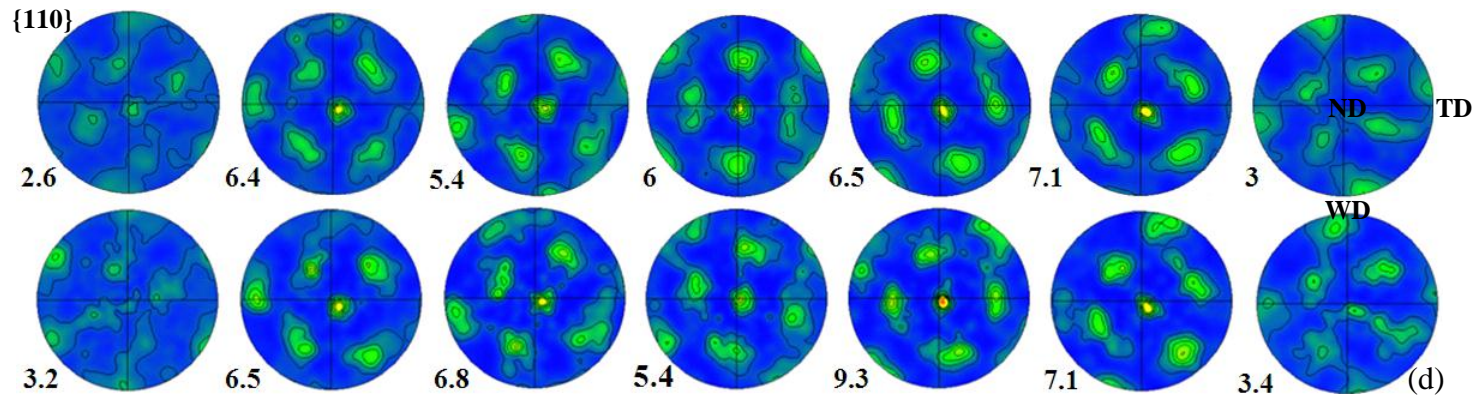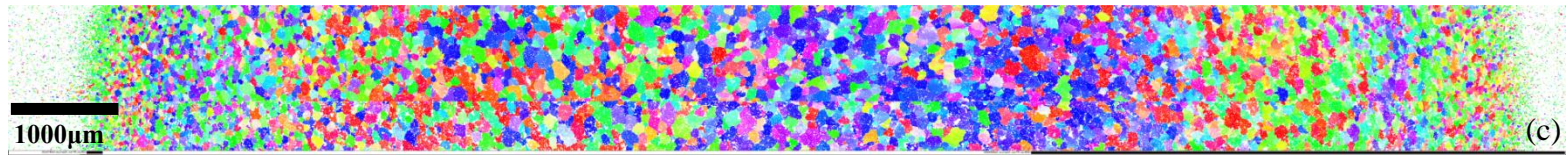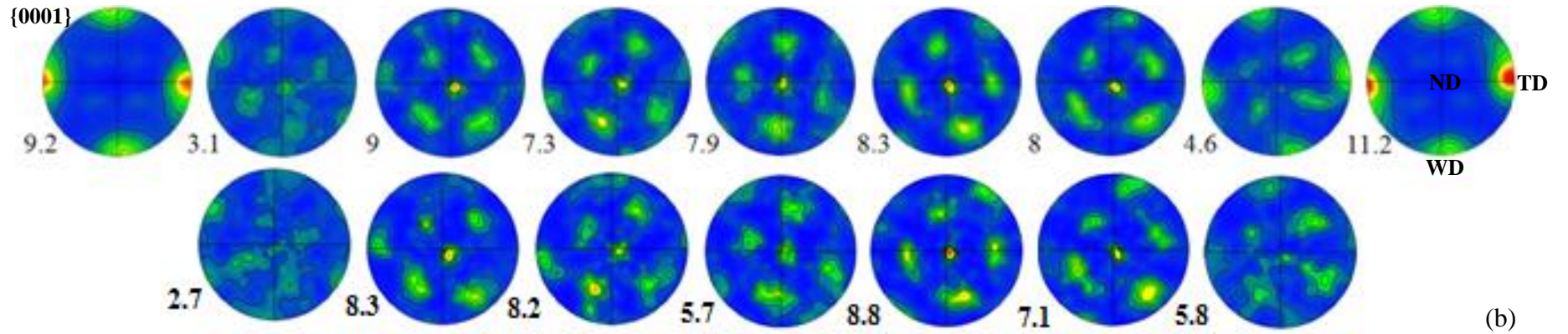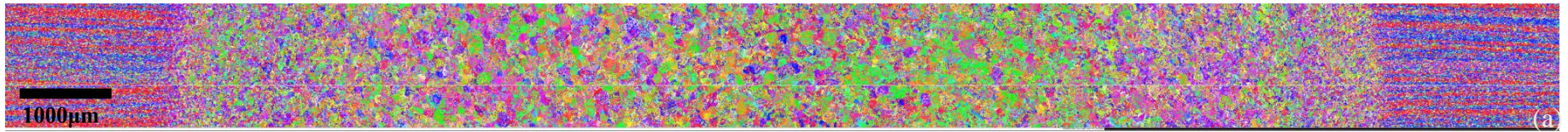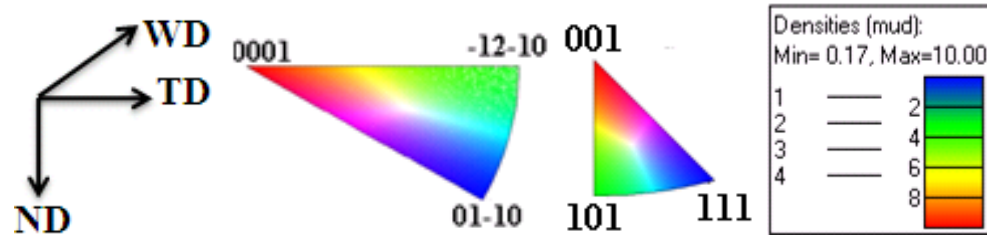
Figure 6.29 EBSD data sized 17138μm×1366μm obtained from the RS to the AS of W20: (a) IPF map and (b) {0001} pole figures of the low temperature α phase; (c) IPF map after reconstruction with superimposed black curves explained in the text; (d) {110} pole figures of the reconstructed high temperature β phase with maximum density

*6.2.2.5 Texture of W21*

EBSD data map sized 16528μm×1372μm was collected from the RS to the AS of the weld zones of W21 as indicated in a red rectangular in the macrograph (Figure 6.30). Figure 6.31(a) and (b) are the IPF maps of the weld zones on a horizontal line and the corresponding {0001} pole figures of the low temperature α phase at the 1-2mm intervals on a horizontal line. Similarly, for the ND at the centre of the weld, Figure 6.31(c) and (d) shows the corresponding texture of the reconstructed high temperature β phase. It should be noted that the welding axes of the map, IPF map colour key for both the α phase and β phase, and pole figure density bar are shown at the bottom of figures. The maximum and minimum density of the {0001} PFs and {110} PFs for both the α and β texture are 8.8 and 5, 7.1 and 3.6, respectively. Similarly, the AS has higher texture strength than the RS.
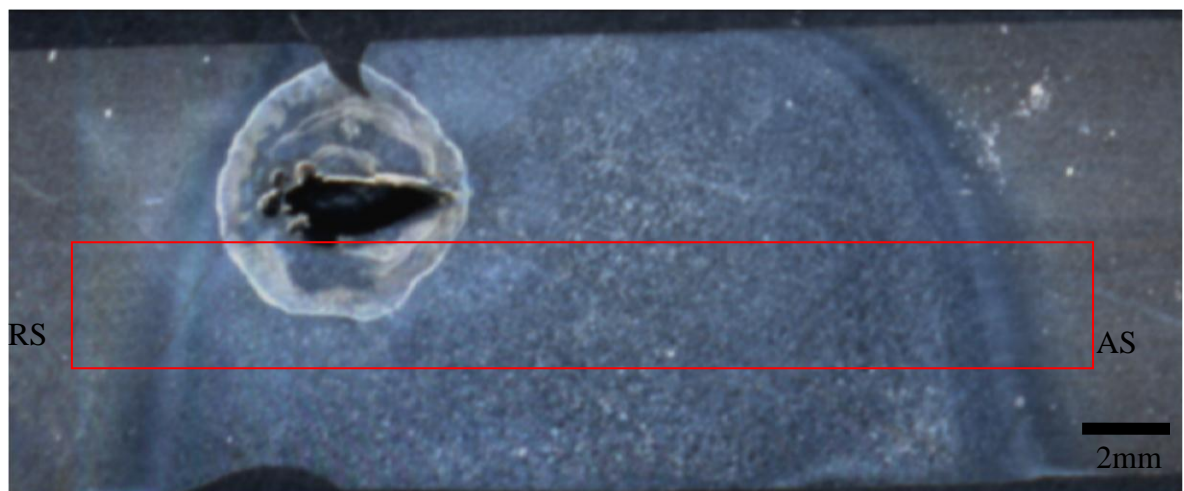


Figure 6.30 Macro section of the weld W21
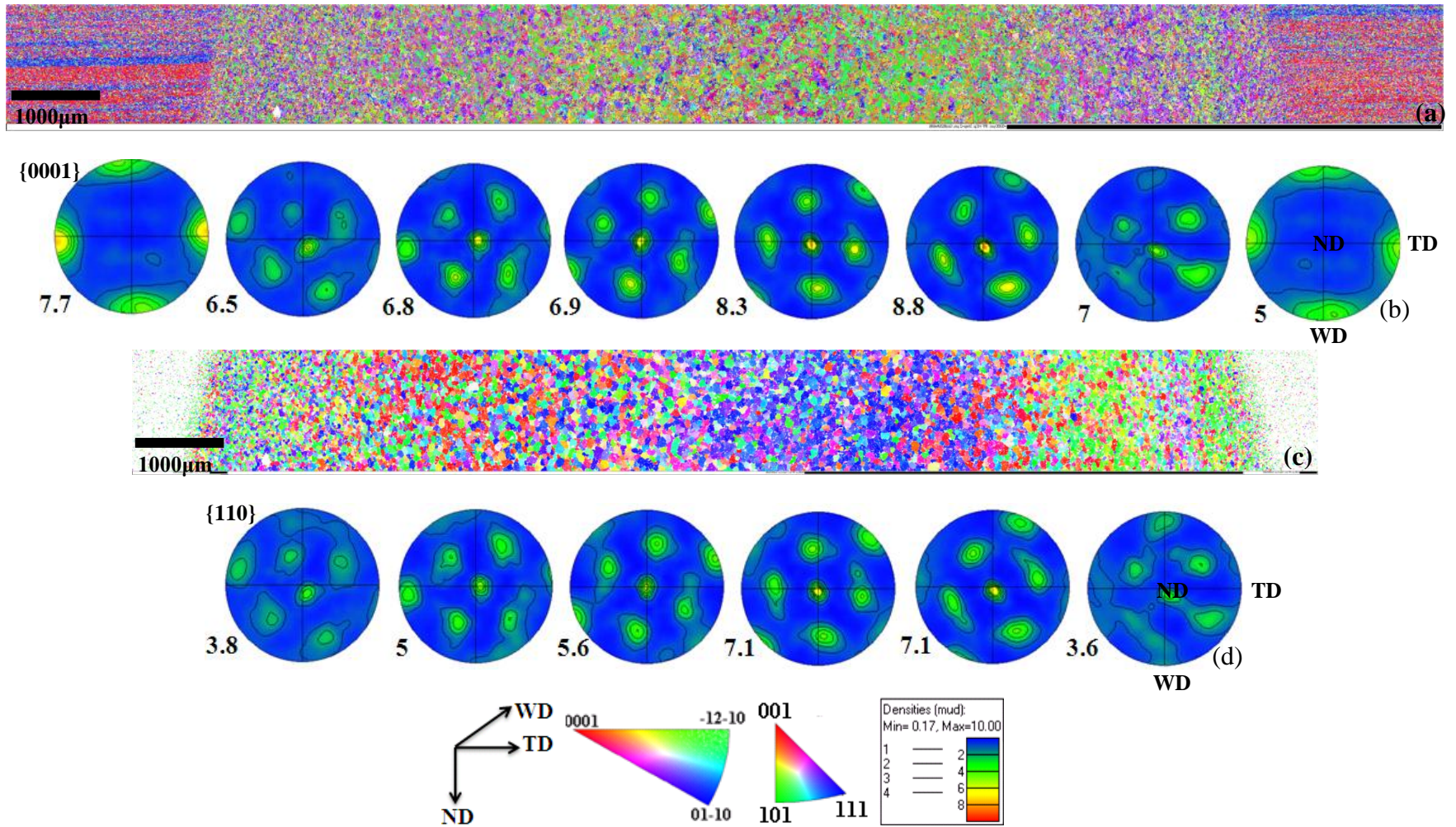
Figure 6.31 EBSD data sized 16528μm×1372μm obtained from the RS to the AS of W21: (a) IPF map and (b) {0001} pole figures of the low temperature α phase; (c) IPF map after reconstruction with superimposed black curves explained in the text; (d) {110} pole figures of the reconstructed high temperature β phase with maximum density

### 6.2.3 Definition of the TMAZ and the HAZ

*6.2.3.1 W4-50mm/min*

Figure 6.32(a) is an IPF map taken from the RS of the welding edge of W4, for convenience, the map has been divided into five zones, corresponding to equiaxed parent structure (A), bimodal structure (B and C), fully transformed lamellar structure (D and E), the α phase (hcp) texture and retained β phase (bcc) texture are represented by the {0001} PFs and {110} PFs, respectively, as shown in Figure 6.32(b) and (c). The welding axes, IPF colour key for the α phase and pole figure density bars are shown at the bottom of the figures. It is clearly seen that the α phase texture starts to change at the bimodal structure (B and C) while the β phase texture of the bimodal structure retains the same as the base material (A). This would suggest that in Section A, B and C, the material has not been deformed because the β texture remains the same but a significant change in α texture has occurred on cooling due to other α variants being produced. Both the α and β texture of section D and E have changed indicating that the material has undergone deformation and thus they must be part of the TMAZ whilst the material in Section B and Section C constitute the HAZ.
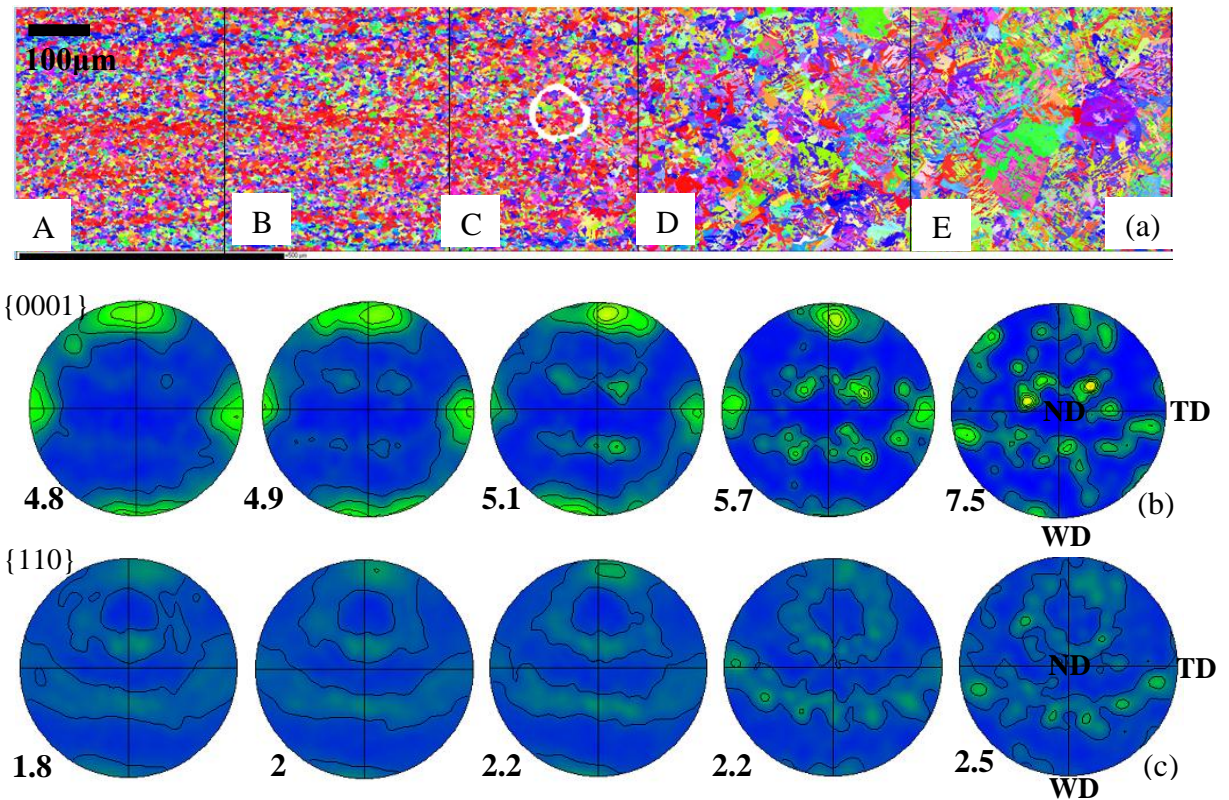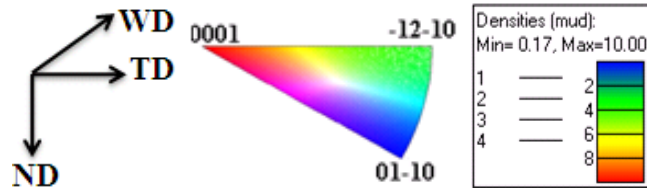
Figure 6.32 (a) IPF map of the transition zone at the RS of W4; (b) {0001} pole figures of the room temperature α phase; (c) {110} pole figures of the room temperature β phase

IPF map taken from the AS of the welding edge of W4 is shown in Figure 6.33(a), which was divided into four zones, corresponding to fully transformed lamellar structure (A), bimodal structure (B), equiaxed structure (C and D), {0001} PFs of the α phase texture and {110} PFs of retained β phase texture are shown in Figure 6.33(b) and (c), respectively. The welding axes, IPF colour key for the α phase and pole figure density bars are shown at the bottom of the figures. The welding axes, IPF colour key for the α phase and pole figure density bars are shown at the bottom. It is seen that in Section B, the α phase texture starts to change due to other α variants being produced, while the β phase texture retains the same as the BM (Section C and D). This meant that in Section B, C and D, the material has not been deformed because the β texture remains the same. Both the α and β texture of Section A have changed indicating that the material has undergone deformation and thus they must be part of the TMAZ whilst the material in Section B constitute the HAZ.



236
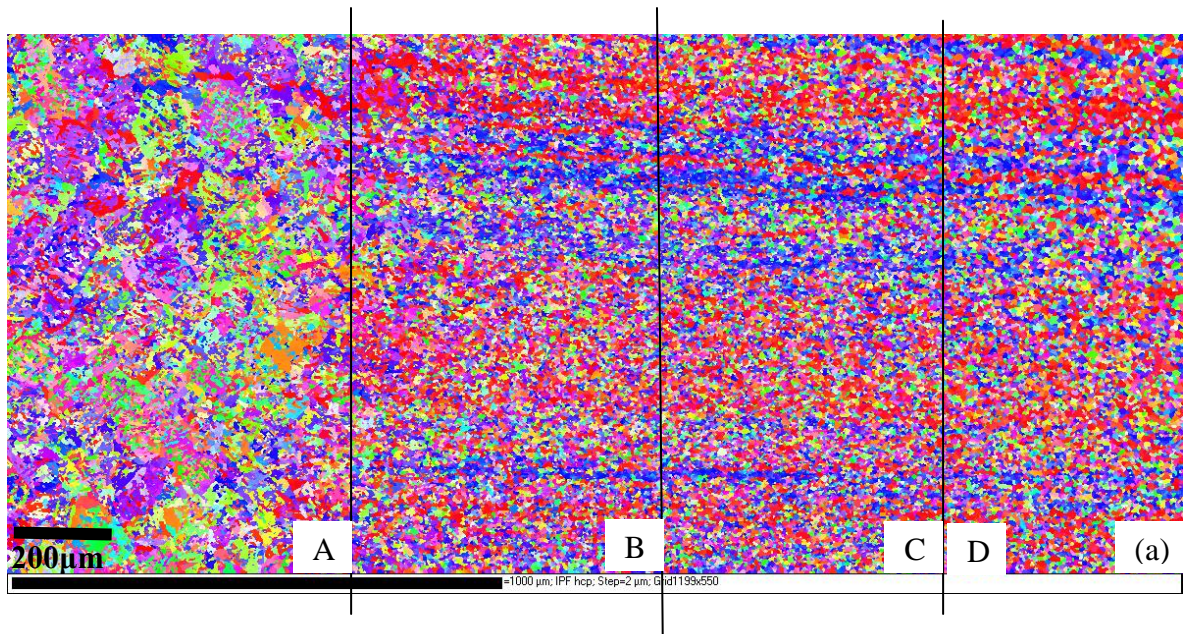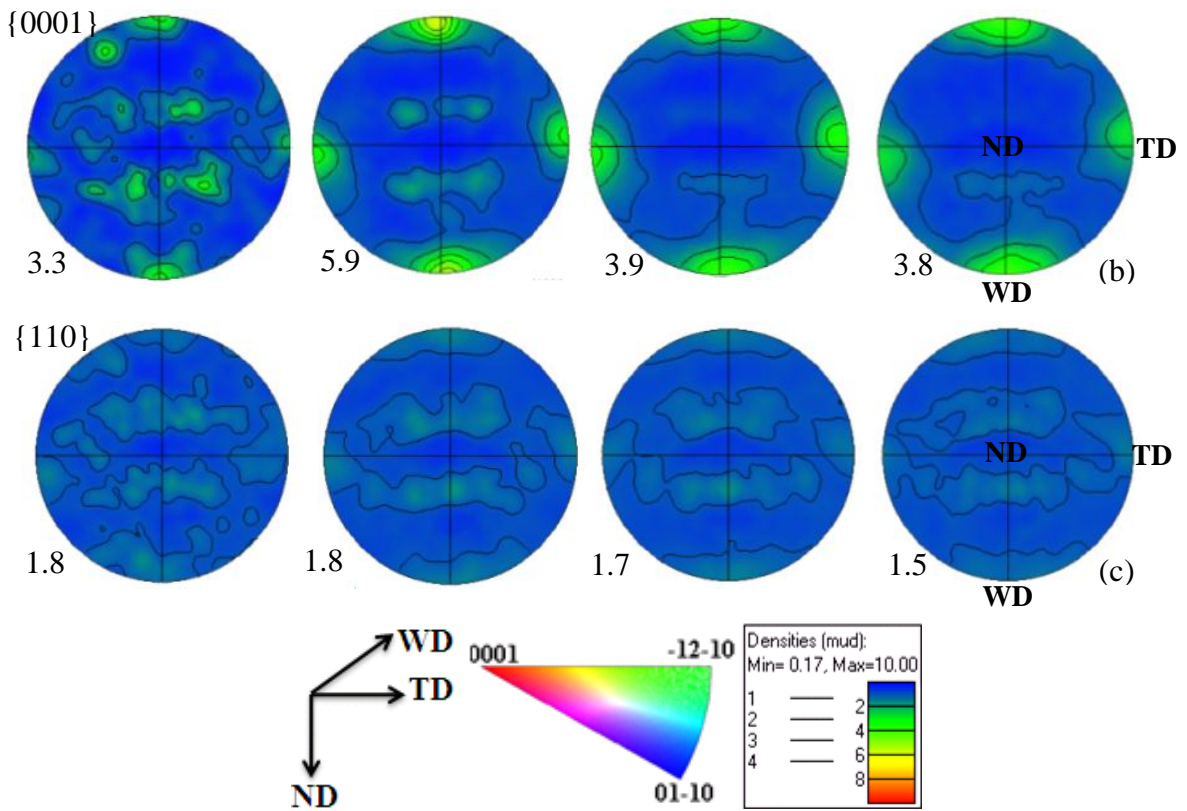
Figure 6.33 (a) IPF map of the transition zone at the AS of W4; (b) {0001} pole figures of the room temperature α phase; (c) {110} pole figures of the room temperature β phase

### 6.2.3.2 W5-100mm/min

Figure 6.34(a) is an IPF map taken from the RS of the welding edge of W5, which has been divided into five zones: equiaxed parent structure (A and B), bimodal structure (C), lamellar structure (D and E). The α phase (hcp) texture and retained β phase (bcc) texture are represented by the {0001} PFs and {110} PFs, respectively, as shown in Figure 6.34(b) and (c). The welding axes, IPF colour key for the α phase and pole figure density bars are shown at the bottom of the figures. The result demonstrates that the α phase texture starts to change at the bimodal structure (C) while the β phase texture of the bimodal structure retains the same as the BM (A+B). This would suggest that in Section A, B and C the material has not been deformed because the β texture remains the same. Both the α and β texture of section D and E have changed indicating that the material has undergone deformation and thus they must be part of the TMAZ whilst the material in Section C constitute the HAZ.
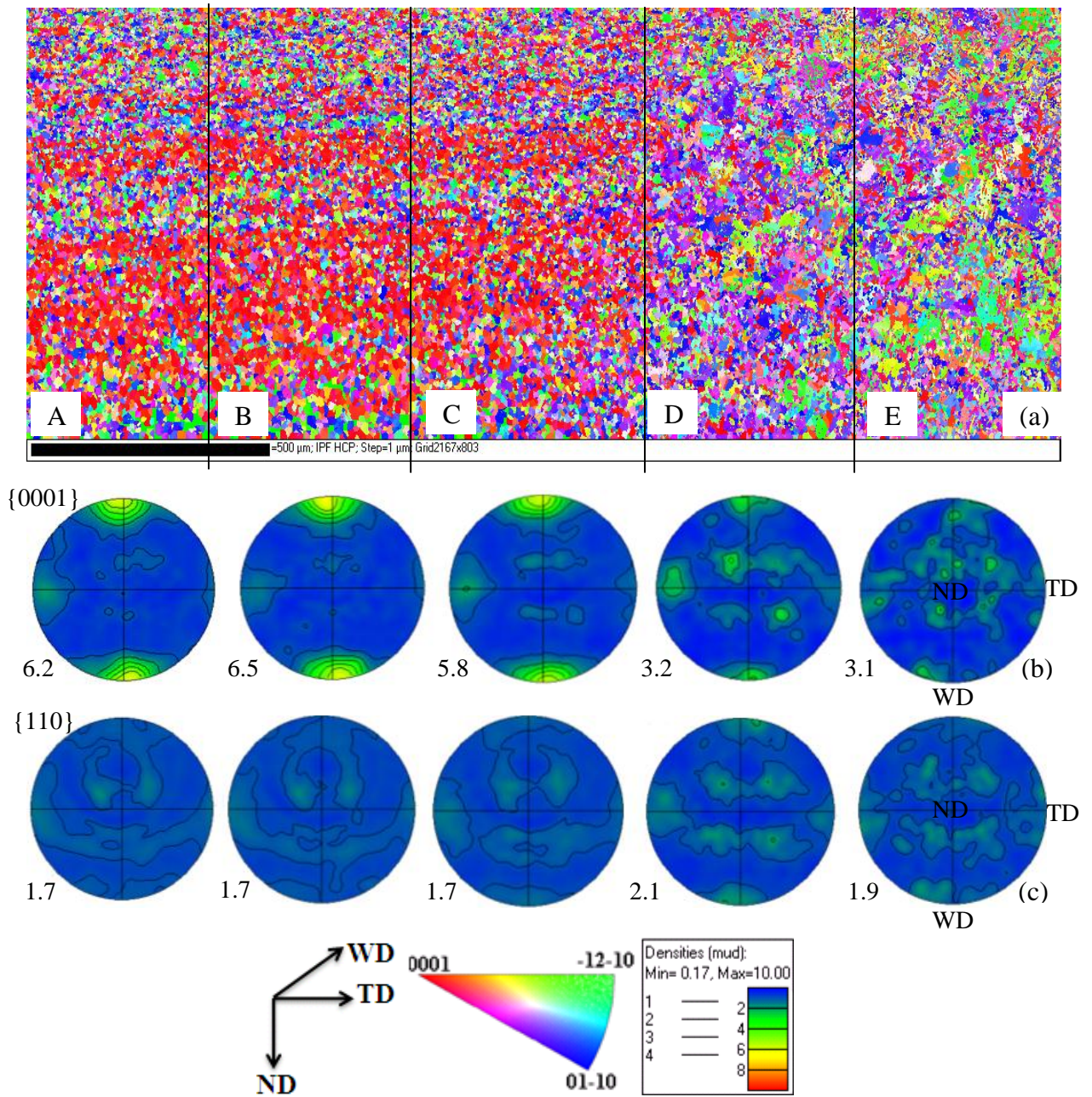
Figure 6.34 (a) IPF map of the transition zone at the RS of W5; (b) {0001} pole figures of the room temperature α phase; (c) {110} pole figures of the room temperature β phase

IPF map taken from the AS of the welding edge of W5 is shown in Figure 6.35(a), which was divided into four zones, corresponding to fully transformed lamellar structure (A), bimodal structure (B), equiaxed parent structure (C and D), {0001} PFs of the α phase texture and {110} PFs of retained β phase texture are shown in Figure 6.35(b) and (c), respectively. The welding axes, IPF colour key for the α phase and pole figure density bars are shown at the bottom of the figures. It is clearly seen that the α phase texture starts to

change at the bimodal structure (Section B) while the β phase texture of the bimodal structure retains the same as the base material (Section C and D). This would suggest that in Section B, C and D, the material has not been deformed because the β texture remains the same as the BM (C and D); Section A has undergone deformation because both the α and β texture have changed and it must be part of the TMAZ whilst the material in Section B constitute the HAZ.
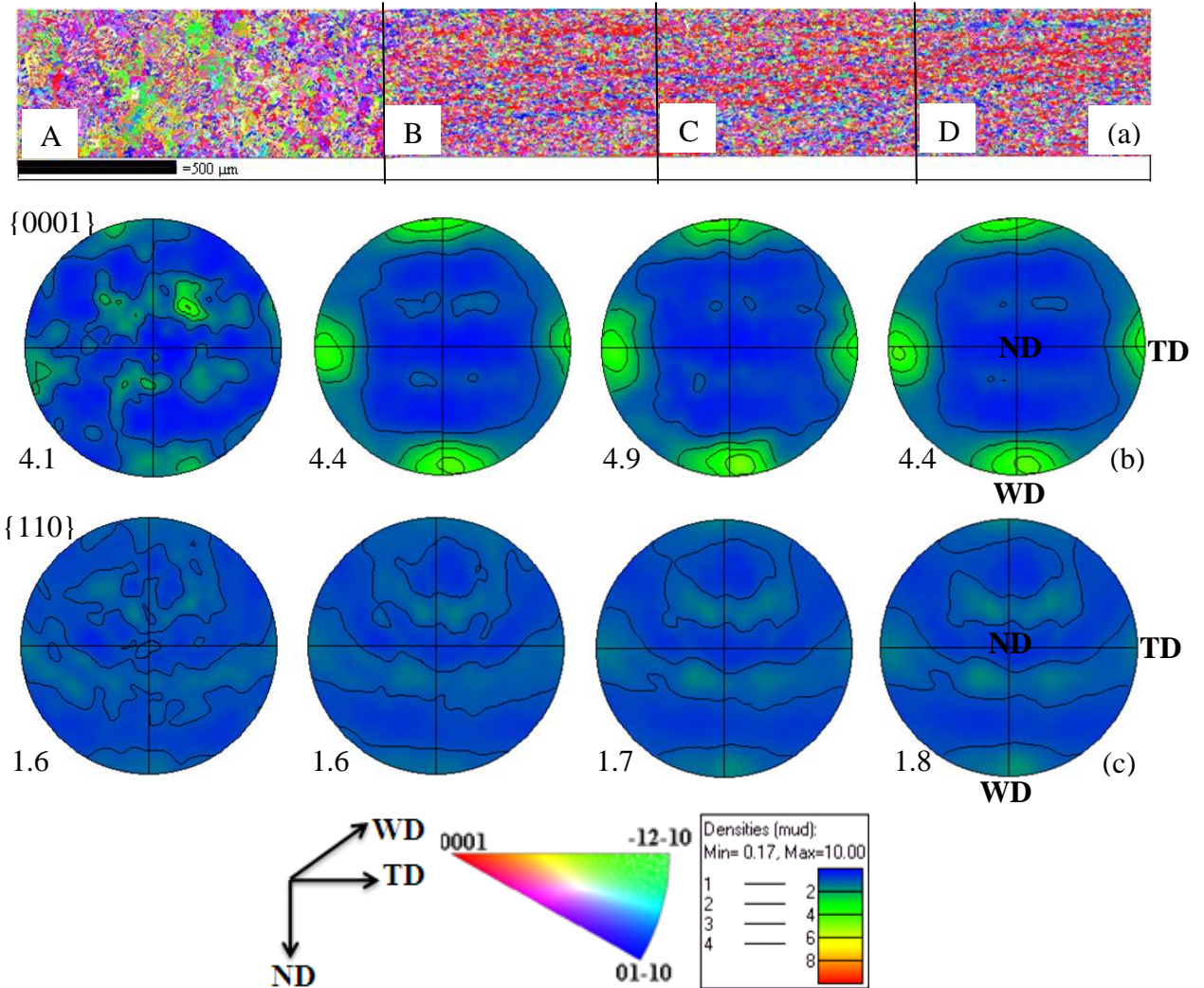


Figure 6.35 (a) IPF map of the transition zone at the AS of W5; (b) {0001} pole figures of the room temperature α phase; (c) {110} pole figures of the room temperature β phase

Figure 6.36(a) is an IPF map taken from the RS of the welding edge of W6 and the map has been divided into four zones: bimodal structure (A), fully transformed lamellar structure (B, C and D), and the α phase (hcp) texture and retained β phase (bcc) texture are represented by the {0001} PFs and {110} PFs, respectively, as shown in Figure 6.36(b) and (c). The welding axes, IPF colour key for the α phase and pole figure density bars are shown at the bottom of the figures. It is seen in Section A that the α phase texture has changed while the β phase texture retains the same as the BM, which indicates that the material in Section A has not been deformed and Section A must be the HAZ. Both the α and β texture of Section B, C and D with lamellar structure have changed indicating that the material has undergone deformation and there is a variation in both the α and β texture of Section B, C and D in terms of rotation of the 45° component and pole intensity. It should be noted that Section B and C have stable 45° component in α texture, while the 45° component in α texture of Section D tends to be diffuse and easily breaks up in to new texture component. This would suggest that Section B and C must be part of the TMAZ and Section D is a part of the SZ.
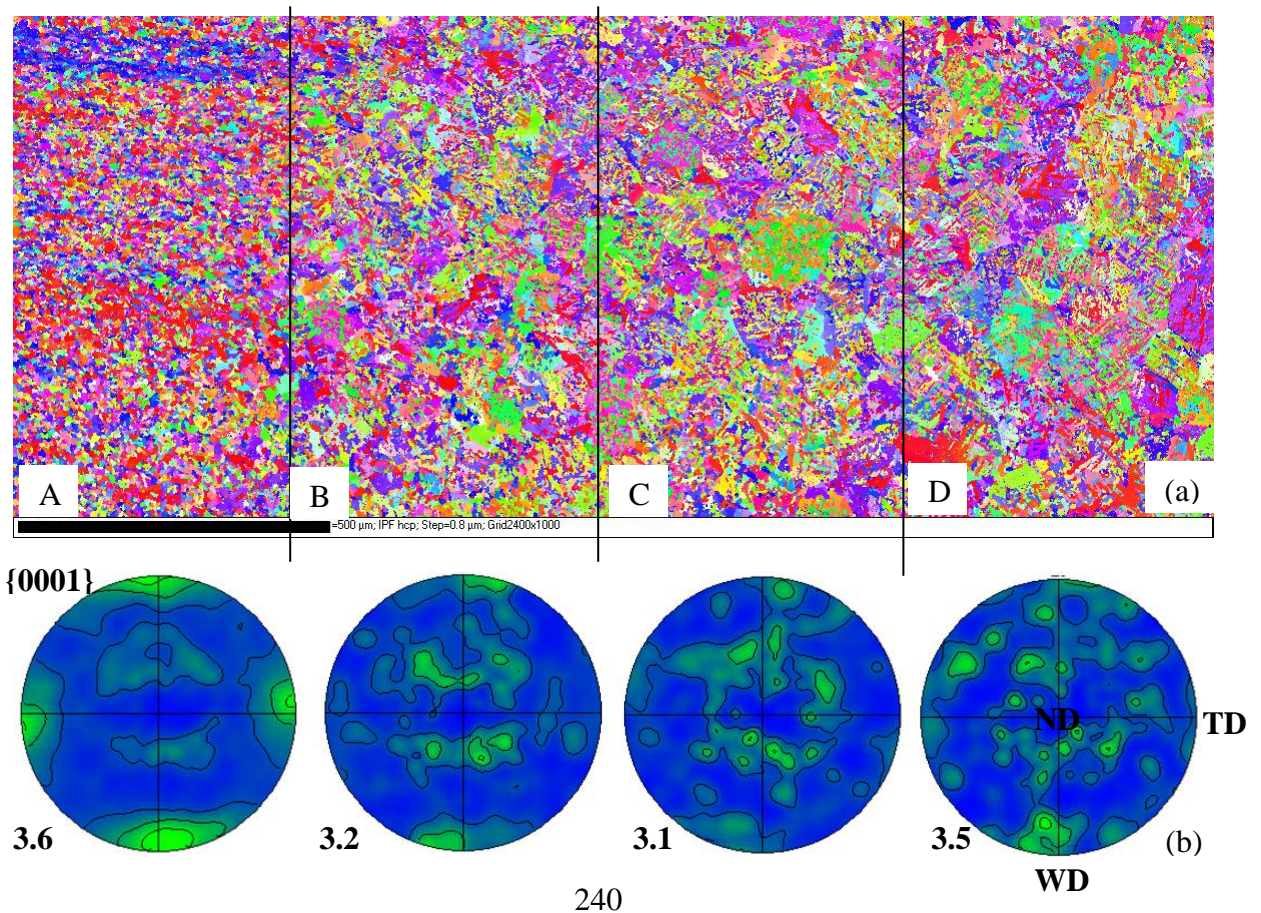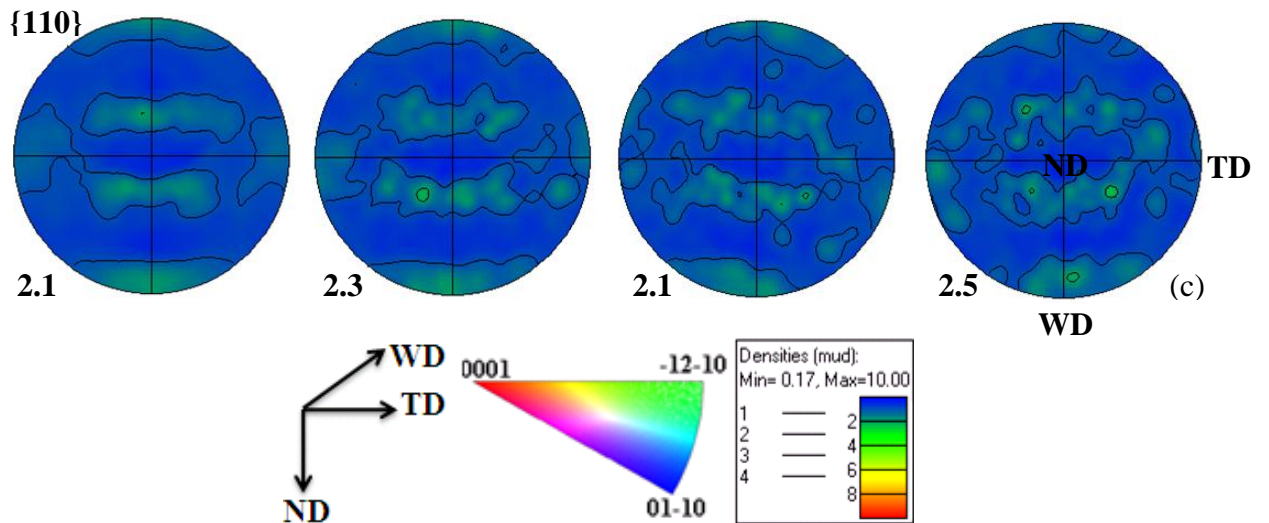
Figure 6.36 (a) IPF map of the transition zone at the RS of W6; (b) {0001} pole figures of the room temperature α phase; (c) {110} pole figures of the room temperature β phase

IPF map taken from the AS of the welding edge of W6 is shown in Figure 6.37(a), which was divided into four zones, they are Section A and B with lamellar structure, Section C with bimodal structure and Section D with equiaxed structure. {0001}PFs of the α phase texture and {110} PFs of retained β phase texture are shown in Figure 6.37(b) and (c), respectively. The welding axes, IPF colour key for the α phase and pole figure density bars are shown at the bottom of the figures. It is seen that the α phase texture starts to change at Section C while the β phase texture of Section C retains the same as the BM (Section D). This would suggest that in Section C and D, the material has not been deformed because the β texture remains the same, thus, the material in Section C constitute the HAZ. Both the α and β texture of Section B and A have changed indicating that the material has undergone deformation and both Section B and A have stable 45° component in α texture, thus they must be part of the TMAZ.

**{0001}**

5.1    4.1    6.8    6.2    (b)

**{110}**

2.4    2.1    1.9    1.9    (c)
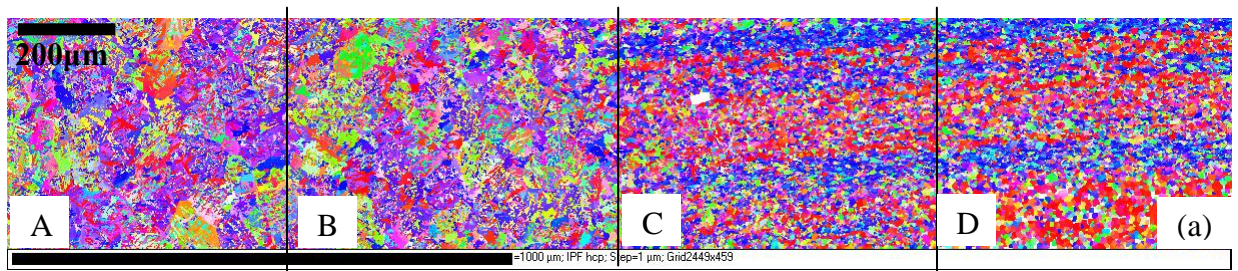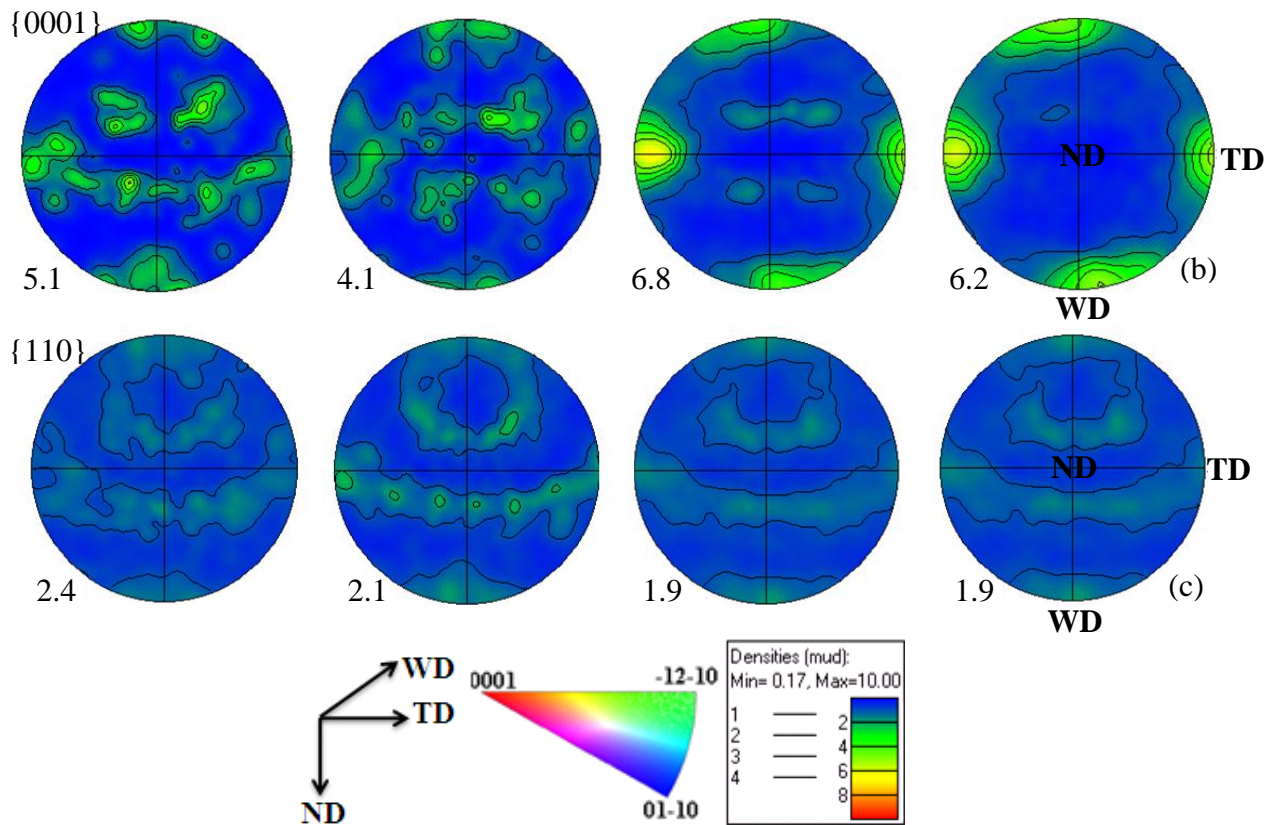
Figure 6.37 (a) IPF map of the transition zone at the AS of W6; (b) {0001} pole figures of the room temperature α phase; (c) {110} pole figures of the room temperature β phase

*6.2.3.4 W19-800rpm*

Figure 6.38(a) is an IPF map taken from the RS of the welding edge of W19, for convenience, the map has been divided into four zones, corresponding to equiaxed parent structure (A+B), bimodal structure (C), fully transformed lamellar structure (D). The α phase (hcp) texture and retained β phase (bcc) texture are represented by the {0001} PFs and {110} PFs, respectively, as shown in Figure 6.38(b) and (c). The welding axes, IPF colour key for the α phase and pole figure density bars are shown at the bottom of the figures. It is clearly seen that the α phase texture starts to change at the bimodal structure (C) while the β phase texture of the bimodal structure retains the same as the base material (A+B). This would suggest that in Section A, B and C the material has not been deformed because the β texture remains the same as the BM (A+B) and the material in Section C constitutes the HAZ. Both the α and β texture of Section D have changed indicating that the material has undergone deformation and thus they must be part of the TMAZ.
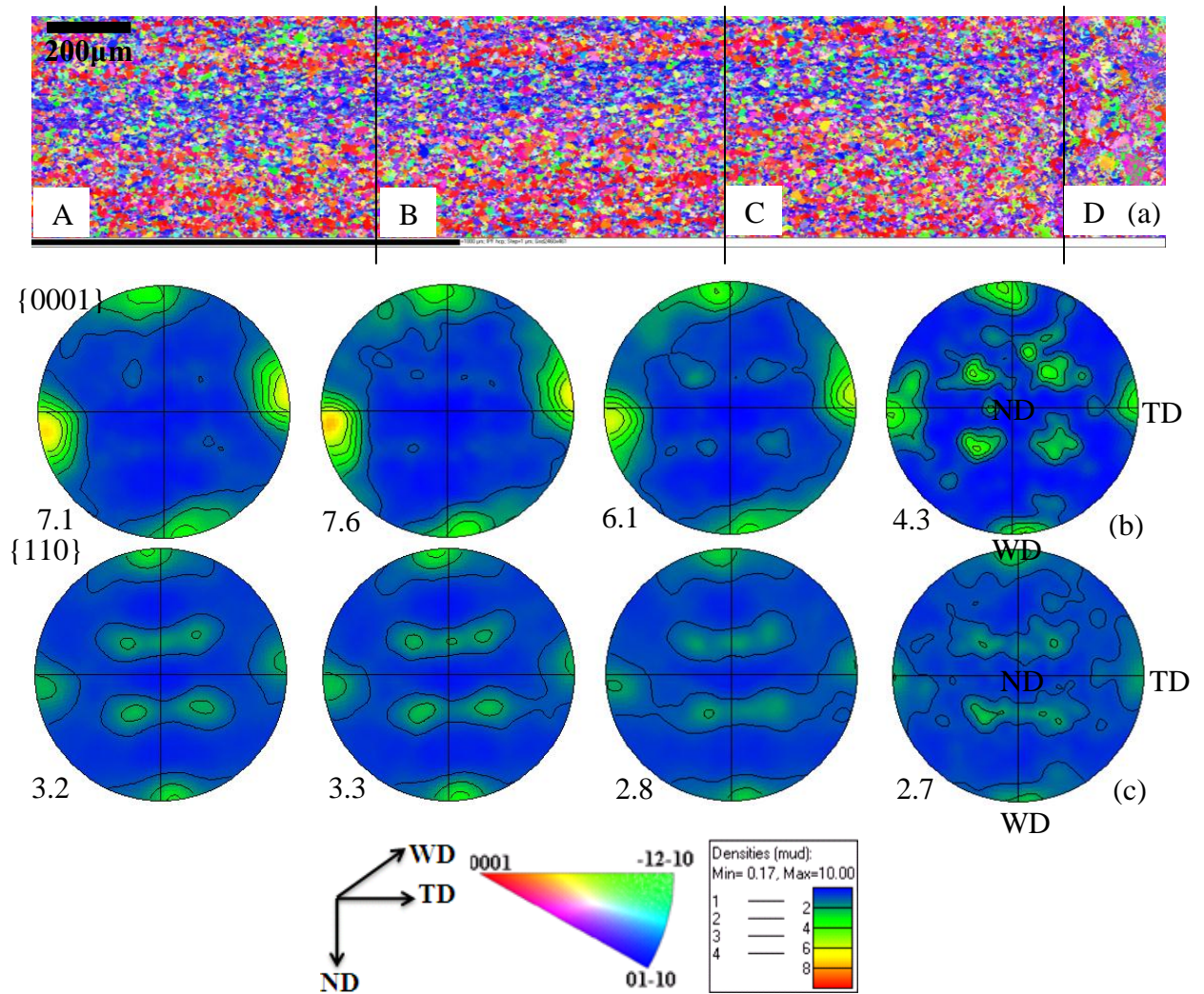
Figure 6.38 (a) IPF map of the transition zone at the RS of W19; (b) {0001} pole figures of the room temperature α phase; (c) {110} pole figures of the room temperature β phase

Figure 6.39(a) shows the IPF map taken from the AS of the welding edge of W19, which was divided into three zones: fully transformed lamellar structure (A), bimodal structure (B), equiaxed parent structure (C), {0001} PFs of the α phase texture and {110} PFs of retained β phase texture are shown in Figure 6.39(b) and (c), respectively. The welding axes, IPF colour key for the α phase and pole figure density bars are shown at the bottom of the figures. It is clearly seen that in Section B, the α phase texture starts to change, while the β phase texture of the bimodal structure retains the same as the BM (Section C). This meant that in Section B and C, the material has not been deformed because the β texture remains the same, thus Section B must be the HAZ. Both the α and β

texture of Section A have changed indicating that the material has undergone deformation and thus they must be part of the TMAZ.
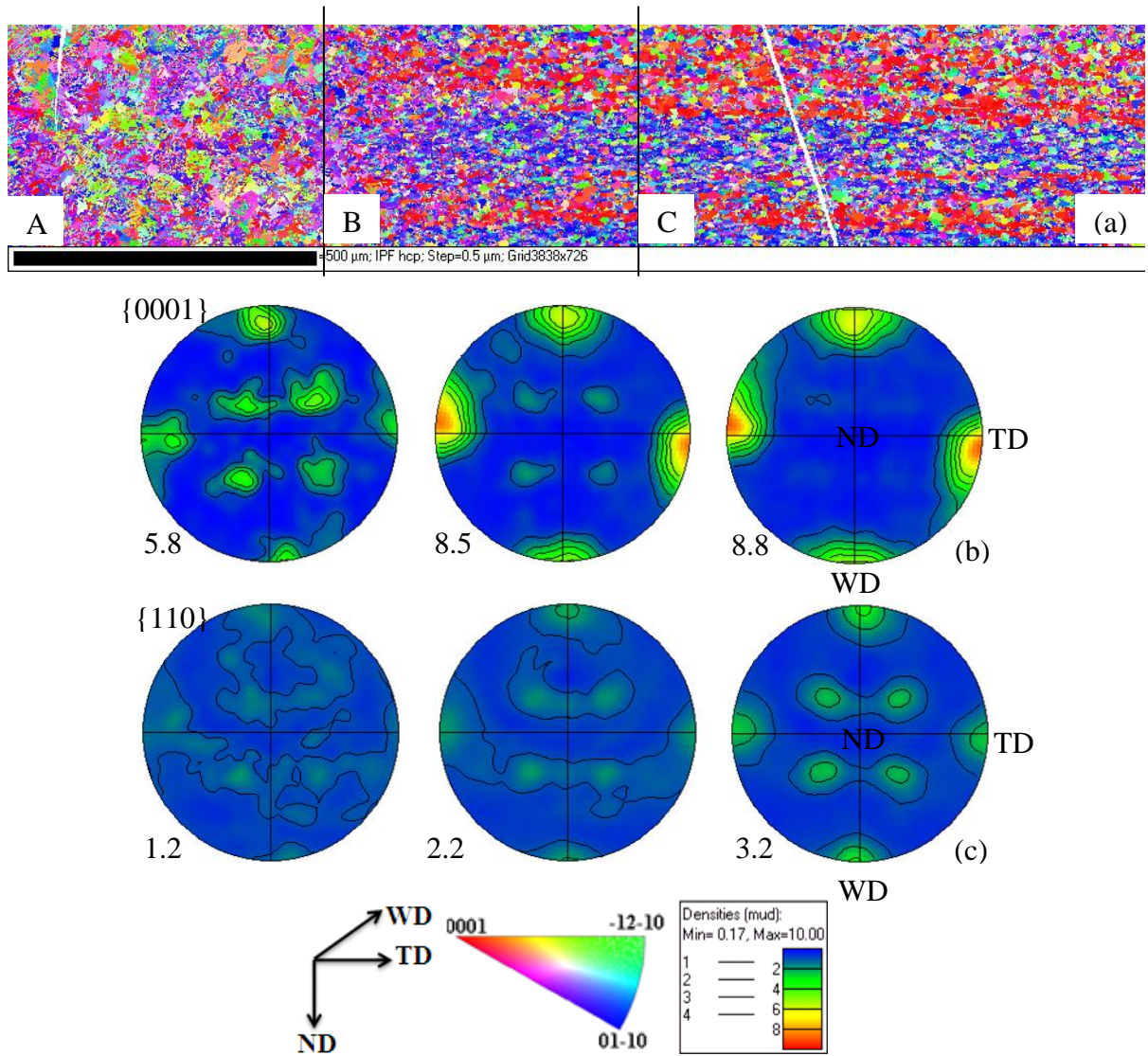


Figure 6.39 (a) IPF map of the transition zone at the AS of W19; (b) {0001} pole figures of the room temperature α phase; (c) {110} pole figures of the room temperature β phase

*6.2.3.5 W20-600rpm*

Figure 6.40 (a) is an IPF map taken from the AS of the welding edge of W20, for convenience, the map has been divided into four zones, corresponding to equiaxed parent structure (A+B), bimodal structure (C), fully transformed lamellar structure (D). The α phase (hcp) texture and retained β phase (bcc) texture are represented by the {0001} PFs

and {110} PFs, respectively, as shown in Figure 6.40(b) and (c). The welding axes, IPF colour key for the α phase and pole figure density bars are shown at the bottom of the figures. It is clearly seen that in Section B, the α phase texture starts to change while the β phase texture of the bimodal structure retains the same as the base material (A). The result demonstrates that the material in Section B has not been deformed because the β texture remains the same and Section B must be the HAZ. Both the α and β texture of Section C and D have changed indicating that the material has undergone deformation and thus they must be part of the TMAZ.
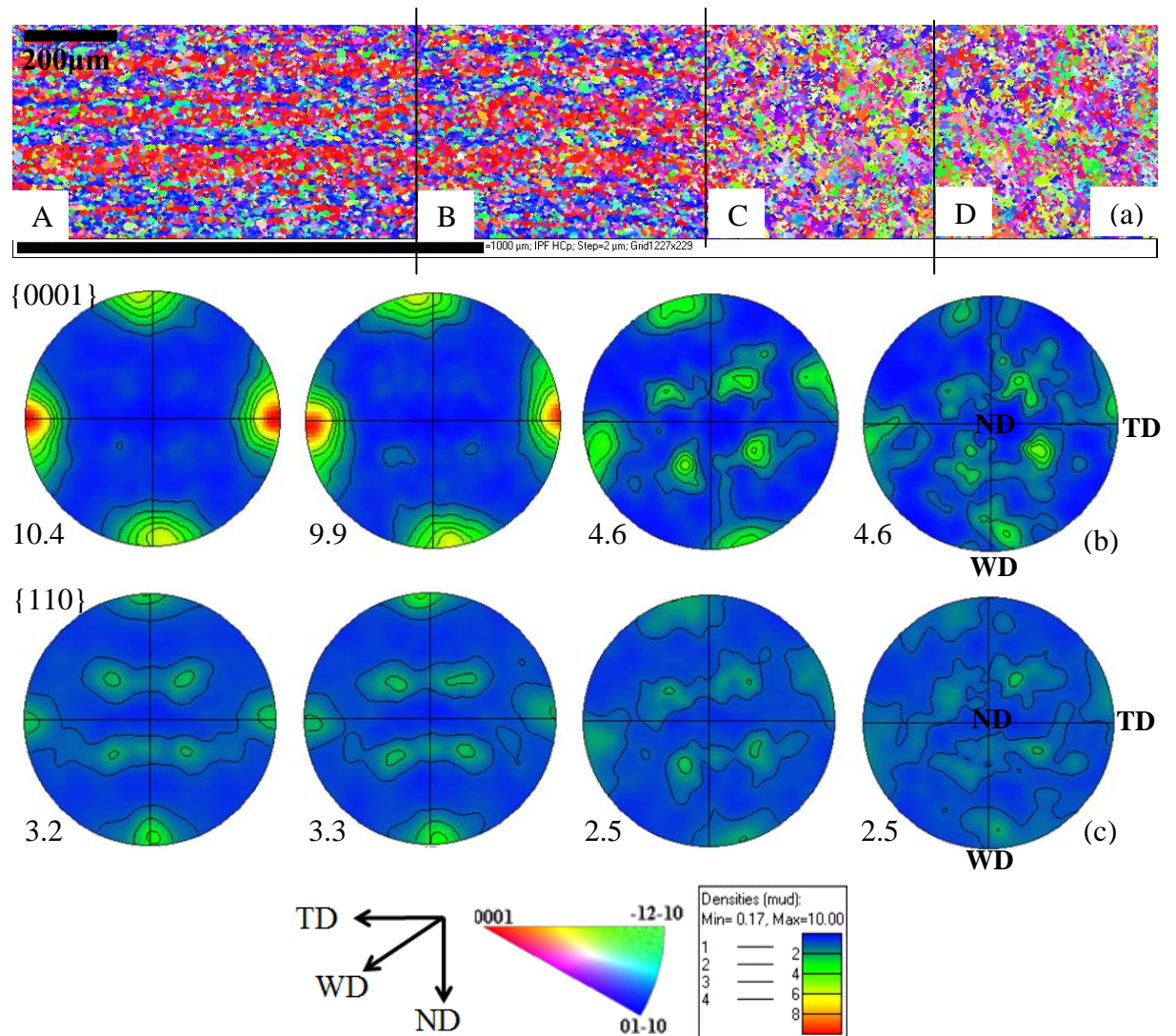


Figure 6.40 (a) IPF map of the transition zone at the AS of W20; (b) {0001} pole figures of the room temperature α phase; (c) {110} pole figures of the room temperature β phase

245

Figure 6.41(a) is an IPF map taken from the RS of the welding edge of W20, which was divided into four zones, corresponding to fully transformed lamellar structure (A+B), bimodal structure (C), equiaxed parent structure (D), {0001} PFs of the α phase texture and {110} PFs of retained β phase texture are shown in Figure 6.41(b) and (c), respectively. The welding axes, IPF colour key for the α phase and pole figure density bars are shown at the bottom of the figures. It was shown that the α phase texture starts to change at Section C while the β phase texture in Section C retains the same as the BM (Section D). This meant that the material has not been deformed in Section C and Section C constitutes the HAZ. Both the α and β texture of Section B and A have changed indicating that the material has undergone deformation and Section B has clear 45° component in α texture while Section A has fuzzy shear texture. Thus, Section B must be the TMAZ and Section A belongs to part of the SZ.
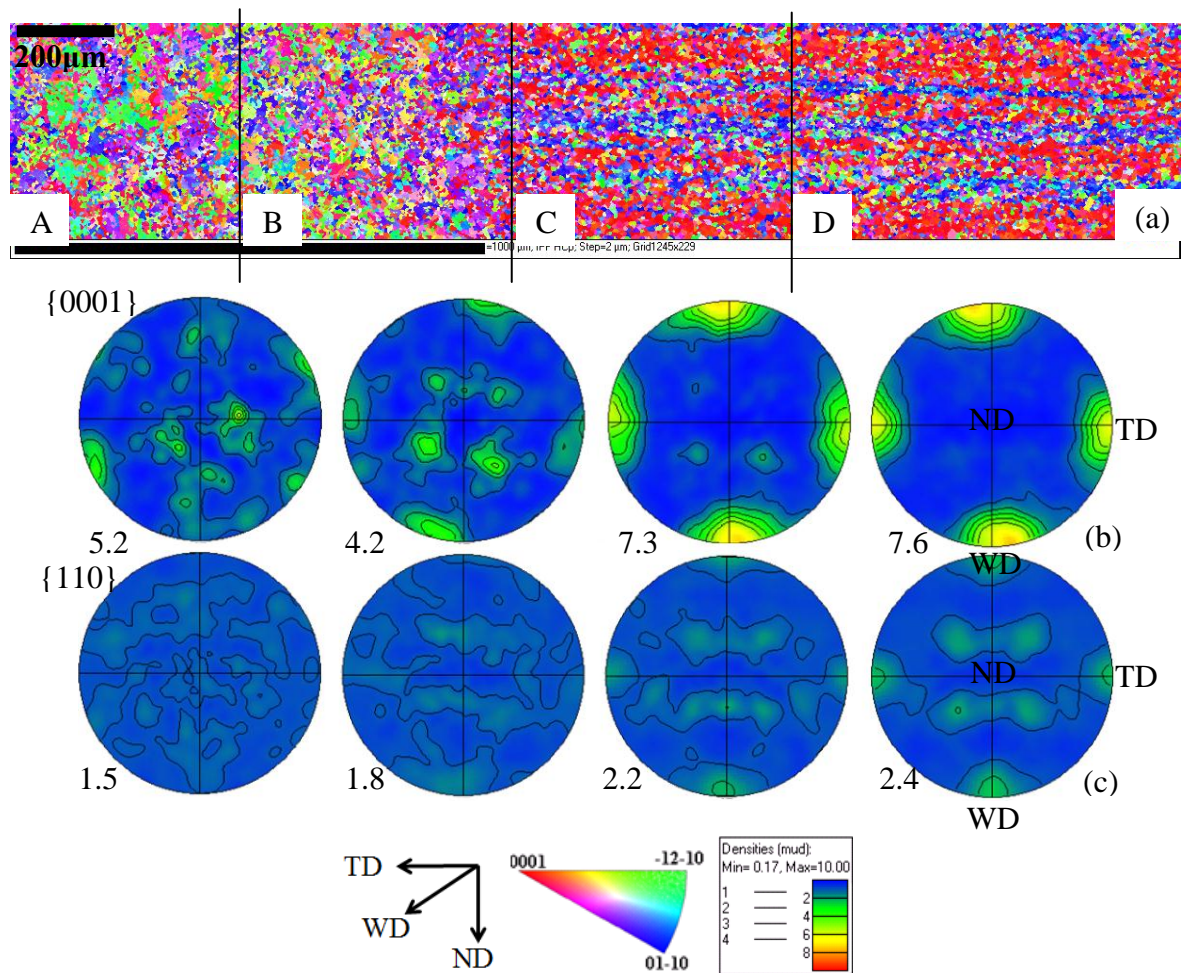


Figure 6.41 (a) IPF map of the transition zone at the RS of W20; (b) {0001} pole figures of the room temperature α phase; (c) {110} pole figures of the room temperature β phase

Figure 6.42(a) is an IPF map taken from the AS of the welding edge of W21, which has been divided into four zones: Section A with equiaxed parent structure, Section C with bimodal structure, Section D with lamellar structure. The α phase (hcp) texture and retained β phase (bcc) texture are represented by the {0001} PFs and {110} PFs, respectively, as shown in Figure 6.42(b) and (c). The welding axes, IPF colour key for the α phase and pole figure density bars are shown at the bottom of the figures. It is seen that in Section C, the α phase texture starts to change while the β phase retains the same as the BM (A). This would suggest that in Section A and B, the material has not been deformed because the β texture remains the same as the BM. Both the α and β texture of Section C have changed indicating that the material has experienced deformation and thus they must be part of the TMAZ whilst the material in Section B constitute the HAZ.
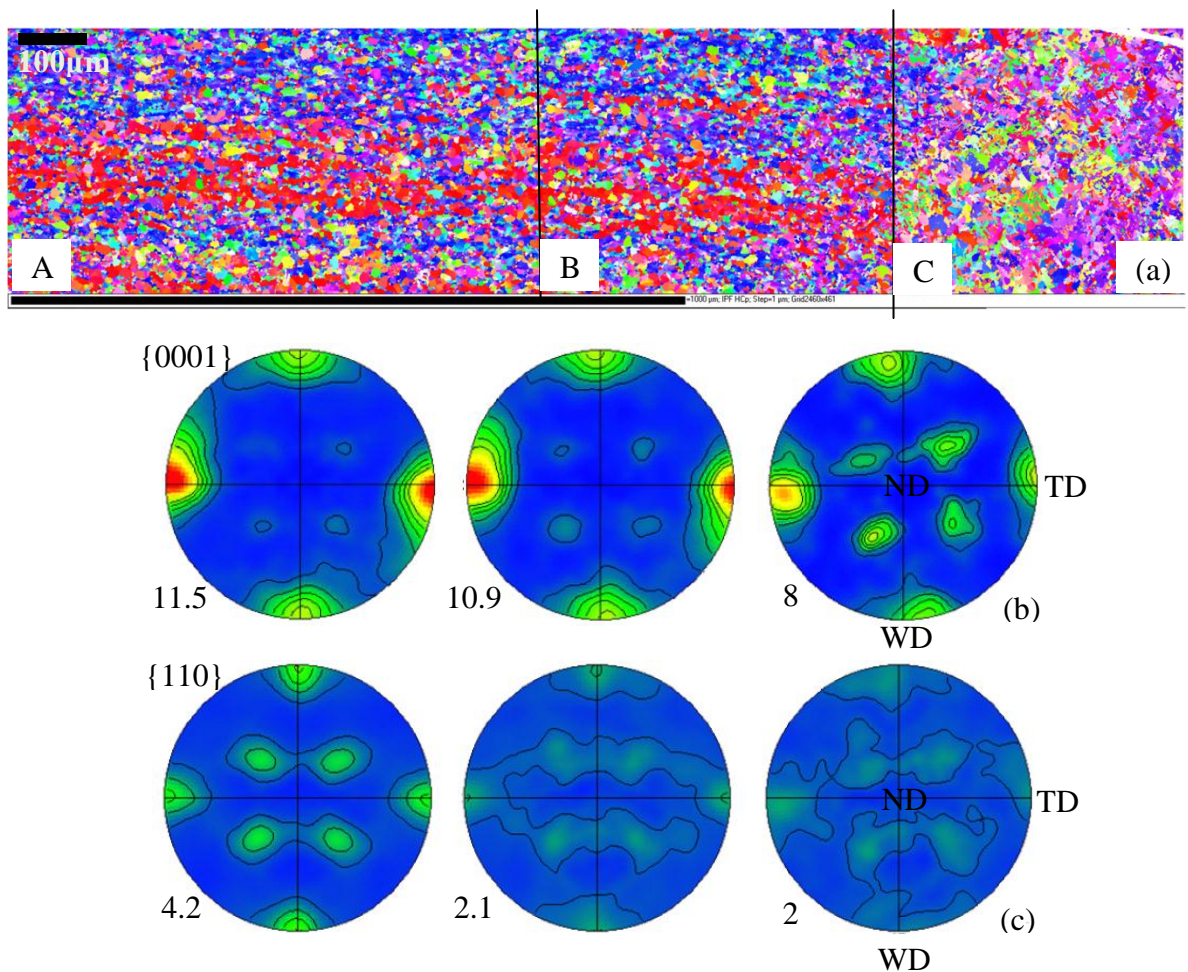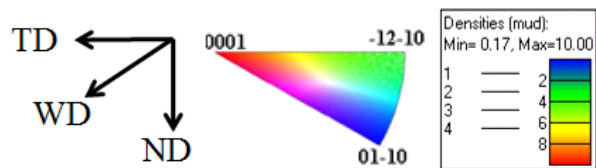
Figure 6.42 (a) IPF map of the transition zone at the AS of W21; (b) {0001} pole figures of the room temperature α phase; (c) {110} pole figures of the room temperature β phase

IPF map taken from the RS of the welding edge of W21 is shown in Figure 6.43(a), and the map was divided into three zones: lamellar structure (A and B), bimodal structure (C) and equiaxed parent structure (D). {0001}PFs of the α phase texture and {110} PFs of retained β phase texture are shown in Figure 6.43(b) and (c), respectively. The welding axes, IPF colour key for the α phase and pole figure density bars are shown at the bottom of the figures. The result demonstrates that the α phase texture starts to change at Section C while the β phase texture of the bimodal structure retains the same as the BM (Section D). Thus, in Section C, the material has not been deformed because the β texture remains the same as the BM. This suggests that Section C must be the HAZ. Both the α and β texture of Section B and Section A have changed indicating that the material has undergone deformation. It is seen from the α texture of Section A and Section B that Section A has developed shear texture showing D1 texture component while an unknown texture type appears in Section B, this unknown texture could be in between 45° component and D1 component. Thus, Section B must be part of the TMAZ.



248
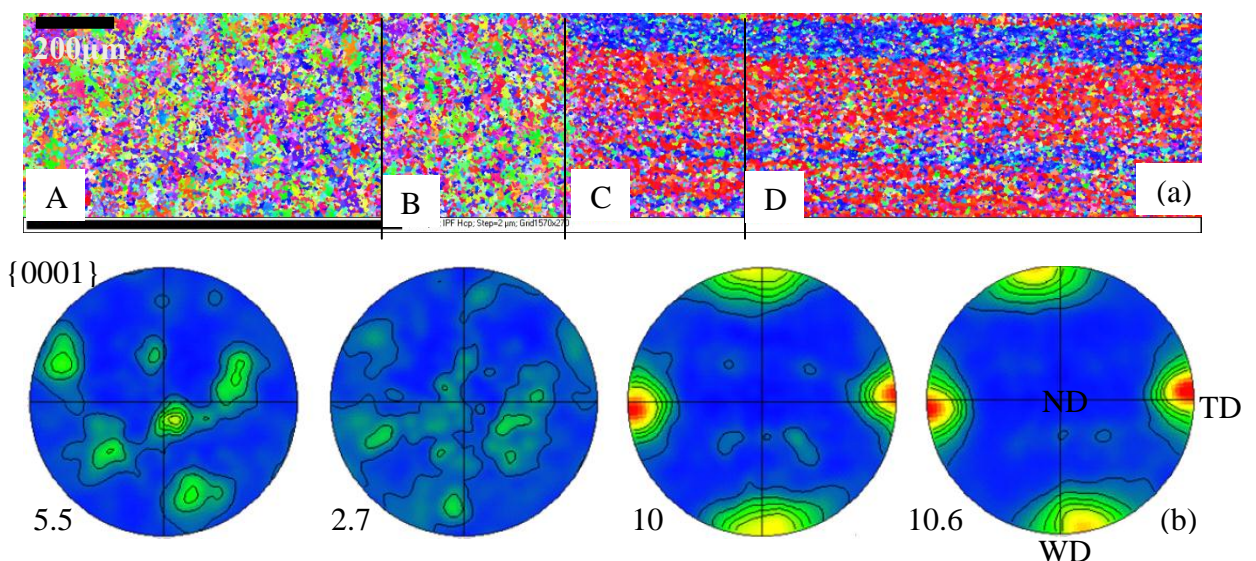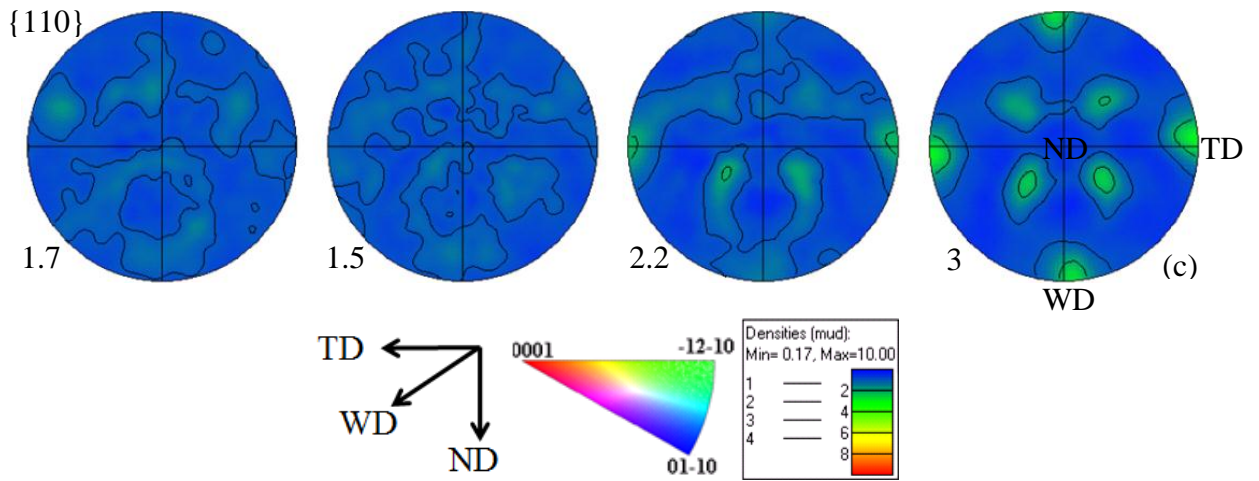
Figure 6.43 (a) IPF map of the transition zone at the RS of W21; (b) {0001} pole figures of the room temperature α phase; (c) {110} pole figures of the room temperature β phase

## 6.3 Misorientation axis distribution

6.3.1 High resolution EBSD maps of the welding edges

In order to investigate detailed texture evolution and texture change in the SZ, the TMAZ, the HAZ and the BM of the cross sections, misorientation analysis based on grain boundary angles and rotation axes were carried out on the four welds W4 (50mm/min and 900rpm), W5 (100mm/min and 900rpm), W19 (150mm/min and 800rpm) and W20 (150mm/min and 600rpm). Texture evolution from the BM to the TMAZ and the SZ can be obtained from the comparison of misorientation difference between different regions in the weld zones in terms of angle and axis, corresponding to the misorientation angle distribution and the rotation axes map. Misorientation angles are represented by grain boundary maps, where misorientation of 15° was used to separate the LAGBs from HAGBs. In misorientation distribution histograms, misorientation angles are often plotted against the relative frequency of themselves. Rotation axes maps are often shown as triangular maps consisting of rotation axes, namely, misorientation axes. Thus, texture evolution can be traced by misorientation analysis consisting of the HAGB spacing and texture strength.

EBSD map sized 2428.8μm×183.6μm taken from the AS of the welding edge of the weld W4 using a 0.2μm step size has been divided into four regions: the BM, the HAZ, the TMAZ and the SZ. Figure 6.44 shows the EBSD maps at the AS of the welding edge of the weld W4. And colour keys for IPF map, welding axes, pole figures are shown at the bottom

of the figures. IPF map is displayed in Figure 6.44(a), where grains are coloured with respect to the WD based on the colour key. Figure 6.44(b) is a grain boundary misorientation map consisting of LAGBs and HAGBs. Misorientation angle distribution plotted against relative frequency in Figure 6.44(c) describes the relative frequency of the misorientation angles ranged from 0° to 94.5°; Figure 6.44(d) shows the rotation axes in the crystal coordinate system at angles of 5°-15°, 25-35°, 55°-68° and 85°-95°. Figure 6.44(d) shows that misorientation axes distributions in the TMAZ, the HAZ and the BM are both characterized by clusters near the $\{0001\}$, $\{01\bar{1}0\}$ and $\{\bar{1}2\bar{1}0\}$ poles. Misorientation axes near the $\{0001\}$ poles consist of 5°-15° and 25°-35° boundaries. Misorientation axes at 55°-68° boundaries are clustering near the $\{\bar{1}2\bar{1}0\}$ poles and misorientations axes tend to cluster around $\{\bar{1}2\bar{1}0\}$poles at 85°-95° boundaries. It is seen that the SZ and the TMAZ have similar misorientation distribution in terms of clustering effect of $\{0001\}$, $\{01\bar{1}0\}$ and $\{\bar{1}2\bar{1}0\}$ poles at the misorientation angles of 5°-15°, 25°-35°, 55°-68° and 85°-95°, however, the SZ has stronger clustering effect of the $\{\bar{1}2\bar{1}0\}$ poles at 55°-68° boundaries. $\{0001\}$ poles at 5°-15° boundaries have stronger clustering effect in the SZ and the TMAZ compared to that in the HAZ, and it is stronger in the HAZ compared to that in the BM. The SZ and the TMAZ have stronger clustering effect of the $\{01\bar{1}0\}$ poles at 85°-95° boundaries than the HAZ which has stronger clustering effect of the $\{01\bar{1}0\}$ poles at 85°-95° boundaries than the BM. Table 6.6 lists the HAGB fraction and texture strength of the BM, the HAZ, the TMAZ and the SZ at the AS of the weld W4. The texture strength mentioned here corresponds to the maximal intensity of the $\{0001\}$ pole figures in unit of MUD.

(a)

(b)

(c)

Figure 6.44 EBSD data taken from the BM, the HAZ, the TMAZ and the SZ at the AS of the welding edge of the weld W4: (a) IPF map: grains are coloured with respect to the WD; (b) grain boundary misorientation map. LAGBs and HAGBs are drawn as silver (2º-15º) and black lines (>15º), respectively; (c) misorientation angle distribution plotted against relative frequency; (d) rotation axes at angles of 5º-15º, 25º-35º, 55º-68º and 85º-95º with respect to the crystal coordinate system

252

Table 6.6 HAGB fraction and texture strength of the BM, the HAZ, the TMAZ and the SZ
at the AS of the weld W4

| Weld zones | BM | HAZ | TMAZ | SZ |
|---|---|---|---|---|
| HAGB fraction, % | 77.5 | 86.4 | 93 | 93.1 |
| Texture strength | 7.8 | 8 | 7 | 15 |

EBSD map sized 1215.6μm×183.6μm using a 0.2μm step size taken from the RS of the welding edge of the weld W4 has been divided into three regions (the TMAZ, the HAZ and the BM). Figure 6.45(a, b) shows EBSD maps of the TMAZ, the HAZ and the BM at the RS of the weld W4. And misorientation analysis results are displayed in Figure 6.45(c). Figure 6.45(d) shows that misorientation axes distributions in the TMAZ, the HAZ and the BM are both characterized by clusters near the $\{0001\}$, $\{01\bar{1}0\}$ and $\{\bar{1}2\bar{1}0\}$ poles. And colour keys for IPF map, welding axes, pole figures are shown at the bottom of the figures. Misorientation axes near the $\{0001\}$ poles consist of 5°-15° and 25°-35° boundaries. And the clustering effect of the $\{0001\}$ poles at 5°-15° boundaries is the highest in the TMAZ and it decreases from the HAZ to the BM; the clustering effect of the $\{0001\}$ poles at 25°-35° boundaries are the same for the TMAZ, the HAZ and the BM; $\{\bar{1}2\bar{1}0\}$ poles cluster at 25°-35° boundaries in the TMAZ only. Misorientations axes at 55°-68° boundaries are clustering near the $\{\bar{1}2\bar{1}0\}$ poles and the clustering effect decrease from the TMAZ to the HAZ and the BM. Misorientations axes tend to cluster around the $\{\bar{1}2\bar{1}0\}$ poles and $\{01\bar{1}0\}$ poles at 85°-95° boundaries. It can be seen that the clustering effect of the $\{\bar{1}2\bar{1}0\}$ poles and $\{01\bar{1}0\}$ poles at 85°-95° boundaries both decrease from the TMAZ to the HAZ and the BM. Table 6.7 lists the HAGB fraction and texture strength of the TMAZ, the HAZ and the BM at the RS of the weld W4. The texture strength corresponds to the maximum intensity of the $\{0001\}$ PFs.



100μm

(a)

(b)


(c)


(d)

254
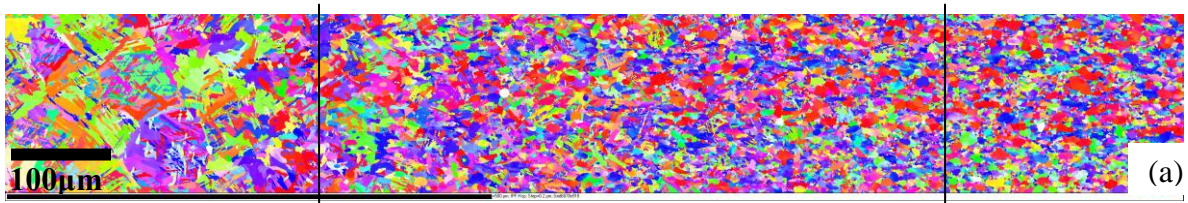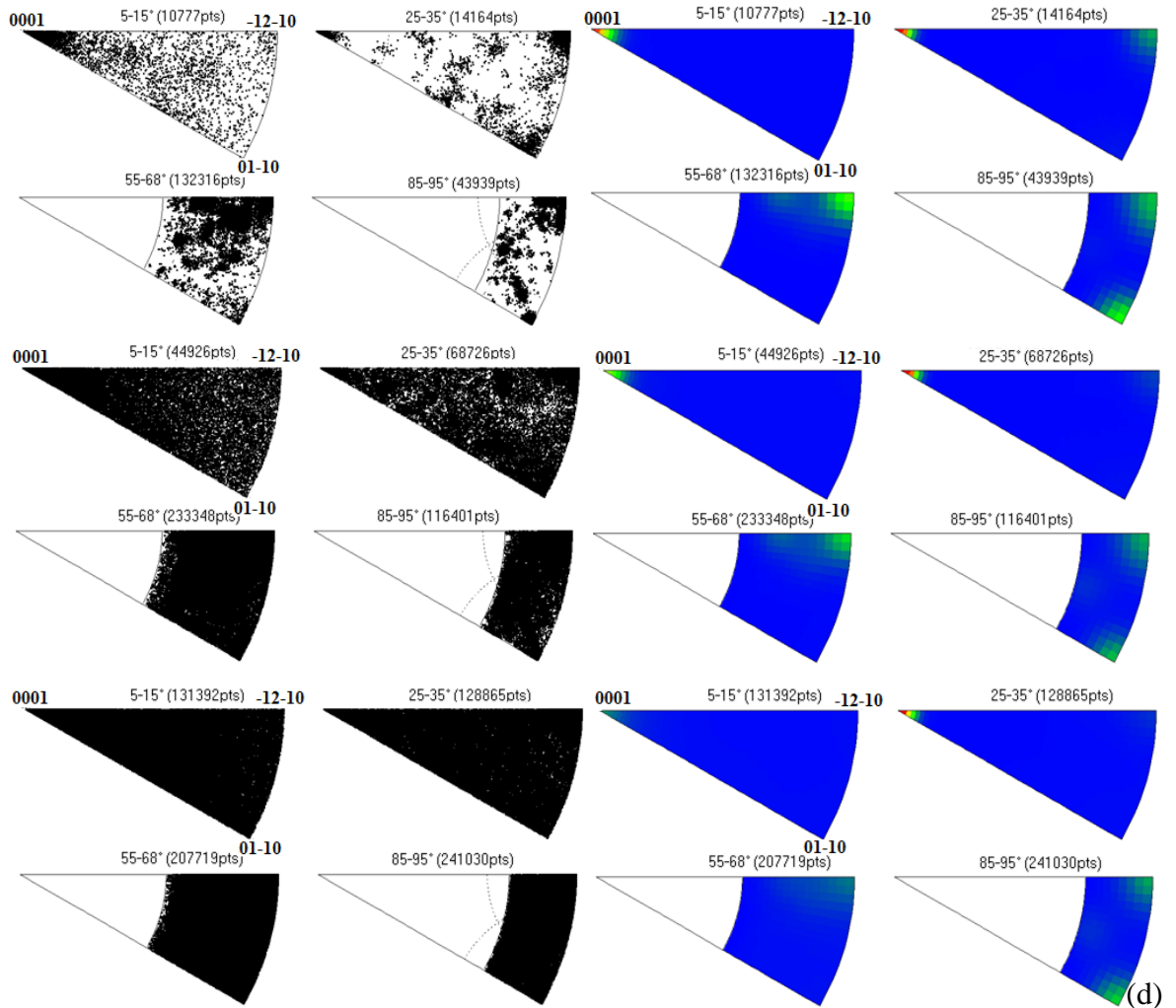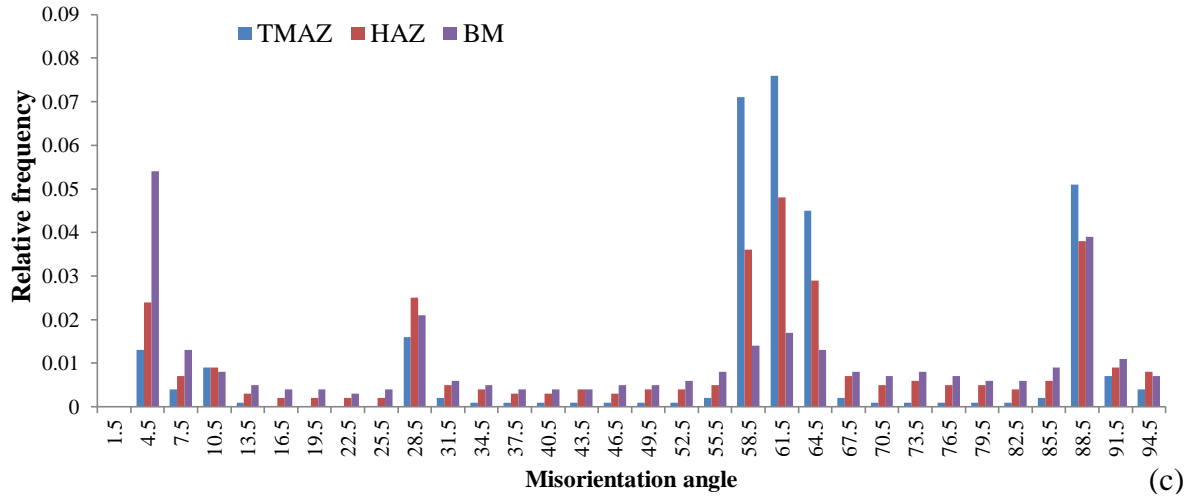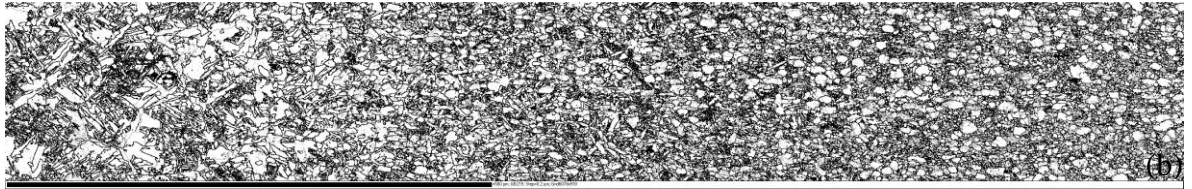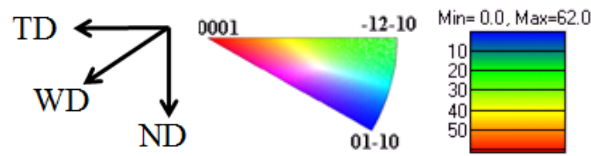
Figure 6.45 EBSD data taken from the TMAZ, the HAZ and the BM at the RS of the welding edge of the weld W4: (a) IPF map. Grains are coloured with respect to the WD; (b) grain boundary misorientation map. LAGBs and HAGBs are drawn as silver (2°-15°) and black lines (>15°), respectively. (c) misorientation angle distribution plotted against relative frequency; (d) rotation axes at angles of 5°-15°, 25°-35°, 55°-68° and 85°-95° with respect to the crystal coordinate system

Table 6.7 HAGB fraction and texture strength of the TMAZ, the HAZ and the BM at the RS of the weld W4

| Weld zones | TMAZ | HAZ | BM |
|---|---|---|---|
| HAGB fraction, % | 99.7 | 87.5 | 75 |
| Texture strength | 7.6 | 4.4 | 4.8 |

EBSD map sized 1491μm×365.5μm using 0.5μm step size taken from the AS of the welding edge of the weld W5 has been divided into three regions: the TMAZ, the HAZ and the BM. Figure 6.46(a and b) shows EBSD maps of the TMAZ, the HAZ and the BM at AS of the weld W5. And misorientation analysis results are displayed in Figure 6.46(c). Figure 6.46(d) shows that misorientation axes distributions in the TMAZ, the HAZ and the BM are both characterized by clusters near the $\{0001\}$, $\{01\bar{1}0\}$ and $\{\bar{1}2\bar{1}0\}$ poles. And colour keys for IPF map, welding axes, pole figures are shown at the bottom of the figures. Misorientation axes near the $\{0001\}$ poles consist of 5°-15° and 25°-35° boundaries for the BM and misorientation axes are clustering near the $\{0001\}$ and $\{\bar{1}2\bar{1}0\}$ poles at 25°-35° boundaries for the HAZ and the TMAZ. Misorientations axes at 55°-68° boundaries are clustering near the $\{\bar{1}2\bar{1}0\}$ poles and misorientations axes tend to cluster around the $\{01\bar{1}0\}$ and $\{\bar{1}2\bar{1}0\}$ poles at 85°-95° boundaries. It is seen that the TMAZ and the HAZ have stronger clustering effect of the $\{01\text{-}10\}$ poles at 55°-68° boundaries compared to the BM and the clustering effect of the $\{\bar{1}2\bar{1}0\}$ poles at 85°-95° boundaries decrease from the TMAZ to the HAZ and the BM. The clustering effect of the $\{01\bar{1}0\}$ poles at 85°-95°

boundaries in the TMAZ is stronger than that in the HAZ and the BM, it should be noted that the HAZ and the BM have the same clustering effect of the $\{01\bar{1}0\}$ poles at 85º-95° boundaries. Table 6.8 lists the HAGB fraction and texture strength of the TMAZ, the HAZ and the BM at the AS of the weld W5. The texture strength corresponds to the maximal intensity of the $\{0001\}$ PFs.



(a)



(b)



(c)
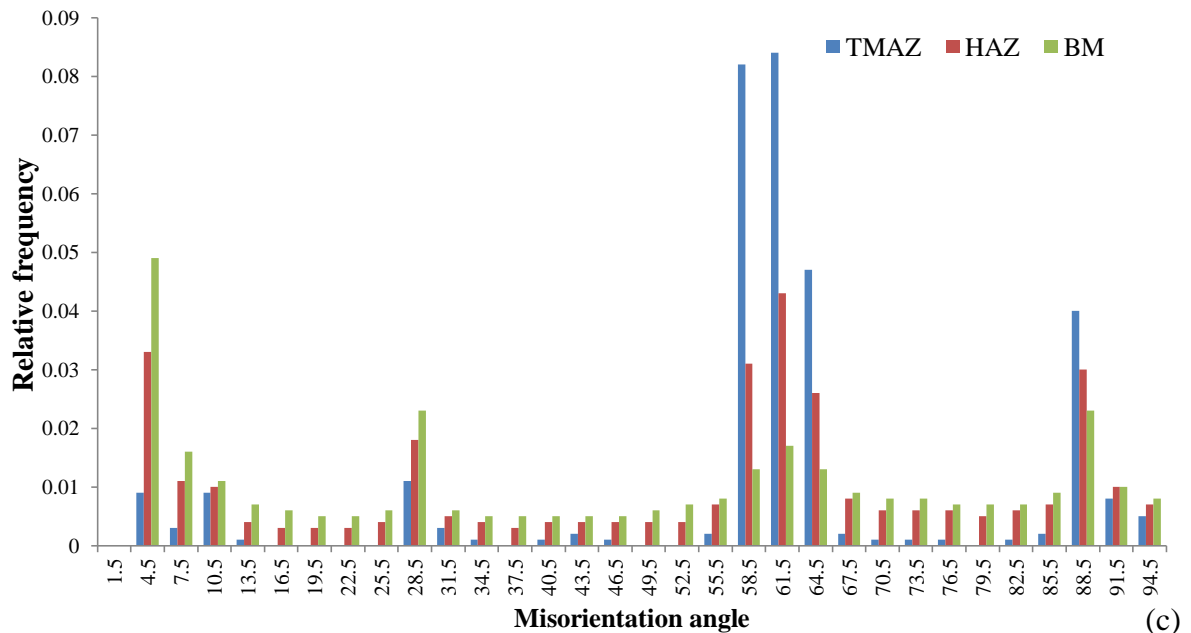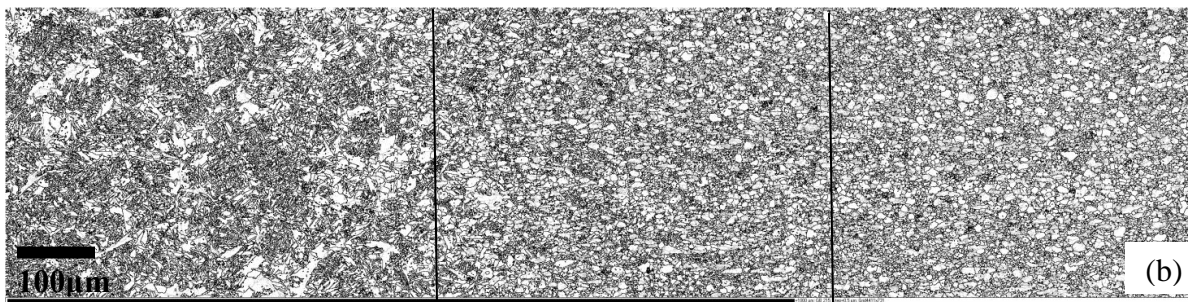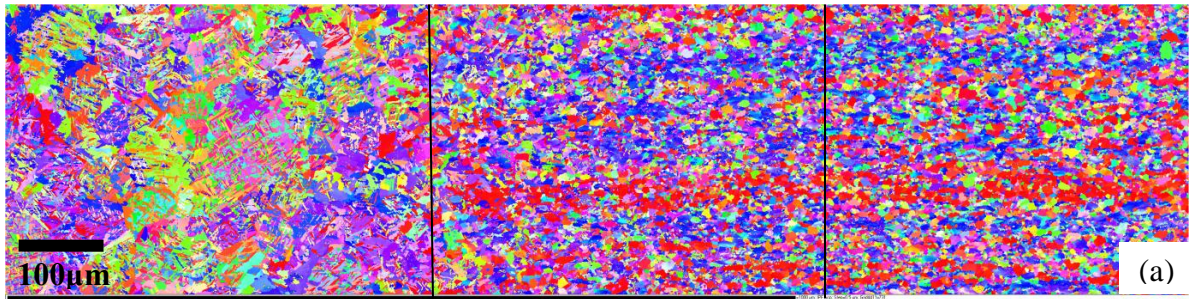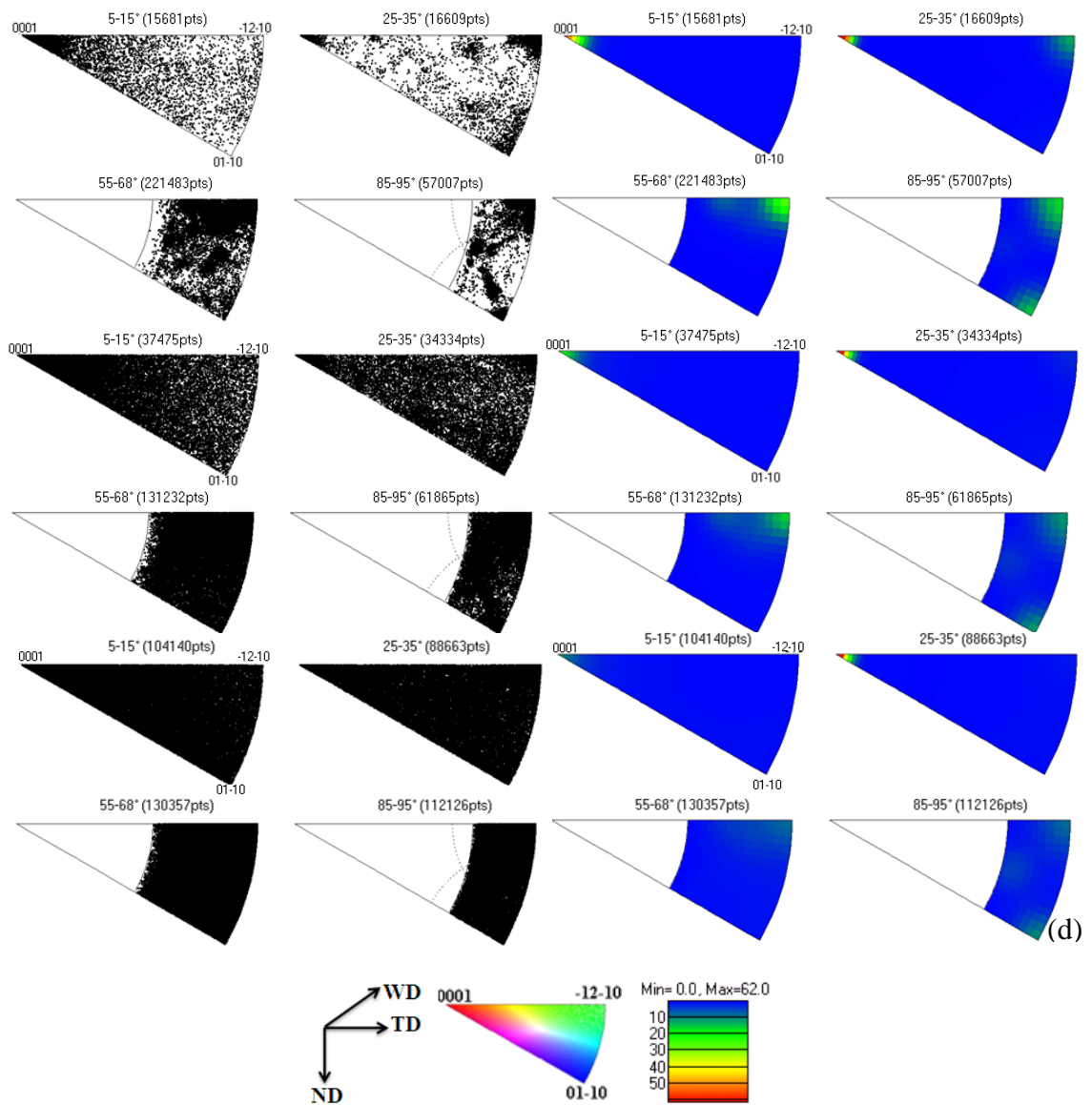
Figure 6.46 EBSD data taken from the TMAZ, the HAZ and the BM at the AS of the welding edge of the weld W5: (a) IPF map; (b) grain boundary misorientation map with LAGBs and HAGBs. (c) misorientation angle distribution plotted against relative frequency; (d) rotation axes with respect to the crystal coordinate system

Table 6.8 HAGB fraction and texture strength of the TMAZ, the HAZ and the BM at the AS of the weld W5

| Weld zones | TMAZ | HAZ | BM |
|---|---|---|---|
| HAGB fraction, % | 93 | 81.8 | 63.6 |
| Texture strength | 6.5 | 5.8 | 4.1 |

EBSD map sized 1211.6μm×183.8μm using a 0.2μm step size taken from the RS of the welding edge of the weld W5 has been divided into three regions: the BM, the HAZ and the TMAZ. Figure 6.47(a and b) shows EBSD maps of the BM, HAZ and TMAZ at AS of the weld W5. And misorientation analysis results are displayed in Figure 6.47(c). Figure 6.47(d) shows that misorientation axes near the {0001} poles consist of 5°-15º and 25°-35° boundaries. Colour keys for IPF map, welding axes, pole figures are shown at the bottom of the figures. It is seen that the clustering effect of the {0001} poles at 5°-15º boundaries is the highest in the TMAZ and it decreases from the HAZ to the BM, whereas, the clustering effect of the {0001} poles at 25°-35º boundaries are the same for the TMAZ, the HAZ and the BM. Misorientations axes at 25°-35° boundaries also cluster near the $\{\bar{1}2\bar{1}0\}$ poles and the clustering effect has weakened significantly from the TMAZ to the HAZ and the BM. Misorientations axes at 55º-68º boundaries are clustering near the $\{\bar{1}2\bar{1}0\}$ poles, the clustering effect of which is the strongest in the TMAZ and it decrease slightly from the TMAZ to the HAZ, however, the clustering effect decreases significantly from the HAZ to the BM. Misorientations axes of the BM, the HAZ and the TMAZ are both characterized by dense clusters near the $\{01\bar{1}0\}$ poles and the weak clusters near the $\{\bar{1}2\bar{1}0\}$ poles at 85º-95° boundaries. It was observed that the clustering effect of the $\{\bar{1}2\bar{1}0\}$ poles at 85º-95° boundaries decreases greatly from the TMAZ to the HAZ and the BM, whereas, the clustering effect of the $\{01\bar{1}0\}$ poles at 85º-95° boundaries is the same for both the TMAZ, the HAZ and the BM. Table 6.9 lists the HAGB fraction and texture strength of the BM, the HAZ and the TMAZ at the RS of the weld W5. The texture strength corresponds to the maximal intensity of the {0001} PFs.

Table 6.9 HAGB fraction and texture strength of the BM, the HAZ and the TMAZ at the RS of the weld W5

| Weld zones | BM | HAZ | TMAZ |
|---|---|---|---|
| HAGB fraction, % | 76.2 | 84 | 90 |
| Texture strength | 5.7 | 5.7 | 6.5 |

(a)

(b)

(c)
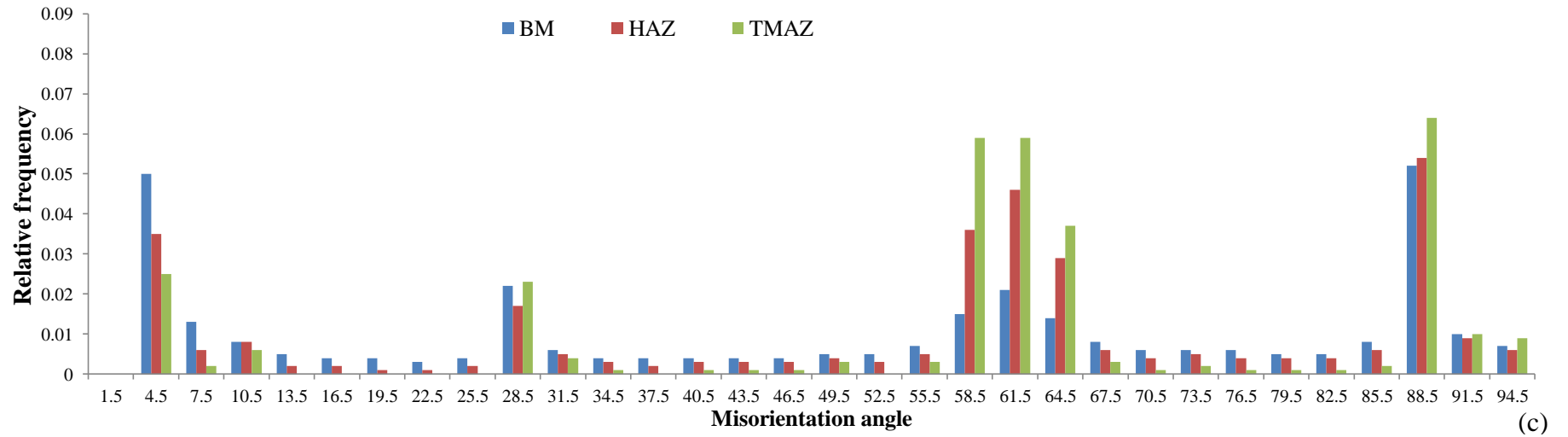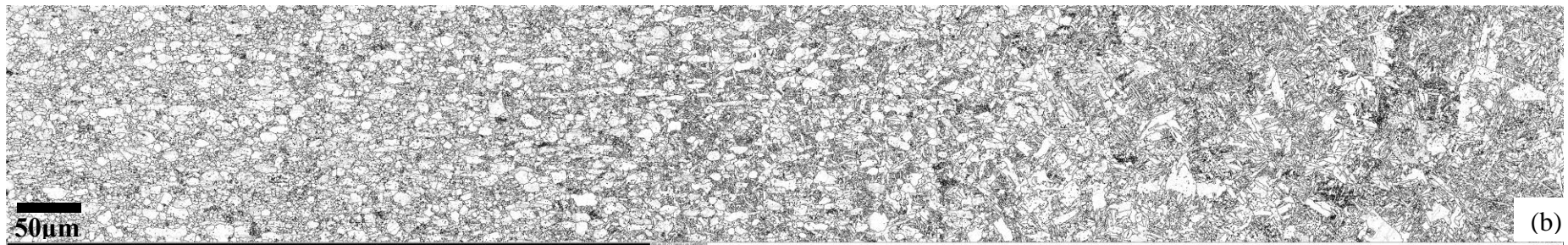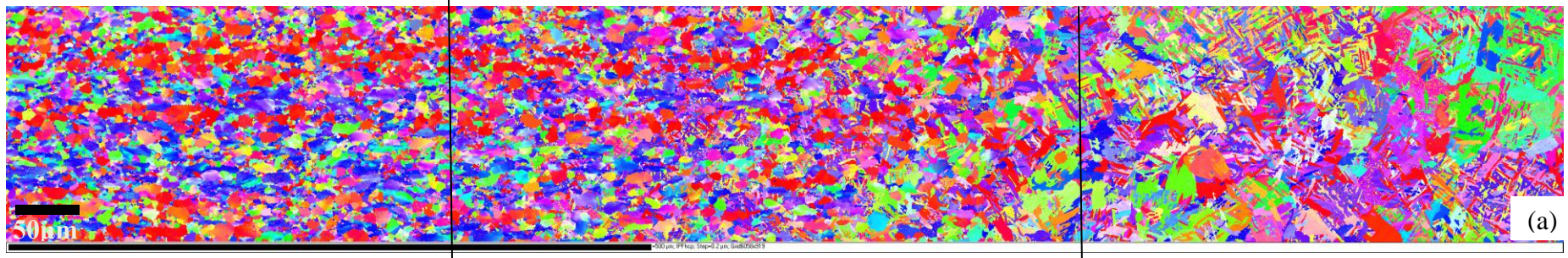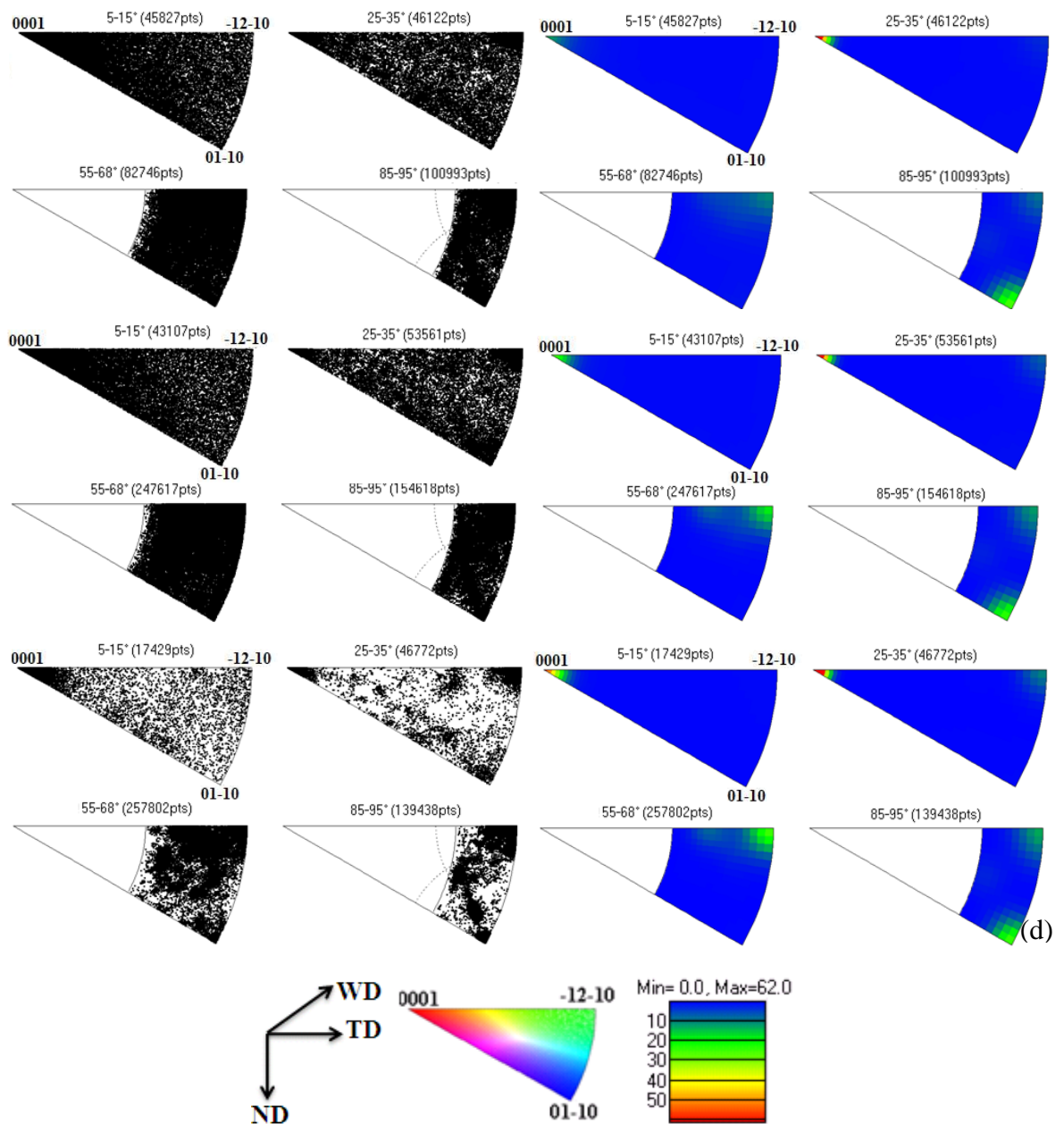
Figure 6.47 EBSD data taken from the BM, the HAZ and the TMAZ at the RS of the welding edge of the weld W5: (a) IPF map. Grains are coloured with respect to the WD according to colour key shown at the bottom of the figures; (b) grain boundary misorientation map. LAGBs and HAGBs are drawn as silver (2º-15º) and black lines (>15º), respectively. (c) misorientation angle distribution plotted against relative frequency; (d) rotation axes at angles of 5º-15º, 25º-35º, 55º-68º and 85º-95º with respect to the crystal coordinate system

EBSD map sized 1496μm×367μm using 0.3μm step size taken from the AS of the welding edge of the weld W19 has been divided into three regions: the TMAZ, the HAZ and the BM. Figure 6.48(a and b) shows EBSD maps of the TMAZ, the HAZ and the BM

at AS of the weld W5. And misorientation analysis results are displayed in Figure 6.48(c). Figure 6.48(d) shows that misorientation axes of of the TMAZ, the HAZ and the BM at 5°-15º and 25°-35° boundaries cluster near the {0001} poles only. Colour keys for IPF map, welding axes, pole figures are shown at the bottom of the figures.

Figure 6.48(d) shows that {0001} poles at 5°-15º boundaries have stronger clustering effect in the TMAZ which becomes much weaker from the TMAZ to the HAZ and the BM; the clustering effect of the {0001} poles at 25°-35º boundaries are the same for the TMAZ, the HAZ and the BM. Misorientations axes at 55º-68º boundaries are clustering near the $\{\bar{1}2\bar{1}0\}$ poles and the clustering effect has weakened from the TMAZ to the HAZ and the BM; misorientations axes tend to cluster around the $\{01\bar{1}0\}$ and $\{\bar{1}2\bar{1}0\}$ poles at 85°-95° boundaries. It is seen that the TMAZ has stronger clustering effect of the $\{\bar{1}2\bar{1}0\}$ poles at 85°-95° boundaries compared to the HAZ which has the same clustering effect as the BM. It can also be seen that the clustering effect of the $\{\bar{1}2\bar{1}0\}$ poles at 85°-95° decreases significantly from the TMAZ to the HAZ and the BM. Table 6.10 lists the HAGB fraction and texture strength of of the TMAZ, the HAZ and the BM at the AS of the weld W19. The texture strength corresponds to the maximal intensity of the {0001} PFs.



(a)



(b)
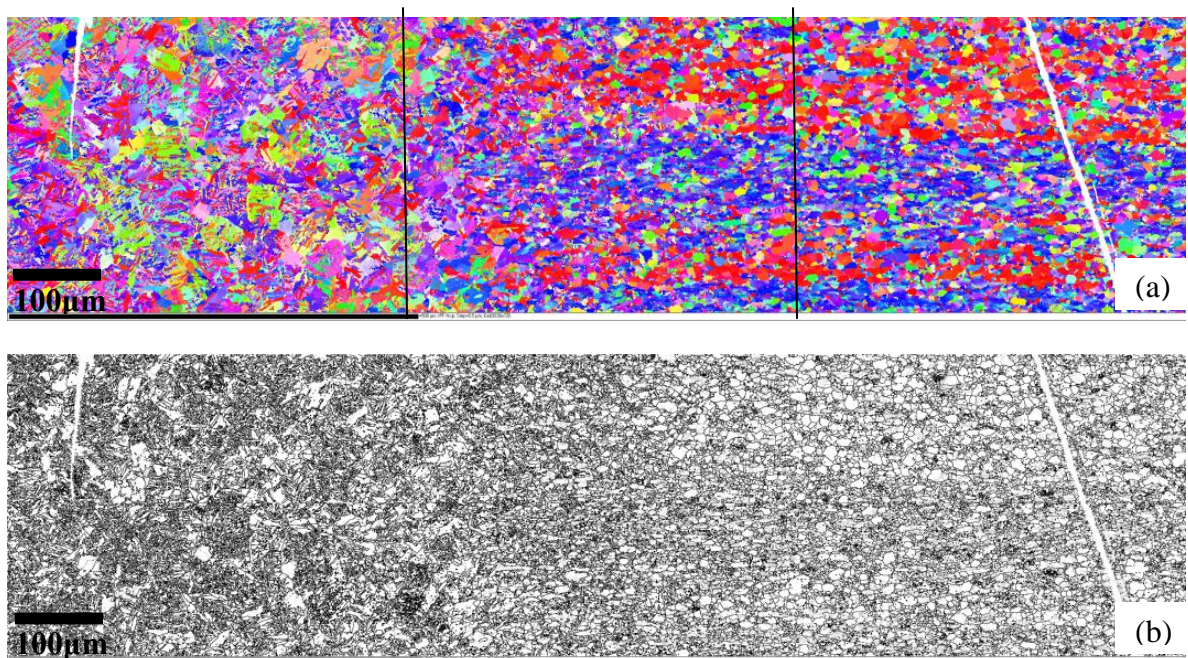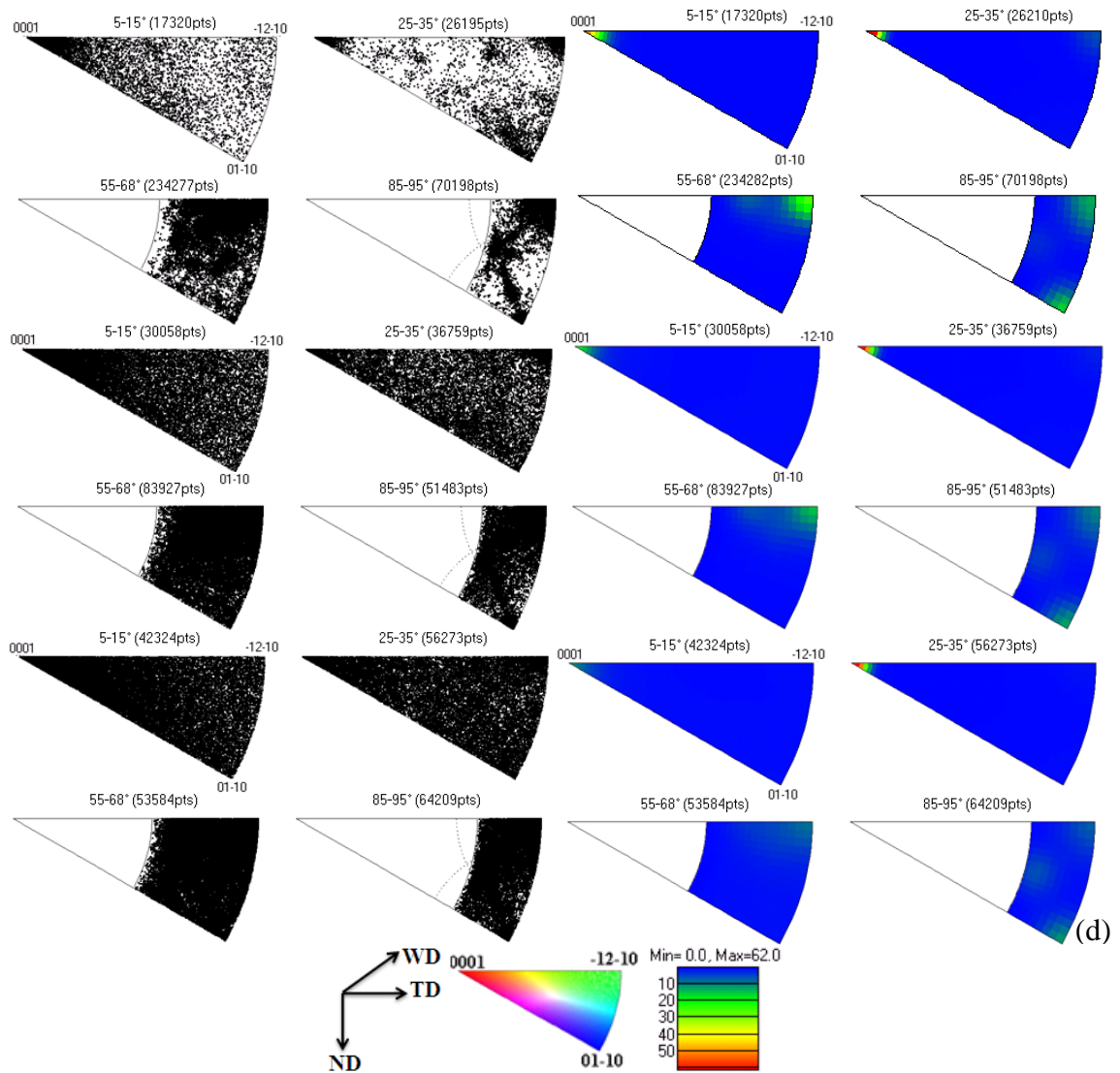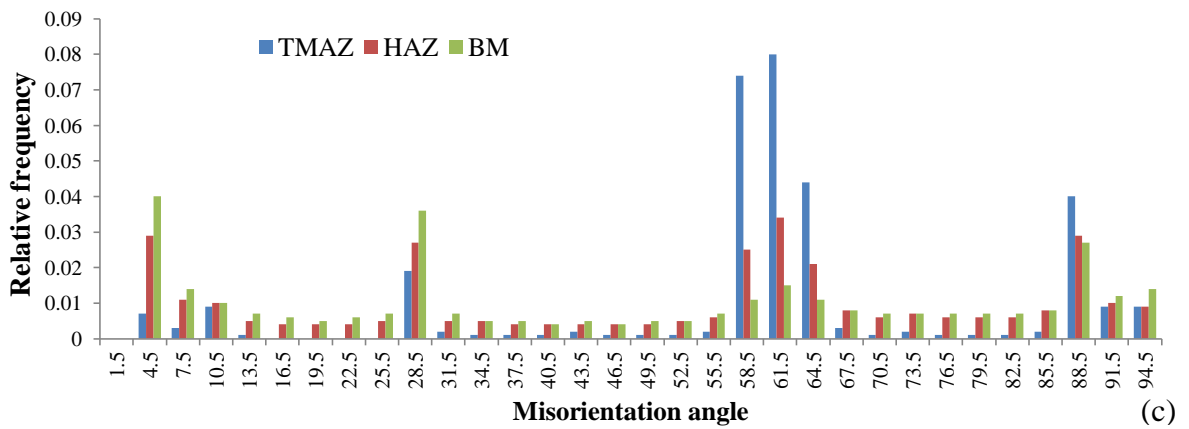
Figure 6.48 EBSD data taken from the TMAZ, the HAZ and the BM at the AS of the welding edge of the weld W19: (a) IPF map; (b) grain boundary misorientation map; (c) misorientation angle distribution plotted against relative frequency; (d) rotation axes at angles of 5º-15º, 25º-35º, 55º-68º and 85º-95º with respect to the crystal coordinate system

Table 6.10 HAGB fraction and texture strength of the TMAZ, the HAZ and the BM at the AS of the weld W19

| Weld zones | BM | HAZ | TMAZ |
|---|---|---|---|
| HAGB fraction, % | 77.7 | 82.5 | 93.7 |
| Texture strength | 8.8 | 8.5 | 5.8 |

EBSD map sized 486.6μm×367.2μm using a 0.2μm step size taken from the RS of the welding edge of the weld W19 has been divided into two regions: the HAZ and the TMAZ. Figure 6.49(a and b) shows EBSD maps of the HAZ and the TMAZ at the RS of the welding edge of the weld W19. And misorientation analysis results are displayed in Figure 6.49(c). Figure 6.49(d) shows rotation axes in the crystal coordinate system at angles of 5º-15º, 25-35º, 55º-68º and 85º-95º. Figure 6.49(d) shows that misorientation axes distributions in the HAZ and the TMAZ are both characterized by clusters near the {0001}, {01$\bar{1}$0} and {$\bar{1}$2$\bar{1}$0} poles. Colour keys for IPF map, welding axes, pole figures are shown at the bottom of the figures. It is seen that misorientation axes at 5º-15º boundaries contain dense clusters near the {0001} poles and the clustering effect decreases significantly from the TMAZ to the HAZ. Misorientation axe at 25°-35º boundaries are clustering near the {0001} and {$\bar{1}$2$\bar{1}$0} poles and the clustering effect of the {0001} poles at 25°-35º boundaries is the same for the TMAZ and the HAZ; the clustering effect of the {$\bar{1}$2$\bar{1}$0} poles at 25°-35º boundaries is stronger in the TMAZ compared to that in the HAZ. And the clustering effect of misorientations axes clustering near the {$\bar{1}$2$\bar{1}$0} poles at 55º-68º boundaries is the same for the TMAZ and the HAZ. Misorientations axes tend to cluster around the {01$\bar{1}$0} and {$\bar{1}$2$\bar{1}$0} poles at 85º-95° boundaries. It is seen that the TMAZ has stronger clustering effect of the {01$\bar{1}$0} poles at 85º-95° boundaries compared to the HAZ and the clustering effect of the {$\bar{1}$2$\bar{1}$0} poles at 85º-95° boundaries is the same for the HAZ and the TMAZ. Table 6.11 lists the HAGB fraction and texture strength of the HAZ and the TMAZ at the RS of the weld W19.
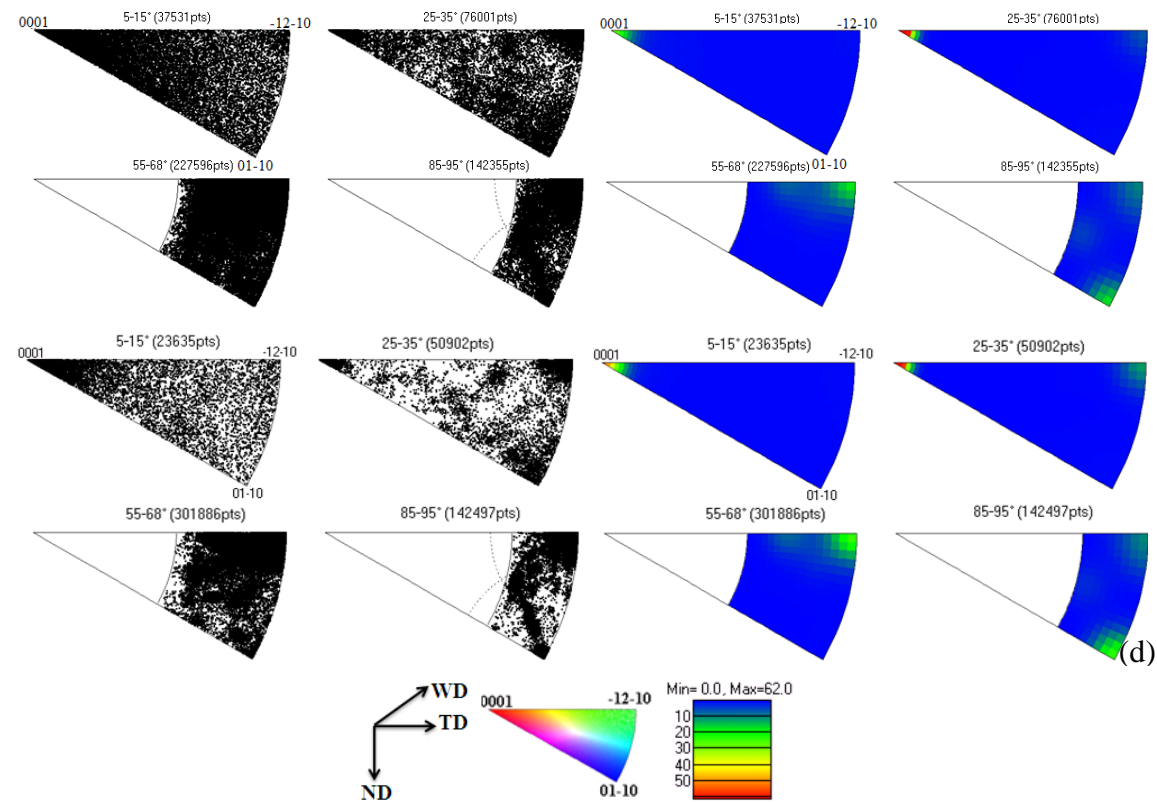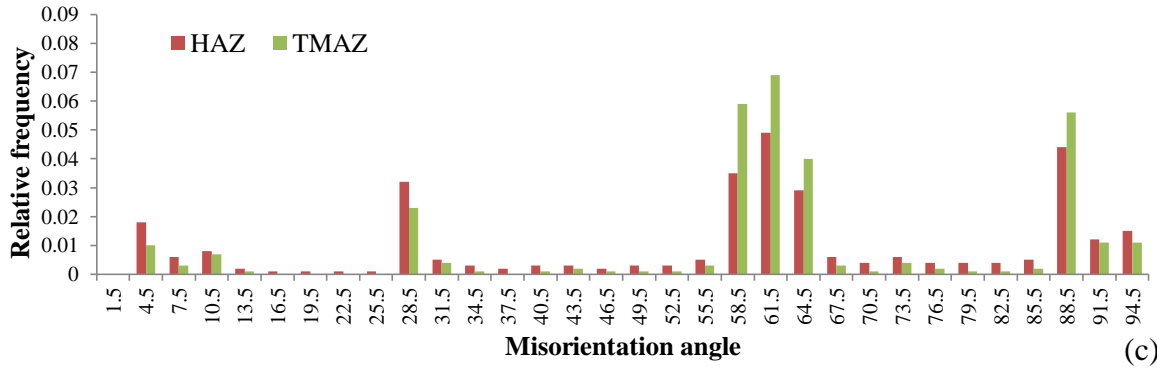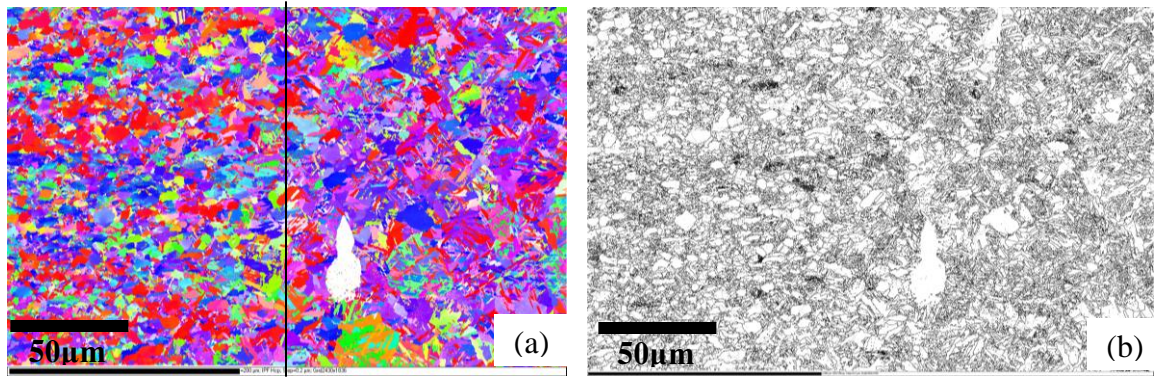
Figure 6.49 EBSD data taken from the HAZ and the TMAZ at the RS of the welding edge of W19: (a) IPF map; (b) grain boundary misorientation map; (c) misorientation angle distribution plotted against relative frequency; (d) rotation axes with respect to the crystal coordinate system

Table 6.11 HAGB fraction and texture strength of the HAZ and the TMAZ at the RS of the weld W19

| Weld zones | HAZ | TMAZ |
|---|---|---|
| HAGB fraction, % | 89.3 | 93.4 |
| Texture strength | 7.6 | 8.6 |

EBSD map sized 2186.4μm×183.9μm using 0.3μm step size taken from the AS of the welding edge of the weld W20 has been divided into four regions (the BM, the HAZ, the TMAZ and the SZ). Figure 6.50(a and b) are the EBSD maps of the four regions at AS of the weld W20. And misorientation analysis results are displayed in Figure 6.50(c). Figure 6.48(d) shows that misorientation axes distributions in the BM, the HAZ, the TMAZ and the SZ are both characterized by clusters near the $\{0001\}$, $\{01\bar{1}0\}$ and $\{\bar{1}2\bar{1}0\}$ poles. Colour keys for IPF map, welding axes, pole figures are shown at the bottom of the figures. Misorientation axes consist of 5-15º and 25°-35º boundaries cluster near the $\{0001\}$ poles only. The $\{0001\}$ poles at 5º-15º boundaries have stronger clustering effect in the SZ and the TMAZ compared to the HAZ, and it is stronger in the HAZ compared to that in the BM, however, the clustering effect of the $\{0001\}$ poles at 5º-15º boundaries is the same for the four regions. Misorientations axes at 55º-68º boundaries are clustering near the $\{\bar{1}2\bar{1}0\}$ poles. Misorientations axes tend to cluster around the $\{01\bar{1}0\}$ and $\{\bar{1}2\bar{1}0\}$ poles at 85º-95° boundaries. It is seen that the clustering effect of the $\{01\bar{1}0\}$ poles at 85º-95° boundaries is the same for the SZ and the TMAZ, and it decreases greatly from the TMAZ to the HAZ and the BM. It should be noted that the clustering effect of the $\{\bar{1}2\bar{1}0\}$ poles at 85º-95º boundaries is very weak in the four regions, however, it has weakened slightly from the TMAZ to the HAZ. Table 6.12 lists the HAGB fraction and texture strength of the BM, the HAZ, the TMAZ and the SZ at the AS of the weld W20.

(a)



(b)



(c)

Figure 6.50 EBSD data taken from the BM, the HAZ, the TMAZ and the SZ at the AS of the welding edge of the weld W5: (a) IPF map. Grains are coloured with respect to the WD; (b) grain boundary misorientation map. LAGBs and HAGBs are drawn as silver (2º-15º) and black lines (>15º), respectively. (c) misorientation angle distribution plotted against relative frequency; (d) rotation axes at angles of 5º-15º, 25º-35º, 55º-68º and 85º-95º with respect to the crystal coordinate system

267

Table 6.12 HAGB fraction and texture strength of the BM, the HAZ, the TMAZ and the SZ at the AS of the weld W20

| Weld zones | BM | HAZ | TMAZ | SZ |
|---|---|---|---|---|
| HAGB fraction, % | 79.5 | 86.5 | 91.5 | 93 |
| Texture strength | 18 | 10 | 6.6 | 5 |

EBSD map sized 707.4μm×130μm using a 0.2μm step size taken from the RS of the welding edge of the weld W20 has been divided into two regions: the TMAZ and the HAZ. Figure 6.51(a and b) shows EBSD maps of the TMAZ and the HAZ at the RS of the weld W20. And misorientation analysis results are displayed in Figure 6.51(c). Figure 6.51(d) shows that misorientation axes distributions in the TMAZ and the HAZ are both characterized by clusters near the $\{0001\}$, $\{01\bar{1}0\}$ and $\{\bar{1}2\bar{1}0\}$ poles. Colour keys for IPF map, welding axes, pole figures are shown at the bottom of the figures. Misorientation axes near the $\{0001\}$ poles consist of 5º-15º and misorientation axes are clustering near the $\{0001\}$ and $\{\bar{1}2\bar{1}0\}$ poles at 25°-35º boundaries. And the clustering effect of the $\{0001\}$ poles at 5°-15º boundaries has weakened slightly from the TMAZ to the HAZ; the clustering effect of the $\{0001\}$ poles at 25°-35º boundaries are the same for the TMAZ and the HAZ. Misorientation axes in the TMAZ has much stronger clustering effect of the $\{\bar{1}2\bar{1}0\}$ poles at 25°-35º boundaries than that in the HAZ. Misorientation axes at 55º-68º boundaries are clustering near the $\{\bar{1}2\bar{1}0\}$ poles and misorientations axes tend to cluster around the $\{01\bar{1}0\}$ and $\{\bar{1}2\bar{1}0\}$ poles at 85º-95° boundaries. It is seen that misorientation axes in the TMAZ has stronger clustering effect of the $\{01\bar{1}0\}$ poles at 85º-95° boundaries compared to that in the HAZ, however, the clustering effect of the $\{\bar{1}2\bar{1}0\}$ poles at 85º-95° boundaries in the TMAZ is the same as that in the HAZ. Table 6.13 lists the HAGB fraction and texture strength of the TMAZ and the HAZ of at the RS the weld W20. The texture strength corresponds to the maximal intensity of the $\{0001\}$ PFs.



50μm

=200 μm; IPF Hcp; Step=0.2 μm; Grid3522x650

(a)
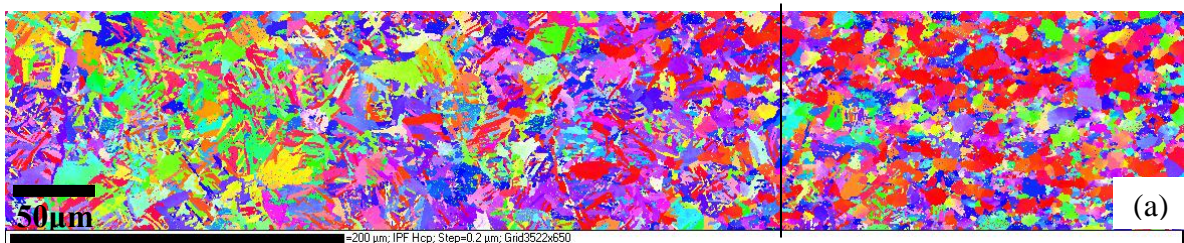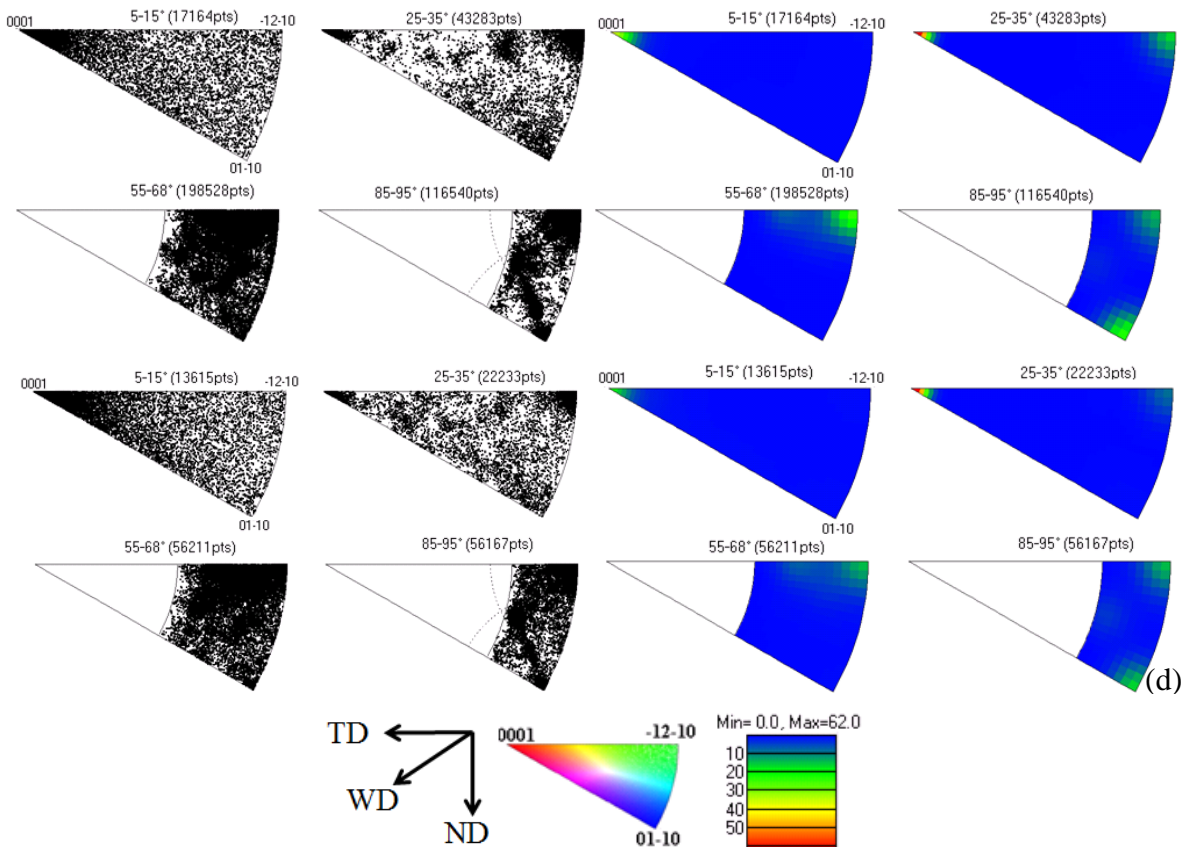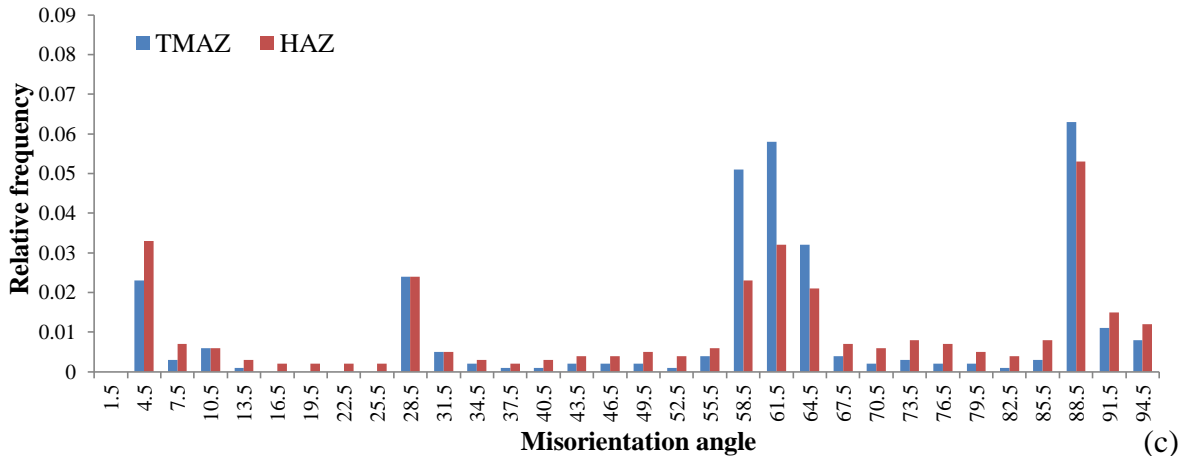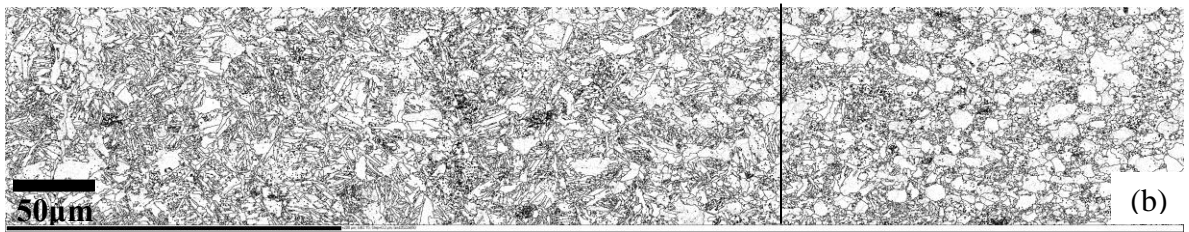
Figure 6.51 EBSD data taken from the TMAZ and the HAZ at the RS of the welding edge of the weld W20: (a) IPF map; (b) grain boundary misorientation map; (c) misorientation angle distribution plotted against relative frequency; (d) rotation axes with respect to the crystal coordinate system

Table 6.13 HAGB fraction and texture strength of the TMAZ and the HAZ at the RS of the weld W20

| Weld zones | TMAZ | HAZ |
|---|---|---|
| HAGB fraction, % | 89.6 | 86.5 |
| Texture strength, MUD | 7.8 | 4.1 |

6.3.2 Misorientation analysis of the SZ from the normal sections

EBSD data of 13000μm×746.2μm using 1.3μm step size were obtained for misorientation analysis, which was taken from the RS to the AS of 5.8.c on the central horizontal line. Figure 6.52 displays grain boundary misorientation map, where grain boundaries with misorientation between 2º to 15º are coloured silver and black is coloured for the grain boundaries with misorientation larger than 15º. Thus, misorientation of 15º was used to separate the LAGBs from the HAGBs. For misorientation analysis, the map has been divided into thirteen parts at 1000μm intervals from the RS to the AS on the central horizontal line. Misorientation angle distribution of the thirteen parts was displayed as relative frequency of misorientation angles plotted against the misorientation angles of 0º to 90º, as shown in Figure 6.53. Part 1, part 2 and part 3 correspond to the BM, the HAZ and the TMAZ; the SZ is composed of part 4, part 5, part 6, part 7, part 8, part 9, part 10, part 11, part 12 and part 13. Table 6.14 shows the HAGB fraction and texture strength across the weld zones of 5.8.c from the RS to the AS on the central horizontal line.

It can be seen that the misorientation angles distributions for the ten regions (part4 to part 13) of the SZ are similar in terms of angles and angle peaks (Figure 6.53). The misorientation angle distributions of the ten regions (part 4 to part 13) in the SZ all consist of a weak low-angle peak at 2º-5º and 10º-13º boundaries, three strongest adjacent peaks in the range of 56º-65º, which is the widest, a strong peak ranging from 86º-90º and a weak peak at 90º-93º boundaries. However, it was shown that 86º-90º boundaries have the strongest peak in the weld centre (part 7 and part 8) compared to that in the other parts, and the weld centre (part 7 and part 8) have the highest HAGB fraction (Table 6.14). Moreover, Table 6.14 shows that texture strength is the highest in the weld centre and the AS has stronger texture strength than the RS. The results demonstrate that the weld centre of 5.8.c

has experienced higher peak weld temperature and more deformation compared to the regions deviated from the weld centre. And the AS has experienced higher peak weld temperature than the RS, which shows agreement with the aforementioned microhardness results in Section 4.4.1 and microstructure characterisation in Chapter 5. Comparison of the evolution of texture across the weld zones can be made by comparing low and high grain boundaries (LAGBs and HAGBs) at the AS and the RS of 5.8.c. It was observed that the texture strengthening from the RS to the AS is resulted from the increase of the HAGB spacing (Table 6.14 and Figure 6.51). This may indicate that the texture strengthening and the development of the grain boundaries from the LAGBs to the HAGBs occur simultaneously. Figure 6.52 shows that misorientation axes distributions in the BM (part1), the HAZ (part 2), the TMAZ (part3) and the SZ (part 4) are both characterized by clusters near the $\{0001\}$, $\{01\bar{1}0\}$ and $\{\bar{1}2\bar{1}0\}$ poles at 5º-15º, 25º-35°, 55º-68º and 85º-95° boundaries. It should be noted that the SZ and the TMAZ have the same clustering effect of poles at 5º-15º, 25º-35°, 55º-68º and 85º-95° boundaries. Misorientation axes cluster near the $\{0001\}$ poles consisting of 5º-15º and 25º-35° boundaries and the $\{0001\}$ poles at 5º-15º and 25º-35° boundaries have stronger clustering effect in the TMAZ compared to that in the HAZ, and it is stronger in the HAZ compared to that in the BM. It is seen that the weak clustering effect of the $\{\bar{1}2\bar{1}0\}$ poles at 25º-35º boundaries decreases from the TMAZ to the HAZ and it was not observed in the BM. Misorientations axes at 55º-68º boundaries are clustering near the $\{\bar{1}2\bar{1}0\}$ poles, and the clustering effect of the $\{\bar{1}2\bar{1}0\}$ poles at 55º-68º boundaries has weakened slightly from the TMAZ to the HAZ and the BM. Misorientations axes tend to cluster around the $\{01\bar{1}0\}$ and $\{\bar{1}2\bar{1}0\}$ poles at 85º-95° boundaries. It is seen that the clustering effect of the $\{\bar{1}2\bar{1}0\}$ poles at 85º-95° boundaries decreases greatly from the TMAZ to the HAZ and the BM. however, the weakest clustering effect of the $\{01\bar{1}0\}$ poles at 85º-95º boundaries is the same for the four regions.

Rotation axes results in Figure 6.53 show that the misorientation axes in the SZ from part 4 to part 13 are both characterized by the dense clusters near the $\{0001\}$ poles at 5º-15º boundaries and the $\{\bar{1}2\bar{1}0\}$ poles at 55º-68º and 85º-95º boundaries, respectively. It was shown that misorientation axes distributions for different regions of the SZ are also similar to each other (Figure 6.53), except for the difference in the clustering effect of the $\{0001\}$ poles at 5º-15º boundaries.
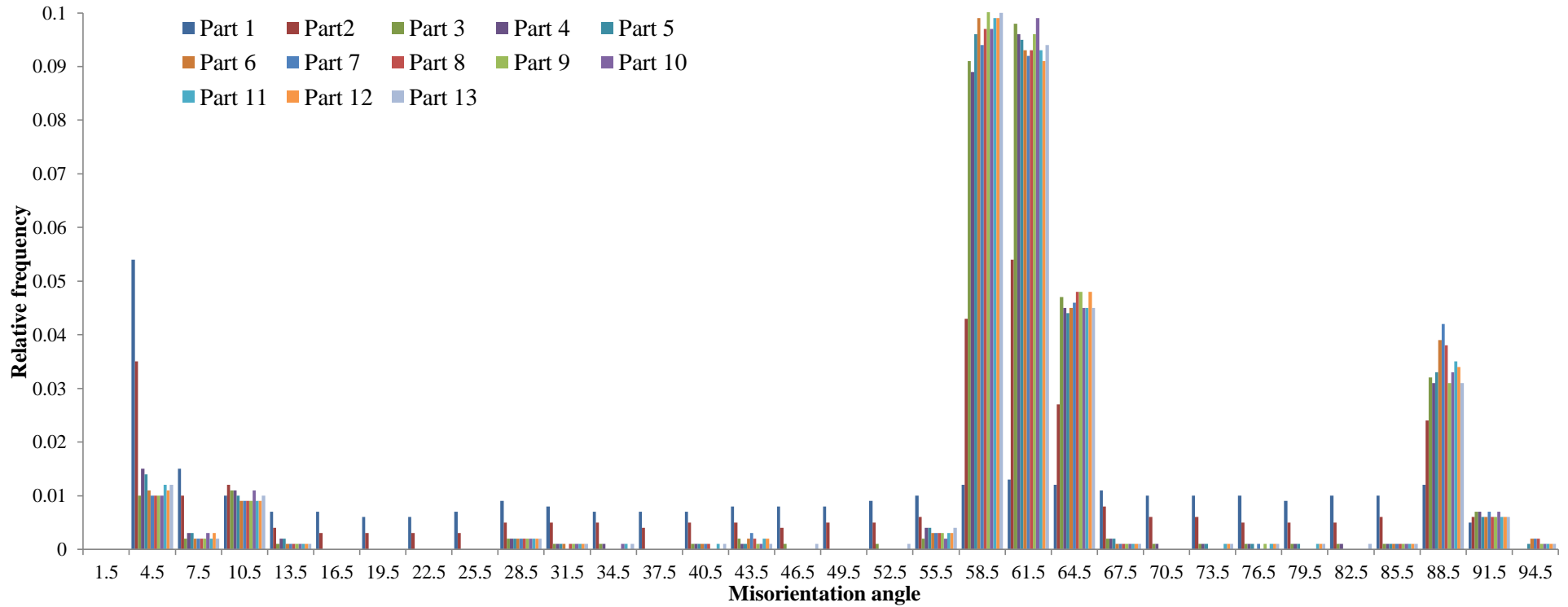
Figure 6.52 Relative frequency of misorientation angles of 0°-94.5° plotted against the misorientation angle from the RS to the AS of 5.8.c

Table 6.14 HAGB fraction and texture strength across the weld zones of 5.8.c from the RS to the AS on the central horizontal line

| Weld region | Part 1 | Part 2 | Part 3 | Part 4 | Part 5 | Part 6 | Part 7 | Part 8 | Part 9 | Part 10 | Part 11 | Part 12 | Part 13 |
|---|---|---|---|---|---|---|---|---|---|---|---|---|---|
| HAGB fraction, % | 73 | 81 | 92.5 | 90.3 | 91 | 92.8 | 93 | 93 | 93 | 92 | 92.5 | 92.4 | 92.2 |
| Texture strength | 6.1 | 2.5 | 4.9 | 7 | 9.9 | 11.2 | 7.7 | 10.4 | 9.6 | 9.2 | 9.5 | 8.4 | 8.9 |

272
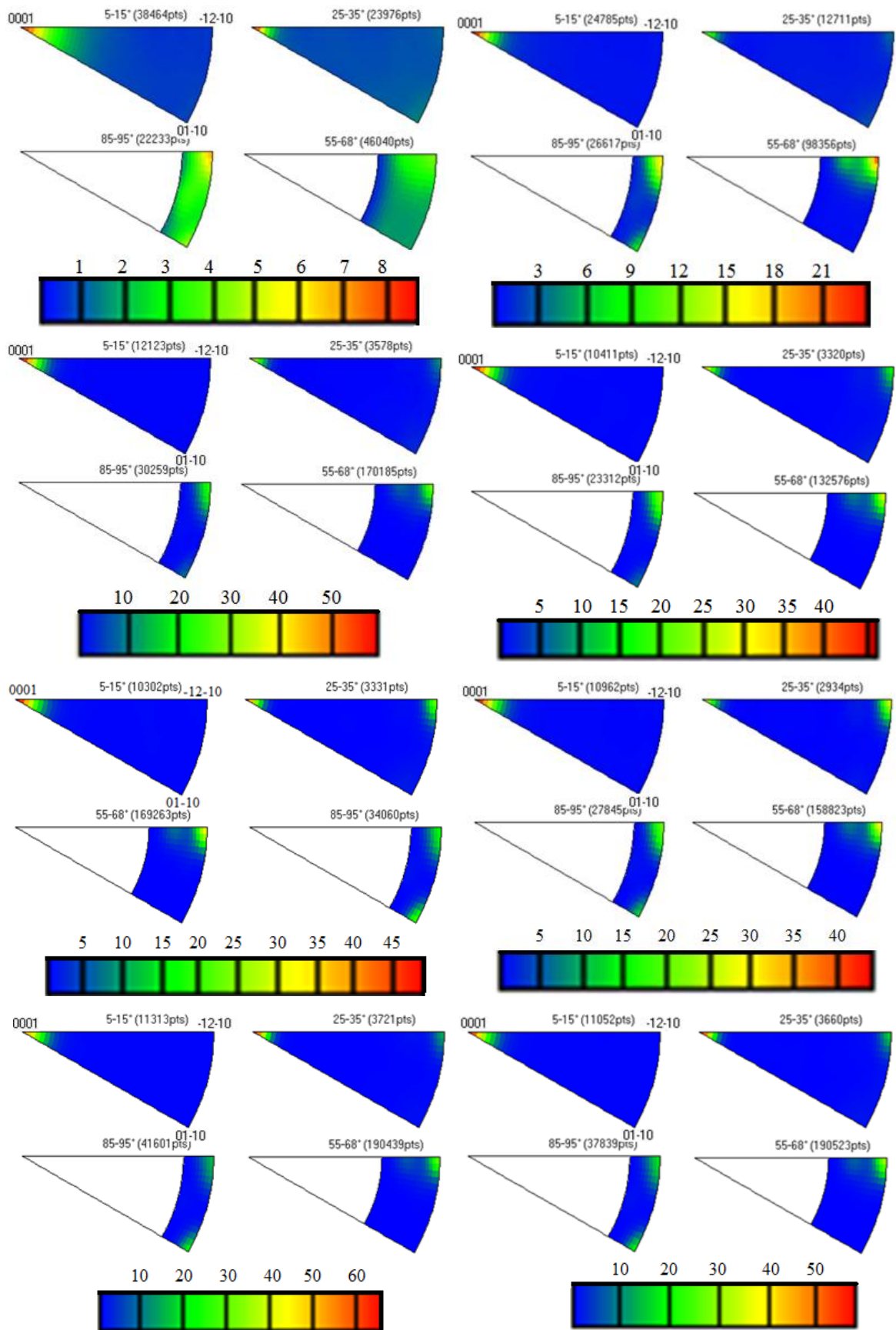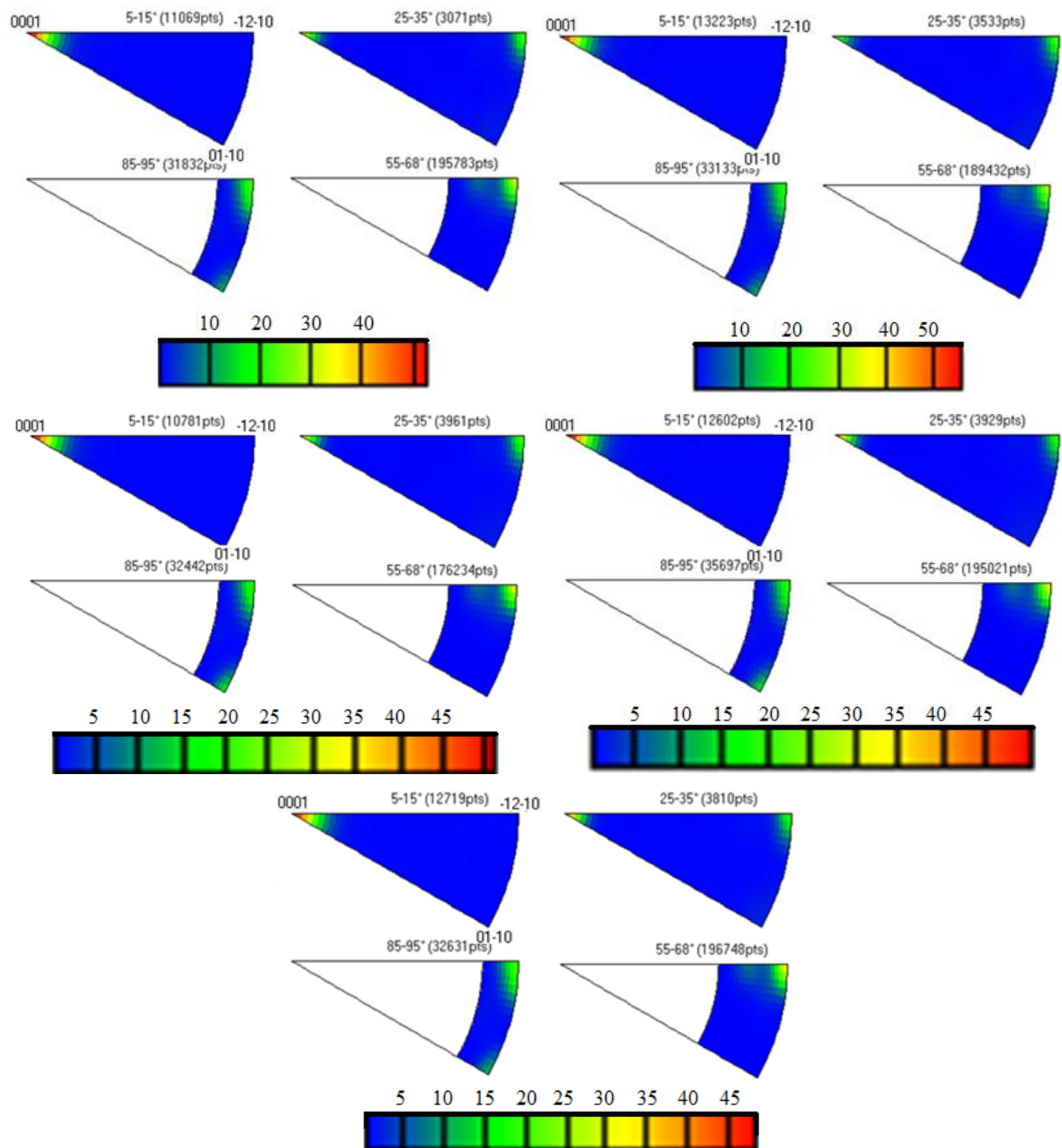
Figure 6.53 Rotation axes at angles of 5º-15º, 25º-35º, 55º-68º and 85º-95º with respect to the crystal coordinate system of each part; part 1, part 2 and part 3 correspond to the BM, the HAZ and the TMAZ, respectively

EBSD data of 9250μm×500μm using a 0.2μm step size were obtained for misorientation analysis, which was taken from the RS to the AS of 6.8.c on the central horizontal line. Figure 6.54 shows the grain boundary misorientation map. For misorientation analysis, the map has been divided into nine parts at approximately 1000μm intervals. Misorientation angle distribution of the nine parts was presented as relative frequency plotted against the

274

misorientation angle of 0º to 94.5º from RS to AS, results of which is shown in Figure 6.54. Table 6.15 shows the HAGB fraction and texture strength across the weld zones of 6.8.c from the RS to the AS. Part 9, part 8 and part 7 correspond to the BM, the HAZ and the TMAZ, the SZ is composed of part 1, part 2, part 3, part 4, part 5 and part 6. Table 6.15 shows the HAGB fraction and texture strength across the weld zones of 6.8.c from the RS to the AS.

Figure 6.54 shows that the misorientation angles distributions for the six regions (part1 to part 6) of the SZ are similar in terms of angles and angle peaks. In the SZ, the misorientation angle distributions of the six regions (part 1 to part 6) all consist of a weak low-angle peak at 2º-5º and 10º-13º boundaries, three strongest adjacent peaks in the widest range of 56º-65º, a strong peak ranging from 86º-90º and a weak peak at 90º-93º boundaries. It is seen in Table 6.15 that the weld centre (part 3 and part 4) have the highest HAGB fraction and the highest texture strength, moreover, the AS has stronger texture strength than the RS. The results again demonstrate that the weld centre of 6.8.c has experienced the highest peak weld temperature. It was also observed that the texture strengthening from the RS to the AS is resulted from the increase of the HAGB spacing (Figure 6.52 and Table 6.15).

Figure 6.55 shows that misorientation axes distributions in the BM (part 9), the HAZ (part 8), the TMAZ (part 7) and the SZ (part 6) are both characterized by clusters near the $\{0001\}$, $\{01\bar{1}0\}$ and $\{\bar{1}2\bar{1}0\}$ poles at 5º-15º, 25º-35°, 55º-68º and 85º-95° boundaries. It should be noted that the SZ and the TMAZ have the same clustering effect of poles at 5º-15º, 25º-35°, 55º-68º and 85º-95° boundaries. It is seen that misorientation axes cluster near the $\{0001\}$ poles consist of 5º-15º and 25º-35° boundaries, and the clustering effect of the $\{0001\}$ poles at 5º-15º and 25º-35° boundaries has weakened significantly from the TMAZ to the HAZ and the BM. The weak clustering effect in the $\{\bar{1}2\bar{1}0\}$ poles at 25º-35º boundaries has decreased greatly from the TMAZ to the HAZ and the BM. Misorientations axes at 55º-68º boundaries are clustering near the $\{\bar{1}2\bar{1}0\}$ poles, and the clustering effect of the $\{\bar{1}2\bar{1}0\}$ poles at 55º-68º boundaries has weakened slightly from the TMAZ to the HAZ, but significantly from the HAZ to and the BM. Misorientations axes tend to cluster around the $\{01\bar{1}0\}$ and $\{\bar{1}2\bar{1}0\}$ poles at 85º-95° boundaries. It is seen that the clustering effect of the $\{\bar{1}2\bar{1}0\}$ poles at 85º-95° boundaries decreases greatly from the TMAZ to the HAZ and

the BM. however, the clustering effect of the $\{01\bar{1}0\}$ poles at 85º-95º boundaries is the same for the three regions.

Rotation axes results in Figure 6.55 show that the misorientation axes in the SZ from part 1 to part 6 are both characterized by dense clusters near the $\{0001\}$ poles at 5º-15º boundaries, $\{\bar{1}2\bar{1}0\}$ poles at 25º-35º boundaries, $\{01\bar{1}0\}$ and $\{\bar{1}2\bar{1}0\}$ poles at 25º-35º, 55º-68º and 85º-95º boundaries, respectively. And the misorientation axes distributions for different regions of the SZ are also similar to each other (Figure 6.51) for part 1, part 2, part 3, part 4 and part 5, however, the clustering effect of the $\{\bar{1}2\bar{1}0\}$ poles at 55º-68º boundaries and 85º-95º boundaries has weakened significantly in part 6 compared to the other five parts.
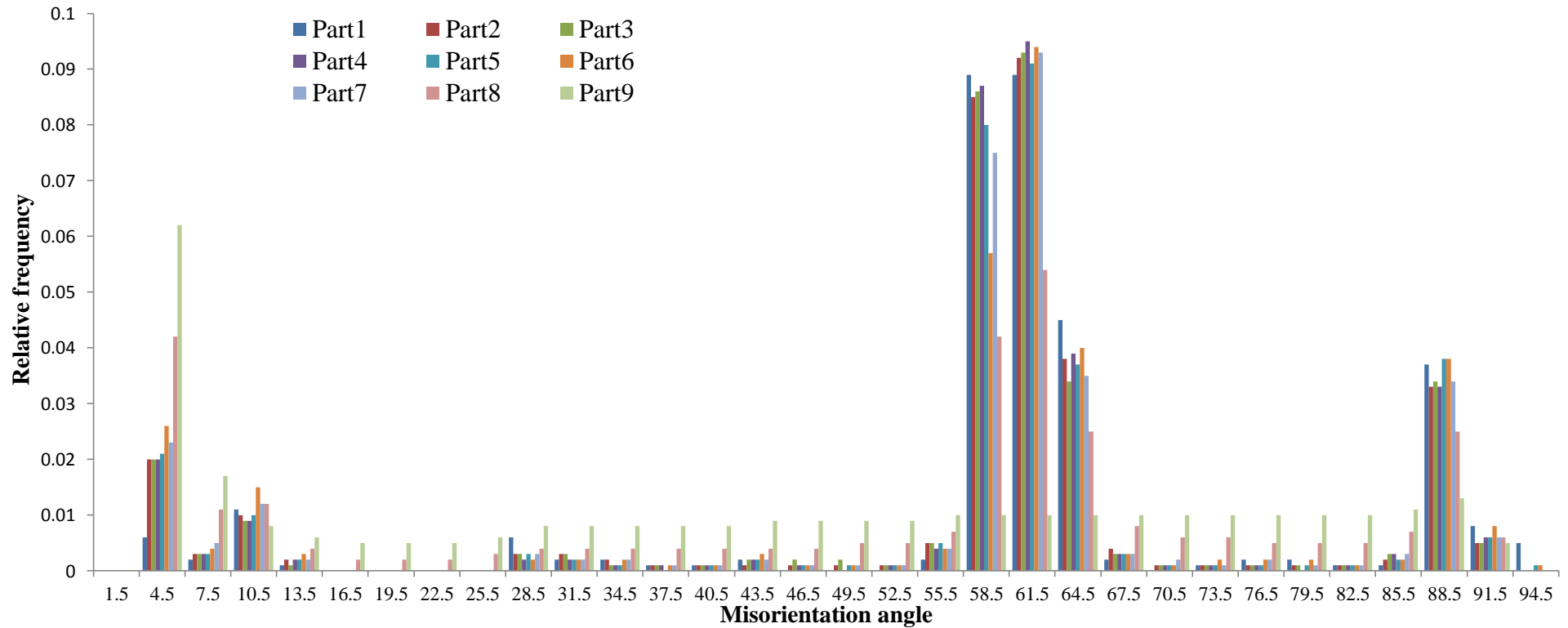
Figure 6.54 Relative frequency of misorientation angles of 0º-94.5º plotted against the misorientation angle from the RS to the AS of 6.8.c

Table 6.15 HAGB fraction and texture strength across the weld zones of 6.8.c from the RS to the AS on the central horizontal line

| Weld region | Part 1 | Part 2 | Part 3 | Part 4 | Part 5 | Part 6 | Part 7 | Part 8 | Part 9 |
|---|---|---|---|---|---|---|---|---|---|
| HAGB fraction, % | 89 | 89 | 89.6 | 89.3 | 88.6 | 85 | 86.7 | 88.2 | 71 |
| Texture strength | 5.2 | 4.4 | 5.3 | 4.2 | 3.6 | 5.2 | 4.2 | 2.2 | 2.5 |
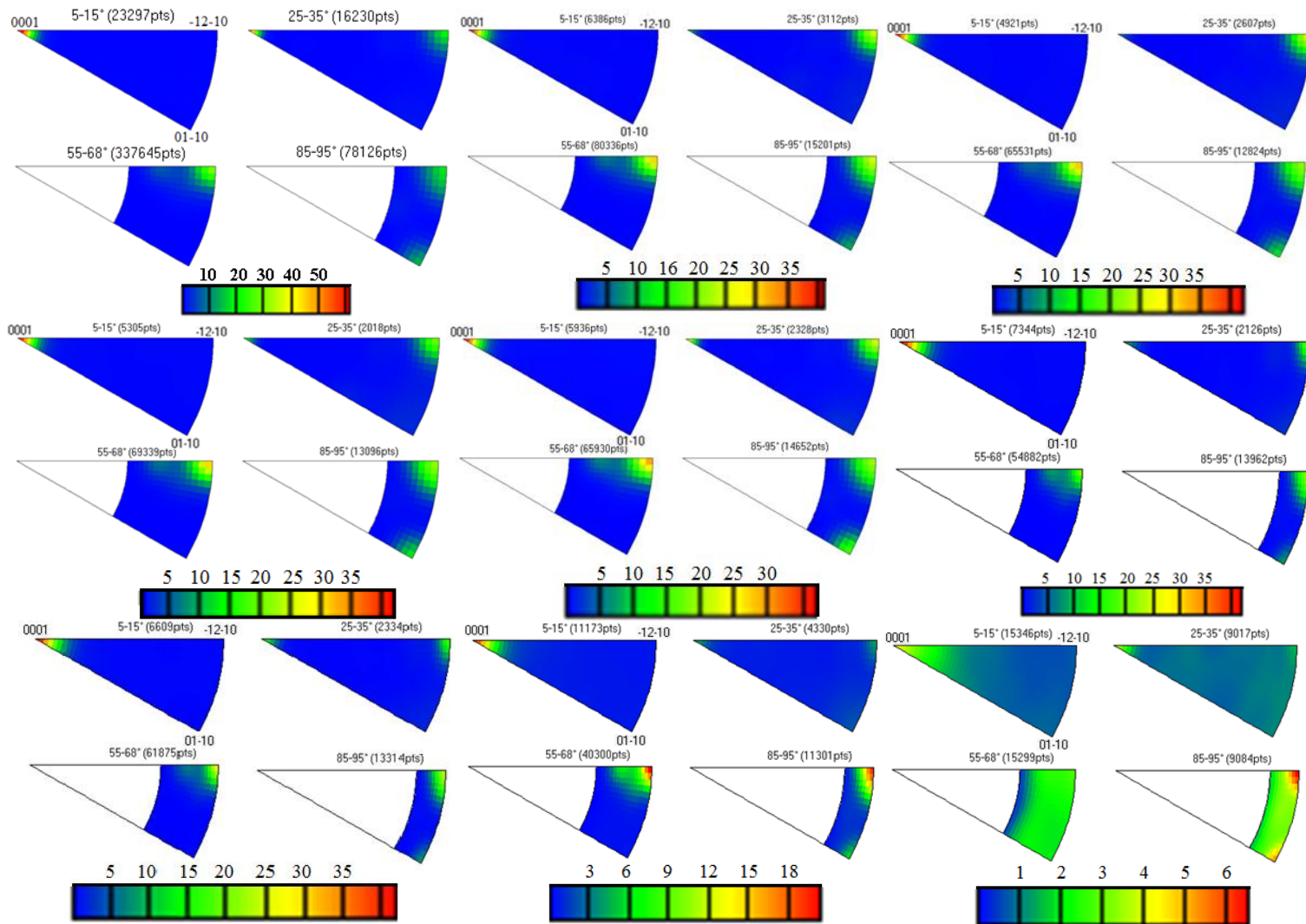
Figure 6.54 Rotation axes at angles of 5º-15º, 25º-35º, 55º-68º and 85º-95º with respect to the crystal coordinate system of each part, where part 7, part 8 and part 9 correspond to the TMAZ, the HAZ and the BM for 6.8.c, respectively

**6.4 Variant selection**

6.4.1 Examples from the three welds W20, W5 and W6

Variant selection was found in the reconstructed high temperature β phase texture in the SZ of the welds. In comparison of Figure 6.7(b) and Figure 6.7(d) in section 6.2 for weld W4, if no variant selection occurs, each {110} pole of the high temperature β phase will correspond to one of the 6 {0001} poles in the low temperature α phase due to the burgers orientation relation; thus, if no variant selection occurs, {0001} PFs of the low temperature α phase would look the same as the {110} PFs of high temperature β phase according to the burgers relationship and both the {0001} PFs and {110} PFs would contain six poles of the same intensity. However, in the {0001} PFs and {110} PFs, one or two of the poles tend to have higher density than other poles and the whole set of {110} PFs contain poles at the same position as the poles of {0001}PFs, but have different intensity compared to {0001}PFs. Moreover, strongest poles are randomly distributed in both the {0001} PFs and {110} PFs indicating a weak variant selection has occurred in W4. Similarly, texture in the probe dominated zone in all the other five welds W5. W6, W19, W20 and W21 have shown weak variant selection in the SZs by comparing the {110} PFs of the reconstructed high temperature β phase and the {0001}PFs of the low temperature α phase, as shown in Figure 6.13 to Figure 6.30 in Section 6.2. However, previous work by Davies et al. (2011) reported that a strong variant selection was observed using 400rpm rotation speed and 60mm/min traverse speed. In this chapter, a detailed variant selection study has been carried out on the three adjacent prior β grains in the centre of the SZ which have fine lamellar structure and EBSD analysis using 0.2μm step size was taken from the weld centre of the cross sections of the three welds W20, W5 and W6, respectively.

Figure 6.56(a) shows the IPF map of the low temperature hcp α phase from the centre of the cross section of the weld W20. The welding axes and IPF colour key are shown at the bottom of the figures. It is seen that GBα grains GBα1 and GBα2 on the two sides of a prior β grain share the same colour red and the {0001} PFs of GBα1 and GBα2 in Figure 6.56(e) are close indicating GBα1 and GBα2 share close orientation. It is seen from Figure 6.56(a) that some α colonies share the same orientation colours as GBα1 and GBα2, about 25% of the α laths inside the prior β2 grain at the right side of GBα2 share the same inverse colours as GBα2. This would suggest that GBα grains may be formed first and the adjacent α laths

have nucleated and grown peripherally from the prior β grain boundary, or the adjacent α colonies have nucleated from GBα which shows agreement with Stanford and Bate (2004) who found that GBα is usually formed first.

Figure 6.56(b) shows the specific grain boundary misorientation map, which was drawn by defined colours according to the misorientation angles between the grain boundaries and the colour key is shown at the bottom of the figures, the colour key systems is defined as: grain boundaries with misorientation angle between 2º to 5º are coloured silver, 5º to 15º are coloured red, purple is coloured for the misorientation between 15º to 40º, misorientation between 40º to 50º are coloured green, Fuchsia is coloured for the misorientation angles between 50º to 70º, black is coloured for the misorientation angles between 70º to 90º and angles larger than 90º are coloured navy blue. Figure 6.55(c) displays a burger disorientation map based on the deviation angle from the burgers angles. The burger disorientation map indicates how misorientations deviate from the closest Burgers Relation. In the colour key system using rainbow colours, pixels with deviation angle less than 3º are coloured from blue to green; pixels with deviation angle less than 6º are coloured from green to red and pixels with deviations more than 6° are coloured white. And more blues are needed in this map to get a good reconstruction (Davies et al., 2011). It can be seen from Figure 6.55(b) that misorientation angle between GBα1 and GBα2 is between 5º to 15º indicating low angle boundary between GBα1 and GBα2. Figure 6.56(d) and Figure 6.56(f) show that the adjacent prior β grains β1 and β2 share common {110} poles and close crystallographic orientation by a rotation of a small angle of less than 2º. And the common {0001} poles of GBα1 and GBα2 are parallel to the common {110} poles. This example shows clearly that when the two adjacent β grains have a close {110} pole, orientation of the α laths at the β/β boundary will have a {0001} pole paralleling to that particular pole (Stanford and Bate, 2004). It should be noted that the colour keys for all the maps in (a-f) are shown at the bottom of the figures.

280
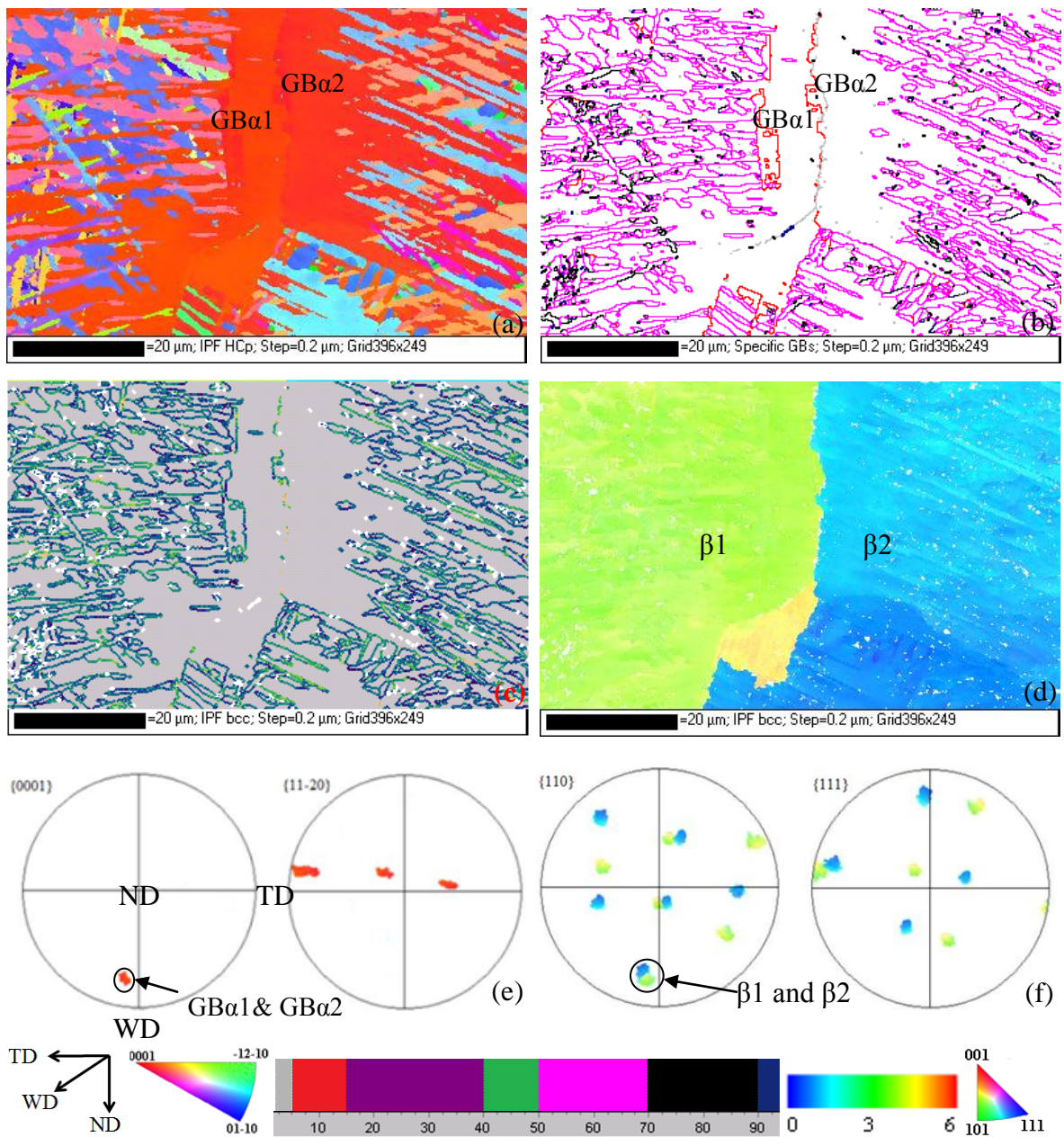
Figure 6.56 Weld W20: (a) grain boundary α (GBα) grains α1 and α2 on the two sides of a prior β grain share the same colour (red) in an IPF map of the low temperature hcp α phase; (b) specific grain boundary misorientation map; (c) a burger disorientation map; (d) IPF map of the reconstructed high temperature bcc β phase showing the corresponding prior β grains; (e) poles in the {0001} and {11$\bar{2}$0} PFs of grain boundary α grains GBα1 and GBα2 indicating GBα1 and GBα2 share close orientation; (f) PFs of β1 and β2 showing β1 and β2 share common {110} poles as indicated in the dark circle

281

Figure 6.57(a) shows α1 (brown) and α2 (green), GBα3 and GBα4 in an Euler colouring map of the low temperature hcp α phase taken from the weld centre of cross section of the weld W5 with welding axes and IPF colour key shown at the bottom of the maps. The two colonies α1 and α2 have difference in both growth directions and crystallographic orientations by a rotation of 160º, as shown in Figure 6.57(d). Figure 6.57(b) is a specific grain boundary misorientation map, colour key of which is shown at the bottom of the maps and it shows that the misorientation angle between the two colonies α1 and α2 is within 40º and 70º. The two α colonies α1 and α2 growing from the same prior β grain boundary into the two adjacent β grains are designated β1 and β2 (Figure 6.57(c)). It was shown in Figure 6.57(e) that β1 has different orientation from β2 indicating there is no orientation relationship between the adjacent β grains β1 and β2 at the β/β boundary. In this case, the adjacent α laths have developed different grain orientations at the prior β grain boundaries and variants were randomly produced on either side of the β/β boundaries (Stanford and Bate, 2004).

It can be seen in Figure 6.57(d) that GBα3 and GBα4 share the same {0001} poles and {11-20} pole indicating GBα3 and GBα4 share the same crystallographic orientation and they could be subgrains of a single GBα grain as indicated in the specific grain boundary misorientation map (Figure 6.57(b)), whereas GBα3 is inside β1 and GBα4 is inside β3. Figure 6.57(f) shows that β1 and β3 share a number of {110} poles and close crystallographic orientation by a rotation of a small angle of less than 2º. In this case, the adjacent α laths across the β/β boundary share a close common {0001} poles and the adjacent α laths have nucleated and grown peripherally from the β/β boundary (Stanford and Bate, 2004).
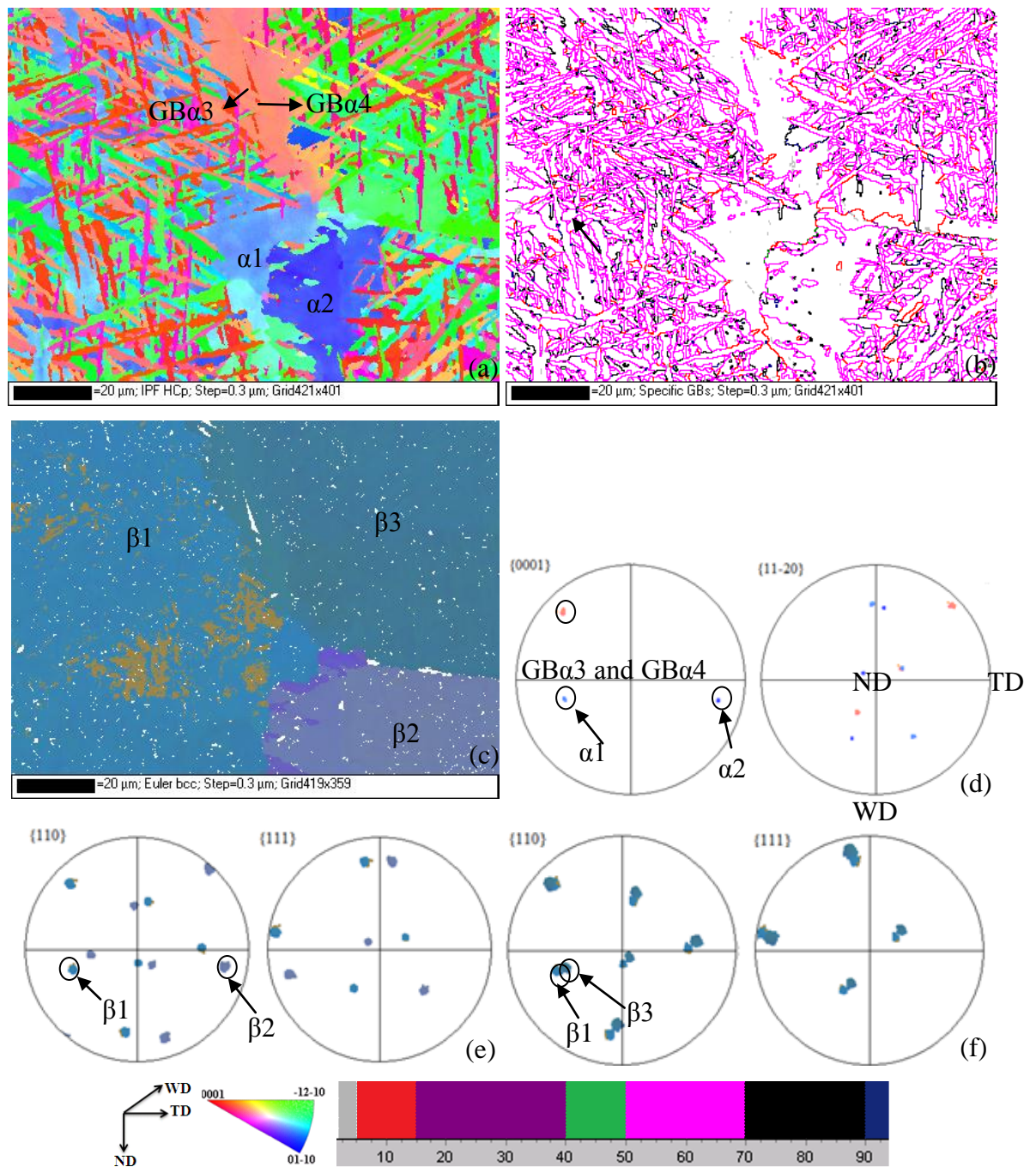
Figure 6.57 Weld W5: (a) α1(brown), α2 (green), GBα3 and GBα4 in an IPF map of the low temperature hcp α phase; (b) specific grain boundary misorientation map; (c) Euler colouring map of the reconstructed high temperature bcc β phase showing the corresponding prior β grains, and they are β1 in blue, β2 in purple and β3 in dark cyan; (d) α PF from α1, α2, GBα3 and GBα4 showing orientations of α crystals; (e) β PF from β1 (blue) and β2 (purple) showing β1 has different orientation from β2; (f) β PF from β1 (blue) and β3 (dark cyan) showing β1 and β3 share common {110} poles as indicated in the dark circles

283

Figure 6.58(a) shows the IPF map of the low temperature hcp α phase taken from the centre of the cross section of the weld W6 with superimposed α colonies α1, α2 and α3 and grain boundary α grains GBα1 and GBα2. The welding axes and IPF colour key are shown at the bottom of the figures. α1 and α2 grow from the same β grain boundary into the two adjacent β grains designated β1 and β2 in Figure 6.58(d), respectively and GBα2 is inside β3. Figure 6.58(b) shows the IPF map of the reconstructed high temperature bcc β phase. GBα and α2 belong to the same prior β grain β1 and α1 was inside β3. α PFs from α1, α2 and GBα1 in Figure 6.58(e) displays that α1, α2 and GBα1 have different orientations from each other, this is an example for grain boundary α between the α laths or colonies that do not share a common {0001} pole. It was demonstrated in Figure 6.58(c) that GBα1 exhibits an orientation as a compromise of the orientations of α colonies α1 and α2 (Stanford and Bate 2004). There was no grain boundary misorientation between GBα2 and the colony α3 as indicated in Figure 6.58(d). It can be seen from Figure 6.58(e) that that β1 (yellow) has different orientation from β3 (dark cyan). The β PFs from β1 and β2 in Figure 6.57(f) indicates that β1 and β2 share two common {110} poles. It is seen that the common {0001} pole for GBα2 and the colony α3 parallels to one of the common {110} poles.



(a)

(b)

(c)

(d)
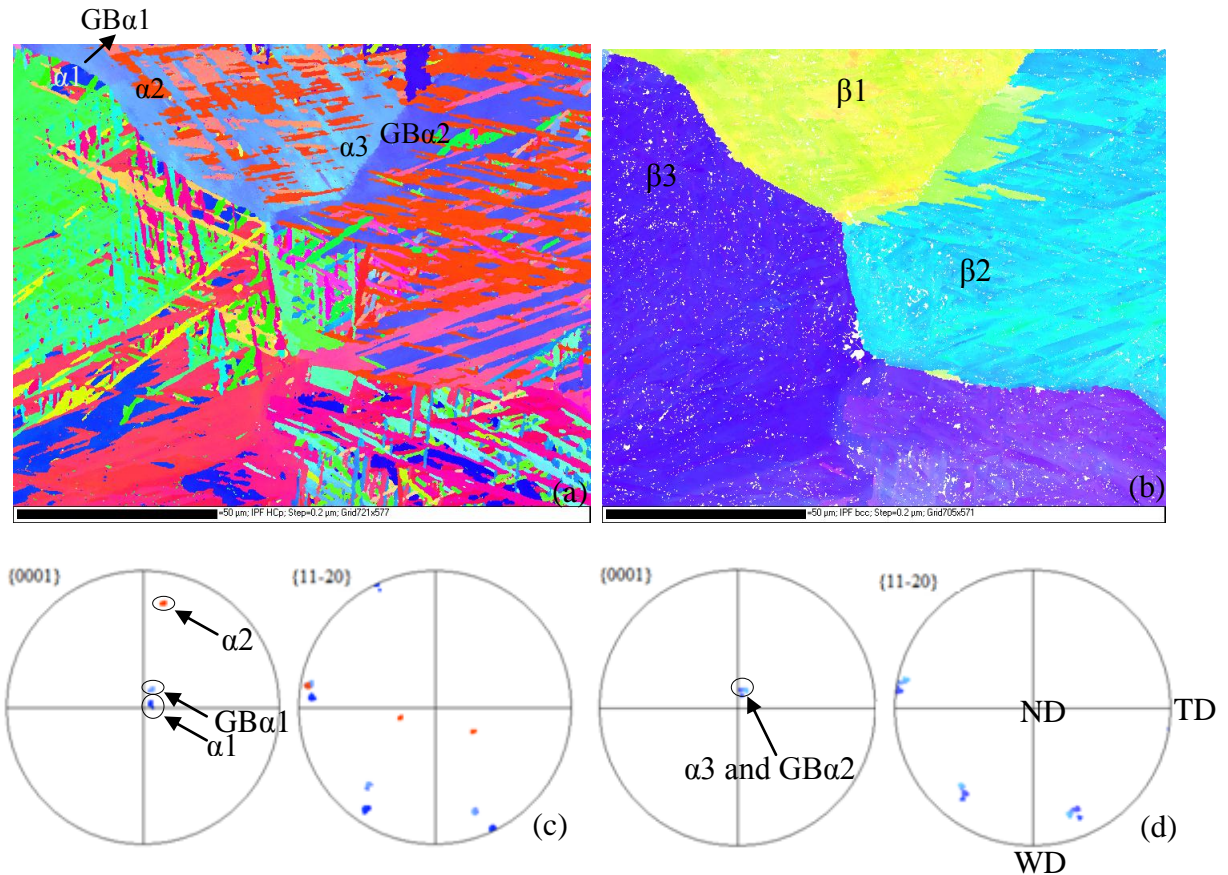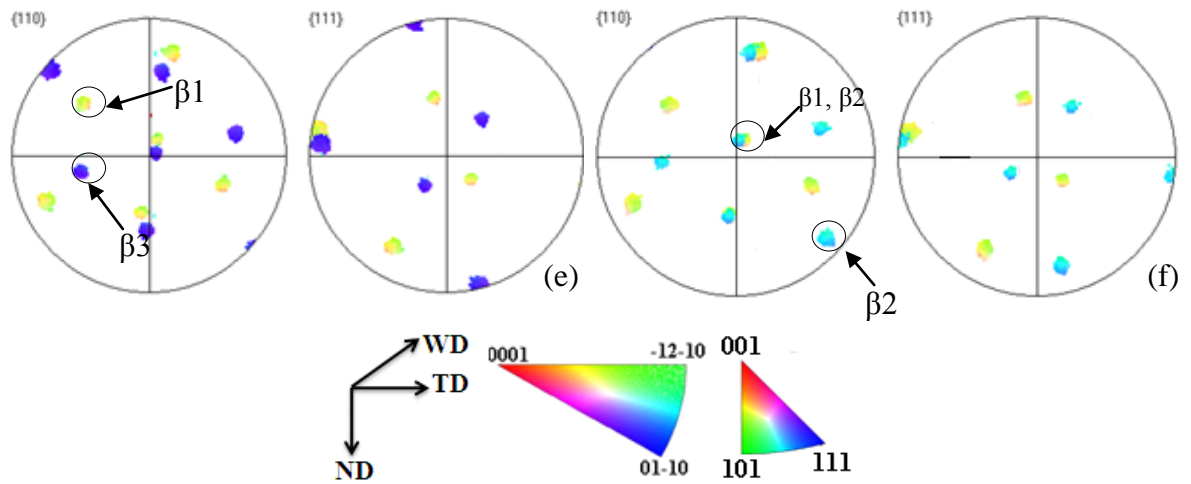
Figure 6.58 Weld W6: (a) α colonies α1(blue) and α2 (red) and grain boundary α (GBα) in an IPF map of the low temperature hcp α phase; (b) IPF map of the reconstructed high temperature bcc β phase showing the corresponding prior β grains, β1 β2 and β3; (c) α PFs from α1, α2 and GBα1; (d) α PFs from α3 and GBα2; (e) β PFs from the prior β grains β1 and β3; (f) β PFs from the prior β grains β1 and β2

6.4.2 Behaviour of the adjacent β grains at β/β grain boundaries

A large β grain was found to produce 12 variants in the case of no variant selection, however, within Figure 6.56 to Figure 6.58, the number of variants within most of the prior β grains was typically less than 12 but in all other instances parent β grains contained a variants of 10 or less than 10, this indicated variant selection. The orientation of the prior β grains are shown by the {110} pole figures. The orientation of the α variants formed at the β/β boundary are shown by the {0001} pole figures. There are three circumstances exist for the orientation relation between the adjacent β grains (Stanford and Bate 2004) and they are (a) the adjacent β grains share one common {110} pole, such as in Figure 6.56(f) of the weld W20; (b) the adjacent β grains have a similar orientation and share a number of common poles, such as in Figure 6.56(f) of the weld W5 and Figure 6.58(f) of the weld W6; (c) the adjacent β grains have no close crystallographic relation, such as in Figure 6.58(f) of the weld W6.

The first relationship between the prior β grains is that the adjacent β grains share one common {110} pole. It was shown in Figure 6.56(f) of W20 that the adjacent β grains share one common {110} pole, GBα1 and GBα2 share common {0001} and {11$\bar{2}$0} poles, β1 and β2 share one common {110} pole but {111} poles are different.

285

The second relationship between the prior β grains is that they are close in orientation, and share a number of {110} poles. In this case it was found that the adjacent α variants across the β/β boundary usually shared a close common (0001) pole (Bhattacharyya et al., 2003). {0001}α PFs from Figure 6.57(f) of the weld W5 showed that orientations of the α colonies were determined by the orientations of GBα grains, e.g. GBα3 and GBα4 as shown in Figure 6.57(a)). GBα3 and GBα4 share common {0001} and {11$\bar{2}$0} poles, β1 and β2 share a number of close {110} poles and {111} poles. GBα3 and GBα4 nucleated first and they had an orientation dependant on the adjacent β orientations and α variants at both sides of the grain boundaries which precipitate at the β grain boundary. Figure 6.58(f) of the weld W6 shows that α3 and GBα2 share a number of close {0001} and {11$\bar{2}$0} poles, β1 and β2 share a number of close {110} poles, but do not share common {111} poles.

The third relationship between the prior β grains is that the adjacent β grains have no close crystallographic relation. Variant selection study in the weld centre of W4C4 suggests that most of the adjacent β grains have no close crystallographic relation and the α variants formed at the boundary do not share any common {0001} poles, however, results are not shown here due to the text limit. In this case, at the grain boundary where the adjacent β grains have no close crystallographic relation, as shown in Figure 6.57(e) of W5 and Figure 6.58(e) and (g) of W6, no crystallographic correlation was found between the α variants across the β/β boundary. It is seen from Figure 6.57(e) that α1 and α2 do not share common {0001} or {11$\bar{2}$0} poles, moreover, {110} poles and {111} poles for β1 are different from β2. Figure 6.58(e) and (f) of W6 shows that α1 from β3, GBα1 and α2 from the same prior β grain β1 have different {0001} and {11$\bar{2}$0} poles from each other. And β1 has different orientations from β3 in terms of {110} and {111} poles.

6.4.3 Variant selection intensity based on the pole intensity

To investigate how variant selection evolves across the weld zones with varying welding parameters, Figure 6.59 plots the pole intensity histograms of the six poles (variants) in the {0001} PF and the {110} PF of the α phase texture and the corresponding reconstructed β phase texture in the SZ from the RS to the AS of the weld zones for all the six welds W4, W5, W6, W19, W20 and W21 (refer to Figure 6.9, Figure 6.15, Figure 6.20, Figure 6.25, Figure 6.29, Figure 6.31). And a key of the six poles (1, 2, 3, 4, 5, and 6 six poles) is shown

at the bottom of the figure. In this work, the difference between the pole intensity of {0001}α PF and the corresponding six poles {110}β PF of the six poles (1 to 6) is given as the absolute value of the subtraction of {0001}α pole intensity and {110}β pole intensity or it is also calculated as the ratio (≥1) of pole intensity of each {0001}α PF versus that of the corresponding {110}β PF or vice versa ({0001}α ↔{110}β). Figure 6.60(a) shows the subtraction of the pole intensity between the {0001}α PF and the corresponding {110}β PF of the six poles (1 to 6) of the weld W4. Figure 6.60(b) shows the ratio of {0001}α ↔{110}β pole intensity for all the six poles. Similarly, Figure 6.60(c-d) shows the difference of the pole intensity for W5 in terms of subtraction and ratio, respectively, Figure 6.60(e-f) is for W6, Figure 6.60(g-h) is for W19, Figure 6.59(i-j) for W20 and Figure 6.60(k-l) is for W21. Figure 6.61(a) and (b) shows the percentage of each pole with the highest pole intensity in {0001} PFs and {110} PFs for all the six poles (1, 2, 3, 4, 5, 6) among all the regions of each weld from the RS to the AS, respectively and the percentage of each variant with the largest subtraction between the {0001} and {110} pole intensity and with the largest ratio of {0001}α ↔{110}β pole intensity for all the six poles among all the regions of each weld from the RS to the AS are shown in Figure 6.61(c) and (d), respectively.

Variant selection intensity is given as the sum of the absolute value of the subtraction of the {0001}α and {110}β pole intensity of the six poles or the sum of the ratio of {0001}α ↔{110}β pole intensity of the six poles. Figure 6.62(a) and (b) shows the variant selection intensity as a function of distance from the weld centre from the RS to the AS of all the six welds in terms of subtraction and ratio, respectively. Variant selection intensity as a function of distance from the weld bottom to the weld surface of all the six welds in terms of subtraction and ratio is shown in Figure 6.62(c) and (d), respectively. Figure 6.62 plots the variant selection intensity as a function of heat input in the weld centre for all the six welds W4, W5, W6, W19, W20 and W21, and the variant selection intensity is calculated as the sum of the subtraction of the pole intensity of {0001}α PF and {110}β PF of the six poles in each weld.

It was demonstrated in Figure 6.59, Figure 6.60, Figure 6.61, Figure 6.62 and Figure 6.63 that the variant selection intensity is the highest in the weld centre; the variant selection intensity increased with increasing heat input, that is to say, the variant selection intensity increased with increasing rotation speed and with decreasing traverse speed; the

regions at the AS deviated from the weld centre has higher variant selection intensity than the regions at the RS deviated from the weld centre; the weld surface has generally higher variant selection intensity than the weld bottom.

It can been seen from the key of the six poles that, in the weld centre, pole 5 lies in the centre of the pole figure and it is parallel to the ND and pole 4 is close to the TD. Figure 6.59(a-l) shows that in the weld centre, the strongest pole intensity of both the {0001} PFs and {110} PFs occurs in the pole 5 for all the six welds except for the weld W4 with pole 4 having the strongest pole intensity, This would suggest that the in the weld centre, strongest pole appears to be the one that is closest to the ND for the five welds W5, W6, W19, W20 and W21 and strongest pole appears to be closest to the TD for the weld W4. Whilst, except for the weld centre, there is no consistency in the occurrence of favorite variants having the highest pole intensity in neither the {0001} PFs nor the {110} PFs for all the six welds. Moreover, pole intensity difference in terms of subtraction and ratio from the RS to the AS of the stir zones for all the six welds W4, W5, W6, W19, W20 and W21 in Figure 6.60(a-l) and Figure 6.62(a-d) suggest that there is no consistency in the occurrence of favorite variants which have the largest intensity difference between the {0001} and {110} pole intensity in terms of subtraction and ratio.

(a)

(b)

(c)

(d)

289

(e)

(f)

(g)

(h)

290

(i)

(j)

(k)

(l)

291
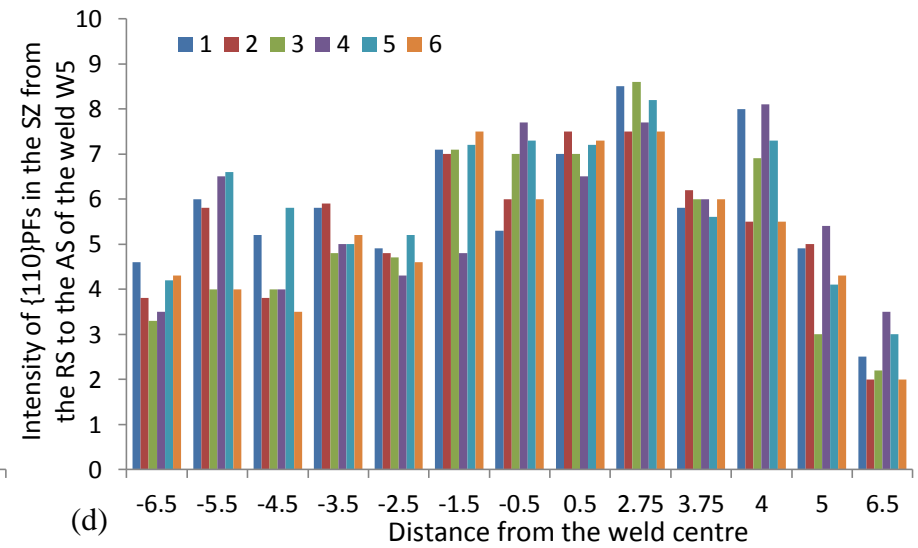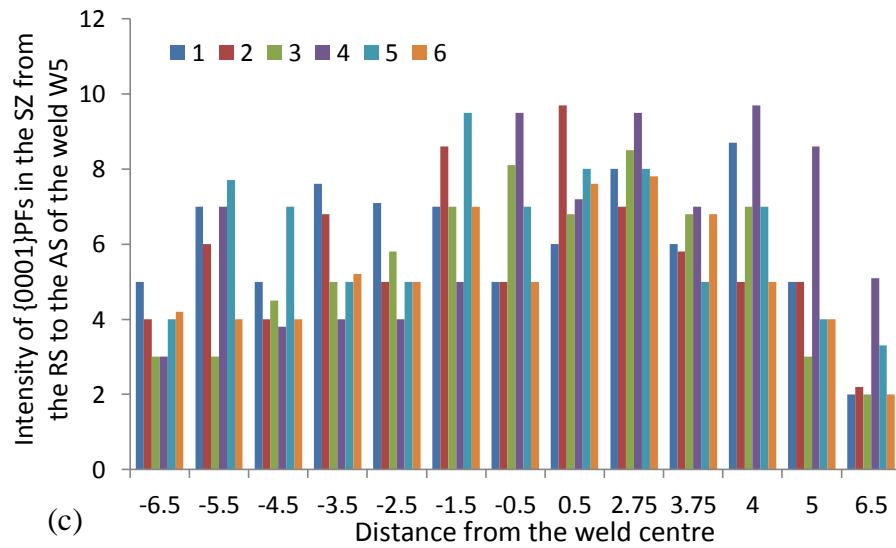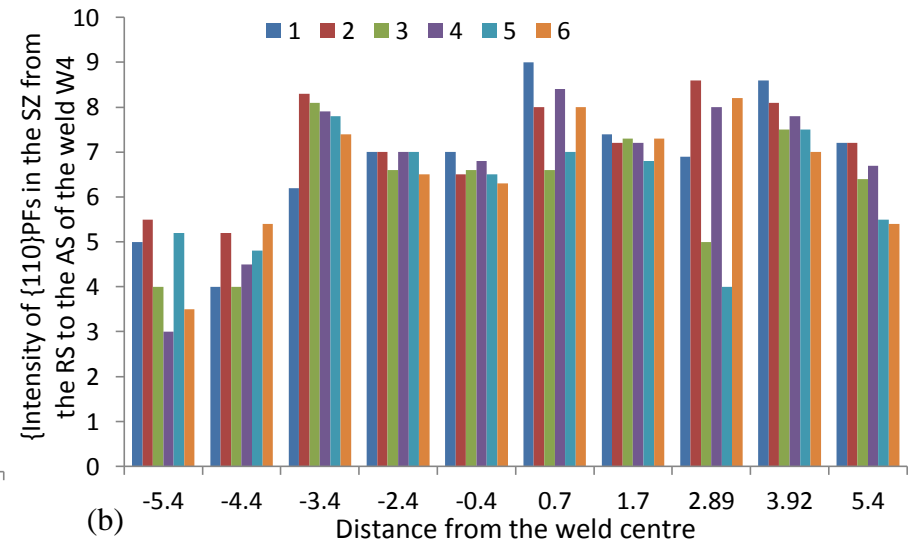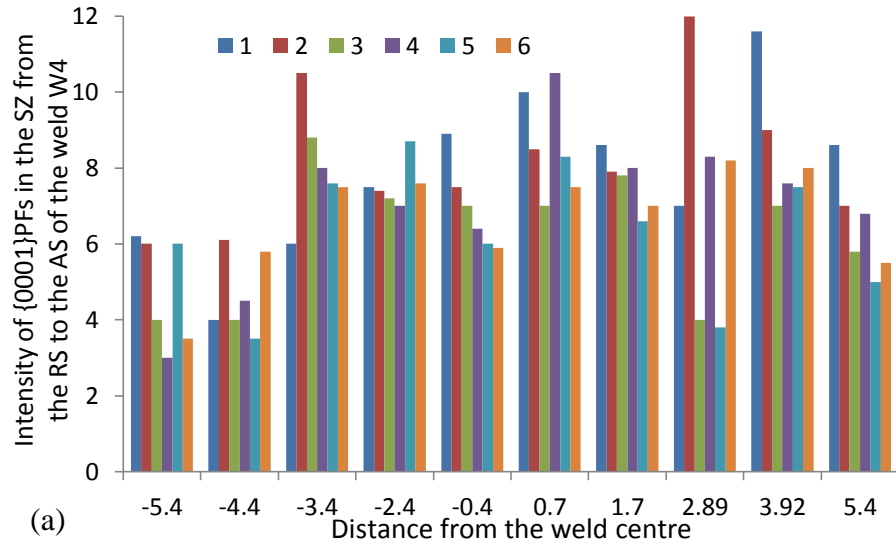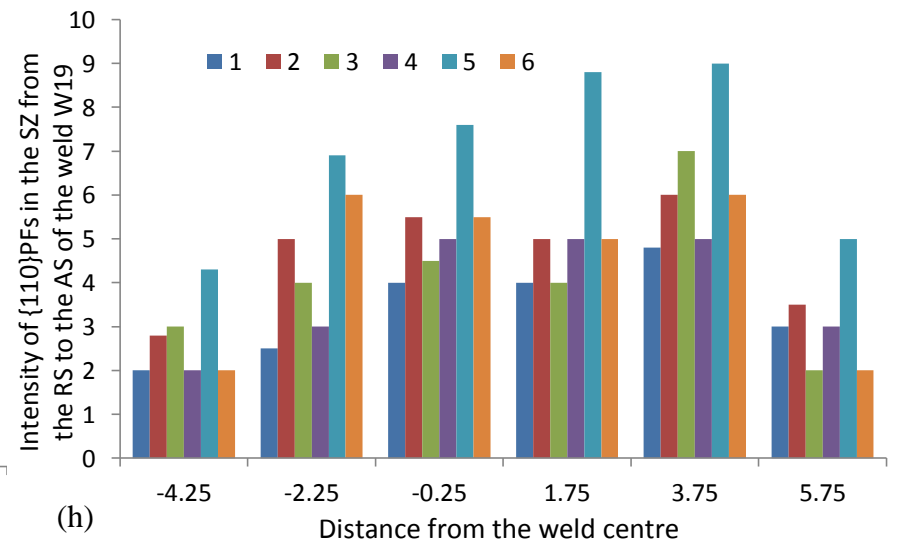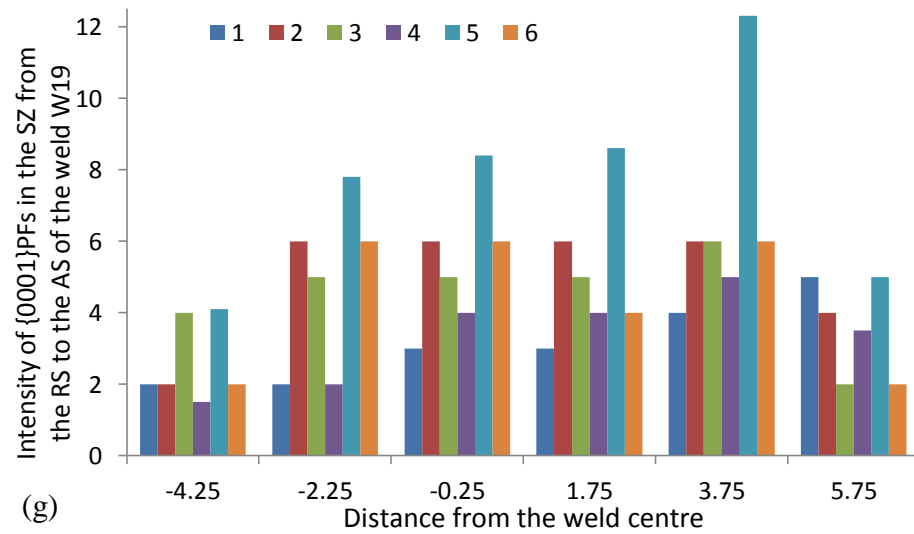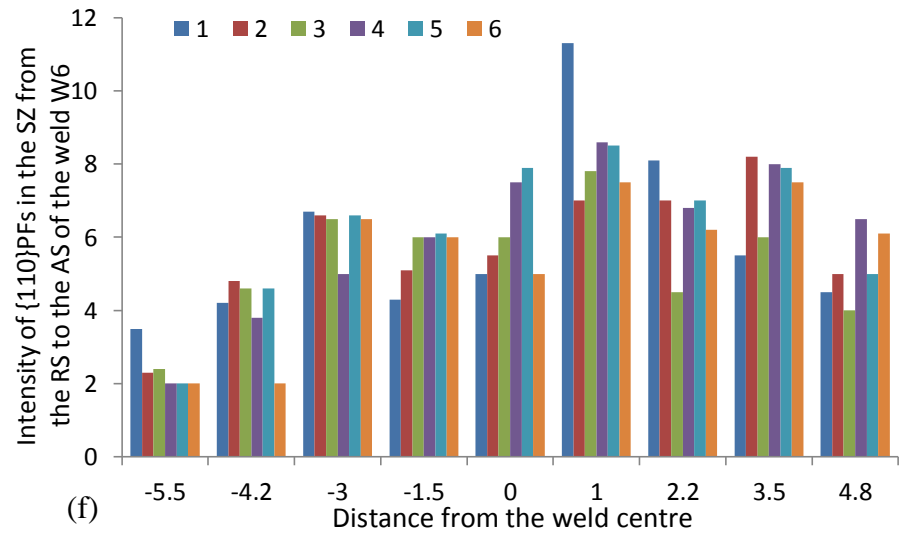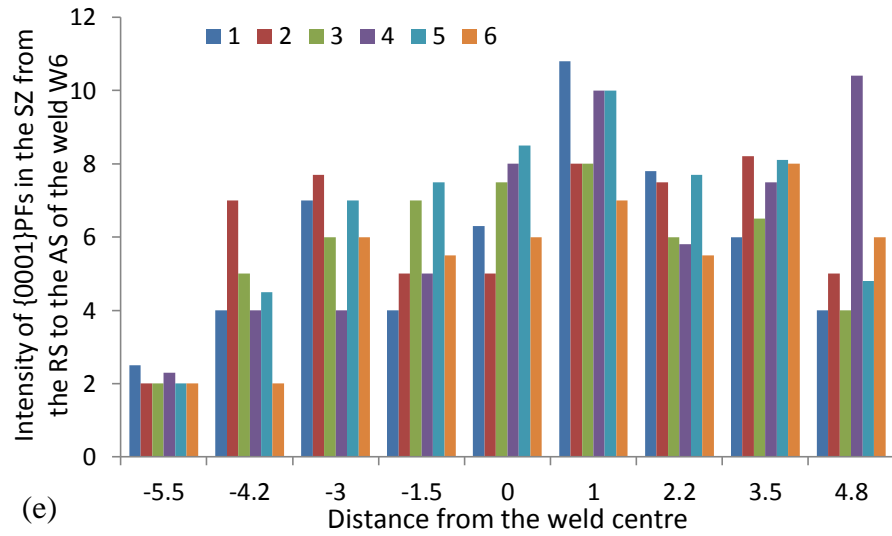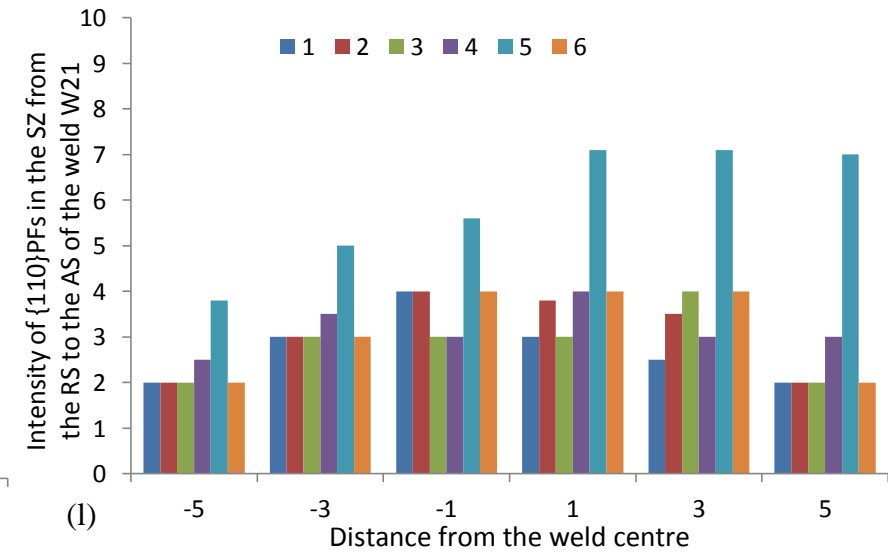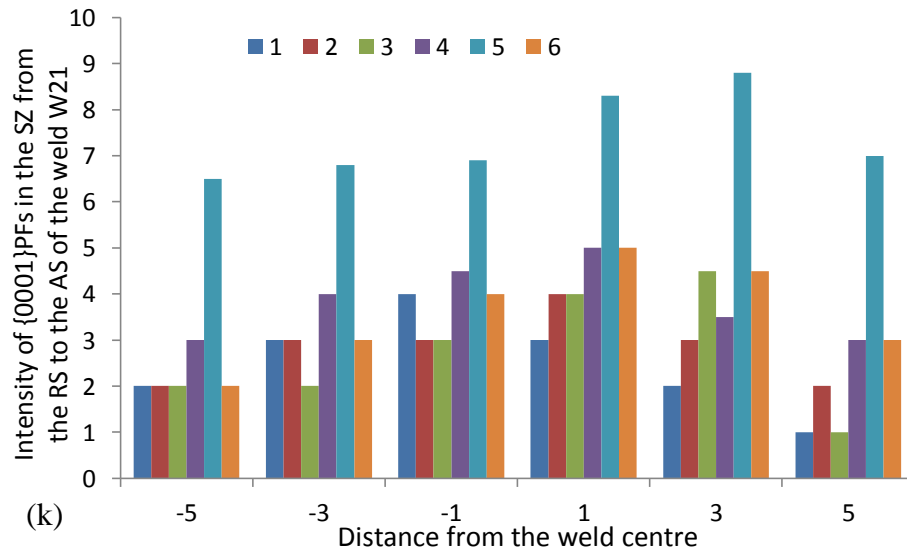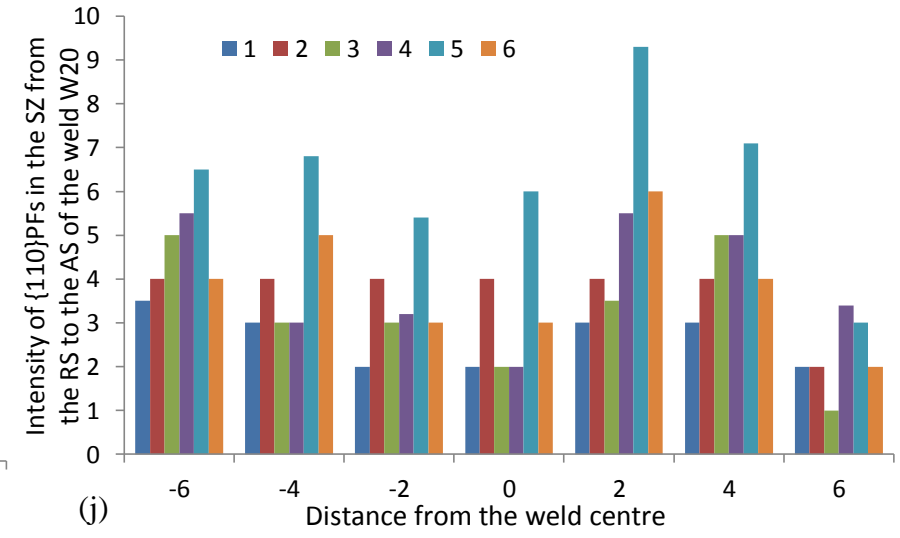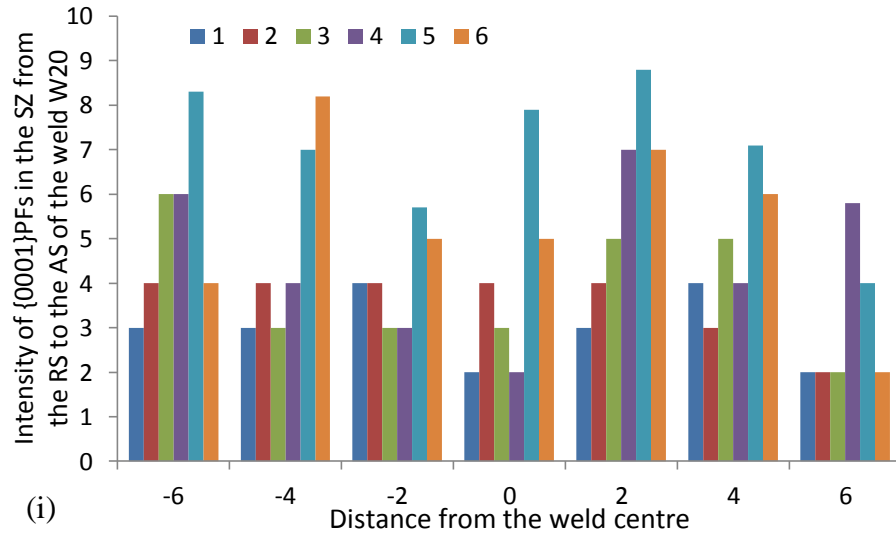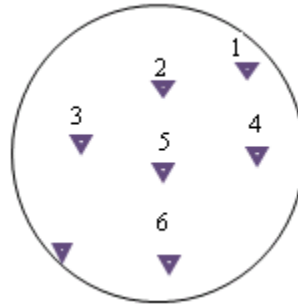
Figure 6.59 Pole intensity histograms of (a) the six poles in the {0001} PF of the α phase texture and (b) the corresponding six poles in the {110} PF of the reconstructed β phase texture in the SZ from the RS to the AS for W4;  Similarly, (c) and (d) for W5, (e) and (f) for W6, (g) and (h) for W19, (i) and (j) for W20, (k) and (l) for W21

(c)

Intensity subtraction between {0001} and {110} PFs of the weld W5

Distance from the weld centre

(d)

Ratio of intensity of {0001}/{110}PFs in the SZ centre of the weld W5

Distance from the weld centre

(e)

Intensity subtraction between {0001} and {110} PFs of the weld W6

Distance from the weld centre

(f)

Ratio of intensity of {0001}/{110}PFs in the SZ centre of the weld W6

Distance from the weld centre

293

(g)

(h)

(i)

(j)

294
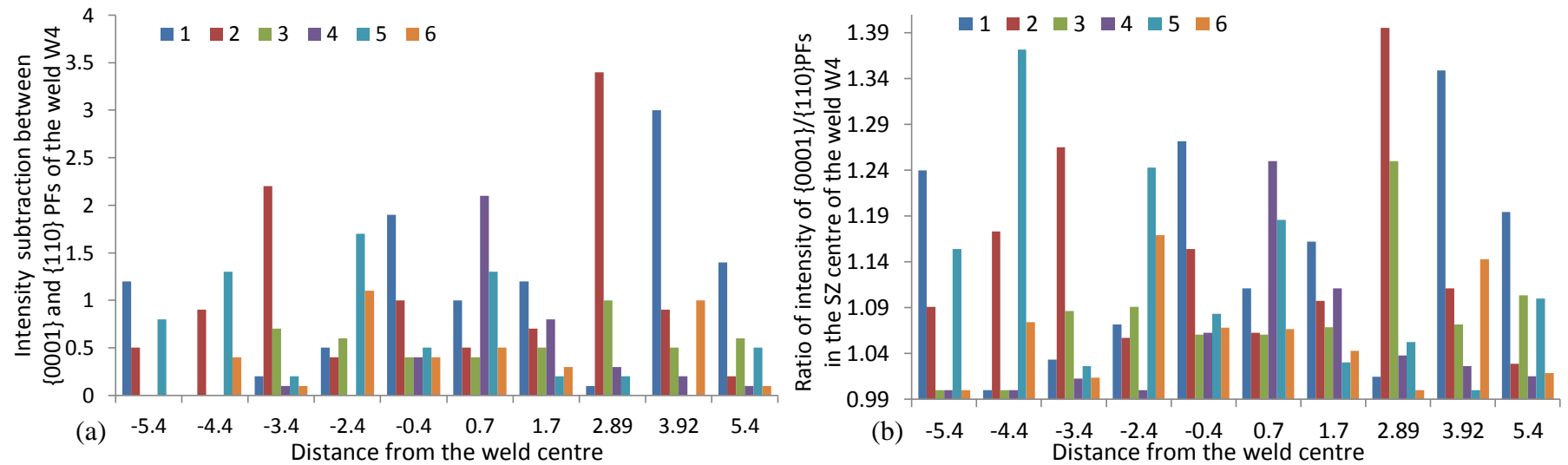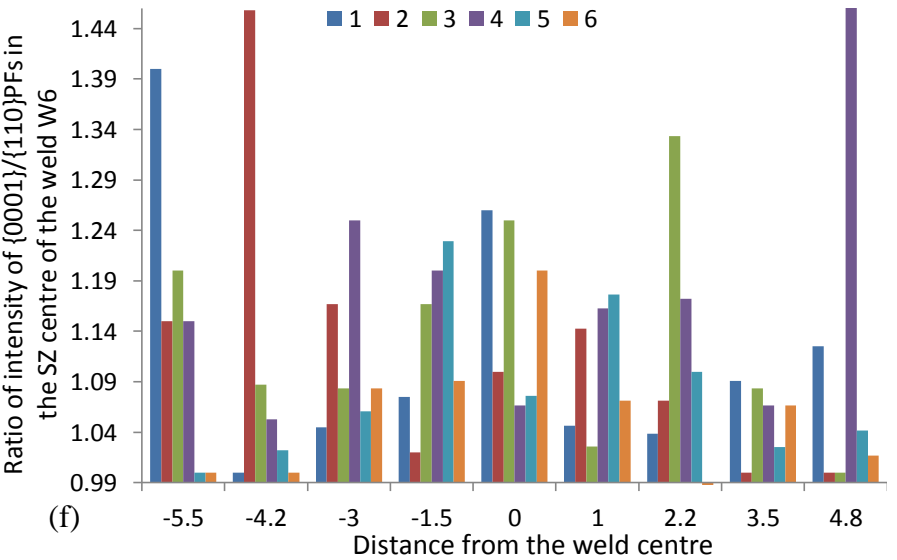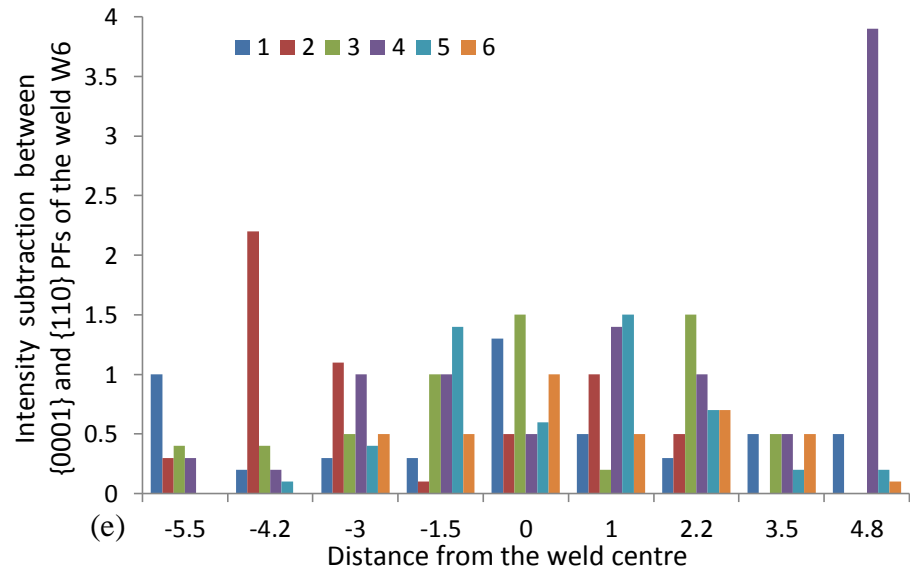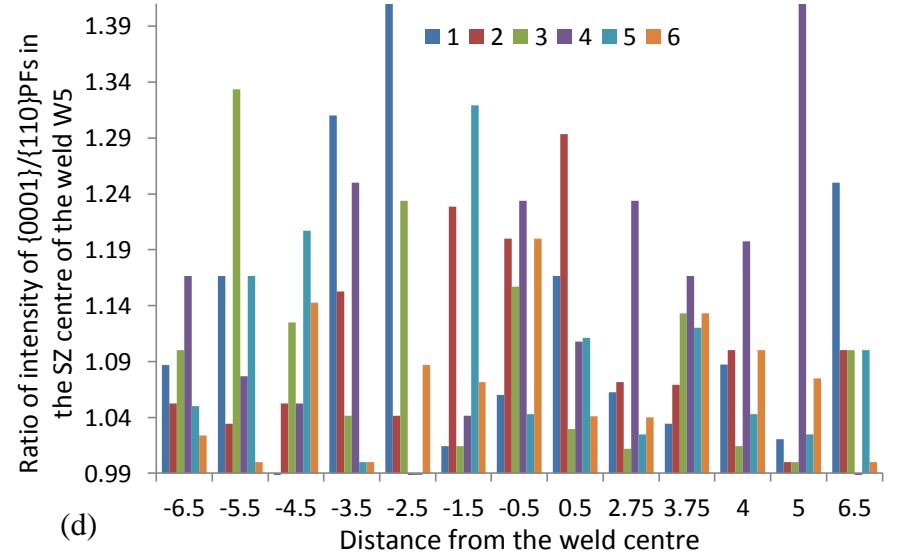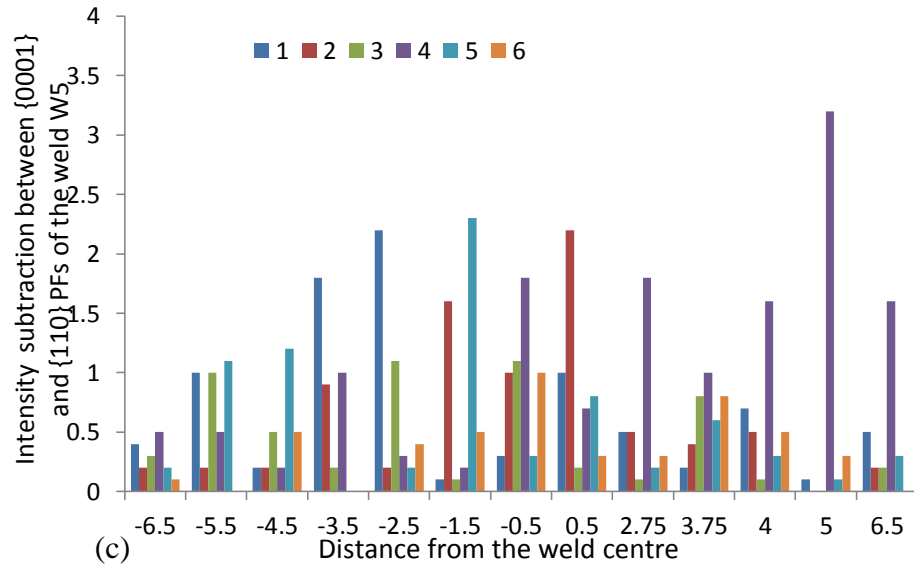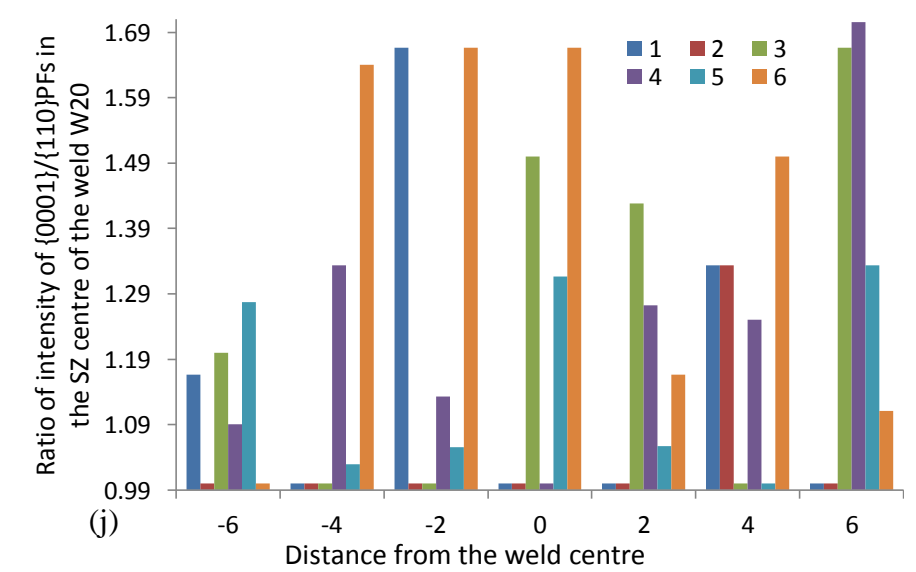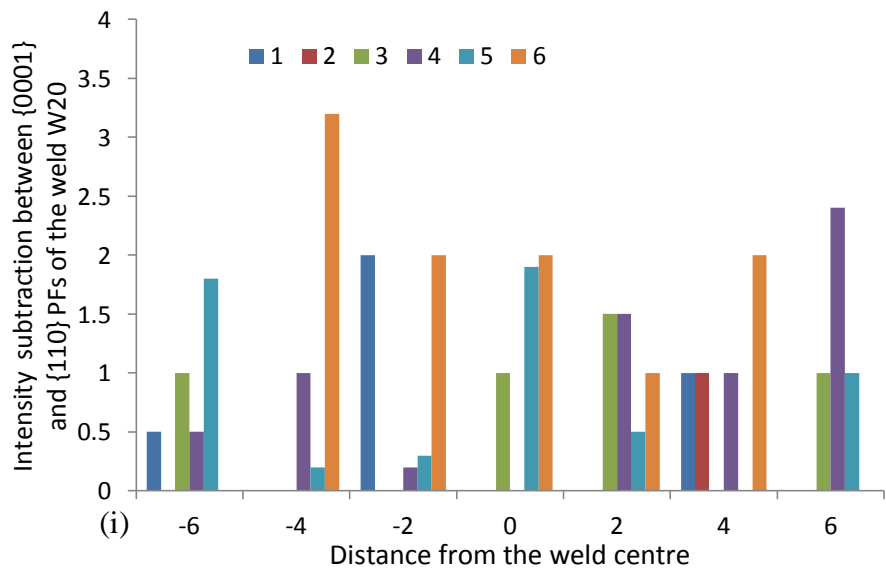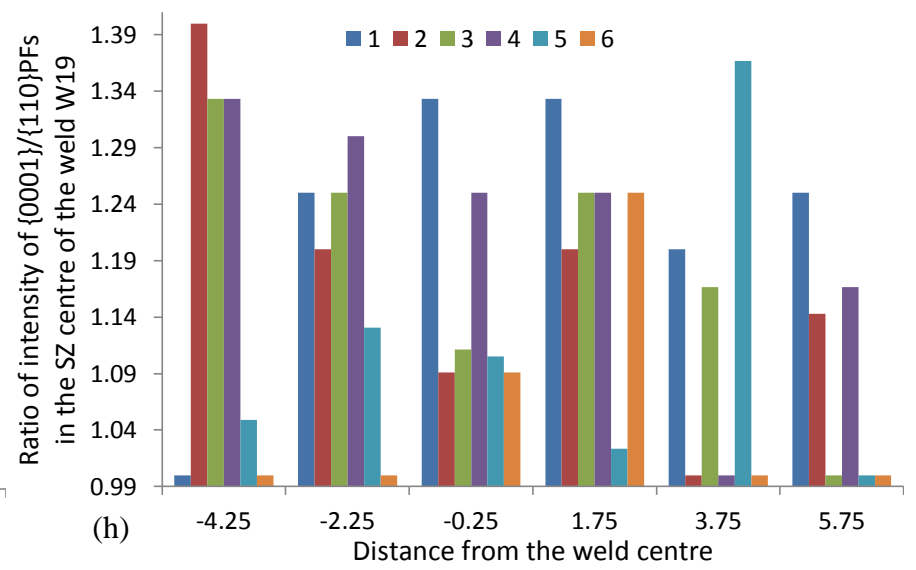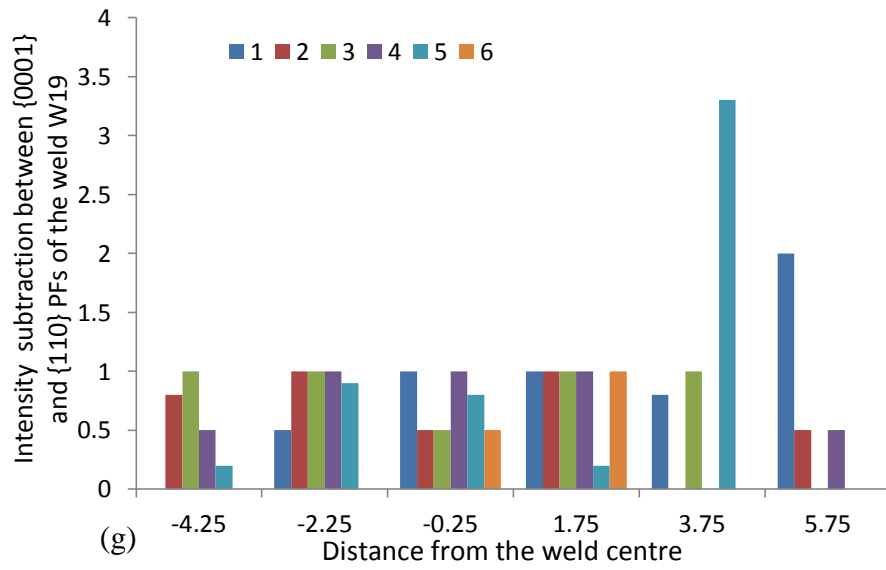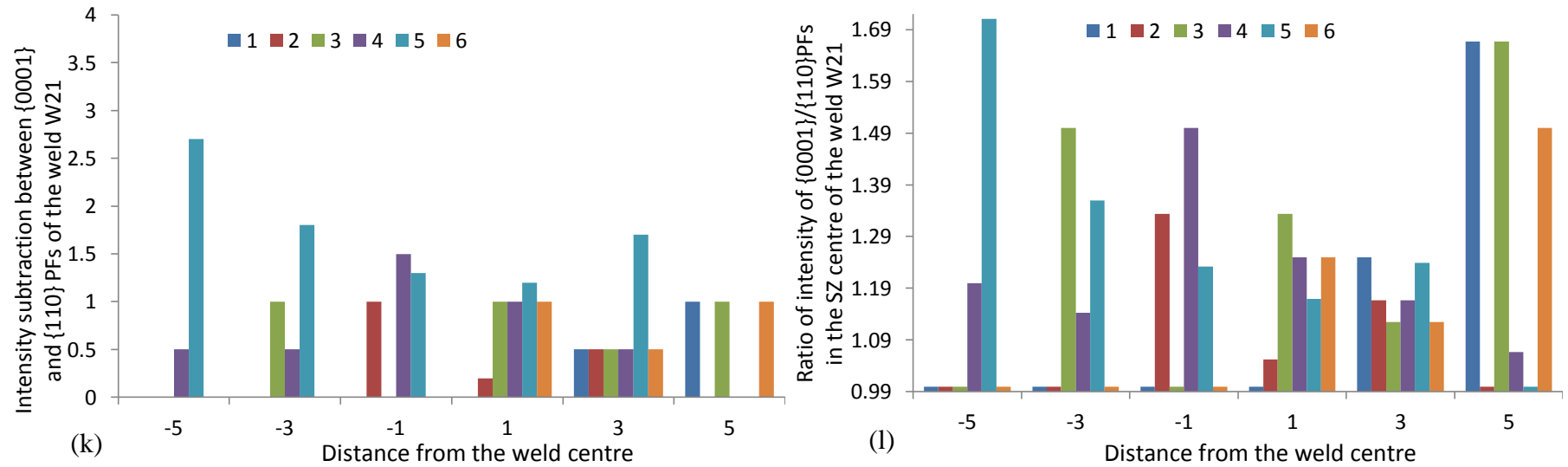
Figure 6.60 Histograms of (a) intensity subtraction between {0001} and {110} PFs and (b) ratio of {0001}α ↔{110}β pole intensity for the six poles 1-6 and in the SZ from the RS to the AS for W4; Similarly, (c) and (d) for W5, (e) and (f) for W6, (g) and (h) for W19, (i) and (j) for W20, (k) and (l) for W21
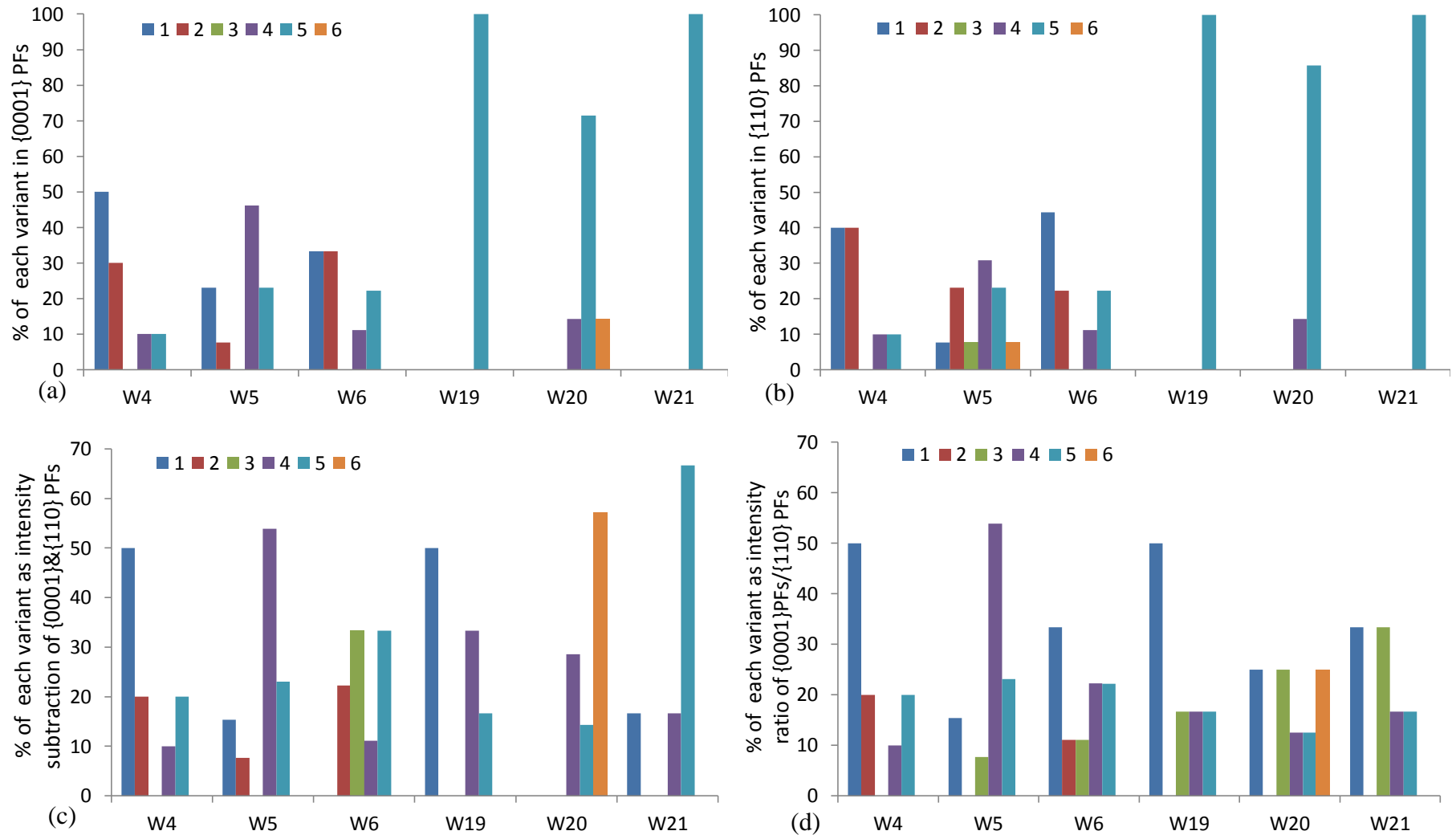
Figure 6.61 Percentage of each variant with the highest pole intensity in (a) {0001}PFs and (b) {110}PFs; Percentage of each variant with (c) the largest subtraction of {0001}and{110} pole intensity and (d) the highest ratio of {0001}α ↔{110}β pole intensity for all the six welds
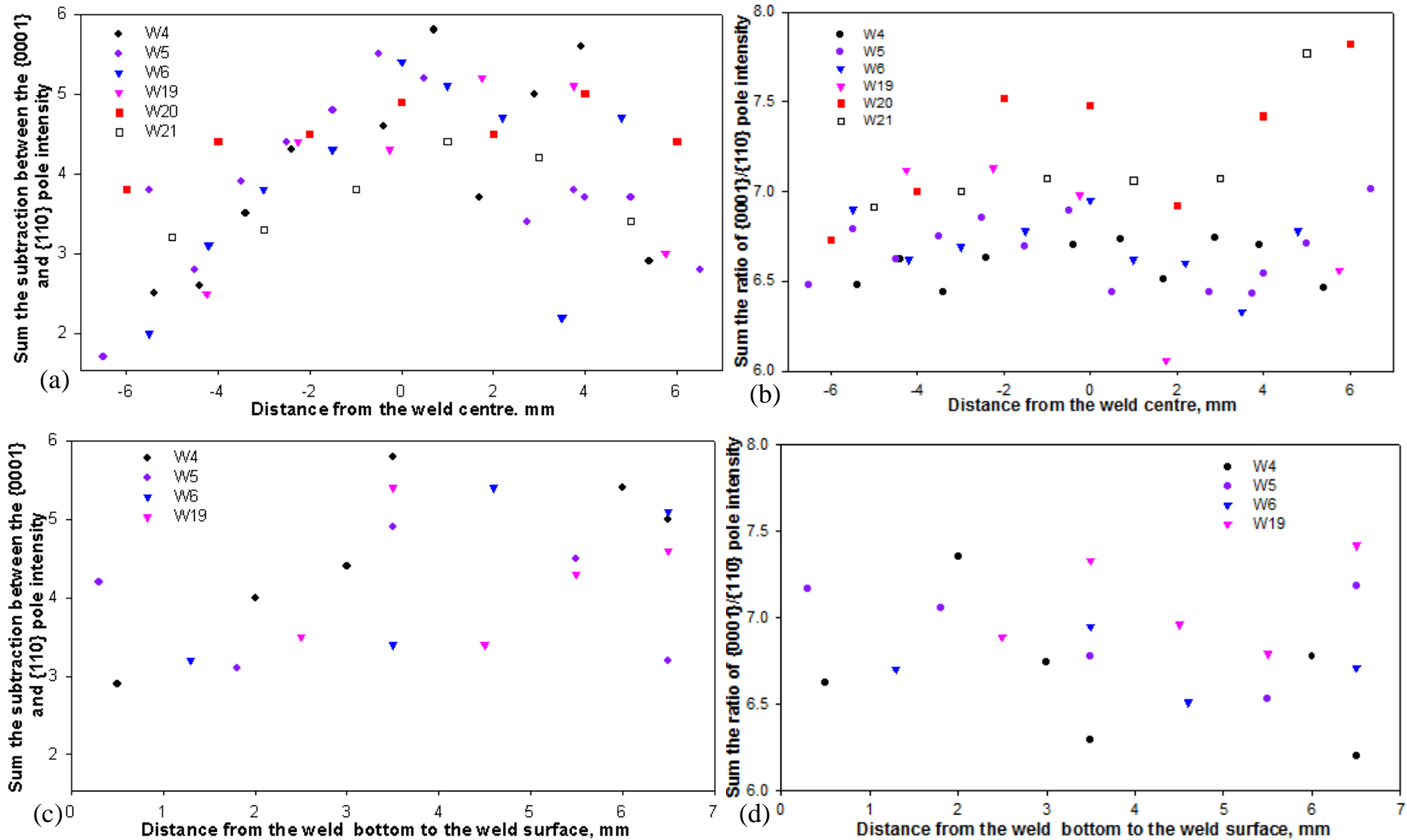
Figure 6.62 Variant selection intensity as a function of the distance from the weld centre from the RS to the AS of all the six welds in terms of the sum of (a) the subtraction between the {0001} and {110} pole intensity, (b) the ratio of {0001}α ↔{110}β pole intensity;  Variant selection intensity as a function of the distance from the weld bottom to the weld surface of the four welds W4, W5, W6 and W19 in terms of the sum of (c) subtraction, (d) ratio
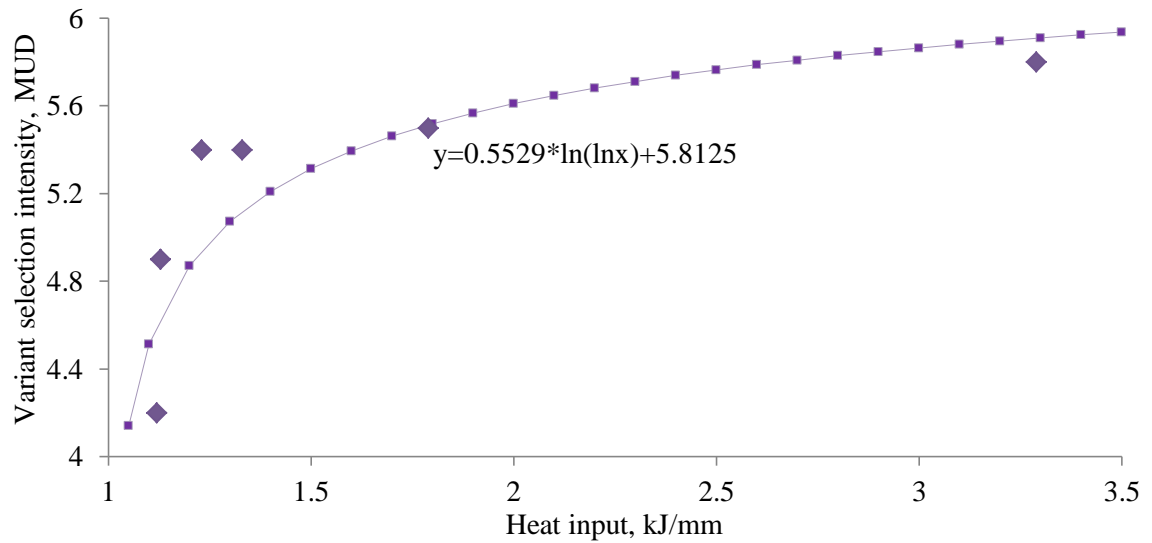
Figure 6.63 Variant selection intensity plotted against heat input in the weld centre for all the six welds

## 6.5 Measurements based on SEM and EBSD data

6.5.1 Grain size measurement of the αp grains in the base material

Manual linear intercept method was used to calculate the αp grain size in the BM and the measurement results were processed by Sigmaplot 10.0 as scatter points in horizontal (X) and vertical (Y) ways and Figure 6.64 shows the average αp grain size plotted against the side sections 4.1.b and 4.5.b, the cross section W4C4, and the normal sections 4.8.b, 6.6.b and 6.8.b. The average αp grain size is the square root of the horizontal and the vertical αp grain size.
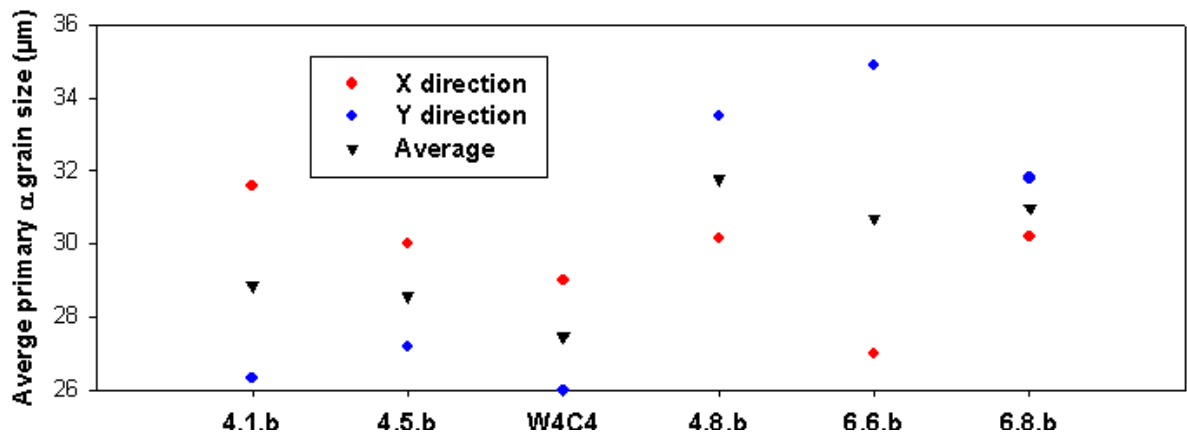


Figure 6.64 Horizontal, vertical and average αp grain size in the BM

6.5.2 Grain size measurement of the prior β grains in lamellar structure

Grain size measurement of the prior β grain size in both the coarse and fine lamellar structure of the weld zones were carried out on a reconstructed grain boundary map based on EBSD data using an in-house software (Davies, 2009) for all the six welds W4, W5, W6, W19, W20 and W21 in terms of cross sections, normal sections and side sections. Manual linear intercept method was used to calculate the prior β grain size and the measurement results were processed by Sigmaplot 10.0. Results of the prior β grain size measurement are shown as two dimensional graphs of average prior β grain size plotted against the distance from the weld centre. The average prior β grain size is taken as the square root value of the horizontal and vertical measurement of prior β grain size. The results of the average prior β grain size and aspect ratio measurement on cross sections W4C4, W5C5 and W6C6 of the three welds W4, W5 and W6 with a constant rotation speed of 900rpm are shown from Figure 6.65(a) to Figure 6.70(a), respectively. Measurements were taken from the RS to the AS of the weld zones on a horizontal line corresponding to the EBSD data of W4C4, W5C5 and W6C6 in section 6.2.2. Similarly, Figure 6.65(b) to Figure 6.70(b) show the results of the average prior β grain size and aspect ratio for the three welds W19, W20 and W21 with a constant traverse speed of 150mm/min, and measurements were taken from the RS to the AS of the weld zones on a horizontal line, corresponding to the EBSD data of W19, W20 and W21 in section 6.2.2.

The average prior β grain size measurement of W4C4 is shown in Figure 6.65(a), which was taken from the RS to the AS on a horizontal line of all the five parts of W4C4 in Section 6.2.2 and aspect ratio (≥1) of prior β grain size in terms of vertical grain size divided by the horizontal grain size or the horizontal grain size divided by the vertical grain size was plotted against distance from the weld centre, as shown in Figure 6.65(b). It is seen that the average prior β grain size was the largest in the weld centre and it decreased gradually from the weld centre to the TMAZ and the weld surface has slightly larger grain size than the weld bottom (Figure 6.65(a)). Figure 6.65(b) shows that the aspect ratio is the smallest in the weld centre and is generally higher at the AS than the RS.
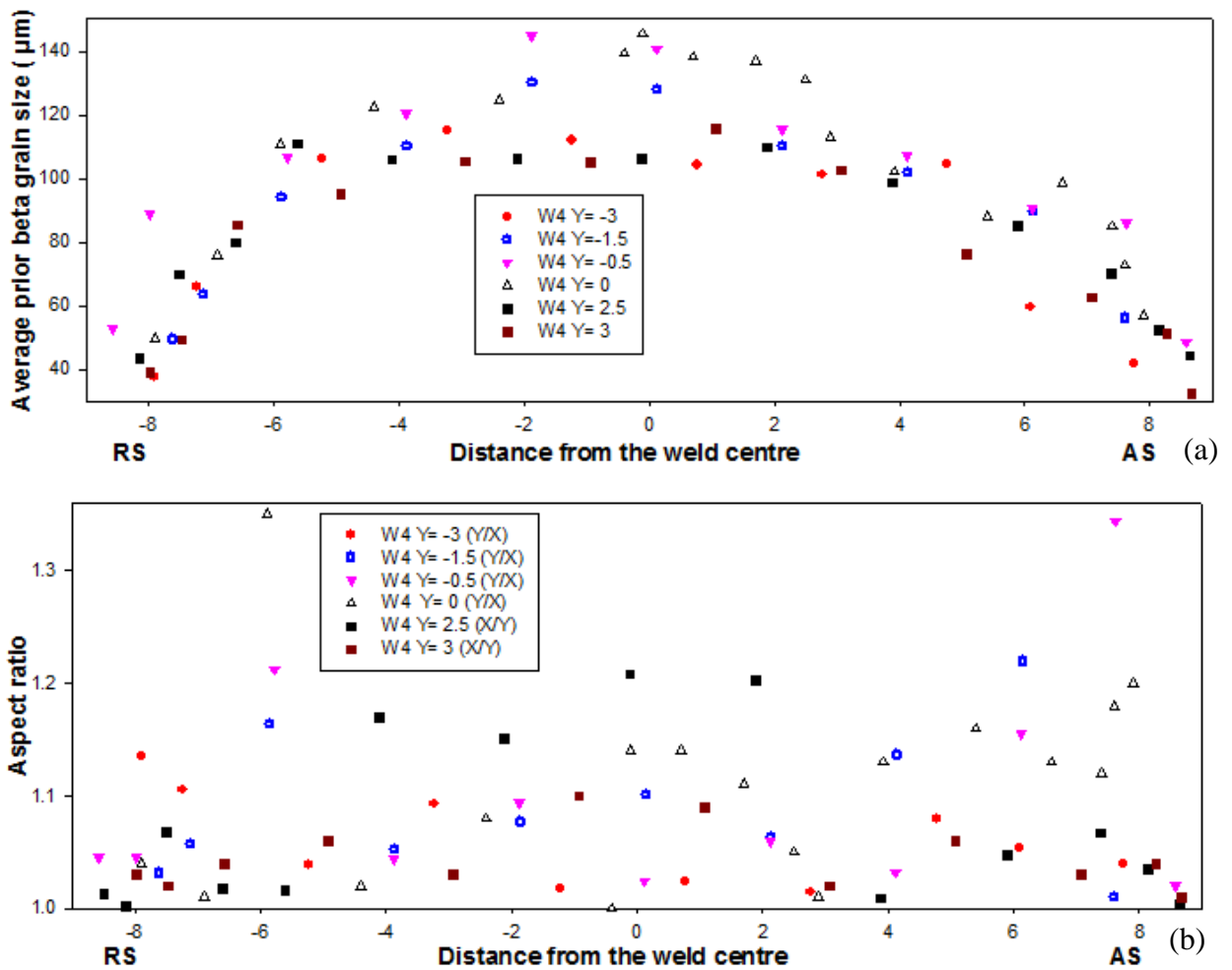
Figure 6.65 (a) Average prior β grain size measurement of W4C4, data was taken from the weld bottom to the weld surface and the corresponding (b) aspect ratio (Y/X: vertical grain size/horizontal grain size; X/Y: horizontal grain size/vertical grain size)

Figure 6.66(a) shows the average prior β grain size measurement of W5C5 taken from the RS to the AS on a horizontal line of all the five parts of W5C5 and aspect ratio of the prior β grain size was plotted against distance from the weld centre, as shown in Figure 6.66(b). Aspect ratio (≥1) can be either the vertical grain size divided by the horizontal grain size or the horizontal grain size divided by the vertical grain size. It was observed that the average prior β grain size was the largest in the weld centre and it decreased gradually from the weld centre to the TMAZ; the weld surface has larger grain size than the weld bottom (Figure 6.66(a)). Only the SZ centre has lower grain aspect ratio and the AS has slight higher grain aspect ratio than the RS indicating more severely deformation has occurred at the AS (Figure 6.66(b)).
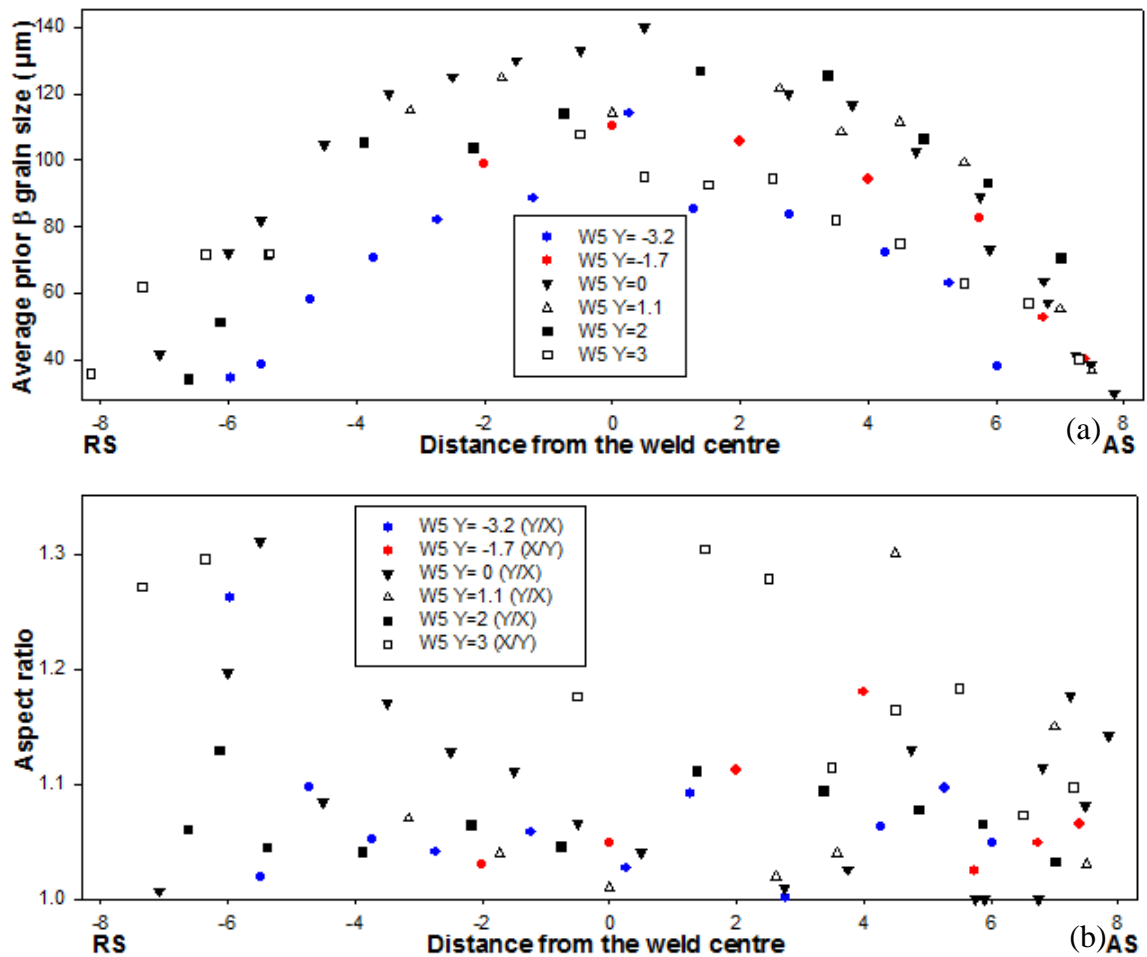
Figure 6.66 (a) Average prior β grain size measurement of W5C5, data was taken from the weld bottom to the weld surface and the corresponding (b) aspect ratio (Y/X: vertical grain size/horizontal grain size; X/Y: horizontal grain size/vertical grain size)

Figure 6.67(a) shows the average prior β grain size measurement of W6C6 taken from the RS to the AS on a horizontal line of all the five parts of W6B6 and aspect ratio of prior β grain size was plotted against distance from the weld centre, as shown in Figure 6.67(b). aspect ratio (≥1) of the prior β grain size can be either the vertical grain size divided by the horizontal grain size or the horizontal grain size divided by the vertical grain size. It was shown in Figure 6.67(a) that the average prior β grain size was the largest in the weld centre and it decreased gradually from the weld centre to the TMAZ; Aspect ratio is larger at the AS than the RS (Figure 6.67(b)).
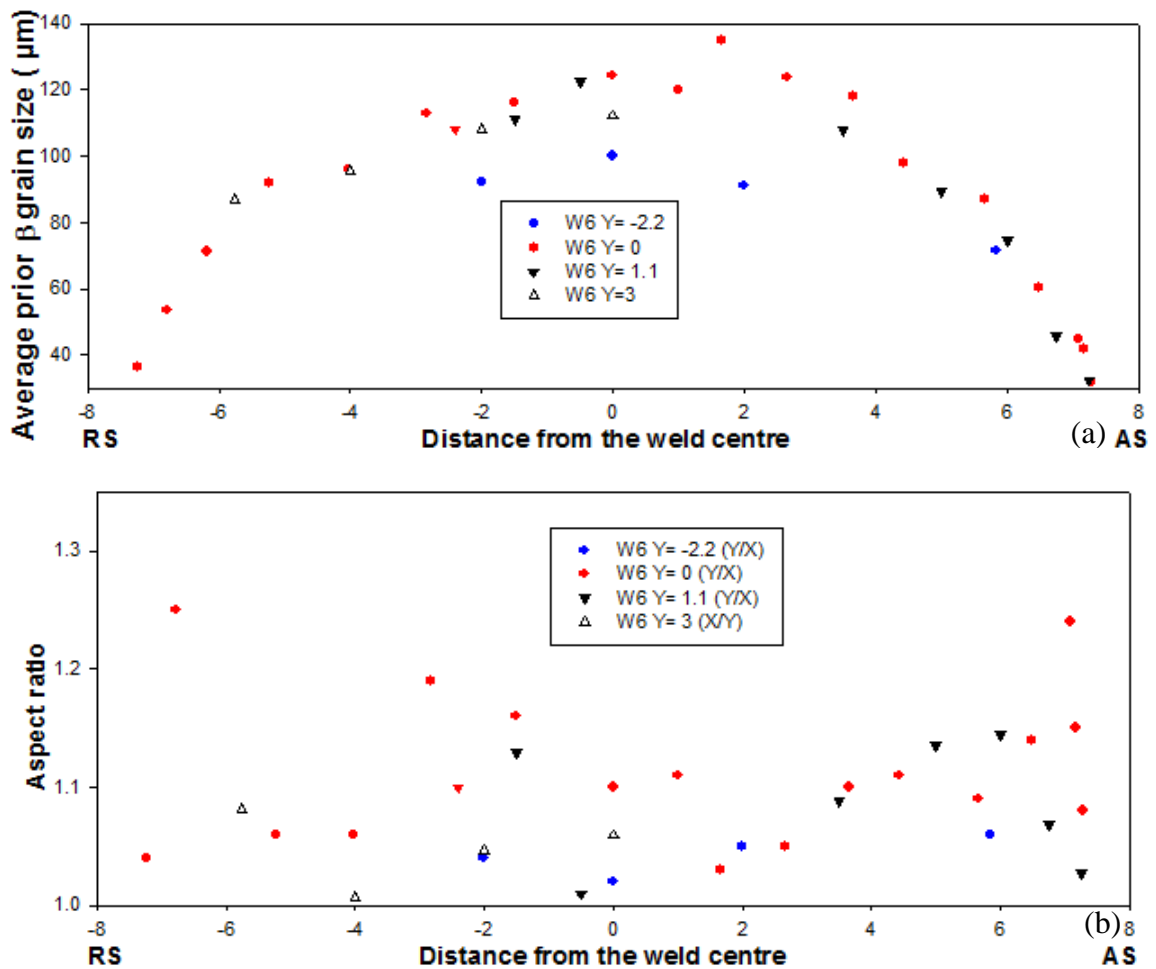
Figure 6.67 (a) Average prior β grain size measurement of W6C6, data was taken from the weld bottom to the weld surface and the corresponding (b) aspect ratio

Figure 6.68(a) shows the average prior β grain size measurement of W19 taken from the RS to the AS on a horizontal line of all the five parts of W19 and aspect ratio of the prior β grain size was plotted against distance from the weld centre as shown in Figure 6.68(b). Aspect ratio (≥1) is the vertical grain size divided by the horizontal grain size (all Y/X). It is seen in Figure 6.68(a) that the prior β grain size is the largest in the weld centre and it decreases gradually from the weld centre to the TMAZ; The average prior β grain size at the AS is much larger than that at the AS indicating the AS has experienced higher peak weld temperature than the RS; the weld surface has larger grain size than the region 1.4mm to the weld bottom. Figure 6.68(b) shows that only the SZ centre has lower grain aspect ratio and the AS has slightly higher grain aspect ratio than the RS indicating more severely deformation has occurred at the AS.
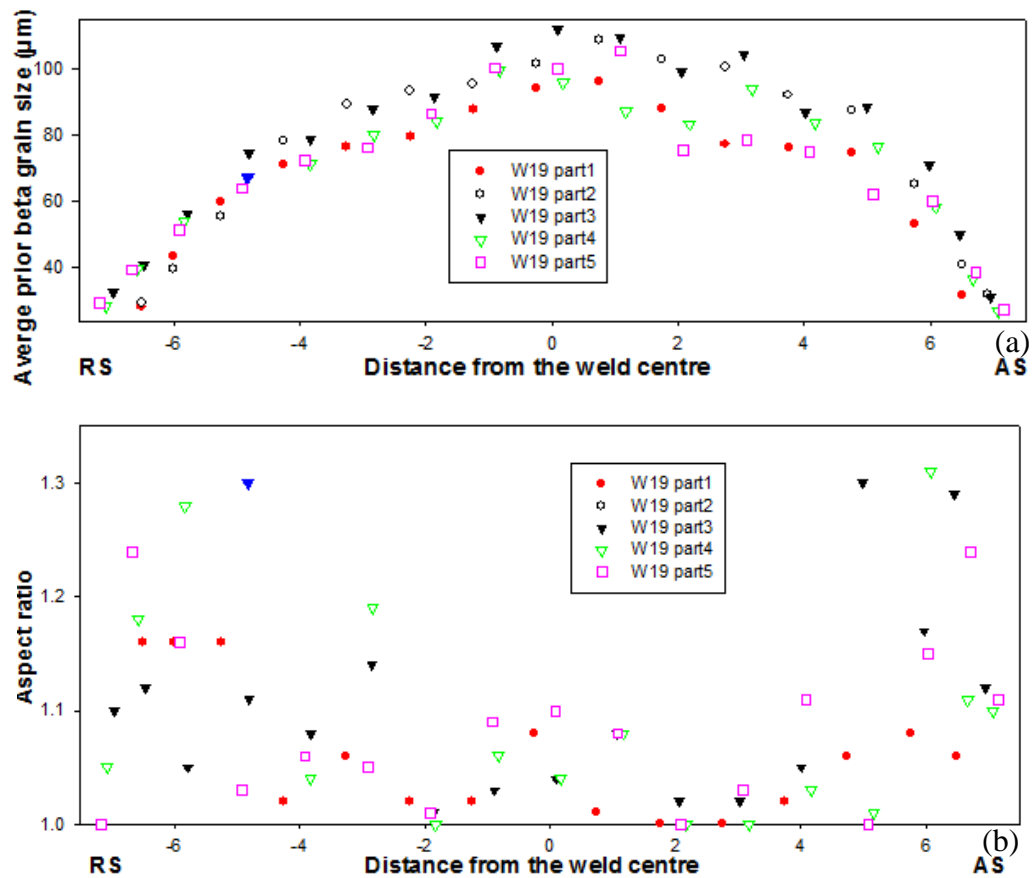
Figure 6.68 (a) Average prior β grain size of the cross section of the weld W19, data was taken from two thirds of the plate thickness to the weld surface, (b) Aspect ratio of the prior β grain size of the five parts (Y/X: vertical grain size/horizontal grain size)

Two average prior β grain size measurements taken from the RS to the AS of W20 on the central horizontal line is shown Figure 6.69(a), and aspect ratio (≥1) of the prior β grain size in terms of the vertical grain size divided by the horizontal grain size was plotted against distance from the weld centre, as shown in Figure 6.69(b). It can be seen that the average prior β grain size at the AS is much larger than that at the RS and this also meant that the AS has experienced higher peak weld temperature than the RS (Figure 6.69(a)). Figure 6.69(b) shows that centre of the SZ has lower grain aspect ratio and the AS has slight higher grain aspect ratio than the RS indicating more severely deformation has occurred at the AS.
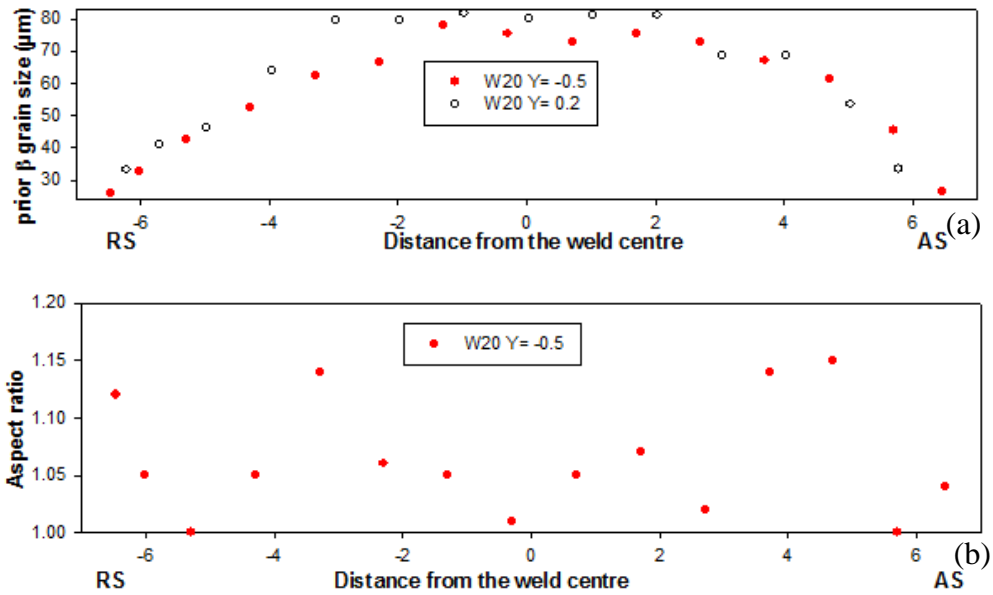
Figure 6.69 (a) Average prior β grain size of the cross section of the weld W20 (b) Aspect ratio (Y/X) of the prior β grain size of the weld centre of W20

Figure 6.70(a) shows the average prior β grain size measurement of W21 taken from the RS to the AS on a horizontal line and aspect ratio (≥1) of the prior β grain size was plotted against distance from the weld centre, as shown in Figure 6.70(b). Aspect ratio (≥1) is the vertical grain size divided by the horizontal grain size. It can be seen from Figure 6.69(a) that the weld centre has the largest prior β grain size and the average prior β grain size at the AS is much larger than that at the RS and this also meant that the AS has experienced higher peak weld temperature than the RS. Figure 6.70(b) shows that aspect ratio of the prior β grain size is the lowest at the AS, and is the highest at the RS.
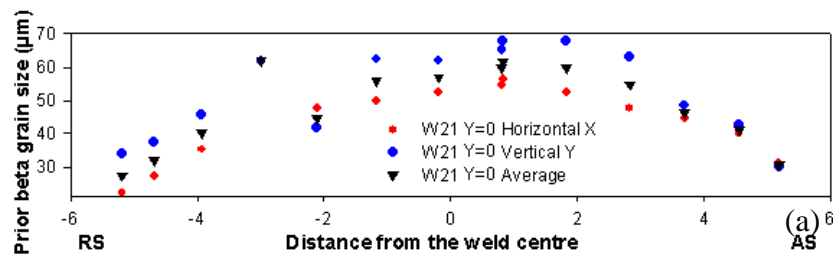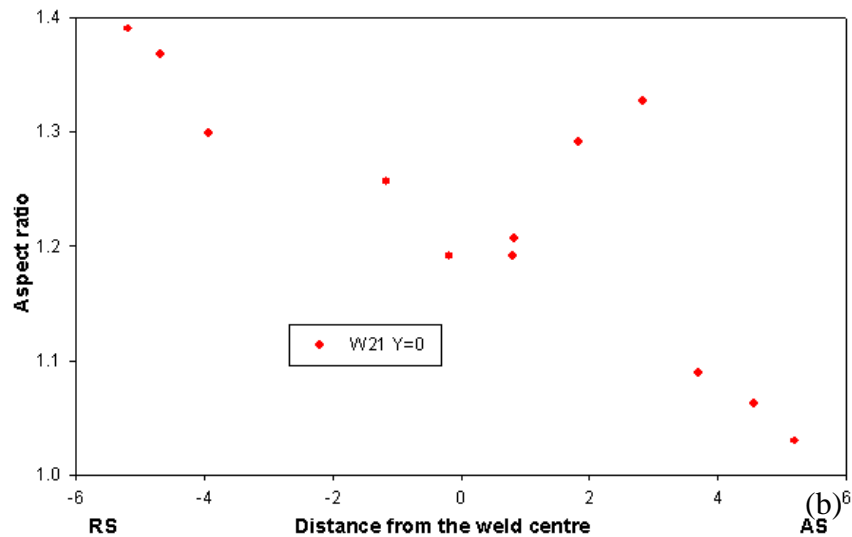
Figure 6.70 (a) Average prior β grain size of the cross section of the weld W21 in both vertical and horizontal directions; (b) aspect ratio of the prior β grain size (Y/X)

Figure 6.71(a) shows the average prior β grain size measurement of the weld centre of the cross section of the weld W4, W5, W6, W19, W20 and W21 on a horizontal line and the corresponding aspect ratio of the prior β grain size of all the cross sections is shown in Figure 6.71(b). It is clearly seen that the prior β grain size decreases with increasing traverse speed and as rotation speed increases, the average prior β grain size increases. Figure 6.71(b) clearly shows that aspect ratio is generally larger at the AS than the RS and the weld centre has the lowest aspect ratio. It was also shown from Figure 6.64(b) to Figure 6.71(b) that the prior β grains are generally larger in the vertical measurement compared to that in the horizontal measurement in the weld centre for all the six welds W4, W5, W6, W19, W20 and W21, this indicates that the prior β grains are elongated along the ND in the weld centre. Figure 6.71(b) shows that W21 has the highest aspect ratio in the weld zones compared to the other five welds.
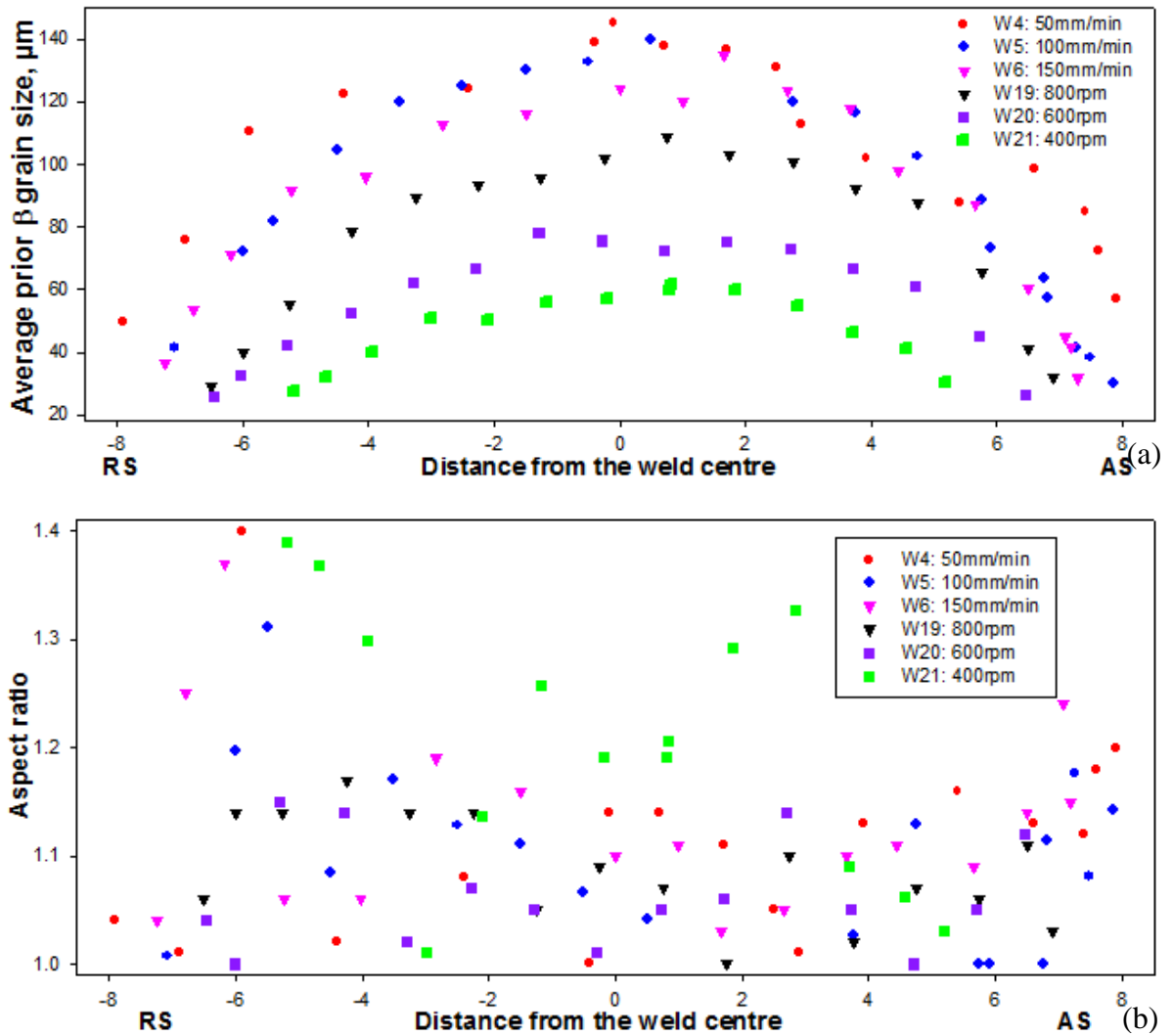
Figure 6.71 (a) Average prior β grain size of the centre of the cross section of the weld W4, W5, W6, W19, W20 and W21; (b) Aspect ratio (all Y/X: vertical grain size/horizontal grain size)) of prior β grain size of all the cross sections

Average prior β grain size measurements taken from the weld centre of all the normal sections of the three welds W4, W5 and W6 is shown in Figure 6.72(a) with vertical error bars and Figure 6.72(b) displays aspect ratio (≥1) of the prior β grain size taken from the weld centre. A comparison can be made for the prior β grain size between all the normal sections from the three welds W4, W5 and W6 in terms of the weld surface, weld centre and weld bottom. It can be seen from Figure 6.72(a) that the normal section 4.7.c from the weld centre of W4 has the largest grain size and the weld bottom of 4.8.c has larger grain size compared to the weld surface of 4.6.c. It was also observed that, in the normal sections for the welds W5 and W6, the largest grain size was found in the normal sections 5.7.c and

306

6.7.c from the weld centre of W5 and W6 and the weld surface (5.6.c and 6.6.c) has larger grain size than the weld bottom (5.8.c and 6.8.c). It is seen from Figure 6.72(a) that the prior β grain size is the largest in the central normal section 4.7.c and it decreases from 4.7.c to 5.7.c and 6.7.c, moreover, the prior β grain size decreased from 4.8.c to 5.8.c and 6.8.c, this again suggests that the prior β grain size decreases with increasing traverse speed from 50 to 100 and 150mm/min in the weld centre and the weld bottom, however, it should be noted that the weld surface of 4.6.c has the smallest grain size compared to 5.6.c and 6.6.c from the weld surface of W5 and W6, which could be attributed to the grain refinement in the W-Re containing region at the weld surface. Figure 6.72(b) shows that the aspect ratio is the highest in the weld centre (4.7.c to 5.7.c and 6.7.c) and the weld surface (5.6.c and 6.6.c) has higher aspect ratio than the weld bottom (5.8.c and 4.8.c).
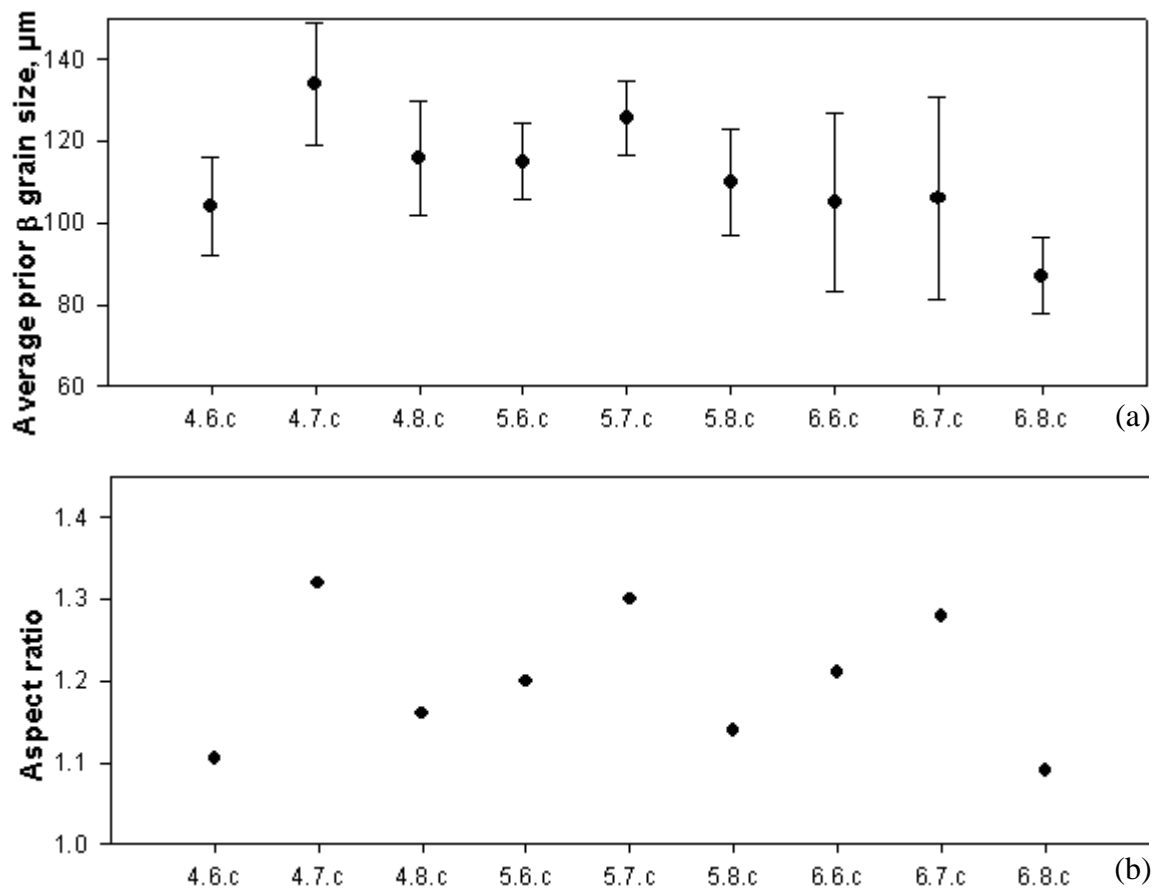


Figure 6.72 Average prior β grain size of the centre of (a) all the normal sections; (b) aspect ratio

Figure 6.73(a) shows the average prior β grain size measurements taken from the weld centre on a horizontal line of all the side sections with vertical error bars and the corresponding aspect ratio of the prior β grain size is shown in Figure 6.73(b). A comparison can be made for the prior β grain size between the side sections from the three welds W4, W5 and W6 by comparing the average prior β grain size of the weld centre on a horizontal line of the side sections. It was shown in Figure 6.73(a) that the prior β grain sizes in the side sections (4.2.c, 4.3.c and 4.4.c) of W4 with the lowest traverse speed are generally greater than that of W5 (5.2.c, 5.3.c and 5.4.c) with medium traverse speed and the side sections of W5 (5.2.c, 5.3.c and 5.4.c) have larger grain size compared to the side sections of W6 (6.2.c, 6.3.c and 6.4.c), this again suggest that the prior β grain size decreases with increasing traverse speed from 50 to 100 and 150mm/min. In comparison of the two side sections 4.2.c and 4.3c taken from the symmetric position with respect to the central vertical line of the cross section at both the AS and the RS, 4.2.c from the AS has slightly larger prior β grain size than 4.3.c from the RS. Similarly, 5.2.c and 6.2.c have slightly larger prior β grain size than 5.3.c and 6.3.c, respectively. Moreover, it is seen in Figure 6.73(b) that aspect ratio of the prior β grain size in the side sections at the AS (4.2.c, 5.2.c and 6.2.c) is larger compared to that in the side sections at the RS (4.3.c, 5.3.c and 6.3.c). This also suggest that the prior β grain size is slightly larger at the AS than the RS and the AS has a greater aspect ratio compared to the RS, indicating materials at the AS have experienced slightly higher peak weld temperature compared to materials at the RS and they have undergone more deformation at the AS compared to materials at the RS.



(a)
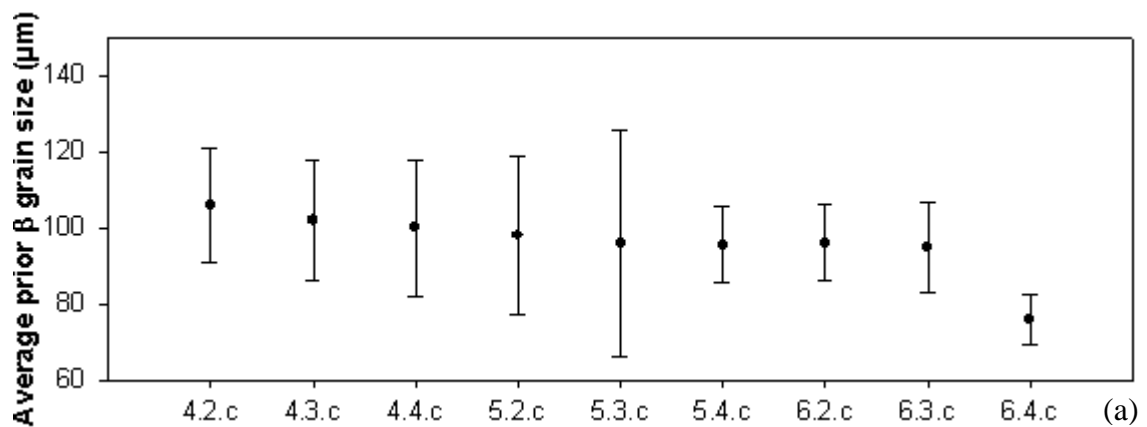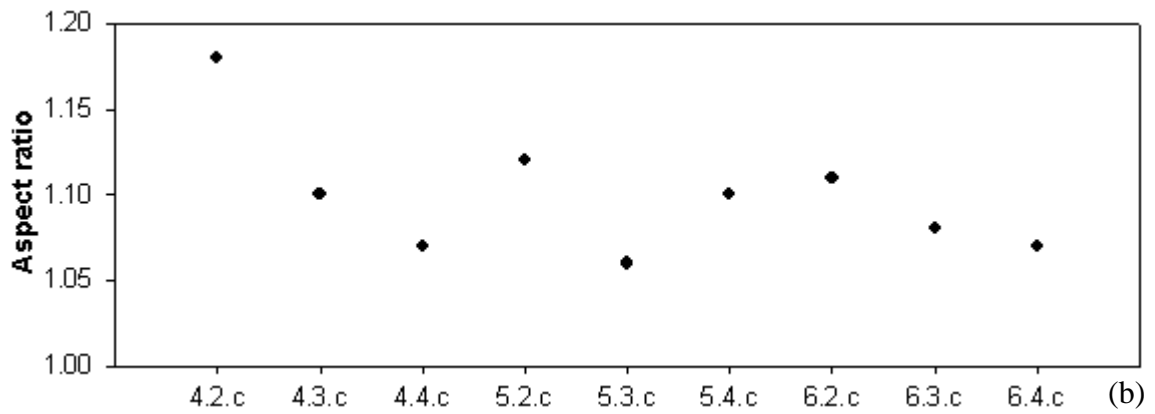
Figure 6.73 Average prior β grain size of the centre of (a) all side sections of all the three welds W4, W5 and W6; (b) aspect ratio

6.5.3 Volume fraction measurement of retained β phase and transformed β phase in the BM and the HAZ

Volume fraction measurement of retained β phase and transformed β phase in the equiaxed and bimodal structure were carried out on Secondary electron micrographs at both the AS and the RS of the welding edge of all the six welds by calculating the volume fraction of retained β phase in the equiaxed structure and the volume fraction of αp phase in the bimodal structure. It should be noted that the volume fraction mentioned here is the area fraction. The results of volume fraction measurement of retained β phase and transformed β phase for the three welds W4, W5 and W6 are shown from Figure 6.74 to Figure 6.76 as two dimensional graphs of scatter points with volume fraction Vv plotted against distance from the weld centre. Similarly, Figure 6.77, Figure 6.78 and Figure 6.79 show the volume fraction measurement of retained β phase and transformed β phase in the equiaxed and bimodal structure at both the AS and the RS of the three welds W19, W20 and W21. Error bars for each micrograph at both the AS and the RS of all the six welds were ±0.01-0.02%. According to the aforementioned study, the volume fraction of retained β phase and transformed β phase increased to 100% in the region with fully lamellar structure, however, the upper limit of volume fraction was defined as 0.8-0.85 due to the difficulty in measuring the volume fraction of the αp grains in the bimodal structure 150μm adjacent to the coarse lamellar structure. It can be clearly seen from Figure 6.74, Figure 6.75 and Figure 6.76 that as the increase of traverse speed, the width of the equiaxed and bimodal structure decreased at both the AS and the RS, and the width of the bimodal structure is

309

much larger at the RS compared to that at the AS for the two welds W4 and W5, which shows agreement with the aforementioned study in Section 5.33. Thus, gradient of the curves became steeper with increasing traverse speed, which means that thermal gradient was the deepest in the weld W6 with the highest traverse speed of 150mm/min, and it decreased with decreasing traverse speed. For example, in the weld centre at the AS of all the three welds W4, W5 and W6, gradients of the blue curves consist of measured points are 40.2º, 48.7º and 55.2º, respectively, thus gradient of the curves increased by 21% and 13% with increasing traverse speed from 50 to 100mm/min and 100 to 150mm/min, respectively. This suggests that the corresponding thermal gradient or temperature gradient increased with increasing traverse speed according to the β approach curve for Ti-6Al-4V (Semiatin and Bieler, 2001; Tamirisakandala et al., 2005). It can be seen that the volume fraction of retained β phase and transformed β phase is higher at the AS than that at the RS for the weld surface, the weld centre and the weld bottom of the three welds W4, W5 and W6 indicating the AS has experienced slightly higher peak weld temperature than the RS.
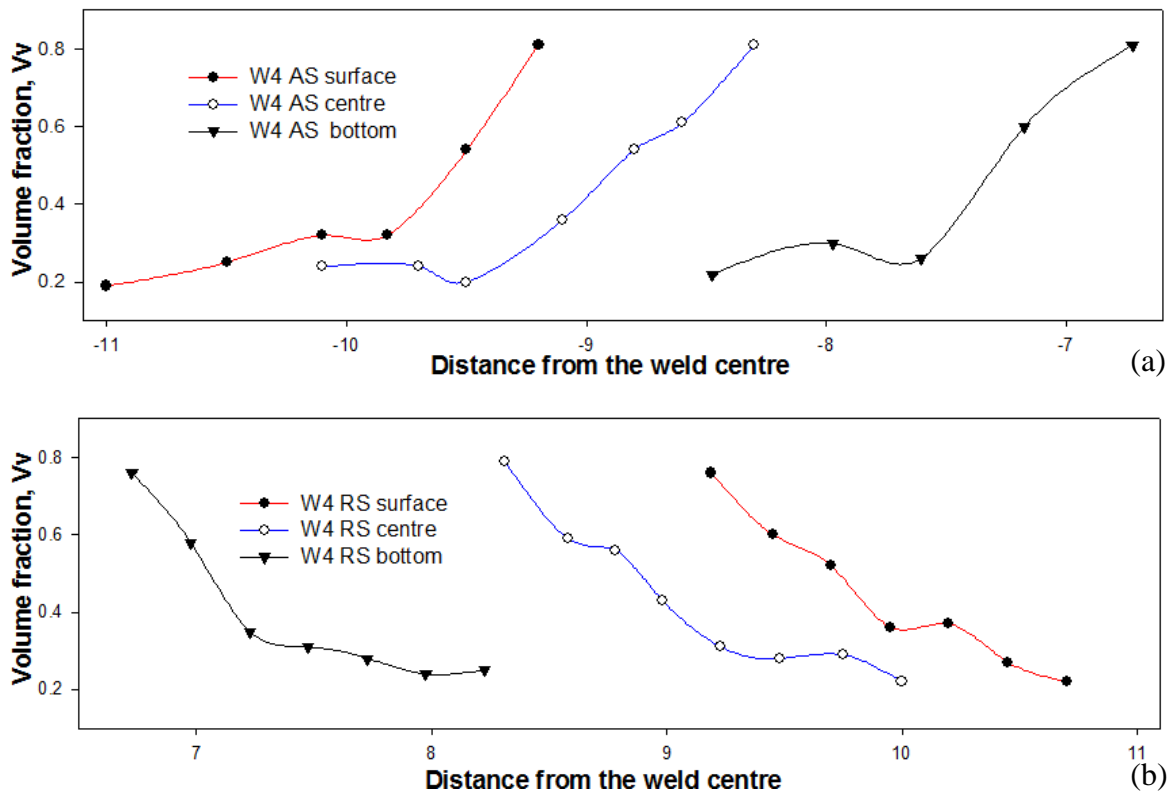


Figure 6.74 Volume fraction of retained β phase and transformed β phase in the equiaxed and bimodal structure at both: (a) the AS and (b) the RS of the welding edge for W4
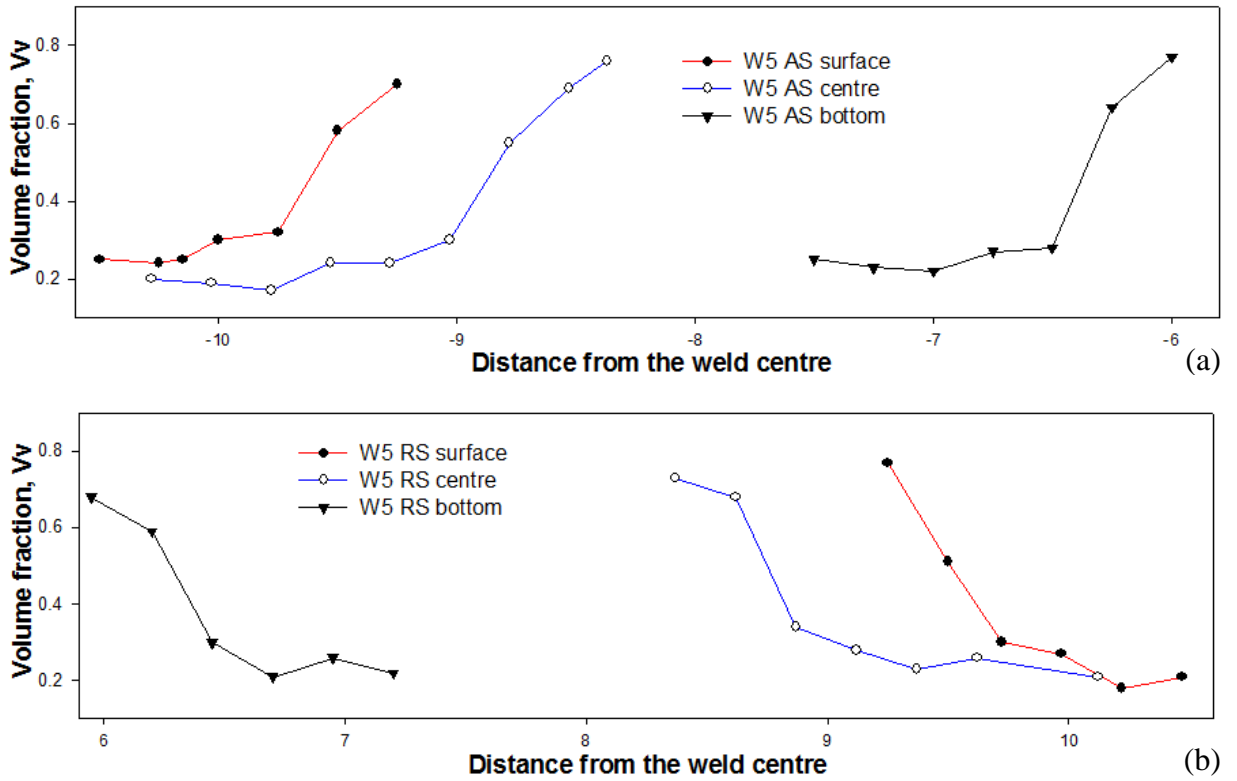
Figure 6.75 Volume fraction of retained β phase and transformed β phase in the equiaxed and bimodal structure at both: (a) the AS and (b) the RS of the welding edge for W5
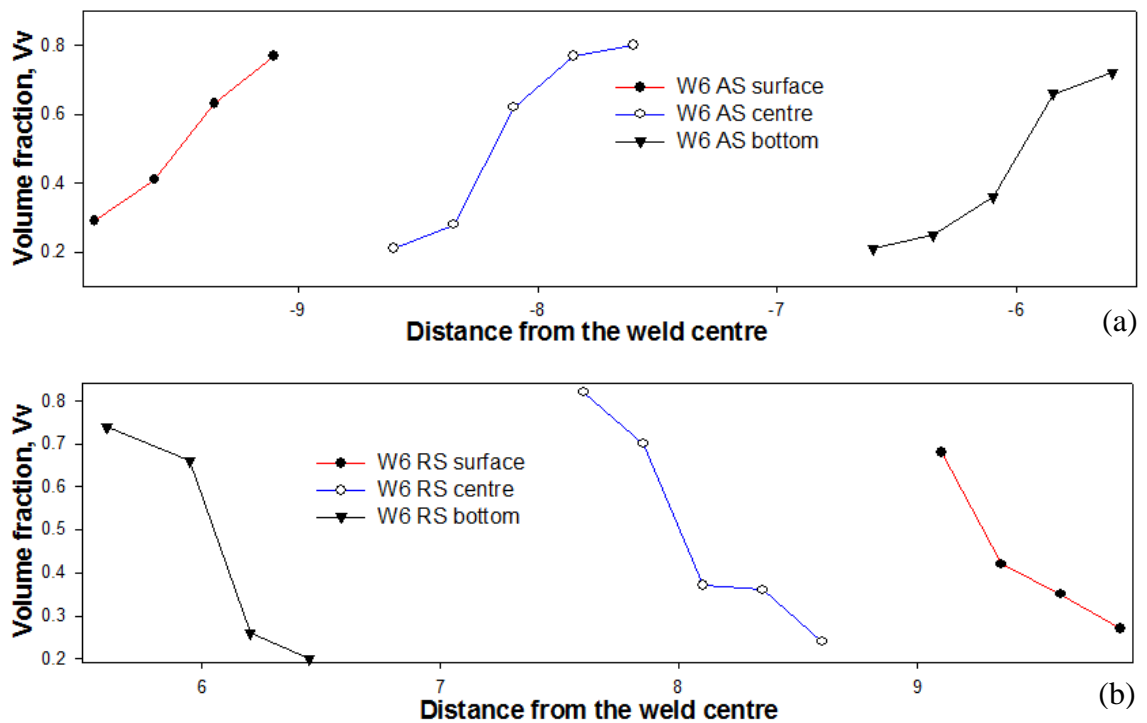


Figure 6.76 Volume fraction of retained β phase and transformed β phase in the equiaxed and bimodal structure at both: (a) the AS and (b) the RS of the welding edge for W6

311

Figure 6.77, Figure 6.78 and Figure 6.79 show that as the decrease of rotation speed, the width of the bimodal structure decreased at both the AS and the RS, which shows agreement with the results in Section 5.3 and the width of the bimodal structure is much larger at the RS compared to the AS for the three welds W19, W20 and W21 with a constant traverse speed. Thus, gradient of the curves became steeper with decreasing rotation speed, and this would suggest that thermal gradient was the deepest in the weld W21 with lowest rotation speed of 400rpm, and it decreased with increasing rotation speed from 400 to 600 and 800rpm. For example, at the AS of the weld centre, gradient of the blue curves increased by 5% and 8% with decreasing rotation speed from 800 to 600rpm and 600 to 400rpm, respectively. It should be noted again that the volume fraction of retained β phase and transformed β phase is higher at the AS than at the RS for both the weld surface, the weld centre and the weld bottom of the three welds W19, W20 and W21 due to the fact that the AS has experienced slightly higher peak weld temperature than the RS.
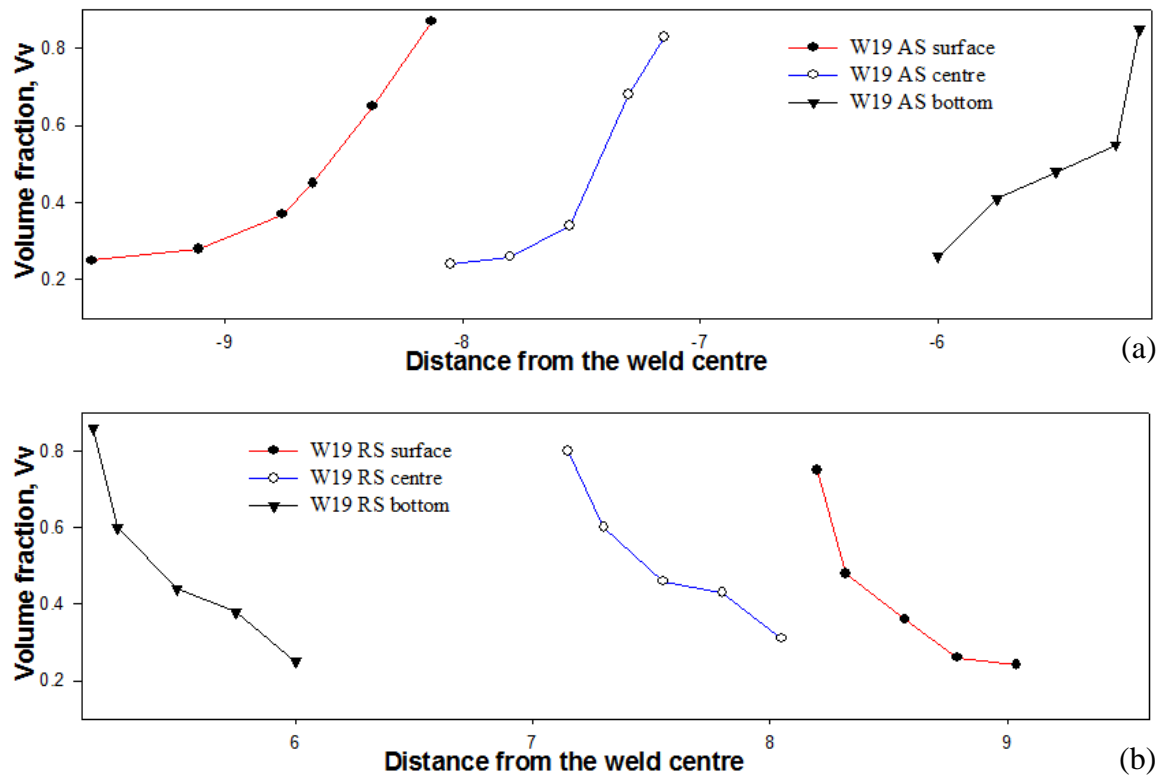


Figure 6.77 Volume fraction of retained β phase and transformed β phase in the equiaxed and bimodal structure at both: (a) the AS and (b) the RS of the welding edge for W19
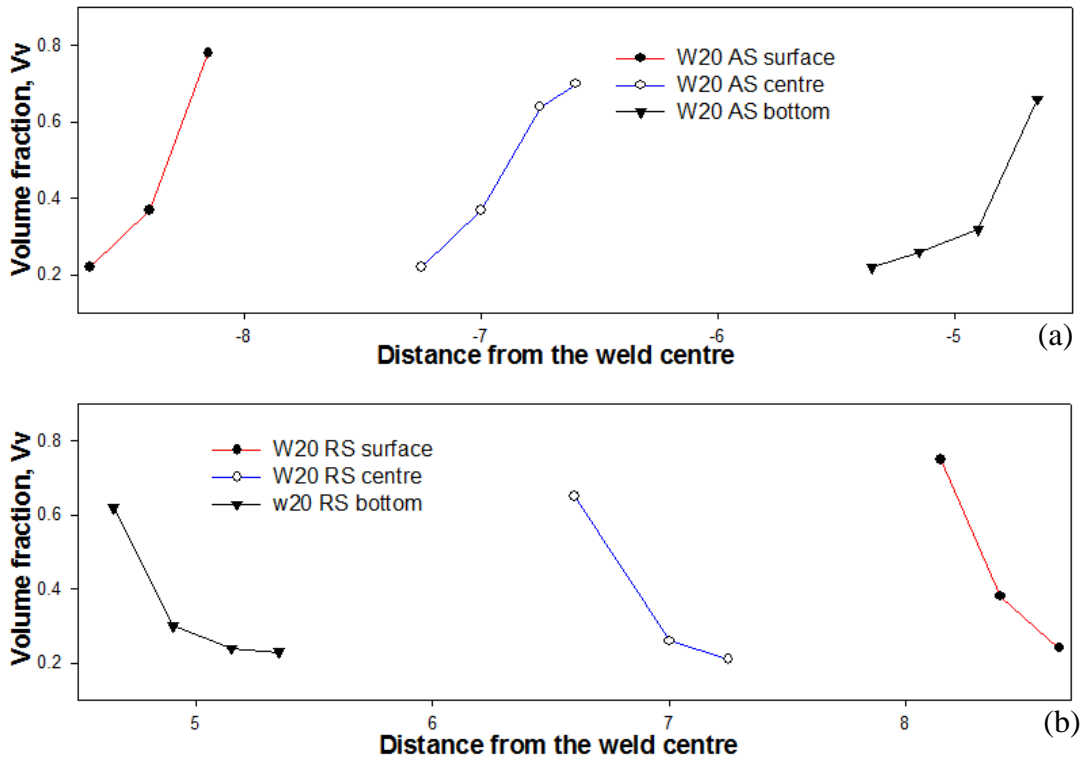
Figure 6.78 Volume fraction of retained β phase and transformed β phase in the equiaxed
and bimodal structure at both: (a) the AS and (b) the RS of the welding edge for W20
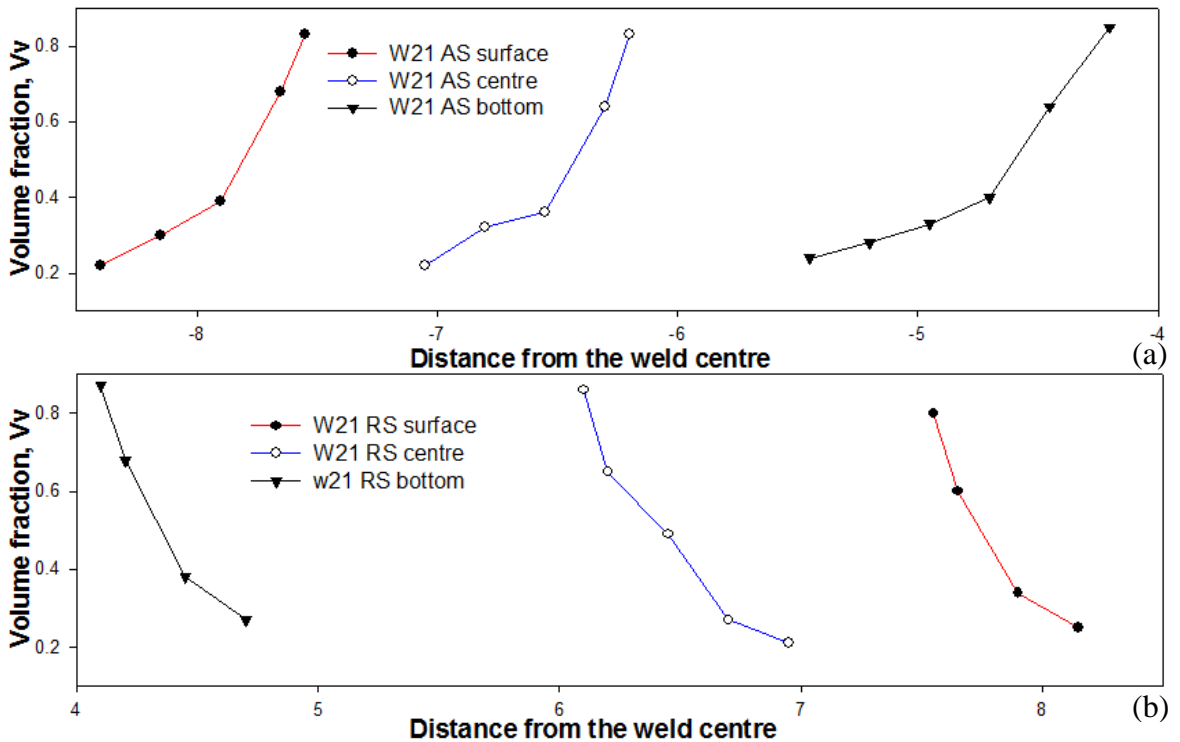


Figure 6.79 Volume fraction of retained β phase and transformed β phase in the equiaxed
and bimodal structure at both: (a) the AS and (b) the RS of the welding edge for W21

6.5.4 Volume fraction measurement of retained β phase in the SZ

Volume fraction measurement of retained β phase in the fine lamellar structure of the SZ was carried out on Secondary electron micrographs using Image J software and the measurement was taken from the normal sections 4.7.b and 5.6.b. Figure 6.80(a) and (b) show the secondary electron micrographs of the adjacent regions taken from 4.7.b on the centre horizontal line at the AS. Figure 6.80(a) is a high resolution secondary electron micrograph of the lamellar region with α+β morphology, as indicated in a red rectangular in Figure 6.80(a). And Figure 6.81(b) is the corresponding image after thresholding in image J, the phase with dark contrast is the α phase and the phase with light contrast is retained β phase, it was measured that volume fraction of the α phase in the lamellar region with α+β morphology is 86%, and volume fraction of retained β phase (light contrast) is 14%. Similarly, a high resolution secondary electron micrograph of the lamellar region with α+β morphology enclosed in a red rectangular in Figure 6.80(b) is shown in Figure 6.82(a) and Figure 6.82(b) shows the corresponding image after thresholding in image J, where volume fraction of the α phase (dark contrast) is about 85%, and volume fraction of retained β phase (light contrast) is 15%.
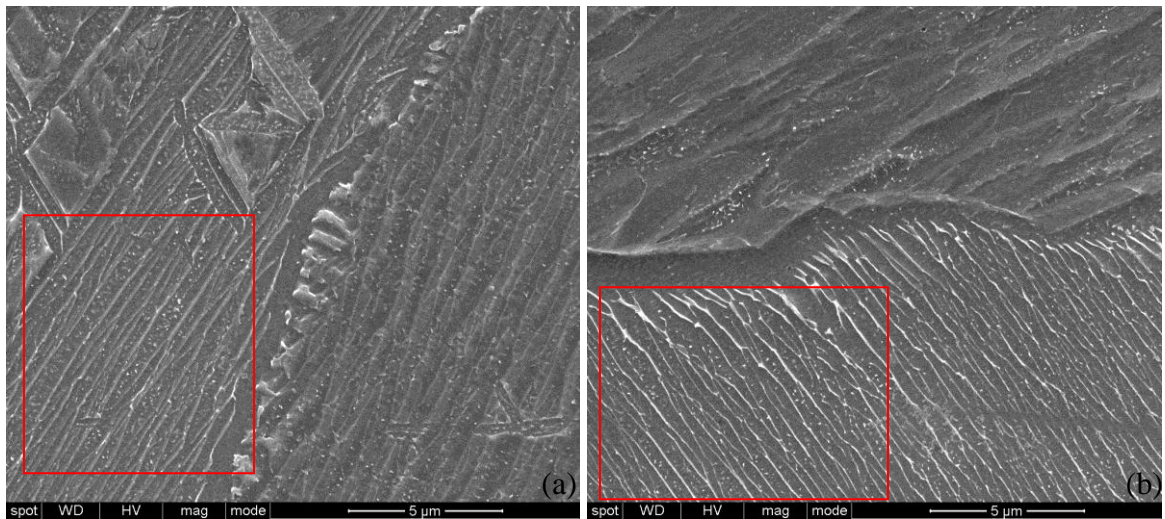


Figure 6.80 (a) (-6.57,-1.03), the thickness of the α laths is between 0.23μm, 0.3μm (mostly), 0.76μm and GBα length is 0.76μm. (b) (-6.6,-1), the thickness of the α laths is between 0.23μm, 0.3μm (mostly), 1.82μm and GBα length is 1.21μm
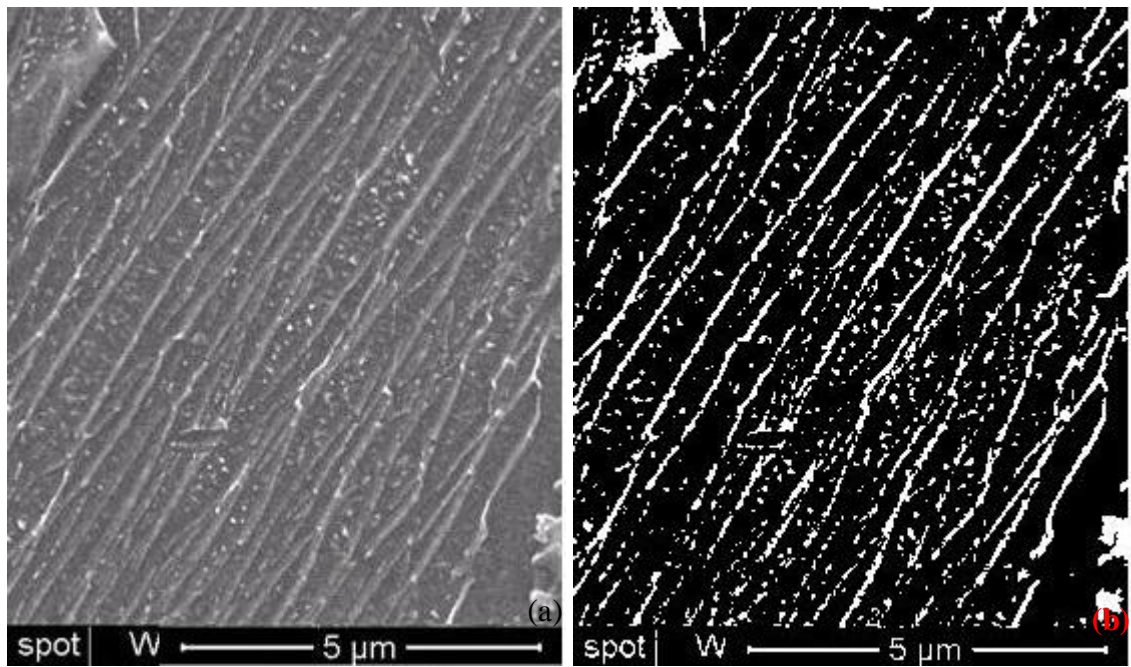
Figure 6.81 High resolution secondary electron micrographs of the lamellar region with
α+β morphology as indicated in the red rectangular in Figure 6.80(a): (a) original graph; (b)
thresholded graph
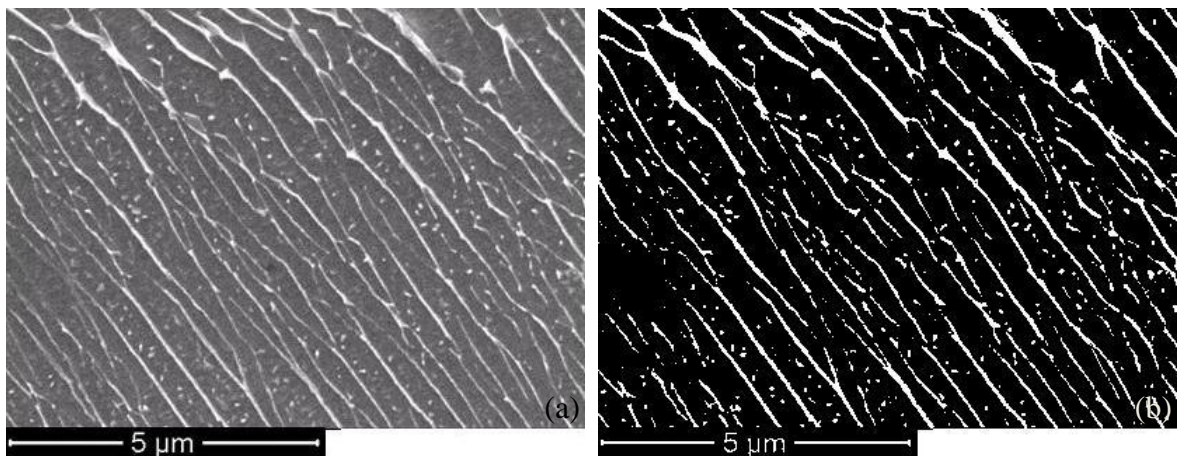


Figure 6.82 High resolution secondary electron micrographs of the lamellar region with
α+β morphology as indicated in the red rectangular in Figure 6.80(b): (a) original graph; (b)
thresholded graph

Figure 6.83(a) shows the secondary electron micrograph of the fine lamellar regions
taken from 2mm to the weld centre at the RS of 5.6.b, and high resolution micrograph of
this region in shown in Figure 6.83(b). Figure 6.84(a) shows a high resolution secondary
electron micrograph of the lamellar region with α+β morphology taken from Figure 6.83(b),

as indicated in a red rectangular. And Figure 6.84(b) is the corresponding image after thresholding in image J. It was measured that the volume fraction of the α phase (dark contrast) in lamellar region with α+β morphology is 89% and volume fraction of retained β phase (light contrast) is 11%.
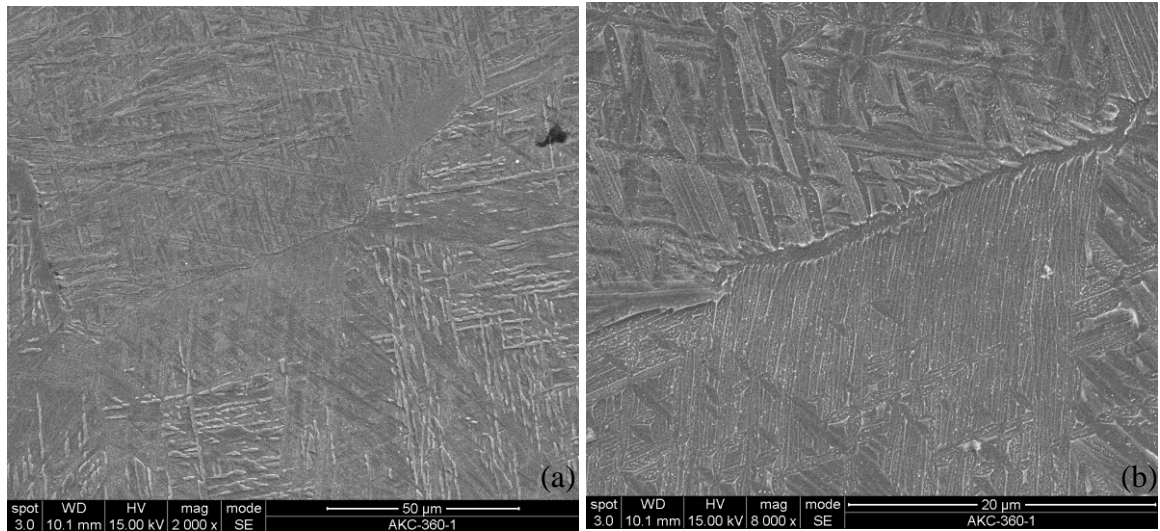


Figure 6.83 (a) micrograph of fine lamellar structure at the RS of 5.6.b and (b) the corresponding high resolution micrograph; The thickness of the α laths is between 0.27μm, 0.54μm (mostly), 1.22μm and GBα length is 1.22 μm
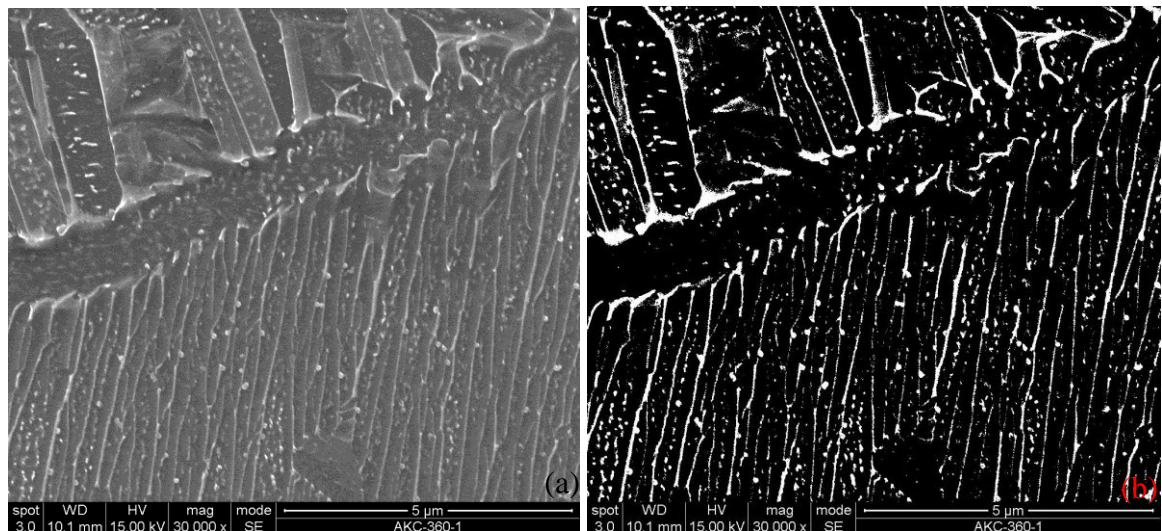


Figure 6.84 High resolution secondary electron micrographs of the lamellar region with α+β morphology as indicated in the red rectangular in Figure 6.83(b): (a) original graph; (b) thresholded graph

6.5.5 Shear strain rate

A method to evaluate shear strain rate generated during FSW was developed by Ahmed, (2009). The calculation method is illustrated in Figure 6.85. The difference between the NG radius ($NG_r$) and the probe tool radius ($P_r$) shown in Figure 6.85(a) will be considered as the thickness of the material sheared ($S_x$) (Ahmed, 2009). The shearing speed ($V_s$) calculation was shown in Figure 6.85(b) using equation 6.1.

$$V_s = 2\omega \, P_r \qquad\qquad (6.1)$$

Where $\omega = 2\pi r/60$ and r is the rotation speed in rpm, the shear strain rate $\overset{g}{\gamma}$ is given in equation 6.2 according to Figure 4.9 using equation 6.1:

$$\overset{g}{\gamma} = \tan \alpha = \frac{V_s}{S_x} \qquad\qquad (6.2)$$
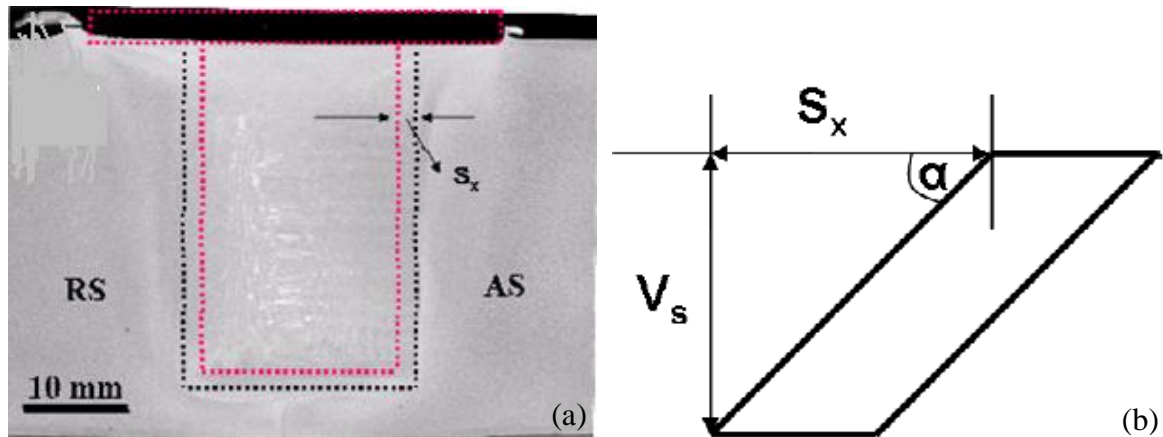


Figure 6.85 (a) A schematic of the tool shape superimposed on the optical macrograph of a FSWed aluminium alloy with a parallel probe tool. Red dashed line represents the tool dimension and black dashed line represents the nugget zone (NG); (b) Schematic of shear strain rate calculation (Ahmed, 2009)

Table 6.16 displays the shear strain rate results of the six welds using equation 6.2. Shear strain rates were calculated on both the weld surface and the weld bottom, it was observed that weld bottom has higher shear strain rate than the weld surface due to thickness of the sheared material Sx at the weld bottom is smaller than that of the weld surface. At the weld bottom, as traverse speed increased from 50 to 100mm/min, there was a large increase in shear strain rate by 34.8%, while shear strain rate increased by 12.8% when traverse speed increased from 100 to 150mm/min; at the weld bottom, shear strain rate decreased by 6% with decreasing rotation speed from 800 to 600rpm and as rotation speed decreased from 600 to 400rpm, shear strain rate decreased by 3%. At the weld surface, shear strain rate increased by 3.4% and 2% when traverse speed increased from 50-100mm/min and 100-150mm/min, respectively; shear strain rate decreased by 18.8% with decreasing rotation speed from 800-600rpm and there was a 16.7% increase in shear strain rate with decreasing rotation speed from 600 to 400rpm. A comparison can be made between the two welds W6 and W19 with rotation speed of 900 and 800rpm by showing that shear strain rate was higher in W6 than that in W19 at both the weld surface and the weld bottom, shear strain rate decreased by 18.3% and 7% at the weld surface and the weld bottom as rotation speed decreased from 900 to 800rpm, respectively. Thus, the shear strain rate generated in both the weld surface and the weld bottom increased with increasing traverse speed and with increasing rotation speed.

Table 6.16 Shear strain rates in the weld zones of all the six welds

| Weld No | W4 | W5 | W6 | W19 | W20 | W21 |
|---|---|---|---|---|---|---|
| Rotation speed, r, rev/min | 900 | 900 | 900 | 800 | 600 | 400 |
| Travel speed, mm/min | 50 | 100 | 150 | 150 | 150 | 150 |
| Thickness of the sheared material around the probe at the surface, Sx, mm | 3 | 2.9 | 2.85 | 3.1 | 2.7 | 2.1 |
| Thickness of the sheared material around the probe at the bottom, Sx, mm | 3.1 | 2.3 | 2.1 | 2 | 1.6 | 1.1 |
| Shear strain rate at the surface, $s^{-1}$, $\pi r \Pr/15 S_x$ | 307.9 | 318.5 | 324.1 | 264.8 | 228.1 | 195.5 |
| Shear strain rate at the bottom, $s^{-1}$, $\pi r \Pr/15 S_x$ | 298 | 401.6 | 439.8 | 410.5 | 384.8 | 373.2 |

## 6.6 Discussion

6.6.1 Effect of welding parameters on texture development

The TMAZ and the HAZ were differentiated by comparing texture of the room temperature α phase and retained β phase changing from the equiaxed structure, the bimodal structure to the coarse lamellar structure. Results of the determination of the TMAZ and the HAZ at both the AS and the RS for all the six welds suggest that bimodal structure belongs to the HAZ and coarse lamellar structure constitutes the TMAZ, as shown from Figure 6.32 to Figure 6.43 for all the six welds W4, W5, W6, W19, W20 and W21. It is seen in {0001} pole figures of the room temperature α phase of all the six welds that the HAZ and the TMAZ both have developed a texture type containing three components and they are TD component, 45º component and WD component, using Ari-Gur and Semiatin's notation (1998), where TD component and WD component refer to the poles orientated into the TD and the WD, respectively, 45º component represents the poles lying in the lines from the

319

pole position to the centre, which is rotated 45º to either the TD or the WD in a pole figure. It can be seen that the BM and the HAZ both have much clearer 45º component, and 45º component appeared to be more diffuse in the TMAZ, which could be attributed to much higher peak weld temperature and more deformation in the TMAZ. However, it should be noted that TD component, 45º component and WD component in TMAZ have been rotated by a small angle compared to that in the HAZ (Figure 6.32(b)-Figure 6.43(b)).

In the region just adjacent to the TMAZ (Figure 6.36 at the RS of W6; Figure 6.43 at the RS of W21), TD and WD components have broken up into random poles or some new components tended to develop in this region. This meant that further into the weld centre, this region has undergone slightly higher peak weld temperature and more deformation compared to the TMAZ and deformation of this region was robust enough to generate a slight texture change, thus, the SZ with fine lamellar structure adjacent to the TMAZ was able to form shear texture by higher temperature and more intensive deformation. Texture of the weld zones at the RS including the SZ, the TMAZ, the HAZ and the BM of the weld W21 shown in Figure 6.43(b) and (c) suggesting that both the α phase texture and the β phase texture are stronger in the SZ compared to that in the TMAZ, moreover, the SZ has developed a simple shear texture, whereas, the TMAZ retained similar but rotated texture component as the texture component in the HAZ. This meant that the SZ has experienced more deformation than the TMAZ, so that both the α phase and β phase have been deformed in the SZ.

It was observed that the reconstructed high temperature β texture exhibit a classic bcc shear texture with D1 shear texture component in the SZ and the low temperature α texture inherited this D1 component from the high temperature β phase, as shown in the {0001} pole figures and {110} pole figures of the α and β phases, where intensity of individual poles within each pole figure varies for all the six welds depending on distance from the weld centre and texture of the α and β phases. As we deviate away from the centre of the weld, the shear texture rotates about the ND but remains the D1 component, as observed by Davies et al. (2011). In the SZ, the {0001} basal plane tends to align with the surface of the pin due to shear deformation imposed by the rotation of the pin. Thus, the {0001} planes tended to align with an ellipsoidal surface resulting in the SZ having basin-shaped characteristics. In the fully transformed lamellar structure in the SZ of the cross sections of the all the six welds, as shown in Figure 6.7(a) to Figure 6.11(a), Figure 6.13(a) to Figure

6.17(a), Figure 6.19(a) to Figure 6.23(a), Figure 6.25(a), Figure 6.29(a) and Figure 6.31(c), the high temperature β phase was successfully reconstructed with 85-87% indexed for all the IPF maps after reconstruction indicating that the SZ material has experienced a peak weld temperature above the $T_\beta$. Whilst, in the equiaxed structure of the BM and the bimodal structure of the HAZ, there was little or no reconstruction again suggesting that the α phase in the HAZ and the BM are not related to burger's relation thus peak weld temperature experienced in the HAZ and the BM are both below the $T_\beta$.

A direct comparison of shear texture developed in the SZ can be made between all the six welds with varying traverse speed and rotation speed by comparing length of the SZ, texture strength and the prior β grain size at the weld surface, the weld centre and the weld bottom. Length of the SZs in the weld centre can be calculated from the IPF maps for all the six welds (Figure 6.8(a), Figure 6.15(a), Figure 6.20(a), Figure 6.25(a), Figure 6.29(a) and Figure 6.31(a)), and they are 14.5mm, 14.2mm and 12.9mm for the three welds W4, W5 and W6 with a constant rotation speed of 900rpm, respectively. Length of the SZs in the weld centre are 12.4mm, 12.1mm, 11.45mm for the three welds W19, W20, W21 with a constant traverse speed, respectively. The results have been confirmed by the secondary electron micrographs. It is seen in both low temperature α texture and high temperature β texture that texture strength is the highest in the weld W4 with the lowest traverse speed, and as traverse speed increases from 50 to 100mm/min, the texture strength decreases and the maximum texture strength of the low temperature α texture decreases from 11.3 to 5.8MUD in the weld surface, from 11.6 to 11.4MUD in the weld centre and from 9.3 to 7.4MUD in the weld bottom, respectively; in the weld centre, the maximum texture strength of the low temperature α texture decreased from 11.6 to 11.4 and 8.4MUD with increasing traverse speed from 50 to 100 and 150mm/min, respectively. In the three welds W19, W20 and W21, as rotation speed decreases from 800 to 600rpm, the maximum texture strength of the low temperature α texture decreased from 12.3 to 8.8MUD in the weld centre, whereas, the maximum texture strength of the α texture retained 8.8MUD in the weld centre with decreasing rotation speed from 600 to 400rpm.

The average prior β grain size in each micrograph at both the AS and the RS (Figure 6.64, Figure 6.66, Figure 6.67, Figure 6.68, Figure 6.69 and Figure 6.70 from the manual measurement results) has been measured based on grain boundary maps of the reconstructed β phase via EBSD data. It was observed that the largest prior β grain size in

the weld centre was 155, 140 and 130μm at tool traverse speed of 50, 100, 150mm/min, respectively. Thus, the prior β grain size decreased with increasing traverse speed. This was due to the fact that lower traverse speed resulted in higher peak weld temperature in the SZ, which provides more time for the growth of the prior β grain in the β phase field during welding. The three welds W19, W20 and W21 with a constant traverse speed of 150mm/min and rotation speed of 400, 600 and 800rpm have the largest prior β grain size of 65, 82 and 115μm in the weld centre, respectively. This suggests that the prior β grains in the SZs of the three welds W19, W20 and W21 increased with increasing rotation speed from 400 to 600 and 800rpm due to higher peak weld temperature and rapid β grain growth in the weld with higher rotation speed. This result shows agreement with Zhang et al. (2008a) and Edwards and Ramulu (2010) who both pointed out that higher rotation speeds resulted in larger prior β grains due to higher peak temperature and longer dwell time in the SZ. And the largest prior β grain size in the weld centre plotted against heat input for all the six welds W4, W5, W6, W19, W20 and W21 in shown Figure 6.86 with vertical error bars and fit curve. It was shown that the prior β grain size increases significantly with increasing heat input from 1.1 to 1.5kJ and increases slightly when heat input increases from 1.5 to 3.3kJ, again suggesting that peak weld temperature in the weld centre increases significantly with increasing rotation speed and increases slightly with decreasing traverse speed. This meant that rotation speed has large effect on peak weld temperature in the weld zones compared to the traverse speed, which shows agreement with Edwards and Ramulu (2010) and they found that varying traverse speed from 50 to 100 and 150mm/min at a rotation speed of 300rpm does not generate variation in peak weld temperature for FSWed Ti-6Al-4V of 12mm thickness. Figure 6.87(a) and (b) plot the largest prior β grain size in the weld centre as a function of traverse speed and rotation speed, respectively. According to the data of Xue et al. (2010), the average grain size in the SZ plotted against both the traverse speed and the rotation speed are shown in Figure 6.88(a) and (b) with vertical error bars and fit curves, respectively. The results from Figure 6.87 again demonstrates that in this work, the rotation speed has much stronger effect on the prior β grain size compared to the traverse speed although heat input has increased greatly as traverse speed increases, which shows agreement with Attallah and Salem (1999) on a high strength aluminium alloy, Commin et al. (2009) on AZ31 magnesium alloy, Xue et al. (2010) on pure copper (Figure 6.87) and Hasan Haji on FSW of steel from the University of Sheffield, who both reported

that, in the SZ, increasing rotation speed leads to an increase in the grain size and the grain size increases with decreasing traverse speed, and both cases are due to the increase of peak weld temperature. However, the tool rotation speed has a large effect on the grain size and at high rotation speed, the traverse speed has little influence on the grain size due to the fact that peak weld temperature was determined by the weld power which is proportional to multiplying the input torque by the rotation speed (Reynolds et al., 2005b)
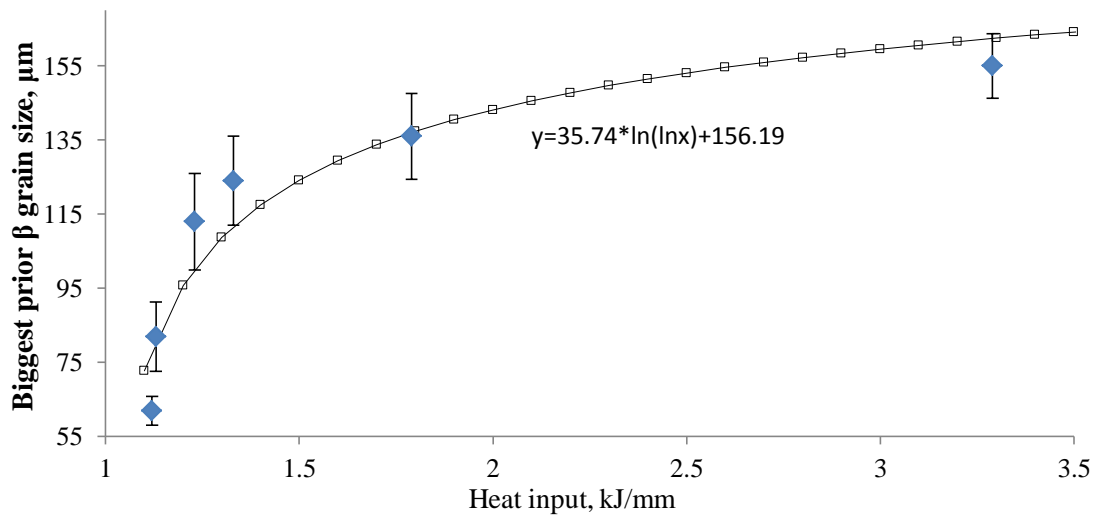


Figure 6.86  Largest prior β grain size in the weld centre plotted against heat input for all the six welds W4, W5, W6, W19, W20 and W21

(b)
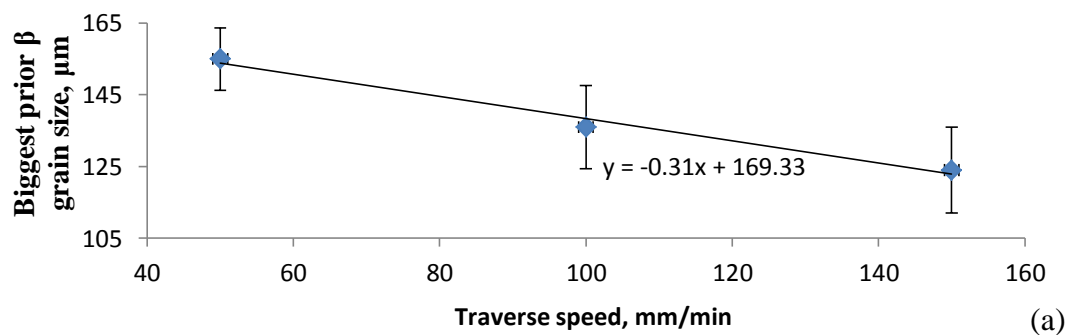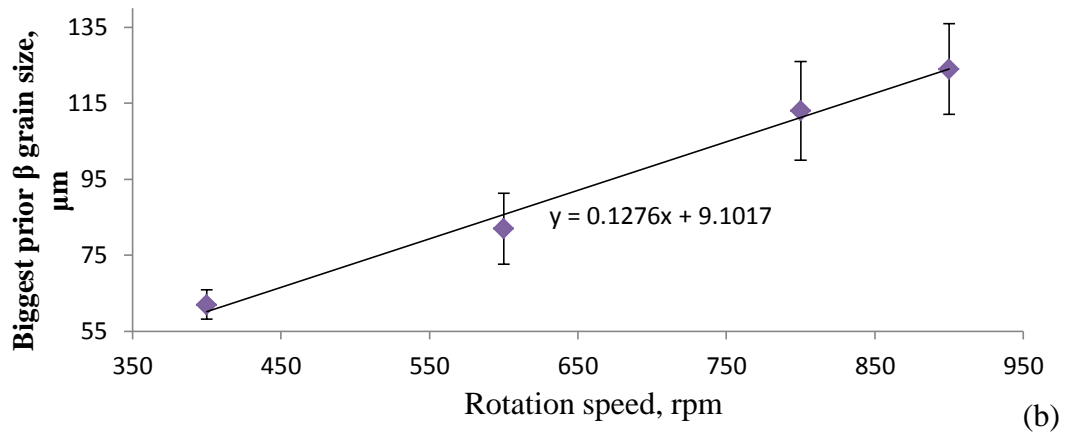
Figure 6.87 The largest prior β grain size in the weld centre as a function of (a) traverse speed and (b) rotation speed



(a)



(b)
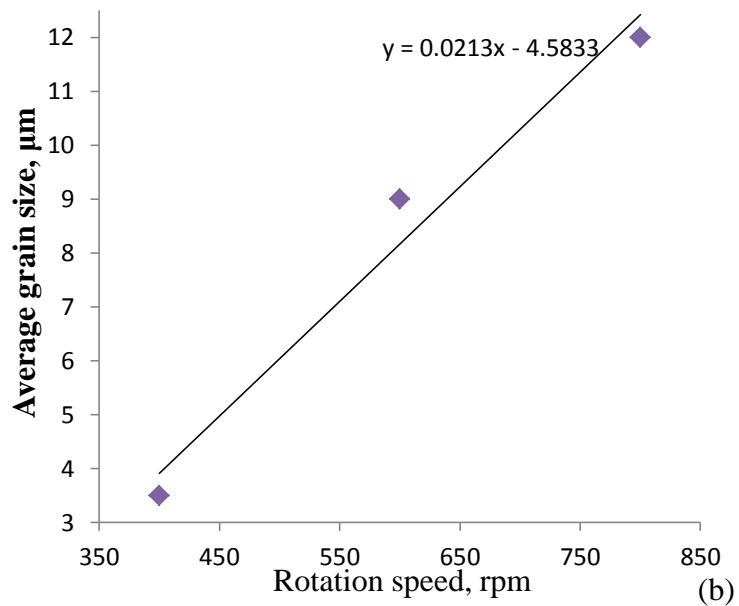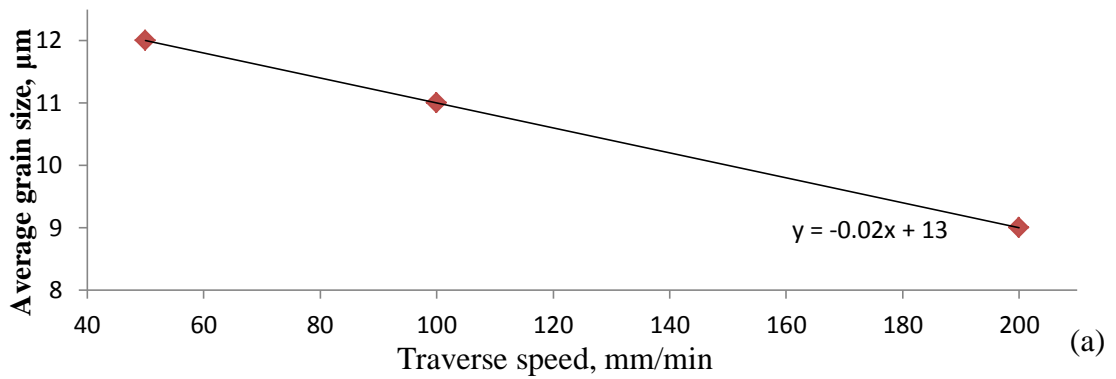
Figure 6.88 Average grain size in the SZ of FSW of pure copper by Xue et al. (2010) plotted against both (a) traverse speed with a constant rotation speed and (b) rotation speed with a constant traverse speed

324

It was observed in the cross sections of all the six welds that, from the TMAZ at the RS to the weld centre and from the weld centre to the TMAZ at the AS, the prior β grain size of the SZ grows rapidly from the welding edge to the weld centre indicating that the weld centre has experienced higher peak weld temperature than the weld edge at both the AS and the RS. This result is in accordance with the previous microstructure results in Chapter 5 that the weld centre has larger grain size compared to the welding edge at both the AS and the RS. It is seen that the prior β grains within the SZ region of distance approximately 2mm to the welding edge at both the AS and the RS were aligned with the SD, as indicated as thick black curves in the reconstructed IPFs of Set2, Set 4 and Set 5 (Figure 6.8, Figure 6.10 and Figure 6.11) of W4; Set1, Set2, set 4 and Set 5 (Figure 6.13, Figure 6.14, Figure 6.16 and Figure 6.17) of W5; Set1, Set3, Set4 and Set 5 (Figure 6.19, Figure 6.21, Figure 6.22 and Figure 6.23) of W6; Figure 6.25 of W19 and this could be resulted from the shearing deformation of material caused by the tool pin during the FSW process which was able to tilt the direction of the prior β grains into a direction paralleling to the SD.

A direct comparison can be made between the two welds W19 (800rpm) and W6 (900rpm) with 150mm/min traverse speed by comparing the texture strength and the prior β grain size at the weld surface (Figure 6.20 of W6, part5 of W19 in Figure 6.25), the weld centre (Figure 6.20 of W6, part2 of W19 in Figure 6.25) and 1mm below the weld centre from the RS to the AS (Figure 6.20 of W6, part1 of W19 in Figure 6.25). The results showed that the texture strength is stronger in W6 than that in W19 as observed at the weld surface, the weld centre and 1mm below the weld centre. W6 has a larger prior β grain size in both the weld surface, the weld centre and 1mm below the weld centre compared to W19 (Figure 6.20, 6.21, 6.22 and Figure 6.25)

In Figure 6.7 to Figure 6.30, it should be noted in the key that the axes for the map and the pole figures are not the same; the inverse colours in the α phase and the reconstructed β phase change with position in the weld within the weld zones and none of the colours were repeatable from the AS to the RS reflecting that the AS and the RS are not symmetric, in fact, the AS has a higher pole intensity than the RS and thus, the texture of the weld zones is much stronger at the AS than the RS due to different material flow condition caused by the tool rotation. It should be noted that the prior β size at the AS is larger than that at the RS for all the six welds, this would again suggest that the AS has experienced higher peak weld temperature than the RS due to stronger material flow at the AS and material flow is

more disruptive on the AS because of the relative directions of tool rotation and translation (Klingensmith et al., 2005).

6.6.2 Misorientation axes

It can be seen that at both the AS and the RS of all the four cross sections of the welds W4, W5, W19, W20 and two normal sections 5.8.c and 6.8.c, the strongest clustering effect of misorientations accumulated near the {0001} basal planes at 25º-35º boundaries for both the TMAZ, the HAZ and the BM and less stronger clustering effect of misorientations axes occured at 55º-68º boundaries (Figure 6.44 and Figure 6.45 for W4; Figure 6.46 and Figure 6.47 for W5, Figure 6.48 and Figure 6.49 for W19, Figure 6.50 and Figure 6.51 for W20; Figure 6.52 for 5.8.c and Figure 6.53 for 6.8.c).

And the misorientation angles across the α/α grain boundaries in misorientation angle distribution histograms at both the AS and the RS for all the four welds W4, W5, W19 and W20 reveal that there were both LAGBs and HAGBs present in the TMAZ, the HAZ and the BM (Figure 6.44, Figure 6.45, Figure 6.46, Figure 6.47, Figure 6.48, Figure 6.49, Figure 6.50, Figure 6.51, Figure 6.52 and Figure 6.53). In the BM, the LAGBs suggest that subdivision of larger α grains has occurred. The HAGBs, on the other hand, cannot be explained by this subdivision mechanism (Pilchak, 2009). Both the LAGB fraction and HAGB fraction significantly increase from the BM to the HAZ and the TMAZ (Figure 6.44 and Figure 6.45 for W4; Figure 6.46 and Figure 6.47 for W5, Figure 6.48 and Figure 6.49 for W19, Figure 6.50 and Figure 6.51 for W20; Figure 6.52 for 5.8.c and Figure 6.53 for 6.8.c). Thus, LAGBs and HAGBs both occurred by deformation. HAGB fraction in the TMAZ also increases significantly (Table 6.14 and Figure 6.52 for 5.8.c; Table 6.15 and Figure 6.54 for 6.8.c despite the new LAGB formation of 5º-15º. It is seen that the HAGB fraction increases as texture strength increases.

It should be noted that 25º-35º boundaries do not correspond to any of the misorientation angles belonging to Burger's orientation relation in the TMAZ or the HAZ or the BM for all the cross sections  W4, W5, W19 and W20 and the two normal sections 5.8.c and 6.8.c , however, they were observed in the SZ of the normal sections 5.8.c and 6.8.c. Table 6.17 shows the misorientation axes at 25º-35º boundaries not having the clusters near the {-12-10} poles for the cross sections of the four welds W4, W5, W19 and W20. It should be

326

noted that except for 25º-35º boundaries, all the other boundaries: 5º-15º, 55º-68º and 85º-95º are strictly related to Burger's orientation relationship, as aforementioned in Section 2..2.3.1. However, 25º-35º boundaries do not correspond to any of these angles, indicating 25º-35º boundaries were not from the misorientation of the adjacent α variants, and we assume that they came from the misorientation between the adjacent prior β grains.

Table 6.17 Misorientation axes at 25º-35º boundaries not having the clusters near {-12-10} poles

|  | W4 | W5 | W19 | W20 |
|---|---|---|---|---|
| AS | the BM and the HAZ | the BM and the HAZ | the BM, the HAZ, the TMAZ | the BM, the HAZ, the TMAZ |
| RS | the BM and the HAZ | the BM | the BM and the HAZ | the BM |

To summarise, texture strengthening from the RS to the AS and from the welding edge to the weld centre is accompanied by the increase of HAGB fraction.

6.6.3 Variant selection mechanism

If no variant selection happens, each {110} pole in the texture of the high temperature β phase will correspond to one of the six {0001} poles in the low temperature α phase due to the burgers orientation relation (Davies et al., 2011) and both poles will share the same position and same intensity. However, as shown in the {0001} PFs of room temperature α phase and the {110} PFs of high temperature β phase from Figure 6.7 to Figure 6.30 in the SZ of the cross section of all the six welds, the corresponding two poles share the same position but with different intensities, this meant that variant selection has occurred in the weld zones.

Recall the variant selection mechanism in Chapter 2, variant selection may be associated with the transformed α laths growing from the prior β grain in titanium alloys at α colonies precipitate from GBα with cooling rate less than 37ºC/s (Davies, 2009) and at low

vanadium contents (<5%) in titanium alloys during slow diffusional transformations (Banerjee et al., 2004; Karthikeyan et al., 2008). Variant selection was previously explained by the preferential nucleation of certain α orientations between the adjacent β grains having nearly parallel {110} poles, which lead to the preferential nucleation of common variants at the β/β boundaries (Bhattacharyya et al., 2003; Stanford and Bate 2004; Bhattacharyya et al., 2007; van Bohemen et al., 2008; Davies et al., 2011). Moreover, Variant selection was partially caused by thermal stresses, internal stresses, deformation, temperature, etc (Moustahfid et al., 1997; Gey and Humbert, 2002; Zeng and Bieler 2005; Humbert et al., 2006; Daymond et al., 2010; Davies et al., 2011; Pilchak et al., 2011).

In this work, orientations between the adjacent β grains can be either: totally related, partially related or not related. Thus the relationship between orientation of the α variants and the prior β grain boundaries has been investigated in all the four welds W20, W5, W6 and W4. Firstly, it is seen in Figure 6.56 of W20 and Figure 6.57(d) of W5 that the orientation of α variants on both side of the prior β grain boundaries were partially determined by the orientation of GBα grains, in another case, GBα grains define the orientation of α variants on one side of the boundaries only (Figure 6.58(f) of W6). Secondly, the orientation of GBα grains are a comprise between the adjacent α laths (Figure 6.58(e) of W6); Last, orientations of the α variants on both sides were not influenced by the prior β grain boundaries (W4, Figure 6.57(d) of W5). Thus, it can be concluded that the selection of α variants was not influenced by GBα grains or the prior β grain boundaries. Variant selection mechanism can be attributed to the result of the preferential nucleation of certain α orientations between the adjacent β grains having nearly parallel <110>, which lead to the preferential nucleation of common variants at the β/β boundaries (Bhattacharyya et al. 2003; Stanford and Bate, 2004). Moreover, Variant selection was partially caused by thermal stresses in Zr–2.5Nb (Daymond et al. 2010). It is seen in Figure 6.60 to Figure 6.63 that there is no consistency in the occurrence of favorite variants having the highest pole intensity in neither the {0001} PFs nor the {110} PFs or the largest intensity difference between the {0001} and {110} pole intensity in terms of subtraction and ratio for all the six welds. Thus, it can be concluded that the selection of α variants was not influenced by GBα grains or the prior β grain boundaries or the welding axes.

6.6.4 Shear texture component comparison

Table 6.18 shows a comparison of shear texture types developed in the SZ of FSW of different alloys including the present study. The table suggests that D2 shear texture component was observed in the SZs of the FSWs with near α alloy Ti-5111 (Knipling and Fonda, 2009), α+β alloy Ti-6Al-4V (Pilchak and Williams 2010; Davies et al., 2011) and β alloy Timetal 21S (Reynolds et al., 2005a), a FSW study of pure iron by Mironov et al., (2008) and the present study both reported that the SZ has D1 shear texture component.

In all the three types of shear texture component D1, D2, E1, E2, F, the rotation of the ideal orientation is opposite to the sense of the shear during the early stages of straining. And at larger strains and higher temperatures, the ideal orientation is rotated in the sense of the shear for D1 and D2 components (Montheillet et al., 1985). Baczynski and Jonas (1996) have observed an increase of D1 and a decrease of D2 with increasing strain from 0.5 to 1.9, and D2 component disappears at strain about 1.9.

Table 6.18 Shear texture types developed in the SZ of different studies

|  | Texture type | FSWed materials | Traverse speed, mm/min | Rotation speed, rpm |
|---|---|---|---|---|
| Reynolds et al., 2005a | D2 | Timetal 21S | 51, 152, 203, 305 | 200 |
| Mironov et al., 2008 | D1 | Pure iron | 60 | 200 |
| Knipling and Fonda, 2009 | D2 | Ti-5111 | 51 | 140 |
| Abbasi et al., 2011 | D1 | X80 steel | Not known | Not known |
| Davies et al., 2011 | D2 | Ti-6Al-4V | 60 | 400 |
| Knipling and Fonda, 2011 | D2, P1 | Ti-5111 | 51 | 140 |
| The present study | D1 | Ti-6Al-4V | 50, 100, 150 | 900 |
|  |  |  | 150 | 800, 600, 400 |

## 6.7 Summary

This chapter gives details about the effect of welding parameters on texture development. Texture analysis were carried out on all the weld zones for all six welds in terms of shear texture in the SZ, differentiation of the TMAZ and the HAZ, misorientation analysis at the welding edges and variant selection study. Manual measurements were also used to calculate the prior β grain size in the SZs and the volume fraction of retained β phase in the HAZ and the BM. The main findings from this chapter are summarised in Figure 6.89.
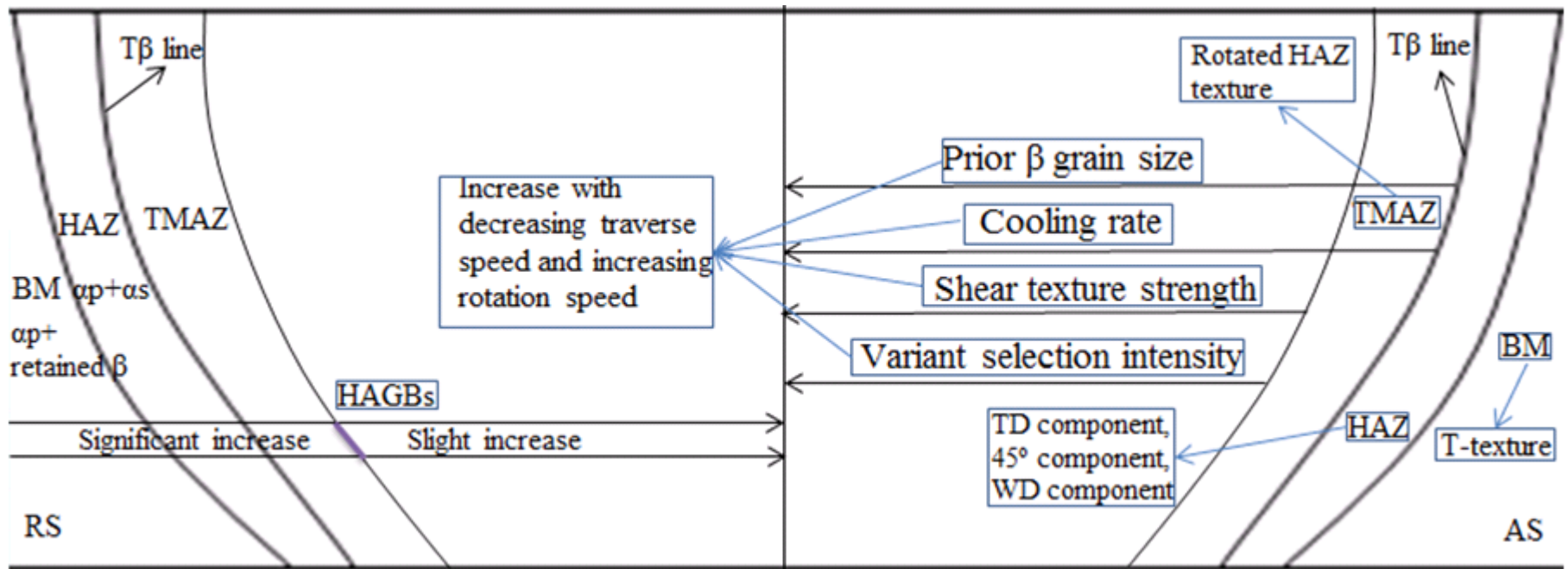
Figure 6.89 A summary of the main findings from Chapter 6

**Chapter 7 General discussions**

**7.1 Introduction**

In this chapter a more detailed discussion of the effects of the major welding parameters, such as traverse speed and rotation speed, will be presented on the surface roughness, microhardness, microstructure and texture of SSFSW of Ti-6Al-4V, in order to find out the optimum welding parameter to produce good weld joints with good surface quality, medium microhardness, small grain size and most importantly, and without significant tool wear.

**7.2 Effect of heat input on the prior β grain size and the thickness of the α laths**

Based on Table 4.3, Table 7.1 shows the data of heat input, the largest prior β grain size and the average thickness of the α laths in the weld centre. Figure 7.1(a) plots the graph with the largest prior β grain size and the average thickness of the α laths against heat input with vertical error bars. And the average thickness of the α laths as a function of largest prior β grain size is shown in Figure 7.1(b). It was shown in Figure 7.1(a) that as heat input decreased from 3.29 to 1.12kJ, the largest prior β grain size in the weld centre decreased significantly from 155 to 62μm and the average thickness of the α laths in the weld centre increased greatly from 0.26 to 4.4μm, which suggests that heat input have large effect on the microstructure unit size such as the prior β grain size and the thickness of the α laths. Figure 7.1(a) also indicates that, when correlating heat input with the welding parameters, the rotation speed has much stronger influence on the microstructure unit size compared to the traverse speed, however, heat input was largely affected by the traverse speed rather than the rotation speed. Figure 7.2 shows the average thickness of the α laths in the middle of the weld plotted against the largest prior β grain size in the weld centre for all the six welds, indicating that the average thickness of the α laths decreased significantly with increasing prior β grain size and the result shows agreement with Gil et al. (2001) who reported that larger β grain size produces smaller α lath thickness due to the decrease of the starting temperature of β-α transformation (Polmear, 1981; Ohmori et al., 1994).

Table 7.1 Data of heat input, the largest prior β grain size and the average thickness of the α laths in the weld centre for all the six welds

| Weld No | W21 | W20 | W19 | W6 | W5 | W4 |
|---|---|---|---|---|---|---|
| Average Heat input, kJ/mm | 3.29 | 1.13 | 1.23 | 1.33 | 1.79 | 1.12 |
| Largest prior β grain size, μm | 62±3.9 | 82±9.36 | 113±13 | 124±12 | 136±11.6 | 155±8.7 |
| Average thickness of the α laths, μm | 4.40±0.5 | 3.75±0.4 | 2.60±0.4 | 0.77±0.2 | 0.48±0.1 | 0.26±0.1 |
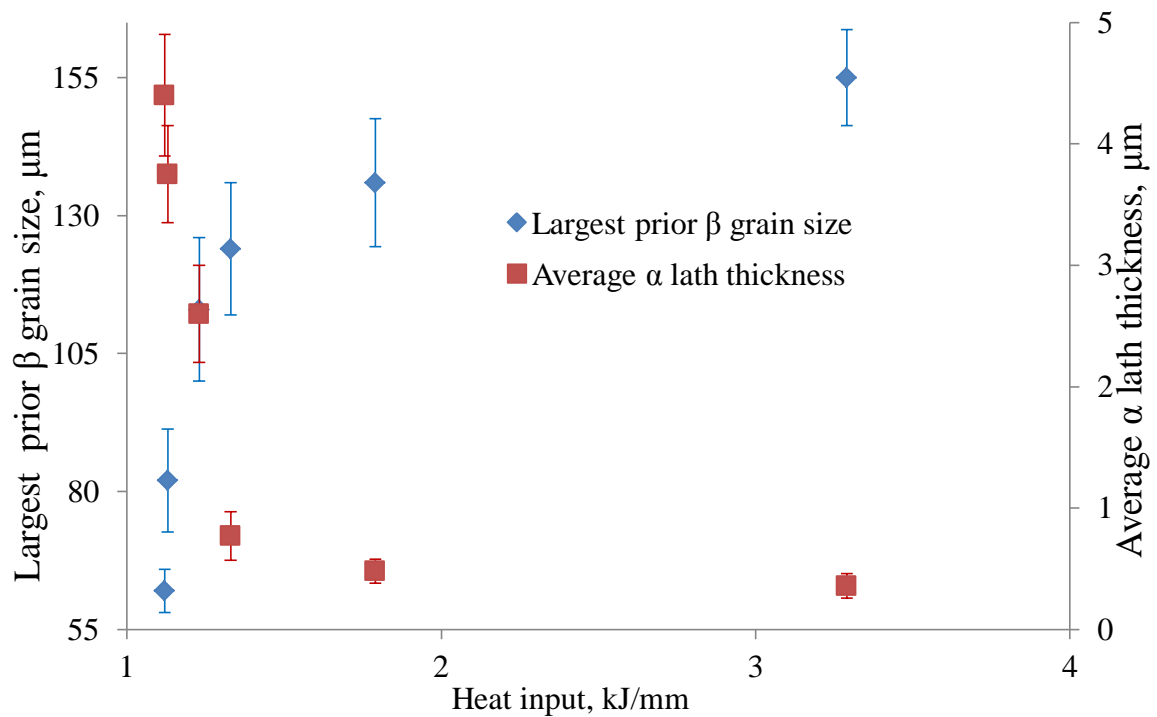


Figure 7.1 Largest prior β grain size and the average thickness of the α laths in the middle of the weld plotted against heat input in the weld centre for all the six welds
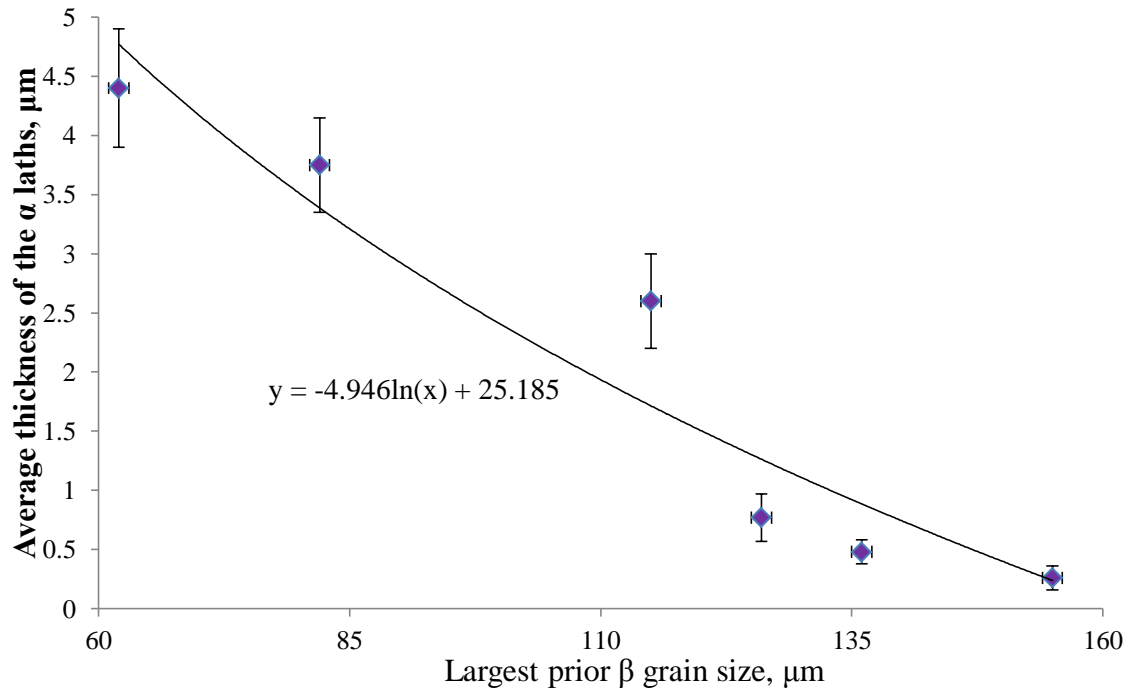
Figure 7.2 The average thickness of the α laths in the middle of the weld plotted against the largest prior β grain size in the weld centre for all the six welds

## 7.3 Effect of the prior β grain size on α morphologies and variant selection

The area fraction of the a morphologies consisting of basketweave α+Widmanstätten α, GBα and Colony α in unit of % as a function of the prior β grain size on the central horizontal line of all the six welds W4, W5, W6, W19, W20 and W21 are shown in Figure 7.3(a), (b) and (c), respectively. It is seen from Figure 7.3(a) that as the prior β grain size increases, the area fraction of basketweave α and Widmanstätten α increases significantly for all the six welds and the largest area fraction of basketweave α and Widmanstätten α in the weld centre increases with increasing rotation speed from 400 to 600, 800 and 900rpm from the four welds W21 to W6 and with decreasing traverse speed from 150 to 100 and 50mm/min from the welds W6 to W4, indicating that the largest area fraction of basketweave α and Widmanstätten α in the weld centre increases with increasing peak weld temperature. Figure 7.3(b) and (c) both show that the area fraction of GBα and Colony α decreases with increasing prior β grain size and the smallest area fraction of GBα and Colony α in the weld centre increased with increasing traverse speed and with decreasing rotation speed.

333
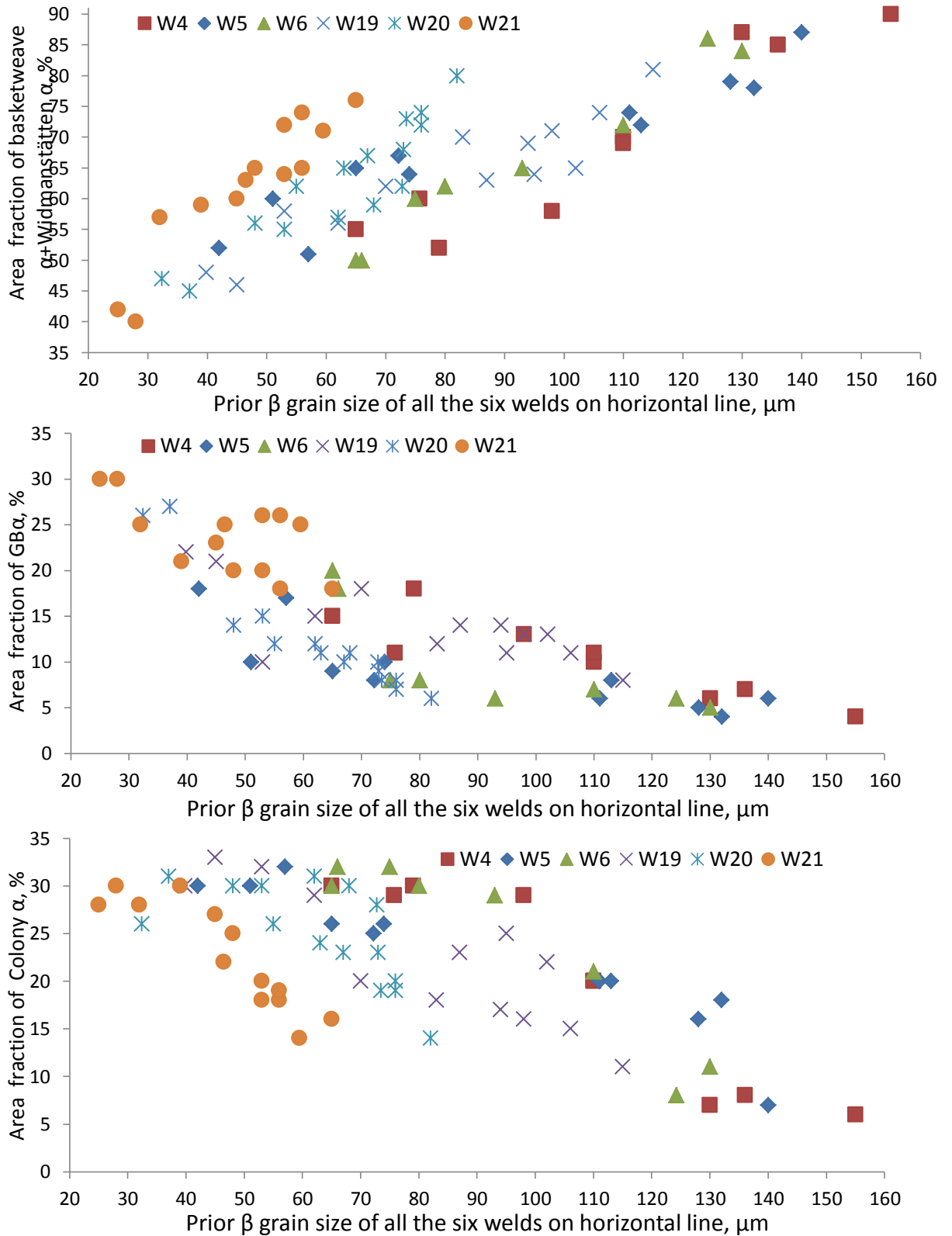
Figure 7.3 The area fraction of the α morphologies: (a) basketweave α and Widmanstätten α, (b) GBα and (c) Colony α plotted against the prior β grain size on the central horizontal line of all the six welds

334

Figure 7.4 shows the variant selection intensity as a function of the prior β grain size on the central horizontal line for all the six welds. It can be seen that as the prior β grain size increases, the variant selection intensity becomes stronger.
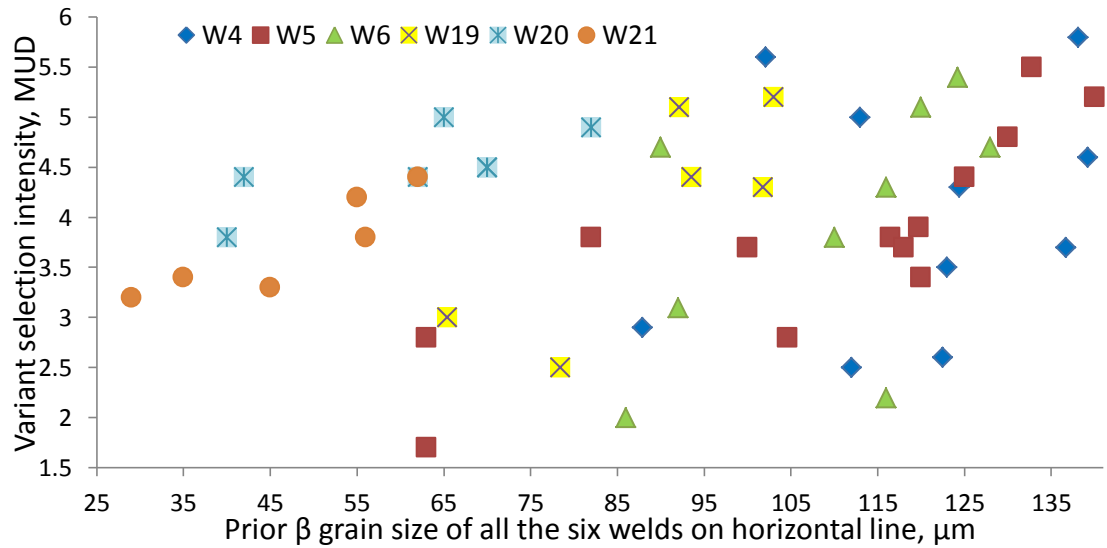


Figure 7.4 Variant selection intensity plotted as a function of the prior β grain size on the central horizontal line for all the six welds

## 7.4 Effect of welding parameters on the process route

Figure 7.5(a) shows swept volume, heat input, the largest prior β grain size and shear texture strength in the SZ, the shear strain rate at the weld surface and the weld bottom given as a function of traverse speed of the three welds W4, W5 and W6. And these parameters given as a function of rotation speed of the welds W19, W20 and W21 are shown in Figure 7.5(b). For the ease of comparison, all the variables start from the value of 1.0 and data for Figure 7.5(a) and (b) are referred to Table 1 and Table 2 in Appendix.

Figure 7.5 shows defect, tool wear, surface quality in terms of smoothness and flatness, microhardness, intensity of variant selection as function of traverse speed and rotation speed, indicating that as traverse speed increased, swept volume, shear strain rate at both the weld surface and the weld bottom increased; swept volume increased with decreasing rotation speed. It is seen that both the traverse speed and rotation speed have large influence on swept volume and the traverse speed has greater effect on swept volume compared to the rotation speed; shear strain rate at the weld surface increases slightly and shear strain

rate at the weld bottom increases greatly as the traverse speed increases. However, shear strain rate at both the weld surface and the weld bottom increased with increasing rotation speed; moreover, there is a large increase in the shear strain rate at the weld surface compared to the shear strain rate at the weld bottom.

It is also seen from Figure 7.5(a) and (b) that heat input, the prior $\beta$ grain size in the lamellar structure and shear texture strength in the SZ both decreased with increasing traverse speed from 50 to 100 and 150mm/min and they both decreased with decreasing rotation speed from 900 to 800, 600 and 400rpm, moreover, the prior $\beta$ grain size has changed greatly with varying traverse speed and rotation speed; the traverse speed has more effect on heat input compared to the rotation speed; the traverse speed and the rotation speed both have relative small effect on shear texture strength.

Microhardness was dependent on heat input, thin higher hardness layers observed in the weld surface and the weld bottom of all the three welds W4, W5 and W6 possibly due to tool wear; Microhardness is much more uniformly distributed in the four welds W6, W19, W20 and W21 with 150mm /min traverse speed. For convenience, Microhardness values are displayed in terms of intensity and represented as three symbols: highest ▲, modest △ and low △. Tool wear was significant and observed at the weld surface and the weld bottom of the weld W4 in terms of the cross section, the normal sections and the side sections at the AS of the weld surface. And a small amount of tool wear was observed in W5, W6 and W19. However, tool wear were not observed in the two welds W20 and W21. Tool wear has been classified into three types with symbols: significant tool wear ★, mild tool wear ☆ and no tool wear ☆ (Figure 7.6).

Surface quality in terms of smoothness and flatness were investigated along the whole weld length and the traverse section of all the six welds. It has previously been found that the weld surface was the least flat in the weld W4 and surface quality increased with increasing traverse speed from 50 to 100 and 150mm/min, whilst the weld W6 has a bump at the AS due to insufficient down force. And the weld surfaces were flat in the three welds W19, W20 and W21. In Figure 7.2, surface quality along the weld length or the WD was represented as straight line indicating smooth and relatively flat surface and curved lines (waves) indicating that the surface was not flat and the magnitude of the waves shows the

intensity of the surface roughness. However, for the weld W6, adjacent to the straight line is an oblique line reflecting the bump at the AS. Porosity was found in the weld W21 through the whole weld thickness, moreover, incomplete penetration was observed at the RS of the two welds W20 and W21 with rotation speed of 600 and 400rpm, respectively. Three types of defect consist of porosity✖, incomplete penetration✖, and no defect ● (Figure 7.6).

Shear texture strength and the intensity of variant selection in the SZ are closely related. In comparison of the cross sections of the four welds W4, W5, W6 and W19 (Figure 6.6-Figure 6.25) in terms of weld surface, weld centre and weld bottom, it can be clearly seen that W4 has strong variant selection and as traverse speed increases, the intensity of variant selection has decreased slightly, and it has decreased slightly with decreasing rotation speed from 900 to 800rpm, moreover, in the weld centre (Figure 6.24 to Figure 6.30) of the three welds W19, W20 and W21, intensity of variant selection decreased with decreasing rotation speed. Intensity of variant selection are represented as three symbols as comparative strong

✹; mild ✸ and not strong ✜ (Figure 7.6).



(a)
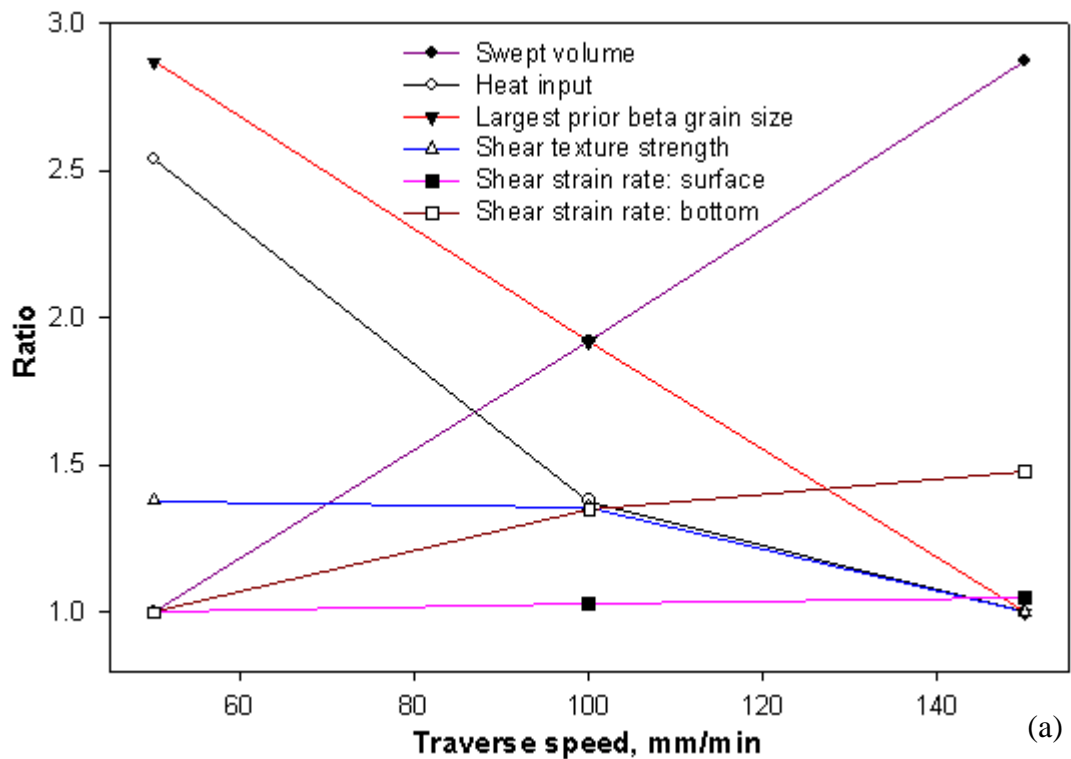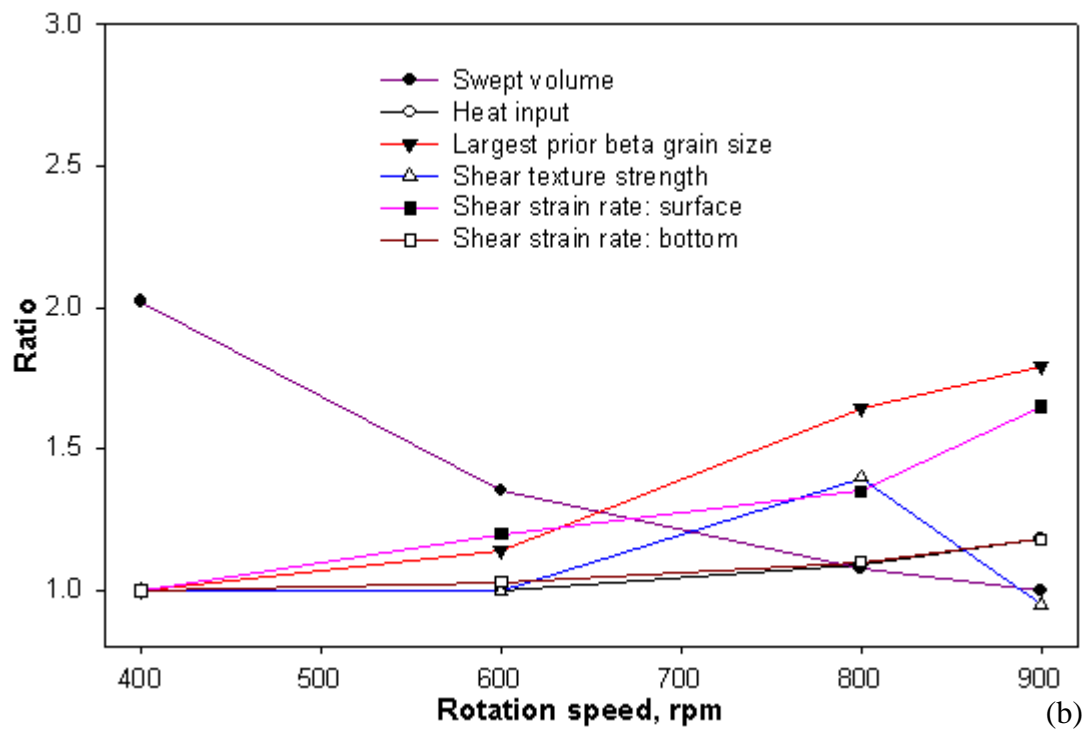
Figure 7.5 The effect of (a) traverse speed and (b) rotation speed on swept volume, heat input, largest prior β grain size in the lamellar structure, shear texture strength in the SZ, and shear strain rate at the weld surface and the weld bottom, respectively
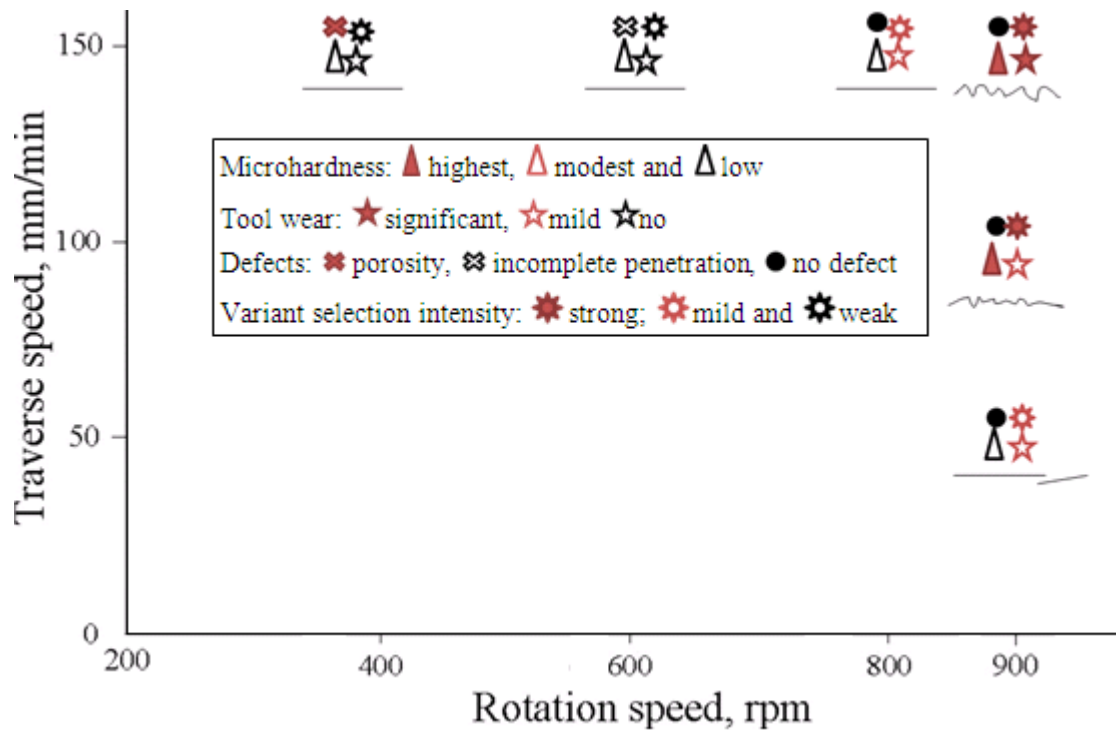


Figure 7.6 Defect, tool wear, surface quality, microhardness, intensity of variant selection as function of traverse speeds and rotation speeds, symbols are explained in the text

Figure 7.7 summarizes a process map for SSFSWed Ti-6Al4V with varying welding parameters based on all the experimental results indicating the influence of traverse speed and rotation speed on the weld regions with different qualities. And Figure 7.9 also shows that the variety of the weld regions consisting of the five weld regions depend on the traverse speed and rotation speed. It is clearly seen that the five weld regions have four different types and they are the weld regions unable to make, the weld regions with porosity and/or incomplete penetration, the weld region with potential tool wear and good weld region with optimum weld parameters which are at rotation speed of 200-600rpm and traverse speed of 50-100mm/min and at traverse speed of 50-150mm/min and rotation speed of 600-800rpm.
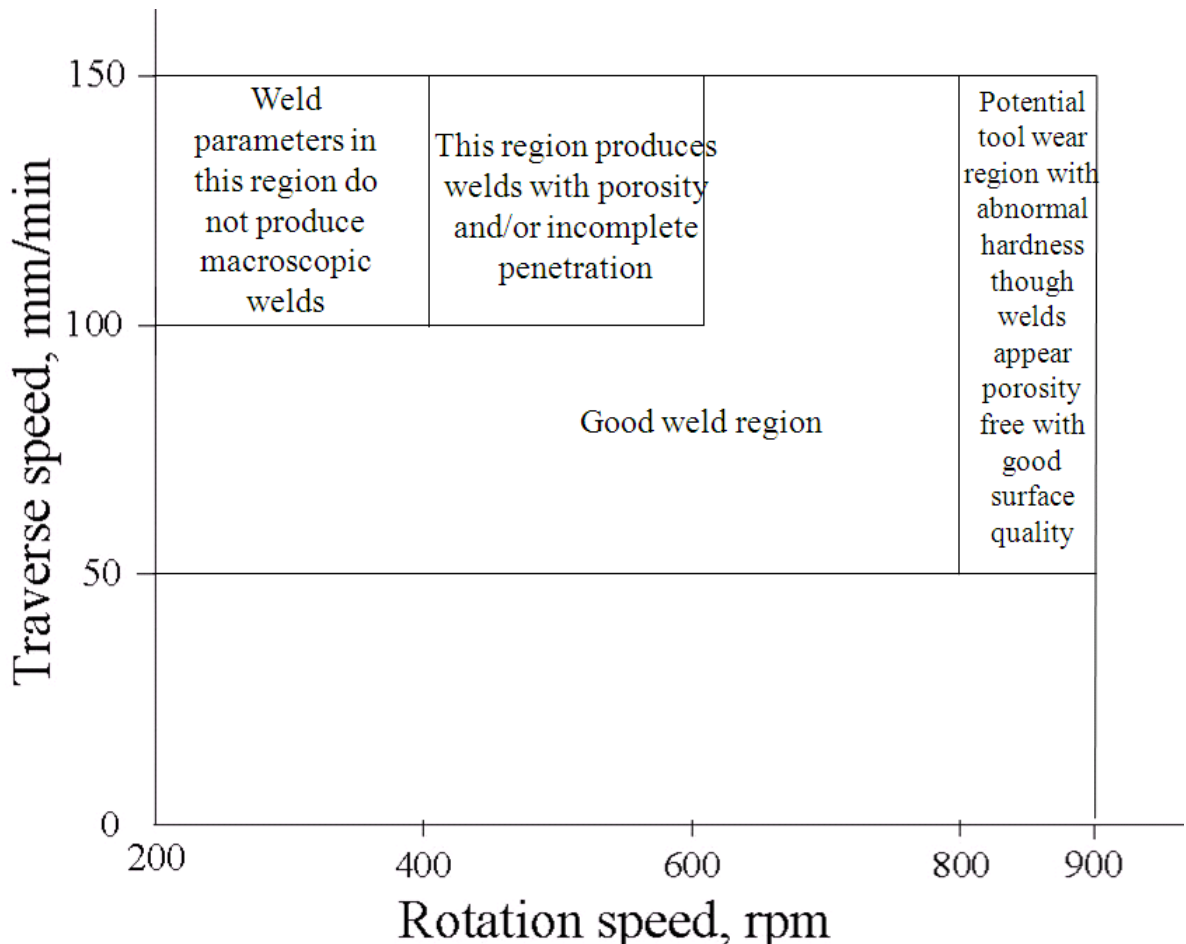


Figure 7.7 Processing map for SSFSWed Ti-6Al-4V with traverse speed of 50-150mm/min and rotation speed of 200-900rpm

**7.4 Summary**

- According to the aformentioned study, heat input in the range 1.2 and 1.3kJ/mm appears to produce optimum weld.

- Shear texture strength and the intensity of variant selection both increases with decreasing traverse speed and increasing rotation speed. And the variant selection intensity becomes stronger with increasing prior β grain size. The prior β grain size increases with increasing heat input as the decrease of the traverse speed and the increase of rotation speed, the area fraction of basketweave α andWidmanstätten α increases significantly with increasing prior β grain size, the area fraction of GBα and colony α in the weld centre decreases with increased with increasing traverse speed and with decreasing rotation speed as the increase of prior β grain size, the average thickness of the α laths decreased significantly with increasing prior β grain size; the rotation speed has much stronger effect on the microstructure unit size (the prior β grain size and the thickness of the α laths) compared to the traverse speed.

- Good weld region with optimum weld parameters are predicted at rotation speed of 200-600rpm and traverse speed of 50-100mm/min and at traverse speed of 50-150mm/min and rotation speed of 600-800rpm.

- Schematic drawing in Figure 7.8 indicates different weld zones (BM, HAZ, TMAZ and SZ), the β transus ($T_β$) line; prior β grain size (in dark circles) along the centre horizontal line and the central vertical line, α morphologies, the thickness of the α laths, cooling rate, thin surface layer with fine grain size, Figure 7.9 is a schematic drawing of crystallographic texture in terms of low temperature {0001}α PFs in different weld zones (BM, HAZ, TMAZ and SZ) and trend of shear texture strength. Table 7.2 concludes the characterisation of microstructure features and texture in the weld zones
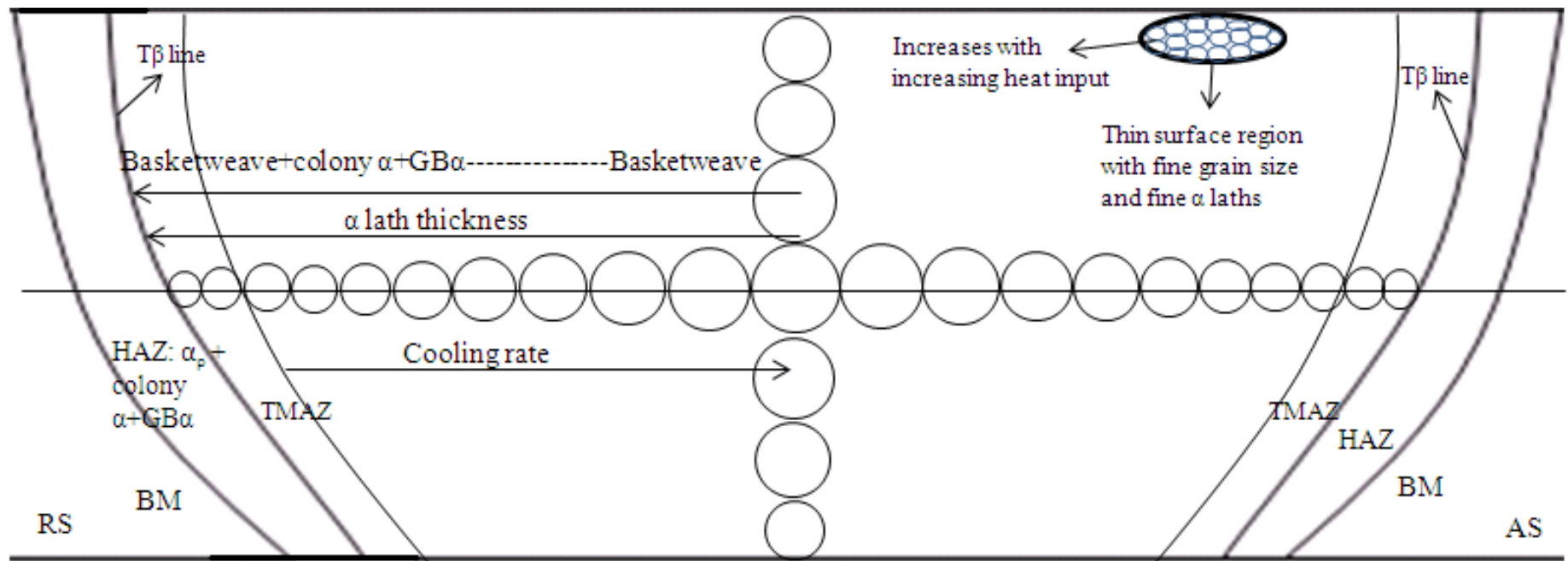
Figure 7.8 Schematic drawing indicates the overall microstructure developed in the weld zones of this study
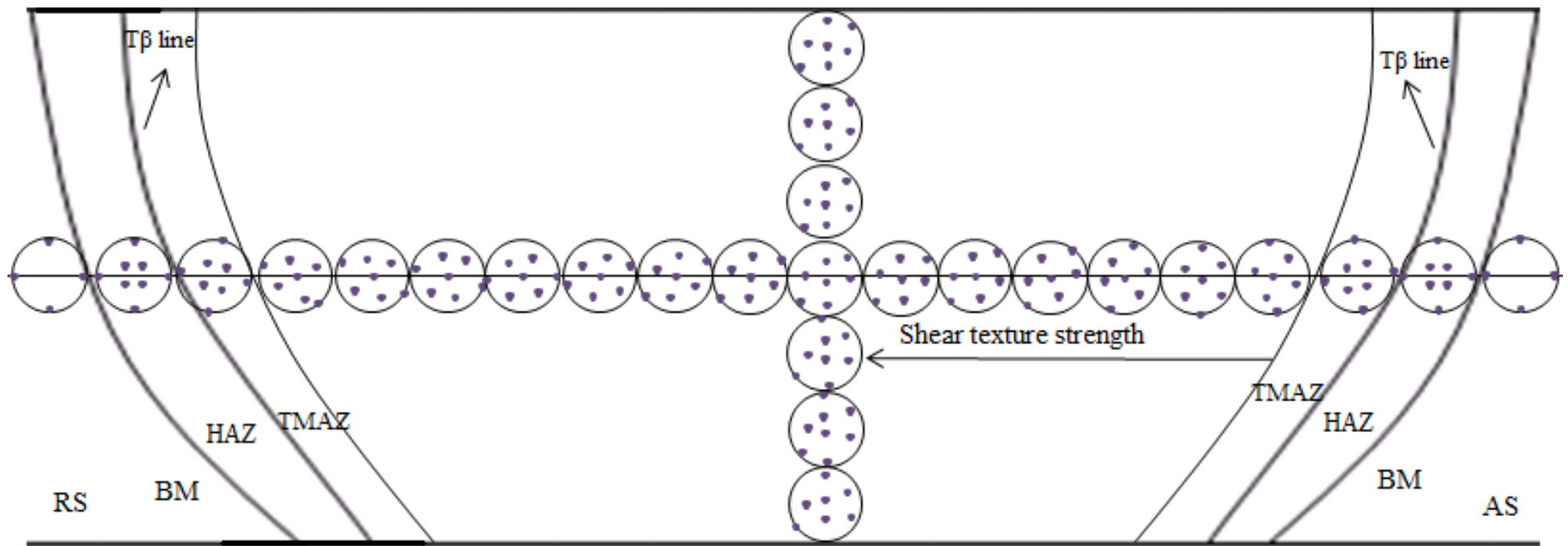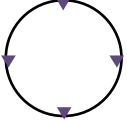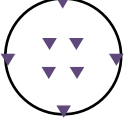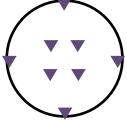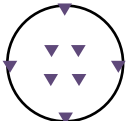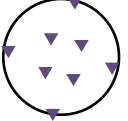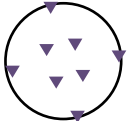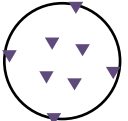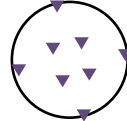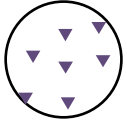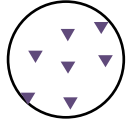
Figure 7.9 Schematic drawing indicates the overall texture developed in the weld zones of this study

Table 7.2 Characterisation of microstructure and texture in the weld zones

| | Microstructure | Texture (Schematic) | | | | Characteristics |
|---|---|---|---|---|---|---|
| | | α phase, {0001} PFs | | Reconstructed β phase, {110} PFs | | |
| BM | Equiaxed structure | | | | | 82% $\alpha_p$ + 18% retained β; classic rolling texture; undeformed region |
| HAZ*[1] | Bimodal structure | | | | | $\alpha_p$ + retained β + transformed $\alpha_s$; undeformed region |
| TMAZ*[2] | Coarse lamellar structure | The RS | The AS | The RS | The AS | 100% transformed $\alpha_s$; rotates along the normal direction as rotated HAZ texture |
| SZ | Fine lamellar structure | | | | | 100% transformed $\alpha_s$; rotated to D1 bcc simple shear texture |

*[1]: width of the HAZ is slightly larger at the RS than that at the AS

*[2]: width of the TMAZ is slightly larger at the AS than that at the RS

343

**Chapter 8 Conclusions**

**8.1 Introduction**

This chapter provides the conclusions for the study on microstructure evolution and crystallographic texture evolution during stationary shoulder friction stir welding of Ti–6Al–4V alloy. The conclusions are divided into three main parts. Firstly, an analysis of the influence of the process parameters of SSFSW on heat input, surface quality and hardness, secondly, a characterization of microstructure of different weld zones and finally, texture evolution in the weld zones consisting of texture development in the weld zones and variant selection study.

**8.2 Effect of process parameters**

1. Traverse force, down force and torque and swept volume increased with increasing traverse speed and decreasing rotation speed.

2. The material has higher heat input at lower traverse speed and the reduction of heat input in not linear; heat input decreased slightly with decreasing rotation speed and the reduction of heat input is linear.

3. The weld surfaces became significantly smoother with increasing traverse speed indicating process stability increases with increasing traverse speed.

4. The weld zones are slightly harder than the base material; hardness at the AS is slightly higher than the RS; thin higher hardness layers were observed in the weld surface of all the three welds and the weld bottom of the weld W4 and W5 produced with the same rotation speed of 900rpm were possibly resulted from the tool material infiltration; W6 with the highest traverse speed has uniform hardness distribution. Microhardness is much more uniformly distributed in the three welds W19, W20 and W21 with 150mm /min traverse speed.

5. Peak weld temperature was the highest in the weld centre and it decreased from the weld centre to the weld surface and from the weld centre to the weld bottom; Peak weld temperature in the weld zones decreased with increasing traverse speed and it increased with increasing rotation rate.

6. The AS has experienced higher peak temperature than the RS for all the three welds as proved by Secondary electron micrographs of the transition zones and hardness test.

7. The prior β grain size increases with increasing heat input as the decrease of the traverse speed and the increase of rotation speed, as the prior β grain size increases, the variant selection intensity becomes stronger and the average thickness of the α laths decreased significantly.

8. The rotation speed has much stronger effect on the microstructure unit size: the prior β grain size and the thickness of the α laths compared to the traverse speed.


## 8.3 Characterization of microstructure

1. Optical and SEM showed that the BM is composed of equiaxed αp grains of 29μm size and retained β, the HAZ has bimodal structure with αp and transformed β phase in the form of coarse lamellar α, namely, secondary α. Fully lamellar structure observed in the TMAZ has undergone deformation.

2. The TMAZ has coarse α laths while the SZ contains fine α laths structure. SZ is characterised by α colonies, GBα, Widmanstätten structure and basketweave structure, where a large amount of α+β lamellar laths were arranged along GBα with interweaved α laths about 1-2μm and thinner β laths less than 0.3μm.

3. In both coarse and fine lamellar structure of the TMAZ and the SZ, the prior β grain size increased with decreasing traverse speed and it increased with increasing rotation speed.

4. Great material flow at the AS of the weld surface from the probe resulted in the "shearing effect" on the weld surface at the AS of all the six welds due to the fact that the material at the RS was pushed to the AS during welding.

5. Width of the bimodal structure at both the AS and the RS decreased with increasing traverse speed and decreasing rotation speed. Thermal gradient became deeper with increasing traverse speed and decreasing rotation speed.

6. Peak weld temperature experienced in the weld centre was the highest and it decreased with increasing distance from the weld centre to both the AS and the RS of the welding edge

7. Tool wear caused by W and Re has occurred in the four welds W4, W5, W6 and W19. W-Re has infiltrated into the welded material in the form of solution resulting in changing of the transformation behaviour, whereupon martensite like structure is formed at normally the same cooling rate as the region next to it does not have dissolved W-Re region which formed lamellar structure.

## 8.4 Characterization of texture

1. Texture of the BM display a classic rolling texture characterised by large elongated macrozones which may cause the fatigue crack. The TMAZ has experienced peak weld temperature above the $T_\beta$, and peak weld temperature in the HAZ is below the $T_\beta$. The simple shear texture component $D1\left(11\bar{2}\right)[111]$ was consistently observed in the SZ and the texture is much stronger at the AS than the RS.

2. Determination of the TMAZ and the HAZ at both the AS and the RS for all the six welds suggest that the bimodal structure belongs to the HAZ and the coarse lamellar structure constitutes the TMAZ.

3. Texture increases and then HAGB fraction increases; texture strengthening from the RS to the AS in the SZ is accompanied by the increase of HAGB fraction.

4. There is a very weak variant selection observed in the SZ due to higher rotating rate of the tool. Selection of the α variants was not influenced by grain boundary α grains or the prior β grain boundaries or the welding axes.

5. Shear texture strength and the intensity of variant selection both increases with decreasing traverse speed and increasing rotation speed

**Chapter 9 Future work**

**9.1 SSFSW process**

Further work needs to be conducted to establish relationships between all of the relevant process parameters and the resulting microstructure and properties of the weld joint. This would again allow the welding parameters to be optimized.

Thermal couples should be embedded in the welds at different positions in further welding tests in order to obtain exact temperature data.

**9.2 Characterization of microstructure**

Further test using TEM will be possible to determine the deformation mode, which was difficult to determine by SEM and EBSD. For example, an analysis of dislocations to determine the active slip systems and twinning systems and a study of recrystallization in the weld zones.

It would be useful to simulate SSFSW by further tests followed with controlled cooling rate. This would give more insight into the microstructure development in different weld zones

It would be useful to carry out thermal modeling of SSFSW of titanium alloys via Abaqus. This would allow a detailed investigation on temperature distribution, material flow and even strain and stress distribution during SSFSW. And modeling work in conjunction with experimental work would help us determine the optimal process parameters.

**9.3 Characterization of texture**

It would be interesting to study the texture modelling although it requires a lot of mathematical and computational skills and is hard to undertake in terms of finding out parameters for the material, e.g. slip systems.

It would be useful to study the effect of texture and variant selection on mechanical properties.

## Appendix

Rotation in the program for all sections in order to rotate into the shear reference frame:
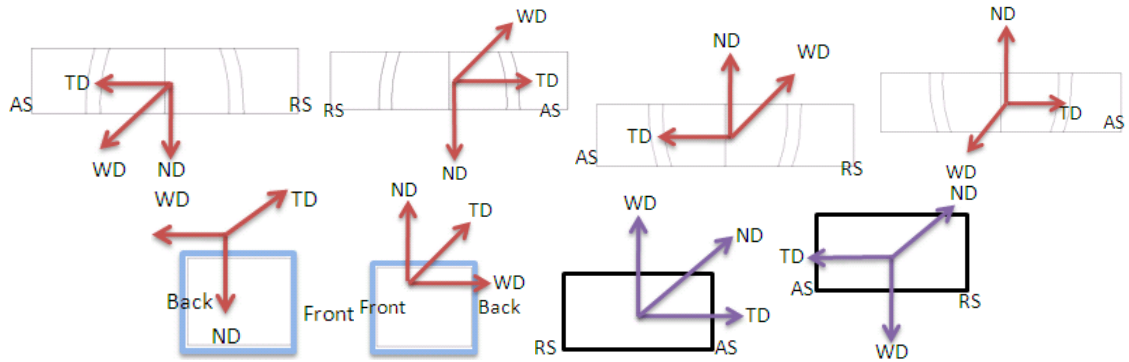


Figure 1 Rotation in the program for the cross sections: 1. Rotate around Z 180 then X 90, 2. Rotate about X 270 in the program, 3. Rotate around X 90 then Z 180, 4. Rotate about X 90 in the program for the side sections and 5. Rotate around X 90, Y 180 and then Z=270, 6. Rotate around X 90, and then Z; for the normal sections: 7. Rotate X around 180 in the program and 8. Rotate around X 180 and then Z 180 in the program

Table 1 Data of swept volume, heat input, largest prior β grain size, shear texture strength in the SZ, the shear strain rate at the weld surface and the weld bottom of all the six welds

| Weld No | W4 | W5 | W6 | W19 | W20 | W21 |
|---|---|---|---|---|---|---|
| Swept volume V, mm$^3$/rev | 6.15 | 11.82 | 17.66 | 19 | 23.88 | 35.74 |
| Average Heat input, kJ/mm | 3.3 | 1.8 | 1.3 | 1.2 | 1.1 | 1.1 |
| Largest prior β grain size, μm | 155 | 136 | 124 | 113 | 82 | 62 |
| Shear texture strength, MUD | 11.6 | 11.4 | 8.4 | 12.3 | 8.8 | 8.8 |
| Shear strain rate at the surface, s$^{-1}$ | 307.9 | 318.5 | 324.1 | 264.8 | 228.1 | 195.5 |
| Shear strain rate at the bottom, s$^{-1}$ | 298 | 401.6 | 439.8 | 410.5 | 384.8 | 373.2 |

Table 2 Ratio data of swept volume, heat input, largest prior β grain size, shear texture strength in the SZ, the shear strain rate at the weld surface and the weld bottom of all the six welds

| Weld No | Swept volume | Heat input | Largest prior beta grain size | Shear texture strength | Shear strain rate at the surface | Shear strain rate at the bottom |
|---|---|---|---|---|---|---|
| W4 | 1.00 | 2.54 | 2.87 | 1.38 | 1.00 | 1.00 |
| W5 | 1.92 | 1.38 | 1.92 | 1.36 | 1.03 | 1.35 |
| W6 | 2.87 | 1.00 | 1.00 | 1.00 | 1.05 | 1.48 |
| W21 | 2.02 | 1.00 | 1.00 | 1.00 | 1.00 | 1.00 |
| W20 | 1.35 | 1.00 | 1.14 | 1.00 | 1.20 | 1.03 |
| W19 | 1.08 | 1.09 | 1.64 | 1.40 | 1.35 | 1.10 |
| W6 | 1.00 | 1.18 | 1.79 | 0.95 | 1.65 | 1.18 |

# References

Abbasi, M., Nelson, T. and Sorensenn, C., 2011, Transformation and Deformation texture study in Friction stir processed API X80 steel, in Friction Stir Welding and Processing VI, The Minerals Metals and Materials Society, edited by: R. Mishra, M. W. Mahoney, Y. Sato, H. Hovanski and R. Verma, TMS (the Minerals, Metals and Materials Society)

Ahmed, T., and H.J. Rack, 1998, Phase transformations during cooling in α+β titanium alloys, Materials Science and Engineering A, 243, p.206-211

Ahmed, M.M.Z., 2009, The Development of Thick Section Welds and Ultra-Fine Grain Aluminium Using Friction Stir Welding and Processing, PhD thesis, The University of Sheffield

Arbegast, J.W., Refill Friction Stir Spot Welding of Aluminium Alloy, 2007, Proceedings of International Seminar on Friction-based Spot Welding Processes. Germany,

Ari-Gur, P. and Semiatin, S.L., 1998, Evolution of microstructure, macrotexture and microtexture during hot rolling of Ti-6Al-4V, Materials Science and Engineering A, 257, p. 118-127

Arthur, F., Croft, R., Goyle, A., Plummer, J. and Xiao, B., 2007, Developing a Mathematical Model Capable of Predicting the Properties of TMCR Steel, MAT 480, the university of Sheffield

Assessment of Stationary Shoulder Friction Stir Welding (SSFSW) for the Joining of Titanium Alloys for a Group of Sponsors PR11708-1, 2007, TWI

Attallah, M.M. and Salem, H.G., 2005, Friction stir welding parameters: a tool for controlling abnormal grain growth during subsequent heat treatment, Materials Science and Engineering A, 391, p. 51-59

Baczynski, J., and Jonas, J. J., 1996, Texture development during the torsion testing of α-iron and two IF steels, Acta Materialia, 44(11), p. 4273-4288

Bania, P.J., 1994, beta titanium alloys and their role in the titanium industry, JOM (The Member Journal of TMS), 46(7), p. 16-19

Banerjee, R., Bhattacharyya, D., Collins, P.C., Viswanathan, G.B. and Fraser, H.L., 2004, Precipitation of grain boundary α in a laser deposited compositionally graded Ti-8Al-xV alloy- an orientation microscopy study, Acta Materialia, 52, p. 45, p. 379.

Banerjee, S., and Mukhoparhyay, P., 2007, Phase transformations: examples from titanium and zirconium alloys, Pergamon Materials series, p. 43, p. 101-120, p. 687-689

Balasubramanian, S., 1998, Polycyrstalline plasticity: application to deformation processing of lightweight metals, PhD thesis, Massachusetts institute of technology

Balasubramanian and Anand, L., 2002, "Plasticity of initially textured hexagonal polycrystals at high homologous temperatures: application to titanium", Acta materialia, 50, p. 133-148

Baufeld, B., Der Biest, O. V. and Dillien, S., 2010, Texture and Crystal Orientation in Ti-6Al-4V Builds Fabricated by Shaped Metal Deposition, Metallurgical and Materials Transactions A, 41(8), p. 1917-1927

Bhattacharyya, D., Viswanathan, G.B., Denkenberger, R., Furrer, D. and Fraser, H.L., 2003, the role of crystallographic and geometrical relationships between α and β phases in an α/β titanium alloy, Acta Materialia, 51, p. 4679-4691

Bhattacharyya, D., Viswanathan, G.B. and Fraser, H.L., 2007, Crystallographic and morphological relationships between β phase and the Widmanstätten and allotriomorphic the α phase at special β grain boundaries in an α/β titanium alloy, Acta Materialia, 55, p. 6765-6778

Biavant, K. L., Pommier, S. and Prioul, C., 2002, Local texture and fatigue crack initiation in a Ti-6Al-4V titanium alloy, Fatigue and Fracture of Engineering Materials and Structures, 25(6), p.527

Blicharski, M., Nourbakhsh, S. and Nutting, J., 1979, Structure and properties of plastically deformed α-Ti, Metal Science, 13(9), p. 516-522(7)

Bowen, A.W., Mcdarmaid, D.S. and Partridge, P.G., 1991, Effect of high-temperature deformation on the texture of a two-phase titanium alloy, Journal of Materials Science, 26, p. 3459

Brinckmann, S., von Strombeck, A., Schilling, C., dos Santos, J.F., Lohwasser, D. and Koçak, M., 2000, Mechanical and Toughness Properties of Robotic-FSW Repair Welds in 6061-T6 Aluminium Alloys, proceedings of the second international Symposium on Friction Stir Welding, 26-28 June 2000, Gothenburg, Sweden

Bunge, H.J., 1982, Texture analysis in materials science, Butterworths and Co, London, p. 4-10, 15, 47

Cantoni, M., 2010, Experimental Methods in Physics, Introduction to EDX,

http://wiki.epfl.ch/mep/documents/MEP%5B09-10%5D_DOWNLOAD/6%20edx.pdf (Accessed 10/11/2010)

Cavaliere, P., Squillace, A. and Panella, F., 2008, Effect of welding parameters on mechanical and microstructural properties of AA6082 joints produced by friction stir welding, journal of materials processing technology, 200, p. 364-372

Charles, C. and Järvstråt, N., 2008, Modelling Ti-6Al-4V microstructure by evolution laws implemented as finite element subroutines: Application to TIG metal deposition, Proceedings of the 8th International Conference on Trends in welding research, 2-6 June 2008, Pine Mountain, Georgia

Chen, C.M. and Kovacevic, R., 2003, Finite element modeling of friction stir welding-thermal and thermomechanical analysis, International Journal of Machine Tools and Manufacture, 43, p. 1319-1326

Chen Z.W. and Maginness, R., 2004, Formation of the weld zones during friction stir welding of Aluminium alloys, Proceedings of the Fifth international symposium on Friction stir welding, 14-16 September 2004, Meta, France

Cheng, D., Huang, J., Zhao, X. and Zhang, H., 2010, Microstructure and superplasticity of laser welded Ti-6Al-4V alloy, Materials and Design, 31, p. 620-623

Channel 5 help files, 2005, project manager version 5.07.0, HKL Thechnology A/S

Chaze, A.M. and Montheillet, F., 1994, in Les Alliages de Titane Beta, Eds. A. Vassel, D. Eylon, and Y. Combres, Editions de la Revue de Metallurgie, Paris, 8, p. 41

Chesnutt, J.C., Rhodes, C.G. and William, J.C., 1976, Relationship between mechanical properties, microstructure and fracture topography in α+β titanium alloys Fractography-

Microscopic cracking processes, ASTM STP 600 (American Society for testing and materials), p. 116-118

Choi, S.H., Shin, E.J. and Seong, B.S., 2007, Simulation of deformation twins and deformation texture in an AZ31 Mg alloy under uniaxial compression, Acta Materialia, 55, p. 1483

Colegrove, P.A. and Shercliff, H.R., 2004, Development of Trivex, Friction stir welding tool, Part 1: two dimensional flow modeling, Science and Technology of Welding and Joining, 9(4), p. 345-351

Colligan, K., 2000, Dynamic material deformation during friction stir welding of Aluminium, Proceedings of the second international Symposium on Friction Stir Welding, 26-28 June 2000, Gothenburg, Sweden

Combres, Y. and Champin, B., 1992, Proc. Colloque GS Ti Aussoi/ proceeding of Ti GS Aussois conference, CNRS (National Center for Scientific Research), p. 143

Commin, L., Dumont, M., Masse, J. E. and Barrallier, L., 2009, Friction stir welding of AZ31 magnesium alloy rolled sheets: Influence of process parameters, Acta Materialia 57, p. 326–334

Crystallographic Institute, 2008, Albert-Ludwigs Freiburg University,

http://www.krist.unifreiburg.de/studium/PraktiKum/PraktiKum_Manuskripte/EBSD/EBSD .pdf (accessed 18/02/2008)

Cullity, B.D, 1978, Elements of X-ray Diffraction, second edition, Addison-Wesley Publishing Company, United States, p. 41-45

Danaf, E.E., Kalidindi, S.R. and Doherty, R.D., 1999, Influence of grain size and stacking-fault energy on deformation twinning in fcc metals, Metallurgical and Materials Transactions A, 30(5), p. 1223-1232

Dawes, C.J. and Thomas, W.M., 1999, Development of improved tool designs for friction stir welding of Aluminium, Proceedings of the first international symposium on Friction stir welding, 14-16 June 1999, Thousand Oaks, California, USA

Davies, P.S., 2009, An Investigation of Microstructure and Texture Evolution in the Near-α Titanium Alloy Timetal® 834, PhD thesis, The University of Sheffield

Davies, P.S., Wynne, B.P., Rainforth, W.M., Thomas M.J. and P.L. Threadgill, 2011, Development of microstructure and crystallographic texture during Stationary Shoulder Friction Stir Welding of Ti-6Al-4V, Metallurgical and Materials Transactions A, 42(8), p. 2278-2289

Dawes, C.J., and Thomas, W.M., 1999, Development of improved tool designs for friction stir welding of Aluminium, Proceedings of the first international symposium on Friction stir welding, 14-16 June 1999, Thousand Oaks, California, USA

Daymond, M.R., Holt, R.A., Cai, S., Mosbrucker, P. and Vogel, S.C., 2010, Texture inheritance and variant selection through an hcp-bcc-hcp phase transformation, Acta Materialia, 58, p. 4053-4066

Ding, R., Guo, Z. X. and Wilson, A., 2002, Microstructural evolution of a Ti-6Al-4V alloy during thermomechanical processing, Materials Science and Engineering A, 327(2), p. 233-245

Ding R., and Guo, Z.X., 2004, Microstructural evolution of a Ti-6Al-4V alloy during β-phase processing: experimental and simulative investigations, Materials Science and Engineering A, 365, p. 172-179

Divinski, S.V., Dnieprenko, V.N. and Ivasishin, O.M., 1998, Effect of phase transformation on texture formation in Ti-base alloys, Materials Science and Engineering A, 243, p. 201-205

Donachie, M.J., 1988, Titanium-A Technical Guide, ASM International, Metals Park, OH, p. 353-365

Donachie, M.J., 2000, Titanium, A Technical Guide, 2nd edition, Materials Park, OH: ASM International, p. 1-5, p. 102-105, p. 381

Dunst, D., and Mecking, H., 1996, Analysis of experimental and theoretical rolling textures of two-phase titanium alloys, Zeitschrift für Metallkunde (Z Metallkd), 87(6), p. 498

Eylon, D., 1994, Metallurgy and Technology of Practical Titanium Alloys, in S. Fujishiro, D. Eylon, T. Kishi (Eds.), TMS, Warrendale, PA, p. 29-34

Edwards, P.D. and Ramulu, M., 2009, Investigation of microstructure, surface andsubsurface characteristics in titanium alloy friction stir welds of varied thicknesses, Science and Technology of Welding and Joining, 14(5), p. 476-483

Edwards, P. and Ramulu, M., 2010, Peak temperatures during friction stir welding of Ti-6Al-4V, Science and Technology of Welding and Joining, 15(6), p. 468-472

Edwards, P., Petersen, M., Ramulu, M. and Boyer, R., 2010, Mechanical Performance of Heat Treated Ti-6Al-4V Friction Stir Welds, Journal Key Engineering Materials, 436, p. 213

Flower, H.M., 1990, Microstructural development in relation to hot working of titanium alloys, Materials Science and Technology, 6, p. 1084-1085

Fonda, R.W. and Knipling, K.E., 2010, Texture development in near-a Ti friction stir welds, Acta Materialia, 58, p. 6452-6463

Fratini, L., Micari, F., Buffa G. and Ruisi, V.F., 2010, A new fixture for FSW processes of titanium alloys, CIRP Annals-Manufacturing Technology, 59, p. 271-274

Fujii, H., Takada, Y., Tsuji N. and Nogi, K., 2004, Friction stir welding of ultrafine grained materials, Proceedings of the Fifth international symposium on Friction stir welding, 14-16 September, 2004, Meta, France

Fujii, H., Sun, Y., Kato H., and Nakata, K., 2010, Investigation of welding parameter dependent microstructure and mechanical properties in friction stir welded pure Ti joints, Materials Science and Engineering A, 527, p. 3386-3391

Fuller, C.B., 2007, Friction stir tooling: tool materials and designs, in Friction stir welding and processing, edited by Rajiv S. Mishra, Murray W. Mahoney, p. 7-35

Gazder, A.A., Dalla Torre, F., Gu, C.F., Davies C.H.J. and Pereloma, E.V., 2006, Microstructure and texture evolution of bcc and fcc metals subjected to equal channel angular extrusion, Materials Science and Engineering A, 415(1-2), p. 126-139

Germain, L., Gey, N., Humbert, M., Bocher P., and Jahazi, M., 2005, An automated method to analyze separately the microtextures of primary $\alpha_p$ grains and the secondary $\alpha_s$ inherited colonies in bimodal titanium alloys, Materials Characterization, 54(3), p.216-222

Germain, L., Gey, N., Humbert, M., Vob, P., Jahazi, M. and Bocher, P., 2008, Texture heterogeneities induced by subtransus processing of near a titanium alloys, Acta Materialia, 56, p. 4298-4308

Gey, N. and Humbert, M., 2002, Characterization of the variant selection occurring during the α→β→the α phase transformations of a cold rolled titanium sheet, Acta Materialia, 50, p. 277-287

Gey, N. and Humbert, M., 2003, Specific analysis of EBSD data to study the texture inheritance due to the β-α phase transformation, Journal of Materials Science, 38, p. 1289-1294

Gil, F.X., Ginebra, M.P., Manero, J.M. and Planell, J.A., 2001, Formation of α-Widmanstätten structure: effects of grain size and cooling rate on the Widmanstätten morphologies and on the mechanical properties in Ti6Al4V alloy, Journal of Alloys and Compounds, 329(1-2), p. 142-152

Glavicic, M.G., Kobryn, P.A., Bieler T.R., and Semiatin, S.L., 2003a, A method to determine the orientation of the high-temperature beta-phase from measured EBSD data for the low-temperature alpha-phase in Ti-6Al-4V, Material Science and Engineering A, 346, p. 50-59

Glavicic, M.G., Kobryn, P.A., Bieler, T.R., and Semiatin, S.L., 2003b, An automated method to determine the orientation of the high-temperature beta-phase from measured EBSD data for the low-temperature alpha-phase in Ti-6Al-4V, Material Science and Engineering A, 351, p. 258-264

Glavicic, M.G., Kobryn, P.A. and Semiatin, S.L., 2004, Validation of an automated EBSD method to deduce the β- phase texture in Ti-6Al-4V with a colony-α microstructure, Material Science and Engineering A, 385, p. 372-376

Goddard, N. D. R., Flower, H.M., and Cope, M., 1989, Proceedings of the 6th World Conference on Titanium, Paris, Les Editions de Physique, ed. P. Lacombe et al., p. 259-264

Gourdet. S., and Montheillet, F., 2000, An experimental study of the recrystallization mechanism during hot deformation of Aluminium, Materials Science and Engineering A, 283, p. 274

Gourdet. S., and Montheillet, F., 2002, Effects of dynamic grain boundary migration during the hot compression of high stacking fault energy metals: Acta Materialia, 50, p. 2801-2812

Gourdet. S., and Montheillet, F., 2003, A model of continuous dynamic recrystallization, Acta Materialia, 51, p. 2688-2694

Goetz, R.L. and Jata, K.V., 2001, Modeling friction stir welding of titanium and Aluminium alloys, Friction Stir Welding and Processing, Indianapolis, USA; 4-8 November, p. 35-42

Gray III, G.T., 1988, Deformation twinning in Al-4.8 wt% Mg, Acta Metallurgica, 36(7), p. 1745

Grujicic, M., Arakere, G., Pandurangan, B., Hariharan, A., Yen, C.F., Cheeseman, B.A. and Fountzoulas, C., 2011, Computational analysis and experimental validation of the friction-stir welding behaviour of Ti-6Al-4V, Proceedings of the Institution of Mechanical Engineers, Part B: Journal of Engineering Manufacture, 225(2), p. 208-223

Harris, D. and Norman, A.F., 2003, Properties of Friction stir welded joints: A review of the literature, EUROSTIR, Progress report presented at the 6th PSG Meeting

Hassan, K.H., Prangnell, P.B., Norman, A.F., Price, D.A. and Williams, S.W., 2003, Effect of welding parameters on nugget zone microstructure and properties in high strength Aluminium alloy friction stir welds, Science and Technology of Welding and Joining, 8, p. 257

Hatherby, M. and Hutchinson, W.B., 1979, An introduction to textures in metals, London, p. 6-7, p. 35-63

Hansen, M., "A cooler weld", 2003, Mechanical Engineering Magazine Online, publication of ASME Int'l

Helder, E. and Subramanian, P.R., 2003, FSW of titanium alloys for aircraft engine components, TMS Annual Meeting

Heurtier, P., Jones, M.J., Desrayaud, C., Driver, J.H., Montheillet, F. and Allehaux, D., 2006, Mechanical and thermal modelling of friction stir welding, Journal of Materials Processing Technology, 171(3), p. 348-57

Hughes, A. and Hansen, N., 1997, High angle boundaries formed by grain subdivision mechanisms, Acta Materialia, 45 (9), p. 3871-3873

Hughes, D.A., Lebensohn, R., Wenk, H.R. and Kumar, A., 2000, Stacking fault energy and microstructure effects on torsion texture evolution. Proc. R. Soc. Lond. A/ Proceedings of the Royal Society A, 456, p. 921-950

Humbert, M., Gey, N. and Germain, L., 2005, Study and Modelling of Some Variant Selections in bcc to hcp Phase Transformations, Materials Science Forum, 495-497, p. 1111-1120

Humbert, M., Germain, L., Gey, N., Bocher, P. and Jahazi, M., 2006, Study of the variant selection in sharp textured regions of bimodal IMI 834 billet, Materials Science and Engineering A, 430, p. 157-164

Humphreys, F.J. and Hatherly, M., 1995, Recrystallisation and related annealing phenonomen, Pergamon, p.497

Humphreys, F.J., 2001, Review Grain and subgrain characterisation by electron backscatter diffraction, Journal of Materials Science, 36, p. 3833-3854

Humphreys, F.J. and Hatherly, M., 2004, Recrystallization and related annealing phenomena second edition, Amsterdam; London: Elsevier, p. 24-35, 154-155, p. 444

Humphreys, F.J., 2004, Recrystallization phenomenon and related annealing Phenomena, p. 12, p. 92-114, p.169-172, p. 427-437, p457

Humphreys, F.J., 2008, University of Manchester,

http://www.recrystallization.info/rexmenu.htm, (Accessed 18/12/2008, but currently not available)

Irving, P. E. and Beevers, C.J., 1974, Microstructural Influences on Fatigue Crack Growth in Ti-6Al-4V, Materials Science and Engineering, 14(3), p. 229-238

Jata, K.V., P.R. Subramanian, A.P. Reynolds, T. Trap and E. Helder, 2004, Friction Stir Welding of Titanium Alloys for Aerospace Applications: Microstructure and Mechanical Behavior, 2004, Proceedings of the fourteenth International offshore and polar engineering conference Toulon, France, 2004

Jiang, X., Davies, P.S., Wynne, B.P. and Threadgill, P.J., 2010, A Microstructure and Crystallographic Texture Investigation of Static Shoulder Friction Stir Welding of Ti-6Al-4V, Proceedings of the 8th International Friction Stir Welding Symposium, 18-20 May 2010, Timmendorfer Strand, Germany

Joshi, V.A., 2006, Titanium Alloys, An Atlas of Structures and Fracture Features, CRC Press Taylor and Francis Group, p. 10, p. 19-26, p. 59, p. 97

Johnson, A.J.W., Bull, C.W., Kumar, K.S. and Briant, C.L., 2003, the influence of microstructure and strain rate on the compressive deformation behavior of Ti-6Al-4V, Metallurgical and Materials Transactions A, 34, p. 295

Jonas, J.J., 1969, The back stress in high temperature deformation, Acta Metallurgica, 17(4), p. 11, p. 397.

Jonas, J.J., Sellars, C.M. and McG. Tegart, W.J., 1969, Strength and structure under hot working conditions, Metallurgical Reviews, 14 (130), p. 1-24

Jourdan, C., Gastaldi, J., Marzo, P. and Grange, G., 1991, In situ statistical study of the nucleation, the variant selection and the orientation memory effect during the β titanium martensitic transformation, Journal of Materials science, 26, p. 4355-4360

Juhas, M.C., Viswanathan, G.B. and Fraser, H.L., 2000, Microstructural Evolution in Ti Alloy Friction Stir Welds, Proceedings of the 2nd Symposium on Friction Stir Welding, 26-28 June 2000, Gothenburg, Sweden

Juhas, M.C., Viswanathan, G.B. and Fraser, H.L., 2001, Proceedings of lightweight alloys for aerospace application, TMS, Warrendal, 2001

Kalidindi, S.R., Salem, A.A. and Doherty, R.D., 2003, Role of Deformation Twinning on Strain Hardening in Cubic and Hexagonal Polycrystalline Metals, Advanced Engineering Materials, 5(4), p. 229-232

Kallee, S. and Mistry, A., 1999, Friction stir welding in the automotive body in white production, First international symposium on friction stir welding, 14-16 June 1999, Thousand Oaks, California, USA

Karthikeyan, T., Dasgupta, A., Saroja, S., Khatirkar, R., Vijayalakshmi, M. and Samajdar, I., 2008, Study of texture and microtexture during β to α + β transformation in a Ti-5Ta-1.8Nb alloy, Materials Science and Engineering A, 485, p. 581-588

Kelly, A., Groves, G.W. and Kidd, P., 2000, Crystallography and Crystal Defects, Revised Edition, John Wiley and Sons Ltd, p. 97-103

Kestenbach, H.J. and Meyers, M.A., 1976, The effect of grain size on the shock-loading response of 304-type stainless steel, Metallurgical and Materials Transactions A, 7(11), p. 1943

Klingensmith, S., DuPont, J.N. and Marder, A.R., 2005, Microstructural Characterization of a Double-Sided Friction Stir Weld on an Superaustenitic Stainless Steel, Welding Journal, 84(5), p. 77S-85S

Knipling, K.E. and Fonda, R.W., 2009, Texture development in the stir zone of near-α titanium friction stir welds, Scripta Materialia, 60, p. 1097-1100

Knipling, K.E. and Fonda, R.W., 2011, Microstructural Evolution in Ti-5111 Friction Stir Welds, Metallurgical and materials transactions A, 42, p. 2312-2320

Kocks, U.F., Tomé, C.N. and Wenk, H.R., 1998, Texture and Anistropy: preferred orientations in polycrystals and their effect on materials properties, Cambridge university Press, p. 169

Kopeliovich, D., 2009, Classification of titanium alloys, Materials forum, Substances and Technologies,
http://www.substech.com/dokuwiki/doku.php?id=classification_of_titanium_alloys
(accessed 02/04/2009)

Lang, B., Zhang, T.C., Li, X.H. and Guo, D.L., 2010, Microstructural evolution of a TC11 titanium alloy during linear friction welding, Journal of Materials Science, 45, p. 6218-6224

Leary, R. K., Merson, E., Birmingham, K., Harvey, D., and Brydson, R., 2010, Microstructural and microtextural analysis of Inter Pulse GTCAW welds in CP-Ti and Ti-6Al-4V, Materials Science and Engineering A, 527, p.7694-7705

Lee. W.B., Lee, C.Y., Chang, W.S., Yeon, Y.M. and Jung, S.B., 2005, Microstructural investigation of friction stir welded pure titanium, Materials Letters, 59(26), p 3315-3318

Leonard, A.J. and Lockyer, S.A., 2003, Flaws in Friction stir welds, Proceedings of the 4th international symposium on Friction Stir Welding, 14-16 May 2003, Utah, USA

Leyens, C. and Peters, M., 2003, Titanium and Titanium Alloys: Fundamentals and Aplications, WILEY-VCH GmbH and Co.KGaA, Weinheim, p. 6, p. 134-165

Li, S., Beyerlein, I.J. and M. A.M. Bourke, 2005, Texture formation during equal channel angular extrusion of fcc and bcc materials: comparison with simple shear, Materials Science and Engineering A, 394, p.7

Lienert, T.J., Jata, K.V., Wheeler, R. and Seetharaman, V., 2000, Friction stir welding of Ti-6Al-4V alloys, Materials Solutions, St. Louis, MO, USA, p. 160-166

Lienert, T.J., Jata, K.V., Wheeler, R. and Seetharaman, V., 2001, Friction stir welding of Ti-6Al-4V Alloys, Proceedings of joining of advanced and specialty materials III, ASM International, Materials Park, 2001

Lienert, T. J., Stellwag, W. L. Jr., Grimmett, B.B. and Warke, R.W., 2003a, Friction Stir Welding Studies on Mild Steel, Suplement to the Welding Journal, Welding Journal, p. 1S-9S

Lienert, T. J., Stellwag, W.L. Jr., and Lehman, L.R., 2003b, Heat input, peak temperatures and process efficiencies for FSW, Proceedings of the 4th international symposium on Friction stir welding, 14-16 May 2003, Utah, USA

Liu, H., Zhou, L., Huang, Y. and Liu, Q., 2010a, Study of the Key Issues of Friction Stir Welding of Titanium Alloy, Journal Materials Science Forum, 638-642, p. 1185-1190

Liu, H., Zhou, L. and Liu, Q.W., 2010b, Microstructural characteristics and mechanical properties of friction stir welded joints of Ti-6Al-4V titanium alloy, Materials and Design, 31(3), p. 1650-1655

Liu, H. and Zhou, L., 2010, Microstructural zones and tensile characteristics of friction stir welded joint of TC4 titanium alloy, Transactions of Nonferrous Metals Society of China, 20, p. 1873-1878

Longhurst, W. R., 2009, Force control of friction stir welding, PhD Dissertation, Vanderbilt University

Lütjering, G. and Williams, J.C., 2003, *Titanium*, Berlin, London, p 18-84, p. 212-222

Lütjering, G., Williams, J.C. and Gysler, A., 1998, Microstructure and Mechanical Properties of Titanium Alloys, in Microstructure and Properties of Materials, eds. J.C.M. Li, World Scientific, Singapore, p. 6-8, p. 19

http://www.worldscibooks.com/etextbook/4311/4311_chap01.pdf  (accessed 02/06/2010)

Ma, Z.Y., Pilchak, A.L., Juhas, M.C. and William, J.C., 2008, Microstructural refinement and property enhancement of cast light alloys via friction stir processing, Scripta Materialia, 58, p. 361-366

Mahajan, S. and Williams, D.F., 1973, Deformation Twinning in Metals and Alloys, International Materials Reviews, 18(2), pp. 43-61(19)

Majdic, M. and Ziegler, G., 1973, Effect of the Metastable beta-Phase Transformations in the Ti-6Al-4V Alloy, Zeitschrift fuer Metallkunde/Materials Research and Advanced Techniques, 64 (11), p.751-758

Mishra, R.S. and Ma, Z.Y., 2005, Friction stir welding and processing, Materials Science and Engineering R-Reports, 50(1-2), p. 4-26

Mironov, S., Zhang, Y., Sato, Y.S. and Kokawa, H., 2008a, Development of grain structure in β-phase field during friction stir welding of Ti-6Al-4V alloy, Scripta Materialia, 59, p. 27-30

Mironov, S., Sato, Y.S. and Kokawa, H., 2008b, Microstructural evolution during friction stir-processing of pure iron, Acta Materialia, 56, p. 2602-2614

Mironov, S., Sato, Y.S. and Kokawa, H., 2009, Development of grain structure during friction stir welding of pure titanium, Acta Materialia, 57, p. 4519-4528

Mironov, S., Sato, Y.S. and Kokawa, H., 2010, Microstructural evolution during friction stir welding of Ti-15V-3Cr-3Al-3Sn alloy, Materials Science and Engineering A, 527, p. 7498-7504

Miyazawa, T., Iwamoto, Y., Maruko, T. and Fujii, H., 2011, Development of Ir based tool for friction stir welding of high temperature materials, Science and Technology of Welding and Joining, 16(2), p. 188

Montheillet, F., Cohen, M. and Jonas, J.J., 1984, Axial stresses and texture development during the torsion testing of Al, Cu and a-Fe, Acta Metallurgica, 32(11), p. 2077-2089

Montheillet, F., Gilormini, P. and Jonas, J.J., 1985, Relation between Axial stresses and texture development during torsion testing: a simplified theory, Acta Metallurgica, 33(4), p. 705-717

Moustahfid, H., Humbert, M. and Philipe, M.J., 1997, Modelling of the texture transformation in a Ti-64 sheet after hot compression, Acta Materialia, 45(9), p. 3785-3790

Nandan, R., DebRoy, T. and Bhadeshia, H.K.D.H., 2008, Recent advances in friction-stir welding- Process, weldment structure and properties, Progress in Materials Science 53, p. 980-1023

Nelson, T.W., Hunsaker, B. and Field, D.P., 1999, Local texture characterization of Friction stir welds in 1100 Aluminium, Proceedings of the 1st international symposium on Friction stir welding, 14-16 June, 1999, Thousand Oaks, California, USA

Nelson, T.W., Zhang, H. and Haynes, T., 2000, Friction stir welding of Aluminium C 6061-boron carbide, Proceedings of the 2nd international Symposium on Friction Stir Welding, 26-28 June, 2000, Gothenburg, Sweden

Nishihara, T. and Nagasaka, Y., 2004, Development of Micro-FSW, Proceedings of the 5th international symposium on Friction stir welding, 14-16 September, 2004, Meta, France

Ohmori, Y., Nakai, K., Ohtsubo, H. and Tsunofuri, M., 1994, Formation of Widmanstätten alpha structure in a Ti-6Al-4V alloy, Materials Transaction, JIM, 35 (4), p. 238–246

Oxford Instruments, Nano Analysis Ltd., EBSD analysis of TiAl alloys for texture and interphase boundary analysis,

http://www.oxford-instruments.com/products/x-ray-microanalysis/ebsd/ebsd-applications/Pages/applications.aspx (Accessed 27/09/2010)

Peel, M.J., Steuwer, A., Withers, P.J., Dickerson, T., Shi, Q. and Shercliff, H., 2006, Dissimilar Friction Stir Welds in AA5083-AA6082, Part I: Process Parameter Effects on

Thermal History and Weld Properties, Metallurgical and materials transactions A, 37, p. 2183

Peters, M., Gysler, A. and Lütjering, G., 1984, Influence of texture on fatigue properties of Ti-6Al-4V, Metallurgical and Materials Transactions A, 15(8), p. 1598

Pilchak, A.L., Juhas, M.C. and Williams, J.C., 2007a, Microstructural Changes Due to Friction Stir Processing of Investment-Cast Ti-6Al-4V, Metallurgical and materials transactions A, 38, p. 401-409

Pilchak, A.L., Juhas, M.C. and Williams, J.C., 2007b, Observations of Tool-Workpiece Interactions during Friction Stir Processing of Ti-6Al-4V, Metallurgical and Materials Transactions A, 38, p. 435-437

Pilchak, A.L., Norfleet, D., Juhas, M.C. and Williams, J.C., 2008, Friction Stir Processing of Investment-Cast Ti-6Al-4V: Microstructure and Properties, Metallurgical and Materials Transactions A, 39(7), p. 1519-1524

Pilchak, A.L., 2009, the effect of friction stir processing on the microstructure, mechanical properties and fracture behavior of investment cast Ti-6Al-4V, PhD Dissertation, The Ohio State University, USA

Pilchak, A.L. and Williams, J.C., 2011, Microstructure and Texture Evolution during Friction Stir Processing of Fully Lamellar Ti-6Al-4V, Metallurgical and materials transactions A, 42(3), p. 773-794

Pilchak, A.L., Tang, W., Sahiner, H., Reynolds, A.P. and Williams, J.C., 2011, Microstructure evolution during Friction Stir Welding of Mill-Annealed Ti-6Al-4V, Metallurgical and materials transactions A, 42(3), p. 753-762

Polmear, I.J., 1981, Light Alloys-Metallurgy of the Light Metals, Edward Arnold, London, p. 167-175

Querin, J.A., Rubisoff, H.A., Schneider, J.A., David, S.A., Roy, T.D., DuPont, J.N., Koseki, T. and Smartt, H.B., 2009, Effect of the weld Tool Geometry on Friction Stir Welded Ti-6Al-4V, Trends in Welding Research, Proceedings of the 8th International Conference, p. 108-112

Ramirez, A.J. and Juhas, M.C., 2003, Microstructural Evolution in Ti-6Al-4V Friction Stir Welds, Materials Science Forum, 426-432, p. 2999

Randle, V. and Engler, O., 2000, Introduction to texture analysis, Amsterdam, Gordon and Breach, p 24-25, p 200-220

Ren, S.R., Ma, Z.Y. and Chen, L.Q., 2007, Effect of welding parameters on tensile properties and fracture behavior of friction stir welded Al-Mg-Si alloy, Scripta Materialia, 56, p. 71-72

Record, J.H., Covington, J.L., Nelson, T.W., Sorensen, C.D., and Webb, B.W., 2004, Fundamental characterization of friction stir welding, Proceedings of the 5th international symposium on Friction stir welding, 14-16 September, 2004, Meta, France

Reynolds, A. and Lockwood, W.D., 1999, Digital image correlation for determination of the weld and base metal constitutive behavior, Proceedings of the 1st international symposium on Friction stir welding, 14-16 June 1999, Thousand Oaks, California, USA

Reynolds, A.P., Hood, E. and Tang, W., 2005a, Texture in friction stir welds of Timetal 21S, Scripta Materialia, 52, p. 491-494

Reynolds, A. P., Tang, W., Khandkar, Z., Khan, J.A. and Lindner, K., 2005b, Relationships between weld parameters, hardness distribution and temperature history in alloy 7050 friction stir welds, Science and Technology of Welding and Joining, 10(2), pp. 190-199

Rubal, M.J., Lipold, J.C., Juhas, M.G., 2010, Microstructure evolution during friction stir processing of Ti-5111, Proceedings of the 8th international symposium on Friction Stir Welding, 18-20 May 2010, Timmendorfer Strand, Germany

Russell, M. J., Friction Stir Welding of titanium alloys - a progress update, Proceedings of the 10th World Conference on Titanium, 13-18 July 2003, Hamburg, Germany

Russell, M.J. and Blignault, C., 2006, Recent developments in Friction Stir Welding of Ti Alloys, Proceedings of the 6th international Symposium on Friction Stir Welding, 10-13 October 2006, Saint Sauveur, Quebec, Canada, ed. P.L. Threadgill

Russell, M.J., Threadgill, P.L., Thomas, M.J. and Wynne, B.P., 2007, "Stationary shoulder friction stir welding of Ti-6Al-4V; process and evaluation", Proceedings of the 11th World Conference on Titanium, 3-7 June 2007, Kyoto, Japan

Salem, A.A., 2000, Chapter 23 of Electron Backscatter Diffraction in Materials Science" by A.J. Schwartz, M. Kumar, Kluwer Academic, New York, p. 324-325

Sato, Y.S., Miyake, M., Kokawa, H., Omori, T., Ishida, K., Imano, S., Park, S.H.C., and Hirano, S., 2011, Development of a cobalt- based alloy FSW tool for high-softening-temperature materials, in Friction Stir Welding and Processing VI, The Minerals Metals and Materials Society, eds. R. Mishra, M. W. Mahoney, Y. Sato, H. Hovanski and R. Verma, TMS (the Minerals, Metals and Materials Society), 2011, p. 3-5

Savolainen, K., Mononen, J., Saukkonen, T., Hänninen, H. and Koivula, J., 2004, Friction stir weldability of coper alloys, Proceedings of the 5th international symposium on Friction stir welding, 14-16 September 2004, Meta, France

Schillinger, W., Bartels, A., Gerling, R., Schimansky, F.P. and Clemens, H., 2006, Texture evolution of the γ- and the α/α2-phase during hot rolling of γ-TiAl based alloys, Intermetallics, 14(3), p. 345

Schwartz, A.J., Kumar, M. and Adams, B.L., 2000, Electron backscatter diffraction in materials science, New York; London, Kluwer Academic

Scialpi, A., De Filipis, L.A.C. and Cavaliere, P., 2007, Influence of shoulder geometry on microstructure and mechanical properties of friction stir welded 6082 Aluminium alloy, Materials and Design, 28, p. 1125-1128

Sellars, C.M., 1978, Recrystallization of metals during hot deformation, Phil. Trans. R. Soc. Lond. A/ Proceedings of the Royal Society A, 288(1350), p. 147

Sellars, C.M. and Tegart, W.J. McG., 1972, Hot Workability, International Metallurgical Reviews, 17(1), p. 1

Semiatin, S.L. and Bieler, T.R., 2001, The effect of alpha platelet thickness on plastic flow during hot working of Ti-6Al-4V with a transformed microstructure, Acta Materialia, 49, p. 3559-3565

Senkov, O.N., Valencia, J.J., Senkova, S.V., Cavusoglu, M. and Froes, F.H., 2002, Effect of cooling rate on microstructure of Ti-6Al-4V forging, Materials Science and Technology, 18, p. 1471-1478

Seshacharyulu, T., Medeiros, S.C., Frazier, W.G., and Prasas, Y.V.R.K., 2000, Hot working of commercial Ti-6Al-4V with an equiaxed α-β microstructure: materials modeling considerations, Materials Science and Engineering A, 284 (1-2), p. 192

Seshacharyulu, T., Medeiros, S.C., Frazier, W.G., and Prasas, Y.V.R.K., 2002, Microstructural mechanisms during hot working of commercial grade Ti-6Al-4V with lamellar starting structure, Materials Science and Engineering A, 325, p. 112-125

Seward, G.G.E., Celotto, S., Prior, D.J., Wheeler, J., Pond, R.C., 2004, In situ SEM-EBSD observations of the hcp to bcc phase transformation in commercially pure titanium, Acta Materialia, 52, p. 821-832

Singh, A.K. and Schwarzer, R.A., 2001, Evolution of cold rolling texture in the binary alloys: Ti-0.4Mn and Ti-1.8Mn, Materials Science and Engineering A, 307, p. 153S

Smith College, 2010, Scanning Electron Microscope (SEM),

http://131.229.114.77/microscopy/semvar.html (Accessed 12/12/2010)

Smith, C.B. and Hinrichs, J.F., 2011, Friction stir welding and related processes, in Innovations in Materials Manufacturing, Fabrication, and Environmental Safety, edited by Mel Schwartz, p. 249-268

Song, M., and Kovacevic, R., 2003, Numerical and experimental study of the heat transfer process in friction stir welding, Journal Proceedings of the Institution of Mechanical Engineers, Part B: Journal of Engineering Manufacture, 217(1), p. 73-85

Sorensen, C.D. and Nelson, T.W., 2003, Progress in polycrystalline cubic boron nitride FSW tooling, Proceedings of the 4th international symposium on Friction stir welding, 14-16 May 2003, Utah, USA

Sorensen, C.D., Nelson, T.W., Parker, S.M. and Steel, R.J., 2004, Innovative technology application in FSW of high softing temperature materials, Proceedings of the 5th international symposium on Friction stir welding, 14-16 September 2004, Meta, France

Sorensen, C.D., 2004, Progress in Friction Stir Welding High Temperature Materials, Proceedings of the Fourteenth International Pipeline Conference, 4-8 October 2004, Calgar, Alberta, Canada

Stanford, N. and Bate, P.S., 2004, Crystallographic variant selection in Ti-6Al-4V, Acta Materialia, 52, p. 5215-5224

Stanford, N., and Bate, P.S., 2005, The Martensitic Transformation Texture in Ti-6Al-4V, Materials Science Forum, 495-497, p. 669-674

Strangwood, M., Davis, C.L. and Attallah, M.M., 2004, Microstructural development and modelling in Friction stir welds of strain-hardenable Al alloy, Proceedings of the 5th international symposium on Friction stir welding, 14-16 September 2004, Meta, France

Subramanian, P.R., Nirmalan, N.V., Young, L.M., Sukamp, P., Larsen, M., Dupree, P.L. and Shukla, A.K., 2003, Effect of microstructural evolution in mechanical and corrosion behavior of friction stir processed Aluminium alloys, friction stir welding and processing II, eds. K.V. Jata, M.W. Mahoney, R.S. Mishra, S.L. Semiatin, and T. Lienert, TMS, p. 235-242

Sutton, M.A., Reynolds, A.P., Yan, J., Yang, B. and Yuan, N., 2006, Microstructure and mixed mode I/II fracture of AA2524-T351 base material and friction stir welds, Engineering Fracture Mechanics, 73(4), p. 391-407

Swygenhoven, H.V., Spaczer, M. and Caro, A., 1999, Microscopic description of plasticity in computer generated metallic nanophase samples: a comparison between Cu and Nii, Acta Materialia, 47(10), p. 3117-3126

Szczepanski, C.J., Jha, S.K., Larsen, J.M. and Jones, J.W., 2008, Microstructural Influences on Very-High-Cycle Fatigue-Crack Initiation in Ti-6246, Metallurgical and materials transactions A, 39, p. 2841-2851

Tamirisakandala, S., Vedam, B.V. and Bhat, R.B., 2003, Recent Advances in the Deformation Processing of Titanium Alloys, Journal of Materials Engineering and Performance, 12, p. 661-673

Tamirisakandala, S., Bhat, R.B., Miracle, D.B., Boddapati, S., Bordia, R., Vanover, R. and Vasudevan, V.K., 2005, Effect of boron on the beta transus of Ti-6Al-4V alloy, Scripta Materialia, 53, p. 220

Takahashi, K., Combres, Y., Chaze, A.M. and Levaillant, C., 1993, Microstructural evolutions of different Ti-6%Al-4%V titanium alloy morphologies during and after hot working simulated by torsion testing, Journal of Metallurgy, Paris, 90(5), p. 600

Thomas, W. M., Nicholas, E. D., Needham, J.C., Murch, M.G., Templesmith, P., and Dawes, C.J., 1991, Friction stir butt welding, International patent application PCT/GB92/02203 and G.B Patent Application 9125978

Thomas, W.M., et al., Oct. 17, 1996, Friction stir welding, G.B. Patent Application, 2,306,366, UK

Thomas, W.M., Munns, I. and Smith, P.T., 1999, Friction Stir welding of an Aluminium alloy-Effect of Tool Geometry, TWI Industrial Memebers Report, No 688

Thomas, W.M., Nicholas, E.D. and Smith, S.D., 2001, Friction stir welding-Tool developments, Aluminium 2001, Proceedings of the TMS 2001 Aluminium automotive and joining sessions, S.K. Das, J.G. Kaufman and T.J. Linert, Ed., TMS, p. 213

Thomas, W.M., Stainers, D.G., Norris, I.M. and de Firas, R., 2002, Friction stir welding tools and developments, FSW seminar, 3 December, 2002, Porto, Portgual

Thomas, W.M., 2003, Friction stir welding- recent developments, THERMEC 2003, 7-11 July, 2003, TMS, Madrid, Spain

Thomas, W.M., Johnson, K.I. and Wiesner, C.S., 2003, Friction stir welding-recent developments in tool and process technologies, Advanced Engineering Materials, 5, p. 485-90

Thomas, M.J., 2005, Crystallographic Texture Analysis of Titanium Aerospace Alloy Ti 834, EBSD Interest Group

Thomas, M.J., NG, B.S., Wynne, B.P. and Threadgill, P., A Novel Friction Stir Welding Technique for Ti-6Al-4V; A Microstructural Investigation, Proceedings of the 11th World Conference on Titanium, 3-7 June 2007, Kyoto, Japan

Thomas, M.J., 2007, the Effect of Thermomechanical Process Parameters on the Microstructure and Crystallographic Texture Evolution of Near-α Aerospace Alloy Timetal®834, PhD thesis, The University of Sheffield

Threadgill, P.L., and Martin, J., 2008, Introduction to Friction Stir Welding, course of The Welding Institute, Sheffield, UK

Threadgill, P.L., 2007, Terminology in friction stir welding, Science and Technology of Welding and Joining, 12(4), p. 357-360

Threadgill, P.L. and Martin, J., 7-9 October, 2008, "Introduction to Friction Stir Welding", course of The Welding Institute, Catcliffe, Yorkshire, UK

Threadgill, P.L., Leonard, A.J., Shercliff, H.R. and Withers, P.J., 2009, Friction stir welding of Aluminium alloys, International Materials Reviews, 54(2), p. 49-52

Timet, 2010, Ti-6Al-4V, http://www.timet.com/index_new.htm (accessed on 12/09/2010)

Van Bohemen, S.M.C., Kamp, A., Petrov, R.H., Kestens, L.A.I. and Sietsma, J., 2008, Nucleation and variant selection of secondary α plates in α+β Ti alloy, Acta Materialia, 56, p. 5907-5914

Vilaca, P., Quintino, L. and dos Santos, J.F., 2005, iSTIR-Analytical thermal model for friction stir welding, Journal of Materials Processing Technology, 169(3), p. 452-465

Wang, S.C, Aindow, M. and Starink, M.J., 2003, Effect of self-accommodation on α/α boundary populations in pure titanium, Acta Materialia, 51, p. 2485-2503

Wanjara, P. and Jahazi, M., 2005, Linear friction welding of Ti-6Al-4V: Processing, microstructure, and mechanical-property inter-relationships, Metallurgical and Materials Transactions A, 36(8), p. 2149-2164

Wang, Y.N. and Huang, J.C., 2003, Review Texture analysis in hexagonal materials, Materials Chemistry and Physics, 81, p. 11-26, p. 10

Warchomicka, F., Poletti, C., Stockinger, M. and Henke, T., 2010, Microstructure evolution during hot deformation of Ti-6Al-4V double cone specimens, International Journal of Material Forming, 3, Supl 1, p. 215- 218

Weiss, I. and Semiatin, S.L., 1999, Thermomechanical processing of alpha titanium alloys-an overview Materials Science and Engineering A, 263(2), p. 243-256

Williams, J.C., 1973, Critical review: Kinetics and phase transformations, in Titanium science and technology, Titanium Science and Technology, Jaffee, R.I. and Burte, H.M. (Eds), Plenum Press, New York, Vol. 3, p. 1428-1433

Xue, P., Xie, G.M., Xiao, B.L., Ma, Z.Y. and Geng, L. 2010, Effect of Heat Input Conditions on Microstructure and Mechanical Properties of Friction-Stir-Welded Pure Copper, Metallurgical and materials transactions A, 41, p. 2010-2021

Yue, Q., Liu, Y., Wang, D., Wang, X., Chu, M. and Shen, J., 2009, Effects of microstructures on mechanical properties of Ti-63 titanium alloy, Rare metals, 28(6), p. 533-536

Zaefferer, S., 2003, A study of active deformation systems in titanium alloys: dependence on alloy composition and correlation with deformation texture, Materials Science and Engineering A, 344, p. 20-28

Zeng, L. and Bieler, T.R., 2005, Effects of working, heat treatment, and aging on microstructural evolution and crystallographic texture of α, α′, α″ and β phases in Ti-6Al-4V wire, Materials Science and Engineering A, 392(1-2), p. 408-412

Zettler, R., Lomolino, S., dos Santos, J.F., Donath, T., Beckmann, F., Lipman, T. and Lohwasser, D., 2004, A study of material flow in FSW of AA 2024-T351 and AA 6056-T4 alloy, Proceedings of the Fifth international symposium on Friction stir welding, 14-16, September 2004, Meta, France

Zhang, Y., Sato, Y.S., Kokawa, H., Park, S.H.C. and Hirano, S., 2008a, Microstructural characteristics and mechanical properties of Ti-6Al-4V friction stir welds, Materials Science and Engineering A, 485, p. 448-455

Zhang, Y., Sato, Y.S., Kokawa, H., Park, S.H.C. and Hirano, S., 2008b, Stir zone microstructure of commercial purity titanium friction stir welded using PCBN tool, Materials Science and Engineering A, 48, p. 25-30

Zhang, Y., Sato, Y.S., Kokawa, H., Park, S.H.C. and Hirano, S., 2010, Grain structure and microtexture in friction stir welded commercial purity titanium, Science and Technology of Welding and Joining, 15(6), p. 500

Zhou, L., Liu, H.J., Liu, P. and Liu, Q.W., 2009, The stir zone microstructure and its formation mechanism in Ti-6Al-4V friction stir welds, Scripta Materialia, 61, p. 596-599

Zhou, L., Liu, H.J. and Liu, Q.W., 2010a, Effect of rotation speed on microstructure and mechanical properties of Ti-6Al-4V friction stir welded joints, Materials and Design, 31(5), p. 2631-2636

Zhou, L., H. J. Liu and Q. W. Liu, 2010b, Effect of process parameters on stir zone microstructure in Ti-6Al-4V friction stir welds, Journal of materials science, 45, p. 39-45

Zhu, Z.S., Gu, J.L. and Chen, N.P., 1995, "Variant selection and phase transformation texture in titanium", Journal of materials science letters, 14, p. 1153-1154

Zhu, S.J., Mukherji, D., Chen, W., Lu, Y.X., Wang, Z.G. and Wahi, R.P., 1998, Steady state creep behaviour of TiC particulate reinforced Ti-6Al-4V composite, Materials Science and Engineering A, 256, p. 301-307

Zhu, Y.T., and Huang, J.Y., Gubicza, J. and Unga´r, T., Hungary, Wang, Y.M. and Ma, E., 2003, Nanostructures in Ti processed by severe plastic deformation, Journal of Materials Research, 18(8), p. 1912-1914